Synergistic Framework for Analysis and Model Assessment in Bridge Aerodynamics and Aeroelasticity

Dissertation

as required for the conferral of the academic degree

Doktor-Ingenieur (Dr.-Ing.)

at the Faculty of Civil Engineering of the

Bauhaus-Universität Weimar

submitted by

Igor Kavrakov

from Skopje, Macedonia

Assessors: Prof. Dr. Guido Morgenthal
Prof. Dr. Giovanni Solari
Prof. Dr. Tom Lahmer

Weimar, June 2019

Abstract

Wind-induced vibrations often represent a major design criterion for long-span bridges. This work deals with the assessment and development of models for aerodynamic and aeroelastic analyses of long-span bridges.

Computational Fluid Dynamics (CFD) and semi-analytical aerodynamic models are employed to compute the bridge response due to both turbulent and laminar free-stream. For the assessment of these models, a comparative methodology is developed that consists of two steps, a qualitative and a quantitative one. The first, qualitative, step involves an extension of an existing approach based on Category Theory and its application to the field of bridge aerodynamics. Initially, the approach is extended to consider model comparability and completeness. Then, the complexity of the CFD and twelve semi-analytical models are evaluated based on their mathematical constructions, yielding a diagrammatic representation of model quality.

In the second, quantitative, step of the comparative methodology, the discrepancy of a system response quantity for time-dependent aerodynamic models is quantified using comparison metrics for time-histories. Nine metrics are established on a uniform basis to quantify the discrepancies in local and global signal features that are of interest in bridge aerodynamics. These signal features involve quantities such as phase, time-varying frequency and magnitude content, probability density, non-stationarity, and nonlinearity.

The two-dimensional (2D) Vortex Particle Method is used for the discretization of the Navier-Stokes equations including a Pseudo-three dimensional (Pseudo-3D) extension within an existing CFD solver. The Pseudo-3D Vortex Method considers the 3D structural behavior for aeroelastic analyses by positioning 2D fluid strips along a line-like structure. A novel turbulent Pseudo-3D Vortex Method is developed by combining the laminar Pseudo-3D VPM and a previously developed 2D method for the generation of free-stream turbulence. Using analytical derivations, it is shown that the fluid velocity correlation is maintained between the CFD strips.

Furthermore, a new method is presented for the determination of the complex aerodynamic admittance under deterministic sinusoidal gusts using the Vortex Particle Method. The sinusoidal gusts are simulated by modeling the wakes of flapping airfoils in the CFD domain with inflow vortex particles. Positioning a section downstream yields sinusoidal forces that are used for determining all six components of the complex aerodynamic admittance. A closed-form analytical relation is derived, based on an existing analytical model. With this relation, the inflow particles' strength can be related with the target gust amplitudes a priori.

The developed methodologies are combined in a synergistic framework, which is applied to both fundamental examples and practical case studies. Where possible, the results are verified and validated. The outcome of this work is intended to shed some light on the complex wind–bridge interaction and suggest appropriate modeling strategies for an enhanced design.

Acknowledgments

I would like to express my sincere and immense gratitude to Professor Guido Morgenthal for his support throughout my studies. His profound "why not" to my naive "it does not work" has taught me how to question in research, making these past four years truly enjoyable. Perhaps more important from the present perspective, I have learned intangibles from him that I cannot describe, and yet I perceive that they will undoubtedly leave a mark on my future career.

Special thanks must go to Professor Giovanni Solari and Professor Tom Lahmer for agreeing to asses this, not particularly brief, dissertation.

I would also like to thank Professor Ahsan Kareem and his research group NatHaz for making me feel welcomed during my stay at the University of Notre Dame. Our fruitful discussions on nonlinear aerodynamics have significantly contributed to the quality of this work.

I am also grateful to Professor Daniele Rocchi, Dr. Tomasso Argentini and Simone Omarini for hosting me at Politecnico di Milano and sharing their invaluable knowledge in experimental bridge aerodynamics. I enjoyed being part of the inspiring environment at PoliMi.

My gratitude also extends to Professor Yaojun Ge and his group for the invitation for the brief stay at Tongji University. The insight that I have gained there on large scale wind tunnel testing during the early stages of this work was stimulating.

Special thanks must go to Professor Klaus Gürlebeck and Dr. Dmitrii Legatiuk for their mathematical rigor on the part of this work related to the abstract nonsense (Category Theory). I am also thankful to Dr. Alfredo Camara from City, University of London for the motivating discussions and productive collaboration on the wind-vehicle-bridge interaction.

I am grateful to Professor Giorgio Diana for his invitation to join the IABSE Working Group "Super long-span bridge aerodynamics". This extends to all contributing members for sharing results to create a benchmark for bridge aerodynamics, that would ultimately help for the successful verification of the core code for this work.

Furthermore, I appreciate the support of Professor Frank Werner and Dr. Lars Abrahamczyk during my time at the GRK 1462. The funding by the German Research Foundation (DFG) in the scope of my employment at the Bauhaus-Universität Weimar is gratefully acknowledged.

Particular thanks go to Dr. Hans Georg Timmler for his continued encouragement. Many thanks go to my colleagues at the MSK and GRK 1462, and especially to my two office mates, Luise Göbel and Tajammal Abbas, and Sebastian Rau. You all made for a positive and pleasant working atmosphere, and provided constructive criticism when needed.

Last and most important, I thank my family and Kalina for their unconditional support, encouragement, and understanding of my "unconventional" working hours.

Contents

List of Figures

List of Tables

Nomenclature

Acronyms

2D	Two dimensional
3D	Three dimensional
CFD	Computational fluid dynamics model
CMBM	Complex mode-by-mode model
CQS	Corrected quasi-steady model
FFT	Fast Fourier transform
HNL	Hybrid nonlinear model
LQS	Linear quasi-steady model
LST	Linear steady model
LU	Linear unsteady model
MBM	Mode-by-mode model
MNL	Modified nonlinear model
MQS	Modified quasi-steady model
NLU	Nonlinear unsteady model
PDF	Probability density function
PSD	Power spectral density
QS	Quasi-steady model
RMS	Root-mean-square
SM	Structural model
SRQ	System response quantity
ST	Steady model
VPM	Vortex particle method
VTG	Velocity-based free-stream turbulence generation

Greek

α	Rotation
α_e	Effective angle of attack
β_B	Biphase randomization factor
β_{sur}	Surrogate biphase randomization factor
β_{in}	Inflow circulation correction factor
$\boldsymbol{\Delta x}$	Point distance vector
$\boldsymbol{\eta}$	Modal state vector
$\boldsymbol{\eta}_o$	State vector
$\boldsymbol{\gamma}_b$	Bound circulation strength vector
$\boldsymbol{\iota}$	Velocity vector induced by vorticity
$\boldsymbol{\kappa}$	Wave number vector
$\boldsymbol{\Lambda}$	Complex eigenvalue matrix
$\boldsymbol{\omega}_u$	Vorticity vector
$\boldsymbol{\phi}$	Complex mode shape vector
$\boldsymbol{\Psi}$	Mode shape matrix
$\boldsymbol{\Theta}$	Phase matrix
$\varkappa_\varepsilon$	Mollified velocity kernel
$\varkappa$	Velocity kernel
$\boldsymbol{\vartheta}$	Random Fourier increment vector
$\boldsymbol{\vartheta}^*$	Normalized $\boldsymbol{\vartheta}$
$\boldsymbol{\Xi}$	Complex eigenvector matrix
$\boldsymbol{\zeta}$	Complex eigenvector
χ	Aerodynamic admittance
Δc	Cell size
Δl_{pan}	Panel length
Δp	Particle release factor
Δ	Increment
δ	Dirac-delta function

ϵ	Metric sensitivity parameter
Γ	Vortex (particle) strength
Γ^*	Gamma function
γ_0	Wake-induced part of γ_b
γ_1	Quasi-steady part of γ_b
Γ_a^{in}	Approximated inflow Γ
Γ_b	Bound vortex strength
γ_b	Bound vortex sheet strength
Γ_m^{in}	Modeled inflow Γ
γ_w	Wake vortex sheet strength
κ	Wave number magnitude
$\kappa_x, \kappa_y, \kappa_z$	Wave numbers
λ	Complex eigenvalue
μ	Similarity parameter
ν	Fluid viscosity
ω	Circular frequency
Φ	Indicial function
Ψ	Mother wavelet
ρ	Fluid density
σ	Standard deviation
$\tau = tU/B$	Reduced time
τ_δ	Reduced time lag
θ	Velocity phase angle
Υ_b	Quadratic phase coupling indicator
Υ_s	Non-stationarity indicator
ε	Core radius
φ^R	Random phase
φ_B	Bispectrum phase
φ_B^R	Random bispectrum phase
$\varphi_D, \varphi_L, \varphi_M$	Dynamic angle of attack
φ_w	Dynamic angle of attack due to wind
ϱ	Gaussian white noise
ϑ	Random Fourier increment
ϑ^*	Normalized ϑ
ξ	Damping ratio
ω_u	Vorticity

Operators & Operations

$(\cdot)\vert$	Linearization
$(\cdot)^+$	Pseudo-inverse
$(\cdot)^T$	Matrix transpose
$\cdot$	Scalar product
$\circ$	Composition
$\dot{(\cdot)}$	Time derivative
$\Im(\cdot)$	Imaginary part
$\langle\cdot\rangle$	Expected value/Ensemble average
$\lfloor\cdot\rfloor$	Floor
$\det(\cdot)$	Determinant
$\Pr(\cdot)$	Probability
∇	Gradient
$\nabla\cdot$	Divergence
$\nabla\times$	Curl
$\odot$	Point-wise multiplication
$\oslash$	Point-wise division
$\otimes$	Tensor product
$\overline{(\cdot)}$	Conjugate complex
∂	Partial derivative
$\Re(\cdot)$	Real part
$\mathrm{sgn}(\cdot)$	Sign
$\times$	Vector product
$\Vert\cdot\Vert$	Second norm
$\vert\cdot\vert$	Absolute value
$(\cdot)'$	Derivative/Reduced-time derivative

Roman

$\boldsymbol{\mathcal{I}}$	Identity tensor
$\boldsymbol{\mathcal{R}}$	Correlation velocity tensor
$\boldsymbol{\mathcal{S}}$	Spectral velocity tensor
$\boldsymbol{b}$	Right-hand side vector
$\boldsymbol{C}$	Modal damping matrix
$\boldsymbol{C}_o$	Damping matrix

$\boldsymbol{c}_x$	Coherence decay coefficient vector
$\boldsymbol{C}_{ae}$	Aerodynamic damping matrix
$\boldsymbol{c}_{ae}$	Row vector of $\boldsymbol{C}_{ae}$
$\boldsymbol{f}$	Modal force vector
$\boldsymbol{f}_o$	Force vector
$\boldsymbol{f}_v$	Vortex shedding force vector
$\boldsymbol{f}_{noi}$	Interior noise force vector
$\boldsymbol{f}_{pr}$	Pressure force vector
$\boldsymbol{G}$	Impedance matrix
$\boldsymbol{H}$	Cholesky lower triangular matrix
$\boldsymbol{I}$	Identity matrix
$\boldsymbol{J}$	Unit matrix
$\boldsymbol{K}$	Modal stiffness matrix
$\boldsymbol{K}_o$	Stiffness matrix
$\boldsymbol{K}_{ae}$	Aerodynamic stiffness matrix
$\boldsymbol{k}_{ae}$	Row vector of $\boldsymbol{K}_{ae}$
$\boldsymbol{M}$	Influence matrix
$\boldsymbol{M}$	Modal mass matrix
$\boldsymbol{M}_o$	Mass matrix
$\boldsymbol{N}$	State input matrix
$\boldsymbol{n}$	Normal vector
$\boldsymbol{O}$	State matrix
$\boldsymbol{O}^*$	Equivalent state matrix
$\boldsymbol{q}$	Modal displacement vector
$\boldsymbol{q}_o$	Displacement vector
$\boldsymbol{S}$	Spectral matrix
$\boldsymbol{s}$	Tangential vector
$\boldsymbol{S}^*$	Two-sided spectral matrix
$\boldsymbol{u}$	Fluid/wind velocity vector
$\boldsymbol{u}^*$	Fluctuating part of $\boldsymbol{u}$
$\boldsymbol{u}_\infty$	Mean part of $\boldsymbol{u}$
$\boldsymbol{x}$	Spatial coordinate vector
$\boldsymbol{x}_\gamma$	Wake sheet position
$\boldsymbol{x}_p$	Particle position
$\boldsymbol{x}_p^{\mathrm{RW}}$	Particle random walk vector
$\boldsymbol{x}_s$	Stiffness center
$\boldsymbol{x}_c$	Gust tracking location
$\boldsymbol{x}_{in}$	Particle release location
$\boldsymbol{Z}$	Velocity kernel location matrices
η_D, η_L, η_M	Phase lag coefficient
$\mathbb{N}$	Set of natural numbers
$\mathbb{N}_0$	Set of natural numbers incl. zero
$\mathbb{R}$	Set of real numbers
$\mathcal{A}$	Metric relative exponent
$\mathcal{B}$	Interface between fluid and solid domain
$\mathcal{D}$	Domain
$\mathcal{D}_\mathcal{B}$	Thin zone adjacent to $\mathcal{B}$
$\mathcal{D}_p$	Patch
$\mathcal{F}$	Fluid domain
$\mathcal{G}$	Solid domain
$\mathcal{M}$	Comparison metric
$\mathcal{M}_\varphi$	Phase metric
$\mathcal{M}_p$	Peak metric
$\mathcal{M}_{\mathrm{pdf}}$	PDF metric
$\mathcal{M}_{\mathrm{rms}}$	RMS metric
$\mathcal{M}_B$	Wavelet-based bispectrum metric
$\mathcal{M}_m$	Magnitude metric
$\mathcal{M}_s$	Stationarity wavelet metric
$\mathcal{M}_{wf}$	Frequency-normalized wavelet metric
$\mathcal{M}_w$	Wavelet metric
$\mathcal{N}$	Normal (Gaussian) distribution
$\mathcal{S}$	Perimeter of $\mathcal{D}_p$
$\mathcal{U}$	Uniform distribution
CL	Confidence level
COI	Cone of influence
IT	Inner triangle
Re	Reynolds number
St	Strouhal number
A_p, A_h, A_a	Frequency-independent coefficients
B	Deck/body width
B_W	Wavelet bispectrum
B_W^F	Filtered wavelet bispectrum
B_W^R	Phase-randomized wavelet bispectrum
BC	Bhattacharyya coefficient
C	Theodorsen function
C_D, C_L, C_M	Static wind coefficients
C'_D, C'_L, C'_M	Static wind coefficients derivatives

$C_D^{hys}, C_L^{hys}, C_M^{hys}$	Aerodynamic hysteresis
$c_p, c_h.c_\alpha$	Damping coefficients
C_x, C_y, C_z	Coherence decay coefficients
coh	Space coherence
D	Drag force
E	Energy spectrum
f	Frequency
F_D, F_L, F_M	Local aerodynamic forces
f_{ce}	Wavelet central frequency
g_b^*	Bispectrum probability of exceedance factor
g_s^*	Stationarity probability of exceedance factor
G_W	Bispectrum amplitude
G_W^F	Filtered bispectrum amplitude
G_W^R	Phase-randomized bispectrum amplitude
h	Vertical displacement
$H_0^{(2)}, H_1^{(2)}$	Hankel functions of second kind
I	Impulse function
i	Imaginary unit
$J_0^{(2)}, J_1^{(2)}$	Bessel functions of first kind
$K = \omega B/U$	Reduced frequency
$K^* = K/2$	Half reduced frequency
k_p, k_h, c_α	Stiffness coefficients
L	Lift force
l_G	Inflow particle band height
l_R	Airfoil distance
L_T	Von Kármán turbulent length scale
L_u, L_v, L_w	Turbulent length scales
l_v	Vorticity support
l_d	Domain length
l_h	Domain height
M	Moment
m_D, m_L, m_M	Aerodynamic center
m_p, m_h, m_α	Inertial masses
N_m	Number of modes
N_n	Number of nodes
N_r	Number of P^{3}M neighboring cells
N_x, N_z	Number of Poisson grid cells
N_{sur}	Number of surrogates
N_f	Number of discrete frequencies
N_{ip}	Number of inflow particles
N_{pan}	Number of panels
N_p	Number of particles
N_{samp}	Number of samples
N_{str}	Number of strips
N_{st}	Number of aerodynamic states
N_s	Number of time-steps
N_{wp}	Number of wind points
O	Objective function
P	Histogram estimate PDF
p	Lateral displacement
P^*, H^*, A^*	Flutter derivatives
P_e	Kernel estimate PDF
p_r	Pressure
Q^*	Dynamic derivatives
R	Correlation
R^*	Correlation coefficient
S	Power spectral density
S^W	Wavelet-based S
s_c	Wavelet scale
t	Time
t_δ	Time lag
TI_u, TI_v, TI_w	Turbulence intensities
U_r	Resultant velocity
$V_r = U/(fB)$	Reduced velocity
W	Wavelet coefficients
W_f	Wavelet normalization factor
x, y, z	Spatial coordinates
d^B	Bhattacharyya distance
T_{c}	Metric normalization time
t_{lag}	Mean time delay
u	Longitudinal fluid/wind velocity
v	Lateral fluid/wind velocity
w	Vertical fluid/wind velocity

Superscripts & Subscripts

$(\cdot)^F$	Airfoil	$(\cdot)_F$	Airfoil
$(\cdot)^{in}$	Inflow	$(\cdot)_{in}$	Inflow
$(\cdot)_0$	Amplitude	$(\cdot)_n$	Normalized (standard score)
$(\cdot)_{\text{rms}}$	Root mean square	$(\cdot)_{se}$	Self-excited
$(\cdot)_{\text{sur}}$	Surrogate	$(\cdot)_s$	Static
$(\cdot)_b$	Buffeting	$(\cdot)_{tr}$	Threshold
$(\cdot)_c$	Center/central/tracking	$(\cdot)_t$	Target (prescribed)

Chapter 1

Introduction

1.1 Motivation and scope

Long-span bridges are unequivocally one of the most remarkable types of structures. Their size, slenderness, and architecture make the design of such structures a challenging engineering task. Apart from the engineering aspect, bridges certainly represent lifelines to society when it comes to commute and logistics of products for basic human needs. Thus, the safety of such structures is of imperial importance, not only for the immediate disastrous effect in the event of their collapse but for the aftermath as well.

The lean design of bridges, such as the Great Belt Bridge (cf. Fig. 1.1), is also their curse as it makes them susceptible to wind-induced vibrations. Having low structural damping, these structures can exhibit high oscillations and potential aeroelastic instabilities that can lead to collapse. Although several bridges have collapsed prior, the unfortunate Tacoma Narrows incident was the real eyeopener for the bridge engineering community that wind action should be considered as a dynamic loading rather than by the pseudo-static approaches used previously. Today, wind-induced vibrations commonly represent the main design criterion for long-span bridges.

Figure 1.1: Great Belt Bridge - Artistic impression (picture courtesy of COWI, from www.cowi.com).

All this makes the accurate representation of the aerodynamic forces essential for a safe, yet reasonable design. Still today in the modern era of computers, experimental wind tunnel testing is the standard for the design of major bridges, providing design forces and assuring structural safety in terms of aerodynamic instabilities. In addition to wind tunnel tests, computer modeling of the aerodynamic forces has proven to be useful as it can be performed on a standard PC, offering higher flexibility in terms of an iterative design and cost reduction. Thus, it becomes an integral part of the common design practice.

Mathematical modeling of the aerodynamic forces is approached either by semi-analytical or Computational Fluid Dynamics (CFD) models. The semi-analytical models directly model the aerodynamic forces using mathematical constructions (e.g. equations) supplemented by experimental or CFD aerodynamic coefficients that account for the fluid-structure interaction. On the contrary, the CFD models discretize the equations of fluid mechanics in a numerical fashion. Thus, this makes the semi-analytical models an intermediate development between the experimental and CFD models. From a modeling perspective, both the semi-analytical and CFD models are mathematical models. As no mathematical model is a perfect representation of the reality, both of these models have questionable reliability in terms of simplifying assumptions and numerical uncertainty.

Traditionally, the semi-analytical models based on experimental aerodynamic coefficients have been used to compute the bridge response, and consequently, the design internal forces. A multitude of semi-analytical models has been proposed over the years. The principal differences in these types of models originate from their underlying physical assumptions. Naturally, the huge variety of semi-analytical models poses the question on their quality and the effect of their underlying assumptions on the structural response for the design wind.

In the past two decades, the application of CFD in bridge aerodynamics has gained considerable momentum, offering substantial insight into the physics of fluid-structure interaction. Commonly, the CFD models are used to determine the aerodynamic coefficients that serve as an input in the semi-analytical models. These models are rather rarely employed to directly compute the bridge response, especially when there is free-stream turbulence involved. This is attributed to the high computational demand and numerical uncertainty, making the CFD models not readily available for three-dimensional (3D) fully coupled aeroelastic analysis.

To address the issues of high computational demand and numerical uncertainty many CFD methods and strategies have emerged. In particular, the two-dimensional (2D) Vortex Particle Method (VPM) has shown a positive outcome for modeling the wind-bridge interaction with sufficient accuracy at an acceptable computational cost. Moreover, the recent extension of the VPM to consider random free-stream turbulence has made this method directly applicable to 2D aeroelastic analyses. On the front of three-dimensionality, the laminar Pseudo-3D VPM has found reasonable successes for accounting the 3D structural behavior by positioning 2D CFD strips along a 3D line-like structure.

In light of the previous points, room for improvement can be identified in terms of aerodynamic model assessment and advancement of the VPM from the aspect of free-stream turbulence. When the initial idea of this work was conceived, the main purpose was to introduce a methodology for comparison and assessment of aerodynamic models. Such a methodology should enable comparison on two levels, qualitatively and quantitative.

As the work progressed over the years, the extensive use of the VPM inspired some advancements of this method. Particularly, a research topic emerged in extending the Pseudo-3D method to consider free-stream turbulence, which would effectively extend this method to perform aeroelastic analyses in turbulent wind conditions. Further, when using the time-domain aerodynamic models a need presented itself for determining the transfer function between the free-stream wind fluctuations and aerodynamic forces, known as the aerodynamic admittance. To tackle this challenge using CFD, a method to simulate deterministic free-stream turbulence was necessary to be developed. Ultimately, the goal of the dissertation is to present all the developments in a coherent and synergistic framework for aerodynamic and aeroelastic analyses of bridges.

1.2 Contribution and dissemination

Several novel methods and methodologies constitute this work. The way this dissertation is written is to follow the necessary steps of the logical order of analysis in terms of firstly introducing all models, methods or methodologies, and then proceeding with their verification, validation or application. In such a way, the novel contribution might not be clearly distinguished from the state of the art, based on the dissertation structure. Thus, the purpose of this and the next section is to delineate the contributions of the work by the author and guide the reader as to where it can be found. Moreover, the idea of writing a monograph is to show how the presented methods connect to one another in the global scope of bridge aerodynamics. In other words, the dissertation presents a synergistic framework for analyses and model assessment in bridge aerodynamics and aeroelasticity. It is noted that for a reader without an extended background in the subject matter, the specific contributions will become clear as this work progresses.

The proposed synergistic framework is presented in Fig. 1.2. Depending on a target output, the framework is to be used to select a model combination required for specific aerodynamic and aeroelastic analysis (cf. Tab. 1.1). With this, analyses due to turbulent or laminar free-stream can be conducted and the response in terms of time-dependent forces or displacements can be compared for different models.

Keeping in mind the synergistic framework, the following new methods and methodology are introduced:

- A comparative methodology for an assessment of aerodynamic models.

  This methodology is constituted of two steps, allowing both qualitative and quantitative comparison. The first step involves evaluation of models based on their mathematical constructions (e.g. equations). This is done by means of a previously developed modeling approach based on Category Theory. First, an extension of the categorical modeling approach is proposed to consider model comparability and completeness. Then, the complexity of semi-analytical and CFD aerodynamic models is evaluated. In the second, quantitative, step the time-dependent forces or response for the aerodynamic models are quantified for the identical input employing comparison metrics for time-histories. Nine metrics are utilized, all constructed on a uniform basis. Seven of these metrics are adapted from former studies, including peak, root-mean-square (RMS), phase, magnitude, probability density function (PDF), wavelet and normalized-wavelet metrics. Additionally, two new metrics are introduced to quantify discrepancy in the potential non-stationary and nonlinear signal features by testing stationarity using surrogates and wavelet bispectrum.

- A Turbulent Pseudo-3D Vortex Particle Method.

  This method is established by combining two previously developed methods for velocity-based free-stream turbulence generation and the laminar Pseudo-3D method. With this, multimode buffeting analysis can be performed using CFD in a Pseudo-3D manner. Using analytical derivations, it is shown that the span-wise correlation of the velocity is maintained within the CFD domain between the strips.

- A method for determination of the complex aerodynamic admittance using the VPM.

  Deterministic free-stream sinusoidal gusts are simulated by modeling the wakes of rotating airfoils in the CFD domain with inflow vortex particles. Positioning a section downstream yields sinusoidal forces and thus all six components of the complex aerodynamic admittance can be determined. A closed-form analytical relation is derived to relate the inflow particles' circulation to the target gust amplitudes, based on an existing analytical model.

- A simple method for computation of the unsteady buffeting forces.

  Based on the Fast Fourier Transform (FFT) and the principle of stable linear systems due to periodic inputs, this method allows simple inclusion of the aerodynamic admittance in the buffeting forces and thus avoiding rational approximation.

Where these novel methods and methodology can be found within the dissertation is noted in the next section (Sec. 1.3). Additionally, the sections that contain these methods are identified by the symbol (*).

Apart from methods and methodologies, several analyses in terms of comparison, verification, and validation are performed that further add to the contribution. Particularly, a complete verification of aerodynamic and aeroelastic analyses of a flat plate is performed for the VPM, using the well-established analytical solution. The author is not aware of such analysis, including verification of the aeroelastic response due to free-stream turbulence, published in the literature.

Moreover, the similarities and discrepancies between a CFD model, taken as a reference, and six semi-analytical models are studied from a perspective of the effect of the model assumptions on the aerodynamic forces/response. The special aspect of this analysis is that the CFD model is used for both flutter and buffeting analysis.

Further, Pseudo-3D analyses are performed that are of high spatial resolution in terms of the number of CFD strips with as many as fifty. This allows consideration of a significant number of modes.

Finally, a validation of the CFD aerodynamic admittance is performed using experimental tests for the first time in terms of both real and imaginary parts.

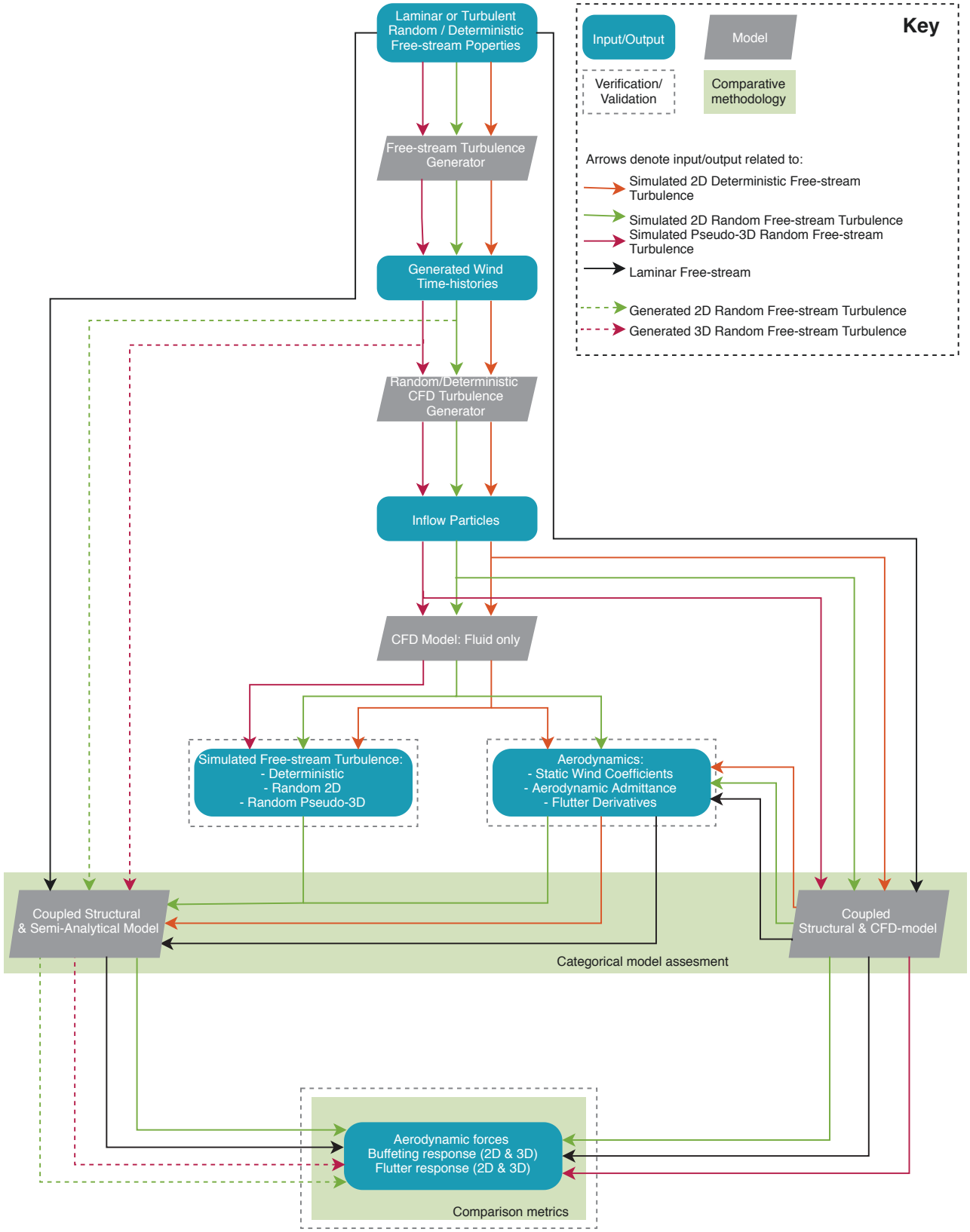

Figure 1.2: Synergistic framework for analyses and assessment of models in bridge aerodynamics and aeroelasticity.

Analysis type (Target output) \ Model	CFD				Semi-analytical	
	Fluid	Fluid & Static boundary	Fluid & Moving boundary	Coupled Structural & Fluid	Aerodynamic force	Coupled Aerodynamic force & Structural
Static analysis + laminar free-stream (Static wind coefficients)		○				
Static analysis + random turbulent free-stream (Buffeting forces, Aerodyn. admittance)	○	○			○	
Static analysis + deterministic turbulent free-stream (Aerodyn. admittance)	○	○				
Forced-vibration analysis + laminar free-stream (Flutter derivatives)			○			
Dynamic analysis + laminar free-stream (Aerostatic response, Flutter velocity)				●		●
Dynamic analysis + random turbulent free-stream (Buffeting response: identical/different input)				●		●

Table 1.1: Models for aerodynamic and aeroelastic analyses within the synergistic framework based on target quantities. Empty circle ○ indicates analysis only in 2D; filled circle ● indicates analysis in both 2D and Pseudo-3D. Some of the target outputs require more than one type of analysis and hence, more than one model.

Publications directly related to the dissertation

Most of the methods and methodologies, that are considered as a contribution of this work, are published/submitted for publication within several scientific articles. Although the author is the main contributor in these articles, it is important to specify and acknowledge the particular contribution of the rest of the authors as per ethical scientific standards. The considered articles, published/submitted before submission of this dissertation, are listed below:

- **Kavrakov, I.**, Kareem, A. and Morgenthal, G.
  "Comparison metrics for time-histories: Application to bridge aerodynamics."
  Under review (Feb. 2019).

- **Kavrakov, I.**, Argentini, T., Omarini, S., Rocchi, D. and Morgenthal, G.
  "Determination of complex aerodynamic admittance of bridge decks under deterministic gusts using the Vortex Particle Method."
  Published (2019): *Journal of Wind Engineering and Industrial Aerodynamics* [165].

- **Kavrakov, I.**, Legatiuk, D., Gürlebeck, K. and Morgenthal, G.
  "A categorical perspective towards aerodynamic models for aeroelastic analyses of bridge decks."
  Published (2019): *Royal Society Open Science* [166].

- **Kavrakov, I.** and Morgenthal, G.
  "Aeroelastic analyses of bridges using a Pseudo-3D Vortex Method and velocity-based synthetic turbulence generation."
  Published (2018): *Engineering Structures* [168].

- **Kavrakov, I.** and Morgenthal, G.
  "A synergistic study of a CFD and semi-analytical models for aeroelastic analysis of bridges in turbulent wind conditions."
  Published (2018): *Journal of Fluids and Structures* [169].

- **Kavrakov, I.** and Morgenthal, G.
  "A comparative assessment of aerodynamic models for buffeting and flutter of long-span bridges."
  Published (2017): *Engineering* [167].

Throughout this project, Guido Morgenthal has played an essential supervisory and advisory roles for all concepts and methods developed herein. Dmitrii Legatiuk and Klaus Gürlebeck provided mathematical rigor to the category-theory related parts, with particular emphasis on the formulation of the new categorical definitions. Tommaso Argentini, Daniele Rocchi and Simone Omarini contribution are related to the validation of the method for determination of the complex aerodynamic admittance. They and their team from Politecnico di Milano, prepared and conducted the experiments that were used for validation of the CFD method for determination of aerodynamic admittance. The author was present during the model building and instrumentation and engaged in extensive discussions. Ahsan Kareem supplied ideas and had a contribution in a supervisory and advisory manner for the comparison metrics, particularly to the wavelet, non-stationary and bispectrum related aspects.

Publications indirectly related to the dissertation

Apart from the articles that directly constitute this work, the author has also contributed to articles as a co-author during the period of this project. In contrast to the directly related publications, these are not explicitly considered in this work and they include the following:

- Diana, G., Stoyanoff, S. [and 18 others, including **Kavrakov, I.**]
  "IABSE Task Group 3.1 benchmark results. Part 2: Numerical analysis of 2-degree-of-freedom bridge deck section based on experimental aerodynamics."
  In press (2019): *Structural Engineering International* [87].
- Diana, G., Stoyanoff, S. [and 18 others, including **Kavrakov, I.**]
  "IABSE Task Group 3.1 benchmark results. Part 1: Numerical analysis of 2-degree-of-freedom bridge deck section based on analytical aerodynamics."
  In press (2019): *Structural Engineering International* [88].
- Camara, A., **Kavrakov, I.**, Nguyen, K. and Morgenthal, G.
  "Complete framework of wind-vehicle-bridge interaction with random road surfaces."
  Published (2019): *Journal of Sound and Vibration* [43].
- Abbas, T., **Kavrakov, I.**, and Morgenthal, G.
  "Methods for flutter stability analysis of long-span bridges: A review."
  Published (2017): *Proceedings of the ICE - Bridge Engineering* [3].

As a part of the Task Group 3.1 "Super Long Span Bridge Aerodynamics" of the International Association for Bridge and Structural Engineering (IABSE), a benchmark for code verification for aeroelastic analyses of bridges is being developed. For this particular task, the author supplied results for blind comparison along with participants from universities and consulting companies worldwide. The results are included in the first two publications above. For the framework of wind-vehicle-bridge interaction, the main code for aeroelastic analyses of bridges, developed for this dissertation, was extended by the author to account for the vehicle-bridge interaction. A contribution was made in the section of semi-analytical models in the review.

Developed software

Three main MATLAB-based codes are developed for the purpose of this work, including:

- An integrated platform for structural dynamics and aeroelastic analyses using semi-analytical aerodynamic models;
- A module of VXflow for the generation of deterministic/random free-stream turbulence;
- A tool for comparison of time-histories.

Used software

Two software packages were used, including:

- SOFiSTiK: A commercial structural Finite Element analysis solver;
- VXflow: An in-house CFD solver based on Vortex Particle Method.

SOFiSTiK was used to obtain the dynamic characteristics in terms of mode shapes and frequencies. All CFD analyses are performed using VXflow, which was supplied and modified by Guido Morgenthal to include the inflow particles for the free-stream turbulence.

1.3 Structure

The work is structured in seven chapters:

Chapter 2 introduces the fundamentals of bridge aerodynamics and aeroelastic phenomena. Main developments in the field of aerodynamic force modeling are reviewed and referenced.

Chapter 3 provides the mathematical formulation and numerical discretization of the structural and aerodynamic models, as well as the modeling and simulation of random free-stream turbulence. As a part of this chapter, two extensions of the VPM are included in terms of the new Turbulent Pseudo-3D VPM and a method for generation of the complex aerodynamic admittance under deterministic gusts.

The comparative methodology is presented in Chapter 4 in two parts, quantitative and qualitative part. In the first part, the categorical modeling approach is revisited, then extended and finally applied to the aerodynamic models formulated in Chapter 3. The adapted comparison metrics for time-histories are presented in the second part.

Chapter 5 is devoted to verification and the fundamental applications of the distinctive parts of the synergistic framework. The behavior of the comparison metrics is firstly studied on generic signals, followed by a verification of both deterministic and random (including Pseudo-3D verification of span-wise coherence) free-stream turbulence. Ultimately, a complete set of aerodynamic and aeroelastic analyses of a flat plate is performed.

As a part of Chapter 6, the synergistic framework is applied for aerodynamic and aeroelastic analyses of three long-span bridges. The purpose is to demonstrate the applicability of the presented methods and methodology. Where possible, validation with experimental results is provided as well.

Chapter 7 offers a summary of the work presented, along with critical remarks, conclusions, and recommendations for further research.

Chapter 2

Wind and Bridges: Synthesis

2.1 Historical perspective

While bridges build with ropes and planks date back to ancient China, the concept of the modern suspension bridges is arguably attributed to the work of Fausto Veranzio published in *Machinae Novae*, 1616. He envisioned a solution for a crossing that involves two parallel metal girders, connected by wooden planks and supported on parallel chains that are mounted on two towers. His solution resembles on what today is considered a suspension bridge. However, it was not until the 1800s when the construction of cable-supported bridges started to gather momentum with the ascent of the steel industry.

Unfortunately, the progress in bridge aerodynamics is predicated on devastating collapses. Several bridges collapsed during severe storms in the 19th century, including e.g., Dryburgh Abbey, UK (1818), Nassau, Germany (1834), Brighton Chain Pier, UK (1836), Menai Strait, UK (1839), Tay Bridge, UK (1879), and Niagara Clifton, USA (1889). An early report by Russel [270] back in 1839 describes the second failure of the Brighton chain-pier (cf. Fig. 2.1)

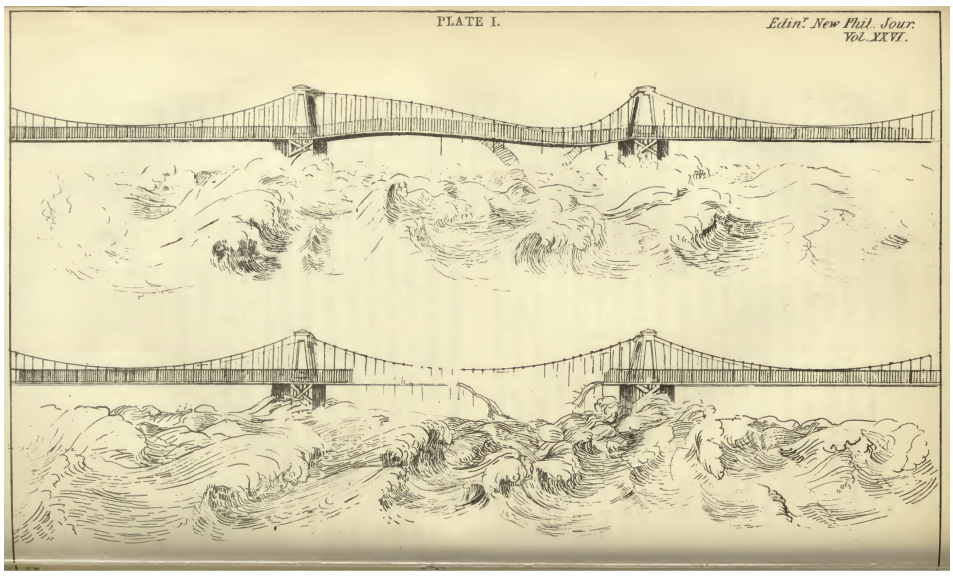

Figure 2.1: Brighton chain-pier collapse: sketch by Leut.-Col. Reid, in an article by Russel [270], 1839 (courtesy of Edinburgh New Philosophical Journal).

in the Edinburgh New Philosophical Journal. He reported the testimony by Leut.-Col. Reid, who was present on the spot when the collapse occurred, including the following excerpt:

> *The same span of the Brighton chain-pier (the third from the shore), has now twice given away in a storm. The first time it happened in a dark night, and the storm was accompanied by much thunder and lightning: the general opinion of those who do not inquire into the causes of such matter was, that it was destroyed by lightning; but the persons employed about the pier, and whose business was to repair it, were satisfied that the first fracture was neither caused by lightning nor waters, but by the wind.*
>
> *The fracture this year was similar to the former, and cause evidently the same. This time, it gave away half hour after mid-day, on 30th of November 1836, and a great number of persons were there to see it.*

Reid then proceeds to describe an event of a typical bridge failure including deck undulation and breaking of hangers. Thus, even back then the engineers were aware of the ruinous effects of the wind. In fact, early attempts to model wind as forces date back to 1759, by the engineer John Smeaton who described the wind forces due to mean wind in the Table of Wind Force for the Royal Society of London [315]. However, it was difficult to describe the forces due to the gust wind speed; hence, the engineers attempted to provide remedies by ingenious solutions such as stiffening of towers and various bracing systems.

At the beginning of the twentieth century, the bridge construction began to prosper remarkably as a result of the inception of Deflection Theory and the advancements in metallurgy. George Washington Bridge and Golden State Bridge broke the one-kilometer milestone in the 1930s,

Figure 2.2: Tacoma Narrows Bridge collapse (picture courtesy of Wikimedia Commons contributors, commons.wikimedia.org).

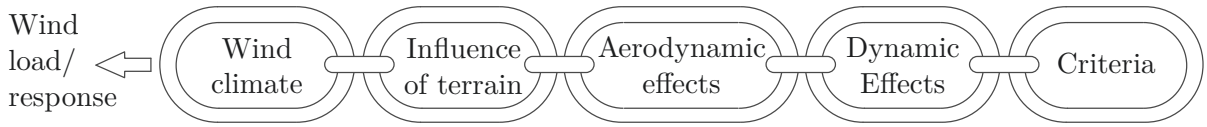

Figure 2.3: Alan G. Davenport Wind Loading Chain, after Isyumov [146].

promising even longer spans. However, the design and construction of cable-supported bridges was hindered by the momentous Tacoma Narrows incident (cf. Fig. 2.2), which unfortunately represent a pivotal point for the birth of modern bridge aerodynamics and aeroelasticity.

After just nineteen months of construction, the Tacoma Narrows Bridge opened to traffic in July 1940. It was considered to be stunningly slender, which elicited much comment at that time [291]. At operational wind speeds, the bridge would oscillate in such a way that vehicles would appear and disappear as one passed the bridge, and thus, it earned the name "Galloping Gertie" [291]. While no wind tunnel tests were performed prior to the design and construction, the violent oscillations in service led the authorities to subsequently request a dynamic structural model and a section model for wind tunnel tests. Before the collapse, Farquharson [104, 105] performed both tests on a small-scale dynamic model and wind tunnel tests on a sectional model. Although a torsional instability did not occur during the test [291], he did warn that the drastic advancements in bridge slenderness "render predictions exceedingly precautions and necessitate greatly extended theoretical investigations" [105]. Only three months after completion in November 1940, the bridge collapsed due to a relatively low wind speed of 19 m/s (cf. Fig. 2.2). The collapse was documented with motion pictures, which showed signs of torsional instability.

In the aftermath of the Tacoma incident, a task group, comprised of the renowned engineers and scientists, O. H. Amman, T. von Kármán and G. B. Woodruff, was assigned to determine the reason of the collapse [8]. A part of the task group's conclusions included the following: "At higher wind velocities torsional oscillations, when once induced, had the tendency to increase their amplitude." This indicated the occurrence of the aeroelastic phenomenon torsional flutter induced by high vertical vibrations that may have been a consequence of vortex-induced vibrations. Describing such phenomena was intractable by the pseudo-static analyses, and the need for new theoretical approaches became apparent.

Pioneering developments were made by Davenport [72, 73, 74] in the 1960s, who laid out the foundation of modern bridge aerodynamics and aeroelasticity and the field of wind engineering in general. He introduced the famous Alan G. Davenport Wind Loading Chain (cf. Fig. 2.3) that indicates all components involved in the design of wind-resistant structures. Following preliminary attempts that relate bridge flutter to airfoil by Bleich [26], Selberg [295] and Klöpper [176], Scanlan and his collaborators [280, 281, 288, 290] described the aerodynamic forces induced by motion that can replicate coupled flutter in bridge aerodynamics. With these research works, the field of bridge aerodynamics started to emerge and gain considerable attention.

Further information on the historical perspectives of bridge aerodynamics and long-span bridges can be found in the excellent book by Scott [291], including the works by Myata [225], Paxton and Mun [253], Rutz and Rens [271] and more recently Larsen and Larose [191].

2.2 Atmospheric wind

The first two links of Davenport's Wind Loading Chain (cf. Fig. 2.3) are related to the earth atmosphere and local terrain properties. In this section, a brief background of the fundamental statistical concepts of atmospheric wind and turbulence is given from a perspective to be utilized for the modeling of aerodynamic forces. The goal is by no means to provide a complete overview on the subject matter.

Wind, or the motion of air w.r.t. the surface of the earth, is fundamentally caused by variable solar heating of the earth's atmosphere [301]. A solar variation between poles yields to pressure and temperature differences, which together with the earth rotation and friction cause movement of air according to the principles of thermodynamics. Four forces play the main role for the air motion including the pressure, centrifugal, Coriolis (i.e. deviating force from a straight line due to earth's rotation) and friction forces. For a point sufficiently far away from the earth's surface, the friction forces are negligible and the mean wind velocity governed by the first three forces is referred to as gradient wind velocity U_{gr} (cf. Fig. 2.4, left).

Close to the surface, the friction effects are not negligible and the influence of the terrain (second link in Davenport's chain) is prominent, resulting in strong wind shears and high turbulence. This region of high retarding shear force and turbulent mixing is referred to atmospheric boundary layer and can extend from a few hundred meters to several kilometers [369]. Of particular interest in wind engineering are the lower 10 % of the atmospheric boundary layer, referred to as the surface boundary layer [248]. The thickness of the atmospheric boundary layer depends on the wind velocity, latitude angle, and terrain. For wind over flat surfaces, the atmospheric boundary layer is significantly thinner than for wind over residential areas (cf. Fig. 2.4, left).

To study the wind and atmospheric turbulence, Panofsky and Dutton [248] offer two perspectives. The first one is based on the fluid equations in terms of modeling the flow dynamics in space and time. Somewhat more heuristic, the second perspective is based on observation and measurements in terms of turbulent statistics. Herein, the statistical descriptors of turbulence are discussed in terms of their physical significance, while the modeling and generation of free-stream turbulence are discussed in Sec. 3.3.

Typically, the fluctuating velocity field is assumed as a stationary Gaussian field when the aerodynamic forces acting on bridges are in question [368], providing significant simplifications for description and simulation of the atmospheric turbulence. These simplifications are briefly discussed later. Looking at the wind velocity $\boldsymbol{u} = \boldsymbol{u}(\boldsymbol{x}; t)$ as a stationary random process in $\mathbb{R}^3$

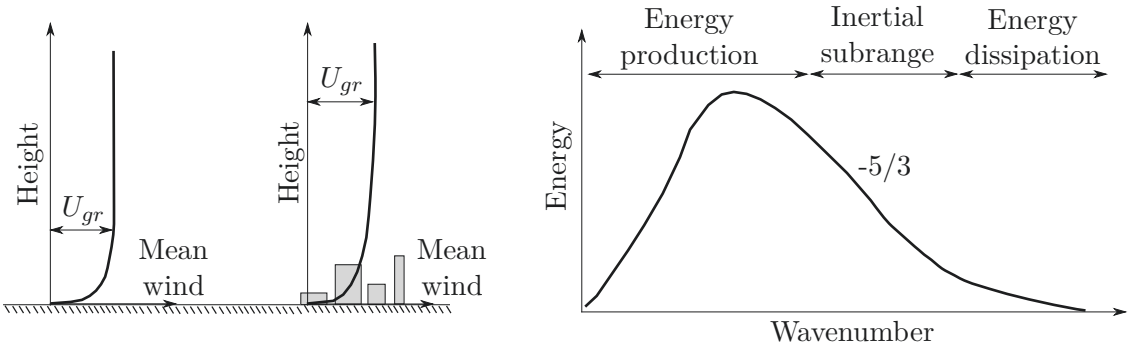

Figure 2.4: Boundary layer over flat and residential areas (left). Energy spectrum in the atmospheric boundary layer (right) (reproduced from Kaimal and Finnigan [158]).

domain with Cartesian coordinate system $\boldsymbol{x} = (x, y, z)$ and time t, it can be separated as

$$\boldsymbol{u}(\boldsymbol{x}; t) = \boldsymbol{u}_\infty(\boldsymbol{x}) + \boldsymbol{u}^*(\boldsymbol{x}; t), \tag{2.1}$$

where

$$\boldsymbol{u}_\infty(\boldsymbol{x}) = \langle \boldsymbol{u}(\boldsymbol{x}; t) \rangle = (U(\boldsymbol{x}), 0, 0) \tag{2.2}$$

is the mean wind speed for $\langle \cdot \rangle$ denoting the time-average operation and

$$\boldsymbol{u}^*(\boldsymbol{x}; t) = (u(\boldsymbol{x}; t), v(\boldsymbol{x}; t), w(\boldsymbol{x}; t)), \tag{2.3}$$

is the fluctuating component. Typically, the coordinate system is selected such that the coordinates x, y, z correspond to the fluctuating velocities u, v, w in the longitudinal, lateral and vertical direction, respectively, while the mean wind speed U is taken to be along the x coordinate (longitudinal direction).

Depending on the convention, the mean wind speed corresponds to an averaging interval of 10 minutes [145] or 1 hour [100]. Several models describe the wind profile for the boundary layer (cf. [301, 315] for an overview). A commonly used mathematical model to describe the mean wind profile $U = U(z)$ in a thermally neutral atmosphere is the logarithmic law:

$$U = \frac{u_{\text{fr}}}{k_0} \ln\left(\frac{z}{z_0}\right), \tag{2.4}$$

where $k_0 \approx 0.4$ is the von Kárman constant, z_0 is the surface length that depends on the terrain, and u_{fr} is the friction or shear velocity that represents the wind stresses on the ground. The logarithmic law in (2.4) is valid for the surface layer [248], which is of main interest in Wind Engineering.

The simplest statistical descriptor of turbulence is the turbulence intensity TI, which is defined for each fluctuating component as

$$TI_u = \frac{\sigma_u}{U}, \quad TI_v = \frac{\sigma_v}{U}, \quad TI_w = \frac{\sigma_w}{U}, \tag{2.5}$$

where σ_a is the standard deviation of a for $a \in \{u, v, w\}$. Typically, turbulence intensities are highly influenced by the terrain. In the case of Gaussian turbulence, the extreme velocity peak corresponding to a certain probability of exceedance can be related to the turbulence intensity.

If one thinks of the atmospheric turbulence as a superposition of swirls or "eddies" with a certain length, then a measure for the average size of an eddy is described by the turbulence length scales [301]. Since the averaged eddy length can be measured in three directions for three fluctuating components, there are a total of nine turbulent spatial length scales.

For e.g., the spatial length scales for points along x direction are obtained as

$$L_{ax} = \frac{1}{\sigma_a^2} \int_0^\infty R_a(\Delta x) \mathrm{d}\Delta x, \tag{2.6}$$

where $a \in \{u, v, w\}$ and $R_a = R_a(\Delta x)$ is the spatial cross-covariance function obtained as follows:

$$R_{ax} = R_{ax}(\Delta x) = \langle a(x; t) a(x + \Delta x; t) \rangle, \tag{2.7}$$

where Δx is a separation distance along the longitudinal (mean wind) coordinate x. It follows from (2.6) that if the length scales are small, R_{ax} is rapidly decaying and vice-versa.

Sir Taylor [319] posed a hypothesis stating that the turbulent eddies are simply convected by the mean wind velocity U, i.e. the turbulence is "frozen". This simply means that

$$a(x; t + t_\delta) = a(x + Ut_\delta; t) = a(x + \Delta x; t), \tag{2.8}$$

where t_δ is a time increment and $a \in \{u, v, w\}$. The length scales in the longitudinal direction can be obtained based on the autocovariance function $R_a = R_a(t_\delta)$ for a time increment t_δ as

$$L_{at} = \frac{U}{\sigma_a^2} \int_0^\infty R_a(t_\delta) \mathrm{d}t_\delta, \tag{2.9}$$

which are referred to as temporal length scales from here on. Assuming Taylor's hypothesis is valid, then the temporal and spatial length scale in the longitudinal direction are identical, i.e. $L_{at} = L_{ax}$. The product L_{at}/U is a time scale that corresponds to the average period of the eddies [369].

Looking at eddies as traveling waves, each eddy can be viewed as a periodic fluctuation with a frequency f that corresponds to an eddy wavelength of U/f. The energy contained for a single point in space is described by the power spectral density (PSD) [211], which can be obtained from the Wiener–Khinchin based on autocorrelation function as

$$S_{aa}^*(\omega) = \int_{-\infty}^\infty R_{aa}(t_\delta) e^{-i\omega t} \mathrm{d}t_\delta, \tag{2.10}$$

where $S_{aa}^* = S_{aa}^*(\omega)$ is the double-sided PSD, $\omega = 2\pi f$ is the circular frequency and i is the imaginary unit for $a \in \{u, v, w\}$. The PSD describes the energy distribution of the turbulence. Three regions are distinguished in the PSD [158]: (i) energy-containing range, where most of the energy is produced by shear and buoyancy; (ii) inertial subrange, where the energy cascade occurs, i.e. transfer of kinetic energy from larger to smaller eddies; and, (iii) dissipation range, in which small, high-frequency eddies are dissipated due to viscosity (cf. Fig. 2.4, right). Thus, the integral of the PSD is directly related to the square of the standard deviation as

$$\sigma_a^2 = \int_{-\infty}^\infty S_a^*(\omega) \mathrm{d}\omega, \tag{2.11}$$

which is a measure of the kinetic energy.

The cross-spectra S_{ab}^* for $a = a(\boldsymbol{x}_j; t)$, $b = b(\boldsymbol{x}_k; t)$ and $a, b \in \{u, v, w\}$ describes the correlation between two points j, k in space (space cross-spectra) and between fluctuating components of a single point (point cross-spectra) in a similar fashion as in (2.10). Based on the spectra and cross-spectra, the complete velocity field can be described in terms of a single-sided spectral matrix $\boldsymbol{S} = \boldsymbol{S}(\omega)$ as follows:

$$\boldsymbol{S} = \begin{pmatrix} \boldsymbol{S}_{uu} & \boldsymbol{S}_{uv} & \boldsymbol{S}_{uw} \\ \boldsymbol{S}_{vu} & \boldsymbol{S}_{vv} & \boldsymbol{S}_{vw} \\ \boldsymbol{S}_{wu} & \boldsymbol{S}_{wv} & \boldsymbol{S}_{ww} \end{pmatrix}, \tag{2.12}$$

where the off-diagonal terms are the cross-spectra.

The mean wind speed, turbulence intensity, and spectral matrix are typical turbulent measures that are obtained from experiments on sites. Models based on both principles of fluid mechanics and empirical observations are then utilized to describe the atmospheric wind, such as, e.g., the logarithmic wind profile (cf. (2.4)). Several models have been developed to describe the PSD, such as the ones being by von Kármán [336] and Kaimal [157] (cf. Solari [302] and Solari and

Piccardo [305] for an excellent overview). The PSD models are briefly reviewed and discussed in Sec. 3.3.

The three assumptions that may be used in some cases to idealize turbulence are the stationarity, homogeneity and isotropy. Stationary turbulence means that the turbulent characteristics do not change over time, i.e. they are time-invariant. Homogeneity is related to the space invariance of the turbulence statistics. This may be true to some extend for wind tunnel studies; however, it is an oversimplification for the atmospheric wind as its characteristics are highly dependent on height. Lastly, isotropy assumes that there is a directional symmetry of the turbulence characteristics. Kaimal and Finnigan [158] and Batchelor [19] give detailed explanation of these assumptions. None of these assumptions hold for atmospheric turbulence; however, they provide useful simplifications for analysis. Throughout this work, the turbulence is assumed to be stationarity homogeneous and in some noted cases, isotropic.

When computing the response of a structure in the frequency domain, the spectral definition of the wind field is sufficient. However, in case of solution in the time domain, the wind field is required to be described as correlated time-histories. One approach of obtaining correlated wind time-histories is by the methods for generation of multivariate stationary Gaussian random processes [159]. These methods include the digital-filtering-based schemes in terms of Auto-Regressive (AR) and Auto-Regressive Moving Average (ARMA) (cf. e.g. [203, 224]) or the spectral-based schemes in terms of wave superposition (cf. e.g. [46, 79, 298]). The latter method is of particular interest for this work and is discussed in detail in Sec. 3.3. Another approach of obtaining wind time-histories, which is of use as inflow conditions for Large Eddy Simulation within the CFD-based methods, is by their simulation as 2D or 3D random processes that comply with the Navier-Stokes equations [178, 365]. The two approaches are briefly discussed in Secs. 3.3 and 3.6.2.

The recent advances in modeling of the wind field are focused on the non-stationary and non-Gaussian storms such as thunderstorms and typhoons. The simulation methods have advanced significantly in the past few decades and their usage is mainly focused on applications, such as low rise buildings, when the effects of aerodynamic damping are not as complex as for bridges in terms of aerodynamic coupling and fluid memory (cf. e.g. Solari and De Gaetano [304], Tamura and Kareem [315] and Tao et al. [317] for excellent summaries). While few studies exist that apply non-stationary winds for aeroelastic analyses of bridges (cf. e.g. [54, 55]), these methods are not well adopted yet as the description of the unsteady aerodynamic forces is based on a stationary aerodynamic coefficients.

2.3 Bluff body aerodynamics

The fields of bluff body aerodynamics and aeroelasticity are wide; thus, this and the next section highlight some basic concepts that are of use for the coming chapters, while comprehensive information can be found in the excellent references [9, 27, 91, 301, 315]. Further specific references are also provided during the discussion of some particular results. The place of these two fields is descriptively incorporated in wind engineering through the third and fourth links in the Davenport's chain (cf. Fig. 2.3).

Unlike airplane wings, civil structures have irregular shapes, yielding complex fluid-structure interaction. Bridge cross sections are typically considered as bluff bodies that involve sharp edges, leading to adverse pressure gradients enabling transitions from laminar to turbulent boundary layer and large circulation regions. Hunt [141] separates three regions that have

distinct flow features, including the (i) free-stream (laminar or turbulent), (ii) near-body region where local (signature) turbulence effect occur, and (iii) the wake. These regions are interrelated and are governed by flow and body characteristics such as turbulent properties, viscous effects and body shape.

The ratio between the inertial and viscous effects of the flow is of cardinal importance for the flow features and wake behind bluff bodies. This ratio is expressed by the Reynolds number:

$$\mathrm{Re} = \frac{UB}{\nu}, \tag{2.13}$$

where ν is the kinematic viscosity, while B is a reference length, typically taken to be the width of the body. At high Reynolds number, the inertial effects of the flow are dominant, leading to laminar to a turbulent transition of the boundary layer. This occurs even for streamlined bodies when there is no separation due to an abrupt change in the geometry.

In case of bluff bodies, separation occurs at moderately low Reynolds number, leading to formation of large eddies in the wake. Increasing the Reynolds number, the flow becomes unstable and thus, the eddies start to alternate leading to the famous von Kármán street, first reported by Bénard in 1908, and then studied in depth by von Kármán in 1911. The frequency of the alternating eddies is linked to the body geometry; thus, the regularity of vortex shedding can be non-dimensiolized by the Strouhal number as

$$\mathrm{St} = \frac{f_{shed} H_D}{U}, \tag{2.14}$$

where f_{shed} is the vortex shedding frequency, while H_D is a reference length, typically taken to be the depth of the body. E.g., fundamental studies on circular cylinders (cf. e.g. Rohsko [266] and Goldburg et al. [120]) indicate Strouhal number of approximately 0.2. Beyond the range of Reynolds number in which the von Kármán street occurs, turbulent mixing prevails in the boundary layer that helps the fluid to be transported with higher momentum [301], yielding narrower wake (i.e. delayed separation) that entails small vortices.

When the free-stream turbulence is additionally involved, the situation is significantly more complex. The effect of the free-stream turbulence on bluff bodies is perplexing and still not well understood. Free-stream turbulence induces fluctuating pressures due to the instantaneous change of direction of the wind speed (angle of incidence), which affects the local turbulence effects by altering the separation points, and influences the wake [234]. These effects are rather complicated and are a topic of extensive research since the 1930s from the seminal works by Dryden [92] and Taylor [318] and is still of a field of major interest (cf. e.g. [141, 297, 366]). Generally, the free-stream turbulence can affect the transition from a laminar to a turbulent boundary layer, particularly for length scales of the same size as the boundary layer thickness [141]. The flow in this region is predominantly three-dimensional with propagating disturbances and instabilities in the lateral direction occur such as the Klebanoff modes [175], puffs and elongated structures [366].

All the above-mentioned effects contribute to the forces felt by an immersed body. Due to the compliance of boundary conditions between the fluid and body, normal and tangential local forces stem on the body surface. Integrated for the whole body, these local forces result in total drag D (horizontal), lift L (vertical) and moment M (torsional) forces. Depending on the body geometry and fluid density ρ, the aerodynamic forces can be non-dimensionalized by means of

the static wind coefficients of drag C_D, lift C_L and moment C_M as follows:

$$\begin{aligned} C_D &= \frac{D}{\frac{1}{2}\rho U^2 B}, \\ C_L &= \frac{L}{\frac{1}{2}\rho U^2 B}, \\ C_M &= \frac{M}{\frac{1}{2}\rho U^2 B^2}, \end{aligned} \tag{2.15}$$

In light of the previously described physical processes, three types of aerodynamic forces can be identified for a stationary bluff body, including: (i) vortex-shedding forces, (ii) forces due to free-stream turbulence (buffeting forces) and (iii) forces due to laminar free-stream (static forces). For an oscillating body under laminar or turbulent free-stream, an additional forcing source is the motion that yields the (iv) self-excited forces (i.e. motion-induced forces). The motion of the body initiates a separation of circulation-carrying eddies that are convected by the free-stream wind. Conserving the momentum of the system, self-excited forces arise to counter the total rotation contained in the motion-induced eddies. Describing these forces that act on a bridge deck is one of the main goals in bride aerodynamics.

2.4 Aeroelastic phenomena

Aeroelasticity is a branch of engineering that is devoted to the studying of interactions between the "AEI" trinity of forces, including the Aerodynamic, Elastic and Inertial forces. Arthur R. Collar [68] conceptualized the AEI trinity in terms of a triangle such that all aeroelastic phenomena can be described by the interaction of the AEI forces. Wind engineers often focus on the aerodynamic forces, while using simple structural dynamics for the structure under the linear assumption. Thus, as in this work, the terms bridge aerodynamics and aeroelasticity are used interchangeably.

Figure 2.5 schematically depicts the structural response w.r.t. the wind speed for both laminar and turbulent free-stream. At moderate wind-speeds for laminar free-stream, the abrupt peaks

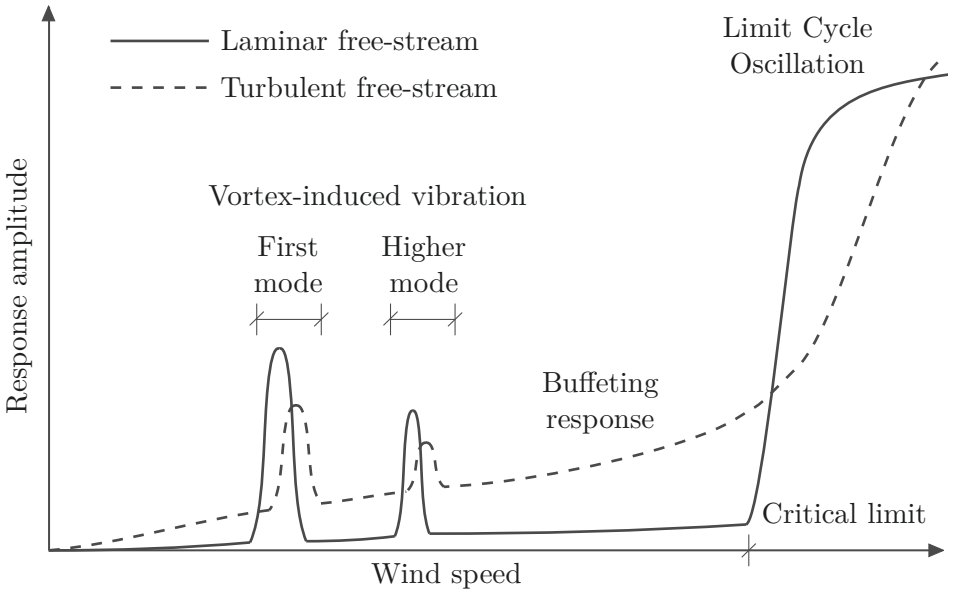

Figure 2.5: Aeroelastic phenomena: structural response against wind speed.

indicate the vortex-induced vibrations as a resonant aeroelastic phenomenon. Increasing wind aeroelastic instability occurs at a certain threshold, resulting in violent amplitudes. Beyond this threshold, oscillations with high, but limiting amplitudes may be observed, commonly termed as limit cycle oscillations. The structural (buffeting) response is significantly larger for turbulent compared to laminar free-stream throughout the whole wind speed range, except at the wind speeds where aeroelastic resonance and instability occurs. For these cases, the influence of free-stream turbulence on the vortex-induced vibrations and aeroelastic instability is still not well understood as it may increase or decrease the severity of the response. In what follows, the aeroelastic phenomena, including the vortex-induced vibrations, aeroelastic instabilities with the post-critical range, and buffeting response are briefly discussed.

Vortex-induced vibration is an aerodynamically nonlinear resonant phenomenon that involves synchronization of the vortex-shedding and the structural vertical vibrations in a particular narrow wind speed range. In this sense, the principal vortex-shedding frequency is close to the structural frequency. Although the shedding frequency is linearly dependent on the velocity (cf. (2.14)), in this narrow wind range, commonly known as lock-in, the vortex-shedding process is controlled by the structural oscillations in terms of the amplitude and phase, leading the principal vortex-shedding frequency to be similar to a structural across-wind frequency. The oscillations are self-limiting due to the nonlinear aerodynamic forces leading to a constant oscillation amplitude in the lock-in range. Specifically, the prediction of oscillation amplitude is the major topic of research as the physical processes that are responsible for the vortex-induced vibrations are not well understood in general for bluff bodies.

Fundamental investigations were initially conducted on circular cylinders that offer substantial insight into the underlying physics of the phenomenon. An excellent overview can be found in the works by Sarpkaya [278], Griffin and Koopmann [122], and Williamson and Govardhan [348]. Bluff bridge decks resemble rectangular cylinders; thus, a correlation can be found in their behavior during vortex-induced vibrations. In terms of bridge design, vortex-induced vibrations are an in-service issue. Thus, the prediction of the resonant amplitude is of importance in order to satisfy a criterion such as comfort or fatigue. Vortex-induced vibrations have occurred for several bridges including, for e.g., the Great Belt Bridge [191], Trans-Tokyo Bay Highway Crossing [110] and Volgograd bridge. Wu and Kareem [357] provide comprehensive summary on vortex-induced vibrations for bridge decks.

The self-excited forces play a minor role compared to the vortex-shedding forces in case of vortex-induced vibrations. However, for the case of aeroelastic instabilities, it is exactly the self-excited forces that are responsible for the violent oscillations of the structure. At high wind speeds, the structural oscillations yield a distinct fluid-structure interaction in a self-feeding manner, leading to diverging amplitudes. The total damping of the system, which is comprised of an aerodynamic and a mechanical part, is incapable of dissipating the induced energy by the flow, resulting in negative damping that causes the oscillations of the body to increase with each cycle. Depending on the motion, three types of aeroelastic instabilities are distinguished including galloping, torsional flutter, and coupled or "classical" flutter. The first type is associated with instability in the vertical direction, the second is a rotational instability, while the third type involves a coupled motion of both vertical and rotational oscillations. Sections that are deep are more prone to galloping and torsional flutter, while the coupled flutter occurs for shallow, streamlined sections that resemble an airfoil. Apart from the shape, other factors that contributes to which type of instability would occur are the vertical and torsional frequencies and their separation for the coupled flutter.

Early investigations on the galloping were done by Den Hartog [78], followed by investigations on square-like sections by, for e.g., Novak [240], Parkinson and Brooks [252] and Mukhopadhuau [231]. A preliminary identifier for galloping is the negative slope of the lift coefficient as is related to the negative aerodynamic damping. Once this negative aerodynamic damping surpasses the structural damping in magnitude, instability occurs. This is also known as the Den Hartog criterion. Typically, D-type sections are prone to flutter. Thus, galloping is more critical for cables and transmission lines rather than bridge decks. A recent literature review on galloping is given by Piccardo et al. [256].

On several occasions, Nakamura and his coworkers [233, 235] studied on several occasions the occurrence of a torsional flutter from a phenomenological point of view, while Washizu [345, 346] highlighted the effect of the aspect ratio. Matsumoto et al. [216] investigated the driving mechanisms of torsional flutter for rectangular and H-type sections, such as the Tacoma Narrows section, which are prone to torsional flutter. In Matsumoto et al. [218], the interaction of torsional flutter with vortex-induced vibration was highlighted, it is believed to be the case of Tacoma Narrows failure.

As a phenomenon, coupled flutter for bridge decks finds its roots in the airfoil theory in the fundamental works by Theodorsen [323] and Wagner [339]. For this type of aeroelastic instability, the torsional and rotational frequency coincide, yielding coupled oscillation with an energy transfer between modes. Studies on coupled airplane flutter go as early as in 1916, as noted in the interesting historical perspective provided by Fung [112]. Matsumoto [216] studied the range of width-to-depth ratio where a transition from torsional to coupled flutter occurs. They concluded that for rectangular prisms with a width-to-depth ratio larger than 10, the instability translates to a coupled flutter. Further general works describing the influence of parameters on flutter can be found by Abbas and Morgenthal [4], while Larsen and Larose [191] give a fundamental perspective on flutter of bridges. An extended literature review on the topic of aeroelastic instabilities is provided by Abbas et al [3].

In the design procedure of bridges, it is ensured that aeroelastic instability is avoided. Beyond the instability threshold and regardless of the type of instability, the self-feeding oscillation ultimately exhibits high nonlinearities on both structural and aerodynamic sides leading to a stable oscillation range, known as limit cycle oscillation. The amplitude is significantly higher compared to vortex-induced vibrations. This phenomenon has been studied for wings and fundamental cases (cf. e.g. Tang and Dowel [316], Dowel et al. [91] and Amandolese et al. [7]). The design of bridges for the limit-cycle-oscillation amplitudes is still only conceptual as a design is not feasible for such high amplitudes.

Buffeting is defined in a broad sense as the unsteady loading of a structure by velocity fluctuations in the oncoming flow [301]. This is not a distinct phenomenon as the aeroelastic resonance and instability. The sources of the buffeting forces were discussed in the previous section. If, additionally, the structure is elastic, the total aerodynamic forces can be seen as a nonlinear composition of the buffeting and self-excited forces. As for coupled flutter, the fundamentals of the buffeting originate from the airfoil theory (cf. e.g. [91, 112]), from the seminal works by Sears [293] and Liepmann [205]. The concepts of application in wind engineering were laid out by Davenport [72, 73]. It is also noted that the influence of free-stream turbulence on the aeroelastic resonance and instability of bridges is still not well understood, as some studies indicate both stabilizing and destabilizing effects for (cf. e.g. [18, 344]).

In addition to the discussed aeroelastic phenomena, other phenomena may occur such as torsional divergence, i.e. aerostatic instability due to negative aerodynamic stiffness, wake buf-

feting and rain wind-induced vibrations [301]. These are not of major concern for this work.

Apart from the comprehensive works given at the beginning of the previous section, excellent references that cover the broad topic of wind engineering in terms of bluff body aerodynamics and aeroelasticity are given by Solari [303], Iriwin [144], Kareem and Wu [161], Fujino and Siringoringo [110], and Larsen and Larose [191].

2.5 Aerodynamic models

The main task of aerodynamic modeling is to describe the wind forces acting on the bridge deck. In bridge aerodynamics and aeroelasticity, generally, three types of models can be distinguished including experimental, semi-analytical and CFD models. Experimental models are small-scale models of a part of the whole structures that are tested in a wind tunnel facility. As noted in the previous chapter, the CFD and semi-analytical models are mathematical models. The former discretizes the fluid governing equations to model the fluid-structure interaction, while the latter accounts for this interaction by introducing aerodynamic coefficients. These aerodynamic coefficients are obtained either experimentally or from CFD analyses. Figure 2.6 schematically depicts the components of fluid structure-interaction for all types of models.

In what follows, a brief literature review is conducted for the mathematical models, while the experimental models are touched upon briefly for the sake of consistency.

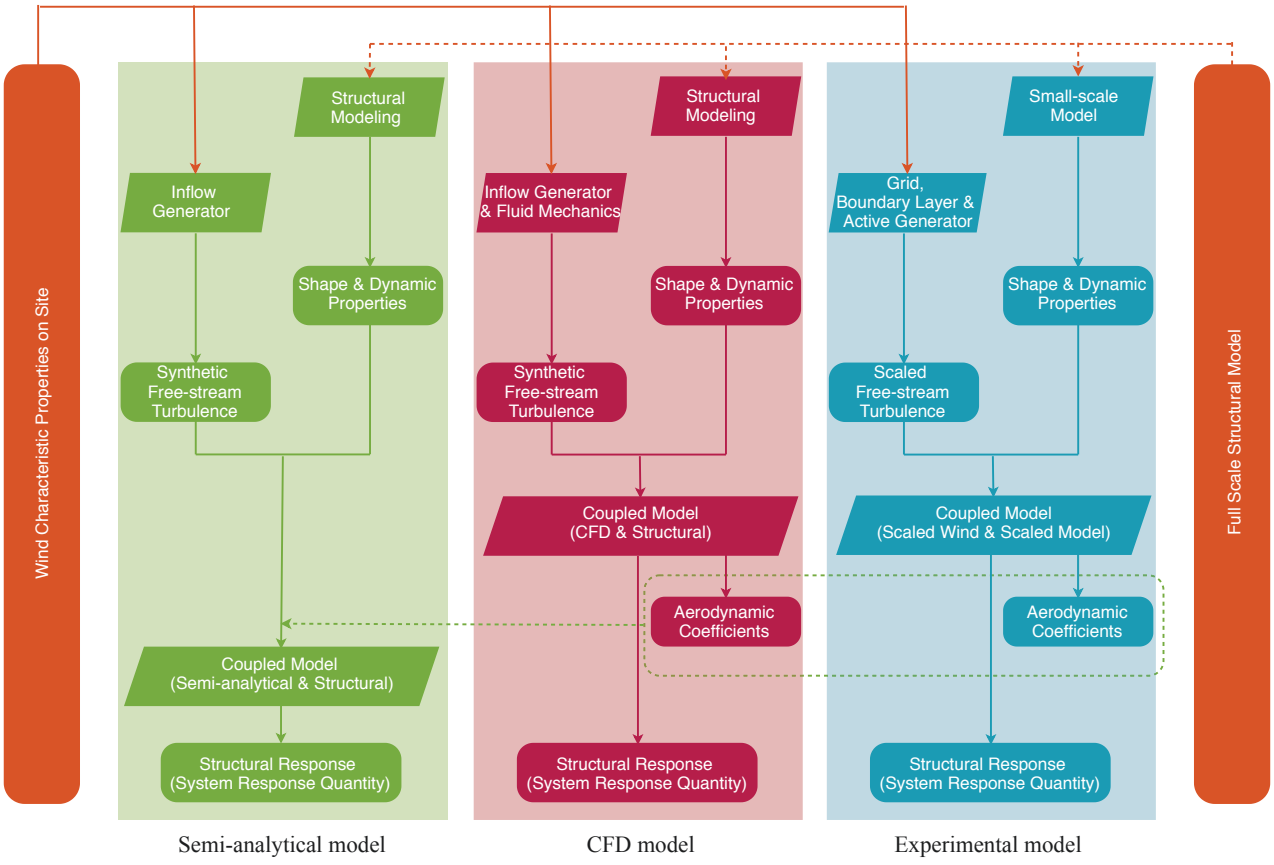

Figure 2.6: Classification of models used in bridge aerodynamics and aeroelasticity.

2.5.1 Experimental models

Experimental wind tunnel testing is still an integral part of the design of bridges. The structural and flow properties are scaled based on non-dimensional numbers such as the Reynolds number, Froude number, and Strouhal number [301]. Depending on the type of tests, three types of models can be distinguished:

i) Section model;

ii) Taut strip model;

iii) Full aeroelastic model.

The first type of model represents the strip assumption and is used to obtain the aerodynamic coefficients such as static wind coefficients, flutter derivatives, and aerodynamic admittance. Moreover, if the model is suspended on springs, the critical wind speeds for vortex-induced vibrations and flutter can be obtained for an idealized 2D situation.

Taut strip models represent the deck of the bridge, without any additional structural elements [187]. It can be suspended in the two setups, static or elastic. Typically, the vertical and torsional frequencies are targeted for the elastic setup. The advantage is that is less expensive than the full aeroelastic models while taking several modes into account and the 3D structure of turbulence.

Full aeroelastic models are typically used in boundary layer wind tunnels and they represent a scaled replica of the bridge on site. Their main purpose is to obtain the bridge response in terms of smooth and turbulent free-stream. They have been used to identify aerodynamic coefficients in some instances as well [369].

2.5.2 Semi-analytical models

The semi-analytical models are generally phenomenological types of models as they attempt to model either one or multiple aeroelastic phenomena. Following this, in bridge aerodynamics, the models can be grouped as models for flutter and buffeting analyses, vortex-induced vibrations and single-degree-of-freedom instabilities (torsional flutter and galloping). While the purpose of the models can overlap to a certain extent, often they cannot offer a complete description of multiple phenomena simultaneously. The models for buffeting and flutter analyses are the main interest herein; thus, they are studied and reviewed in depth. These models revolve around two pivotal assumptions: quasi-steady and linear unsteady assumptions.

The quasi-steady assumption is the starting point in bridge aerodynamics for modeling the buffeting and self-excited forces. The models based on this assumption trace back to galloping of circular cylinders (cf. [252]) and quasi-steady flat-plate theory (cf. e.g. [112]). The unsteadiness or the so-called fluid memory is neglected in the case of quasi-steady theory. However, due to the nonlinear relationship between the effective angle of attack and static wind coefficients, the mathematical model of the system results in a coupled nonlinear equations of motion. The application of the quasi-steady theory in time domain is rather straightforward, which resulted in its extensive use over the years (cf. e.g. [179, 255]).

In order to take into account the fluid memory of the aerodynamic forces up to a certain degree, Diana et al. [80] introduced the corrected quasi-steady model, in which the slope of static wind coefficients is modified to account for the fluid memory at a certain reduced frequency by a correction coefficient. This was later extended to the band superposition scheme, by splitting

the wind frequency spectrum in bands for which different correction coefficient was applied [82]. Borri and Costa [33] extended this by approximating the static wind coefficient up to the third order of Taylor's expansion. A similar approach was used by Su et al. [313] where the unsteady information contained in the flutter derivatives was used for a single reduced frequency near the first mode yielding in a frequency-independent scheme. The effect of the aerodynamic damping resulting from the torsional motion, described by the aerodynamic center, is neglected in some studies (cf. e.g. [1, 312]).

The linear unsteady assumption takes into account the fluid memory in the aerodynamic forces by frequency-dependent aerodynamic coefficients. Davenport [72, 73] adopted the concept of linear aerodynamic admittance for line-like structures from the airfoil theory [205, 293] to represent the unsteadiness of the buffeting forces. For the motion-induced forces, Scanlan and his coworkers (cf. e.g. [280, 281, 283]) introduced linear frequency-dependent coefficients, i.e. Scanlan's flutter derivatives, which correspond to Theodorsen's [323] analytical expression for an airfoil. The concept of aerodynamic admittance for bridge decks is similar as for an airfoil: it represents a transfer function between incoming wind fluctuations and forces. After establishing the linear unsteady theory for bridge decks, many frameworks were developed for multimode coupled buffeting and flutter analyses in the frequency domain (cf. e.g. [147, 163, 208, 368]), supported by the fact that the flutter derivatives, wind spectra, and aerodynamic admittances are all described in the frequency domain [284]. However, the main advantage of the time domain is the potential for consideration of structural and aerodynamic nonlinearities. The inherent linear unsteady behavior of the buffeting and motion-induced forces in time domain is modeled by a linear superposition of elementary response functions. These functions in bridge aerodynamics are conventionally termed as indicial (unit-step) or unit-impulse functions.

Scanlan et al. [288] introduced the indicial functions for bluff bodies which are the time-domain counterpart of the aerodynamic derivatives and admittance, which for flat plate correspond to the analytical Wagner [339] and Küssner [184] functions, respectively. The experimental identification is cumbersome since it is difficult to simulate a step function; therefore, the extraction of the unsteady information is convenient from the flutter derivatives (cf. e.g. [45, 69]) by means of rational approximation. Recently, Miranda et al. [76] developed a formulation based on indicial functions that explicitly separates the inertial and circulatory contribution leading to a consistent approach based on Wagner's function for an airfoil.

Pointing out the redundancy in the indicial function formulation, Bucher and Lin [41] proposed a formulation based on the impulse functions. As for the indicial function, a rational approximation is also applicable for the impulse functions [347]. Wu and Kareem [361] did a comparative study between these two formulations and concluded generally there is no superiority between these two kernels for the description of linear aerodynamic forces.

Boonyapinyo et al. [31] conducted one of the first comprehensive buffeting and flutter analyses in time domain utilizing a state-space approach. Almost concurrently, Chen and Kareem [61] formulated a framework based on impulse function, extending for aerodynamic admittance. The latter two studies focused on computing the response using impulse functions. Based on the indicial function formulation, several studies introduced frameworks for aeroelastic analyses including the ones by Costa and Borri [69] and Zhang [375].

To account for the ambiguity of the aerodynamic center in the quasi-steady based model, Øiseth et al. [244] introduced the modified quasi-steady model that interpolates the flutter derivatives at a certain frequency using linear least-squares fit. The contribution of the unsteady forces is crucial for the low reduced velocities, while the aerodynamic nonlinearity governs the

low reduced velocity part. Utilizing this logic, Chen and Kareem [59] developed a hybrid nonlinear model by utilizing the quasi-steady model for the low-frequency component of the wind spectrum based on which response, the high-frequency component of the wind is linearized. Diana et al. [85] validated this premise for a similar model with experiments.

Recent developments in the semi-analytical models attempt to describe nonlinear aerodynamic behavior. One group involve models approximating the of dynamic hysteretic wind coefficients using rheological and polynomial models (cf. e.g. [84, 86]) or neural networks (cf. [356]), while the other is based on nonlinear convolution with fading memory scheme using Volterra series (cf. [362, 364]). From the recent development, the Volterra series is the closest model to describe the underlying physics of bridge aerodynamics.

Apart from the models for buffeting and flutter analyses, semi-analytical models in bridge aerodynamics are developed with a special purpose to determine vortex-induced vibration (cf. e.g. [83, 96]) and nonlinear single-degree-of-freedom flutter (cf. e.g. [236, 373]).

2.5.3 Computational fluid dynamics models

With the application of the numerical CFD methods for Wind Engineering problems, a new field, Computational Wind Engineering, has emerged. The CFD methods have been used for a wide variety of applications such as aerodynamic and aeroelastic analyses of buildings, bridge decks, riser pipes, off-shore wind turbines, etc. Blocken [29] gives an excellent perspective of the realm of Computational Wind Engineering. For the purpose of this study, the narrow application of CFD modeling in Computational Bridge Aerodynamics is of interest.

There are several ways how to discretize the fluid equations and solve numerically the fluid-structure interaction. Perhaps, the most widely applied method is the Finite Volume Method, which discretizes the Navier-Stokes equations on a Eulerian grid, enabling conservation of the volume for all cells and the overall flow volume. Another approach is the conventional Finite Element method that utilizes the variational formulation of the fluid equations for the discretization. Perhaps the most straightforward grid-based method is the Finite Difference Method, which was attractive in the early beginnings of Computational Wind Engineering.

As an alternative to the grid-based methods, the Lagrangian 2D Discrete Vortex Method has proven to be robust and efficient for flow simulation in a relatively wide field of application, especially for free-field bluff body aerodynamics problems. Within this method, the vorticity field is discretized by particles, carrying concentrated circulation [70]. This has enabled to study the flow past complex geometries with a good accuracy for a reasonable computational cost.

As all scales of turbulence cannot be resolved using Direct Numerical Simulation due to computational restraints, another issue that is of particular importance for the CFD models is the turbulence modeling. Turbulent models are based on spatial-averaging Large Eddy Simulation (LES), time-averaging Reynolds Averaged Navier-Stokes (RANS) or their combination Detached Eddy Simulation (DES). Moreover, particular care should be also put on modeling the contribution of turbulence on the subgrid scales. Mostly, the models for turbulence modeling have been utilized for the grid-based CFD methods. Comprehensive information on grid-based methods and turbulence modeling can be found in, e.g., Ferziger and Peric [107].

Grid-based methods

Commonly, grid-based methods have served for CFD models for obtaining the static wind coefficients and flutter derivatives. A significant number of studies have been published in recent years; thus, only a fraction of these are mentioned herein.

Fujiwara et al. [111] reported one of the earliest applications of the Finite Difference Method to study the aerodynamic behavior of a bridge deck in terms of static wind coefficients and even determined the vortex-induced vibration amplitudes. Using the same method, Kuroda [183] studied the Great Belt section on a stationary grid without a turbulence model at a Reynolds number in the order 10^5. The mean pressure distribution and static wind coefficients were obtained and the agreement with the experimental static wind coefficients was evaluated as good noting the discrepancies in the lift due to insufficient modeling of railings and crash barriers.

Two early attempts to utilize the Finite Volume Method are the one by Selvam et al. [296] and the one Bruno et al. [37, 38]. The latter studies utilized the code FLUENT by Ansys to determine the static wind coefficients and flutter derivatives of a bridge deck, as well as to study the effect of barriers. Similarly, studies that involve of the flutter derivatives and static wind coefficients based on the Finite Volume Method in 2D involve the ones by Vairo [332], Nieto et al. [239] and Brusiani [40]. The latter study also provided a comparison of sub-grid turbulence models and noted that differences may arise based on the choice of a turbulence model.

With the ascent of computer power, CFD studies have emerged that consider the 3D fluid behavior for applications in bridge aerodynamics under laminar free-stream. Bai et al. [15] utilized a 3D DES Finite Volume CFD model to determine the flutter derivatives and noted that the need for 3D analyses is crucial for bluff bridge sections. Comparing the pressure on the deck due to sinusoidal motion, Sarkic et al. [277] noted the limitation of the 2D Unsteady RANS compared to 3D LES.

Motion-induced indicial functions were obtained using the Finite Element Method and RANS turbulence model by Turbelin and Gibert [330] and Brar et al. [35]. Fransos and Bruno [109] used the standard implementation of the Finite Volume Method in FLUENT to determine the Wagner function. Generally, the time-step is a major culprit for numerical uncertainties when ideal unit-step functions are applied for all CFD method.

Applications based on the grid-based CFD methods have seldom focused on directly determining the aeroelastic response for laminar free-stream. Fradsen [108] determined the free oscillation flutter using a Finite Element based code Spectrum by Anysis for the Great Belt Bridge. She found the critical limit to be in good correspondence with wind tunnel tests. Utilizing 3D LES, Sarwar and Ishihara [279] determined the vortex-induced vibrations for a bluff bridge deck including counter-measures. To validate their implementation, they initially compared their results for a rectangular prism to former experimental results.

The recent trend for applications of the grid-based methods is to determine the critical velocity including the limit cycle oscillation amplitudes. E.g., Ying et al. [370] determined the limit cycle oscillation amplitudes for two bridge decks using 2D RANS Finite Element CFD model and compared the results with experiments, yielding fair correspondence, while Lee et al. [196] utilized similar CFD model and an implicit coupling scheme to determine the limit cycle oscillation amplitudes of Tacoma Narrows bridge. However, the author is not aware of a grid-based CFD application considering 3D structural behavior yet.

Aeroelastic and aerodynamic analyses involving free-stream turbulence and grid-based CFD methods are scarce. A part of this may be attributed to the lack of computationally efficient, yet sufficiently validated methods for the inflow boundary conditions. In a rudimentary fashion, the aerodynamic admittance and gust induced indicial functions have been computed by Ujema et al. [331], Bruno et al. [39] and Turbelin and Gibert [330]. The author is not aware of other grid-based CFD study presenting 3D buffeting analysis, other than the one by Kim et al. [172]. They used a RANS Finite Element CFD model which did not involve verification of the free-stream turbulence within the CFD domain.

Discrete Vortex Method

Pioneering works for the application of CFD in bridge aerodynamics could be traced in the late 80s and early 90s of the past century. One of the first applications of the Discrete Vortex Method for bridge decks was by Bienkiwicz [22] and Kutz [21]. They used this method to compute the pressure and static wind coefficients of a static rectangular prism and a bridge deck.

A few years later, Walther [342] and Larsen [341] used their code DVMflow to study the aerodynamic behavior of a bridge deck on numerous occasions. Initially, they mostly conducted aerodynamic analyses to determine the static wind coefficients and flutter derivatives (cf. e.g. [190, 193]). Their code was also used by Farsani et al. [106] to compute indicial functions for a bridge deck and by Ebrahimnejad et al. [95] to develop a reduced-order model of the flutter derivatives.

Similar applications in terms of only aerodynamic analyses (i.e. no aeroelasticity) were made by Taylor and Vezza [320], who used their code to compute the aerodynamic forces due to forced oscillation of a square cylinder and later to study the stability of a footbridge [321]. Further, Ge and Xiang [115] compared the Discrete Vortex Method to grid-based methods based on the flutter derivatives and static wind coefficients for several bridge decks. Although differences were noted, they were not substantial.

Morgenthal's [226, 227] implementation of the 2D Vortex Method, VXflow, was used to compute the static wind coefficients and flutter derivatives for several bridge decks, as well as for aeroelastic analyses in terms of vortex-induced vibrations of the Great Belt Bridge and flutter analysis of the Millau viaduct. Results were compared to wind tunnel tests for several case-studies, yielding good correspondence.

Wilden and Graham [349, 350] developed a Pseudo-3D vortex method that accounts for the 3D structural behavior of riser-pipes during vortex-induced vibrations by positioning 2D fluid strips along the structure. Based on this idea, Morgenthal and McRobie [229] introduced their implementation of a laminar Pseudo-3D vortex method in the field of bridge aerodynamics to study vortex-induced vibrations. Later, VXflow was successfully validated for vortex-induced vibrations of Niteroi bridge for an enhanced GPU implementation [229]. Abbas [2] attempted to utilize the laminar Pseudo-3D method in VXflow for flutter analysis with few slices and five modes.

An important milestone of the 2D vortex method was overcome by Prendergast [257] and McRobie [258] in terms of modeling of free-stream turbulence. They introduced a velocity-based free-stream turbulence generation that can simulate free-stream turbulence in the CFD domain. Incorporating this method in Morgenthal's VXflow, the first application to study 2D buffeting response of a bridge deck using the Discrete Vortex Method was made.

Rassmusen et al. [261] used the velocity-based turbulence generation method and Walther's DVMflow to determine the aerodynamic admittance of the Great Belt Bridge. Using the same implementation, Hejlesen et al. [134] determined the aerodynamic admittance for four bridge decks and validated a part of the results with former wind tunnel studies.

Recently, Tolba and Mogenthal [326] extended the laminar Pseudo-3D Vortex Method to account for the isotropic free-stream turbulence by introducing a particle-based turbulence generation. With this, the idea of using a Pseudo-3D CFD method for buffeting analysis was established. The difference between this method and Prendergast's velocity-based method is that the circulation of the inflow particles is generated directly instead as a by-product of a velocity field. The authors argued that with the velocity-based turbulence generation method "the correlations are not maintained in the process of their transformation to inflow vortex particles" [326]. However, it was not shown to what extent is the loss of the span-wise correlation.

2.5.4 Comparative studies

A large number of semi-analytical models have stimulated the need for model assessment. Several comparative studies have emerged that compare various semi-analytical aerodynamic models based on various quantities of interest. Additionally, the semi-analytical models have been compared with CFD models and experimental models in terms of verification and validation.

A comparison of results from the frequency- and time-domain computations for the linear unsteady model has been targeted by several studies. To perform such a comparison for the buffeting response, Chen and Kareem [61] utilized the RMS and averaged PSD. Øiseth et al [245] also compared several formulations of the elementary indicial and impulse functions with the frequency-domain counterpart based on the RMS and PSD as quantities of interest. The critical flutter velocity was additionally compared directly as a unique parameter. Similarly, the critical flutter limit has been a quantity of interest for several other comparative studies (cf. e.g. [194, 273]).

Another comparison perspective is to quantify the influence of the aerodynamic assumptions on the aeroelastic response. Petrini et al. [255] compared several time-domain models based on the quasi-steady and linear unsteady assumptions. Their comparative discussion on the buffeting response is based on the PDF, mean values and envelopes (i.e. peak) quantities and by looking at the time-histories qualitatively. Wu and Kareem [359] performed an extensive comparison of linear and non-linear aerodynamic models in the time domain. Therein, the buffeting response was compared for identical input wind time-histories based on the RMS and looking at the time-histories qualitatively. Most of the studies that introduce nonlinear semi-analytical models (cf. e.g. [59, 85, 86, 360]) also compare or validate the buffeting response, qualitatively, based on the time-histories, or, quantitatively, in terms of RMS, peak and seldom PSD. Moreover, various schematics are often offered (cf. e.g. [255, 364]) to ease the understanding of how these models relate to one another and which is of higher complexity, i.e. better.

2.6 Research questions

This section presented a compact overview of the different components for modeling of the wind effects on bridges. Following a brief introduction of atmospheric turbulence and bridge aerodynamics and aeroelasticity, an emphasis was put on the review of mathematical aerodynamic models and their comparative studies. In light of this, several research gaps can be identified.

First, the complexity of semi-analytical and CFD aerodynamic models in terms of their mathematical constructions has not been evaluated based on a sound mathematical approach such as graph or category theory. Although one can intuitively say which model is more complex, and hence, better, such an approach is necessary to formally support this kind of statements.

Second, there is still no procedure based on well-established local or global quantities (metrics) for comparison of time-dependent models in bridge aerodynamics. Although the RMS and PSD may be sufficient for comparison of linear models under Gaussian input, a more intrinsic procedure is required to quantify the nonlinear and non-stationary features of the nonlinear aerodynamic models.

Third, there is still the possibility to employ the velocity-based turbulence generation to the Pseudo-3D Vortex Methods. Using this type of free-stream turbulence would offer certain advantages over the particle-based method such as partial consideration of anisotropy.

Finally, a CFD method for the determination of the aerodynamic admittance under deterministic gusts has not yet been developed. Using such a method would make the the determination of the six-component complex aerodynamic admittance feasible.

In the following chapters, an attempt is made to partially address these yet unresolved problems.

Chapter 3

Modeling in Bridge Aerodynamics

3.1 Introduction

Having reviewed some of the recent developments in the field of bridge aerodynamics previously, this chapter presents the theoretical formulation and certain aspects of selected and novel aerodynamic models and methods. Before describing the structure of this chapter and its contents, the coupled model of wind-bridge interaction is approached conceptually.

The coupled model consists of two models describing the immersed structure and surrounding fluid. Thus, the modeling domain $\mathcal{D}$ entails a body domain $\mathcal{G}$ and a fluid domain $\mathcal{F}$, such that $\mathcal{D} = \mathcal{G} \cup \mathcal{F}$, including an interface $\mathcal{B}$ that encompasses $\mathcal{G}$, as depicted in Fig. 3.1 (left). Aside from the structural and fluid model, appropriate boundary conditions are satisfied on the interface. In what follows, the structural and fluid models are formulated, with particular emphasis on the aerodynamic forces acting on the body as a consequence of the fluid-structure interaction.

Initially, the structural model is briefly outlined in Sec. 3.2 as it is of secondary importance for the purpose of this work. Next, the modeling random free-stream turbulence is revisited in Sec. 3.3, firstly by describing the free-stream turbulence using the spectral representation, and then by explaining the generation process of fluctuating wind velocities as stationary Gaussian random processes. In this sense, the free-stream turbulence then serves as an input for the aerodynamic models of the buffeting forces.

Since the semi-analytical aerodynamic models for bridge decks rest on the foundations of the analytical model for a flat plate, this model is first briefly discussed in Sec. 3.4 in terms of steady,

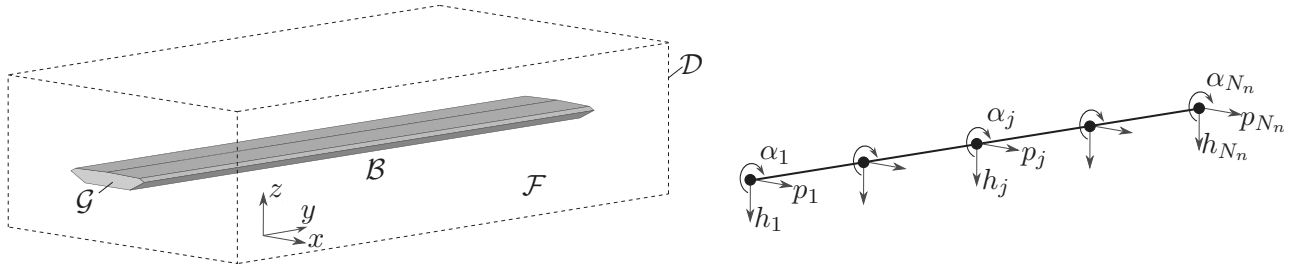

Figure 3.1: Coupled model of wind-bridge interaction: formulation (left); discretization of the structural model (right).

linear unsteady and quasi-steady aerodynamic assumptions. These assumptions represent the pivotal points of twelve semi-analytical models defined in Sec. 3.5. Ten of these models are implemented in a computer code that is used in the applications' chapters. Moreover, a simple method for computation of the buffeting forces based on the FFT is given in Sec. 3.5.7.

Further, a CFD model based on the VPM as a numerical discretization scheme is formulated in Sec. 3.6. Two particular extensions of the VPM models are revisited including the velocity-based method for simulating random free-stream turbulence and the laminar Pseudo-3D method. These two extensions represent a basis for the new turbulent Pseudo-3D VPM, introduced in Sec. 3.6.4.

Aerodynamic coefficients represent the link between the CFD and semi-analytical models. Methods for determination of the aerodynamic coefficients are briefly recalled towards the end of the chapter, in Sec. 3.7. As a part of this section, a novel method for the determination of the complex aerodynamic admittance under deterministic gusts is introduced as well.

Apart from introducing new methods, the main notion of the chapter is to formally define the aerodynamic models, which complexity is evaluated utilizing a category theory-based approach in the next chapter. As the foundation of this modeling approach is the mathematical constructions (i.e. equations), the models are defined in such a manner to offer a clear distinction where assumptions are made in their formulation.

3.2 Structural model

The governing equations of the body (i.e. bridge deck) can take a wide variety of forms depending on the physical assumptions made. Adopting weaker assumptions, the structural model can be formulated in a complex manner in terms of nonlinear partial differential equations from solid mechanics. Alternatively, the structural model can be constructed in a simplified fashion by reducing dimensions in terms of plate and beam theories and posing stronger assumptions such as linearity. As the structural model is of secondary importance in this work, the bridge deck is modeled by the Euler-Bernoulli linear beam theory using the standard Finite Element Method for the spatial discretization (cf. e.g. [20, 67]).

The domain of the body $\mathcal{B}$ (cf. Fig. 3.1, left) is reduced to a beam model in $\mathbb{R}^3$ domain with $N_n \in \mathbb{N}$ number of nodes at discrete locations $\boldsymbol{x}_{sj} = (x_{sj}, y_{sj}, z_{sj})$, for $j \in \{1, \dots, N_n\}$ (cf. Fig. 3.1, right). Since most of the aerodynamic models are developed for sectional models in $\mathbb{R}^2$ domain, each node corresponds to three degrees of freedom in the vertical direction $h = h(\boldsymbol{x}_s; t)$, lateral direction $p = p(\boldsymbol{x}_s; t)$ and torsional rotation about the bridge axis $\alpha = \alpha(\boldsymbol{x}_s; t)$. The governing equation of motion for a system in dynamic equilibrium is

$$\boldsymbol{M}_o \ddot{\boldsymbol{q}}_o + \boldsymbol{C}_o \dot{\boldsymbol{q}}_o + \boldsymbol{K}_o \boldsymbol{q}_o = \boldsymbol{f}_o, \tag{3.1}$$

where $\boldsymbol{M}_o$, $\boldsymbol{C}_o$, $\boldsymbol{K}_o$ are the mass, damping and stiffness matrices, respectively, while $\boldsymbol{f}_o = \boldsymbol{f}_o(t)$ is the force vector comprised of the drag $D = D(\boldsymbol{x}_s; t)$, lift $L = L(\boldsymbol{x}_s; t)$ and moment $M = M(\boldsymbol{x}_s; t)$ forces at all locations $\boldsymbol{x}_s$. The displacement vector is denoted as $\boldsymbol{q}_o = \boldsymbol{q}_o(t)$ along with its corresponding time derivatives $\dot{\boldsymbol{q}}_o = \dot{\boldsymbol{q}}_o(t)$ and $\ddot{\boldsymbol{q}}_o = \ddot{\boldsymbol{q}}_o(t)$.

The size of the coupled matrices and vectors in (3.1) is in $\mathbb{R}^{3N_n \times 3N_n}$ and $\mathbb{R}^{3N_n \times 1}$, respectively; hence, the numerical solution can be computationally demanding for large N_n. Under the linear assumption, (3.1) can be reduced by the mode generalized approach as

$$\boldsymbol{M}\ddot{\boldsymbol{q}} + \boldsymbol{C}\dot{\boldsymbol{q}} + \boldsymbol{K}\boldsymbol{q} = \boldsymbol{f}, \tag{3.2}$$

where the modal mass, damping and stiffness matrices are

$$\boldsymbol{M} = \boldsymbol{\Psi}^T \boldsymbol{M}_o \boldsymbol{\Psi}, \quad \boldsymbol{C} = \boldsymbol{\Psi}^T \boldsymbol{M}_o \boldsymbol{\Psi}, \quad \boldsymbol{K} = \boldsymbol{\Psi}^T \boldsymbol{K}_o \boldsymbol{\Psi}, \tag{3.3}$$

respectively, while the modal displacement $\boldsymbol{q} = \boldsymbol{q}(t)$ and force vectors $\boldsymbol{f} = \boldsymbol{f}(t)$ yield

$$\boldsymbol{q} = \boldsymbol{\Psi}^T \boldsymbol{q}_o, \quad \boldsymbol{f} = \boldsymbol{\Psi}^T \boldsymbol{f}_o, \tag{3.4}$$

respectively, for $(\cdot)^T$ denoting transpose operation. The modal velocity $\dot{\boldsymbol{q}} = \dot{\boldsymbol{q}}(t)$ and acceleration $\ddot{\boldsymbol{q}} = \ddot{\boldsymbol{q}}(t)$ vectors can be obtained in a similar fashion as the modal displacements. In (3.3) and (3.4), $\boldsymbol{\Psi}$ is the mode shape matrix which is formulated from the mode shapes $\boldsymbol{\psi}$ (i.e. eigenvectors), which obtained from the eigenvalue analysis of (3.1).

The modal matrices in (3.3) are diagonal with size in $\mathbb{R}^{N_m \times N_m}$, while the length of the modal vectors is in $\mathbb{R}^{N_m \times 1}$, where $N_m \in \mathbb{N}$ is the number of selected vibration modes. Although the maximum number of modes is $N_m = 3N_n$, usually few modes have a significant contribution to the response for wind-induced loads. Hence, the system order is significantly reduced, rendering efficient computation of (3.2).

The aerodynamic forces acting on the bridge deck are typically formulated in $\mathbb{R}^2$ domain, while their span-wise correlation is imposed by the structural motion and the wind field in case of free-stream turbulence. This is a consequence of the strip assumption, which will be discussed as a part of the critical remarks in the last chapter. Therefore, it is useful to define the structural model (SM) in $\mathbb{R}^2$ as a three-degree-of-freedom system as

$$\mathbf{SM} := \begin{cases} m_p \ddot{p} + c_p \dot{p} + k_p p = D, \\ m_h \ddot{h} + c_h \dot{p} + k_h h = L, \\ m_\alpha \ddot{\alpha} + c_\alpha \dot{\alpha} + k_\alpha \alpha = M, \end{cases} \tag{3.5}$$

where $m_p = m_h$ is the inertial mass; m_α is the mass moment of inertia; c_p, c_h, c_α are the damping coefficients and k_p, k_h, k_α are the spring stiffnesses, all in terms of lateral p, vertical h and rotational α displacements, respectively. For this system, the modal displacement and force vectors yield $\boldsymbol{q} = (p, h, \alpha)$ and $\boldsymbol{f} = (D, L, M)$, respectively. The advancement in time of (3.2) and (3.5) is performed by the standard Newmark-beta method (cf. e.g. [67]).

3.3 Synthetic free-stream turbulence

In this section, the method for the generation of free-stream turbulence as a stationary Gaussian process is briefly explained. Initially, the free-stream turbulence is described based on the spectral representation, utilizing the adapted von Kármán spectra for engineering applications. The wind velocities are then generated as multivariate stationary Gaussian random processes.

The generated wind velocities are used for two purposes, namely: (i) to obtain buffeting forces for the semi-analytical aerodynamic models, and (ii) to simulate free-stream turbulence for the CFD model. The latter requires further steps to impose the governing equations of the fluid, which will be discussed later in Secs. 3.6.2 and 3.6.4.

3.3.1 Spectral representation of the wind field

Consider a zero-mean homogeneous fluctuating fluid velocity $\boldsymbol{u}^* = \boldsymbol{u}^*(\boldsymbol{x})$ as a continuous stationary stochastic process in $\mathbb{R}^3$. The correlation velocity tensor $\boldsymbol{\mathcal{R}} = \boldsymbol{\mathcal{R}}(\boldsymbol{\Delta x})$ for separation distance $\boldsymbol{\Delta x} = (\Delta x, \Delta y, \Delta z)$ can be obtained in a similar fashion as in (2.7) (cf. e.g. [19, 211]). Taking an ensemble average for the tensor product of the velocity vectors yields

$$\boldsymbol{\mathcal{R}}(\boldsymbol{\Delta x}) = \langle \boldsymbol{u}^*(\boldsymbol{x}) \otimes \boldsymbol{u}^*(\boldsymbol{x} + \boldsymbol{\Delta x}) \rangle \,, \tag{3.6}$$

where $\otimes$ denotes the tensor product and $\langle \cdot \rangle$ the ensemble-average operation. Same symbol is used for time and ensemble averaging since all stochastic processes are considered to be mean-ergodic in this work. The correlation tensor is Hermitian, i.e. $\boldsymbol{\mathcal{R}}(\boldsymbol{\Delta x}) = \boldsymbol{\mathcal{R}}(-\boldsymbol{\Delta x}) = \overline{\boldsymbol{\mathcal{R}}}(\boldsymbol{\Delta x})$, for $\overline{(\cdot)}$ denoting conjugate complex operation. Analogous to the Wiener-Khinchin theorem (2.10), the spectral velocity tensor $\boldsymbol{\mathcal{S}} = \boldsymbol{\mathcal{S}}(\boldsymbol{\kappa})$ is obtained by taking the Fourier transform of (3.6) as

$$\boldsymbol{\mathcal{S}}(\boldsymbol{\kappa}) = \frac{1}{(2\pi)^3} \int_{-\infty}^{\infty} \boldsymbol{\mathcal{R}}(\boldsymbol{\Delta x}) \exp(-i\boldsymbol{\kappa} \cdot \boldsymbol{\Delta x}) \mathrm{d}\boldsymbol{\Delta x}, \tag{3.7}$$

where $\int_{-\infty}^{\infty} \mathrm{d}\boldsymbol{\Delta x} = \iiint_{\infty}^{\infty} \mathrm{d}\Delta x \mathrm{d}\Delta y \mathrm{d}\Delta z$ and $\boldsymbol{\kappa} = (\kappa_x, \kappa_y, \kappa_z)$ is the wavenumber vector. Similarly as the correlation tensor, the spectral tensor is Hermitian, i.e. $\boldsymbol{\mathcal{S}} = \overline{\boldsymbol{\mathcal{S}}}$.

For isotropic turbulence and incompressible flow [19], the spectral tensor becomes

$$\boldsymbol{\mathcal{S}} = \frac{E}{4\pi\kappa^4} \left(\boldsymbol{\mathcal{I}}\kappa^2 - \boldsymbol{\kappa} \otimes \boldsymbol{\kappa} \right), \tag{3.8}$$

where $E = E(\kappa)$ is the energy spectrum of turbulence, $\boldsymbol{\mathcal{I}}$ is the identity tensor, while κ is the wavenumber magnitude, obtained as

$$\kappa = \|\boldsymbol{\kappa}\| = \sqrt{\kappa_x^2 + \kappa_y^2 + \kappa_z^2}. \tag{3.9}$$

Based on the energy spectrum, the turbulent kinetic energy (TKE) per unit mass is

$$\mathrm{TKE} = \int_0^{\infty} E(\kappa) \mathrm{d}\kappa = \frac{1}{2} \left\langle \|\boldsymbol{u}^*(\boldsymbol{x})\|^2 \right\rangle = \frac{1}{2} \left(\sigma_u^2 + \sigma_v^2 + \sigma_w^2 \right) = \frac{3}{2} \sigma_{\mathrm{iso}}^2, \tag{3.10}$$

where $\sigma_j^2 = \sigma_{iso}^2$ for $j \in \{u, v, w\}$ is the variance of turbulent wind fluctuations. This relates the turbulence intensity (cf. Sec. 2.2) to the energy spectrum. von Kármán [336] suggested an interpolation formula of the energy spectrum based on reasoning from Navier-Stokes equations. The well-known von Kármán energy spectrum (cf. e.g. [247, 352]) is given by

$$E = \frac{55}{9} \frac{\Gamma^*(5/6)}{\sqrt{\pi}\Gamma^*(1/3)} \frac{\sigma_{iso}^2 \kappa^4 L_T^5}{\left[1 + (kL_T)^2\right]^{17/6}}, \tag{3.11}$$

where Γ^* is the gamma function and L_T is the von Kármán length scale. By specifying the length scale and variance of the fluctuations, the complete wind field is defined analytically. However, it is difficult to measure the spectral tensor directly.

Alternatively, the velocity field can be described by the spectral matrix (cf. e.g. [212, 247]), which is significantly easier to be determined from experiments. The relation between the two-sided spectral velocity matrix $\boldsymbol{S}_{\boldsymbol{u}}^* = \boldsymbol{S}_{\boldsymbol{u}}^*(\kappa_x, \Delta y, \Delta x)$ and spectral tensor for points in the $y - z$ plane is

$$\boldsymbol{S}_{\boldsymbol{u}}^*(\kappa_x; \Delta y, \Delta x) = \int_{-\infty}^{\infty} \boldsymbol{\mathcal{S}}(\boldsymbol{\kappa}) \exp\left[i(\kappa_y \Delta y + \kappa_z \Delta z)\right] \mathrm{d}\boldsymbol{\kappa}_{\perp}, \tag{3.12}$$

where $\int_{-\infty}^{\infty} \mathrm{d}\boldsymbol{\kappa}_{\perp}, = \iint_{\infty}^{\infty} \mathrm{d}\kappa_y \mathrm{d}\kappa_z$, with the spectral matrix being Hermitian, i.e. $\boldsymbol{S}_{\boldsymbol{u}}^* = \overline{\boldsymbol{S}_{\boldsymbol{u}}^*}$. Principally, there is no additional information in the spectral matrix compared to the spectral tensor [212, 213]. However, it is significantly easier to obtain the parameters that define the spectral matrix from a practical aspect. The entries of this matrix are defined in what follows.

One-point spectra

For a single point, the spectrum in the longitudinal direction is obtained by substituting (3.11) and (3.8) in (3.12) and setting $\Delta y = \Delta z = 0$. Proceeding with the integration [212, 352], the longitudinal spectrum yields

$$S_u^*(\kappa_x) = S_{uu}^*(\kappa_x; 0, 0) = \frac{\Gamma^*(5/6)}{\sqrt{\pi}\Gamma^*(1/3)} \frac{\sigma_u^2 L_T}{\left[1 + (\kappa_x L_T)^2\right]^{5/6}}. \tag{3.13}$$

From this, the more commonly used single-sided spectrum $S_u(f)$, which is dependent on the frequency $f = U\kappa_x/(2\pi)$, is obtained as

$$S_u(f) = 2S_u^*(f) = \frac{4\pi}{U} S_u^*(\kappa_x). \tag{3.14}$$

The von Kármán length scale is common (i.e. resultant) to all three components of the spectral tensor. From (3.13), the longitudinal length scale L_u is obtained as

$$L_u = \frac{\sqrt{\pi}\Gamma^*(5/6)}{\Gamma^*(1/3)} L_T \cong \frac{3}{4} L_T. \tag{3.15}$$

In this form, L_u is interpreted in the same way as in Sec. 2.2, i.e. as averaged length of the eddies. Changing (3.14) and (3.15) into (3.13), the von Kármán longitudinal spectrum becomes

$$\frac{f S_u(f)}{\sigma_u^2} = \frac{4 f L_u/U}{\left[1 + 70.8(f L_u/U)^2\right]^{5/6}}. \tag{3.16}$$

In a similar manner as for the longitudinal spectra, the lateral and vertical spectra can be obtained as

$$S_j^*(\kappa_x) = S_{jj}^*(\kappa_x, 0, 0) = \frac{1}{2} \frac{\Gamma^*(5/6)}{\sqrt{\pi}\Gamma^*(1/3)} \frac{\sigma_j^2 L_T \left[1 + 8/3(\kappa_x L_T)^2\right]}{\left[1 + (\kappa_x L_T)^2\right]^{11/6}}, \text{ for } j \in \{v, w\}. \tag{3.17}$$

Taking the lateral L_v and vertical L_w length scales as

$$L_v = L_w = \frac{1}{2} \frac{\sqrt{\pi}\Gamma^*(5/6)}{\Gamma^*(1/3)} L_T \cong \frac{3}{8} L_T, \tag{3.18}$$

and using (3.14) in (3.17), the single-sided Kármán lateral and vertical spectra yield

$$\frac{f S_j(f)}{\sigma_j^2} = \frac{4 f L_j/U \left[1 + 755.2(f L_j/U)^2\right]}{\left[1 + 283.2(f L_j/U)^2\right]^{11/6}}, \text{ for } j \in \{v, w\}. \tag{3.19}$$

Some properties can be deduced from the analytical one-point spectra for isotropic turbulence. First, all one-point cross-spectra are zero, i.e. $S_{jk}/S_{jk} = 0$ for $j, k \in \{u, v, w\}$ such that $j \neq k$; hence, the variance of the cross velocity component is also zero $\sigma_{jk} = 0$. Second, it can be gathered from (3.18) and (3.15) that the longitudinal length scale is two-times larger than the lateral and vertical length scales, i.e. $L_u/L_v = L_u/L_w = 2$. Third, the ratio between the longitudinal and lateral or longitudinal spectra amounts to $S_v/S_u = S_w/S_u = 4/3$ for a large part of the frequencies.

Two-point spectra

The cross-spectra between points $\boldsymbol{x}_j = (x_j, y_j, z_j)$ and $\boldsymbol{x}_k = (x_k, y_k, z_k)$ at distance $\boldsymbol{\Delta x}_{jk} = (0, \Delta y_{jk}, \Delta z_{jk})$ is denoted as

$$S^*_{a_j b_k}(\kappa_x) = S^*_{ab}(\kappa_x; \Delta y_{jk}, \Delta z_{jk}), \quad \text{for } a, b \in \{u, v, w\}\,; \quad j, k \in \{1, \dots, N_{wp}\}\,, \tag{3.20}$$

where $N_{wp} \in \mathbb{N}$ is the number of points in the fluid domain. The cross-spectra can be obtained in a similar way as the point spectra, by substituting (3.8) and (3.11) in (3.12) for $\|\boldsymbol{\Delta x}_{jk}\| \neq 0$.

A more meaningful physical interpretation is obtained by the use of coherence, i.e. the normalized cross-spectra. The magnitude-squared coherence is given by

$$coh^2_{a_j b_k}(f) = coh^2_{ab}(f; \Delta y_{jk}, \Delta z_{jk}) = \frac{\Re\left[S_{a_j b_k}(f)\right]^2 + \Im\left[S_{a_j b_k}(f)\right]^2}{S_a(f) S_b(f)}, \tag{3.21}$$

where $\Re(\cdot)$ and $\Im(\cdot)$ denote the real and imaginary parts, respectively. As derived by Irwin [143], the coherences for the von Kármán energy spectrum yield the following:

$$\begin{aligned}
coh_{u_j u_k}(f) &= 0.994\left[A_t^{5/6} K_{5/6}(A_t) - 0.5 A_t^{11/6} K_{1/6}(A_t)\right], \\
coh_{v_j v_k}(f) &= 0.994\left[A_t^{5/6} K_{5/6}(A_t) + \frac{283.2(fL_v/U)^2}{1 + 755.2(fL_v/U)^2} A_t^{11/6} K_{1/6}(A_t)\right], \\
coh_{w_j w_k}(f) &= 0.994\left[A_t^{5/6} K_{5/6}(A_t) - \frac{1}{1 + 755.2(fL_w/U)^2} A_t^{11/6} K_{1/6}(A_t)\right],
\end{aligned} \tag{3.22}$$

where $K_{5/6} = K_{5/6}(A_t)$ and $K_{1/6} = K_{1/6}(A_t)$ are modified Bessel functions of second kind and

$$A_t = 0.747 \frac{\|\Delta \boldsymbol{x}\|}{L_u} \sqrt{1 + 70.8(fL_u/U)^2}. \tag{3.23}$$

Isotropy also implies that the cross-coherence $coh_{u_j w_k} = 0$; however, $coh_{uv} \neq 0$ [181].

Wind engineering adaptation

Isotropic conditions are rarely met in the atmospheric boundary layer. The measured turbulence variances in the atmosphere depend on the height above ground, roughness length, mean wind velocity, and Coriolis parameter. Generally, the relation $\sigma_w < \sigma_v < \sigma_u$ is obtained for anisotropic turbulence. From a collection of measurements close to the ground, Solari and Piccardo [305] give estimates of the turbulence ratios of $\langle \sigma_v / \sigma_u \rangle = 0.75$ and $\langle \sigma_v / \sigma_w \rangle = 0.50$. Similarly, the ratio of the length scales do not agree with the ratio of 2 obtained previously for the von Kármán spectra, i.e. $\langle L_u / L_v \rangle = 4$ and $\langle L_u / L_w \rangle = 10$.

To obtain a design spectra, a generic spectral function, such as (3.16) and (3.19), is fitted to measurement data using parameters such as the length scales. Various spectral functions have been proposed in the literature as the von Kármán spectra are not consistent with the atmospheric conditions and Kolomorgov's hypotheses in the high-frequency range due to anisotropy and shear (i.e. inhomogeneity) [301]. Some of the most widely used models of spectral distribution include the ones by Haris [132], Kaimal [157], and ESDU [100] (cf. [248, 302, 305] for an excellent overview). While these models usually result in a better fit to measurements, the main disadvantage is that they are mostly empirical and do not have a general energy spectrum (cf. (3.11)); thus, they lack spectral tensor description of the velocity field (cf. (3.8)).

Furthermore, the von Kármán coherence does not comply with the measurements as a consequence of the anisotropic behavior. Based on the principle of geometric similarity, Davenport [73, 74] introduced a simple, yet useful, expression for the coherence. Extended for all three directions [305], Davenport coherence is given as follows:

$$coh_{jk} = coh_{a_j b_k}(\Delta \boldsymbol{x}; f) = \exp\left(-\frac{f}{U}\boldsymbol{c}_x \cdot |\Delta \boldsymbol{x}|\right), \tag{3.24}$$

where $\boldsymbol{c}_x = (C_x, C_y, C_z) > 0$ is the coherence decay coefficient vector, and $|\cdot|$ denotes a point-wise absolute value. The concept of geometric similarity implies that the coherence w.r.t. the normalized distance $f\Delta j/U$ for $j \in \{x, y, z\}$ is similar, and $coh \to 1$ for $f \to 0$. This is not the case for the von Kármán coherence (cf. Fig. 3.2, right). There has been many modifications of the Davenport coherence (cf. Solari [305] for discussion and review). In some formulations, (3.24) contains nine coherence decay coefficients, which can be used to fit the measured data. Vickery [334] proposed to utilize the second norm instead of the absolute value in (3.25). The extended format [267, 305] of Vickery's coherence reads

$$coh_{jk} = coh_{a_j b_k}(\Delta \boldsymbol{x}; f) = \exp\left(-\frac{f}{U}\left\|\boldsymbol{c}_x \odot \Delta \boldsymbol{x}\right\|\right), \tag{3.25}$$

where $\odot$ denotes a point-wise multiplication. This formulation is termed as Vickery coherence.

To describe the free-stream turbulence, the von Kármán point-spectra (cf. (3.16) and (3.19)) and Vickery coherence (cf. (3.25)) are used in this work. The Davenport coherence (3.24) is utilized in some instances for CFD-based free-stream turbulence to simplify the Vickery coherence. Since aerodynamic forces in the span-wise direction are neglected, the lateral spectrum amounts to $S_v = 0$. Further, the point cross-spectra is neglected, i.e. $S_{uw} = 0$. The reason for this is due to the particular simulation method of free-stream turbulence for the CFD model, which will be discussed in Sec. 3.6.2. The general formulation of the spectral matrix finally yields

$$S_{a_j a_k} = S_{a_j a_k}(\Delta \boldsymbol{x}; f) = \sqrt{S_a S_a} coh_{jk} \exp\left(-i 2\pi f \theta_{jk}\right), \tag{3.26}$$

where $a \in \{u, w\}$ and θ_{jk} is the phase angle for points separated in the stream-wise direction. Based on Taylor's hypothesis [194], this angle is obtained as

$$\theta_{jk} = \frac{\Delta x_{jk}}{U}. \tag{3.27}$$

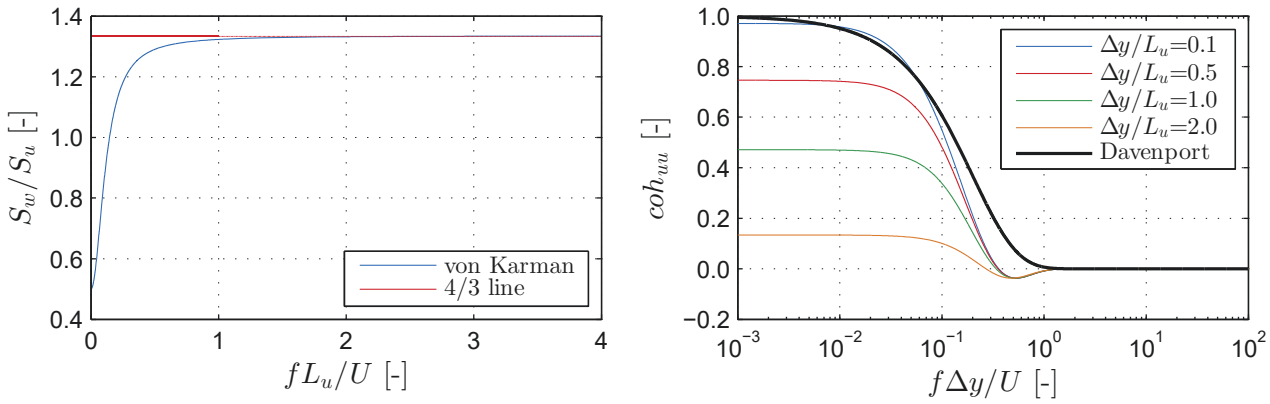

Figure 3.2: Properties of von Kármán spectra: ratio between vertical and longitudinal fluctuations (left); comparison of von Kármán spectra velocity coherence for points with different lateral separation with the Davenport coherence. If there is only lateral separation the Davenport coherence is similar to the Vickery coherence.

The incentive for using the von Kármán spectra is that they are based on the Navier-Stokes equations and the energy spectrum, which gives a physical representation of the turbulence field to a certain extent. This is of particular importance for the simulation of free-stream turbulence for the CFD model. Moreover, the 4/3 ratio of the lateral and vertical spectrum w.r.t. the longitudinal spectrum is retained as there is local isotropy in the inertial subrange [248] (cf. Fig. 3.2, left). Several studies (cf. e.g. [44, 140, 254]) have reported that the von Kármán describes relatively well the atmospheric turbulence with for the design of structures with low natural frequencies [301]. The condition of the coherence to asymptotically tend to unity for low frequencies is generally not true in atmospheric [212, 214] or wind tunnel conditions [187]; however, several studies have shown the principle geometric similarity to be sufficiently adequate for wind engineering purposes (cf. e.g. [44, 140, 182, 254, 305]). With this, a rather flexible description of the spectral matrix (cf. (3.26)) is obtained.

It is noted that to obtain synthetic free-stream turbulence that satisfies the continuity condition of the Navier-Stokes equations, a description based on the spectral tensor is required [178]. This is not of particular importance for the semi-analytical models; however, it can result in a loss of the TKE for the CFD model. For atmospheric turbulence, Mann [212] proposed such tensor based on the rapid distortion theory, which has been validated with measurements from the atmosphere [75, 212]. Since the free-stream turbulence herein is simulated as a one-dimensional multivariate process, rather than two- or three-dimensional, the continuity equation is additionally imposed for the CFD model, as discussed further in Sec. 3.6.2.

3.3.2 Generation of stationary Gaussian processes

Once the spectral matrix is defined, the next step involves the generation of spatially correlated wind time-histories as random stationary Gaussian processes using the spectral method (cf. e.g. [79, 298, 299]). Initially, the concept of spectral representation for a univariate process is explained. Based on the same principles, the generation of the wind field as a multivariate process is established.

Univariate process

Consider a zero-mean univariate one-dimensional random process $u = u(t)$ with two-sided spectrum $S_u^* = S_u^*(\omega)$. Utilizing the spectral representation by Priestley [259], a random process can be described using a stochastic integral as a

$$u(t) = \int_{-\infty}^{\infty} \exp(i\omega t)\, \mathrm{d}\vartheta(\omega), \tag{3.28}$$

where $\vartheta = \vartheta(\omega)$ is a complex random process with random increment $\mathrm{d}\vartheta = \mathrm{d}\vartheta(\omega)$, describing the random phases and spectral amplitudes. Assuming the spectrum is continuous and $S_u^*(\omega) \geq 0$, a normalized version of the spectral process (cf. e.g. [210, 249]) is obtained as

$$\vartheta^*(\omega) = \int_{-\infty}^{\omega} \frac{\mathrm{d}\vartheta(\omega_1)}{\sqrt{S_u^*(\omega_1)}} \mathrm{d}\omega_1, \tag{3.29}$$

which simplifies (3.28) as

$$u(t) = \int_{-\infty}^{\infty} \exp(i\omega t)\, \sqrt{S_u^*(\omega)} \mathrm{d}\vartheta^*(\omega). \tag{3.30}$$

The increments $\mathrm{d}\vartheta^*$ of the normalized spectral process (i.e. normalized random Fourier increment) are orthogonal; thus, they satisfy the following orthogonality conditions:

$$\begin{aligned} \langle \mathrm{d}\vartheta^*(\omega) \rangle &= 0, \\ \left\langle \mathrm{d}\vartheta^*(\omega)\mathrm{d}\overline{\vartheta^*}(\omega) \right\rangle &= \mathrm{d}\omega, \\ \left\langle \mathrm{d}\vartheta^*(\omega_1)\mathrm{d}\overline{\vartheta^*}(\omega_2) \right\rangle &= 0, \qquad \text{for } \omega_1 \neq \omega_2. \end{aligned} \tag{3.31}$$

Rewriting (3.30) as

$$\begin{aligned} u(t) &= \int_0^\infty \exp(i\omega t)\sqrt{S_u^*(\omega)}\mathrm{d}\vartheta^*(\omega) + \int_{-\infty}^0 \exp(i\omega t)\sqrt{S_u^*(\omega)}\mathrm{d}\vartheta^*(\omega) \\ &= \int_0^\infty \exp(i\omega t)\sqrt{S_u^*(\omega)}\mathrm{d}\vartheta^*(\omega) + \int_0^\infty \exp(-i\omega t)\sqrt{S_u^*(-\omega)}\mathrm{d}\vartheta(-\omega), \end{aligned} \tag{3.32}$$

and since the increments are Hermitian for real processes i.e. $d\vartheta^*(-\omega) = d\overline{\vartheta^*}(\omega)$ [46], the spectral representation of $u = u(t)$ reduces to

$$u(t) = 2\Re\left[\int_0^\infty \exp(i\omega t)\sqrt{S_u^*(\omega)}\mathrm{d}\vartheta^*(\omega)\right], \tag{3.33}$$

which represents a Fourier-Stieltjes integral. The normalized Fourier increment can be described by $\mathrm{d}\vartheta^*(\omega) = \varrho\mathrm{d}\omega$, where $\varrho = \varrho(\omega)$ is a complex-valued, uncorrelated white noise with unit variance; hence, (3.33) yields

$$u(t) = 2\Re\left\{\int_0^\infty \exp(i\omega t)\sqrt{S_u^*(\omega)}\varrho(\omega)\mathrm{d}\omega\right\}. \tag{3.34}$$

Assuming constant spectral amplitudes, the white noise can be represented using a random phase $\varphi^R \sim \mathcal{U}[0, 2\pi)$ for each harmonic, where $\mathcal{U}$ denotes the uniform distribution. Taking this into account, the discrete form of (3.34) yields

$$u(t) = 2\Re\left[\sum_{l=0}^{N_f-1} \sqrt{S_u^*(\omega_l)\Delta\omega}\exp\left[i\omega_l t + i\varphi_l^R\right]\right], \tag{3.35}$$

where $N_f \in \mathbb{N}$ is the number of discrete frequencies and $\Delta\omega$ is the increment of the circular frequency. It is easy to realize from (3.35) that FFT can be used to generate random signals by introducing a random phase for a prescribed spectral density.

Multivariate process

In the case of a multivariate one-dimensional correlated process, the fluctuating velocity field can be discretized on N_{wp} number of points as follows [249]:

$$\boldsymbol{u}^*(\boldsymbol{x};t) \implies \boldsymbol{u}^*(t) = \left\{u_1(t), \ldots, u_{N_{wp}}(t), w_1(t), \ldots, w_{N_{wp}}(t)\right\}. \tag{3.36}$$

In a similar fashion as for a univariate process (cf. (3.28)), the velocity field can be described as

$$\boldsymbol{u}^*(t) = \int_{-\infty}^\infty \exp(i\omega t)\,\boldsymbol{H}(\omega)\mathrm{d}\boldsymbol{\vartheta}^*(\omega), \tag{3.37}$$

where now $\boldsymbol{\vartheta}^*$ is a normalized Fourier increment vector corresponding to the $3N_{wp}$ points, satisfying the following orthogonality conditions:

$$\begin{aligned} \langle \mathrm{d}\boldsymbol{\vartheta}^*(\omega) \rangle &= \mathbf{0}, \\ \left\langle \mathrm{d}\boldsymbol{\vartheta}^*(\omega) \mathrm{d}\overline{\boldsymbol{\vartheta}^*}^T(\omega) \right\rangle &= \mathrm{d}\omega \boldsymbol{J}_{N_{wp}}, \\ \left\langle \mathrm{d}\boldsymbol{\vartheta}^*(\omega_1) \mathrm{d}\overline{\boldsymbol{\vartheta}^*}^T(\omega_2) \right\rangle &= \mathbf{0}, \quad \text{for } \omega_1 \neq \omega_2. \end{aligned} \tag{3.38}$$

where $\boldsymbol{J}_{N_{wp}}$ is a unit matrix (all ones) of size in $\mathbb{R}^{N_{wp} \times N_{wp}}$. The matrix $\boldsymbol{H} = \boldsymbol{H}(\omega)$ satisfies the condition

$$\boldsymbol{S}_{\boldsymbol{u}}^* = \overline{\boldsymbol{H}} \boldsymbol{H}^T, \tag{3.39}$$

where $\boldsymbol{S}_{\boldsymbol{u}}^* = \boldsymbol{S}_{\boldsymbol{u}}^*(\omega)$ is the two-sided spectral matrix which is obtained from (3.26). Thus, in the same analogy to (3.30) for S_u^*, the $\boldsymbol{H}$ matrix contains information regarding the spectral density of the velocity at each point in the diagonal terms. In addition, information regarding the correlation between different points is contained in the off-diagonal terms. Since $\boldsymbol{S}_{\boldsymbol{u}}^*$ is positive definite, $\boldsymbol{H}$ is obtained in (3.39) using Cholesky decomposition. The matrix $\boldsymbol{H}$ represents a complex, lower triangular matrix and it can be represented as

$$\boldsymbol{H} = \sqrt{\boldsymbol{H} \odot \overline{\boldsymbol{H}}} \odot \exp(\boldsymbol{\Theta}), \tag{3.40}$$

where

$$\boldsymbol{\Theta} = \tan^{-1}\left[\Im\left(\boldsymbol{H}\right) \oslash \Re\left(\boldsymbol{H}\right)\right], \tag{3.41}$$

for $\oslash$ denoting the point-wise division.

There are various ways to discretize (3.37), akin to (3.35). Taking (3.40) and (3.41) into account, the efficient discretization by Ruan and McLaughlin [269] and Ding et al.[89] is utilized herein, yielding the following for each process in $\boldsymbol{u}(t)$:

$$a_j(t) = 2\sqrt{\Delta\omega}\Re\left\{\sum_{k=1}^{N_{wp}} \sum_{l=0}^{N_f-1} |H_{jk}(\omega_l)| \exp\left[i\omega_{kl}t + i\Theta_{jk}(\omega_l) + i\varphi_{kl}^R\right]\right\}, \tag{3.42}$$

where $j \in \{1, \ldots, N_{wp}\}$, $a \in \{u, w\}$, $\varphi^R \sim \mathcal{U}[0, 2\pi)$ is a random phase angle, $\omega_l = l\Delta\omega + \Delta\omega/2$ is the single indexing frequency; $\omega_{kl} = l\Delta\omega + k/N_{wp}\Delta\omega$ is the double indexing frequency, $N_f \in \mathbb{N}$ is number of discrete frequencies which corresponds to the upper cutoff frequency $\omega_{\max} = \Delta\omega N_f$, for frequency increment $\Delta\omega$. It is clear from (3.42) that besides the summation over the frequencies, there is a summation over all points, accounting for the cross-correlation. Only the vertical and longitudinal fluctuating velocities are considered in (3.42) and (3.36). Additionally, the one-point cross-spectrum is neglected, i.e. $S_{uw} = 0$. Therefore, the summation in (3.42) is only over N_{wp} instead of $2N_{wp}$, resulting in independent generation of the longitudinal and vertical fluctuations.

Numerical implementation using the Fast Fourier transform

Looking at (3.42), it is obvious that one may take advantage of the FFT to improve the computational efficiency for the generation of wind fluctuations. Noting that $\boldsymbol{H}$ is a lower triangular matrix, (3.42) can be reformulated as

$$a_{j,p} = a_j(p\Delta t) = 2\sqrt{\Delta\omega}\Re\left(\sum_{k=0}^{j} C_{jkp}\right), \tag{3.43}$$

where $a \in \{u, w\}$, $p \in \{0, \ldots, N_s - 1\}$, $N_s = 2N_f$ is the number of time-steps such that $N_s \in \mathbb{N}$, Δt is the time-increment,

$$C_{jkp} = \sum_{l=0}^{N_s-1} B_{jkl} \exp\left(i \frac{2\pi}{N_s} lp\right), \tag{3.44}$$

where

$$B_{jkl} = \begin{cases} |H_{jk}(\omega_l)| \exp\left[i\Theta_{jk}(\omega_l) + i\varphi_{kl}^R\right], & \text{for } 0 \leq l < N_f, \\ 0, & \text{for } N_f \leq l < N_s. \end{cases} \tag{3.45}$$

It can be seen that (3.44) is the inverse FFT of (3.45), which can be solved efficiently utilizing standard FFT libraries. Depending on the definition of the inverse FFT, (3.44) might require multiplication by the number of steps N_s.

3.4 Analytical model: Flat plate

The fundamentals of the modeling of forces in bridge aerodynamics essentially rests on the classical airfoil theory. To be able to assess the semi-analytical aerodynamic models, quantify the effect of aerodynamic assumptions and provide an intrinsic discussion, the essentials of the classical airfoil theory are briefly revisited herein. Thus, the goal is not to provide an extensive overview, rather form foundations for the formulation of the semi-analytical models. Hence, the expressions for the aerodynamic forces are given directly, based on pioneering studies such as the ones by Wagner [339], Küssner [184], Theodorsen [323], Sears [293] and von Kármán and Sears [338], which are summarized in the excellent works by Jones [154], Fung [112], Bisplinghoff et al. [23], and more recently by Dowel [91].

The airfoil is assumed to be infinitely thin, i.e. as a flat plate with chord B in $\mathbb{R}^2$ (cf. Fig. 3.3, left). Two degrees of freedom are considered to completely describe the flat plate motion, in the vertical h and rotational α directions, corresponding to the lift L and moment M forces, respectively. The stiffness center is positioned at the middle of the flat plate, i.e. $\boldsymbol{x}_s = (0, 0)$. At angle $\alpha = 0$, the mean wind speed U is parallel to the flat-plate. The behavior of the aerodynamic forces can be fully described for three states, including steady motion, oscillation, and free-stream vertical gust w. For these states, the following assumptions hold: the flow is potential, the disturbance of the velocity potential is small (i.e. linear superposition principle applies) and the flow leaves the trailing edge smoothly (i.e. the Kutta condition).

Before proceeding further, it is useful to define the following non-dimensional relations, which will be used throughout this work:

$$\tau = \frac{tU}{B}, \quad K = \frac{\omega B}{U}, \quad K^* = \frac{K}{2}, \quad V_r = \frac{2\pi}{K} = \frac{U}{fB}, \tag{3.46}$$

where τ is the reduced time; K is the reduced frequency w.r.t. a circular frequency ω of motion or gust; K^* is the reduced frequency for half chord; and V_r is the reduced velocity. In the following, the aerodynamic forces are obtained for steady, unsteady and quasi-steady aerodynamics.

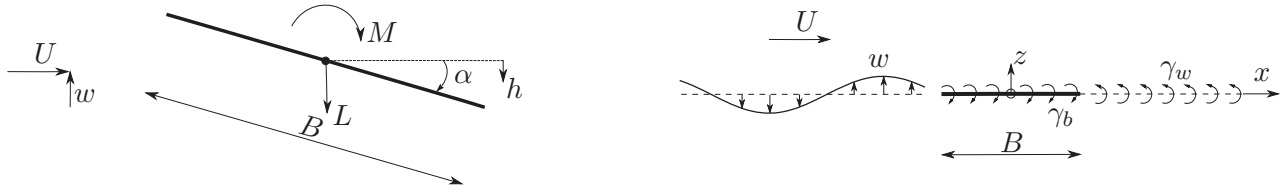

Figure 3.3: Flat plate aerodynamic model: aerodynamic forces acting on a flat plate (left); sources of vorticity due to motion and free-stream gust (right).

3.4.1 Steady aerodynamics

Consider a flat plate under a mean wind speed U at static angle α_s (i.e. time-independent). For a steady flow the forces are time-independent, i.e. $L = L(\boldsymbol{x}_s, \alpha_s)$ and $M = M(\boldsymbol{x}_s, \alpha_s)$. Based on the Kutta-Jukowski theorem, the total lift acting on the airfoil at angle α_s is obtained by integrating the net strength of the bound vortex sheet $\gamma_b = \gamma_b(\boldsymbol{x}, \alpha_s)$ as

$$L = -\rho U \int_{-B/2}^{B/2} \gamma_b(x)\mathrm{d}x = \rho U \Gamma_b, \tag{3.47}$$

where $\Gamma_b = \Gamma_b(\boldsymbol{x}_b)$ is a concentrated bound vortex strength at $\boldsymbol{x}_b = (x_b, z_b)$. The bound vortex sheet strength γ_b is dependent on the downwash velocity $w_a = w_a(\boldsymbol{x})$ on the surface of the flat plate. Since γ_b can be analytically determined (cf. e.g. [23, 112]), the analytical solution for the lift and moment yield

$$L = -\frac{1}{2}\rho U^2 B 2\pi\alpha_s, \quad M = \frac{1}{2}\rho U^2 B^2 \frac{\pi}{2}\alpha_s. \tag{3.48}$$

From (3.48), it can be gathered that the resultant lift force is acting at the front quarter-point, i.e. the concentrated vortex is positioned at $x_b = -0.25B$. Comparing (2.15) and (3.48), the lift and moment coefficients yield

$$C_L = 2\pi\alpha_s = C'_L\alpha_s, \quad C_M = \frac{\pi}{2}\alpha_s = C'_M\alpha_s, \tag{3.49}$$

where the $C'_L = \mathrm{d}C_L/\mathrm{d}\alpha_s$ and $C'_M = \mathrm{d}C_M/\mathrm{d}\alpha_s$ are the derivatives of the lift and moment coefficients w.r.t. α_s, as (3.49) is obviously a linear expression.

3.4.2 Unsteady aerodynamics

Consider a flat plate in an unsteady flow. The aerodynamic forces originate from the motion of the flat plate and free-stream gusts, for which the following three elementary cases are distinguished: translatory harmonic motion (Case 1), rotational harmonic motion (Case 2) and free-stream sinusoidal vertical gust (Case 3). For the motion-induced forces due to harmonic oscillations (Case 1 and Case 2), complete closed-form expressions were first given by Theodrsen [323]. Herein, the formulation by von Kármán and Sears [338] and Sears [293] is used for all elementary cases, as it offers more explicit physical interpretation.

In an unsteady flow, the bound vortex sheet is time-dependent, i.e. $\gamma_b = \gamma_b(x;t)$ for $-B/2 \leq x \leq B/2$ (cf. Fig 3.3, right). Further, there is a vortex sheet in the wake that is induced by the motion with strength $\gamma_w = \gamma_w(x;t)$ for $B/2 \leq x < \infty$. The strength of the bound vortex sheet can be separated as $\gamma_b = \gamma_0 + \gamma_1$, where γ_0 is the quasi-steady part, which would be the total circulation if the wake had no effect, while γ_1 is the wake-induced part, which corresponds to the

strength of the wake vortex sheet γ_w based on the Kelvin circulation theorem. The self-excited aerodynamic forces are obtained using the law of conservation of momentum (which is directly related to the total vortex sheet strength). Hence, the aerodynamic forces are constituted of three parts, namely: (i) quasi-steady part, corresponding to γ_0; (ii) wake part, corresponding to γ_1; and (iii) apparent mass, corresponding to the inertial effects. The aerodynamic forces are dependent on the downwash velocity $w_a = w_a(x;t)$ on the plate surface. For the two cases of oscillations, the lift and moment yield the following:

Case 1. Translatory oscillation: $w_a(x;t) = \dot{h}(t)$

$$\begin{aligned} &L_{\dot{h}}^{\mathrm{QS}} = -\frac{1}{2}\rho U^2 B 2\pi \left(\alpha + \frac{\dot{h}}{U}\right), \quad L_{\dot{h}}^{\mathrm{AM}} = -\frac{1}{4}\rho B^2 \pi \left(U\dot{\alpha} + \ddot{h}\right), \quad L_{\dot{h}}^{\mathrm{W}} = L_{\dot{h}}^{\mathrm{QS}} \left[1 - C(K^*)\right], \\ &M_{\dot{h}}^{\mathrm{QS}} = -L_{\dot{h}}^{\mathrm{QS}} \frac{B}{4}, \qquad\qquad M_{\dot{h}}^{\mathrm{AM}} = 0, \qquad\qquad M_{\dot{h}}^{\mathrm{W}} = -L_{\dot{h}}^{\mathrm{W}} \frac{B}{4}. \end{aligned} \tag{3.50}$$

Case 2. Rotational oscillation: $w_a(x;t) = x\dot{\alpha}(t)$ for $-B/2 \leq x \leq B/2$

$$\begin{aligned} &L_{\dot{\alpha}}^{\mathrm{QS}} = -\frac{1}{2}\rho U^2 B 2\pi \frac{0.25 B\dot{\alpha}}{U}, \quad L_{\dot{\alpha}}^{\mathrm{AM}} = 0, \qquad\qquad L_{\dot{\alpha}}^{\mathrm{W}} = L_{\dot{\alpha}}^{\mathrm{QS}} \left[1 - C(K^*)\right], \\ &M_{\dot{\alpha}}^{\mathrm{QS}} = 0, \qquad\qquad M_{\dot{\alpha}}^{\mathrm{AM}} = -\frac{\pi}{128}\rho c^4 \dot{\alpha}, \quad M_{\dot{\alpha}}^{\mathrm{W}} = -L_{\dot{\alpha}}^{\mathrm{W}} \frac{B}{4}, \end{aligned} \tag{3.51}$$

where the superscripts QS, W and AM correspond to the quasi-steady, wake and apparent mass parts, respectively, while $C = C(K^*)$ is the Theodorsen complex function given as

$$C = \frac{H_1^{(2)}}{H_1^{(2)} + iH_0^{(2)}}, \tag{3.52}$$

for $H_0^{(2)} = H_0^{(2)}(K^*)$ and $H_1^{(2)} = H_1^{(2)}(K^*)$ being Hankel functions of second kind.

Next, consider a harmonic motion comprised of translatory and rotational oscillations (i.e. Case 1 and 2 combined). The total downwash velocity of the flat plate $w_a = w_a(x;t)$ is then

$$w_a = \dot{h} + \alpha U + \dot{\alpha} x. \tag{3.53}$$

Applying the results from (3.50) to the first two terms and from (3.51) to the last term in (3.53), the unsteady self-excited aerodynamic force yield the following:

$$\begin{aligned} L_{se}^{\mathrm{US}} &= -\frac{\pi}{4}\rho B^2 \left(\ddot{h} + U\dot{\alpha}\right) - \frac{1}{2}\rho U^2 B 2\pi C(K^*) \left(\alpha + \frac{\dot{h}}{U} + \frac{0.25 B\dot{\alpha}}{U}\right), \\ M_{se}^{\mathrm{US}} &= -\frac{\pi}{8}\rho B^3 \left(U\dot{\alpha} + \frac{B}{16}\ddot{\alpha}\right) + \frac{1}{2}\rho U^2 B^2 \frac{\pi}{2} C(K^*) \left(\alpha + \frac{\dot{h}}{U} + \frac{0.25 B\dot{\alpha}}{U}\right), \end{aligned} \tag{3.54}$$

which is exactly the form given by Theodorsen [323].

The unsteady buffeting forces due to free-stream sinusoidal gust $w = w(x;t) = w_0 \sin(\omega t)$ can be obtain analogous to (3.50) and (3.51). Instead of the influence of the wake, in this case, the unsteadiness in the aerodynamic forces originates from uneven downwash velocity distribution. Denoting this contribution by the superscript E, the aerodynamic forces yield

Case 3. Sinusoidal gust: $w_a(x;t) = w_0 \exp[i\omega(t - x/U)]$ for $-B/2 \le x \le B/2$

$$\begin{aligned} L_b^{\mathrm{US}} &= -L_w^{\mathrm{QS}} + L_w^{\mathrm{E}} = -L_w^{\mathrm{QS}} + L_w^{\mathrm{QS}}[1 - \chi(K^*)] = -\frac{1}{2}\rho U^2 B 2\pi \chi(K^*)\frac{w}{U}, \\ M_b^{\mathrm{US}} &= -L_b^{\mathrm{US}}\frac{B}{4} = \frac{1}{2}\rho U^2 B^2 \frac{\pi}{2}\chi(K^*)\frac{w}{U}, \end{aligned} \tag{3.55}$$

where $\chi = \chi(K^*)$ is the Sears complex aerodynamic admittance, given as

$$\chi = (J_0 - iJ_1)\, C + iJ_1, \tag{3.56}$$

where $J_0 = J_0(K^*)$ and $J_1 = J_1(K^*)$ are Bessel functions of the first kind.

Summing up the buffeting and self-excited parts, the total unsteady aerodynamic forces yield

$$\begin{aligned} L^{\mathrm{US}} &= -\frac{\pi}{4}\rho B^2\left(\ddot{h} + U\dot{\alpha}\right) - \frac{1}{2}\rho U^2 B 2\pi\left[C(K^*)\left(\alpha + \frac{\dot{h}}{U} + \frac{0.25B\dot{\alpha}}{U}\right) + \chi(K^*)\frac{w}{U}\right], \\ M^{\mathrm{US}} &= -\frac{\pi}{16}\rho B^3\left(U\dot{\alpha} + \frac{B\ddot{\alpha}}{8}\right) + \frac{1}{2}\rho U^2 B^2\frac{\pi}{2}\left[C(K^*)\left(\alpha + \frac{\dot{h}}{U} + \frac{0.25B\dot{\alpha}}{U}\right) + \chi(K^*)\frac{w}{U}\right]. \end{aligned} \tag{3.57}$$

The first term in each expression of (3.57) corresponds to the apparent mass effect. Each term in the square brackets represents an angle corresponding to a particular motion component or the gust. Thus, these terms can be realized as an effective unsteady angle of attack

$$\alpha_e^{\mathrm{US}} = C(K^*)\left(\alpha + \frac{\dot{h}}{U} + \frac{0.25B\dot{\alpha}}{U}\right) + \chi(K^*)\frac{w}{U}. \tag{3.58}$$

The unsteady forces in (3.57) are of mixed nature, i.e. they contain frequency- and time-dependent terms. Wagner [339] and Küssner [184] formulated the unsteady problem in pure time-domain (in fact, chronologically earlier than Theodorsen [323] and Sears [293]), by means of indicial functions corresponding to elementary unit-step motion or gust. The unsteady aerodynamic forces $L^{\mathrm{UN}} = L^{\mathrm{UN}}(\boldsymbol{x}_s;\tau)$ and $M^{\mathrm{UN}} = M^{\mathrm{UN}}(\boldsymbol{x}_s;\tau)$ dependent of the reduced time τ are given as follows:

$$\begin{aligned} L^{\mathrm{UN}} &= -\frac{\pi}{4}\rho U^2\left(h'' + B\alpha'\right) - \frac{1}{2}\rho U^2 B 2\pi\Bigg\{\int_{-\infty}^{\tau}\Phi_{se}(\tau - \tau_1)\left[\alpha'(\tau_1) + \frac{h''(\tau_1)}{B} + 0.25\alpha''(\tau_1)\right]\mathrm{d}\tau_1 \\ &\qquad + \int_{\infty}^{\tau}\Phi_b(\tau - \tau_1)\frac{w'(\tau_1)}{U}\mathrm{d}\tau_1\Bigg\}, \\ M^{\mathrm{UN}} &= -\frac{\pi}{16}\rho B^2 U^2\left(\alpha' + \frac{\alpha''}{8}\right) + \frac{1}{2}\rho U^2 B^2\frac{\pi}{2}\Bigg\{\int_{-\infty}^{\tau}\Phi_{se}(\tau - \tau_1)\left[\alpha'(\tau_1) + \frac{h''(\tau_1)}{B} + 0.25\alpha''(\tau_1)\right]\mathrm{d}\tau_1 \\ &\qquad + \int_{\infty}^{\tau}\Phi_b(\tau - \tau_1)\frac{w'(\tau_1)}{U}\mathrm{d}\tau_1\Bigg\}, \end{aligned} \tag{3.59}$$

where $\Phi_{se} = \Phi_{se}(\tau)$ and $\Phi_b = \Phi_b(\tau)$ are the Wagner and Küssner indicial response functions corresponding to unit step motion and sharp-edged gust, respectively. The prime subscript of the time-dependent terms in (3.59) denotes differentiation w.r.t reduced time, such that

$$h' = \frac{\mathrm{d}h}{\mathrm{d}\tau} = \frac{\mathrm{d}t}{\mathrm{d}\tau}\frac{\mathrm{d}h}{\mathrm{d}t} = \frac{\mathrm{d}t}{\mathrm{d}\tau}\dot{h} = \frac{B}{U}\dot{h}, \quad h'' = \frac{\mathrm{d}^2h}{\mathrm{d}\tau^2} = \left(\frac{\mathrm{d}t}{\mathrm{d}\tau}\right)^2\frac{\mathrm{d}^2h}{\mathrm{d}t^2} + \frac{\mathrm{d}^2t}{\mathrm{d}\tau^2}\frac{\mathrm{d}h}{\mathrm{d}t} = \frac{B}{U}\frac{\mathrm{d}t}{\mathrm{d}\tau}\ddot{h} = \frac{B^2}{U^2}\ddot{h}. \tag{3.60}$$

Similar expressions can be obtained for the rotation. The duality between the frequency and time-domain in (3.57) and (3.59) is realized by means of Fourier-integral superposition, as noted by Garrick [113]. Hence, the relations between the functions of Wagner-Theodorsen and Küssner-Sears yield

$$\Phi_{se}(\tau) = \frac{1}{2\pi i}\int_{-\infty}^{\infty} \frac{C(K^*)}{K^*}\exp(iK^*2\tau)\mathrm{d}K^*, \quad \Phi_b(\tau) = \frac{1}{2\pi i}\int_{-\infty}^{\infty} \frac{\chi(K^*)}{K^*}\exp\left[iK^*(2\tau-1)\right]\mathrm{d}K^*, \tag{3.61}$$

respectively, for $\tau > 0$. It is noted that the reduced time is based on full chord herein, instead of half chord as commonly adopted (cf. e.g. [23, 113]). The preceding integrals are singular at the origin; hence, they are evaluated using the Cauchy's residue theorem. As the integrals yield relatively complicated relations, it is often resorted to approximate forms of Φ_{se} and Φ_b (cf. e.g. [23, 112]), such as:

$$\begin{aligned} \Phi_{se} &\cong 1 - 0.165\exp(-0.089\tau) - 0.335\exp(-0.6\tau), \\ \Phi_b &\cong 1 - 0.5\exp(-0.26\tau) - 0.5\exp(-2\tau), \end{aligned} \tag{3.62}$$

which were obtained by Jones [153] and Sears and Sparks [294], respectively. As noted by Giesing et al. [118], Φ_b in (3.62) is for a gust acting at the leading edge of the flat plate. Theodorsen and Sears functions are depicted in Fig. 3.4 (left), more conveniently w.r.t. the reduced velocity. Both are complex-valued, meaning there is a phase difference between the aerodynamic forces and corresponding motion or gust. Analogous, Wagner and Küssner functions (cf. Fig. 3.4, right) give the rise-time due to unit-step input motion and gust, respectively, at $\tau = 0$. In essence, all of these functions describe the influence of fluid memory.

3.4.3 Quasi-steady aerodynamics

In quasi-steady aerodynamics, it is assumed that the aerodynamic forces are not influenced by the wake effect or non-uniformity of the gust distribution, i.e. unsteadiness of the flow. In other words, the effect of fluid memory is neglected. This corresponds to the following asymptotic

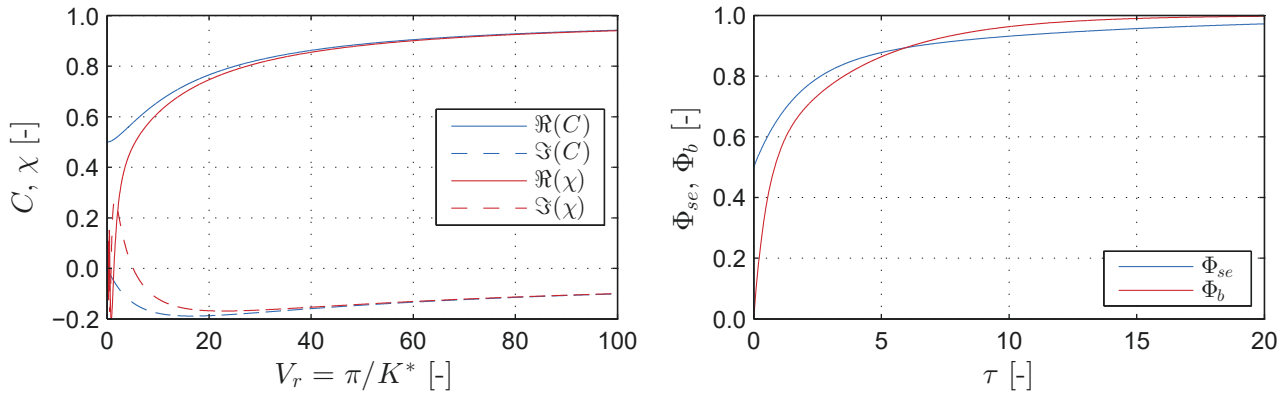

Figure 3.4: Unsteadiness of aerodynamic forces acting on a flat plate: real and imaginary parts of the frequency-dependent Theodorsen (C, cf. (3.52)) and Sears (χ, cf. (3.56)) functions (left); approximation (cf. (3.62)) of the time-domain indicial self-excited Wagner Φ_{se} and buffeting Küssner Φ_b functions (right).

cases (cf. Fig. 3.4):

$$\begin{aligned} \lim_{V_r\to\infty} C(V_r) = 1, \quad \lim_{V_r\to\infty} \chi(V_r) = 1, \\ \lim_{\tau\to\infty} \Phi_{se}(\tau) = 1, \quad \lim_{\tau\to\infty} \Phi_b(\tau) = 1. \end{aligned} \tag{3.63}$$

For these limiting cases, it can be gathered from from (3.50), (3.51) and (3.55) that the forces due to the wake and uneven velocity distribution tend to vanish. Hence, using (3.63) in (3.57) or (3.59), the quasi-steady aerodynamic forces yield

$$\begin{aligned} L^{\mathrm{QS}} &= -\frac{\pi}{4}\rho B^2\left(\ddot{h} + U\dot{\alpha}\right) - \frac{1}{2}\rho U^2 B 2\pi\left(\alpha + \frac{w}{U} + \frac{\dot{h}}{U} + \frac{0.25B\dot{\alpha}}{U}\right), \\ M^{\mathrm{QS}} &= -\frac{\pi}{8}\rho B^3\left(U\dot{\alpha} + \frac{B}{16}\ddot{\alpha}\right) + \frac{1}{2}\rho U^2 B^2 \frac{\pi}{2}\left(\alpha + \frac{w}{U} + \frac{\dot{h}}{U} + \frac{0.25B\dot{\alpha}}{U}\right). \end{aligned} \tag{3.64}$$

It is noted that in some formulations of the quasi-steady theory (cf. e.g. [112]), the apparent mass effect is not taken into account completely. Analogous to the forces, the quasi-steady effective angle of attack is obtained from (3.58) as

$$\alpha_e^{\mathrm{QS}} = \alpha + \frac{w}{U} + \frac{\dot{h}}{U} + \frac{0.25B\dot{\alpha}}{U}. \tag{3.65}$$

3.5 Semi-analytical models

Having introduced the fundamentals of flat plate aerodynamics, the semi-analytical models of aerodynamic forces for bridge decks are presented in this section. In fact most of these models are based on the principles of steady, quasi-steady and unsteady aerodynamics of a flat plate. In essence, the quasi-steady and unsteady state can be considered as aerodynamic assumptions. These two assumptions represent a pivotal point for most of the semi-analytical models; hence, it is useful to define them for bridge decks in a more formal manner.

Adapted from Fung [112], the quasi-steady assumption is defined for the purpose of this work as follows:

Definition 3.1 (Quasi-steady assumption)**.** *The aerodynamic characteristics of a bridge deck for a time-variable angle of attack at any instant of time are the same as the characteristics for an equivalent constant angle of attack.*

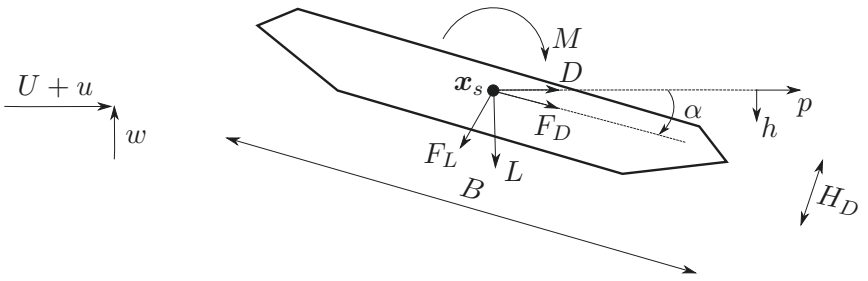

Figure 3.5: Coordinate system of three-degree-of-freedom wind-bridge interaction.

Correspondingly, the linear unsteady assumption is defined as follows:

Definition 3.2 (Linear unsteady assumption)**.** *The aerodynamic characteristics of a bridge deck for a time-variable angle of attack, at any instant of time, are the same as the characteristics considering the evolution of the angle of attack for small amplitudes, where linearity and the superposition principle apply.*

The wind-structure interaction is described for the system depicted in Fig. 3.5. The deck is with width B and depth H_D. The structural model is the one defined in (3.5) for three degrees of freedom. For convenience, three contributions are distinguished in the force vector (and its components) $\boldsymbol{f} = \boldsymbol{f}(\boldsymbol{f}_s, \boldsymbol{f}_b, \boldsymbol{f}_{se})$, corresponding to the static $\boldsymbol{f}_s = \boldsymbol{f}_s(\alpha_s)$ (due to mean wind), buffeting $\boldsymbol{f}_b = \boldsymbol{f}_b(t)$ and self-excited $\boldsymbol{f}_{se} = \boldsymbol{f}_{se}(t)$ parts of the aerodynamic forces. A total of ten models are considered, namely: steady (ST), linear steady (LST), quasi-steady (QS), linear quasi-steady (LQS), corrected quasi-steady (CQS), modified quasi-steady (MQS), mode-by-mode (MQS), complex mode-by-mode (CMBM) and hybrid nonlinear (HNL) model. All these models are implemented in a computer code, including the generation of fluctuating wind velocities. Moreover, two advanced models, the modified nonlinear (MNL) and nonlinear unsteady (NLU), are briefly outlined for the purpose of model assessment using the categorical modeling approach in the next chapter.

3.5.1 Steady model

First, the ST model is introduced. It is essentially based on (3.48), taking that the static wind coefficients can be nonlinear (cf. Fig. 3.6). In this case, the steadiness refers to the structure, i.e. the aerodynamic forces are independent of the motion [255], although it may be argued that the terminology implies steady flow. Nevertheless, the buffeting forces are accounted for in a quasi-steady manner. The ST model is formulated as

$$\mathbf{ST} := \begin{cases} D = F_L \sin\varphi_w + F_D \cos\varphi_w, \quad L = F_L \cos\varphi_w - F_D \sin\varphi_w, \quad M = F_M, \\ F_D = \dfrac{1}{2}\rho U_r^2 B C_D(\alpha_e), \quad F_L = -\dfrac{1}{2}\rho U_r^2 B C_L(\alpha_e), \quad F_M = \dfrac{1}{2}\rho U_r^2 B^2 C_M(\alpha_e), \\ \alpha_e = \alpha_s + \varphi_w, \quad \varphi_w = \arctan\left(\dfrac{w}{U+u}\right), \quad U_r = \sqrt{(U+u)^2 + w^2}, \end{cases} \tag{3.66}$$

where α_s is the angle of attack at static equilibrium due to static aerodynamic forces and $\varphi_w = \varphi_w(t)$ is the dynamic angle of attack due to free-stream turbulence, both constituting the effective angle of attack $\alpha_e = \alpha_e(t)$. The resultant velocity is denoted as U_r. From (3.66) it can be gathered that for an arbitrary trend of the static wind coefficients C_D, C_L and C_M, the aerodynamic forces are nonlinearly dependent on the effective angle of attack. Thus, the static and buffeting forces do not abide by the superposition principle.

3.5.2 Linear steady model

The static wind coefficients from wind tunnel experiments are usually determined up to a certain angle of attack (e.g. ± 15 deg). Hence, extrapolation is required for effective angles outside this range for the aerodynamic forces in (3.66). Alternatively, the aerodynamic forces may be linearized at the static angle of attack that also offers mathematical simplifications. In the case of streamlined bridge decks, this is a fair assumption for the lift and moment coefficients as they are generally linear within this range (cf. Fig. 3.6).

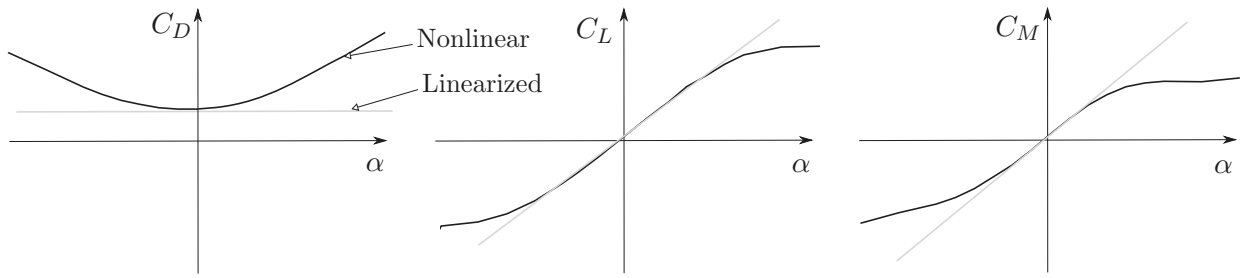

Figure 3.6: Typical nonlinear and corresponding linearized static wind coefficients of a bridge deck: drag (left); lift (center) and moment (right).

For e.g., using Taylor's expansion for the lift force in (3.66) yields

$$L|_{\alpha_s} = \frac{1}{2}\rho[(U+u)^2+w^2]B\left\{[-C_L(\alpha_s) - C'_L(\alpha_s)\varphi_w]\cos(\varphi_w) - [C_D(\alpha_s) + C'_D(\alpha_s)\varphi_w]\sin(\varphi_w)\right\}, \tag{3.67}$$

where $C'_L = C'_L(\alpha_s)$ and $C'_D = C'_D(\alpha_s)$ are the derivatives of the lift and drag coefficients at the static angle of attack α_s. Further, using small angle approximation (i.e. $\sin(\varphi_w) = \tan(\varphi_w) = \varphi_w$ and $\cos(\varphi_w) = 1 - \varphi_w^2/2$) and neglecting the squared terms of fluctuating velocity products, (3.67) is simplified to

$$L = \frac{1}{2}\rho U^2 B\left[-C_L - C'_L\frac{w}{U} - C_D\frac{w}{U} - 2C_L\frac{u}{U}\right], \tag{3.68}$$

where $C_L = C_L(\alpha_s)$ and $C_M = C_M(\alpha_s)$. The first term in the brackets corresponds to the static part L_s, while the other terms correspond to the buffeting part L_b. Similar expressions can be obtained for the drag and moment forces. Based on this, the LST model yields

$$\mathbf{LST} := \begin{cases} D = D_s + D_b, \quad L = L_s + L_b, \quad M = M_s + M_b, \\ D_s = \frac{1}{2}\rho U^2 B C_D, \quad L_s = -\frac{1}{2}\rho U^2 B C_L, \quad M_s = \frac{1}{2}\rho U^2 B^2 C_M, \\ D_b = \frac{1}{2}\rho U^2 B\left[2C_D\frac{u}{U} + (C'_D - C_L)\frac{w}{U}\right], \\ L_b = -\frac{1}{2}\rho U^2 B\left[2C_L\frac{u}{U} + (C'_L + C_L)\frac{w}{U}\right], \\ M_b = \frac{1}{2}\rho U^2 B^2\left(2C_M\frac{u}{U} + C'_M\frac{w}{U}\right). \end{cases} . \tag{3.69}$$

3.5.3 Quasi-steady model

Introducing the motion-induced contribution to the effective angle of the ST model in (3.66) (cf. e.g. [33, 58, 179]), the QS model is obtained as

$$\mathbf{QS} := \begin{cases} D = F_L\sin\varphi_D + F_D\cos\varphi_D, \quad L = F_L\cos\varphi_L - F_D\sin\varphi_L, \quad M = F_M, \\ F_D = \frac{1}{2}\rho U_{rD}^2 B C_D(\alpha_{eD}), \quad F_L = -\frac{1}{2}\rho U_{rL}^2 B C_L(\alpha_{eL}), \quad F_M = \frac{1}{2}\rho U_{rM}^2 B^2 C_M(\alpha_{eM}), \\ \alpha_{ej} = \alpha_s + \alpha + \varphi_j, \quad \varphi_j = \arctan\left(\frac{w + \dot{h} + m_j B\dot{\alpha}}{U + u - \dot{p}}\right), \\ U_{rj} = \sqrt{(U+u-\dot{p})^2 + (w + \dot{h} + m_j B\dot{\alpha})^2}, \quad \text{for } j \in \{D, L, M\}, \end{cases} \tag{3.70}$$

where φ_j is the dynamic angle of attack including wind and motion terms, while m_j coefficients specify the position of the aerodynamic center [27]. The preceding expressions comply with Definition 3.1. When compared with flat plate quasi-steady aerodynamics (cf. (3.64) and (3.65)), it can be gathered that the QS model in bridge aerodynamics additionally accounts for the aerodynamic nonlinearity in the static wind coefficients (i.e. quasi-steady nonlinearity). However, the apparent mass effects are disregarded in (3.70).

The aerodynamic center m_j specifies a point at which an equivalent (resultant) downwash velocity due to angular motion is positioned. In the case of a flat plate, it can be seen from (3.65) that the aerodynamic center corresponds to the front quarter-point, i.e. $m_j = 0.25$. Specifying the same point in bridge aerodynamics can result in significant underestimation of the critical velocity corresponding to torsional instability. For a flat-plate, the contribution of the angular velocity is canceled out due to the apparent mass forces (cf. (3.64)). In bridge aerodynamics, the self-excited forces are dependent on the downwash at multiple points due to large flow separation [359]. Hence, an equivalent point should be obtained by selecting an appropriate quasi-steady state. In this case, this is done by utilizing the flutter derivatives. However, there is no well-established method for obtaining this point. This will be discussed further in Ch. 6.

3.5.4 Linear quasi-steady model

Similarly, as for the LST model, the LQS model is obtained by linearizing the QS model at the static angle of attack, employing the same assumptions as in (3.67) and (3.68). The LQS model yields the following formulation:

$$
\mathbf{LQS} := \begin{cases}
D = D_s + D_b + D_{se}, \quad L = L_s + L_b + L_{se}, \quad M = M_s + M_b + M_{se}, \\
D_s = \dfrac{1}{2}\rho U^2 B C_D, \quad L_s = -\dfrac{1}{2}\rho U^2 B C_L, \quad M_s = \dfrac{1}{2}\rho U_r^2 B^2 C_M, \\
D_b = \dfrac{1}{2}\rho U^2 B \left[2C_D \dfrac{u}{U} + (C_D' - C_L)\dfrac{w}{U}\right], \\
L_b = -\dfrac{1}{2}\rho U^2 B \left[2C_L \dfrac{u}{U} + (C_L' + C_L)\dfrac{w}{U}\right], \\
M_b = \dfrac{1}{2}\rho U^2 B^2 \left(2C_M \dfrac{u}{U} + C_M' \dfrac{w}{U}\right), \\
D_{se} = \dfrac{1}{2}\rho U^2 B \left[(C_D' - C_L)\dfrac{\dot{h} + m_D B\dot{\alpha}}{U} + C_D'\alpha - 2C_D \dfrac{\dot{p}}{U}\right], \\
L_{se} = -\dfrac{1}{2}\rho U^2 B \left[(C_L' + C_D)\dfrac{\dot{h} + m_L B\dot{\alpha}}{U} + C_L'\alpha - 2C_L \dfrac{\dot{p}}{U}\right], \\
M_{se} = \dfrac{1}{2}\rho U^2 B^2 \left(C_M' \dfrac{\dot{h} + m_M B\dot{\alpha}}{U} + C_M'\alpha - 2C_M \dfrac{\dot{p}}{U}\right).
\end{cases} \tag{3.71}
$$

Compared to the ST model (cf. (3.69)), the LQS model includes the contribution of self-excited forces D_{se}, L_{se}, M_{se}. Moreover, the LQS model resembles more the QS model of a flat plate (cf. (3.64)) than the QS model in bridge aerodynamics (cf. (3.70)), as it is linear. The effect of fluid memory is neglected in both QS and LQS models.

3.5.5 Linear unsteady model

Unlike to the LQS model, the LU model takes into account the unsteadiness of aerodynamic forces. As for a flat plate, the LU model is formulated also in time and frequency domain. Moreover, in addition to the indicial elementary function in the time-domain, the LU model can be also formulated based on impulse functions. As shown further, these formulations are equivalent in a mathematical sense.

Since the LU model is perhaps the most widely used model, an extended explanation is given herein compared to the rest of the semi-analytical models. The time- and frequency-domain formulations are first reviewed, followed by their interrelations and analogies with the flat-plate and quasi-steady aerodynamics. Finally, numerical implementation is briefly discussed.

Frequency-domain formulation

In the frequency domain, the fluid memory is included by introducing a frequency-dependent aerodynamic coefficient in analogy to Theodorsen and Sears functions in (3.57). The self-excited forces in the extended Scanlan's formulation (cf. e.g. [163, 280, 289, 290]) yield the following:

$$\begin{aligned}
D_{se}^{\mathrm{LU}} =& \frac{1}{2}\rho U^2 B\left(KP_1^*\frac{\dot{p}}{U} + KP_2^*\frac{B\dot{\alpha}}{U} + K^2P_3^*\alpha + K^2P_4^*\frac{p}{B} + KP_5^*\frac{\dot{h}}{U} + K^2P_6^*\frac{h}{B}\right),\\
L_{se}^{\mathrm{LU}} =& \frac{1}{2}\rho U^2 B\left(KH_1^*\frac{\dot{h}}{U} + KH_2^*\frac{B\dot{\alpha}}{U} + K^2H_3^*\alpha + K^2H_4^*\frac{h}{B} + KH_5^*\frac{\dot{p}}{U} + K^2H_6^*\frac{p}{B}\right),\\
M_{se}^{\mathrm{LU}} =& \frac{1}{2}\rho U^2 B^2\left(KA_1^*\frac{\dot{h}}{U} + KA_2^*\frac{B\dot{\alpha}}{U} + K^2A_3^*\alpha + K^2A_4^*\frac{h}{B} + KA_5^*\frac{\dot{p}}{U} + K^2A_6^*\frac{p}{B}\right).
\end{aligned} \tag{3.72}$$

This formulation is of a mixed nature as it contains frequency-dependent flutter derivatives $P_j^* = P_j^*(K)$, $H_j^* = H_j^*(K)$ and $A_j^* = A_j^*(K)$ for $j \in \{1,\dots,6\}$, based on the reduced frequency of motion K (cf. (3.46)), while the displacements are time-dependent, i.e. $p = p(t)$, $h = h(t)$ and $\alpha = \alpha(t)$. Similarly, as for a flat plate, Davenport [72, 73] included the unsteadiness in the buffeting forces for bridge decks utilizing general aerodynamic admittances. In an extended format (cf. e.g. [58, 73, 147]), the buffeting forces are formulated as:

$$\begin{aligned}
D_b^{\mathrm{LU}} =& \frac{1}{2}\rho U^2 B\left[2C_D\chi_{Du}\frac{u}{U} + (C_D' - C_L)\chi_{Dw}\frac{w}{U}\right],\\
L_b^{\mathrm{LU}} =& -\frac{1}{2}\rho U^2 B\left[2C_L\chi_{Lu}\frac{u}{U} + (C_L' + C_D)\chi_{Lw}\frac{w}{U}\right],\\
M_b^{\mathrm{LU}} =& \frac{1}{2}\rho U^2 B^2\left(2C_M\chi_{Mu}\frac{u}{U} + C_M'\chi_{Mw}\frac{w}{U}\right),
\end{aligned} \tag{3.73}$$

where $\chi_{Dj} = \chi_{Dj}(K)$, $\chi_{Lj} = \chi_{Lj}(K)$ and $\chi_{Mj} = \chi_{Mj}(K)$ for $j \in \{u, w\}$ are the complex aerodynamic admittance functions corresponding to the drag, lift and moment forces, respectively, all dependent on the reduced frequency of the free-stream turbulence K. The formulation (3.73) also contains frequency- ($\chi = \chi(K)$) and time-dependent terms ($u = u(t)$ and $w = w(t)$).

To obtain pure a frequency-domain formulation for the three-degree-of-freedom system, the self-excited force vector $\mathbf{f}_{se}$ can be expressed as

$$\boldsymbol{f}_{se} = \boldsymbol{K}_{se}\boldsymbol{q} + \boldsymbol{C}_{se}\dot{\boldsymbol{q}}, \tag{3.74}$$

Moving this vector on the right-hand side in (3.5) yields

$$\boldsymbol{M}\ddot{\boldsymbol{q}} + (\boldsymbol{C} - \boldsymbol{C}_{ae})\,\dot{\boldsymbol{q}} + (\boldsymbol{K} - \boldsymbol{K}_{ae})\,\boldsymbol{q} = \boldsymbol{f}_s + \boldsymbol{f}_b, \tag{3.75}$$

where

$$\boldsymbol{K}_{ae} = \boldsymbol{K}_{ae}(K) = \frac{1}{2}\rho U^2 K^2 \begin{bmatrix} P_4^* & P_6^* & BP_3^* \\ H_6^* & H_4^* & BH_3^* \\ BA_6^* & BA_4^* & B^2A_3^* \end{bmatrix}, \tag{3.76}$$

and

$$\boldsymbol{C}_{ae} = \boldsymbol{C}_{ae}(K) = \frac{1}{2}\rho U B K \begin{bmatrix} P_1^* & P_5^* & BP_2^* \\ H_5^* & H_1^* & BH_2^* \\ BA_5^* & BA_1^* & B^2A_2^* \end{bmatrix}, \tag{3.77}$$

represent the aerodynamic stiffness and damping matrices, respectively. Taking the Fourier transform, (3.75) is obtained in a pure frequency-domain formulation as

$$\left[-\omega^2\boldsymbol{M} + i\omega(\boldsymbol{C} - \boldsymbol{C}_{ae}) + (\boldsymbol{K} - \boldsymbol{K}_{ae})\right]\hat{\boldsymbol{q}} = \boldsymbol{f}_s + \hat{\boldsymbol{f}}_b, \tag{3.78}$$

where $\hat{\boldsymbol{q}} = \hat{\boldsymbol{q}}(\omega)$ and $\hat{\boldsymbol{f}}_b = \hat{\boldsymbol{f}}_b(\omega)$ are the Fourier transforms of the modal displacement and modal buffeting force vectors, respectively.

In case of flutter analysis, the buffeting forces are neglected and the critical flutter velocity is identified based on the eigenvalue problem

$$\boldsymbol{G}\hat{\boldsymbol{q}} = 0, \tag{3.79}$$

where

$$\boldsymbol{G} = \boldsymbol{G}(\omega, U) = -\omega^2\boldsymbol{M} + i\omega(\boldsymbol{C} - \boldsymbol{C}_{ae}) + (\boldsymbol{K} - \boldsymbol{K}_{ae}), \tag{3.80}$$

is the impedance matrix. As noted by Scanlan and his coworkers [147, 148, 163, 289], nontrivial solution of (3.79) is obtained if the determinant of the impedance matrix vanishes, indicating negative damping threshold. As the impedance matrix is complex, the flutter condition is formulated as

$$|\det(\boldsymbol{G})| = 0. \tag{3.81}$$

From (3.80) and (3.81), it can be gathered that the system is dependent on two variables: the wind speed U and oscillation frequency ω. The critical wind speed U_{cr} is sought by fixing a value of U, and evaluating condition (3.81) in a frequency range of interest. If the condition is not met, the velocity is increased until U_{cr} is obtained.

The buffeting response is computed by a spectral analysis of (3.78). The PSD of the modal displacements matrix $\boldsymbol{S}_{\boldsymbol{q}} = \boldsymbol{S}_{\boldsymbol{q}}(\omega)$ is obtained based on the PSD of the buffeting forces $\boldsymbol{S}_{\boldsymbol{f}_b} = \boldsymbol{S}_{\boldsymbol{f}_b}(\omega)$ and the impermanence matrix from (3.80). Finally, the PSD of the system displacement matrix $\boldsymbol{S}_{\boldsymbol{q}_o} = \boldsymbol{S}_{\boldsymbol{q}_o}(\omega)$ is obtained, in which the diagonal members correspond to each degree of freedom. Summarizing, the following relations constitute the determination of the buffeting response:

$$\boldsymbol{S}_{\boldsymbol{f}_b} = \hat{\boldsymbol{f}}_b\left(\overline{\hat{\boldsymbol{f}}_b}\right)^T, \quad \boldsymbol{S}_{\boldsymbol{q}} = \boldsymbol{G}^{-1}\boldsymbol{S}_{\boldsymbol{f}_b}\left(\overline{\boldsymbol{G}^{-1}}\right)^T, \quad \boldsymbol{S}_{\boldsymbol{q}_o} = \boldsymbol{\Psi}^T\boldsymbol{S}_{\boldsymbol{f}_b}\boldsymbol{\Psi}. \tag{3.82}$$

The formulation of the buffeting force vector $\boldsymbol{f}_b$ is based on (3.73) and the PSD of the wind fluctuations in (3.26) in a straightforward manner. Principally, the method for multimode analyses for the whole deck is the equivalent of the three-degree-of-freedom system. In this case, the aerodynamic stiffness, damping, and buffeting force matrices are formulated using the standard Finite Element principles. It is noted that the flutter derivatives and aerodynamic admittances should be obtained corresponding to the static angle of attack, based on an aerostatic analysis.

Time-domain formulation

As for a flat plate, the aerodynamic forces acting on a bridge deck may be formulated in a pure time-domain form in terms of indicial response functions due to unit-step input. Perhaps one of the earliest formulation of the self-excited forces in terms of indicial functions was done by Scanlan et al. [288], followed by many studies that included or excluded various terms (cf. e.g. [45, 69, 76, 133, 282, 284, 287]). Corresponding to the flat plate model formulated by (3.59), formulation of the LU model in the time domain by indicial functions is formally defined as follows:

$$
\mathbf{LU} := \begin{cases}
D = D_s + D_b + D_{se}, \quad L = L_s + L_b + L_{se}, \quad M = M_s + M_b + M_{se}, \\
D_s = \frac{1}{2}\rho U^2 B C_D, \quad L_s = -\frac{1}{2}\rho U^2 B C_L, \quad M_s = \frac{1}{2}\rho U^2 B^2 C_M, \\
D_b = \frac{1}{2}\rho U^2 B \left[2C_D \int_{-\infty}^{t} \Phi_{Du}(t-t_1)\frac{\dot{u}(t_1)}{U}\mathrm{d}t_1 + (C'_D - C_L)\int_{-\infty}^{t} \Phi_{Dw}(t-t_1)\frac{\dot{w}(t_1)}{U}\mathrm{d}t_1 \right], \\
L_b = -\frac{1}{2}\rho U^2 B \left[2C_L \int_{-\infty}^{t} \Phi_{Lu}(t-t_1)\frac{\dot{u}(t_1)}{U}\mathrm{d}t_1 + (C'_L + C_D)\int_{-\infty}^{t} \Phi_{Lw}(t-t_1)\frac{\dot{w}(t_1)}{U}\mathrm{d}t_1 \right], \\
M_b = \frac{1}{2}\rho U^2 B^2 \left[2C_M \int_{-\infty}^{t} \Phi_{Mu}(t-t_1)\frac{\dot{u}(t_1)}{U}\mathrm{d}t_1 + C'_M \int_{-\infty}^{t} \Phi_{Mw}(t-t_1)\frac{\dot{w}(t_1)}{U}\mathrm{d}t_1 \right], \\
D_{se} = \frac{1}{2}\rho U^2 B \Bigg[(C'_D - C_L)\int_{-\infty}^{t} \Phi_{Dh}(t-t_1)\frac{\ddot{h}(t_1)}{U}\mathrm{d}t_1 + C'_D \int_{-\infty}^{t} \Phi_{D\alpha}(t-t_1)\dot{\alpha}(t_1)\mathrm{d}t_1 \\
\qquad + (C'_D - C_L)\int_{-\infty}^{t} \Phi_{D\dot{\alpha}}(t-t_1)\frac{m_D B\ddot{\alpha}(t_1)}{U}\mathrm{d}t_1 - 2C_D \int_{-\infty}^{t} \Phi_{Dp}(t-t_1)\frac{\ddot{p}(t_1)}{U}\mathrm{d}t_1 \Bigg], \\
L_{se} = -\frac{1}{2}\rho U^2 B \Bigg[(C'_L + C_D)\int_{-\infty}^{t} \Phi_{Lh}(t-t_1)\frac{\ddot{h}(t_1)}{U}\mathrm{d}t_1 + C'_L \int_{-\infty}^{t} \Phi_{L\alpha}(t-t_1)\dot{\alpha}(t_1)\mathrm{d}t_1 \\
\qquad + (C'_L + C_D)\int_{-\infty}^{t} \Phi_{L\dot{\alpha}}(t-t_1)\frac{m_L B\ddot{\alpha}(t_1)}{U}\mathrm{d}t_1 - 2C_L \int_{-\infty}^{t} \Phi_{Lp}(t-t_1)\frac{\ddot{p}(t_1)}{U}\mathrm{d}t_1 \Bigg], \\
M_{se} = \frac{1}{2}\rho U^2 B^2 \Bigg[C'_M \int_{-\infty}^{t} \Phi_{Mh}(t-t_1)\frac{\ddot{h}(t_1)}{U}\mathrm{d}t_1 + C'_M \int_{-\infty}^{t} \Phi_{M\alpha}(t-t_1)\dot{\alpha}(t_1)\mathrm{d}t_1 \\
\qquad + C'_M \int_{-\infty}^{t} \Phi_{M\dot{\alpha}}(t-t_1)\frac{m_M B\ddot{\alpha}(t_1)}{U}\mathrm{d}t_1 - 2C_M \int_{-\infty}^{t} \Phi_{Mp}(t-t_1)\frac{\ddot{p}(t_1)}{U}\mathrm{d}t_1 \Bigg],
\end{cases}
\tag{3.83}
$$

where $\Phi_{Dj} = \Phi_{Dj}(t)$, $\Phi_{Lj} = \Phi_{Lj}(t)$ and $\Phi_{Mj} = \Phi_{Mj}(t)$ are the drag, lift and moment buffeting indicial functions for $j \in \{u, w\}$ or self-excited indical functions for $j \in \{h, p, \alpha, \dot{\alpha}\}$. The indicial functions are obtained either directly from experimental and CFD tests, or indirectly from the flutter derivatives. Determining the indicial functions in such a manner, it is difficult to isolate the term corresponding to the angular velocity $\Phi_{\dot{\alpha}}$. Thus, this term is generally neglected in the analysis and it is kept only in the formulation herein. Moreover, Bucher and Lin [41, 42] and Wu and Kareem [361] note that the terms corresponding to the indicial function corresponding to the angular rotation Φ_{α} contains most of the information w.r.t. the angular velocity $\dot{\alpha}$, i.e. $\Phi_{\dot{\alpha}}$ is redundant.

Alternatively, to the indicial function approach, the formulation of the buffeting forces by impulse functions has been widely utilized (cf. e.g. [31, 41, 42, 56, 61, 208]). Utilizing impulse functions, the self-excited forces yield

$$\begin{aligned}
D_{se}^{\mathrm{LU}} &= \frac{1}{2}\rho U^2 B\Bigg[(C_D' - C_L)\int_{-\infty}^{t} I_{Dh}(t-t_1)\frac{h(t_1)}{B}\mathrm{d}t_1 + C_D'\int_{-\infty}^{t} I_{D\alpha}(t-t_1)\alpha(t_1)\mathrm{d}t_1 \\
&\qquad - 2C_D\int_{-\infty}^{t} I_{Dp}(t-t_1)\frac{p(t_1)}{B}\mathrm{d}t_1\Bigg], \\
L_{se}^{\mathrm{LU}} &= -\frac{1}{2}\rho U^2 B\Bigg[(C_L' + C_D)\int_{-\infty}^{t} I_{Lh}(t-t_1)\frac{h(t_1)}{B}\mathrm{d}t_1 + C_L'\int_{-\infty}^{t} I_{L\alpha}(t-t_1)\alpha(t_1)\mathrm{d}t_1 \\
&\qquad - 2C_L\int_{-\infty}^{t} I_{Lp}(t-t_1)\frac{p(t_1)}{B}\mathrm{d}t_1\Bigg], \\
M_{se}^{\mathrm{LU}} &= \frac{1}{2}\rho U^2 B^2\Bigg[C_M'\int_{-\infty}^{t} I_{Mh}(t-t_1)\frac{h(t_1)}{B}\mathrm{d}t_1 + C_M'\int_{-\infty}^{t} I_{M\alpha}(t-t_1)\alpha(t_1)\mathrm{d}t_1 \\
&\qquad - 2C_M\int_{-\infty}^{t} I_{Mp}(t-t_1)\frac{p(t_1)}{B}\mathrm{d}t_1\Bigg],
\end{aligned} \tag{3.84}$$

while the buffeting forces are

$$\begin{aligned}
D_b^{\mathrm{LU}} &= \frac{1}{2}\rho U^2 B\left[2C_D\int_{-\infty}^{t} I_{Du}(t-t_1)\frac{u(t_1)}{U}\mathrm{d}t_1 + (C_D' - C_L)\int_{-\infty}^{t} I_{Dw}(t-t_1)\frac{w(t_1)}{U}\mathrm{d}t_1\right] \\
L_b^{\mathrm{LU}} &= -\frac{1}{2}\rho U^2 B\left[2C_L\int_{-\infty}^{t} I_{Lu}(t-t_1)\frac{u(t_1)}{U}\mathrm{d}t_1 + (C_L' + C_D)\int_{-\infty}^{t} I_{Lw}(t-t_1)\frac{w(t_1)}{U}\mathrm{d}t_1\right], \\
M_b^{\mathrm{LU}} &= \frac{1}{2}\rho U^2 B^2\left[2C_M\int_{-\infty}^{t} I_{Mu}(t-t_1)\frac{u(t_1)}{U}\mathrm{d}t_1, + C_M'\int_{-\infty}^{t} I_{Mw}(t-t_1)\frac{w(t_1)}{U}\mathrm{d}t_1\right].
\end{aligned} \tag{3.85}$$

In (3.84) and (3.85), $I_{Dj} = I_{Dj}(t)$, $I_{Lj} = I_{Lj}(t)$ and $I_{Mj} = I_{Mj}(t)$ are the drag, lift and moment buffeting impulse functions for $j \in \{u, w\}$ or self-excited impulse functions for $j \in \{h, p, \alpha\}$.

The impulse and indicial functions are the time-domain counterparts of the flutter derivatives; hence, they account for the effect of fluid memory. They are equivalent in terms of the information that they can contain mathematically, by the same analogy as unit-step and impulse response functions. Let $a = a(t)$ be the system input (i.e. motion or gust) and $b = b(t)$ be the system output (i.e. forces). The system output can be written using either unit-impulse response function $I = I(t)$ or unit-step (indicial) response function $\Phi = \Phi(t)$, corresponding to a unit-impulse and unit-step input in terms of Duhamel integral. This yields

$$b(t) = a(0)\Phi(t) + \int_0^t \dot{a}(t_1)\Phi(t-t_1)\mathrm{d}t_1 = a(t)\Phi(0) + \int_0^t a(t_1)\dot{\Phi}(t-t_1)\mathrm{d}t_1 = \int_0^t a(t_1)I(t-t_1)\mathrm{d}t_1, \tag{3.86}$$

from where it follows

$$I(t) = \Phi(0)\delta(t) + \dot{\Phi}(t), \tag{3.87}$$

where $\delta(t)$ is the Dirac delta function. A self-explanatory graphical illustration of the unit-step and unit-impulse response is given in Fig. 3.7.

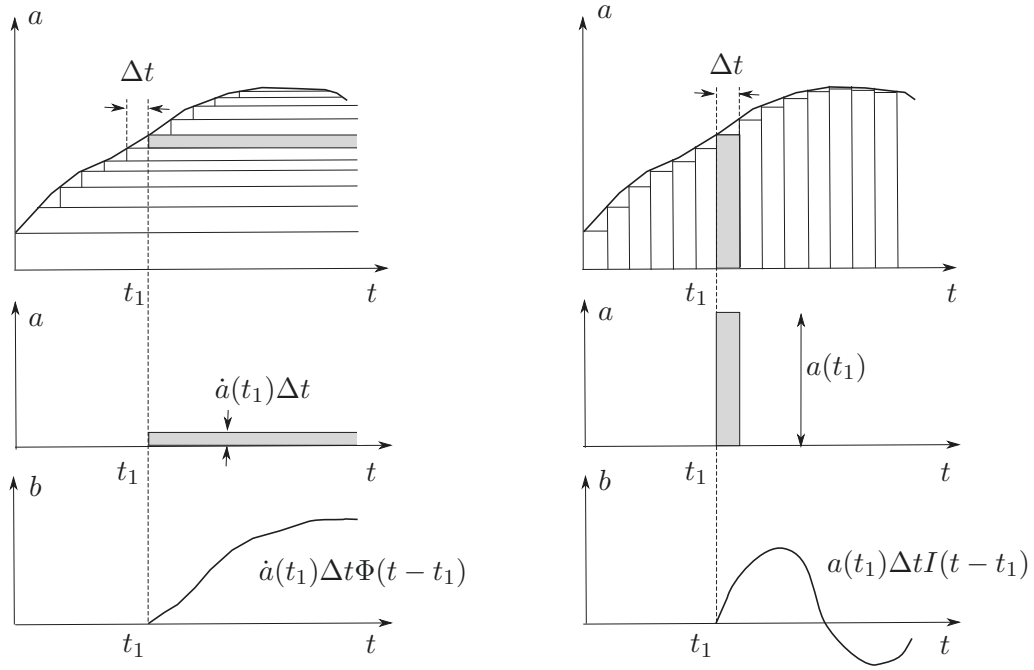

Figure 3.7: Duhamel integral for unit-step (left) and unit-impulse (right) input functions: total input (top); elementary input (center); elementary response (bottom). Adapted from von Kármán and Biot [337] and Fung [112].

In bridge aerodynamics, the impulse and indicial functions are commonly obtained from the flutter derivatives based on a general approximate form, utilizing rational approximation. The minor differences between the two formulations lie mainly in this approximate form and the determination of the coefficients, which will be briefly discussed later.

As an alternative to the indicial and impulse function formulation, the LU model has been formulated in the time domain using rheological models [85] or directly approximating the aerodynamic trusnfer function corresponding to the impedance (cf. (3.80)) using second-order polynomials [156]. As noted further, all formulations are equivalent if the unsteady information is obtained from the flutter derivatives.

Time and frequency domain interrelations

Mathematically, the frequency-domain formulation (cf. (3.72) and (3.73)) and the time-domain formulation using indicial (cf. (3.83)) or impulse (cf. (3.84) and (3.85)) functions are equivalent. This means that they are all representation of a model which is linear and can account for the fluid memory. Herein, the relations between these formulations are briefly revisited to be able to perform rational approximation and finally obtain a pure time-domain form of the LU model.

The lift due to vertical excitation can be expressed as follows:

$$\begin{aligned} L_h^{\mathrm{LU}} &= \frac{1}{2}\rho U^2 B \left(K H_1^* \frac{\dot{h}}{U} + K^2 H_4^* \frac{h}{B} \right) \\ &= -\frac{1}{2}\rho U^2 B (C_L' + C_D) \int_{-\infty}^{t} \Phi_{Lh}(t - t_1) \frac{\ddot{h}(t_1)}{U} \mathrm{d}t_1 \\ &= -\frac{1}{2}\rho U^2 B (C_L' + C_D) \int_{-\infty}^{t} I_{Lh}(t - t_1) \frac{h(t_1)}{B} \mathrm{d}t_1. \end{aligned} \tag{3.88}$$

Noting the relations in (3.60), and performing integration by parts with a change of variables on the term involving the indicial function

$$\int_{-\infty}^{t} \Phi_{Lh}(t-t_1)\frac{\ddot{h}(t_1)}{U}\mathrm{d}t_1 = \int_{-\infty}^{\tau} \Phi_{Lh}(\tau-\tau_1)\frac{h''(\tau_1)}{B}\mathrm{d}\tau_1 = \Phi_{Lh}(0)\frac{h'}{B} + \int_{0}^{\tau} \Phi'_{Lh}(\tau_1)\frac{h'(\tau-\tau_1)}{B}\mathrm{d}\tau_1, \tag{3.89}$$

and

$$I_{Lh}(\tau) = \frac{B}{U}I_{Lh}(t), \quad \Phi_{Lh}(\tau) = \Phi_{Lh}(t), \tag{3.90}$$

(3.88) can be expressed w.r.t. the reduced time as

$$\begin{aligned} L_h^{\mathrm{LU}} &= \frac{1}{2}\rho U^2 B\left(KH_1^*\frac{h'}{B} + K^2H_4^*\frac{h}{B}\right) \\ &= -\frac{1}{2}\rho U^2 B(C'_L + C_D)\left[\Phi_{Lh}(0)\frac{h'}{B} + \int_0^{\tau}\Phi'_{Lh}(\tau-\tau_1)\frac{h'(\tau_1)}{B}\mathrm{d}\tau_1\right] \\ &= -\frac{1}{2}\rho U^2 B(C'_L + C_D)\int_{-\infty}^{\tau} I_{Lh}(\tau-\tau_1)\frac{h(\tau_1)}{B}\mathrm{d}\tau_1. \end{aligned} \tag{3.91}$$

To obtain (3.91) in a pure frequency-domain form, the Fourier transform is performed, in analogy with flat plate in (3.61). According to the convolution theorem, convolution is simply multiplication in the frequency domain, i.e.

$$\int_{-\infty}^{\infty} a(t_1)b(t-t_1)\mathrm{d}t_1 = \int_{-\infty}^{\infty} a(t-t_1)b(t_1)\mathrm{d}t_1 = \hat{a}(f)\hat{b}(f). \tag{3.92}$$

Taking the Fourier transform of (3.91) w.r.t. the reduced frequency K and using the convolution theorem, (3.91) can be expressed for harmonic motion in the frequency domain as

$$\begin{aligned} \hat{L}_h^{\mathrm{LU}} &= \frac{1}{2}\rho U^2 B\left(K^2H_1^*\frac{i\hat{h}}{B} + K^2H_4^*\frac{\hat{h}}{B}\right) \\ &= -\frac{1}{2}\rho U^2 B(C'_L + C_D)\left[\Phi_{Lh}(0)K\frac{i\hat{h}}{B} + \hat{\Phi}'_{Lh}K\frac{i\hat{h}}{B}\right] \\ &= -\frac{1}{2}\rho U^2 B(C'_L + C_D)\hat{I}_{Lh}\frac{\hat{h}}{B}, \end{aligned} \tag{3.93}$$

where the identity

$$\hat{h}' = iK\hat{h} \tag{3.94}$$

is used for the velocity terms. Thus, relations between the flutter derivatives, self-excited impulse and indicial functions can be obtained from (3.93) in the frequency domain for L_h.

In a similar fashion, relations can be obtained for the rest of the self-excited forces, yielding the following identities:

$$\begin{aligned}
\hat{I}_{Dh} &= iK\left[\Phi_{Dh}(0)+\hat{\Phi}'_{Dh}\right] &&= \frac{K^2}{(C'_D-C_L)}\left(iP_5^*+P_6\right),\\
\hat{I}_{D\alpha} &= \left[\Phi_{D\alpha}(0)+\hat{\Phi}'_{D\alpha}\right] &&= \frac{K^2}{C'_D}\left(iP_2^*+P_3^*\right),\\
\hat{I}_{Dp} &= iK\left[\Phi_{Dp}(0)+\hat{\Phi}'_{Dp}\right] &&= -\frac{K^2}{2C_D}\left(iP_1^*+P_4^*\right),\\
\hat{I}_{Lh} &= iK\left[\Phi_{Lh}(0)+\hat{\Phi}'_{Lh}\right] &&= -\frac{K^2}{(C'_L+C_D)}\left(iH_1^*+H_4^*\right),\\
\hat{I}_{L\alpha} &= \left[\Phi_{L\alpha}(0)+\hat{\Phi}'_{L\alpha}\right] &&= -\frac{K^2}{C'_L}\left(iH_2^*+H_3^*\right),\\
\hat{I}_{Lp} &= iK\left[\Phi_{Lp}(0)+\hat{\Phi}'_{Lp}\right] &&= \frac{K^2}{2C_L}\left(iH_5^*+H_6^*\right),\\
\hat{I}_{Mh} &= iK\left[\Phi_{Lh}(0)+\hat{\Phi}'_{Lh}\right] &&= \frac{K^2}{C'_M}\left(iA_1^*+A_4^*\right),\\
\hat{I}_{M\alpha} &= \left[\Phi_{M\alpha}(0)+\hat{\Phi}'_{M\alpha}\right] &&= \frac{K^2}{C'_M}\left(iA_2^*+A_3^*\right),\\
\hat{I}_{Mp} &= iK\left[\Phi_{Mp}(0)+\hat{\Phi}'_{Mp}\right] &&= -\frac{K^2}{2C_M}\left(iA_5^*+A_6^*\right).
\end{aligned} \tag{3.95}$$

As the aerodynamic admittance functions are complex, i.e. $\chi = \Re(\chi)+i\Im(\chi)$, the same approach can be used for the buffeting forces as for the self-excited forces. Taking the lift force due to vertical gust as an example, the following identity holds:

$$\begin{aligned}
L_w^{\mathrm{LU}} &= -\frac{1}{2}\rho U^2 B\left(C'_L+C_D\right)\left(\Re(\chi_{Lw})+i\Im(\chi_{Lw})\right)\frac{w}{U}\\
&= -\frac{1}{2}\rho U^2 B(C'_L+C_D)\int_{-\infty}^{t}\Phi_{Lw}(t-t_1)\frac{\dot{w}(t_1)}{U}\mathrm{d}t_1\\
&= -\frac{1}{2}\rho U^2 B(C'_L+C_D)\int_{-\infty}^{t}I_{Lw}(t-t_1)\frac{w(t_1)}{B}\mathrm{d}t_1.
\end{aligned} \tag{3.96}$$

Noting similar relations as in (3.60), (3.89) and (3.90), the lift force in (3.96) can be expressed w.r.t. the reduced time as

$$\begin{aligned}
L_w^{\mathrm{LU}} &= -\frac{1}{2}\rho U^2 B\left(C'_L+C_D\right)\left(\Re(\chi_{Lw})+i\Im(\chi_{Lw})\right)\frac{w}{U}\\
&= -\frac{1}{2}\rho U^2 B(C'_L+C_D)\left[\Phi_{Lw}(0)\frac{w}{U}+\int_0^{\tau}\Phi'_{Lw}(\tau-\tau_1)\frac{w'(\tau_1)}{U}\mathrm{d}\tau_1\right]\\
&= -\frac{1}{2}\rho U^2 B(C'_L+C_D)\int_{-\infty}^{\tau}I_{Lw}(\tau-\tau_1)\frac{w(\tau_1)}{U}\mathrm{d}\tau_1.
\end{aligned} \tag{3.97}$$

Taking the Fourier transform of (3.97) yields

$$\begin{aligned}\hat{L}_w^{\mathrm{LU}} &= -\frac{1}{2}\rho U^2 B\left(C_L' + C_D\right)\left(\Re(\chi_{Lw}) + i\Im(\chi_{Lw})\right)\frac{\hat{w}}{U} \\ &= -\frac{1}{2}\rho U^2 B(C_L' + C_D)\left[\Phi_{Lw}(0)\frac{\hat{w}}{U} + \hat{\Phi}'_{Lw}\frac{\hat{w}}{U}\right] \\ &= -\frac{1}{2}\rho U^2 B(C_L' + C_D)\hat{I}_{Lw}\frac{\hat{w}}{U},\end{aligned} \tag{3.98}$$

which gives the relation between the buffeting impulse and indicial functions and aerodynamic admittance in the frequency domain. For all aerodynamic forces due to incoming gusts, the following relation holds:

$$\hat{I}_{jk} = \Phi_{jk}(0) + \hat{\Phi}'_{jk} = \Re(\chi_{jk}) + i\Im(\chi_{jk}), \quad \text{for } j \in \{D, L, M\}, \quad k \in \{u, w\}. \tag{3.99}$$

Rational function approximation and numerical implementation

Although the indicial functions can be obtained experimentally, the common process is to approximate them based on the flutter derivatives and aerodynamic admittances, utilizing the identities in (3.95) and (3.99). A general approximate form for the indicial functions based on a flat plate (cf. (3.62)) is expressed as

$$\Phi = \Phi_{se} = \Phi_b = 1 - \sum_{j=1}^{N_{st}} A_j \exp\left(-d_j\tau\right), \tag{3.100}$$

where A_j are linear coefficients and d_j are unsteady state coefficients that can be seen as a cascade of filters for $N_{st} \in \mathbb{N}_0$ number of aerodynamic states, that account for the unsteady behavior of the aerodynamic forces. The number of states is different for each set of flutter derivatives; however, selecting in the range for $N_{st} = 3 - 5$ usually suffices [347]. It can be seen that as $\tau \to 1$, the indicial function tends to the quasi-steady state, i.e. $\Phi = 1$. Several studies have also proposed alternative forms of (3.100). For e.g., Caracoglia and Jones [45] suggest replacing the unity in the first term with an additional coefficient A_0, by which the quasi-steady state is based on the flutter derivatives, while Jung [155] utilized cubic splines. However, the form (3.100) is used herein as it bears the most physically insightful meaning [361, 375].

From (3.100), the approximate indicial function at $\tau = 0$ and its first derivative yield

$$\Phi(0) = 1 - \sum_{j=1}^{N_{st}} A_j, \quad \Phi' = \sum_{j=1}^{N_{st}} A_j d_j \exp\left(-d_j\tau\right). \tag{3.101}$$

The Laplace transform is defined as

$$\tilde{a}(s) := \int_0^\infty a(t)\exp\left(-st\right)\mathrm{d}t, \tag{3.102}$$

where s is the Laplace integration variable, taken to be purely on the imaginary axis, i.e. $s = iK$. Summing the terms in (3.101) and performing the Laplace transform yields

$$\Phi(0) + \tilde{\Phi}' = 1 - \sum_{j=1}^{N_{st}} A_j + \sum_{j=1}^{N_{st}} A_j d_j \frac{1}{d_j + iK} = 1 - \sum_{j=1}^{N_{st}} \left(\frac{A_j K^2}{d_j^2 + K^2} + i\frac{A_j d_j K}{d_j^2 + K^2}\right). \tag{3.103}$$

This form is suitable to determine the unknown coefficients A_j and d_j for the indicial functions, based on the flutter derivatives and aerodynamic admittance functions. Comparing the left-hand side of (3.103), it can be seen that it is very similar to the expressions in (3.95), with the difference being one corresponding to the Laplace and to the Fourier transform. As the Laplace transform is performed purely on the imaginary axis, the Fourier transform can be generalized as Laplace transform, as discussed by Fung [112]. With this generalization, the expressions in (3.95) hold for a divergent oscillation. Thus, for e.g., in case of the lift indicial function due to vertical motion Φ_{Lh}, these unknown coefficients are related to the flutter derivatives as

$$H_1^* = \frac{(C_L' + C_D)}{K}\left(1 - \sum_{j=1}^{N_{st}} \frac{A_j K^2}{d_j^2 + K^2}\right), \quad H_4^* = (C_L' + C_D)\sum_{j=1}^{N_{st}} \frac{A_j d_j}{d_j^2 + K^2}. \tag{3.104}$$

Correspondingly, the A_j and d_j coefficients for the lift indical function due to vertical gust are related to the aerodynamic admittance function (cf. (3.99)) as

$$\Re(\chi_{Lw}) = \left(1 - \sum_{j=1}^{N_{st}} \frac{A_j K^2}{d_j^2 + K^2}\right), \quad \Im(\chi_{Lw}) = \sum_{j=1}^{N_{st}} \frac{A_j d_j}{d_j^2 + K^2}. \tag{3.105}$$

Based on the data in the flutter derivatives and aerodynamic admittance functions, (3.104) and (3.105) represent a nonlinear optimization problem with A_j and d_j as design variables, which can be formulated as follows:

$$\text{OP}: \begin{cases} \min\limits_{A,d} O(K, A, d), \\ \text{subject to: } d > 0, \end{cases} \tag{3.106}$$

where $O = O(K, A, d)$ is the objective function in terms of square-root error. For e.g., the objective function for the lift due to vertical motion is formulated as

$$\begin{aligned} O_{Lh} = \sum_{k=1}^{N_{samp}} \Bigg\{ &\left[H_1^*(K_p) - \frac{(C_L' + C_D)}{K_p}\left(1 - \sum_{j=1}^{N_{st}} \frac{A_j K_p^2}{d_j^2 + K_p^2}\right)\right]^2 \\ &+ \left[H_4^*(K_p) - (C_L' + C_D)\sum_{j=1}^{N_{st}} \frac{A_j d_j}{d_j^2 + K_p^2}\right]^2 \Bigg\}, \end{aligned} \tag{3.107}$$

or for the lift due to vertical gust as

$$O_{Lw} = \sum_{p=1}^{N_{samp}} \left\{ \left[\Re[\chi_{Lw}(K_p)] - \left(1 - \sum_{j=1}^{N_{st}} \frac{A_j K_p^2}{d_j^2 + K_p^2}\right)\right]^2 + \left[\Im[\chi_{Lw}(K_p)] - \sum_{j=1}^{N_{st}} \frac{A_j d_j}{d_j^2 + K_p^2}\right]^2 \right\}, \tag{3.108}$$

where K_p are the distinct reduced frequencies at which the flutter derivatives or aerodynamic admittance functions are determined from experiments or CFD analysis for a number of samples $N_{samp} \in \mathbb{N}$. Similar relations can be obtained for the remaining indicial functions, based on (3.95). The nonlinear optimization problem is solved utilizing the standard nonlinear least-squares technique, as proposed by Scanlan [288]. Further modifications have been proposed to refine the optimization process such as modification in the algorithm (cf. e.g. [45]) or by fixing values of the state coefficients d_j (cf. e.g. [194, 375]). Generally, these modifications influence the goodness-of-fit, which was not an issue in this work.

The impulse functions are obtained using a rational approximation as it is difficult to perform impulse excitation experimentally or numerically. As noted in (3.87), the impulse and indicial functions are related. If this relationship is true even for the approximative form of the impulse function, then based on (3.101) and

$$\Phi'(0) = \sum_{j=1}^{N_{st}} A_j d_j, \quad \Phi'' = -\sum_{j=1}^{N_{st}} A_j d_j^2 \exp\left(-d_j \tau\right), \tag{3.109}$$

the following relation can be obtained for the impulse functions corresponding to vertical h and lateral p displacements:

$$I_p = I_h = (1 - \sum_{j=1}^{N_{st}} A_j)\delta'(\tau) + \sum_{j=1}^{N_{st}} A_l d_j \left[\delta(\tau) - d_j \exp\left(d_j \tau\right)\right], \tag{3.110}$$

while the approximate form of the impulse functions corresponding to rotation α and gusts, u and w, yields

$$I_u = I_w = I_\alpha = \delta(\tau) - \sum_{j=1}^{N_{st}} A_j \left[\delta(\tau) - d_j \exp\left(-d_j \tau\right)\right]. \tag{3.111}$$

Instead of using two separate formulations, the self-excited impulse functions are commonly approximated based on the so-called Roger's approximation [265, 324, 325] in wing aerodynamics (cf. e.g. [31, 61, 194, 347] for applications in bridge aerodynamics). Roger's approximation for the self-excited forces is given as

$$I_{se} = A_1 \delta(\tau) + A_2 \delta'(\tau) + A_3 \delta''(\tau) + \sum_{j=1}^{N_{st}} A_{j+3} \left[\delta(\tau) - d_j \exp\left(-d_j \tau\right)\right]. \tag{3.112}$$

Analogous, the approximate form for the buffeting impulse functions include an additional term:

$$I_b = A_1 \delta(\tau) + \sum_{j=1}^{N_{st}} A_{j+1} \left[\delta(\tau) - d_j \exp\left(-d_j \tau\right)\right]. \tag{3.113}$$

Taking the Laplace transform of (3.112) and (3.113) yield

$$\begin{aligned} \tilde{I}_{se} &= A_1 + A_2 iK + A_3 (iK)^2 + \sum_{j=1}^{N_{st}} A_{j+3} \left[1 - d_j \frac{1}{d_j + iK}\right] \\ &= A_1 + A_2 iK + A_3 K^2 + \sum_{j=1}^{N_{st}} \left(\frac{A_{j+3} K^2}{d_j^2 + K^2} + i \frac{A_{j+3} d_j K}{d_j^2 + K^2}\right), \end{aligned} \tag{3.114}$$

and

$$\tilde{I}_b = A_1 + \sum_{l=1}^{N_{st}} A_{j+1} \left[1 - d_j \frac{1}{d_j + iK}\right] = A_1 + \sum_{j=1}^{N_{st}} \left(\frac{A_{j+1} K^2}{d_j^2 + K^2} + i \frac{A_{j+1} d_j K}{d_j^2 + K^2}\right), \tag{3.115}$$

respectively. Based on these relations and (3.95) and (3.99), the following bi-level nonlinear optimization problem can be formulated:

$$\text{BOP}: \begin{cases} \min\limits_{d} O(K, A, d), \\ \text{subject to: } d > 0, \\ \text{where } d \text{ solves:} \begin{cases} \min\limits_{A} O(K, A, d), \end{cases} \end{cases} \tag{3.116}$$

where, for e.g., the objective function for the lift impulse function due to vertical is given as

$$O_{Lh} = \sum_{p=1}^{N_{samp}} \left\{ \left[H_4^*(K_p) + \frac{(C_L' + C_D)}{K_p^2} \left(A_1 + A_3 K_p^2 + \sum_{j=1}^{N_{st}} \frac{A_{j+3} K_p^2}{d_j^2 + K_p^2} \right) \right]^2 + \left[H_1^*(K_p) + \frac{(C_L' + C_D)}{K_p} \left(A_2 + \sum_{j=1}^{N_{st}} \frac{A_{j+3} d_j}{d_j^2 + K_p^2} \right) \right]^2 \right\}, \tag{3.117}$$

while for the lift impulse function due to vertical gust as

$$O_{Lw} = \sum_{p=1}^{N_{samp}} \left\{ \left[\Re[\chi_{Lw}(K_p)] - \left(A_1 + \sum_{j=1}^{N_{st}} \frac{A_{j+1} K_p^2}{d_j^2 + K_p^2} \right) \right]^2 + \left[\Im[\chi_{Lw}(K_p)] - \sum_{j=1}^{N_{st}} \frac{A_{j+1} d_j}{d_j^2 + K_p^2} \right]^2 \right\}. \tag{3.118}$$

The bi-level optimization problem in (3.116) is comprised of a linear lower-level optimization, where the coefficients A_j are sought, and a nonlinear higher-level optimization process, where the nonlinear coefficients d_j are the design variables. The linear optimization is solved utilizing the linear least-squares algorithm, while a constrained Nelder-Mead simplex algorithm is used for the upper optimization task. It is noted that, (3.116) can be formulated in the same manner as the standard optimization problem for the indicial functions in (3.106) and solved using a nonlinear least-squares algorithm. Obtaining the unknown coefficients as a bi-level optimization problem was proposed by Tiffany and Adams [324, 325]. They indicate that using bi-level optimization reduces the computational costs for the nonlinear process and fit of the linear part do not rely on the convergence properties of the nonlinear algorithm.

Both indicial and impulse response functions are obtained from the fluter derivatives and aerodynamic admittances. Hence, they cannot account for additional unsteady information than the one included in these linear frequency-dependent coefficients. Taking this into account, and the relation (3.87), it can be argued that they are equivalent mathematical constructions in terms of the aerodynamic assumptions (i.e. both linear and unsteady). However, the goodness-of-fit of the impulse functions seem to be superior using the present formulation due to the additional coefficients in (3.112) and (3.113), and the advantage of the bi-level optimization in (3.116) as opposed to the nonlinear optimization in (3.106). On the other hand, the indicial response functions offer better physical interpretation as the rise-time of the unsteady forces can be directly observed (i.e. the fluid memory), as argued by Wu and Kareem in [361]. Several studies have been conducted comparing the two types of approximations (cf. e.g. [58, 195, 245, 361]) based on several criteria such as mathematical formulation and numerical uncertainty, most rendering the conclusion of their equivalence. However, the differences in the goodness-of-fit of both formulations to the derivatives may bring discrepancies in the response [245]. Nevertheless, this is dependent on the particular set of flutter derivatives.

In the numerical implementation, the convolution of the memory part contained in the indicial and impulse functions (i.e. exponential part in (3.100), (3.111) and (3.112)) can be of high computational cost for a large number of time steps. Hence, the memory term can be reduced utilizing recursive functions (cf. [195, 375]). For e.g., the lift force due to vertical displacements

using indicial functions (cf. (3.91) and (3.100)) can be written as

$$\begin{aligned} L_h(\tau) &= -\frac{1}{2}\rho U^2 B(C'_L + C_D)\int_{-\infty}^{\tau} \Phi_{Lh}(\tau-\tau_1)\frac{h''(\tau_1)}{U}\mathrm{d}\tau_1 \\ &= -\frac{1}{2}\rho U^2 B(C'_L + C_D)\int_{-\infty}^{\tau} \left\{1 - \sum_{j=1}^{N_{st}} A_j \exp[-d_j(\tau-\tau_1)]\right\}\frac{h''(\tau_1)}{U}\mathrm{d}\tau_1 \\ &= -\frac{1}{2}\rho U^2 B(C'_L + C_D)\frac{h'(\tau)}{U} + \sum_{j=1}^{N_{st}}\frac{1}{2}\rho U^2 B(C'_L + C_D)\int_{-\infty}^{\tau} A_j \exp[-d_j(\tau-\tau_1)]\frac{h''(\tau_1)}{U}\mathrm{d}\tau_1 \\ &= -\frac{1}{2}\rho U^2 B(C'_L + C_D)\frac{h'(\tau)}{U} + \sum_{j=1}^{N_{st}} L^*_{hj}(\tau). \end{aligned} \tag{3.119}$$

The terms L^*_{hj} represent the reduction in the lift due to the unsteady states, which can be separated into two parts:

$$\begin{aligned} L^*_{hj}(\tau) =& \frac{1}{2}\rho U^2 B(C'_L + C_D)\int_{-\infty}^{\tau-\Delta\tau} A_j \exp[-d_j(\tau-\Delta\tau+\Delta\tau-\tau_1)]\frac{h''(\tau_1)}{U}\mathrm{d}\tau_1 \\ &+ \frac{1}{2}\rho U^2 B(C'_L + C_D)\int_{\tau-\Delta\tau}^{\tau} A_j \exp[-d_j(\tau-\tau_1)]\frac{h''(\tau_1)}{U}\mathrm{d}\tau_1. \end{aligned} \tag{3.120}$$

It can be seen that the first term in the preceding expression includes the lift reduction at $\tau - \Delta\tau$, where $\Delta\tau$ denotes the reduced time-step. Moreover, assuming that the integrand under the second term changes linearly between $\tau - \Delta\tau$ and τ, the following is obtained:

$$L^*_{hj}(\tau) \cong \exp(-d_j\Delta\tau)L^*_{hj}(\tau-\Delta\tau) + \frac{1}{2}\rho U^2 B(C'_L + C_D)A_j \exp\left(-d_j\frac{\Delta\tau}{2}\right)\frac{h''(\tau-\frac{\Delta\tau}{2})}{U}\Delta\tau. \tag{3.121}$$

Since the force at τ is required to obtain the displacements at the same point in time, the displacements are known until $\tau - \Delta\tau$. Hence, the term $h''(\tau - \Delta\tau/2)$ can approximated using Taylor's series. By simple expansion until the first order, (3.121) yields

$$L^*_{hj}(\tau) \cong \exp(-d_j\Delta\tau)L^*_{hj}(\tau-\Delta\tau) + \frac{1}{2}\rho U^2 B(C'_L + C_D)A_j \exp\left(-d_j\frac{\Delta\tau}{2}\right)\frac{h'(\tau-\Delta\tau)}{U}\Delta\tau. \tag{3.122}$$

Several studies have proposed reduced numerical schemes for the solution of the convolution integral (cf. e.g. [195, 245]). Some of these schemes tend to converge faster than (3.122) w.r.t. the reduced time-step $\Delta\tau$; however, they require higher computational effort in computing the last term in (3.121). Alternatively, a pilot run can be conducted using the "full" convolution reduced scheme in (3.119) and then verify the result with (3.122), as it is done in this study. The remaining convolution integrals involving the rest of indicial functions in (3.83) and impulse functions in (3.84) and (3.85) can be reduced in a similar fashion.

Interrelations with flat plate and quasi-steady aerodynamics

For a state of $\tau \to \infty$, the indicial functions in (3.83) tend asymptotically to unity, i.e. $\Phi \to 1$, in a similar fashion as for flat plate (cf. (3.63)). In that case, the LU model in time domain (3.83) reduces to the LQS model in (3.71). Alternatively, the flutter derivatives of the LU model can be related to their quasi-steady asymptotes at the limit $V_r \to \infty$. Comparing (3.71) and (3.72),

the following relations are obtained:

$$\begin{aligned}
&P_1^* = -\frac{2C_D}{K}, && P_2^* = \frac{(C_D' - C_L)m_D}{K}, && P_3^* = \frac{C_D'}{K^2}, && P_4^* = 0, && P_5^* = \frac{C_D' - C_L}{K}, && P_6^* = 0,\\
&H_1^* = -\frac{C_L' + C_D}{K}, && H_2^* = -\frac{(C_L' + C_D)m_L}{K}, && H_3^* = -\frac{C_L'}{K^2}, && H_4^* = 0, && H_5^* = \frac{2C_L}{K}, && H_6^* = 0,\\
&A_1^* = \frac{C_M'}{K}, && A_2^* = \frac{C_M' m_M}{K}, && A_3^* = \frac{C_M'}{K^2}, && A_4^* = 0, && A_5^* = -\frac{2C_M}{K}, && A_6^* = 0.
\end{aligned} \tag{3.123}$$

When performing rational approximation, the asymptotes of the flutter derivatives can be set according to (3.123), which reduces the numerical uncertainty due to extrapolation at high reduced velocities. The aerodynamic admittances in the quasi-steady state simply yield

$$\chi_{jk} = 1, \quad \text{for } j \in \{D, L, M\}, \quad k \in \{u, w\}. \tag{3.124}$$

As noted previously in Sec. 3.5.3, the aerodynamic center can be obtained based on the flutter derivatives from (3.123) as

$$m_D = \frac{KP_2^*}{K^2 P_3^* - C_L}, \quad m_L = \frac{KH_2^*}{K^2 H_3^* - C_D}, \quad m_M = \frac{KA_2^*}{K^2 A_3^*}. \tag{3.125}$$

For high reduced velocities, the aerodynamic center tends to an asymptotic value, which represents the equivalent quasi-steady state. Selecting a reduced velocity of $V_r \geq 16$ for the aerodynamic center in (3.125) can be regarded as equivalent quasi-steady state in bridge aerodynamic, as noted by Diana and his coworkers [80, 85].

The flutter derivatives can be obtained based on flat plate unsteady aerodynamics. Assuming harmonic motion and relating (3.72) to (3.54) [301], the following equivalences are obtained:

$$\begin{aligned}
H_1^* &= -2\pi \frac{1}{K^2} K\Re(C), & A_1^* &= \frac{\pi}{2}\frac{1}{K^2} K\Re(C),\\
H_2^* &= -2\pi \frac{1}{K^2}\left[\frac{K}{4} + \Im(C) + \frac{K\Re(C)}{4}\right], & A_2^* &= \frac{\pi}{2}\frac{1}{K^2}\left[-\frac{K}{4} + \Im(C) + \frac{K\Re(C)}{4}\right],\\
H_3^* &= -2\pi \frac{1}{K^2}\left[\Re(C) - K\Im(C)\right], & A_3^* &= \frac{\pi}{2}\frac{1}{K^2}\left[\frac{K^2}{32} + \Re(C) - \frac{K\Im(C)}{4}\right],\\
H_4^* &= 2\pi \frac{1}{K^2}\left[\frac{K^2}{4} + K\Im(C)\right], & A_4^* &= -\frac{\pi}{2}\frac{1}{K^2} K\Im(C),
\end{aligned} \tag{3.126}$$

where $C = C(K^*)$ is Theodorsen function (cf. (3.52)) for $K^* = K/2$. Based on this formulation, the flutter derivatives contain the apparent mass forces. Caracoglia and Jones [45] argued that the general formulation of the unsteady self-excited forces should not contain the apparent mass terms contained in (3.72); hence, any term not multiplied to $C(K^*)$ should be disregarded. Moreover, the rotation-related derivatives, H_2^*, H_3^*, A_2^* and A_3^*, contain both imaginary and real part of $C(K^*)$. This is due to the contribution related to the angular velocity in (3.54), which is not explicitly modeled in (3.72). Neglecting the contribution proportional to K for these derivatives and the apparent mass effect results in the following equivalences:

$$
\begin{aligned}
H_1^* &= -2\pi\frac{1}{K^2}K\Re(C), \quad A_1^* = \frac{\pi}{2}\frac{1}{K^2}K\Re(C),\\
H_2^* &= -2\pi\frac{1}{K^2}\Im(C), \qquad A_2^* = \frac{\pi}{2}\frac{1}{K^2}\Im(C),\\
H_3^* &= -2\pi\frac{1}{K^2}\Re(C), \qquad A_3^* = \frac{\pi}{2}\frac{1}{K^2}\Re(C),\\
H_4^* &= 2\pi\frac{1}{K^2}K\Im(C), \qquad A_4^* = -\frac{\pi}{2}\frac{1}{K^2}K\Im(C).
\end{aligned}
\tag{3.127}
$$

Changing this formulation into (3.95) and using flat plate slopes of the static wind coefficients (cf. (3.49)), all indicial functions are similar, i.e. $\Phi_{Lh} = \Phi_{L\alpha} = \Phi_{Mh} = \Phi_{M\alpha} = \Phi_{se}$, as it is in the flat plate case (cf. (3.59)). The formulation (3.127) will be used for verification of the rational approximation of indicial functions. However, to verify the derivatives from numerical simulations or experiments, the relations in (3.126) should be used as the contribution of the apparent mass and angular velocity to the forces cannot be separated. In the case of the buffeting forces, it is clear from (3.73) and (3.54) that only Sears admittance should be used.

3.5.6 Mode-by-mode model

The simplification in the MBM model is the disregard of aerodynamic coupling. This means that the cross-terms in the LU model (cf. (3.83)) are neglected, yielding the following formulation:

$$
\mathbf{MBM} := \begin{cases}
D = D_s + D_b + D_{se}, \quad L = L_s + L_b + L_{se}, \quad M = M_s + M_b + M_{se},\\
D_s = \frac{1}{2}\rho U^2 B C_D, \quad L_s = -\frac{1}{2}\rho U^2 B C_L, \quad M_s = \frac{1}{2}\rho U^2 B^2 C_M,\\
D_b = \frac{1}{2}\rho U^2 B\left[2C_D\int_{-\infty}^{t}\Phi_{Du}(t-t_1)\frac{\dot{u}(t_1)}{U}\mathrm{d}t_1 (C_D' - C_L)\int_{-\infty}^{t}\Phi_{Dw}(t-t_1)\frac{\dot{w}(t_1)}{U}\mathrm{d}t_1\right],\\
L_b = -\frac{1}{2}\rho U^2 B\left[2C_L\int_{-\infty}^{t}\Phi_{Lu}(t-t_1)\frac{\dot{u}(t_1)}{U}\mathrm{d}t_1\right.\\
\qquad\qquad \left. + (C_L' + C_D)\int_{-\infty}^{t}\Phi_{Lw}(t-t_1)\frac{\dot{w}(t_1)}{U}\mathrm{d}t_1\right],\\
M_b = \frac{1}{2}\rho U^2 B^2\left[2C_M\int_{-\infty}^{t}\Phi_{Mu}(t-t_1)\frac{\dot{u}(t_1)}{U}\mathrm{d}t_1 + C_M'\int_{-\infty}^{t}\Phi_{Mw}(t-t_1)\frac{\dot{w}(t_1)}{U}\mathrm{d}t_1\right],\\
D_{se} = \frac{1}{2}\rho U^2 B 2C_D\int_{-\infty}^{t}\Phi_{Dp}(t-t_1)\frac{\ddot{p}(t_1)}{U}\mathrm{d}t_1\\
L_{se} = -\frac{1}{2}\rho U^2 B(C_L' + C_D)\int_{-\infty}^{t}\Phi_{Lh}(t-t_1)\frac{\ddot{h}(t_1)}{U}\mathrm{d}t_1,\\
M_{se} = \frac{1}{2}\rho U^2 B^2\left[C_M'\int_{-\infty}^{t}\Phi_{M\alpha}(t-t_1)\dot{\alpha}(t_1)\mathrm{d}t_1\right.\\
\qquad\qquad \left. + C_M'\int_{-\infty}^{t}\Phi_{M\dot{\alpha}}(t-t_1)\frac{m_M B\ddot{\alpha}(t_1)}{U}\mathrm{d}t_1\right].
\end{cases}
\tag{3.128}
$$

Due to its simplicity and computational efficiency in the frequency domain, the conventional MBM model was utilized in the past for buffeting analysis (cf. e.g. [281, 289]). Based on the frequency-domain formulation of the LU model given in (3.78), the MBM model in the frequency domain yields

$$\left[-\omega^2 \boldsymbol{M} + i\omega(\boldsymbol{C} - \boldsymbol{I}\boldsymbol{C}_{ae}) + (\boldsymbol{K} - \boldsymbol{I}\boldsymbol{K}_{ae})\right] \hat{\boldsymbol{q}} = \boldsymbol{f}_s + \hat{\boldsymbol{f}}_b, \tag{3.129}$$

where $\boldsymbol{I}$ is the identity matrix which suppresses the aerodynamic coupling. Formulated in such a way, the system in (3.129) is decoupled, i.e. the off-diagonal term in all matrices are zero.

3.5.7 Complex mode-by-mode model

The CMBM model is presented herein, including a new simple method for computation of the buffeting forces based on Fourier transform.

To account for the aerodynamic coupling and still solve a frequency-independent system for the self-excited forces, the CMBM was introduced by Chen and Kareem [57] and later on revisited by Øiseth et al. [245]. The method is based on the complex modal decomposition technique. Rearranging (3.75), the system can be expressed in the state-space as

$$\dot{\boldsymbol{\eta}}_o = \boldsymbol{O}\boldsymbol{\eta}_o + \boldsymbol{N}(\boldsymbol{f}_s + \boldsymbol{f}_b), \tag{3.130}$$

where $\boldsymbol{\eta}_o = \boldsymbol{\eta}_o(t)$ is the state vector, $\boldsymbol{O} = \boldsymbol{O}(K)$ is the state matrix, dependent on the reduced frequency K, and $\boldsymbol{N}$ is the input matrix. These are obtained as

$$\boldsymbol{\eta}_o = \begin{pmatrix} \boldsymbol{q} \\ \dot{\boldsymbol{q}} \end{pmatrix}, \quad \boldsymbol{O} = \begin{bmatrix} \boldsymbol{0} & \boldsymbol{I} \\ -\boldsymbol{M}^{-1}(\boldsymbol{K} - \boldsymbol{K}_{ae}) & -\boldsymbol{M}^{-1}(\boldsymbol{C} - \boldsymbol{C}_{ae}) \end{bmatrix}, \quad \boldsymbol{N} = \begin{bmatrix} \boldsymbol{0} \\ \boldsymbol{M}^{-1} \end{bmatrix}. \tag{3.131}$$

The effect of the self-excited forces can be studied through complex eigenvalue analysis for an eigenvalue problem of (3.130) as

$$(\boldsymbol{O} - \lambda \boldsymbol{I})\boldsymbol{\zeta} = \boldsymbol{0}, \quad \boldsymbol{\zeta} = \begin{pmatrix} \boldsymbol{\phi} \\ \lambda \boldsymbol{\phi} \end{pmatrix}, \tag{3.132}$$

where the vector $\boldsymbol{\zeta}$ is the complex eigenvector with size in $\mathbb{R}^{2N_m \times 1}$, $\boldsymbol{\phi}$ is the complex mode shape vector with size in $\mathbb{R}^{N_m \times 1}$ and λ is the complex eigenvalue, defined as

$$\lambda = -\xi\omega + i\omega\sqrt{1 - \xi^2}, \tag{3.133}$$

where ω and ξ are the frequency and damping ratio of the complex mode. Since the size of the matrix $\boldsymbol{O}$ is in $\mathbb{R}^{2N_m \times 2N_m}$, there are $2N_m$ roots of the characteristic polynomial; therefore the complex modes $\boldsymbol{\phi}_j$ and complex eigenvalues λ_j are obtained along with their complex conjugates $\boldsymbol{\phi}_{j+N_m} = \overline{\boldsymbol{\phi}}_j$ and $\lambda_{j+N_M} = \overline{\lambda}_j$ for $j \in \{1, \ldots, N_m\}$, respectively. Since $\boldsymbol{O}$ is frequency-dependent, iterative complex eigenvalue analysis is required for each mode until the assumed frequency converges with the imaginary part $\Im(\lambda)$. In the case of flutter analysis, the critical velocity U_{cr} is determined for a zero damping ratio of any complex mode, i.e. $\Re(\lambda) \geq 0$.
In the frequency-domain buffeting analysis, the transfer function between the buffeting forces and modal responses is computed for each frequency increment (cf. (3.82)). Thus, generally the complex eigenvalue analysis is not required. However, the method in the frequency domain described in Sec. 3.5.5 requires multiple matrix inversion operations and can be computationally costly. In the MBMC model, it is assumed that the peaks at the complex eigenvalues in the

system transfer function have the most influence on the response; thus, the state matrix $\boldsymbol{O}$ can be approximated by equivalent state matrix $\boldsymbol{O}^*$, that is based on the complex eigenvalues and satisfy the condition:

$$\boldsymbol{\Xi}^{-1}\boldsymbol{O}^*\boldsymbol{\Xi} = \boldsymbol{\Lambda}, \tag{3.134}$$

where $\boldsymbol{\Xi}$ is a matrix with size in $\mathbb{R}^{2N_m \times 2N_m}$ and it contains the complex eigenvectors $\boldsymbol{\zeta}_j$ such that $\boldsymbol{\zeta}_{j+N_m} = \overline{\boldsymbol{\zeta}}_j$ for $j \in \{1, \ldots, N_m\}$ and satisfies the orthogonality condition $\boldsymbol{\Xi}^{-1}\boldsymbol{\Xi} = \boldsymbol{I}$. The eigenvalue matrix $\boldsymbol{\Lambda}$ is a diagonal matrix containing the eigenvalues λ_j and their complex conjugates $\lambda_{j+N_m} = \overline{\lambda}_j$. In this way the state vector $\boldsymbol{\eta}_o$ can be expressed in terms of complex modal coordinates as

$$\boldsymbol{\eta}_o = \boldsymbol{\Xi}\boldsymbol{\eta}, \tag{3.135}$$

where the modal state vector $\boldsymbol{\eta} = \boldsymbol{\eta}(t)$ contains the complex modal displacements such that $\eta_{j+N_m} = \overline{\eta}_j$ for $j \in \{1, \ldots, N_m\}$ and (3.130) can be decoupled as

$$\dot{\boldsymbol{\eta}} = \boldsymbol{\Lambda}\boldsymbol{\eta} + \boldsymbol{\Xi}^{-1}\boldsymbol{N}(\boldsymbol{f}_s + \boldsymbol{f}_b). \tag{3.136}$$

Since the preceding equation is decoupled and frequency independent, it can be solved in the time domain without rational approximation for the self-excited forces.

To be able to define the MNL model explicitly in the time domain, the self-excited forces are derived for the three-degree-of-freedom system in (3.5). For this system, the modal displacements are

$$\boldsymbol{q} = \sum_{j=1}^{3} \left(\boldsymbol{\phi}_j \eta_j + \overline{\boldsymbol{\phi}}_j \overline{\eta}_j \right). \tag{3.137}$$

The self-excited force vector can be described in terms of aerodynamic stiffness and damping matrices as in (3.74). E.g., the lift force due to vertical motion yields

$$L_h = \frac{1}{2}\rho U B \left[U K^2 H_4^*(K) \sum_{j=1}^{3} \left(\phi_{2j}\eta_j + \overline{\phi}_{2j}\overline{\eta}_j \right) + BKH_1^*(K) \sum_{j=1}^{3} \left(\phi_{2j}\dot{\eta}_j + \overline{\phi}_{2j}\overline{\dot{\eta}}_j \right) \right]. \tag{3.138}$$

The whole system in (3.131) has the same complex eigenvalues as in (3.136). The main assumption in the MBMC model is that the self-excited forces can be modeled by interpolating the aerodynamic stiffness and damping matrices at the complex modal frequencies as

$$L_h = \frac{1}{2}\rho U B \left[U \sum_{j=1}^{3} K_{cj}^2 H_4^*(K_{cj}) \left(\phi_{2j}\eta_j + \overline{\boldsymbol{\phi}}_j \overline{\eta}_j \right) + B \sum_{j=1}^{3} K_{cj} H_1^*(K_{cj}) \left(\phi_{2j}\dot{\eta}_j + \overline{\phi}_{2j}\overline{\dot{\eta}}_j \right) \right], \tag{3.139}$$

where $K_{cj} = K_{cj}(\lambda_j)$ is the reduced frequency corresponding to the complex eigenfrequencies.

Summarizing, the CMBM model is defined as follows:

$$
\textbf{CMBM} := \begin{cases}
D = D_s + D_b + D_{se}, \quad L = L_s + L_b + L_{se}, \quad M = M_s + M_b + M_{se}, \\
D_s = \dfrac{1}{2}\rho U^2 B C_D, \quad L_s = -\dfrac{1}{2}\rho U^2 B C_L, \quad M_s = \dfrac{1}{2}\rho U^2 B^2 C_M, \\
D_b = \dfrac{1}{2}\rho U^2 B \Bigg[2C_D \displaystyle\int_{-\infty}^{t} \Phi_{Du}(t-t_1)\frac{\dot{u}(t_1)}{U}\mathrm{d}t_1 \\
\qquad\qquad + (C_D' - C_L) \displaystyle\int_{-\infty}^{t} \Phi_{Dw}(t-t_1)\frac{\dot{w}(t_1)}{U}\mathrm{d}t_1 \Bigg], \\
L_b = -\dfrac{1}{2}\rho U^2 B \Bigg[2C_L \displaystyle\int_{-\infty}^{t} \Phi_{Lu}(t-t_1)\frac{\dot{u}(t_1)}{U}\mathrm{d}t_1 \\
\qquad\qquad + (C_L' + C_D) \displaystyle\int_{-\infty}^{t} \Phi_{Lw}(t-t_1)\frac{\dot{w}(t_1)}{U}\mathrm{d}t_1 \Bigg], \\
M_b = \dfrac{1}{2}\rho U^2 B^2 \Bigg[2C_M \displaystyle\int_{-\infty}^{t} \Phi_{Mu}(t-t_1)\frac{\dot{u}(t_1)}{U}\mathrm{d}t_1 \\
\qquad\qquad + C_M' \displaystyle\int_{-\infty}^{t} \Phi_{Mw}(t-t_1)\frac{\dot{w}(t_1)}{U}\mathrm{d}t_1 \Bigg], \\
D_{se} = \displaystyle\sum_{j=1}^{3} \left[\boldsymbol{k}_{ae1}(K_{cj})\boldsymbol{\phi}_j\eta_j + \boldsymbol{k}_{ae1}(K_{cj})\overline{\boldsymbol{\phi}}_j\overline{\eta}_j + \boldsymbol{c}_{ae1}(K_{cj})\boldsymbol{\phi}_j\eta_j + \boldsymbol{c}_{ae1}(K_{cj})\overline{\boldsymbol{\phi}}_j\overline{\eta}_j \right], \\
L_{se} = \displaystyle\sum_{j=1}^{3} \left[\boldsymbol{k}_{ae2}(K_{cj})\boldsymbol{\phi}_j\eta_j + \boldsymbol{k}_{ae2}(K_{cj})\overline{\boldsymbol{\phi}}_j\overline{\eta}_j + \boldsymbol{c}_{ae2}(K_{cj})\boldsymbol{\phi}_j\eta_j + \boldsymbol{c}_{ae2}(K_{cj})\overline{\boldsymbol{\phi}}_j\overline{\eta}_j \right], \\
M_{se} = \displaystyle\sum_{j=1}^{3} \left[\boldsymbol{k}_{ae3}(K_{cj})\boldsymbol{\phi}_j\eta_j + \boldsymbol{k}_{ae3}(K_{cj})\overline{\boldsymbol{\phi}}_j\overline{\eta}_j + \boldsymbol{c}_{ae3}(K_{cj})\boldsymbol{\phi}_j\eta_j + \boldsymbol{c}_{ae3}(K_{cj})\overline{\boldsymbol{\phi}}_j\overline{\eta}_j \right],
\end{cases}
\tag{3.140}
$$

where $\boldsymbol{k}_{aen} = \boldsymbol{k}_{aek}(K_{cj})$ and $\boldsymbol{c}_{aek} = \boldsymbol{c}_{aek}(K_{cj})$ are row vectors of size in $\mathbb{R}^{1\times 3}$ that correspond to the k-th row of the aerodynamic stiffness and damping matrices in (3.76) and (3.77), respectively. For each complex mode, these vectors depend on the reduced frequency $K_{cj} = K_{cj}(\lambda_j)$ corresponding to the complex eigenfrequency $\Im(\lambda_j)$.

Method for computation of the unsteady buffeting forces based on FFT*

The buffeting forces in the MBMC still are modeled as for the LU model, i.e. they require rational approximation as pointed out by Chen and Kareem in [57]. Øiseth et al. [245] did not include fluid memory in the buffeting forces. Herein, a novel method is presented in order to avoid rational approximation, which is indeed the motivation for the MBMC model.
The method utilizes the principles of a response of stable linear systems due to periodic inputs [67]. In this case, the buffeting force is the response, which is, in fact, stable and linear, while the wind fluctuations are the input. Assuming that the wind fluctuations are stationary periodic signals (as previously defined in Sec. 3.3), the buffeting forces in (3.73) can be obtained using the Fourier transform for a given time-domain wind fluctuations, i.e. $u = u(t)$ and $w = w(t)$. Noting the convolution theorem in (3.92), the aerodynamic admittance can be simply multiplied to the Fourier transform of the wind fluctuations and then transferred back to the time domain

using the inverse Fourier transform. Taking this into account, e.g., the lift buffeting force yields

$$L_{bw}(t) = \frac{1}{2}\rho U^2 B(C_L' + C_D) \int_{-\infty}^{\infty} \chi_{Lw}(f) \frac{\hat{w}(f)}{U} \exp(2\pi i f t) \mathrm{d}f. \tag{3.141}$$

For periodic input and stable output, the difference between using the Fourier instead of the Laplace transform as for rational approximation is that there is an additional assumption that the transient part (fluid memory) of the initial part of the force is zero. It is later shown in Sec. 5.4.5 that this influence is insignificant. As wind fluctuations are commonly generated before solving (3.5) or (3.136), the FFT can be directly employed for the discrete solution of the circular convolution implied in (3.141). Since the force and the wind fluctuations are real signals, the admittance has the Hermitian symmetry, i.e. $\chi_{Lw}(f) = \overline{\chi}_{Lw}(-f)$. It is clear that instead of rational approximation of χ_{Lw}, interpolation or fitting in the frequency domain can be used which is more convenient in bridge aerodynamics especially for noisy experimentally obtained admittance functions (cf. e.g. [187]). The method could also be applied for admittance functions obtained from the spectral method with zero lag, i.e. $\Im(\chi)$=0. However, it should be mentioned that this implies that the admittance is a non-causal filter, i.e. the lift force depends on future inputs. Since the generated wind fluctuation signals are a superposition of integer harmonic signals, the Gibbs effect and spectral leakage are avoided. Figure 3.8 depicts the presented method schematically.

This method for computation of the buffeting forces can also be applied to any model that includes the fluid memory such as the LU or HNL models. The computational time is significantly reduced for the solution of the second-order differential equation (cf. (3.5)). Instead of solving the linear convolution integral, FFT is used once before the analysis. Alternatively, the buffeting forces can be directly generated by modifying the spectral matrix of the wind fluctuations (3.26) with the aerodynamic admittance as in [62]. However, in this case, the aerodynamic nonlinearities in the HNL model, such as the dependency of aerodynamic parameters on the effective angle of attack cannot be accounted for, as noted by Chen and Kareem [56]. In the case of experimentally obtained admittance functions containing finite data set, the extrapolation of the admittance for the high reduced velocity is by assuming quasi-steady values. If rational function approximation is utilized, this problem is solved simply by utilizing the analytic continuation of the impulse or indicial response functions.

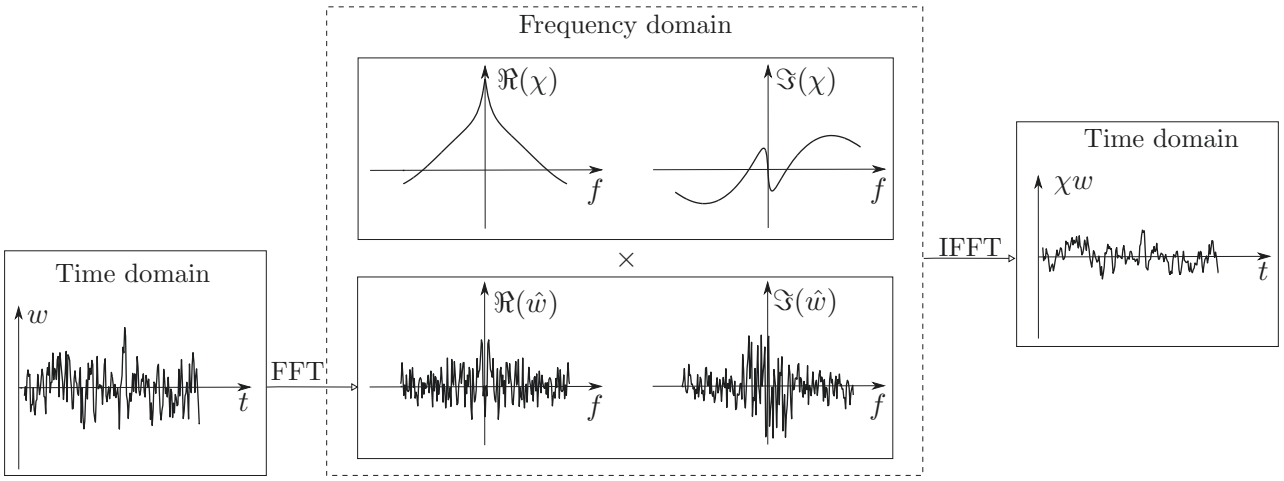

Figure 3.8: Graphical illustration of the method of computation of the unsteady buffeting forces based on the FFT.

3.5.8 Modified quasi-steady model

In order to avoid rational approximation in the LU model and reduce the ambiguity of the aerodynamic center in the LQS model, Øiseth et al. [244] introduced the MQS model. In this model, the self-excited forces are obtained by substituting the flutter derivatives in (3.72) with frequency-independent coefficients that neglect the unsteady contribution. With this, and assuming the buffeting forces are modeled as for the LQS model (3.71), the formulation of the MQS model yields the following:

$$\mathbf{MQS} := \begin{cases} D = D_s + D_b + D_{se}, \quad L = L_s + L_b + L_{se}, \quad M = M_s + M_b + M_{se}, \\ D_s = \dfrac{1}{2}\rho U^2 B C_D, \quad L_s = -\dfrac{1}{2}\rho U^2 B C_L, \quad M_s = \dfrac{1}{2}\rho U_r^2 B^2 C_M, \\ D_b = \dfrac{1}{2}\rho U^2 B \left[2C_D \dfrac{u}{U} + (C_D' - C_L)\dfrac{w}{U}\right], \\ L_b = -\dfrac{1}{2}\rho U^2 B \left[2C_L \dfrac{u}{U} + (C_L' + C_L)\dfrac{w}{U}\right], \\ M_b = \dfrac{1}{2}\rho U^2 B^2 \left(2C_M \dfrac{u}{U} + C_M' \dfrac{w}{U}\right), \\ D_{se} = \dfrac{1}{2}\rho U^2 B \left(A_{p1}\dfrac{\dot{p}}{U} + A_{p2}\dfrac{B\dot{\alpha}}{U} + A_{p3}\alpha + A_{p4}\dfrac{p}{B} + A_{p5}\dfrac{\dot{h}}{U} + A_{p6}\dfrac{h}{B}\right), \\ L_{se} = \dfrac{1}{2}\rho U^2 B \left(A_{h1}\dfrac{\dot{h}}{U} + A_{h2}\dfrac{B\dot{\alpha}}{U} + A_{h3}\alpha + A_{h4}\dfrac{h}{B} + A_{h5}\dfrac{\dot{p}}{U} + A_{h6}\dfrac{p}{B}\right), \\ M_{se} = \dfrac{1}{2}\rho U^2 B^2 \left(A_{a1}\dfrac{\dot{h}}{U} + A_{a2}\dfrac{B\dot{\alpha}}{U} + A_{a3}\alpha + A_{a4}\dfrac{h}{B} + A_{a5}\dfrac{\dot{p}}{U} + A_{a6}\dfrac{p}{B}\right), \end{cases} \tag{3.142}$$

where $A_{pj} = A_{pj}(V_{rc1})$, $A_{hj} = A_{hj}(V_{rc2})$ and $A_{aj} = A_{aj}(V_{rc3})$ for $j \in \{1, \ldots, 6\}$ are frequency-independent coefficients taking into account the averaged fluid memory at specific reduced velocity of oscillation V_{rck} for $k \in \{1, 2, 3\}$. Comparing (3.72) and (3.142), the following relations are obtained:

$$A_{pj} = K_{c1} P_j^*, \quad A_{hj} = K_{c2} H_j^*, \quad A_{aj} = K_{c3} A_j^*, \quad \text{for } j \in \{1, 2, 5\}, \tag{3.143}$$

$$A_{pj} = K_{c1}^2 P_j^*, \quad A_{hj} = K_{c2}^2 H_j^*, \quad A_{aj} = K_{c3}^2 A_j^*, \quad \text{for } j \in \{3, 4, 6\}. \tag{3.144}$$

The frequency-independent coefficients are obtained either by using linear least-square fit or by secant approximation to the flutter derivatives. The secant approximation is at a selected value of V_{rck} (equivalently, K_{ck}), that is based on an oscillation frequency for each direction of motion (translation or rotation), i.e. $k \in \{1, \ldots, 3\}$. In the first case, V_{rc} is obtained implicitly, while in the latter, V_{rc} is typically based on the first natural frequency for each direction. The frequency-independent coefficients can be also related to the approximation of the impulse response function (cf. (3.112)), in a sense that the A_1 coefficient corresponds to the stiffness-related frequency-independent coefficients A_p (cf. (3.144)), while A_2 coefficient corresponds to the damping-related frequency-independent coefficients A_p (cf. (3.143)).

3.5.9 Corrected quasi-steady model

The idea of the CQS model is to retain the nonlinearity considered in the QS model as an advantage over the LU model, while partially modeling the unsteadiness. Diana et al. [80]

proposed the CQS model by modifying the slope of the static wind coefficients in (3.70) with dynamic derivatives that take into account an averaged fluid memory. The CQS model is formulated as

$$\mathbf{CQS} := \begin{cases} D = F_L \sin\varphi_D + F_D \cos\varphi_D, \quad L = F_L \cos\varphi_L - F_D \sin\varphi_L, \quad M = F_M, \\ F_D = \dfrac{1}{2}\rho U_{rD}^2 B C_D^*(\alpha_{eD}), \quad F_L = -\dfrac{1}{2}\rho U_{rL}^2 B C_L^*(\alpha_{eL}), \quad F_M = \dfrac{1}{2}\rho U_{rM}^2 B^2 C_M^*(\alpha_{eM}), \\ \alpha_{ej} = \alpha_s + \alpha + \varphi_j, \quad \varphi_j = \arctan\left(\dfrac{w + \dot{h} + m_j B\dot{\alpha}}{U + u - \dot{p}}\right), \\ U_{rj} = \sqrt{(U + u - \dot{p})^2 + (w + \dot{h} + m_j B\dot{\alpha})^2}, \\ C_j^*(\alpha_{ej}) = C_j(\alpha_s) + \displaystyle\int_{\alpha_s}^{\alpha_e} Q_j^*(\alpha_1, V_{rc}) C_j'(\alpha_1) \mathrm{d}\alpha_1, \quad \text{for } j \in \{D, L, M\}, \end{cases} \tag{3.145}$$

where $C_j^* = C_j^*(\alpha_{ej})$ are the corrected static wind coefficients based on the dynamic derivatives $Q_j^* = Q_j^*(V_{rc}, \alpha_{ej})$. The dynamic derivatives are either obtained from dynamic tests or more commonly, from the flutter derivatives. In the latter case, the equivalences between the dynamic derivatives and the flutter derivatives are obtained from (3.145) and (3.72), yielding

$$Q_D^* = \frac{K_c^2 P_3^*}{C_D'}, \quad Q_L^* = -\frac{K_c^2 H_3^*}{C_L'}, \quad Q_M^* = \frac{K_c^2 A_3^*}{C_M'}. \tag{3.146}$$

For the CQS model, the flutter derivatives are required at various angles of attack, i.e. $P_3^* = P_3^*(\alpha, V_{rc})$, $H_3^* = A_3^*(\alpha, V_{rc})$, $A_3^* = A_3^*(\alpha, V_{rc})$, and are interpolated at specific reduced velocity V_{rc}, based on the averaged frequency of oscillation f_c. In this work, f_c is computed as $f_c = (f_h + f_\alpha)/2$, with f_h and f_α being the frequencies of the first vertical and torsional modes, respectively. Since the contribution to the effective angle of attack of wind fluctuations and motion cannot be separated, the same correction coefficients account for both averaged fluid memory in the buffeting and self-excited forces. The implied assumption here is that the fluid memory of the self-excited and buffeting forces are essentially the same. Some studies have correlated the flutter derivatives and the admittance functions in an analytical and an experimental way (cf. e.g. [11, 286, 287, 328]). However, these correlations do not hold for the flat plate analytical solution.

3.5.10 Hybrid nonlinear model

Chen and Kareem [59] introduced the HNL model under the premise that the effect fluid memory is insignificant at high reduced velocities and the nonlinearity is governing the aerodynamic forces, while for low reduced velocities, the effect of fluid memory is dominant. In the HNL, the effective angle of attack is split into a low- and a high-frequency component denoted as α_e^l and α_e^h, respectively. For the low-frequency part, the QS model is utilized to compute the forces (cf. (3.70)), and for the high-frequency component, the LU model is employed (cf. (3.83)), linearized at the low-frequency angle of attack α_e^l. Taking this into account, the HNL model is

defined as follows:

$$\textbf{HNL} := \begin{cases} D = D^{QS}(\alpha_e^l) + D^{LU}(\alpha_e^h)|_{\alpha_e^l}, \quad L = L^{QS}(\alpha_e^l) + L^{LU}(\alpha_e^h)|_{\alpha_e^l}, \\ M = M^{QS}(\alpha_e^l) + M^{LU}(\alpha_e^h)|_{\alpha_e^l}, \quad \alpha_{ej} = \alpha_{ej}^l + \alpha_{ej}^h, \\ \alpha_{ej}^l = \alpha_s + \alpha^l + \arctan\left(\dfrac{w^l + \dot{h}^l + m_j B\dot{\alpha}^l + n_j \dot{w}^l}{U + u^l - \dot{p}^l}\right). \quad \text{for } j \in \{D, L, M\}. \end{cases} \tag{3.147}$$

In Chen and Kareem's formulation of the NLU model in [59], the effective angle of attack is in a similar form as for the QS model (cf. (3.70)). Herein, the formulation recently presented by Diana et al. [85] is employed, which introduces the coefficient n_j that accounts for the phase lag between the wind fluctuations and quasi-steady aerodynamic force in the low-frequency range. This coefficient is obtained based on the aerodynamic admittance of vertical fluctuations as

$$n_j = \frac{\Re(\chi_{jw})}{\Im(\chi_{jw})} \frac{V_r}{2\pi} \frac{B}{U}. \tag{3.148}$$

As for the aerodynamic center, a reduced velocity should be selected for n_j at which the phase becomes negligible (i.e. equivalent quasi-steady state). In bridge aerodynamics, this is usually for reduced velocities amounting to $V_r \geq 15$. Correspondingly, the cut-off frequency should be chosen in such a manner to accommodate for the validity of the quasi-steady assumption in the low-frequency band of α_e^l. Alternatively, this threshold can be taken similar to the first natural frequency [59]. It is noted that the HNL model is not fully nonlinear or fully unsteady; rather a hybrid model, based on the intrinsic understanding of the aerodynamic force.

3.5.11 Advanced models

Two additional models, MNL and HNL, are given in this section to evaluate their complexity based on the categorical modeling approach in the next chapter. No numerical implementation of these models is considered in this work. The reasons are briefly discussed after these models are presented.

The MNL model approximates the aerodynamic hysteresis in a nonlinear fashion, yielding the following formulation of the aerodynamic forces:

$$\textbf{MNL} := \begin{cases} D = \dfrac{1}{2}\rho U_{rj}^2 B \left[-C_L^{hys}(\alpha_{eL}) \sin\varphi_D + C_D^{hys}(\alpha_{eD}) \cos\varphi_D\right], \\ L = -\dfrac{1}{2}\rho U_{rj}^2 B \left[C_L^{hys}(\alpha_{eL}) \cos\varphi_L + C_D^{hys}(\alpha_{eD}) \sin\varphi_L\right], \quad M = \dfrac{1}{2}\rho U_{rj}^2 B^2 C_M^{hys}(\alpha_{eM}), \\ \alpha_{ej} = \alpha_s + \alpha + \varphi_j, \quad \varphi_j = \arctan\left(\dfrac{w + \dot{h} + m_j B\dot{\alpha}}{U + u - \dot{p}}\right), \\ U_{rj} = \sqrt{(U + u - \dot{p})^2 + (w + \dot{h} + m_j B\dot{\alpha})^2}, \quad \text{for } j \in \{D, L, M\}, \end{cases} \tag{3.149}$$

where $C_j^{hys} = C_j^{hys}(\alpha_e, \dot{\alpha_e}, V_{rc})$ is the aerodynamic hysteresis. There are several ways how to approximate the aerodynamic hysteresis, e.g., using rheological models [84] or artificial neural networks [356]. For illustration, herein approximation using polynomials is utilized (cf. [86, 359]), which introduces an additional assumption that the fluid memory due to wind fluctuations and motion is similar. The aerodynamic hysteresis then yields

$$C_j^{hys} = C_j(\alpha_s) + \sum_{k,l}^{N_c} A_{jkl} \alpha_{ej}^k(V_{rc}) \dot{\alpha}_{ej}^l(V_{rc}), \tag{3.150}$$

where A are the approximation coefficients for a polynomial of degree $N_c \in \mathbb{N}_0$. The experimental or numerical aerodynamic hysteresis generally differs for various V_r; however, the approximated aerodynamic hysteresis is obtained at a specific reduced velocity V_r based on the frequency of oscillation. Alternatively, the aerodynamic hysteresis can be averaged for the whole range of reduced velocities V_r including a rheological model for the instability range [86] or the band-superposition scheme can be used for splitting the wind-spectrum in multiple frequency "bands" [359].

One of the most recently developed semi-analytical models is the NLU model, based on the nonlinear indicial functional. Since a general nonlinear indicial functional is presently unavailable for bridge decks, Wu and Kareem [360, 364] introduced a reduced scheme based on a finite sum of multidimensional convolution integrals accounting for higher-order nonlinear effects. Based on their formulation, the mathematical formulation of the NLU model is given as follows:

$$
\mathbf{NLU} := \begin{cases}
D = \frac{1}{2}\rho U^2 B \Bigg[\Phi_D^0 + \sum\limits_k \int_{-\infty}^{t} \Phi_{Dk}^{\mathrm{I}}(t-t_1)\dot{k}(t_1)\mathrm{d}t_1 \\
\qquad\qquad + \sum\limits_{k,l} \int_{-\infty}^{t}\int_{-\infty}^{t} \Phi_{Dkl}^{\mathrm{II}}(t-t_1,t-t_2)\dot{k}(t_1)\dot{l}(t_2)\mathrm{d}t_1\mathrm{d}t_2 + \dots \Bigg], \\
L = -\frac{1}{2}\rho U^2 B \Bigg[\Phi_L^0 + \sum\limits_k \int_{-\infty}^{t} \Phi_{Lk}^{\mathrm{I}}(t-t_1)\dot{k}(t_1)\mathrm{d}t_1 \\
\qquad + \sum\limits_{k,l} \int_{-\infty}^{t}\int_{-\infty}^{t} \Phi_{Lkl}^{\mathrm{II}}(t-t_1,t-t_2)\dot{k}(t_1)\dot{l}(t_2)\mathrm{d}t_1\mathrm{d}t_2 + \dots \Bigg], \\
M = \frac{1}{2}\rho U^2 B^2 \Bigg[\Phi_M^0 + \sum\limits_k \int_{-\infty}^{t} \Phi_{Mk}^{\mathrm{I}}(t-t_1)\dot{k}(t_1)\mathrm{d}t_1 \\
\qquad + \sum\limits_{k,l} \int_{-\infty}^{t}\int_{-\infty}^{t} \Phi_{Mkl}^{\mathrm{II}}(t-t_1,t-t_2)\dot{k}(t_1)\dot{l}(t_2)\mathrm{d}t_1\mathrm{d}t_2 + \dots \Bigg], \\
\text{for } k,l \in \left\{u, w, \dot{p}, \dot{h}, \alpha, \dot{\alpha}\right\},
\end{cases}
\tag{3.151}
$$

where $\Phi^0 = \Phi^0(t)$, $\Phi^{\mathrm{I}} = \Phi^{\mathrm{I}}(t)$, and $\Phi^{\mathrm{II}} = \Phi^{\mathrm{II}}(t)$ are the zeroth, first and second-order indicial functions. Higher-order indicial functions can be introduced in a similar fashion. It is convenient to formulate the NLU model in a Volterra series formalism, by using the analogies between the unit-step and unit-impulse functions [360]. With this, the well-established methods for identification of the Volterra kernels due to unit-impulse input are readily applicable.

From a perspective of numerical implementation, the MNL model is relatively straightforward. The main issue why this model was not considered in the analyses is the lack of a well-established method for the determination of the aerodynamic hysteresis. For highly nonlinear behavior at high oscillation amplitudes, the hysteresis exhibits non-periodic (i.e. non-repetitive) behavior (cf. e.g. [376]). The studies that utilize the MNL model commonly show a smooth hysteretic curve (cf. e.g. [86, 359]), which is probably the result of some kind of averaging at each angle. Moreover, high-frequency content in the forces due to vortex shedding and numerical noise can affect significantly the reliability of the aerodynamic hysteresis when it is obtained based on CFD using the VPM. Hence, first a standard method of determining the aerodynamic

hysteresis should be established before assessing this model in a quantitative manner for a practical example.

The determination of the kernels for the NLU model requires significant output data either from wind tunnel tests or CFD analyses. For e.g., the second-order indicial function Φ^{II} in (3.151) requires separate analyses at each time couple $t - t_1$ and $t - t_2$, which can yield a significant number of experimental tests or simulation runs. Alternatively, the Volterra kernels can be obtained by determining their frequency response counterparts from multi-frequency input [206]. For e.g., the second-order kernel requires dual-frequency input. The number of frequency couples grows quadratically; thus, it can yield a significant number of separate tests. Although the NLU model has been utilized for predicting vortex-induced vibrations (cf. e.g. [368]), the author is not aware of a study that presents full buffeting and flutter analyses of a bridge (2D or 3D), utilizing the NLU model based on CFD or experimental kernels. Hence, the practical application of the model is not yet well-established. Moreover, the NLU model requires burdensome numerical implementation. Nevertheless, from the preliminary investigations in previous studies, the model seems quite promising [360, 362, 363, 364]. Thus, although only conceptual, the mathematical constructions are included for the categorical evaluation of model complexity in the next chapter. However, to be able to quantitatively asses the model and have certain reliability of the results, further studies are required.

3.6 Computational fluid dynamics model

In this section, the CFD model is formulated as an alternative to the semi-analytical models. The VPM is adopted for the numerical discretization of the fluid governing equations. Initially, a brief background of the governing equation and numerical discretization of the VPM is given, followed by the velocity-based method for free-stream turbulence. Then, the Pseudo-3D vortex method with laminar free-stream is revisited to finally introduce a novel turbulent Pseudo-3D method based on the velocity-based free-stream turbulence.

3.6.1 Vortex particle method

The problem is defined for an oscillating body immersed into a fluid in $\mathbb{R}^2$ (cf. Fig. 3.9). The mathematical constructions of the fluid motion, boundary conditions with the corresponding aerodynamic forces are given in the following. Without being exhaustive, the brief formulation is essentially based on excellent works by Chorin and Marsden [65], Leonard [198], Cottet and Koumoutsakos [70] and Wu [353], and for further information, the reader is referred to these references.

Fluid motion

Considering an incompressible fluid flow with constant kinematic viscosity ν in a domain $\mathcal{F}$ in $\mathbb{R}^2$, the fluid motion is governed by the Navier-Stokes equations for conservation of the momentum:

$$\frac{\partial \boldsymbol{u}}{\partial t} + (\boldsymbol{u} \cdot \boldsymbol{\nabla})\, \boldsymbol{u} = -\frac{1}{\rho} \boldsymbol{\nabla} p_r + \nu \boldsymbol{\nabla}^2 \boldsymbol{u}, \tag{3.152}$$

and the incompressibility condition through continuity equation:

$$\boldsymbol{\nabla} \cdot \boldsymbol{u} = 0, \tag{3.153}$$

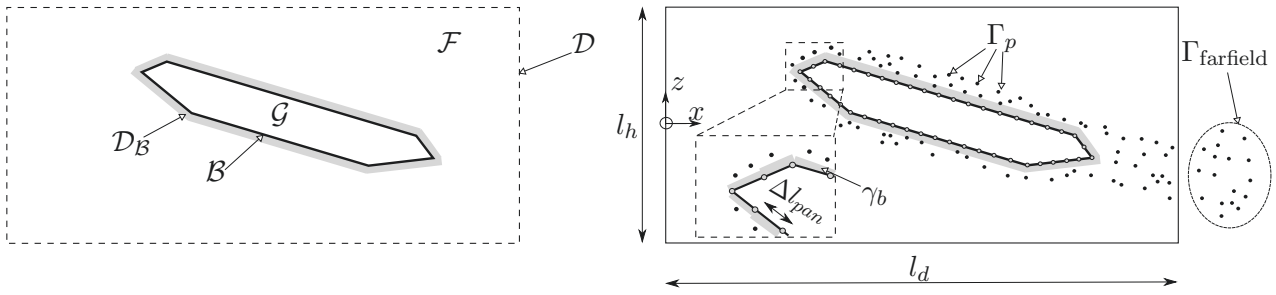

Figure 3.9: Coupled CFD model in 2D: formulation (left); numerical discretization (right).

where the velocity vector is $\boldsymbol{u} = \boldsymbol{u}(\boldsymbol{x};t) = (u(\boldsymbol{x};t), 0, w(\boldsymbol{x};t))$ and $p_r = p_r(\boldsymbol{x};t)$ is the pressure for $\boldsymbol{x} = (x, 0, z)$. Taking the curl of (3.152) and applying the incompressibility condition in (3.153) yields the vorticity transport equation:

$$\frac{\partial \omega_u}{\partial t} + (\boldsymbol{u} \cdot \boldsymbol{\nabla})\, \boldsymbol{\omega}_u = \nu \boldsymbol{\nabla}^2 \boldsymbol{\omega}_u, \tag{3.154}$$

where the curl of the velocity vector delivers

$$\boldsymbol{\nabla} \times \boldsymbol{u} = \boldsymbol{\omega}_u, \tag{3.155}$$

where $\boldsymbol{\omega}_u = \boldsymbol{\omega}_u(\boldsymbol{x};t) = (0, \omega_u(\boldsymbol{x};t), 0)$ is the vorticity vector. The only relevant component of the vorticity in $\mathbb{R}^2$ is the one perpendicular to the fluid plane, i.e. vorticity is a scalar field. For an inviscid fluid, the vorticity transport equation reduces to

$$\frac{\partial \omega_u}{\partial t} + (\boldsymbol{u} \cdot \boldsymbol{\nabla})\, \omega_u = 0. \tag{3.156}$$

Utilizing the following identity

$$\boldsymbol{\nabla} \times (\boldsymbol{\nabla} \times \boldsymbol{u}) = \boldsymbol{\nabla}(\boldsymbol{\nabla} \cdot \boldsymbol{u}) - \boldsymbol{\nabla}^2 \boldsymbol{u}, \tag{3.157}$$

and the continuity condition in (3.153), the velocity field can be obtained from the vorticity field by the following inverted kinematic relation:

$$\boldsymbol{\nabla}^2 \boldsymbol{u} = -\boldsymbol{\nabla} \times \boldsymbol{\omega}_u. \tag{3.158}$$

The preceding expression represents a Poisson equation, which can be solved using Green's function as

$$\boldsymbol{u}(\boldsymbol{x}) = \boldsymbol{u}_\infty - \frac{1}{2\pi} \int_\mathcal{D} \frac{(\boldsymbol{x} - \boldsymbol{z}) \times \boldsymbol{\omega}_u(\boldsymbol{z})}{|\boldsymbol{x} - \boldsymbol{z}|^2} \mathrm{d}\boldsymbol{z}, \tag{3.159}$$

where $\boldsymbol{u}_\infty$ is the mean fluid velocity vector (cf. (2.2)). Commonly, (3.159) is referred to as the Biot-Savart relation.

Boundary conditions

The no-penetration and no-slip velocity boundary conditions (cf. Fig. 3.9, left) yield

$$\boldsymbol{u}_\mathcal{B} \cdot \boldsymbol{n}_\mathcal{B} = \boldsymbol{u}_\mathcal{G} \cdot \boldsymbol{n}_\mathcal{B}, \tag{3.160}$$

$$\boldsymbol{u}_\mathcal{B} \cdot \boldsymbol{s}_\mathcal{B} = \boldsymbol{u}_\mathcal{G} \cdot \boldsymbol{s}_\mathcal{B}, \tag{3.161}$$

respectively. Herein, the fluid velocity on the boundary is denoted as $\boldsymbol{u}_{\mathcal{B}} = \boldsymbol{u}_{\mathcal{B}}(\boldsymbol{x}_{\mathcal{B}}; t)$, $\boldsymbol{x}_{\mathcal{B}} = (x_{\mathcal{B}}, 0, z_{\mathcal{B}})$ is the interface (i.e boundary) coordinate vector on the interface $\mathcal{B}$, $\boldsymbol{u}_{\mathcal{G}} = \boldsymbol{u}_{\mathcal{G}}(\boldsymbol{x}_{\mathcal{B}})$ is the body surface velocity, $\boldsymbol{n}_{\mathcal{B}}$ and $\boldsymbol{s}_{\mathcal{B}}$ are vectors normal and tangential to the body surface, respectively. Satisfying the boundary conditions in (3.160) and (3.161), the vorticity on the boundary is obtained through the Biot-Savart relation (3.159), yielding

$$\frac{1}{2\pi}\int_{\mathcal{D}_{\mathcal{B}}} \frac{(\boldsymbol{x}_{\mathcal{B}} - \boldsymbol{x}) \times \boldsymbol{\omega}_u(\boldsymbol{x})}{|\boldsymbol{x}_{\mathcal{B}} - \boldsymbol{x}|^2} \mathrm{d}\mathcal{D}_{\boldsymbol{x}} = \boldsymbol{\iota}_{\mathcal{B}} - (\boldsymbol{u}_{\mathcal{B}} - \boldsymbol{u}_{\infty}), \tag{3.162}$$

where $\mathcal{D}_{\mathcal{B}}$ is a thin zone adjacent to the surface $\mathcal{B}$ (cf. Fig. 3.9), and

$$\begin{aligned}\boldsymbol{\iota}_{\mathcal{B}}(\boldsymbol{x}_{\mathcal{B}}) = &-\frac{1}{2\pi}\int_{\mathcal{D}\setminus\mathcal{D}_{\mathcal{B}}} \frac{(\boldsymbol{x}_{\mathcal{B}} - \boldsymbol{x}) \times \boldsymbol{\omega}_u(\boldsymbol{x})}{|\boldsymbol{x}_{\mathcal{B}} - \boldsymbol{x}|^2} \mathrm{d}\mathcal{D}_{\boldsymbol{x}} + \frac{1}{2\pi}\oint_{\mathcal{B}} \frac{(\boldsymbol{x}_{\mathcal{B}} - \boldsymbol{x}) \times [\boldsymbol{u}(\boldsymbol{x}) \times \boldsymbol{n}_{\mathcal{B}}(\boldsymbol{x})]}{|\boldsymbol{x}_{\mathcal{B}} - \boldsymbol{x}|^2} \mathrm{d}\mathcal{B}_{\boldsymbol{x}} \\ &+ \frac{1}{2\pi}\oint_{\mathcal{B}} \frac{(\boldsymbol{x}_{\mathcal{B}} - \boldsymbol{x})[\boldsymbol{u}(\boldsymbol{x}) \cdot \boldsymbol{n}_{\mathcal{B}}(\boldsymbol{x})]}{|\boldsymbol{x}_{\mathcal{B}} - \boldsymbol{x}|^2} \mathrm{d}\mathcal{B}_{\boldsymbol{x}},\end{aligned} \tag{3.163}$$

is the velocity induced from the vorticity without the contribution of $\mathcal{D}_{\mathcal{B}}$. The subscript $\boldsymbol{x}$ denotes the integration variable for $\mathcal{D}_{\boldsymbol{x}}$ and $\mathcal{B}_{\boldsymbol{x}}$.

In the vorticity-velocity formulation in $\mathbb{R}^2$, the no-slip and no-penetration conditions represent two equations for one unknown vorticity component. Hence, only one velocity component can be prescribed in (3.162). The present study adopts the implementation by Morgenthal [226] and Morgenthal and Walther [230], which makes use of the no-penetration condition in (3.160), although several studies utilize the no-slip condition instead (cf. e.g. [98, 353, 354]). Instead of solving (3.162) for the vorticity, the vortex methods make use of the vortex sheets bound to the surface. The strength of the vortex sheets can be obtained from the vorticity as

$$\boldsymbol{\gamma}_b = \lim_{l_b \to 0} \int_0^{l_b} \boldsymbol{\omega}_u \mathrm{d}\boldsymbol{n}_{\mathcal{B}}, \tag{3.164}$$

where $\boldsymbol{\gamma}_b = \boldsymbol{\gamma}(\boldsymbol{x}_{\mathcal{B}}; t) = (0, \gamma_b(\boldsymbol{x}_{\mathcal{B}}; t), 0)$ is the strength of the vortex sheet. Applying (3.164) and the no-penetration condition (3.159) to (3.162) yields the following:

$$\left[\frac{1}{2\pi}\int_{\mathcal{B}} \frac{(\boldsymbol{x}_{\mathcal{B}} - \boldsymbol{x}) \times \boldsymbol{\gamma}_b(\boldsymbol{x})}{|\boldsymbol{x}_{\mathcal{B}} - \boldsymbol{x}|^2} \mathrm{d}\mathcal{B}_{\boldsymbol{x}}\right] \cdot \boldsymbol{n}_{\mathcal{B}} = [\boldsymbol{\iota}_{\mathcal{B}} - (\boldsymbol{u}_{\mathcal{B}} - \boldsymbol{u}_{\infty})] \cdot \boldsymbol{n}_{\mathcal{B}}. \tag{3.165}$$

Since the strength of the vortex sheet is the unknown variable, (3.165) represents a boundary value problem. The unique solution of this problem is imposed by an additional equation corresponding to the Kelvin circulation theorem, as shown by Walther [341, 342] and Walther and Larsen [341]. This theorem in terms of global vorticity conservation is given as follows:

$$\frac{\mathrm{d}}{\mathrm{d}t}\int_{\mathcal{D}} \omega_u(\boldsymbol{x}) d\boldsymbol{x} = 0. \tag{3.166}$$

As noted by Wu and Thompson [355], the no-slip condition in (3.161) is imposed implicitly as a consequence of (3.165) and (3.156) for the prescribed no-penetration condition.

Aerodynamic forces

The total aerodynamic forces acting on the body are obtained from the conservation of momentum as

$$\boldsymbol{f} = -\rho\frac{\mathrm{d}}{\mathrm{d}t}\int_{\mathcal{D}} \boldsymbol{\omega}_u(\boldsymbol{x}) \times \boldsymbol{x} \mathrm{d}\boldsymbol{x}. \tag{3.167}$$

Alternatively, by assuming the low friction forces, which is a fair assumption for bridge decks, the aerodynamic forces can be obtained by integrating the pressure over the perimeter as

$$\boldsymbol{f} \cong \boldsymbol{f}_{pr} = \oint_{\mathcal{B}} p_r(\boldsymbol{x}) \boldsymbol{n}_{\mathcal{B}}(\boldsymbol{x}) \mathrm{d}\mathcal{B}_x. \tag{3.168}$$

The pressure gradient can be obtained from the strength of the vortex sheet as

$$\frac{\partial p_r}{\partial s_{\mathcal{B}}} = -\frac{\partial \gamma_b}{\partial t}. \tag{3.169}$$

Numerical discretization

In the VPM, the vorticity field is discretized by vortex particles (cf. Fig. 3.9, right), characterized by their location $\boldsymbol{x}_p = \boldsymbol{x}_p(t) = (x_p(t), 0, z_p(t))$ and strength $\boldsymbol{\Gamma}_p = \boldsymbol{\Gamma}_p = (0, \Gamma_p, 0)$, as follows

$$\omega_u(\boldsymbol{x}; t) = \sum_{p=1}^{N_p} \delta(\boldsymbol{x} - \boldsymbol{x}_p(t)) \Gamma_p, \tag{3.170}$$

where $N_p \in \mathbb{N}$ is the number of particles. The vortex strength corresponds to an integral of a small patch of vorticity $\mathcal{D}_p$ or, equivalently, to a line integral of the velocity over the patch's perimeter $\mathcal{S}$:

$$\Gamma_p = \int_{\mathcal{D}_p} \omega_u(\boldsymbol{x}) \mathrm{d}\boldsymbol{x} = \oint_{\mathcal{S}} \boldsymbol{u}(\boldsymbol{x}) \boldsymbol{n}_s \mathrm{d}s, \tag{3.171}$$

where $\boldsymbol{n}_s$ is a tangential vector of the patch perimeter. Utilizing (3.170), the discrete form of Biot-Savart relation (3.159) for particle's velocity in an Eulerian frame of reference yields

$$\boldsymbol{u}(\boldsymbol{x}_p) = \frac{\partial \boldsymbol{x}_p}{\partial t} = \boldsymbol{u}_\infty - \frac{1}{2\pi} \sum_{j=1}^{N_p} \frac{(\boldsymbol{x}_p - \boldsymbol{x}_j) \times \boldsymbol{\Gamma}_j}{|\boldsymbol{x}_j - \boldsymbol{x}|^2} = \boldsymbol{u}_\infty - \sum_{j=1}^{N_p} \varkappa(\boldsymbol{x}_p - \boldsymbol{x}_j) \Gamma_j, \tag{3.172}$$

where $\varkappa = \varkappa(\boldsymbol{x}_p - \boldsymbol{x})$ is the velocity kernel. To approximate for the numerical instabilities in the denominator in (3.172), the velocity kernel is substituted by mollified velocity kernel $\varkappa_\varepsilon$. There are various kernels which can be used (cf. e.g. [14, 64]). Herein, the second-order Gaussian kernel is employed, given as:

$$\varkappa_\epsilon(\boldsymbol{x}_p - \boldsymbol{x}_j) = \frac{1}{2\pi} \frac{(\boldsymbol{x}_p - \boldsymbol{x}_j) \times \boldsymbol{n}_y}{|\boldsymbol{x}_p - \boldsymbol{x}_j|^2} \left[1 - \exp\left(-\frac{|\boldsymbol{x}_p - \boldsymbol{x}_j|^2}{\epsilon^2} \right) \right], \tag{3.173}$$

where ϵ is the core radius that assures smooth cut-off distance.

The vorticity transport equation (3.154) is solved in two steps using the operator spitting technique by Chorin [64]. Within this technique, the convection and diffusion are solved sequentially. In the convection step, the kinematics of the particles is obtained by solving the Poisson equation (3.158) and Biot-Savart relation (3.172). As the computational cost of directly solving (3.172) is $\mathcal{O}(N_p^2)$, number of fast numerical algorithms have been developed over the years, which are mainly based either on the fast multipole method (cf. e.g. [17, 48]) or the vortex-in-cell (VIC) method (cf. e.g. [16, 66, 137]), which were recently reviewed by Yokota and Obi [371]). The latter method solves Poisson equation (3.158) on a regularized grid utilizing the FFT and (3.158) for the sub-grid particle velocities (3.158), which reduces the computational cost to $\mathcal{O}(N_p \log N_p)$. For this, the unbounded domain is approximated bounded computational domain of size $l_d \times l_h$ (cf. Fig. 3.9,right), which is discretized by $N_x \times N_z$ FFT grid. Herein,

the efficient P^{3}M algorithm is utilized [137], adapted for immersed interfaces by Morgenthal and Walther [230]. Recent developments of the VIC methods involve multi-resolution grids (cf. e.g. [97, 135, 262]); however, the basic VIC and P^{3}M algorithm are deemed sufficient for the present application.

The time-advancement in the convection step of the inviscid Euler equation (3.156) is approximated by the standard Runge-Kutta time-marching techniques. Next, the diffusion step in (3.154) is solved using the random walk method by Chorin [64]. Within this method, the particles' locations are perturbed in a random direction with a random magnitude. Thus, the particles' position $\boldsymbol{x}_{p,j}$ at time-step j are first advanced to $\boldsymbol{x}_{p,j+1/2}$ and then diffused to the final position $\boldsymbol{x}_{p,j+1}$ at step $j+1$ for $j \in \{1, \ldots, N_s\}$, where $N_s \in \mathbb{N}$ is the number of time-steps. For first-order Runge-Kutta, the convection and diffusion steps yield

$$\boldsymbol{x}_{p,k+1/2} = \boldsymbol{x}_{p,k} + \boldsymbol{u}_{p,k}\Delta t, \quad \boldsymbol{x}_{p,k+1} = \boldsymbol{x}_{p,k+1/2} + \boldsymbol{x}_p^{\mathrm{RW}}, \tag{3.174}$$

respectively, where $\boldsymbol{x}_p^{\mathrm{RW}}$ is the random walk vector with variance $\sigma^2_{|x^{\mathrm{RW}}|} = \sqrt{4\nu\Delta t}$.

For the discretization of an immersed body, the boundary element method is utilized [164]. The geometry of the body is discretized on a finite number of panels $N_{pan} \in \mathbb{N}$ with approximately uniform length Δl_{pan}, at which surface there is a linear variation of the strength of the bound vortex sheets. The boundary conditions are enforced at the center of each panel, yielding the following discrete approximation of of (3.165) and (3.166):

$$\boldsymbol{M}\boldsymbol{\gamma}_b = \boldsymbol{b}, \tag{3.175}$$

where $\boldsymbol{M}$ is the influence matrix that is of size in $\mathbb{R}^{N_{pan}+1 \times N_{pan}}$ and $\boldsymbol{b}$ is the right-hand side vector of (3.162) that is in $\mathbb{R}^{N_{pan}+1 \times 1}$. The formulation of the $\boldsymbol{M}$ matrix is given in [164, 226]. The system in (3.175) contains Kelvin circulation theorem as appended separate equation, given as a sum of the contributions to the total circulation as:

$$\sum \Gamma_{\mathrm{system}} = \sum \Gamma_{\mathrm{particles}} + \sum \Gamma_{\mathrm{farfield}} + \sum \Gamma_{\mathrm{boundary}} + \sum \Gamma_{\mathrm{body}} = 0. \tag{3.176}$$

Since the system is overdetermined, the $\boldsymbol{b}$ vector is computed utilizing the least-squares method and it includes the induced velocities on the panels. The aerodynamic forces can be then found from the strength of the bound vortex sheets from (3.169) in a straightforward manner.

The computer code VXflow, developed by Morgenthal [226], is utilized for the numerical implementation of the VPM herein. The code is adapted for highly efficient GPU and OpenCL parallel architecture and it has been verified and validated numerous times (cf. e.g. [52, 226, 228, 229, 230, 251]). Often the parameters in the VPM are experience-based for unresolved simulations; however, particular guidelines exist that yield consistent results. Unless noted otherwise, the core-radius is selected to maintain overlapping between particles, once released from the boundaries, i.e. $\epsilon/\Delta l_{pan} = 1.2$. This overlapping represents a convergence criterion [70], which in this case is satisfied at least near the surface as no re-meshing is used. The number of neighboring Poisson cells N_r for correction of the sub-grid velocities in the P^{3}M algorithm typically amounts to $N_r = 3$, which assures less than 1% error. For more information on numerical implementation, the reader is referred to the Ph.D. thesis of Morgenthal [226].

3.6.2 Velocity-based free-stream turbulence

The velocity-based free-stream turbulence generation (VTG) method was developed by Prendergast [257] and Prendergast and McRobie [258]. It represents a two-step method involving

generating wind velocities on a ladder and subsequently converting them into inflow particles. Herein, it is briefly explained with a different perspective to the mathematical formulation.

Assuming finite vorticity support, i.e. the vorticity is restricted to the modeled domain, the incoming free-stream turbulence can be represented as initial conditions in terms of vorticity field, extending upstream of the section as

$$\omega_u(\boldsymbol{x}; t_0) = \omega_{ut0}. \tag{3.177}$$

where $\omega_{ut0} = \omega_{ut0}(\boldsymbol{x}; t_0)$ is the initial vorticity field at initial time t_0. The vorticity field can be discretized by inflow particles using (3.170) as

$$\omega_u(\boldsymbol{x}; t_0) = \sum_{p=1}^{N_{ip}} \delta\left(\boldsymbol{x} - \boldsymbol{x}_p(t_0)\right) \Gamma_p^{in}, \tag{3.178}$$

where Γ_p^{in} is the inflow particles' circulation (i.e. strength), positioned at regularized discrete gird $\boldsymbol{x}_p$ at $t = t_0$ and N_{ip} is the number of inflow particles. Utilizing Taylor's hypothesis, it is assumed that the particles are convected downstream only by the mean velocity, thus each particles' trajectory at time t is described as

$$\boldsymbol{x}_p(t) = \boldsymbol{x}_p(t_0) + \boldsymbol{u}_\infty t. \tag{3.179}$$

Hence, it can be described which particle, described by its position $\boldsymbol{x}_p$, is occupying a fixed point $\boldsymbol{x}_{in} = (x_{in}, 0, z_{in})$ at time t by setting $\boldsymbol{x}_{in} = \boldsymbol{x}_p(t)$.

The initial conditions of the voriticity in (3.177), i.e. the free-stream turbulence, can be applied by inserting vortex particles with circulation Γ_p^{in} at multiple fixed positions $\boldsymbol{x}_{in}$ upstream of the section (i.e. a band of particles, cf. Fig. 3.10) through time. For discretized time, the particles are inserted at a constant time-interval $\Delta t_{in} = \Delta p \Delta t$, where $\Delta p \in \mathbb{N}$ is the particle-release factor that accounts for the difference between the particle injection time-step Δt_{in} and simulation time-step Δt. This yields circulation at $\boldsymbol{x}_{in}$ at time-step j:

$$\Gamma_{p,j}^{in} = \Gamma_p^{in}(\boldsymbol{x}_{in}; j\Delta t_{in}), \tag{3.180}$$

for $j \in \{1, \ldots, \lfloor N_s/\Delta p \rfloor\}$, where $\lfloor \cdot \rfloor$ is the floor function. The goal is to determine $\Gamma_{p,j}^{in}$ for prescribed statistical properties of the turbulent velocity field.

In the first step, Prendergast [257] positioned a sampling ladder surrounding the particle inflow band to generate the inflow circulation for a prescribed velocity field (cf. Fig. 3.10). At each node of the ladder, two-component correlated velocity field is simulated as a multivariate stationary Gaussian process as described in Sec. 3.3.

In the second step, the approximate inflow circulation is obtained by utilizing (3.171) and approximating the velocity distribution of a quadratic cell by the corner-point velocities (i.e. linear velocity variation, cf. Fig. 3.10). This yields the following:

$$\begin{aligned}
\Gamma_a^{in} &= \left(\frac{\partial w}{\partial x} - \frac{\partial u}{\partial z}\right) \Delta c^2 \\
&= \left[\frac{(w_k + w_n) - (w_j + w_p)}{2\Delta c} - \frac{(u_p + u_n) - (u_j + u_k)}{2\Delta c}\right] \Delta c^2 \\
&= \frac{\Delta c}{2} \left(w_k + w_n - w_j - w_p - u_p - u_n + u_j + u_k\right),
\end{aligned} \tag{3.181}$$

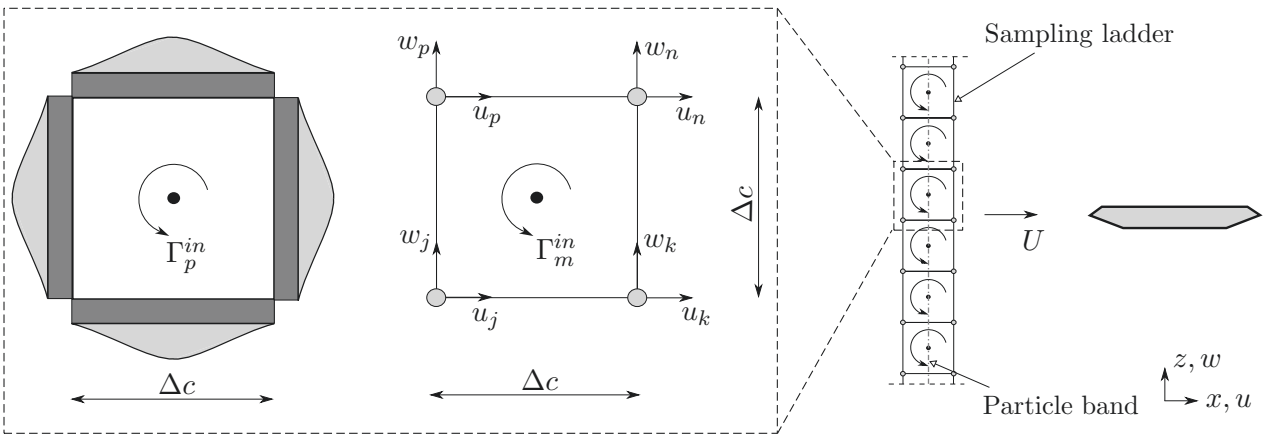

Figure 3.10: Simulation of random-free stream turbulence for the CFD model using the VTG. The velocity is generated at the nodes of the sampling ladder positioned upstream of the deck (right). The inflow circulation injected on the particle band is obtained based on linear velocity distribution (dark gray) and then corrected for the actual nonlinear distribution (light gray).

where Δc is the cell size. For a single point vortex, the actual circulation Γ_p^{in} is based on a nonlinear velocity distribution (light gray area in Fig. 3.10, left), while the approximated circulation Γ_a^{in} is obtained from a linear velocity (dark gray area in Fig. 3.10, left). Hence, a factor of $\pi/2$ should be applied in order to account for the nonlinear velocity distribution. The modeled vortex Γ_m^{in} is then obtained as follows:

$$\Gamma_m^{in} = \beta_{in}\Gamma_p^{in} = \beta_{in}\frac{\pi}{2}\Gamma_a^{in}, \tag{3.182}$$

where β_{in} is a correction factor of the modeled circulation. In the case of a single vortex, this correction factor amounts to $\beta_{in} = 1$. However, for a ladder of particles, this factor is reduced due to the cancellation of the errors on the cell boundaries resulting in values $\beta_{in}\pi/2 \to 1$ for isotropic turbulence. Prendergast [257] refers to this effect to as "smudging of the vorticity", which will be briefly studied in Ch. 5. The cell size Δc is obtained using Taylor's hypothesis as $\Delta c = U\Delta t_{in}$.

Injecting particles upstream in the domain introduces non-zero net circulation in the domain. Hence, Kelvin circulation theorem (cf. (3.176)), needs to be modified to account for the free-stream circulation as

$$\sum \Gamma_{\text{system}} = \sum \Gamma_{\text{particles}} + \sum \Gamma_{\text{farfield}} + \sum \Gamma_{\text{surface}} + \sum \Gamma_{\text{body}} - \sum \Gamma_{\text{free-stream}} = 0. \tag{3.183}$$

The conversion of ladder velocities to particles in (3.182) was validated on an actual 2D flow, represented by the numerical solution of the Navier-Stokes equations by Chaudhury and Morengthal [51]. Therein, the velocity field was recorded on a ladder, positioned in the wake of a bluff body. The flow was then reproduced using (3.182), yielding satisfactory results.

The divergence-free condition on the velocity field, enforced by the continuity condition in (3.153), does not apply to the generated velocity field using the presented method in Sec. 3.3. This is a consequence of the generation of the velocity field as a 1D multivariate random process instead of a 2D process; hence, there is no relation between the longitudinal and vertical wavenumbers. In the vorticity transport equation (3.154), the divergence-free condition is implicit. Hence, there is a loss of TKE when the kinematic constraints of the Navier-Stokes equations are applied to the generated velocity field. Further, the spectral matrix in (3.12) is derived on a 3D

spectral tensor, instead of a 2D. The turbulent energy transfer is different in 2D than in 3D due to the inverse energy cascade (cf. e.g. [30, 222, 223]). All these factors, and additionally the numerical issue with finite vorticity support contribute to the loss of TKE. Alternatively, the divergence-free condition can be incorporated in the generation of the wind time-histories as multivariate 2D processes (cf. Wu [365] for an excellent overview) or by imposing this conditions in an intermediate step (cf. Kondo et al. [177]), as per common practice for the grid-based CFD methods in terms of Large Eddy Simulations. However, the presented turbulent Pseudo-3D method in Sec. 3.6.4 requires the velocity field to be divergence-free in the 2D fluid strips while retaining the correlation between the strips. This is neither a 2D nor 3D case; thus, the typical CFD inflow methods that are divergence-free do not apply. This is the reason why these methods were not utilized to avoid the loss of TKE. Moreover, by extensive analyses of the turbulent characteristics based on ESDU spectra, it was shown that the free-stream turbulence retains the statistical properties using the velocity-based turbulence generation method (cf. e.g. [134, 257, 261]. As seen in Ch. 5, using isotropic von Kármán spectra yields even better results.

As noted in Sec 3.3.1, the cross-spectrum between the two velocity components, i.e. $S_{uw} = 0$, is neglected in VTG even for anisotropic free-stream turbulence. In the atmospheric boundary layer, the point cross-spectra does not equal to zero for anisotropic turbulence, as measured by many experimental studies (cf. [302, 305] for a summary) and described analytically for the second-order structure of turbulence by Mann's tensor [212]. Nevertheless, the effect of the point cross-spectra on the bridge response is commonly considered to be negligible relative to the overall uncertainty in the modeling of the wind field (cf. e.g. [60, 246, 329]). Although generating the wind as a 1D multivariate process can account for the point cross-spectrum S_{uw}, the one-dimensionality assumption neglects the phase information between the two velocity components, i.e. there is no relation between their corresponding wavenumbers. This is why this assumption is deemed reasonable and was included in the original VTG by Prendergast [257]. Moreover, the computational time for generation of wind time-histories is reduced significantly in this case as both fluctuation components can be generated independently, reducing the size of the cross-spectral matrix $\boldsymbol{S_u}$ by a factor of two, as noted in Sec. 3.3.

Having defined the free-stream turbulence as an initial condition, from (3.154), (3.159), (3.165), (3.166), (3.177) and (3.167), the final formulation of the CFD model can be defined as:

$$\textbf{CFD} := \begin{cases} \dfrac{\partial \omega_u}{\partial t} + (\boldsymbol{u}\cdot\boldsymbol{\nabla})\,\omega_u = \nu\boldsymbol{\nabla}^2\omega_u, \quad \boldsymbol{u}(\boldsymbol{x}) = \boldsymbol{u}_\infty - \dfrac{1}{2\pi}\displaystyle\int_{\mathcal{D}} \frac{(\boldsymbol{x}-\boldsymbol{z})\times\boldsymbol{\omega}_u(\boldsymbol{z})}{|\boldsymbol{x}-\boldsymbol{z}|^2}\mathrm{d}\boldsymbol{z}, \\ \left[\dfrac{1}{2\pi}\displaystyle\int_{\mathcal{B}} \frac{(\boldsymbol{x}_{\mathcal{B}}-\boldsymbol{x})\times\boldsymbol{\gamma}_b(\boldsymbol{x})}{|\boldsymbol{x}_{\mathcal{B}}-\boldsymbol{x}|^2}\mathrm{d}\mathcal{B}_x\right]\cdot\boldsymbol{n}_{\mathcal{B}} = [\boldsymbol{\iota}_{\mathcal{B}} - (\boldsymbol{u}_{\mathcal{B}}-\boldsymbol{u}_\infty)]\cdot\boldsymbol{n}_{\mathcal{B}}, \\ \dfrac{\mathrm{d}}{\mathrm{d}t}\displaystyle\int_{\mathcal{D}}\omega_u(\boldsymbol{x})d\boldsymbol{x} = 0, \quad \omega_u(\boldsymbol{x};t_0) = \omega_{ut0}, \quad \boldsymbol{f} = -\rho\frac{d}{dt}\displaystyle\int_{\mathcal{D}}\boldsymbol{\omega}_u(\boldsymbol{x})\times\boldsymbol{x}\mathrm{d}\boldsymbol{x}. \end{cases} \tag{3.184}$$

3.6.3 Laminar Pseudo-3D vortex method

The laminar Pseudo-3D VPM attempts to include the structural behavior in $\mathbb{R}^3$ while modeling the fluid in $\mathbb{R}^2$ by planes (strips) along the span by employing the strip assumption (cf. Fig. 3.11). It was first used for bridges by Morgenthal and his co-workers [228, 229]. The structure is modeled using 3D representation as in (3.1). With this, several improvements can be made, despite the simplification of the 3D flow effects. These improvements include: (i) varying cross-sectional geometry along the structure, (ii) varying mean wind speed for each section and most importantly, (iii) the inclusion of an arbitrary number of structural modes

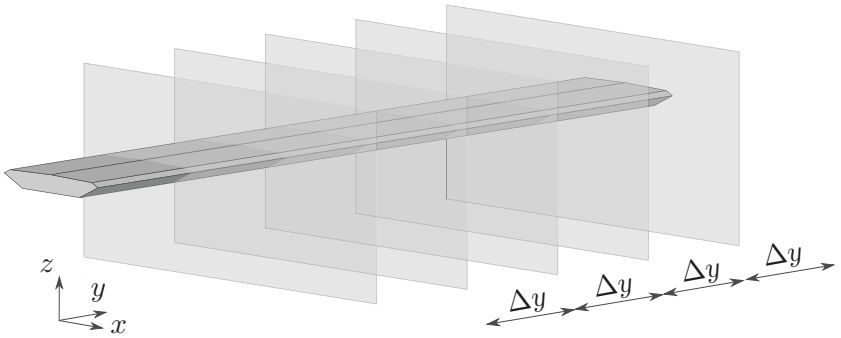

Figure 3.11: Concept of the Pseudo-3D VPM: discretization of the fluid domain on 2D planes (strips) along a line-like structure.

which are necessary for adequate representation of 3D structural behavior. It is noted that laminar Pseudo-3D VPM stands for laminar free-stream, not laminar flow. In the same manner, turbulent Pseudo-3D VPM stands for turbulent free-stream.

The concept is straightforward: the force vector required for the external force required in (3.1) is assembled for $N_{str} \in \mathbb{N}$ number of strips as follows:

$$\boldsymbol{f}_o = (D_1, L_1, M_1, \dots, D_{N_{str}}, L_{N_{str}}, M_{N_{str}}) \,, \tag{3.185}$$

where D_j, L_j and M_j for $j \in \{1, 2, \cdots, N_{str}\}$ are the drag lift and moment force for the j-th strip. These forces are obtained from each strip by 2D CFD simulations, which are coupled by the structural model. For the representation of the structural model, a full (cf. (3.1)) or reduced (cf. (3.2)) system can be used. In the case of laminar free-stream, it is reasonable to assume that the self-excited forces are fully correlated over one element, as noted by Scanlan [285]. This assumption was further examined in a numerical study by Bai et al.[15], where it was observed that the 3D coherence effects in the wake have a minor effect on the flutter derivatives for streamlined decks. However, the energy transfer between modes can severely affect the flutter limit [114], and thus, it is necessary to consider the 3D dynamic behavior of the structure.

3.6.4 Turbulent Pseudo-3D vortex method*

In the case of free-stream turbulence, the 3D effects of the flow are perplexing. A novel turbulent Pseudo-3D VPM is presented herein that attempts to replicate the incoming turbulent fluctuations in $\mathbb{R}^2$, while retaining the velocity span-wise correlation in an empirical manner. The motivation is to obtain the dynamic response of a bridge deck due to an incoming turbulent wind, rather than to simulate free-stream coherent turbulent structures in detail.

A multivariate velocity field is generated on spatially correlated ladders, positioned upstream of each 2D fluid plane (cf. Fig. 3.12). The inflow particles are obtained at the center of each cell from the ladder by the VTG method. Assuming that (3.181) is able to correctly model the node velocities by the inflow particles, the span-wise correlation will be thus retained. However, there is a loss of TKE as the divergence-free condition is not imposed on the generated velocity field (cf. Sec. 3.6.2). Thus, a loss of span-wise correlation of the simulated velocities is expected.

Herein, further analytical expressions are derived to study the span-wise correlation of the circulation, and thus, the correlated velocity field between slices. The investigation is conducted

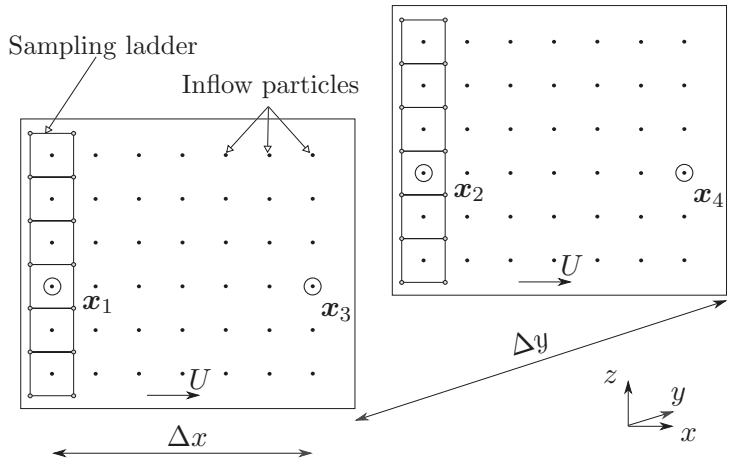

Figure 3.12: Concept of turbulent Pseudo-3D VPM based on VTG: sampling ladders and the position of inflow particles convected by the mean velocity U for two slices at distance Δy.

in two parts, in which: (i) it is shown how the span-wise coherence of the circulation $coh_{\Gamma_1\Gamma_2}$ at points $\boldsymbol{x}_1$ and $\boldsymbol{x}_2$ relates to the span-wise coherence of the velocity at these two points $coh_{u1u2} = coh_{12}$ for the two types coherence functions, Vickery (3.25) and a proposed modified one; and (ii) it is shown that the span-wise correlation, and thus coherence of the circulation is retained for points $\boldsymbol{x}_3$ and $\boldsymbol{x}_4$ as the particles are convected in the fluid domain, based on Taylor's hypothesis (cf. Fig. 3.12).

In the first part, initially the cross-correlation $R_{\Gamma_A\Gamma_B} = R_{\Gamma_A\Gamma_B}(t_\delta)$ of lag t_δ is defined for the circulation at two points, $\boldsymbol{x}_A = (x_A, y_A, z_A)$ and $\boldsymbol{x}_B = (x_B, y_B, z_B)$, located at the center of for any two cells. Utilizing (3.181) and assuming $S_{uw} = S_{wu} = 0$ for the cross-terms (cf. Sec. 3.3), the cross-correlation of the circulation at points $\boldsymbol{x}_A$ and $\boldsymbol{x}_B$ is obtained as follows:

$$\begin{aligned} R_{\Gamma_A\Gamma_B} = R_{\Gamma_A\Gamma_B}(t_\delta) = \frac{\Delta c^2}{4}\Big\langle & [w_{kA}(t) + w_{nA}(t) - w_{jA}(t) - w_{pA}(t)] \\ & \times [w_{kB}(t+t_\delta) + w_{nB}(t+t_\delta) - w_{jB}(t+t_\delta) - w_{pB}(t+t_\delta)] \\ & + [u_{pA}(t) + u_{nA}(t) - u_{jA}(t) - u_{kA}(t)] \\ & \times [u_{pB}(t+t_\delta) + u_{nB}(t+t_\delta) - u_{jB}(t+t_\delta) - u_{kB}(t+t_\delta)] \Big\rangle, \end{aligned} \tag{3.186}$$

where the subscript A and B denote the center point of the cell for the corner velocities. The circulations $\Gamma_A = \Gamma_A(\boldsymbol{x}_A; t)$ and $\Gamma_B = \Gamma_B(\boldsymbol{x}_B; t)$ are not assigned to two particular particles, rather to each particle injected into the domain at time t. Using unique symmetry relation $R_{ab}(t_\delta) = R_{ba}(-t_\delta)$ for two stationary random processes, $a = a(t)$ and $b = b(t)$, the following can be obtained:

$$S_{ab} + S_{ba} = S_{ab} + \overline{S_{ab}} = 2\Re\left[S_{ab}\right]. \tag{3.187}$$

Applying the Wiener-Khinchin theorem (2.10) on (3.186) and using (3.187) yields

$$\begin{aligned} S_{\Gamma_A\Gamma_B} = \frac{\Delta c^2}{4}\Big[& S_{w_{kA}w_{kB}} + S_{w_{nA}w_{nB}} + S_{w_{jA}w_{jB}} + S_{w_{pA}w_{pB}} \\ & + 2\Re\left(S_{w_{kA}w_{nB}} - S_{w_{kA}w_{jB}} - S_{w_{kA}w_{pB}} - S_{w_{nA}w_{jB}} - S_{w_{nA}w_{pB}} + S_{w_{jA}w_{pB}}\right) \\ & + S_{u_{kA}u_{kB}} + S_{u_{nA}u_{nB}} + S_{u_{jA}u_{jB}} + S_{u_{pA}u_{pB}} \\ & + 2\Re\left(-S_{u_{kA}u_{nB}} + S_{u_{kA}u_{jB}} - S_{u_{kA}u_{pB}} - S_{u_{nA}u_{jB}} + S_{u_{nA}u_{pB}} - S_{w_{jA}u_{pB}}\right)\Big] \end{aligned} \tag{3.188}$$

for the circulation cross-spectrum $S_{\Gamma_A\Gamma_B} = S_{\Gamma_A\Gamma_B}(\boldsymbol{x}_A, \boldsymbol{x}_B; f)$ between the two arbitrary points, $\boldsymbol{x}_A$ and $\boldsymbol{x}_B$. Using the same analogy as in (3.26), the cross-spectra of the circulation of two points can be described as

$$S_{\Gamma_A\Gamma_B} = \sqrt{S_{\Gamma_A\Gamma_A} S_{\Gamma_B\Gamma_B}} coh_{\Gamma_A\Gamma_B} = S_\Gamma coh_{\Gamma_A\Gamma_B}. \tag{3.189}$$

Next, consider two points $\boldsymbol{x}_1 = (x_o, y_o, z_o)$ and $\boldsymbol{x}_2 = (x_o, y_o + \Delta y, z_o)$ in the vicinity of two cells located at two separate slices (cf. Fig. 3.12). To show that the circulation at these points is correlated, the cross-spectrum should not amount to zero, i.e. $S_{\Gamma_1\Gamma_2} \neq 0$.

The cross-spectrum of the circulation for velocity field based on the Vickery coherence (cf. (3.25)) is derived first. The limiting value of the velocity coherence between $\boldsymbol{x}_1$ and $\boldsymbol{x}_2$ for the ratio $\Delta c/\Delta y \to 0$ yields

$$\lim_{\Delta c/\Delta y \to 0} coh(\Delta x, \Delta y, \Delta z; f) = coh(0, \Delta y, 0; f) = coh_{12}, \tag{3.190}$$

for $\Delta x, \Delta z \in \{0, \Delta c\}$. Plugging this into (3.188), the limiting case of the circulation cross-spectrum $S^{lim}_{\Gamma_1,\Gamma_2}$ for $\boldsymbol{x}_1$ and $\boldsymbol{x}_2$ yields

$$\begin{aligned} S^{lim}_{\Gamma_1\Gamma_2} = S^{lim}_{\Gamma_1\Gamma_2}(\Delta c; f) =& \frac{\Delta c^2}{4} S_w coh_{12} \Big\{ 4 + 2\Re\Big[1 - \exp(-i2\pi f\theta_{12}) - \exp(-i2\pi f\theta_{12}) \\ & - \exp(-i2\pi f\theta_{12}) - \exp(-i2\pi f\theta_{12}) + 1 \Big] \Big\} \\ & + \frac{\Delta c^2}{4} S_u coh_{12} \Big\{ 4 + 2\Re\Big[-1 + \exp(-i2\pi f\theta_{12}) - \exp(-i2\pi f\theta_{12}) \\ & - \exp(-i2\pi f\theta_{12}) + \exp(-i2\pi f\theta_{12}) - 1 \Big] \Big\}, \end{aligned} \tag{3.191}$$

where $\theta_{12} = \Delta c/U$ is the angular phase shift. Utilizing only the real part of Euler's formula, (3.191) reduces to

$$S^{lim}_{\Gamma_1\Gamma_2} = 2\Delta c^2 S_w \left[1 - \cos\left(\frac{2\pi f \Delta c}{U} \right) \right] coh_{12}. \tag{3.192}$$

The preceding equation shows that the circulation at the points $\boldsymbol{x}_1$ and $\boldsymbol{x}_2$ is correlated as it includes the spatial coherence term. To separate the parts due to space coherence and point spectrum as in (3.189), the point circulation spectrum $S_\Gamma = S_\Gamma(\Delta c, f)$ should be obtained. Two more assumptions are posed to obtain the limiting case of the point-spectrum $S^{lim}_\Gamma = S^{lim}_\Gamma(\Delta c, f)$. Strictly speaking, Taylor's hypothesis impels that the longitudinal coherence coefficient $C_x = 0$ [181]. Further, assuming that the product $fC_z\Delta c/U \to 0$ yields

$$\lim_{fC_z\Delta c/U \to 0} coh(\Delta x, 0, \Delta z; f) = 1, \quad \text{for } \Delta x, \Delta z \in \{0, \Delta c\}. \tag{3.193}$$

Plunging this into (3.188), the limiting case of the circulation spectrum yields

$$\begin{aligned} S^{lim}_\Gamma =& \frac{\Delta c^2}{4} S_w \Big\{ 4 + 2\Re\Big[1 - \exp(-i2\pi f\theta_{12}) - \exp(-i2\pi f\theta_{12}) - \exp(-i2\pi f\theta_{12}) \\ & - \exp(-i2\pi f\theta_{12}) + 1 \Big] \Big\} \\ & + \frac{\Delta c^2}{4} S_u \Big\{ 4 + 2\Re\Big[-1 + \exp(-i2\pi f\theta_{12}) - \exp(-i2\pi f\theta_{12}) - \exp(-i2\pi f\theta_{12}) \\ & + \exp(-i2\pi f\theta_{12}) - 1 \Big] \Big\}, \end{aligned} \tag{3.194}$$

which reduces to

$$S_{\Gamma}^{lim} = 2\Delta c^2 S_w \left[1 - \cos\left(\frac{2\pi f \Delta c}{U}\right)\right]. \tag{3.195}$$

Substituting (3.195) into (3.192) yields

$$S_{\Gamma_1\Gamma_2}^{lim} = S_{\Gamma}^{lim} coh_{12}. \tag{3.196}$$

The preceding equation clearly shows that the limiting case of the cross-spectrum of the circulation is constituted of two terms, the point spectrum and space coherence. Hence, the limit value of the circulation coherence equals the velocity coherence, for a velocity field based on the Vickery coherence. This yields the following:

$$coh_{\Gamma_1\Gamma_2}^{lim} = coh_{u_1u_2} = coh_{12}. \tag{3.197}$$

The expression in (3.196) shows that limiting case of the circulation for $\Delta c/\Delta y \to 0$ is correlated in the span-wise direction in a similar manner as any velocity component at points $\boldsymbol{x}_1$ and $\boldsymbol{x}_2$.

At a late stage of this work it was realized that, if a modified coherence for the velocity field is used, (3.188) could be substantially reduced without the additional assumptions as for a velocity field based on the Vickery coherence. The proposed modified coherence is obtained as a hybrid between the Vickery (cf. (3.25)) and Davenport coherence (cf. (3.24)) as follows:

$$coh_{jk} = coh_{a_jb_k}(\Delta\boldsymbol{x}; f) = \exp\left[-\frac{f}{U}\left(C_y\,|\Delta y| + \sqrt{C_x^2\Delta x^2 + C_z^2\Delta z^2}\right)\right], \tag{3.198}$$

which can be separated for $\boldsymbol{x}_1$ and $\boldsymbol{x}_2$ as

$$coh(\Delta x, \Delta y, \Delta z; f) = coh(0, \Delta y, 0; f)coh(\Delta x, 0, \Delta z; f) = coh_{12}coh(\Delta x, 0, \Delta z; f), \tag{3.199}$$

for $\Delta x, \Delta z \in \{0, \Delta c\}$. Plunging this into (3.188) for $\boldsymbol{x}_1$ and $\boldsymbol{x}_2$ and using the point spectrum S_Γ the following can be obtained:

$$S_{\Gamma_1\Gamma_2} = S_\Gamma coh_{12}, \tag{3.200}$$

which is of similar form as in (3.196), without the additional assumptions of $\Delta c/\Delta y \to 0$, $fC_z\Delta c/U \to 0$ and $C_x = 0$ (cf. (3.190) and (3.193)). This shows that for a velocity field based on the proposed modified coherence function (cf. (3.198)), the circulation coherence is the same as the velocity coherence for any $\Delta c/\Delta y$ ratio and C_x.

Next, the circulation coherence for a velocity field based on the Vickery coherence is studied. Figure 3.13 presents the circulation coherence $coh_{\Gamma_1\Gamma_2}$ from the full spectrum (cf. (3.188)) for varying $\Delta c/\Delta y$ ratio (i.e. without any assumptions). From the figure, it can be seen that the circulation coherence $coh_{\Gamma\Gamma}$ is generally reduced compared to the velocity coherence coh_{12}. For the limiting case of $\Delta c/\Delta y = 0$, the circulation coherence matches the velocity coherence, i.e. (3.197) holds. In the case of smaller ratios that are not equal to zero, the circulation coherence reduces. This is because $S_{\Gamma_1\Gamma_2}$ would attain lower values than S_Γ as the Δy^2 term is present in the negative exponential of the Vickery coherence (cf. (3.25)). The circulation coherence matches the velocity coherence for a velocity field based on the proposed coherence function (cf. (3.198)), regardless of the $\Delta c/\Delta y$ ratio, i.e. the principle of geometric similarity applies in this case (cf. Sec. 3.3.1).

To conclude the first part of the investigation, the quality of the span-wise correlation of the simulated velocities at the beginning of the CFD domain should not depend on the choice of

velocity coherence function. This is only true if the modeled particles in (3.182) replicate the nodal velocities exactly. However, as the generated nodal velocities are not divergence-free in the $x-z$ plane, a loss of span-wise correlation is expected. In this case, it will be shown during the flow verification in Sec. 5.3.1 that the modified velocity coherence (cf. (3.198)) yields better results. This is purely a numerical consequence as the coherence of the circulation based on the Vickery coherence attains lower values (cf. Fig. 3.13), which makes it prone to numerical noise. For a single strip, both the Vickery and modified coherence are similar.

In the second part of the investigation, it is shown that the cross-correlation of the circulation for the points $\boldsymbol{x}_1$ and $\boldsymbol{x}_2$ at the ladder is similar as for the downwind points $\boldsymbol{x}_3 = (x_o+\Delta x, y_o, z_o)$ and $\boldsymbol{x}_4 = (x_o + \Delta x, y_o + \Delta y, z_o)$ (cf. Fig. 3.12). Under Taylor's hypothesis, the longitudinal distance x relates to a time lag τ_r as $\tau_r = \Delta x/U$. Using the stationarity assumption, the cross-correlation possess the property $R(t_\delta) = R(t_\delta + t_r)$ and it can be expressed as follows:

$$\begin{aligned} R_{\Gamma_1\Gamma_2}(t_\delta) &= \langle \Gamma(x_o, y_o, z_o; t)\Gamma(x_o + \Delta x, y_o, z_o; t + t_\delta)\rangle \\ &= \langle \Gamma(x_o, y_o, z_o; t + t_r)\Gamma(x_o + \Delta x, y_o, z_o; t + t_\delta + t_r)\rangle \\ &= \langle \Gamma(x_o, y_o + \Delta y, z_o; t)\Gamma(x_o + \Delta x, y_o + \Delta y, z_o; t + t_\delta)\rangle \\ &= R_{\Gamma_3\Gamma_4}(t_\delta). \end{aligned} \tag{3.201}$$

The latter equation shows, that the span-wise correlation of the circulation, and thus, velocity, is retained in the along-wind direction.

Recently, Tolba and Morgenthal [326] also utilized the idea of introducing empirically correlated free-stream turbulence to the Pseudo-3D VPM. Therein, a particle-based free-stream turbulence generation was introduced instead of using the VTG explained in the previous section. For the particle-based free-stream turbulence, the circulation of the particles is directly generated, instead of first generating a velocity field as in the VTG. The incentives to utilize the VTG for the turbulent Pseudo-3D VPM are the meaningful advantages of (i) partial consideration of anisotropy in the flow, and (ii) ability to prescribe the PSD for both fluctuating components of the velocity. These two points, and the fact that a velocity field is generated instead of vorticity, makes the VTG method both more flexible and intuitive. On the other hand, the span-wise correlation is directly enforced on the inflow particles for the particle-based method.

The energy transfer between turbulent eddies is different in 2D and 3D. However, the turbulent

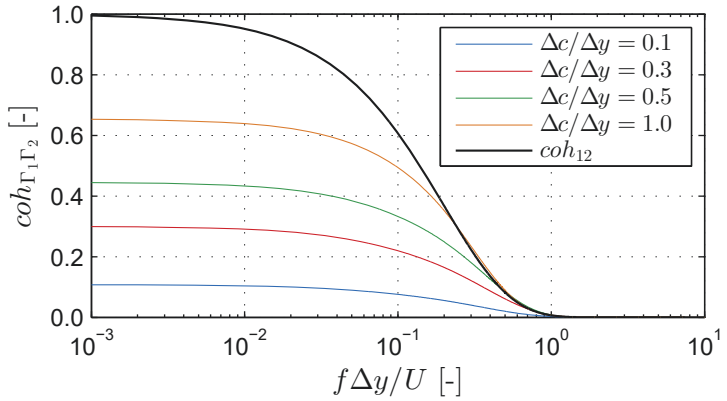

Figure 3.13: Span-wise circulation coherence based on a generated velocity field using the Vickery coherence (cf. (3.25)). For $\Delta c/\Delta y = 0$, the circulation coherence tends to the velocity coherence $coh_{\Gamma_1\Gamma_2} = coh_{12}$. For a generated velocity field using the proposed modified coherence (cf. (3.24)), the circulation coherence is always equal to the velocity coherence.

Pseudo-3D VPM aims to model the large-scale eddies which carry the largest part of the turbulent energy and are critical for the aerodynamic response. The correlation in these eddies is higher than in the small eddies and for high Reynolds number, the advection is dominant. For fluid-structure interaction, a drawback of the turbulent Pseudo-3D VPM is the disregard of the 3D effects which result in increased correlation and reduced magnitude of the buffeting forces w.r.t. their 2D counterparts. Presently, the strip assumption is utilized, as it is difficult to empirically increase the span-wise correlation for the buffeting forces only, since they are nonlinearly coupled with the self-excited forces. The effect of the strip assumption is discussed in detail as a part of critical remarks in the last chapter.

3.7 Determination of aerodynamic coefficients

The aerodynamic coefficients represent the link between the semi-analytical models and a CFD or an experimental model. With the CFD and semi-analytical models being introduced previously, CFD-based methods for determination of the aerodynamic coefficients are presented here. Initially, simple methods extraction of the static wind coefficients and flutter derivatives are briefly recalled. Next, a recently introduced method for determination of the aerodynamic admittance for random gusts is revisited. Finally, a novel method for determination of the aerodynamic admittance under deterministic gusts is introduced.

3.7.1 Static wind coefficients

The determination of the static wind coefficients is straightforward: the averaged (i.e. static) forces of stationary body are normalized w.r.t. the free-stream pressure and a characteristic dimension. Thus, the static forces are obtained as a time-averaged mean of the fluctuating forces at a static angle of attack as

$$D_s(\alpha_s) = \langle D(\alpha_s;\tau)\rangle\,, \quad L_s(\alpha_s) = \langle L(\alpha_s;\tau)\rangle\,, \quad M_s(\alpha_s) = \langle M(\alpha_s;\tau)\rangle\,, \tag{3.202}$$

based on which, the static wind coefficients are obtained as

$$C_D(\alpha_s) = \frac{2D_s(\alpha_s)}{\rho U^2 B}, \quad C_L(\alpha_s) = \frac{2L_s(\alpha_s)}{\rho U^2 B}, \quad C_M(\alpha_s) = \frac{2M_s(\alpha_s)}{\rho U^2 B^2}. \tag{3.203}$$

From a practical aspect, it is important that the time-varying mean of the static wind coefficient converges to a certain value. As the simulation time needs to be set beforehand, usually maintaining the total reduced time interval in the order of $\tau \approx 50 - 200$ suffices to filter the vortex-shedding effects. In such a way, it is ensured that at least 50 chords of a wake are used for the analysis. Moreover, it is important that the Reynolds number is maintained throughout the aeroelastic analyses. Some studies (cf. e.g. Larose [186]) determine the static wind coefficients under turbulent free-stream to compute the aerodynamic admittance. However, this would only average the local non-stationary and nonlinear buffeting effects, as for simulation time $\tau \to \infty$, the gust frequency $f \to 0$ if the strip assumption is valid.

3.7.2 Flutter derivatives

As seen in the previous section, the flutter derivatives correspond to the linear unsteady part of the self-excited forces. Hence, it is crucial that they are determined for displacements that yield aerodynamic forces in the linear range. There are mainly two methods of determining the flutter

derivatives: forced (cf. e.g. [85]) and free vibration (cf. e.g. [263]). Within the first method, the section is forced to oscillate with a prescribed target amplitude and frequency, resulting in aerodynamic forces. The flutter derivatives are then obtained simply as a transfer function in terms of magnitude and phase. In case the free-vibration method, the flutter derivatives are extracted from the damping and stiffness of a system, oscillating for an initial displacement.

Although the free-vibration method is useful in experiments due to the costs of constructing a forced rig, there is great deal of uncertainty in the system identification. Thus, as per common practice for CFD-analyses, the flutter derivatives are determined using forced vibration. To obtain all eighteen flutter derivatives, sinusoidal motion is applied at the stiffness center $\boldsymbol{x}_s$ of the deck in one of three directions: sway, heave and pitch. For each of these cases, the corresponding flutter derivatives are obtained by rearranging (3.72) and taking the Fourier transform, yielding the following:

$$\begin{aligned}
&\text{Sway: } \boldsymbol{q}(\boldsymbol{x}_s;t) = (p_0(\boldsymbol{x}_s),0,0)\exp(i\omega_t t), \quad P_4^*(V_{rt}) + iP_1^*(V_{rt}) = \frac{2\hat{D}_{se}(V_{rt})}{\rho U\pi^2 V_{rt}^2 \hat{p}(V_{rt})},\\
&H_6^*(V_{rt}) + iH_5^*(V_{rt}) = \frac{2\hat{L}_{se}(V_{rt})}{\rho U\pi^2 V_{rt}^2 \hat{p}(V_{rt})}, \qquad A_6^*(V_{rt}) + iA_5^*(V_{rt}) = \frac{2\hat{M}_{se}(V_{rt})}{\rho U\pi^2 B V_{rt}^2 \hat{p}(V_{rt})},
\end{aligned} \tag{3.204}$$

$$\begin{aligned}
&\text{Heave: } \boldsymbol{q}(\boldsymbol{x}_s;t) = (0,h_0(\boldsymbol{x}_s),0)\exp(i\omega_t t), \quad P_6^*(V_{rt}) + iP_5^*(V_{rt}) = \frac{2\hat{D}_{se}(V_{rt})}{\rho U\pi^2 V_{rt}^2 \hat{h}(V_{rt})},\\
&H_4^*(V_{rt}) + iH_1^*(V_{rt}) = \frac{2\hat{L}_{se}(V_{rt})}{\rho U\pi^2 V_{rt}^2 \hat{h}(V_{rt})}, \qquad A_4^*(V_{rt}) + iA_1^*(V_{rt}) = \frac{2\hat{M}_{se}(V_{rt})}{\rho U\pi^2 B V_{rt}^2 \hat{h}(V_{rt})},
\end{aligned} \tag{3.205}$$

$$\begin{aligned}
&\text{Pitch: } \boldsymbol{q}(\boldsymbol{x}_s;t) = (0,0,\alpha_0(\boldsymbol{x}_s))\exp(i\omega_t t), \quad P_3^*(V_{rt}) + iP_2^*(V_{rt}) = \frac{2\hat{D}_{se}(V_{rt})}{\rho U\pi^2 B V_{rt}^2 \hat{\alpha}(V_{rt})},\\
&H_3^*(V_{rt}) + iH_2^*(V_{rt}) = \frac{2\hat{L}_{se}(V_{rt})}{\rho U\pi^2 B V_{rt}^2 \hat{\alpha}(V_{rt})}, \qquad A_3^*(V_{rt}) + iA_2^*(V_{rt}) = \frac{2\hat{M}_{se}(V_{rt})}{\rho U\pi^2 B^2 V_{rt}^2 \hat{\alpha}(V_{rt})},
\end{aligned} \tag{3.206}$$

where p_0, h_0 and α_0 are the motion amplitudes, while the subscript t denotes prescribed (target) value. Alternatively to the direct computation using the Fourier transform, the flutter derivatives are obtained directly by performing linear least squares fit to the forces [193].

The motion amplitudes should be selected as such to ensure that the self-forces are in the linear range. For an initial indication, it is beneficial to check the linear range of the static wind coefficients (cf. Fig. 3.6)). Some studies (cf. e.g. [190, 193, 276, 277]), the displacement amplitudes are selected in the range of $0.04 < k_0/B < 0.06$ for $k \in \{p,h\}$ and 1 deg$< \alpha_0 <$ 8 deg. A fairly comprehensive review on displacement amplitudes is given in Abbas et al. [3], co-written by the author. In pitch case, this range is generally valid and is best decided based on the static wind coefficients, which represent the first indicator for aerodynamic nonlinearity. However, for the sway and heave cases, it is more sensible to select the amplitude based on an effective angle $\alpha_e = \dot{k}_0/U$ for $k = \{p,h\}$, in the same range as for the pitch case as performed by Argentini [11]. In such a way, the displacement amplitude varies for each reduced velocity and the linear range can be identified based on the static wind coefficients as for the rotation.

3.7.3 Aerodynamic admittance for random gusts

The two approaches for determination of the aerodynamic admittance in bridge aerodynamics are based on random and deterministic free-stream turbulence. Computation of the aerody-

namic admittance using the vortex methods was first conducted by Rasmussen et al. [261] and is based on the VTG, discussed in Sec. 3.6.2. Herein, this approach is briefly revisited.

Consider a stationary deck, subjected to random free-stream turbulence. When random free-stream fluctuations are considered as input, the determination of the aerodynamic admittance is obtained for the whole reduced velocity range V_r. Naturally, the free-stream turbulence includes fluctuations in both longitudinal and vertical directions. Thus, only three admittance component can be obtained. From the PSD of (3.73), the squared-absolute value of the aerodynamic admittances can be obtained as

$$\begin{aligned}
|\chi_D|^2 = |\chi_{Du}|^2 = |\chi_{Dw}|^2 &= \frac{4S_{D_b}}{\rho^2 U^2 B^2 \left[4C_D^2 S_u + \left(C_D' - C_L\right)^2 S_w\right]}, \\
|\chi_L|^2 = |\chi_{Lu}|^2 = |\chi_{Lw}|^2 &= \frac{4S_{L_b}}{\rho^2 U^2 B^2 \left[4C_L^2 S_u + \left(C_L' + C_D\right)^2 S_w\right]}, \\
|\chi_M|^2 = |\chi_{Mu}|^2 = |\chi_{Mw}|^2 &= \frac{4S_{M_b}}{\rho^2 U^2 B^4 \left(4C_M^2 S_u + {C_M'}^2 S_w\right)},
\end{aligned} \tag{3.207}$$

where $S_{D_b} = S_{D_b}(\boldsymbol{x}_s; f)$, $S_{L_b} = S_{L_b}(\boldsymbol{x}_s; f)$ and $S_{M_b} = S_{M_b}(\boldsymbol{x}_s; f)$ are the PSD of the drag, lift and moment buffeting forces, respectively. The fluctuating velocities are tracked down in the CFD domain at point $\boldsymbol{x}_c$, based on which the corresponding PSDs, $S_u = S_u(\boldsymbol{x}_c; f)$ and $S_u = S_u(\boldsymbol{x}_c; f)$, are determined. Rassmussen et al. [261] and Hejlesen et al. [134] position the velocity tracking point $\boldsymbol{x}_c$ at an approximate distance of one chord B upstream of the leading edge, i.e. $\boldsymbol{x}_s - \boldsymbol{x}_c = (B, 0, 0)$. Herein, the gust-tracking point is selected to be at the stiffness center, i.e. $\boldsymbol{x}_s \equiv \boldsymbol{x}_c$. Hence, the PSDs of the wind velocity fluctuations are determined from a simulation considering only the free-stream turbulence, that is, without a body in the CFD domain. With this, the wind spectrum is obtained at the same point where the forces are acting. Moreover, and the influence of the deck on the incoming flow is not taken into account. However, the LU model does not capture this effect anyway. As for the flutter derivatives, the selected turbulence intensity should ensure linear buffeting forces. Typically, the range for 3 % $\leq \sigma_w/U \leq$ 10 % for the vertical component is used. This range corresponds to a standard deviation of an effective angle $\alpha_e = w/U$ in the range from 1.5 deg to 6 deg.

Experimentally, the random free-stream turbulence is generated either by a grid or in boundary-layer wind tunnels [123, 186, 187, 209, 274]. Unlike the admittance obtained from the 2D VPM, the experiments consider the 3D structure of the turbulence in a statistical manner through its PSD and coherence function.

3.7.4 Aerodynamic admittance for deterministic gusts*

The second approach for determination of the aerodynamic admittance is based on deterministic free-stream turbulence in terms of sinusoidal gusts with a single prescribed frequency. This section presents a novel method based on the VPM to determine the aerodynamic admittance in its complex form. The method is based on the idea of an active turbulence generator, which has been extensively utilized in experimental tests (cf. e.g. [11, 81, 85, 129, 151]).

An active turbulence generator represents a set of two or more pitching airfoils, oscillating with a single frequency. For an out-of- or in-phase motion of two airfoils, longitudinal or vertical sinusoidal gusts are generated in the region between the wakes of the airfoils, respectively. The

gusts generated in such a way are considered to be fully correlated in the span-wise direction, which complies with the strip assumption. Positioning a deck section downstream of the active turbulence generator yields sinusoidal buffeting forces. Unlike the aerodynamic admittance for random free-stream turbulence, this configuration allows determination of the real and imaginary part of all six aerodynamic admittances as amplitude and phase modulation, respectively, between the sinusoidal buffeting forces and wind gusts.

Consider two fundamental cases of incoming sinusoidal longitudinal $u_c = u_0 \exp(i\omega_t)$ and vertical $w_c = w_0 \exp(i\omega t)$ gusts with on a target frequency ω_t. Rearranging (3.73) and taking the Fourier transform, six components of the aerodynamic admittance can be obtained for the two fundamental cases as follows:

$$\begin{aligned} \text{Longitudinal: } \boldsymbol{u}^*(\boldsymbol{x}_c;t) = (u_0(\boldsymbol{x}_c),0,0)\exp(i\omega_t t), \quad \chi_{Du}(V_{rt}) &= \frac{\hat{D}_b(V_{rt})}{\rho U B C_D \hat{u}(V_{rt})}, \\ \chi_{Lu}(V_{rt}) = \frac{-\hat{L}_b(V_{rt})}{\rho U B C_L \hat{u}(V_{rt})}, \qquad \chi_{Mu}(V_{rt}) &= \frac{\hat{M}_b(V_{rt})}{\rho U B^2 C_M \hat{u}(V_{rt})}. \end{aligned} \tag{3.208}$$

$$\begin{aligned} \text{Vertical: } \boldsymbol{u}^*(\boldsymbol{x}_c;t) = (0,0,w_0(\boldsymbol{x}_c))\exp(i\omega_t t), \quad \chi_{Dw}(V_{rt}) &= \frac{2\hat{D}_b(V_{rt})}{\rho U B\left(C_D' - C_L\right)\hat{w}(V_{rt})}, \\ \chi_{Lw}(V_{rt}) = \frac{-2\hat{L}_b(V_{rt})}{\rho U B\left(C_L' + C_D\right)\hat{w}(V_{rt})}, \quad \chi_{Dw}(V_{rt}) &= \frac{2\hat{M}_b(V_{rt})}{\rho U B^2 C_M' \hat{w}(V_{rt})}, \end{aligned} \tag{3.209}$$

where u_0 and w_0 are the gust amplitudes at a gust-tracking point $\boldsymbol{x}_c$, while the subscript t denotes prescribed (target) value. It is clear that all aerodynamic admittance functions in (3.208) and (3.209) are in its complex form and can be obtained at various prescribed reduced velocities V_{rt}.

In what follows, a concept of a numerical active turbulence generator is explained, which can be used to generate free-stream sinusoidal gusts using the VPM, in terms of inflow particles. A closed-form expression is derived that relates the inflow particles' strength to the gust amplitudes. This expression is based on an existing mathematical model. Finally, a previously developed inverse method that relates particles' strength and gust amplitudes is briefly revisited. The inverse method is used to verify the derived closed-form expression in Sec. 5.3.2.

Concept

Figure 3.14 depicts the concept of the presented method. Two fictitious airfoils, F_A and F_B, are assumed to be oscillating upstream of the section and outside a CFD domain, constituting an active turbulence generator. The motion of the airfoils is rotational, sinusoidal and with same amplitudes. The pitching angles for the two airfoils, $\alpha_{F_A} = \alpha_{F_A}(t)$ and $\alpha_{F_B} = \alpha_{F_B}(t)$, are

$$\alpha_{F_A} = \alpha_{F0}\exp\left(i\omega_t t\right), \;\; \alpha_{F_B} = \alpha_{F0}\exp\left(i\omega_t t + i\varphi_F\right), \tag{3.210}$$

where α_{F0} is the oscillation amplitude and φ_F is the phase between the motion of the two foils.

In the CFD domain, only the wakes of the airfoils are modeled by releasing particles carrying concentrated circulation Γ_F^{in}. Once the particles are released in the CFD domain, their motion is governed by the Navier-Stokes equations, which are numerically solved utilizing the VPM (cf. Sec. 3.6.1). The particles are introduced at two particle release locations, $\boldsymbol{x}_{F_A} = (0,0,-l_R/2)$

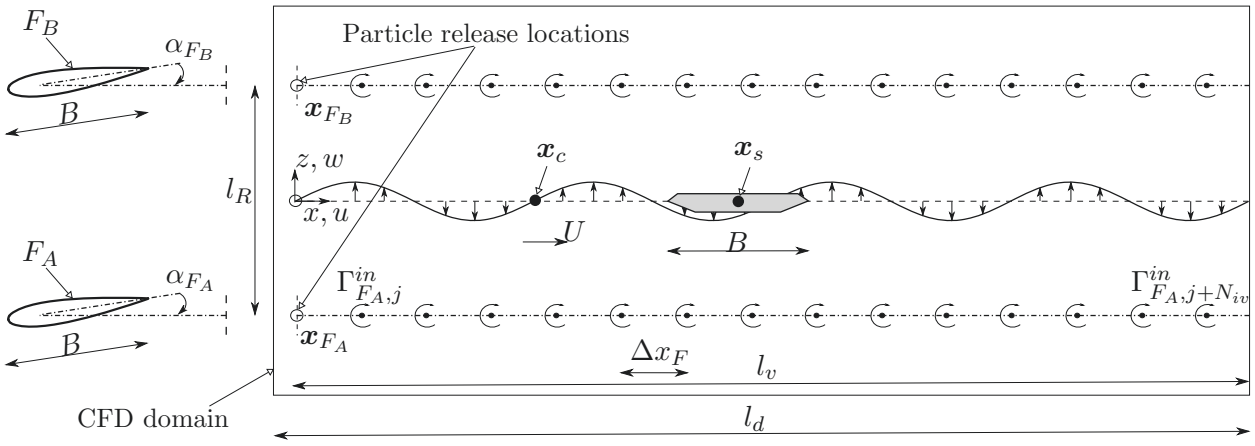

Figure 3.14: Concept of numerical active turbulence generator for generation of deterministic free-stream turbulence for determination of the complex aerodynamic admittance using the VPM.

and $\boldsymbol{x}_{F_B} = (0, 0, l_R/2)$, at a constant time interval $\Delta t_{in} = \Delta p \Delta t$, where $\Delta p \in \mathbb{N}$ is the particle-release factor and Δt is the simulation time-step. In case the oscillation of the airfoils is sinusoidal, the inflow discrete circulation for both airfoils, $\Gamma^{in}_{F_A} = \Gamma^{in}_{F_A}(\boldsymbol{x}_{F_A}; j)$ and $\Gamma^{in}_{F_B} = \Gamma^{in}_{F_B}(\boldsymbol{x}_{F_B}; j)$, yield

$$\begin{aligned} \Gamma^{in}_{F_A,j} &= \Gamma^{in}_{F}(\boldsymbol{x}_{F_A}; j\Delta t_{in}) = \Gamma^{in}_{F0} \exp\left(i\omega_t j \Delta t_{in}\right), \\ \Gamma^{in}_{F_B,j} &= \Gamma^{in}_{F}(\boldsymbol{x}_{F_B}; j\Delta t_{in}) = \Gamma^{in}_{F0} \exp\left(i\omega_t j \Delta t_{in} + i\varphi_F\right), \end{aligned} \tag{3.211}$$

where $j \in \{1, \ldots, \lfloor N_s/\Delta p \rfloor\}$ for $N_s \in \mathbb{N}$ number of steps. The circulation amplitude depends on the temporal discretization, that is, $\Gamma_{F0} = \Gamma_{F0}(\Delta t_{in})$. Assuming Taylor's hypothesis holds, the spatial and temporal discretization are related as $\Delta x_F = U \Delta t_{in}$, where Δx_F is the particle spacing.

If $\Gamma^{in}_{F_A}$ and $\Gamma^{in}_{F_B}$ are in-phase ($\varphi_F = 0$) or out-of-phase ($\varphi_F = \pi$), a vertical or horizontal sinusoidal gust is obtained, respectively, at a gust-tracking point on the centerline, i.e. $\boldsymbol{x}_c = (x_c, 0, 0)$. However, this is only true if the following assumptions hold:

i) the vorticity shed from an airfoil into the wake is concentrated at the mean chord line and is convected by the mean velocity (planar wake assumption);

ii) the wakes are non-interfering and infinite, and the point $\boldsymbol{x}_c$ is located sufficiently downstream of the particle release locations (i.e. the airfoils).

Positioning a section downstream of the particle release locations results in sinusoidal aerodynamic forces. Hence, the aerodynamic admittances can be in a computed straightforward manner (cf. (3.208) and (3.209)). In light of the previous explanation, the presented method consists of two essential steps and one optional step, in which:

a) the inflow particles' strength Γ^{in}_F (cf. (3.211)) is computed a-priori of the CFD simulations for a prescribed gust amplitude, u_{t0} or w_{t0}, and frequency f_t;

b) a CFD simulation with a stationary body is conducted including inflow particles;

c) (optional) a CFD simulation without a body is conducted including inflow particles.

The optional step is included in case the gust-tracking point $\boldsymbol{x}_c$ is selected to be at the stiffness center, i.e. $\boldsymbol{x}_c \equiv \boldsymbol{x}_s$. In this case, the effect of the section on the incoming gust is not taken

into account and the imaginary part of the admittance is obtained for wind fluctuations at the stiffness center, which is the situation for the linear unsteady model based on the airfoil theory.

Modeling flapping airfoils using concentrated vortices has been used for experiments in a form of mathematical models based on airfoil theory, to determine the airfoil flapping angles w.r.t. gust amplitudes (cf. e.g. [130, 309]). Recently, Chawdhury et al. [50] used the concept of counter-rotating vortices in the VPM to simulate pulsating flow, i.e. longitudinal gusts with significantly longer lengths than the CFD domain, to study the performance of flutter-based energy harvesters. For that purpose, a simple discrete model based on the Biot-Savart relation (3.159) was developed to relate the inflow circulation and longitudinal gust amplitudes. That model is inapplicable for the gust lengths required for the aerodynamic admittance.

The presented method extends the concept for sinusoidal gusts in the VPM by Chawdhury et al. [50] in two manners, first to consider co-rotating vortices to simulate vertical gusts, and second, it offers an analytical relation between the inflow particles strength and gust amplitude. In other words, the circulation amplitude of the released particles Γ_{F0}^{in} for a prescribed gust amplitude, u_{ct0} or w_{ct0}, in step a) is obtained from a closed-form expression. This expression is derived based on an airfoil theory-based mathematical model by Stapountzis [309]. It is noteworthy to mention that, the prescribed gust amplitude in step a) is only to provide an approximate value, which will be later corrected by the one tracked in the CFD domain within steps b) or c). The prescribed gust amplitude should also ensure that, up to a certain extent, the aerodynamic forces remain linear.

Mathematical model

The mathematical model, that is used to determine circulation amplitude Γ_{F0}^{in} (cf. (3.211)) for prescribed gust amplitudes, practically enforces the two assumptions i) and ii). These assumptions are required for a gust at point $\boldsymbol{x}_c$ along the centerline to be sinusoidal. In order to relate the pitching angle amplitude of the airfoils α_{F0} to the circulation amplitude Γ_{F0}, and hence, to prescribed gust amplitudes u_{t0} or w_{t0}, two additional assumptions are required since the wakes' are modeled utilizing the flat plate theory (cf. Sec. 3.4), namely:

iii) the airfoils are idealized as flat plates and the oscillation amplitudes are sufficiently small, so that linear unsteady theory applies;

iv) the Kutta-Jukowski condition is constantly fulfilled.

For an oscillating airfoil, which trailing edge is positioned at $(0, 0, z_F)$, the induced velocity at a point on the centerline $\boldsymbol{x}_c$ can be obtained by using the Biot-Savart relation (cf. (3.159)) as follows:

$$\begin{aligned} u_c^F &= u^F(\boldsymbol{x}_c; t) = -\frac{z_F}{2\pi} \int_0^\infty \frac{\gamma_F(x)}{(x_c - x)^2 + z_F^2} \mathrm{d}x, \\ w_c^F &= w^F(\boldsymbol{x}_c; t) = -\frac{1}{2\pi} \int_0^\infty \frac{(x_c - x)\gamma_F(x)}{(x_c - x)^2 + z_F^2} \mathrm{d}x, \end{aligned} \tag{3.212}$$

where, $\gamma_F = \gamma_F(\boldsymbol{x}_\gamma; t)$ is strength of the wake vortex sheet of the airfoil at point $\boldsymbol{x}_\gamma = (x, 0, z_F)$, which is concentrated along the line $z = z_F$ (cf. assumption (i)). Assumption (ii) is implied in (3.212) by neglecting the bound circulation, as the point $\boldsymbol{x}_c$ is assumed to be sufficiently downstream.

For two oscillating airfoils with non-interfering wakes, the fluctuating velocity components at

the centerline yield

$$u_c = u_c^{F_A} + u_c^{F_B}, \quad w_c = w_c^{F_A} + w_c^{F_B}. \tag{3.213}$$

To obtain a solution for the mathematical model in (3.212) and (3.213), two methods are used, referred to as "Analytical" and "Inverse" method.

Analytical forward method

For an airfoil performing sinusoidal rotation with prescribed frequency ω_t, the strength of the wake vortex sheet is also sinusoidal, i.e $\gamma_F = \gamma_{F0} \exp(i\omega_t t)$. Based on the assumptions (i-iv), Stapountzis [308, 309] gives a closed-form solution of (3.212) as follows:

$$\begin{aligned} u_c^F &= -\operatorname{sgn}(z_F) \frac{A}{2} \exp\left[-\frac{2K_t^*}{B}|z_F| + i\left(\omega_t t - \frac{2K_t^*}{B}x_c\right)\right], \\ w_c^F &= i\frac{A}{2} \exp\left[-\frac{2K_t^*}{B}|z_F| + i\left(\omega_t t - \frac{2K_t^*}{B}x_c\right)\right], \end{aligned} \tag{3.214}$$

where sgn is the sign function, K_t^* is the prescribed reduced frequency w.r.t. half chord (cf. (3.46)). For airfoils rotating about the front quarter point, $A = A(K_t^*)$ is given as follows:

$$A = -4U\alpha_{F0} \frac{1 + iK_t^*}{H_1^{(2)} + iH_0^{(2)}}. \tag{3.215}$$

where $H_1^{(2)} = H_1^{(2)}(K_t^*)$ and $H_0^{(2)} = H_0^{(2)}(K_t^*)$ are Hankel functions of the second kind.

In the present configuration, two airfoils are positioned at $\boldsymbol{x}_{F_A}$ and $\boldsymbol{x}_{F_B}$ (cf. Fig. 3.14). The velocities at the centerline can be obtained by changing (3.214) into (3.213). For in-phase oscillations of the airfoils, $u_c^{F_A} = -u_c^{F_B}$ and $w_c^{F_A} = w_c^{F_B}$; hence, the velocities at the centerline yield

$$u_c = 0, \quad w_c = iA \exp\left[-\frac{K_t^* l_R}{B} + i\left(\omega_t t - \frac{2K_t^*}{B}x_c\right)\right]. \tag{3.216}$$

Correspondingly, for out-of-phase oscillations of the airfoils, $u_c^{F_A} = u_c^{F_B}$ and $w_c^{F_A} = -w_c^{F_B}$; hence, the velocities at the centerline are

$$u_c = -A \exp\left[-\frac{K_t^* l_R}{B} + i\left(\omega_t t - \frac{2K_t^*}{B}x_c\right)\right], \quad w_c = 0. \tag{3.217}$$

In the experimental studies [310] the aim is to have a closed-form solution that relates the oscillation amplitude of the airfoils α_{F0} to the gust amplitudes w_{c0} and u_{c0}. To relate the gust amplitude to the circulation in a closed-form solution, the following relations are derived.

First, consider the case for in-phase oscillating airfoils, i.e. $\Gamma_{F_A}^{in} = \Gamma_{F_B}^{in} = \Gamma_F^{in}$. Changing (3.215) into (3.216) for the vertical velocity and using the non-dimensional time τ (cf. (3.46)) yields

$$\alpha_{F0} = -\frac{w_c\left(H_1^{(2)} + iH_0^{(2)}\right)}{4U(1 + iK_t^*)\,i} \exp\left[\frac{K_t^* l_R}{B} - i\left(2K_t^*\tau - \frac{2K_t^*}{B}x_c\right)\right]. \tag{3.218}$$

For a sinusoidal rotational motion of the airfoils, the vertical velocity is also sinusoidal, i.e. $w_c = w_c(\tau) = w_{c0} \exp(iK_t^*\tau)$. Furthermore, the circulatory lift deficiency of such airfoils due to the unsteady behavior is accounted by Theodorsen function $C = C(K_t^*)$ (cf. (3.52)). This

means that the effective quasi-steady angle of oscillation $\alpha_e^{\mathrm{QS}} = \alpha_F$ is replaced with the effective unsteady angle $\alpha_e^{\mathrm{US}} = \alpha_e^{\mathrm{QS}}/C = \alpha_F/C$ (cf. (3.58) and (3.65)). Changing this in (3.218), yields

$$\alpha_e^{\mathrm{US}} = -C\frac{w_{c0}\left(H_1^{(2)} + iH_0^{(2)}\right)}{4U\left(1+iK_t^*\right)i}\exp\left[\frac{K_t^* l_R}{B} - i\left(2K_t^*\tau - \frac{2K_t^*}{B}x_c\right)\right], \tag{3.219}$$

The bound circulation $\Gamma_b = \Gamma_b(\tau)$ is obtained based on the Kutta-Jukowski theorem and the unsteady effective angle as $\Gamma_b = U\pi\alpha_e^{\mathrm{UN}}B$ (cf. (3.47) and (3.57)). Taking this into account and changing for Theodorsen function (cf. (3.52)) into (3.219), the bound circulation reduces to

$$\Gamma_b = \frac{w_{c0}\pi B H_1^{(2)}}{4\left(1+iK_t^*\right)i}\exp\left(\frac{K_t^* l_R}{B} + i2K_t^*\tau\right). \tag{3.220}$$

In the preceding expression, the term $2K_t^*/Bx_c$ and the sign under the exponential in (3.219) are neglected. These terms account for the phase between the circulation at the particle release locations and velocity fluctuations at point $\boldsymbol{x}_c$. This phase is obsolete for the present purpose.

The discrete circulation shed in the wake due to change of angle of the airfoil during time $\Delta\tau_{in} = \Delta t_{in}U/B$ is $\Gamma_F^{in} = \Gamma_F^{in}(\tau) = \Gamma_b(\tau - \Delta\tau_{in}) - \Gamma_b(\tau)$. Taking this into account and discretizing the non-dimensional time as $\tau = j\Delta\tau$, the following relation is obtained:

$$\Gamma_{F,j}^{in} = \frac{w_{c0}\pi B H_1^{(2)}}{4\left(1+iK_t^*\right)i}\exp\left(\frac{K_t^* l_R}{B}\right)\left[\exp\left(-i2K_t^*\Delta\tau_{in}\right) - 1\right]\exp\left(i2K_t^* j\Delta\tau_{in}\right). \tag{3.221}$$

for $j = \{1, \ldots, N_s\}$. Similarly, for the out-of-phase motion in (3.217), i.e. $\Gamma_{F_A}^{in} = \Gamma_F^{in}$ and $\Gamma_{F_B}^{in} = -\Gamma_F^{in}$, the following relation is obtained:

$$\Gamma_{F,j}^{in} = \frac{u_{c0}\pi B H_1^{(2)}}{4\left(1+iK_t^*\right)}\exp\left(\frac{K_t^* l_R}{B}\right)\left[\exp\left(-i2K_t^*\Delta\tau_{in}\right) - 1\right]\exp\left(i2K_t^* j\Delta\tau_{in}\right). \tag{3.222}$$

Both (3.221) and (3.222), represent the relation between the inflow circulation Γ_F^{in} and gust amplitudes for in-phase w_{c0} and out-of-phase motion u_{c0} of the airfoils, respectively. These expressions can be written in a reduced form as

$$\Gamma_{F,j}^{in} = \Gamma_{F0}^{in}\exp\left(i2K_t^* j\Delta\tau_{in}\right), \tag{3.223}$$

which is similar to (3.211) for non-dimensional time. The amplitude of the circulation is the same for vertical or longitudinal sinusoidal gusts with similar prescribed amplitudes $u_{ct0} = w_{ct0}$. Neglecting the phase, the final closed-form solution for the circulation amplitude $\Gamma_{F0}^{in} = \Gamma_{F0}^{in}(\Delta\tau_{in})$ yields

$$\begin{aligned}\Gamma_{F0}^{in} &= \left|\frac{w_{ct0}\pi B H_1^{(2)}}{4\left(1+iK_t^*\right)i}\exp\left(\frac{K_t^* l_R}{B}\right)\left[\exp\left(-i2K_t^*\Delta\tau_{in}\right) - 1\right]\right| \\ &= \left|\frac{u_{ct0}\pi B H_1^{(2)}}{4\left(1+iK_t^*\right)}\exp\left(\frac{K_t^* l_R}{B}\right)\left[\exp\left(-i2K_t^*\Delta\tau_{in}\right) - 1\right]\right|.\end{aligned} \tag{3.224}$$

Discrete inverse method

Harding and Bryden [130] introduced a discrete inverse method for the solution of the mathematical model. In this method, the strength of the wake vortex sheet in (3.212) and (3.213) is

discretized on discrete particles by utilizing the discrete Biot-Savart relation (cf. (3.172)). The assumptions (i) and (ii) are enforced by specifying the inflow particles' position apriori at the mean chord line, uniformly distributed at distance Δx_F. For the configuration in Fig. 3.14, the discrete velocities at $\boldsymbol{x}_c$ at step j yield

$$\begin{aligned} u_{c,j} &= \sum_{k=j}^{N_{ip}+j-1} Z_{u,jk} \left(\Gamma^{in}_{F_A,k} - \Gamma^{in}_{F_B,k} \right), \\ w_{c,j} &= \sum_{k=j}^{N_{ip}+j-1} Z_{w,jk} \left(\Gamma^{in}_{F_A,k} + \Gamma^{in}_{F_B,k} \right), \end{aligned} \tag{3.225}$$

where $j \in \{1, \ldots, \lfloor N_s/\Delta p \rfloor\}$ and $N_{ip} \in \mathbb{N}$ are number of inflow particles considered in the spatial range of summation for the inverse method l_v^{inv}. The matrices $\boldsymbol{Z}_u$ and $\boldsymbol{Z}_w$ are obtained by using (3.172), considering that at each step j, the velocities are influenced only by N_{ip} number of particles. Thus, these matrices are of size in $\mathbb{R}^{\lfloor N_s/\Delta p \rfloor \times \lfloor N_s/\Delta p \rfloor + N_{ip}}$, and are obtained as follows:

$$\begin{aligned} Z_{u,jk} &= \begin{cases} \dfrac{l_R}{4\pi \left[\left(x_c - x_{F,k} \right)^2 + \dfrac{l_R^2}{4} \right]}, & \text{for } j \le k \le j + N_{ip} - 1, \\ 0, & \text{otherwise;} \end{cases} \\ Z_{w,jk} &= \begin{cases} \dfrac{-\left(x_c - x_{F,k} \right)}{2\pi \left[\left(x_c - x_{F,k} \right)^2 + \dfrac{l_R^2}{4} \right]}, & \text{for } j \le k \le j + N_{ip} - 1, \\ 0, & \text{otherwise.} \end{cases} \end{aligned} \tag{3.226}$$

The circulation can be obtained for prescribed velocities, u_{ct} and w_{ct}, by reversing (3.225) as

$$\begin{cases} \Gamma^{in}_{F_A,k} - \Gamma^{in}_{F_B,k} &= \displaystyle\sum_{j=1}^{N_s} Z^{+}_{u,kj} u_{ct,j} \\ \Gamma^{in}_{F_A,k} + \Gamma^{in}_{F_B,k} &= \displaystyle\sum_{j=1}^{N_s} Z^{+}_{w,kj} w_{ct,j} \end{cases}, \tag{3.227}$$

where $\boldsymbol{Z}_u^+$ and $\boldsymbol{Z}_w^+$ are the pseudo-inverse matrices of $\boldsymbol{Z}_u$ and $\boldsymbol{Z}_w$, respectively, as no unique inverse is feasible since the system is overdetermined. The Moore-Penrose method is utilized for the pseudo-inverse operation. The system in (3.227) is solved as simultaneous equations at each time-step. [130] further relate the circulation Γ_F^{in} to the airfoil angles α_F.

The inverse method is given herein to verify the closed-form solution derived in (3.224). Furthermore, it is noted that the prescribed velocities in the inverse method by (3.227) do not need to be sinusoidal. In fact, they can be arbitrary functions, as experimentally validated by Harding et al. [131]. Thus, the inverse method is more flexible than the analytical; however, the latter is preferred for sinusoidal functions as it is more computationally efficient and avoids the error in least-squares fit in the pseudo-inverse operation. This error in the inverse method for sinusoidal velocity fluctuations can be reduced, up to a certain extent, by taking longer l_v^{inv} than the spatial length of summation l_v of the CFD domain (cf. Fig. 3.14).

3.8 Summary

The theoretical foundation of various aspects of modeling in the field of bridge aerodynamics was addressed in this chapter. The wind-structure interaction was formulated as a coupled model, constituted of a structural and an aerodynamic model. Without loss of generality, the structural model of the deck was defined using the linear theory as it is of secondary importance for this work. To increase computational efficiency, the order of the structural system was reduced using the modal representation.

Next, the stochastic wind field was represented by discrete points with defined spatial and temporal correlation, using the spectral representation. At these points, wind time-histories can be then generated as multivariate stationary Gaussian processes. These time-histories represent an input for the aerodynamic models that replicate the buffeting forces.

Having a model for the free-stream turbulence, the modeling of the wind forces acting on a bridge deck was approached in two manners: using CFD and semi-analytical models. Before defining the semi-analytical models for bridge decks, the analytical models for a flat plate were briefly revisited as the basic principles in bridge aerodynamics stem from these analytical models. Two main assumptions were considered as pivotal points: linearity and quasi-steadiness. Mainly based on these two assumptions, twelve semi-analytical models were defined, of which ten are implemented in a computer code. Moreover, a simple method for computation of the buffeting forces based on the FFT was introduced as a part of the CMBM model.

Further, the 2D CFD model was formulated based on the vorticity transport equation including boundary conditions of an immersed body and free-stream turbulence as an initial condition. Formulated as such, it is convenient to discretize the CFD model using the VPM that yields favorable results at reasonable computational costs, despite unresolved turbulent scales and lack of turbulence modeling. The free-stream turbulence was discretized using the VTG, in which the circulation of the inflow particles is obtained from a generated velocity field.

The laminar Pseudo-3D VPM was then revisited as an extension of the 2D VPM that accounts for the 3D structural behavior while modeling the fluid in 2D strips along the span. Based on this method and the VTG method for free-stream turbulence, a novel velocity-based turbulent Pseudo-3D VPM was presented. It was shown, in an analytical manner, that the free-stream turbulence remains correlated in the CFD domain between the fluid strips for points downstream of particle release locations.

Finally, methods for determination of the static wind coefficients, flutter derivatives and aerodynamic admittance for random free-stream were recalled. In this sense, a new method for determination of the aerodynamic admittance for deterministic free-stream was introduced. The method was based on modeling the wakes of two flapping airfoils by inflow particles, yielding sinusoidal gusts along the centerline. Moreover, a closed-form expression was derived that relates inflow particles' circulation to a prescribed gust amplitude.

In the next chapter, the aerodynamic models formulated herein are evaluated using a categorical modeling approach. Verification of the novel methods is performed in Ch. 5.

Chapter 4

Comparative Methodology

4.1 Introduction

The CFD and semi-analytical models presented in the previous chapter can be classified as mathematical models as these models are derived from physical laws and assumptions. This chapter presents a comparative methodology for the comparison of aerodynamic models. The methodology is constituted of two parts and it deals with model comparison in both qualitative and quantitative manner. In the first part, a categorical modeling approach is applied to the aerodynamic models to evaluate them qualitatively. The output of the aerodynamic models is then compared in a quantitative manner in the second part using comparison metrics for time-histories. Although some studies refer to such procedures as verification and validation (cf. e.g. [241, 243, 268]), the term "comparative" is used herein as it is more general. In this sense, verification can be viewed as a comparison with a benchmark analytical model (i.e results), while validation as a comparison with an experimental model (i.e results). Before presenting both individual parts of the comparative methodology, a brief overview of comparison and assessment of mathematical models is given herein, from a general point of view and irrespective of the field of application.

Comparison and assessment of mathematical models require consideration of the complete modeling process. The modeling process is comprised of setting up a mathematical model, introducing input parameters for the specific problem, and calculation of the results performed analytically or numerically. In each of these stages of the modeling process, different types of uncertainties can arise resulting in loss of model quality. Therefore, it is necessary to identify possible sources of uncertainty influencing the final model. Generally speaking, three types of sources of uncertainties can be distinguished (cf. e.g. [243, 268]): (i) model inputs, (ii) numerical approximation, and (iii) model form. The first two sources of uncertainties are related to practical aspects of modeling such as errors in numerical approximation, programming mistakes, and parameter uncertainty. The source of uncertainty related to the model form originates from violating the basic physical assumptions of models, i.e. conceptual errors. This type of uncertainty requires careful treatment and intrinsic knowledge of the physical assumptions implied in the mathematical models since violating basic model assumptions influences the complete modeling process, and therefore, is of critical importance for the practical use of models.

The task of assessment of models based on their physical assumptions, i.e. by taking into account only their mathematical constructions independently of a specific engineering example,

requires tools of abstract mathematics supporting the idea of finding universal properties of models. The universal properties of models, such as model complexity or model robustness, are properties that are common for all mathematical models, without any particular engineering field or application. Several modeling methodologies exploring the idea to work with tools of abstract mathematics, such as graph theory [170], abstract Hilbert spaces [93, 94], abstract algebraic approach [197, 237], have been proposed in recent years. Recently, an approach for model evaluation based on category theory was proposed by Gürlebeck et al. [125]. Although it is clear, that any mathematical formalism can be chosen to serve as a basis for a more formal modeling approach, in this monograph, the abstract category theory-based modeling approach is utilized and further developed. The motivation for choosing this approach is twofold, namely: (i) the abstract nature of category theory supports the idea of assessment of models only based on their mathematical constructions regardless of the engineering field of application; (ii) although categorical constructions are naturally abstract, it is straightforward to keep track of their real physical and engineering interpretations in the category theory-based modeling methodology. To the author's knowledge, a real-world application of the category theory-based modeling methodology has not been presented yet.

A practical interpretation of the results obtained by the application of the category theory-based modeling methodology requires a quantitative characteristic. The quantitative characteristic should indicate clearly the influence of particular modeling assumptions, identified on the abstract level, on the final result in engineering practice. For this purpose, the term system response quantity (SRQ) of interest is utilized herein, which is typically regarded as the outcome of the modeling process [243]. As an example from the field of bridge aeroelasticity, a typical SRQ can be the deck displacements for buffeting analyses or the stiffness/damping of the system when the aerodynamic stability is of interest.

In most of the comparative studies in the field of bridge aerodynamics (cf. Sec. 2.5.4), the SRQ is usually selected to be either the aerodynamic force or the aeroelastic displacements. For model assessment in the time domain, this effectively constitutes a comparison of time-histories. Thus, a comparison is conducted typically in two manners: (i) quantitatively, in terms of a global quantity such as the RMS or peak; and (ii) qualitatively, in terms of time-histories or power spectral densities. However, each comparative study is carried out case-by-case since a unified procedure for quantitative comparison of time-histories in bridge aerodynamics is not available. Moreover, with the development of nonlinear aerodynamic models (cf. e.g. [47, 86, 356, 360]), the assumption of aerodynamic linearity is no longer posed. Thus, this provides a need for quantification of the discrepancies in the nonlinear and non-stationary features of the time-histories such as multi-frequency output for a single-frequency input, complex hysteresis behavior (cf. Fig. 4.1) and high skewness and kurtosis of the output PDF for a Gaussian input.

The literature on methods for comparing time-histories is vast. Without being exhaustive, former studies can be found in field of mechanical systems [152], cavitation in fluid-structure interaction [307], seismology [180], geophysics [351], economics [28], shock of floating platforms [322], crash simulations in vehicle designs [275], etc. The commonality of all methods is that the similarity of the time-history is measured by an absolute or relative metric. Hence, these metrics are used to quantify the discrepancies in certain signal features such as magnitude, phase, frequency content, PDF, etc. For this purpose, various metrics have been developed based on global and local quantities such as peak, RMS error, averaged time-delay, statistical divergences, coefficient of determination, coefficient of correlation, etc. A comprehensive review of metrics available is given by Hora and Campos [138]. Generally, the selection of metrics for comparison is based on the field of application as different signal features are of interest.

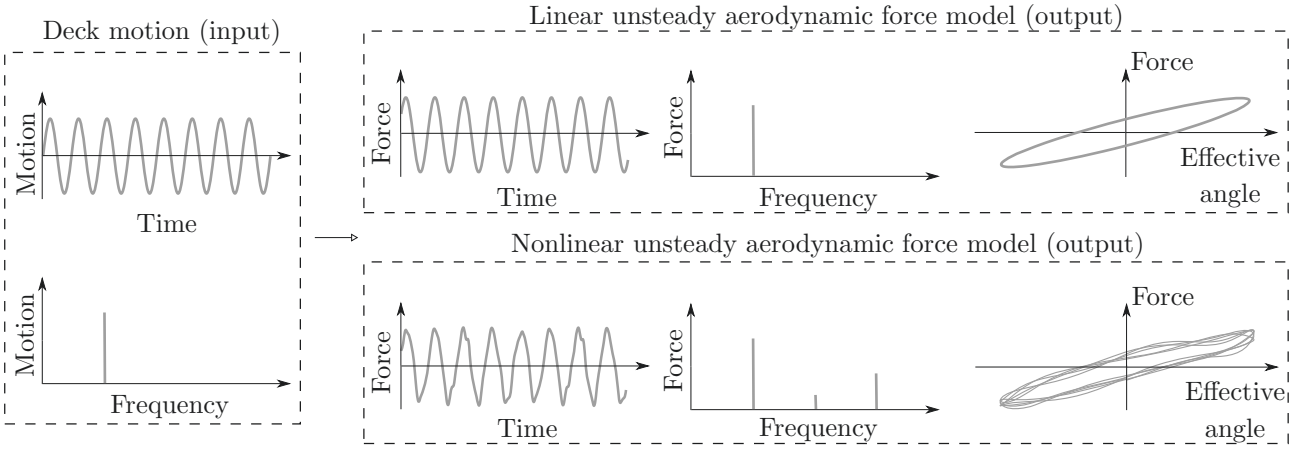

Figure 4.1: Linear and nonlinear aerodynamic forces acting on a bridge deck due to sinusoidal input motion.

In light of the previous overview of qualitative and quantitative aspects of the modeling process, a comparative methodology is presented in this chapter to provide a basis for the comparison of aerodynamic models. The methodology involves two levels of comparison: qualitative and quantitative. First in Sec. 4.2, the aerodynamic models presented in the previous chapter are evaluated in a qualitative manner utilizing the categorical modeling approach. An extension of the categorical modeling approach is further presented to adapt this approach for the present purpose. This extension entails a definition of model completeness and model comparability. The final outcome of the qualitative evaluation is a structure that clearly distinguishes which model is better based on its assumptions (i.e. universal model properties).

Having evaluated the aerodynamic models on an abstract level, the effect of model assumptions on a particular SRQ can be studied in a quantitative manner. For this purpose, a unified set of comparison metrics for time-histories is presented in Sec. 4.3. The metrics are tailored to quantify global and local discrepancies of two time-histories, which are of interest when two aerodynamic models are compared in the time domain with identical input. A total of nine metrics are constructed on a uniform basis. Seven of these metrics are adapted from former studies and recast to facilitate the current application, including peak, RMS, phase, magnitude, PDF, wavelet and frequency-normalized wavelet metrics. Moreover, two additional metrics are introduced to quantify the discrepancies in possible non-stationary and quadratic nonlinear parts of the signals by testing stationarity with wavelet-based surrogates and wavelet-based bispectrum, respectively.

4.2 Aerodynamic modeling: A categorical perspective

The goal of this section is to extend and apply the categorical modeling approach to the field of bridge aerodynamics. Initially, some preliminaries from category theory are briefly recalled. Then, the fundamental concept of the categorical modeling approach for mathematical models is outlined. To this end, a novel extension is presented in terms of model comparability and model completeness. Finally, the aerodynamic models presented in Ch. 3 are employed to serve for a real-world application of the categorical modeling approach.

4.2.1 Preliminaries from category theory

The categorical preliminaries presented herein are based on the excellent works by Adowey [5] and, perhaps more accessible for engineers, Spivak [306]. For complete information on category theory, the reader is referred to these works.

Generally speaking, category theory can be seen as an abstract theory of functions studying different mathematical structures (objects) and relations between them. The definition of a category is the starting point in category theory, which is defined as follows:

Definition 4.1 (Category [5])**.** *A category consists of the following data:*

(i) Objects: $\mathrm{A}_1, \mathrm{A}_2, \mathrm{A}_3, \ldots$

(ii) Arrows: $g_1, g_2, g_3 \ldots$

(iii) For each arrow g*, there are given objects:*

$$\mathrm{dom}(g), \quad \mathrm{cod}(g)$$

called the domain and codomain of g*. One writes:*

$$g \colon \mathrm{A}_1 \longrightarrow \mathrm{A}_2$$

to indicate that $\mathrm{A}_1 = \mathrm{dom}(g)$ *and* $\mathrm{A}_2 = \mathrm{cod}(g)$*.*

(iv) Given arrows $g_1 \colon \mathrm{A}_1 \longrightarrow \mathrm{A}_2$ *and* $g_2 \colon \mathrm{A}_2 \longrightarrow \mathrm{A}_3$*, i.e. with:*

$$\mathrm{cod}(g_1) = \mathrm{dom}(g_2)$$

there is given an arrow:

$$g_2 \circ g_1 \colon \mathrm{A}_1 \longrightarrow \mathrm{A}_3$$

called the composite of g_1 *and* g_2*.*

(v) For each object A*, there is given an arrow* $1_A \colon \mathrm{A} \longrightarrow \mathrm{A}$ *called the identity arrow of* A*.*

These data are required to satisfy the following laws: $g_1 \circ (g_2 \circ g_3) = (g_1 \circ g_2) \circ g_3$ *(associativity) and* $g \circ 1_{\mathrm{A}_1} = g = 1_{\mathrm{A}_2} \circ g$ *for all* $g \colon \mathrm{A}_1 \longrightarrow \mathrm{A}_2$ *(unit).*

A category is anything that satisfies this definition; thus, very general objects can be put together to form a category by specifying relations between objects via the arrows. With this, a category can be considered as an abstract algebra of functions (i.e. arrows), with the composition operation $\circ$ as primitive.

The next logical step would be to establish relations between the objects of the categories. These "relations" or, more formally, mappings can be defined by the notion of a functor as:

Definition 4.2 (Functor [5])**.** *A functor* $F \colon \mathbf{C}_1 \longrightarrow \mathbf{C}_2$ *between categories* $\mathbf{C}_1$ *and* $\mathbf{C}_2$ *is a mapping of objects to objects and arrows to arrows, in such a way that:*

(i) $F(g \colon \mathrm{A}_1 \longrightarrow \mathrm{A}_2) = F(g) \colon F(\mathrm{A}_1) \longrightarrow F(\mathrm{A}_2)$*;*

(ii) $F(1_{\mathrm{A}_1}) = 1_{F(\mathrm{A}_1)}$*;*

(iii) $F(g_1 \circ g_2) = F(g_1) \circ F(g_2)$*.*

That is, F respects domains and codomains, identity arrows, and composition.

As seen in the following, the objects and arrows within the categorical modeling approach are practically sets. Finally, the following objects may be included in some categories:

Definition 4.3 (Initial and terminal objects [5])**.** *In category* $\mathbf{C}$*, an object:*

(i) 0 *is initial if for any object* A *there is an unique mapping*

$$0 \longrightarrow \mathrm{A};$$

(ii) 1 *is terminal if for any object* A *there is an unique mapping*

$$\mathrm{A} \longrightarrow 1.$$

Having defined functors and categories separately, one could think that functors can be used to relate two categories in terms of product. Thus, the following definitions are defined:

Definition 4.4 (Product of categories [5])**.** *The product of two categories* $\mathbf{C}_1$ *and* $\mathbf{C}_2$*, written as*

$$\mathbf{C}_1 \times \mathbf{C}_2$$

has objects of the form $(\mathrm{A}_1, \mathrm{A}_2)$*, for* $\mathrm{A}_1 \in \mathbf{C}_1$ *and* $\mathrm{A}_2 \in \mathbf{C}_2$*, and arrows of the form:*

$$(g_1, g_2) : (\mathrm{A}_1, \mathrm{A}_2) \longrightarrow (\mathrm{A}_1', \mathrm{A}_2')$$

for $g_1 : \mathrm{A}_1 \longrightarrow \mathrm{A}_1' \in \mathbf{C}_1$ *and* $g_2 : \mathrm{A}_2 \longrightarrow \mathrm{A}_2' \in \mathbf{C}_2$*. Composition and units are defined componentwise, that is*

$$(g_1', g_2') \circ (g_1, g_2) = (g_1' \circ g_1, g_2' \circ g_2)$$
$$1_{(A_1, A_2)} = (1_{A_1}, 1_{A_2}).$$

There are two obvious projection function

$$\mathbf{C}_1 \xleftarrow{\pi_1} \mathbf{C}_1 \times \mathbf{C}_2 \xrightarrow{\pi_2} \mathbf{C}_2,$$

defined by $\pi_1(\mathrm{A}_1, \mathrm{A}_2) = \mathrm{A}_1$ *and* $\pi_1(g_1, g_2) = g_1$*, and similarly for* π_2*.*

Definition 4.5 (Functor category [5])**.** *Given the categories* $\mathbf{C}_1$ *and* $\mathbf{C}_2$*, then a category which has as objects functors* $\mathbf{F} : \mathbf{C}_1 \longrightarrow \mathbf{C}_2$*, and as arrows the natural transformations between two of such functors is called a functor category* $\mathbf{C}_1^{\mathrm{C}_2} = \mathrm{Funct}(\mathbf{C}_1, \mathbf{C}_2)$*.*

4.2.2 Categorical approach to modeling

Before employing the categorical language to aerodynamic models, a precise definition of what is considered a mathematical model is necessary. For this purpose, the definition of a mathematical model by Babuska and Oden [13] is utilized, which reads:

Definition 4.6 (Mathematical model [13])**.** *A collection of mathematical constructions that provide abstractions of a physical event consistent with a scientific theory proposed to cover that event.*

This definition implies that first assumptions are made regarding some physical event (i.e. phenomenon), based on which a model is constructed using mathematical formulations.

The concept of the categorical approach to mathematical models for engineering application was introduced by Gürlebeck et al. [125]. Hence, the approach explained in the following is mainly based on their work. Consider a category $\mathbf{Model}_1$ that contains mathematical models utilized to model a specific physical phenomenon, such as the aerodynamic forces arising from motion and free-stream turbulence. To formally introduce the mathematical models as objects of a category, the following definition is constructed:

Definition 4.7 (Objects of a category of mathematical models [125])**.** *Let* $\mathbf{Model}_1$ *be a category of mathematical models describing a given physical phenomenon. Then for all objects of* $\mathbf{Model}_1$ *the following assumptions hold:*

(i) objects are finite sets – set of assumptions of a mathematical model, denoted by $\mathbf{Set}_{\mathrm{A}}$*, where* A *is a corresponding mathematical model;*

(ii) arrows are relations between these sets;

(iii) for each set of assumptions and its corresponding model exists a mapping $\mathbf{Set}_{\mathrm{A}} \overset{S}{\mapsto} \mathrm{A}$*;*

(iv) all objects are related to mathematical models acting in the same physical domain.

Further remarks can be made be on the assumptions in the preceding definition. First, having finite sets of model assumptions as objects in the category is one possible way to approach mathematical models. Alternatively, the models can be directly represented by mathematical expressions (equations). However, in this case, it will be more difficult to distinguish models, since the same set of assumptions can be formalized differently in terms of final equations. For e.g., the LU model in terms of impulse or indicial functions (cf. (3.83), (3.84) and (3.85)). Second, assumption (ii) allows clear relations between models in terms of model assumptions and thus, mathematical models. As seen in the following, this can be used to formulate the definition of model complexity. Finally, the mapping S in (iii) allows for the model complexity to be based solely on its assumptions and independent of the input parameters. With this, the relations between the models is independent of particular values of input parameters. In some cases, the mapping S can be invertible leading to a unique reconstruction of a mathematical model from its set of assumptions. However, this is not possible in a general case.

The relations between objects in the category $\mathbf{Model}_1$ (cf. Definition 4.7) are given by the following definition:

Definition 4.8 (Complexity of mathematical models [125])**.** *Let* A_1 *and* A_2 *be mathematical models in a category* $\mathbf{Model}_1$*. The model* A_1 *has higher complexity than model* A_2 *iff* $\mathbf{Set}_{\mathrm{A}_1} \subset \mathbf{Set}_{\mathrm{A}_2}$*, but* $\mathbf{Set}_{\mathrm{A}_2} \not\subset \mathbf{Set}_{\mathrm{A}_1}$*. Consequently, two models are called equal iff* $\mathbf{Set}_{\mathrm{A}_2} = \mathbf{Set}_{\mathrm{A}_1}$*.*

The definition implies that model complexity can only be a binary relation in a category of models and is considered to be the universal model property. Defined in such a way, the complexity of models is neither related to the definition of complexity typically used in computer science (complexity of an algorithm) nor to the definition of complexity used for a statistical model, where the number of parameters is served as a complexity measure. Thus, the introduced complexity definition represents in a unique way the complexity of a mathematical model in general, based on the difference in the underlying physical assumptions.

Alternatively, the sets of assumptions between two models do not have to adhere to Definition 4.8, i.e. one cannot precisely say which model is more complex than the other. Thus, to refine the structure of the category of mathematical models for the two cases in which the models are or are not complexity-related, one can introduce two types of categories with total or partial orders:

Definition 4.9 (Partially ordered models [125])**.** *Let* $\mathbf{Model}_1$ *be a category of mathematical models with n objects, and let* X *be the set of all physical assumptions used in this category. Assume that objects of* $\mathbf{Model}_1$ *can be ordered according to Definition 4.8 as* $\mathbf{Set}_{A_j} \subset \mathbf{Set}_{A_k}$ *for* $j < k$*. Then the category* $\mathbf{Model}_1$ *contains totally ordered models iff* $\mathrm{X} = \mathbf{Set}_{\mathrm{A}_1} \cup \mathbf{Set}_{\mathrm{A}_2} \cup \ldots \cup \mathbf{Set}_{\mathrm{A}_n}$ *and* $\mathbf{Set}_{\mathrm{A}_n} = \mathrm{X}$*, otherwise, the category* $\mathbf{Model}_1$ *contains partially ordered models.*

Finally, the categorical approach also accounts for coupled problems in engineering such as the fluid-structure interaction. In such cases, a coupled model, comprised of two or more partial models, is necessary. Thus, a coupled model is defined based on Definitions 4.4 and 4.5 as:

Definition 4.10 (Objects of a category of coupled models [125])**.** *Consider two categories of mathematical models* $\mathbf{Model}_1$ *and* $\mathbf{Model}_2$*. Then the coupling of models from these categories constitutes a category* $\mathbf{Model}_{12}$ *with objects satisfying the following conditions:*

(i) objects are finite sets – set of assumptions of a coupled mathematical model, denoted again by $\mathbf{Set}_{\mathrm{A}_1}$*, where* A_1 *is a corresponding coupled mathematical model, and arrows are relations between these sets;*

(ii) set of assumptions $\mathbf{Set}_{\mathrm{A}_{12}}$ *of a coupled mathematical model is defined by*

$$\mathbf{Set}_{\mathrm{A}_{12}} := \mathbf{F}_1\left(\mathbf{Set}_{\mathrm{A}_1}\right) \cup \mathbf{F}_2\left(\mathbf{Set}_{\mathrm{A}_2}\right),$$

where $\mathbf{Set}_{\mathrm{A}_1}$ *and* $\mathbf{Set}_{\mathrm{A}_2}$ *are sets of assumptions of mathematical models from* $\mathbf{Model}_1$ *and* $\mathbf{Model}_2$*, correspondingly,* $\mathbf{F}_1$ *and* $\mathbf{F}_2$ *are functor categories* $\mathrm{Funct}(\mathbf{Model}_1\mathbf{Model}_{12})$ *and* $\mathrm{Funct}(\mathbf{Model}_2\mathbf{Model}_{12})$*, respectively. Moreover, the following statements for* $\mathbf{Set}_{\mathrm{A}}$ *are true*

$$a)\ \left(\mathbf{Set}_{\mathrm{A}_1} \cup \mathbf{Set}_{\mathrm{A}_2}\right) \subset \mathbf{Set}_{\mathrm{A}_{12}}; \quad b)\ \mathbf{Set}_{\mathrm{A}_{12}} \not\subset \left(\mathbf{Set}_{\mathrm{A}_1} \cup \mathbf{Set}_{\mathrm{A}_2}\right).$$

(iii) a coupled mathematical model A_{12} *is a pair* $(\mathrm{A}_1, \mathrm{A}_2)$*, i.e.* $\mathbf{Model}_{12}$ *provides the structure of a category of coupled mathematical models.*

This definition corresponds to the following diagram

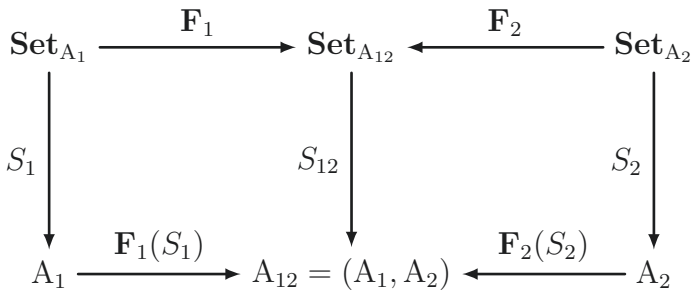

Practical meaning of this definition is the following: property (i) implies that a coupling of mathematical models produces again a mathematical model, meaning that complexity definition

can be used again to order coupled models now; and property (ii) underlines that the set of assumptions of a coupled model is obtained by actions of functors on the sets of assumptions of models being coupled, and not by a simple unification of these sets.

4.2.3 Extension of the categorical approach to modeling*

Before applying the categorical approach to the problems in bridge aerodynamics, several advancements are made to make the approach more suitable for the task at hand. First, a definition of a simplest and most complex model is introduced as follows:

Definition 4.11 (Simplest and most complex models)**.** *Consider a category of mathematical models* $\mathbf{Model}_1$ *with n objects. Let* X *be the set of all physical assumptions used in this category. Let* $\{\mathrm{A}_1, \mathrm{A}_2, \ldots, \mathrm{A}_n\}$ *be the set of all models associated with the sets of assumptions from* $\mathbf{Model}_1$*. Then, the model* A_n *is the simplest model in* $\mathbf{Model}_1$ *iff* $\mathbf{Set}_{\mathrm{A}_n} = \mathrm{X}$*; additionally, the model* A_1 *is the most complex model in* $\mathbf{Model}_1$ *iff* $\mathbf{Set}_{\mathrm{A}_1} \subset \mathbf{Set}_{\mathrm{A}_j} \subset \mathrm{X}\ \forall j = 2, \ldots, n$*.*

Combining this definition with Definition 4.9 and Definition 4.3, the following corollary is immediately obtained:

Corollary 4.1. *In totally ordered categories of mathematical models the simplest and the most complex models exist, and they represent the initial and terminal objects, respectively.*

By using the definition of complexity (cf. Definition 4.8), a comparison of different models can be performed. Particularly, the effect of specific assumptions on a selected SRQ can be evaluated. Such comparison works perfectly in the case of totally ordered categories of models. However, if a given category contains only partially ordered models, then models that are not under the complexity relation cannot be compared directly. To illuminate this point, consider, for e.g., the LU and QS semi-analytical aerodynamic models, and let the deck displacement be a SRQ. By studying the SRQ from both models, one observes discrepancies which are due to the assumptions of linearity or quasi-steadiness. However, a precise specification of the assumption causing the discrepancy in the SRQ is not possible, since the models are not complexity-related to each other. To overcome this problem and to allow a clear comparison of model assumptions in practice, the following definition is introduced:

Definition 4.12 (Comparability of mathematical models)**.** *Let* A_1*,* A_2 *and* A_3 *be models from a category of mathematical models* $\mathbf{Model}_1$*. The models* A_1*,* A_2 *and* A_3 *are called directly comparable iff they are complexity-related. Further, the models* A_1*,* A_2 *are called relatively comparable w.r.t. model* A_3 *iff* $\mathrm{A}_1 \cup \mathrm{A}_2$ *(the union implies the union of the corresponding sets of assumptions) and* A_3 *are complexity-related, i.e.*

$$(\mathbf{Set}_{\mathrm{A}_1} \cup \mathbf{Set}_{\mathrm{A}_2}) \subseteq \mathbf{Set}_{\mathrm{A}_3} \quad \textit{or} \quad \mathbf{Set}_{\mathrm{A}_3} \subseteq (\mathbf{Set}_{\mathrm{A}_1} \cup \mathbf{Set}_{\mathrm{A}_2}).$$

In the preceding definition, the direct comparability is simply the application of complexity definition, and in a totally ordered category, all models are directly comparable. The relative comparability practically implies that for a comparison of two models, which are not complexity-related, a third model is required, which is either simpler or more complex than both of the models. From the point of view of a diagrammatic representation of models, the relative comparability addresses the branching point in the diagram. It is important to note that, in

case of the relative comparability, one cannot draw a conclusion which model outcome is of higher quality based on a simpler model, rather only study the effect of excluding assumptions from the set of assumptions of the simpler model.

When comparing two models, the effect of the assumptions on a selected SRQ needs to be evaluated quantitatively. Typically, measures, such as mean squared error or L^2 error, are used to quantify the model output quality. Since a specific choice of the measure is problem dependent, such measures can be more generally referred to as a *comparison metric*. From bridge aerodynamics perspective, the time-dependent aerodynamic response or forces are commonly used as SRQ; thus, the comparison metrics quantify the discrepancies in the time-histories of these quantities. The actual form of these comparison metrics for time-histories is discussed in detail in Sec. 4.3. Generally, a comparison requires a selection of a reference model, based on which the relative effect of excluding/adding an assumption w.r.t a selected SRQ is studied. Depending on the reference model, two types of comparison can be distinguished, forward and backward, both defined by the following:

Definition 4.13 (Forward and backward comparison)**.** *Let a comparison metric $\mathcal{M}$ quantify the difference of a SRQ between the models A_1 and A_2, where A_1 is chosen to be the reference model. The following types of comparison can be defined:*

(i) forward comparison, if $\mathbf{Set}_{\mathrm{A}_2} \subseteq \mathbf{Set}_{\mathrm{A}_1}$, and the comparison metric $\mathcal{M}$ is denoted as $\mathcal{M}_{SRQ}^{\mathrm{A}_1,\mathrm{A}_2}$;

(ii) backward comparison, if $\mathbf{Set}_{\mathrm{A}_1} \subseteq \mathbf{Set}_{\mathrm{A}_2}$, and the comparison metric $\mathcal{M}$ is denoted as $\overline{\mathcal{M}_{SRQ}^{\mathrm{A}_1,\mathrm{A}_2}}$.

The comparison metrics can be considered in a deterministic or probabilistic fashion. By taking the parameter and numerical uncertainty of the models into account, the comparison metric can be considered as a random variable with a corresponding probability distribution. Hence, the effect of assumptions on a selected SQR will be also considered in a probabilistic manner. Moreover, sensitivity analysis can be performed w.r.t. a certain comparison metric to better understand the influence of parameter and numerical uncertainty on the effect of model assumptions. It is noteworthy to mention that a validation metric, which is commonly used in the verification and validation [241], is, in fact, a special case of a comparison metric. In the case of a validation metric, deterministic or probabilistic, the experimental results are always chosen to be the reference. Moreover, conclusions if a reference model, simpler or more complex, is an appropriate representation of reality cannot be drawn, based only on the categorical modeling approach. This requires appropriate validation with experimental results for each particular case-study.

From practical point of view, it is beneficial to introduce the following definition:

Definition 4.14 (Model completeness)**.** *Let* A *be a model from a category* $\mathbf{Model}_1$*. The model* A *is called complete w.r.t. a certain physical phenomenon iff its corresponding set of assumptions* $\mathbf{Set}_{\mathrm{A}}$ *allows to describe that phenomenon without any additional modification.*

In practice, model completeness implies a subdivision of models in a given category into (discrete) subcategories of models w.r.t. physical phenomena these models are able to describe, based on the physical mechanisms they account for. Such a clear structure simplifies comparative analysis of models, since it narrows the set of models for a specific physical phenomenon of interest prior to comparison, depending on specific purposes of the analysis.

4.2.4 Aerodynamic modeling via categorical approach*

The coupled model for wind-bridge interaction is described based on the categorical modeling approach as a real-world application of an abstract concept. Two partial models constitute the coupled model for wind-bridge interaction: fluid model in terms of aerodynamic forces and a structural model. Both of these models are defined in $\mathbb{R}^2$. Considering a $\mathbb{R}^2$ instead of $\mathbb{R}^3$ domain is itself an assumption (i.e. strip assumption). Nevertheless, defining both partial models in $\mathbb{R}^2$ is compliant with (iv) from Definition 4.7 and is sufficient for the demonstration of the concept of aerodynamic modeling via categorical approach.

First, the structural model SM from (3.5) is considered to be an object of category **StrutModel**. Second, all thirteen aerodynamic force models defined in Ch. 2 are included in the category **AeroModel**, i.e. $\{\mathrm{ST}, \mathrm{LST}, \mathrm{QS}, \mathrm{LQS}, \mathrm{LU}, \mathrm{MBM}, \mathrm{CMBM}, \mathrm{CQS}, \mathrm{MQS}, \mathrm{HNL}, \mathrm{MNL}, \mathrm{NLU}, \mathrm{CFD}\}$. According to Definition 4.10, sets of assumptions in category **CoupModel** are obtained as:

$$\mathbf{Set}_{\mathrm{C}} := \boldsymbol{T}(\mathbf{Set}_{\mathrm{Sm}}) \cup \boldsymbol{F}(\mathbf{Set}_{\mathrm{A}}), \tag{4.1}$$

where SM is the structural model and A can be any model from **AeroModel**. The assumption of linearity in the structural model SM can have a significant influence on the structural behavior along with the aerodynamic model assumptions. This is particularly evident at high wind speeds and in the post-flutter regime in terms of limit cycle oscillations [10, 49, 236]. However, the main interest of this study is the aerodynamic models; thus, only the sets of assumptions for the models in **AeroModel** are defined. Before proceeding with the constriction of the sets of assumptions, the following remark is made:

Remark 4.1. *Sets of assumptions introduced in Definition 4.7 are assumed to be written by the help of a natural language. An alternative way would be listing directly mathematical formalization of the assumptions. However, it would lead to a more complicated construction, since strongly speaking, the formalized assumptions do not necessarily form sets. To make the application more transparent, the formalized assumptions are listed and referenced as sets of assumptions, implying that each formalized assumption corresponds to the same assumption written in a natural language.*

The CFD model (cf. (3.184)) is formulated by assuming the fluid is incompressible and homogeneous, with conservative body forces. Thus, the set of assumptions takes the following form:

$$\mathbf{Set}_{\mathrm{CFD}} := \left\{ \frac{\partial \rho}{\partial t} = 0, \nabla \rho = 0, \nabla \times \boldsymbol{f}_{\mathrm{body}} = 0 \right\}, \tag{4.2}$$

where $\boldsymbol{f}_{\mathrm{body}}$ is the body force vector. The origin of the aerodynamic coefficients in the semi-analytical models is dependent on the model, CFD or experimental, from which they are obtained and its input. Since the semi-analytical models are basically "phenomenological" models, their predictive capabilities are limited by their mathematical constructions and the information contained in the aerodynamic coefficients. Thus, the aerodynamic coefficients are based on and valid for certain input properties of the model they are obtained from, such as frequency content and amplitude (motion or gust) and Reynolds number. Depending on the range of application, the aerodynamic coefficients can be assumed insensitive to variations of these input parameters in some cases (e.g., Reynolds number dependency for bridge decks), while in others not (e.g., Reynolds number dependency for cables). Herein, it is assumed that all aerodynamic coefficients are obtained from the CFD model, meaning that a semi-analytical model is a

reduced-order model from the Navier-Stokes equations. Hence, $\mathbf{Set}_{\mathrm{CFD}}$ is a subset of the sets of assumptions corresponding to all semi-analytical models. The validity of the 2D Navier-Stokes equations and the Vortex Method and how well they represent a realistic situation is not in the scope of the present discussion. Nevertheless, if the aerodynamic coefficients are validated with experimental data in a statistical sense, as it has been conducted in many instances in bridge aerodynamics for the vortex method (cf. Sec. 2.5.3), it is reasonable to assume that the CFD model is a close approximation of the reality. Therefore, the set of assumptions for the NLU model (cf. (3.151)) is constructed as a superset of $\mathbf{Set}_{\mathrm{CFD}}$ as

$$\mathbf{Set}_{\mathrm{NLU}} := \mathbf{Set}_{\mathrm{CFD}} \cup \{\boldsymbol{f}_v = 0; \boldsymbol{f}_{noi} = 0; \boldsymbol{f}(t) = \boldsymbol{f}(\boldsymbol{a}(t))\}\,, \tag{4.3}$$

where $\boldsymbol{f}_v$ and $\boldsymbol{f}_{noi}$ are vectors representing the forces due to vortex-shedding and interior noise, respectively. The third assumption indicates that the forces are time-invariant due to input $\boldsymbol{a} = \boldsymbol{a}(t)$ including the wind fluctuations and structural motion. Although the higher-order indicial functions account for a portion of aerodynamic nonlinearity and fading fluid memory, they cannot replicate the complete aerodynamic behavior simulated by the Navier-Stokes equations. Hence, the NLU model does not account for the forces due to vortex shedding and interior noise. The term "interior noise" is used here to allude to aerodynamic phenomena which can be chaotic such as wake instability, laminar-turbulent transition (Reynolds number), local separation and reattachment. The physical relation between the interior noise and the aerodynamic forces is not well-established and can yield time-variant output (aerodynamic forces) for time-invariant input (motion or incoming gusts). This cannot be captured by the NLU model (cf. Wu and Kareem [362] for discussion). Therefore, the relation in the mathematical constructions between the CFD and NLU models is not as clear as the subsequent relations between the semi-analytical models.

The LU model (cf. (3.83)) includes the fluid memory in a linear sense. Therefore, $\mathbf{Set}_{\mathrm{LU}}$ can be formulated as a superset of $\mathbf{Set}_{\mathrm{NLU}}$, yielding

$$\mathbf{Set}_{\mathrm{LU}} := \mathbf{Set}_{\mathrm{NLU}} \cup \{\boldsymbol{f} = \boldsymbol{f}|_{\alpha_s}\}\,, \tag{4.4}$$

Herein, the linearization implies that the first-order kernel is equal to the corresponding indicial function $\Phi^I = A_1\Phi$, for A_1 being coefficient that accounts for the quasi-steady asymptotes, while the products involving higher-order kernels are neglected. The coefficient A_1 for the corresponding indicial functions can be easily obtained by comparing (3.83) and (3.151).

Despite having similar complex dynamic properties in terms of eigenfrequencies and modes with the LU, the CMBM model (cf. (3.140)) interpolates the aerodynamic transfer matrix at certain reduced frequencies K_{cj} (i.e. reduced velocities V_{rcj}), for $j \in \{1, \ldots, 3\}$ corresponding to the complex eigenfrequencies. With this, the CMBM model accounts for an averaged fluid memory at the complex eigenfrequencies. For the LU model, the reduced velocity V_r represents an interval $[0, \infty)$, while for the MQS model, V_{rcj} are case-dependent coefficients, and therefore, $V_{rcj} \subset V_r$. This means that the CMBM model is a special case of the LU model; thus, $\mathbf{Set}_{\mathrm{CMBM}}$ is a superset of $\mathbf{Set}_{\mathrm{LU}}$ and it yields

$$\mathbf{Set}_{\mathrm{CMBM}} := \mathbf{Set}_{\mathrm{LU}} \cup \{V_r = V_{rc}\}\,. \tag{4.5}$$

Practically, this means that the aerodynamic stiffness and damping matrices (cf. (3.76) and (3.77)) are interpolated at each complex frequency as $\boldsymbol{K}_{ae} = \boldsymbol{K}_{ae}(V_{rcj})$, $\boldsymbol{C} = \boldsymbol{C}_{ae}(V_{rcj})$, respectively. As an example, this was shown in (3.139) for the lift force due to vertical motion.

The MQS model considers the averaged fluid memory only in the motion-induced forces by interpolating the flutter derivatives at a specific reduced velocity V_{rcj} for $j \in \{1, \dots, 3\}$ (cf. (3.142)). Theoretically, this reduced frequency can be selected in a similar way as the CMBM model, although the complex eigenfrequencies are generally unknown. However, the complex mode shapes $\boldsymbol{\phi}_j$ and eigenfrequencies λ_j for the MQS model are assumed to be similar to the ones for the system in still air, $\boldsymbol{\psi}_j$ and ω_j. Hence, $\mathbf{Set}_{\mathrm{CMBM}}$ is a subset of $\mathbf{Set}_{\mathrm{MQS}}$, which is constructed as follows:

$$\mathbf{Set}_{\mathrm{MQS}} := \mathbf{Set}_{\mathrm{CMBM}} \cup \left\{ \Phi_{Lu} = 1; \Phi_{Lw} = 1; \Phi_{Mu} = 1; \Phi_{Mw} = 1; \lambda_j = \omega_j; \boldsymbol{\phi}_j = \boldsymbol{\psi}_j \right\}, \tag{4.6}$$

for $j \in \{1, \dots, 3\}$. Plugging these assumptions in (3.140), it can be easily shown that (3.142) can be obtained, taken that the modal displacements are real for a system in still air.

While the MBM model (cf. (3.128)) accounts for the fluid memory in a similar fashion as the LU model, it neglects the aerodynamic coupling by ignoring the cross products in (3.83). Hence, $\mathbf{Set}_{\mathrm{MBM}}$ is formulated as a superset of $\mathbf{Set}_{\mathrm{LU}}$ as

$$\begin{aligned} \mathbf{Set}_{\mathrm{MBM}} := \mathbf{Set}_{\mathrm{LU}} \cup \{ & \Phi_{Dh}\dot{h} = 0; \Phi_{D\alpha}\dot{\alpha} = 0; \Phi_{D\dot{\alpha}}\ddot{\alpha} = 0; \Phi_{Lp}\dot{p} = 0; \\ & \Phi_{L\alpha}\dot{\alpha} = 0; \Phi_{L\dot{\alpha}}\ddot{\alpha} = 0; \Phi_{Mp}\dot{p} = 0; \Phi_{Mh}\dot{h} = 0 \}. \end{aligned} \tag{4.7}$$

The MNL model (cf. (3.149)) accounts for the aerodynamic nonlinearity and averaged fading fluid memory by selecting a specific reduced velocity V_{rc} for the approximation of the aerodynamic hysteresis. Accounting only for a specific reduced velocity makes the MNL model a special case of the NLU model. For the MNL model, it is additionally assumed that the forces are independent of the origin of the effective angle. By origin, it is meant whether this angle is computed from wind fluctuations, motion or as a combination of the two. Thus, $\mathbf{Set}_{\mathrm{MNL}}$ is obtained as follows:

$$\mathbf{Set}_{\mathrm{MNL}} := \mathbf{Set}_{\mathrm{NLU}} \cup \left\{ V_r = V_{rc}; \boldsymbol{f}\left(\frac{w}{U+u}\right) = \boldsymbol{f}\left(\frac{\dot{h}}{U-\dot{p}}\right) = \boldsymbol{f}\left(\frac{mB\alpha}{U-\dot{p}}\right) \right\}. \tag{4.8}$$

In such way, the frequency-domain counterparts of the higher-order kernels in (3.151) can be approximated by a frequency-independent polynomial, yielding (3.149).

Neglecting the hysteretic behaviour of the aerodynamic coefficients in the MNL model, the CQS model is independent of the derivative of the effective angle of attack $\dot{\alpha_e}$ (cf. (3.145) and (3.149)). With this, the corresponding set of assumptions for the CQS model yields

$$\mathbf{Set}_{\mathrm{CQS}} := \mathbf{Set}_{\mathrm{MNL}} \cup \left\{ \sum_{k,l}^{N_c} A_{kl} \alpha_e^k(\omega_c) \dot{\alpha_e}^{\,l}(\omega_c) = \sum_{k}^{N_c} A_k \alpha_e^k(\omega_c) \dot{\alpha_e}^{\,0}(\omega_c) \right\}, \tag{4.9}$$

where the A_k coefficients can be obtained as N_c degree polynomial of the integral term in (3.145).

The QS model (cf. (3.70)) is a special case of the CQS model, where instead of a specified reduced velocity V_{rc}, it is assumed that the system is mapped to an equivalent state at infinite time. Thus, we formulate $\mathbf{Set}_{\mathrm{QS}}$ as a superset of $\mathbf{Set}_{\mathrm{CQS}}$ as

$$\mathbf{Set}_{\mathrm{QS}} := \mathbf{Set}_{\mathrm{CQS}} \cup \{ V_{rc} \to \infty \}, \tag{4.10}$$

meaning that the correction coefficients (cf. (3.145)) are unity under the quasi-steady assumption, i.e. $Q_j^* = 1$. Precisely, the variable coefficient V_{rc} is assumed to be the limit case towards infinity. Therefore, $V_{rc} \to \infty$ is a subset of the variable coefficient V_{rc}.

Although the HNL model (cf. (3.147)) is partially able to replicate the nonlinear behavior while accounting for the fluid memory in the high-frequency range, this model cannot be considered as fully nonlinear nor fully unsteady. Therefore, the only semi-analytical model, having a set of assumptions as a subset of $\mathbf{Set}_{\mathrm{HNL}}$, is the NLU model. This yields

$$\mathbf{Set}_{\mathrm{HNL}} := \mathbf{Set}_{\mathrm{NLU}} \cup \left\{ V_r \to \infty \text{ for } \alpha_e^l; \boldsymbol{f} = \boldsymbol{f}|_{\alpha_e^l} \text{ for } \alpha_e^h \right\}. \tag{4.11}$$

The mathematical relations between (3.151) and (3.147) can be obtained utilizing Volterra frequency-response functions (cf. Carassale et al. [47] for detail relations).

The LQS model (cf. (3.71)) is linear and neglects the fluid memory; hence, $\mathbf{Set}_{\mathrm{LQS}}$ is obtained as

$$\begin{aligned} \mathbf{Set}_{\mathrm{LQS}} :=& \mathbf{Set}_{\mathrm{MQS}} \cup \{V_{rc} \to \infty\} \\ =& \mathbf{Set}_{\mathrm{QS}} \cup \{\boldsymbol{f} = \boldsymbol{f}|_{\alpha_s}\} \\ =& \mathbf{Set}_{\mathrm{HNL}} \cup \left\{ \boldsymbol{f} = \boldsymbol{f}|_{\alpha_s} \text{ for } \alpha_e^l; V_r \to \infty \text{ for } \alpha_e^h \right\}. \end{aligned} \tag{4.12}$$

By setting $V_{rc} \to \infty$, the frequency-independent coefficients in the MQS attain to their quasi-steady value, which can be obtained simply by comparing (3.71) and (3.142). Since the LU model is more widely used than the MQS model, it is noteworthy to mention that the LQS model can be directly obtained from the frequency-domain formulation of the LU model by the asymptotic values of the flutter derivatives in (3.123). The linearization is performed using the same analogy as in (3.67).

Disregarding the motion-induced forces, generally leads to an inaccurate prediction of the aerodynamic forces, especially for high wind velocities. As the ST model (cf. (3.66)) accounts for the aerodynamic nonlinearity and does not include the motion-induced forces, $\mathbf{Set}_{\mathrm{ST}}$ is constructed as a superset of $\mathbf{Set}_{\mathrm{QS}}$ as

$$\begin{aligned} \mathbf{Set}_{\mathrm{ST}} := \mathbf{Set}_{\mathrm{QS}} \cup \Bigg\{ & \alpha_e = \alpha_s + \alpha + \phi = \alpha_s + \phi; \\ & \phi = \arctan\left(\frac{w + \dot{h} + mB\dot{\alpha}}{U + u - \dot{p}}\right) = \arctan\left(\frac{w}{U+u}\right) \Bigg\}. \end{aligned} \tag{4.13}$$

The LST model (cf. (3.69)) neglects the motion-induced forces and fluid memory in the buffeting forces. Correspondingly, $\mathbf{Set}_{\mathrm{LST}}$ is formulated as a superset of $\mathbf{Set}_{\mathrm{MBM}}$, $\mathbf{Set}_{\mathrm{LQS}}$, and $\mathbf{Set}_{\mathrm{ST}}$ as

$$\begin{aligned} \mathbf{Set}_{\mathrm{LST}} :=& \mathbf{Set}_{\mathrm{LQS}} \cup \Bigg\{ (C_D' - C_L)\frac{\dot{h} + m_D B\dot{\alpha}}{U - \dot{p}} = 0; C_D'\alpha = 0; (C_L' + C_D)\frac{\dot{h} + m_L B\dot{\alpha}}{U - \dot{p}} = 0; \\ & C_L'\alpha = 0; C_M'\frac{\dot{h} + m_M B\dot{\alpha}}{U - \dot{p}} = 0; C_M'\alpha = 0 \Bigg\} \\ =& \mathbf{Set}_{\mathrm{MBM}} \cup \left\{ \Phi_{Lp}\dot{p} = 0; \Phi_{Lh}\dot{h} = 0; \Phi_{M\alpha}\dot{\alpha} = 0; \Phi_{M\dot{\alpha}}\ddot{\alpha} = 0 \right\} \\ =& \mathbf{Set}_{\mathrm{ST}} \cup \{\boldsymbol{f} = \boldsymbol{f}|_{\alpha_s}\}. \end{aligned} \tag{4.14}$$

Based on sets of assumptions used for the models in category **AeroModel** (i.e. from (4.2) to (4.14)), the following diagram can be constructed:

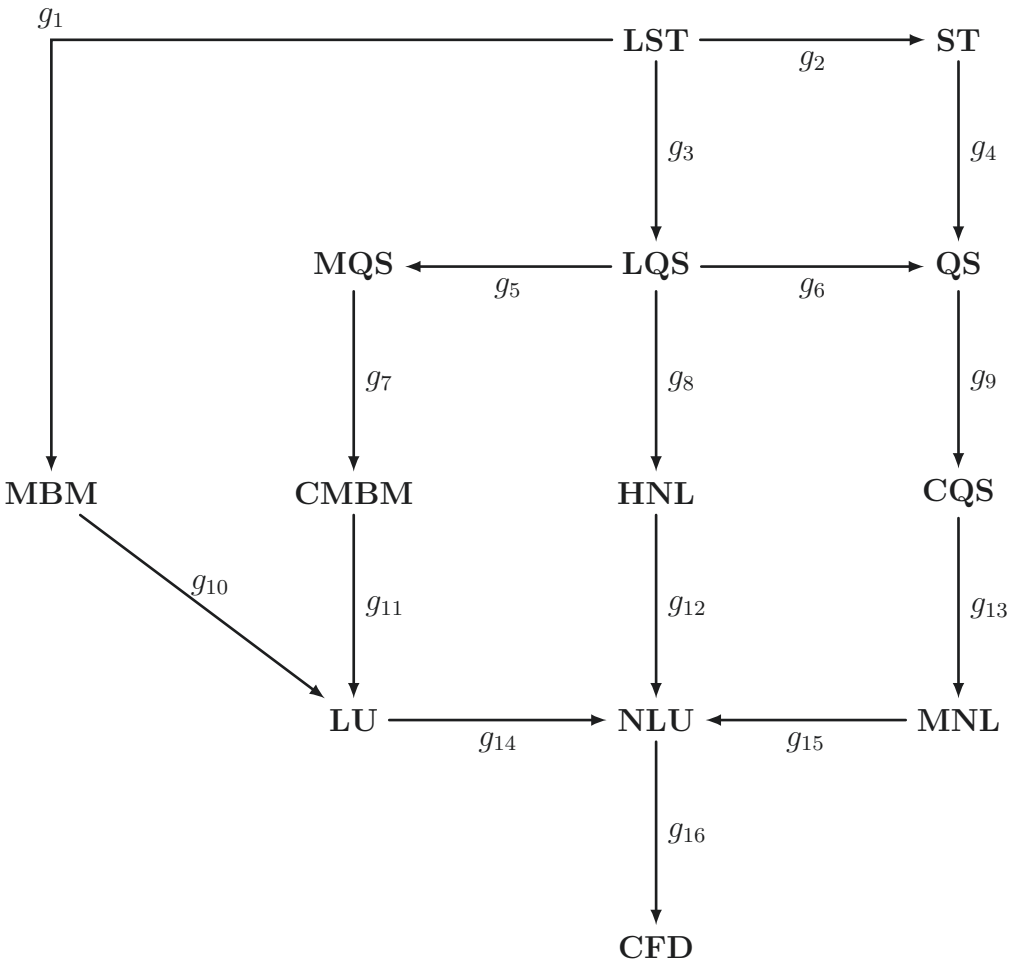

By using Definitions 4.8, 4.9 and 4.11, the following conclusions can be drawn from the diagram of category **AeroModel**: (i) **AeroModel** is a category with partially ordered models; (ii) the CFD model is the most complex aerodynamic model since $\mathbf{Set}_{\mathrm{CFD}} \subset \mathbf{Set}_{\mathrm{A}}$, where A is any model in the category **AeroModel**; (iii) the NLU model is the most complex semi-analytical aerodynamic model since $\mathbf{Set}_{\mathrm{NLU}} \subset \mathbf{Set}_{\mathrm{A}}$, where A is any model in the category **AeroModel**, except the CFD model; (iv) the LST is the simplest aerodynamic model since $\mathbf{Set}_{\mathrm{LST}} = \mathrm{X}$, where X are all aerodynamic assumptions considered in the category **AeroModel**.

Additionally, we see from the diagram that each arrow g_i between models increases complexity. With the increase of the model complexity, one can study the effect of the underlying assumptions in the models based on a selected SRQ. Taking into account Definition 4.12, and the fact that **AeroModel** is a category with partially ordered models, it is evident that a direct comparison of SRQ for any two models from **CoupModel** is not possible. E.g., a direct comparison of LU and QS models is not possible, since the former includes the linear fluid memory, whilst the latter neglects the fluid memory and is nonlinear. This point will be further elaborated in Ch. 6 for one of the applications.

Depending on the wind characteristics, structural properties, and deck shape, several phenomena may occur during the wind-bridge interaction such as vortex-induced vibrations, buffeting response, and aeroelastic instabilities. Although all models in **CoupModel** account for the fluid-structure up to a certain extent, not all are complete w.r.t. all of these phenomena. Herein, Definition 4.14 is used w.r.t. the aeroelastic phenomenon *classical flutter* for the models of **CoupModel**. To precisely define the term classical flutter in bridge aerodynamics, the

definition given by Simiu and Scanlan [301] is utilized, which reads: "[Classical flutter] implies an aeroelastic phenomenon in which two degrees of freedom of a structure, rotation, and vertical translation, couple together in a flow-driven, unstable oscillation." From this definition, it is clear that a model that considers concurrently the aerodynamic and structural behavior is required to simulate flutter. Since the partial differential equations on the structural side for model SM (cf. (3.5)) are decoupled (this is a coupling of degrees of freedom, not mathematical models), the coupling occurs on the aerodynamic side due to the self-excited forces.

The assumption which permits for an aerodynamic model to account for classical flutter is the disregard of aerodynamic coupling. This assumption is also implied by the disregard of the self-excited forces. The sets of assumptions which include this particular assumption are $\mathbf{Set}_{\mathrm{MBM}}$ (cf. (4.7)), $\mathbf{Set}_{\mathrm{ST}}$ (cf. (4.13)) and $\mathbf{Set}_{\mathrm{LST}}$ (cf. (4.14)). Consider a category of aerodynamic models **FlutterModel**, which set of assumptions X does not contain the assumption that the aerodynamic coupling is neglected. The category **FlutterModel** can be obtained as a sub-category from **AeroModel** by a functorial mapping as follows:

$$\mathbf{FlutterModel} \overset{I}{\mapsto} \mathbf{AeroModel}. \tag{4.15}$$

The models included in **FlutterModel** are a sub-collection of the models from **AeroModel**, i.e. {LQS, QS, MQS, CMBC, LU, HNL, CQS, MNL, NLU, CFD}. Subsequently, it is straightforward to define a category **CoupModelF** that contains a coupled model C, which is obtained in similar manner as in (4.1), with the difference that the aerodynamic model A can be any model from **FlutterModel** instead of **AeroModel**. Finally, it can be stated that the models in **CoupModelF** are complete w.r.t. classical flutter phenomenon.

4.3 Comparison metrics for time-histories*

For the aerodynamic models in the categorical diagram of the preceding section, the SRQ of interest is generally based on time-dependent quantities such as the response and forces. In this case, the SRQ generally represents a particular signal feature in terms of phase, magnitude, frequency-content, etc. This section presents a unified set of nine comparison metrics time-histories. All metrics are constructed to quantify global and local discrepancies in the signal features of interest in bridge aerodynamics.

Various signal features (local or global) can attain magnitudes of a different order. Therefore, it is beneficial to construct the comparison metrics in such a manner that their range of values is in the interval between zero and one. To facilitate this, the comparison metrics for time-histories are defined in a unified manner by the following:

Definition 4.15 (Comparison metric for time-histories)**.** *Let $a = a(t)$ and $b = b(t)$, $t \in [0, T]$ be output time-histories of time-dependent models A_1 and A_2 calculated at the same spatial position. A comparison metric $\mathcal{M}_{\mathrm{SRQ}}^{\mathrm{A}_1,\mathrm{A}_2}$ that quantifies the difference of a SRQ, based on a and b, is defined as:*

$$\mathcal{M}_{\mathrm{SRQ}}^{\mathrm{A}_1,\mathrm{A}_2}(a, b) := \exp(-\varepsilon \mathcal{A}),$$

where $\mathcal{A} = \mathcal{A}(a, b)$ is the relative exponent and $\varepsilon > 0$ is a sensitivity parameter. The following properties apply:

(i) $\mathcal{M}_{\mathrm{SRQ}}^{\mathrm{A}_1,\mathrm{A}_2} = 1$*, for equal SRQ for a and b;*

(ii) $0 < \mathcal{M}_{\mathrm{SRQ}}^{\mathrm{A}_1,\mathrm{A}_2} < 1$*, for finite difference of a SRQ for a and b,*

(iii) $\mathcal{M}_{\mathrm{SRQ}}^{\mathrm{A}_1,\mathrm{A}_2} = 0$*, for infinite difference of a SRQ for a and b or when a particular signal property is available for a, while not available for b and vice versa.*

From this definition, the relative exponent $\mathcal{A}$ for each metric accounts for the discrepancies of a particular feature of the time-histories, while the sensitivity parameter $\varepsilon > 0$ is introduced to adjust the sensitivity of different metrics. What is meant by signal property in (iii) is e.g. when one signal is stationary, while the other. Thus, quantification of the discrepancies in for the non-stationary parts is obsolete.

A total of nine metrics are presented, including: (i) phase $\mathcal{M}_{\varphi}$, (ii) peak M_p, (iii) RMS $\mathcal{M}_{\mathrm{rms}}$, (iv) magnitude $\mathcal{M}_m$, (v) PDF $\mathcal{M}_{\mathrm{pdf}}$, (vi) wavelet $\mathcal{M}_w$, (vii) frequency-normalized wavelet $\mathcal{M}_{wf}$, (viii) stationarity $\mathcal{M}_s$, and (ix) wavelet-based bispectrum $\mathcal{M}_b$ metrics. The first seven metrics are adapted from former studies and recast to facilitate the current application, while the last two are introduced as new.

As noted in the previous section, the term "validation metrics" is used by some authors instead of comparison metrics in case of time-histories as well (cf. e.g. [242, 275, 322]). The reason for this is that the comparison is conducted w.r.t. experiments. Moreover, the comparison (or validation) metrics are sometimes related to metrics in terms of statistical distance measures [322]. Herein, such relation is not implied, since some properties of the distance such as identity, symmetry and triangular inequality pose additional constraints that do not have a particular advantage for the present application.

In the following, all of the metrics are defined by their relative exponent and are tailored according to the underlying physics of wind-bridge interaction. When introducing the metrics, the incentives for targeting the particular signal feature are also discussed from a perspective of bridge aerodynamics.

4.3.1 Phase metric

The phase metric accounts for the mean phase discrepancy between two signals. A time-lag between the input wind fluctuations or motion and the output aerodynamic forces is a typical representation of the fluid memory [356]. Various studies have proposed different approaches to evaluate the phase (cf. e.g. [116, 307]). Herein, the phase metric introduced by Sarin et al. [275] is used, as its definition using an exponential function is compliant with the unified manner for comparison metrics adopted in this study. Thus, the relative exponent yields

$$\mathcal{A}_{\varphi} := \frac{t_{\mathrm{lag}}}{T_c}, \tag{4.16}$$

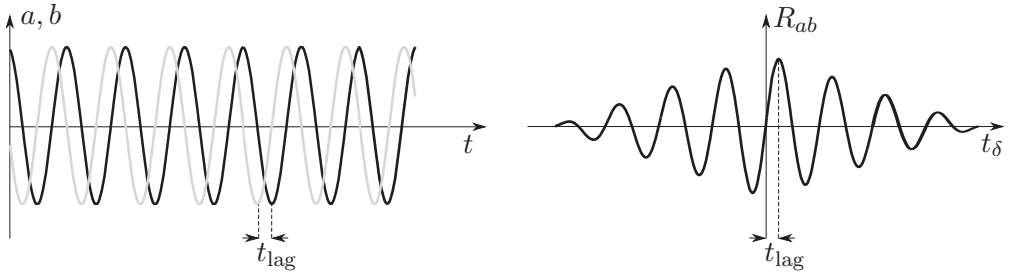

Figure 4.2: Determination of mean time delay between two signals (black $a = a(t)$ and gray $b = b(t)$, left), based on cross-correlation (right).

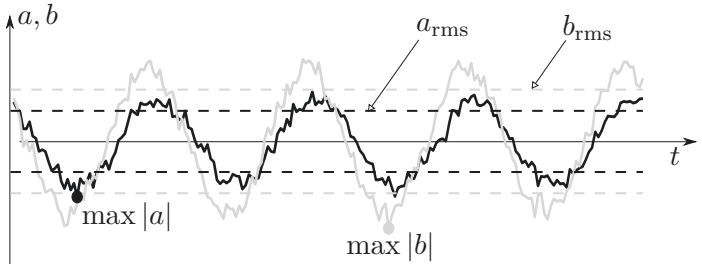

Figure 4.3: Illustration of the global quantities: RMS and absolute peak of two signals (black $a = a(t)$ and gray $b = b(t)$) used for the corresponding metrics.

where mean time delay t_{lag} is obtained from the cross-correlation of the two signals R_{ab} as

$$t_{\text{lag}} = \arg\max_{t_\delta} \langle a(t)b(t+t_\delta)\rangle = \arg\max_{t_\delta} R_{ab}(t_\delta), \tag{4.17}$$

which is schematically depicted in Fig. 4.2. The normalization time T_c is time that is considered to be a significant delay between the signals; hence, it is case-dependent, as discussed later.

Since the cross-correlation is practically sliding the two signals on top of each other, t_{lag} corresponds to the time for which the integral product of both signals is the largest. Hence, the t_{lag} represents a time-shift for which the signals would have the largest similarity in a linear statistical sense, i.e. it represents a mean phase. For signals with different frequency modulations, the phase metric might not carry a sensible meaning.

4.3.2 Peak metric

The peak values of the aeroelastic response are the design criteria for bridges. Thus, how well the aerodynamic models are able to replicate the peak value is of major importance. This is of particular interest for nonlinear aerodynamic models as the peak value may not be directly related to the statistical moments of the forces/response, despite the input wind being Gaussian.

The relative exponent for the peak metric is based on the absolute maximum value of the signals (cf. Fig. 4.3) and is defined as

$$\mathcal{A}_p := \frac{|\max|a| - \max|b||}{\max|a|}. \tag{4.18}$$

4.3.3 Root mean square metric

The utility of the RMS for time-histories is due to its physical interpretation as it is closely related to the signal energy. Moreover, for Gaussian signals with zero mean, the RMS equals the variance, and hence, it is sufficient to compare the PDFs. The relative exponent for the RMS metric is obtained as the relative difference of the RMS of both signals w.r.t. the RMS of the reference signal (cf. Fig. 4.3), yielding

$$\mathcal{A}_{\text{rms}} := \frac{\left|\sqrt{\frac{1}{T}\int_0^T [a(t)]^2\,\mathrm{d}t} - \sqrt{\frac{1}{T}\int_0^T [b(t)]^2\,\mathrm{d}t}\right|}{\sqrt{\frac{1}{T}\int_0^T [a(t)]^2\,\mathrm{d}t}}. \tag{4.19}$$

In many assessment studies of aerodynamic models in bridge aerodynamics, the RMS of the response time-histories has been utilized as a basis for comparison (cf. e.g. [61, 245, 359]). It has been shown to be useful, particularly when comparing linear aerodynamic models in the frequency and time domain for a Gaussian free-stream turbulence [245]. However, for nonlinear models, comparing only the RMS of the aerodynamic forces/response does not provide complete information on the discrepancies for all time-history features.

4.3.4 Magnitude metric

The peak and RMS metrics are based on a global and averaged amplitude discrepancies, respectively. To further study the differences of the magnitude in a time-localized manner, a relative magnitude metric is required. A straightforward way to determine the local amplitude discrepancies would be to compute the RMS deviation of the signals' amplitude and normalize w.r.t. the RMS of the reference signal. In the field of economics, such a comparison coefficient is commonly known as Theil's coefficient of inequality [28]. However, a simple subtraction of two signals might result in large values if the signals are phase-shifted or in the presence of noise, which would unrealistically portrait the situation. In bridge aeroelasticity, such local discrepancies can be a result of vortex shedding and/or interior noise, which entails chaotic aerodynamic phenomena such as wake instability, laminar-turbulence transition, local separation and reattachment (cf. e.g. [362]).

Sarin et al. [275] propose to preprocess the original time-histories utilizing the dynamic time warping algorithm to alleviate some of the local phase-shifts and very high-frequency components. Utilizing the dynamic time warping, the peaks of the signals are aligned in a nonlinear fashion by stretching, but not scaling. Taking this into account, the relative exponent for the magnitude metric yields the following:

$$\mathcal{A}_m := \frac{\sqrt{\frac{1}{N_w}\sum_{j=1}^{N_w}\left(a_{w,j}-b_{w,j}\right)^2}}{\sqrt{\frac{1}{N_w}\sum_{j=1}^{N_w}\left(a_{w,j}\right)^2}}, \tag{4.20}$$

where $a_{w,j}$ and $b_{w,j}$ for $j \in \{1,\ldots,N_w\}$ are the warped versions of the original discretized time-histories a_k and b_k for $k \in \{1,\ldots,N_s\}$, respectively, and N_w is the number of warped steps, which is not necessarily the same with the number of time-steps N_s of the original discretized signals.

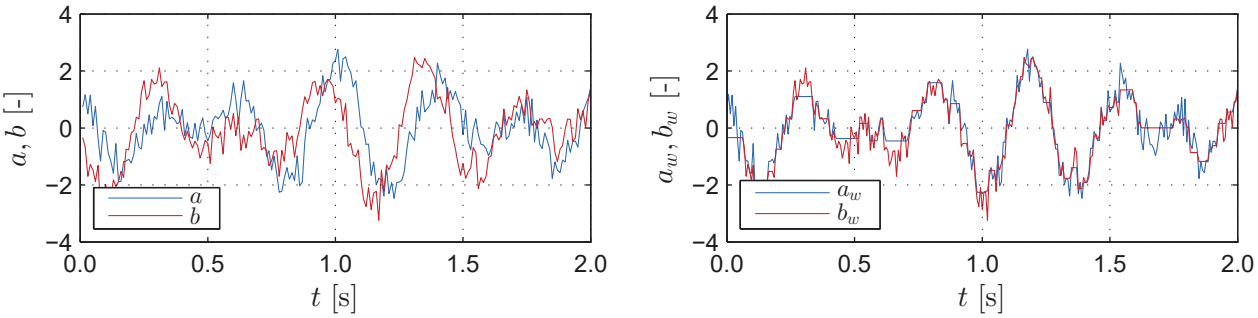

Figure 4.4: Effect of dynamic time warping: example of original (left) and warped (right) time-histories of two harmonic signals with distinct phase-shift and additional Gaussian noise.

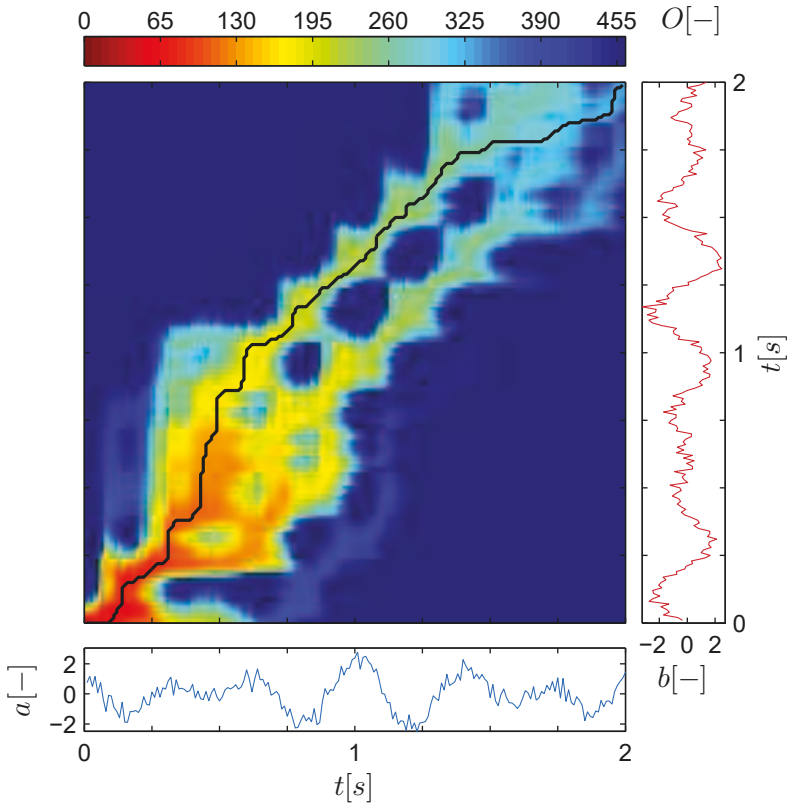

Figure 4.5: Effect of dynamic time warping: accumulated cost matrix O of the dynamic time warping algorithm for two signals in Fig. 4.4, including the optimal warping path (thick black line).

To illustrate the effect of dynamic time warping, consider two biharmonic signals with distinct phase-shift for each harmonic and additional Gaussian noise (cf. Fig. 4.4, left). The dynamic time warping algorithm consists of initially computing an accumulated cost matrix $O_{jk} = \min(O_{j-1,k-1}, O_{j,k-1}, O_{j-1,k}) + d(x_j, y_k)$ for $j, k \in \{1, \ldots, N_s\}$, based on a local distance measure $d(a_j, b_k)$ such as for e.g. Euclidean distance [232]. A sequence of pairs of indices $A_n = [j, k]$ is sought which minimizes a cumulative cost $O_c = \sum_1^{N_w} O[A_n]$. The sequence A_j is the optimal warping path, which is subjected to the following constraints: (i) A_n is monotonically increasing, (ii) A_n progresses one step at a time, (iii) the boundary values are $A_1 = [1, 1]$ and $A_{N_w} = [N_s, N_s]$. The lower the cumulative cost, the more the signals are similar to each other, and visa-versa. For the particular example, the accumulated cost matrix and optimal warping path (the black line) are shown in Fig. 4.5. Based on the ordered pair of indices in A_n, the values of the discrete signals a_j and b_k are correspondingly ordered, resulting in warped signals which can be directly compared w.r.t. the isolated magnitude discrepancies (cf. Fig. 4.4, right). The cumulative cost is an indicator of the amount of shifting of the signals to obtain their warped counterparts. However, this is not taken into account within the magnitude metric as it is assumed that O_c corresponds to the phase and local frequency shifts, which are not of interest for this metric.

4.3.5 Probability density function metric

In regions with large flow separation, the statistical description of the local pressure distribution can differ significantly from a Gaussian, despite Gaussian free-stream turbulence (cf. e.g. [126, 161]). As a result, the higher-order moments of the PDF, such as skewness and kurtosis, can

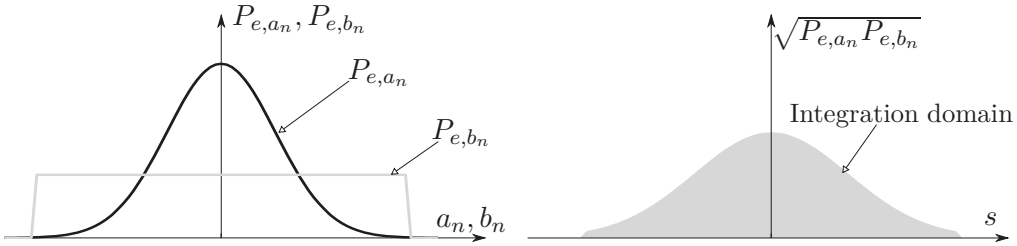

Figure 4.6: PDF metric: estimated PDFs of two normalized (standard score) signals (left); integration area (right).

attain high values. Such non-Gaussian features can occur in the local pressure variation on rooftop cladding [126] as well as the tail of the PDF of the buffeting forces acting on bridge decks. The distortion between the input and output PDF is a property of nonlinear models; hence, it represents an important signal feature to be quantified in bridge aerodynamics and aeroelasticity.

In statistics, two PDFs are compared by utilizing statistical distance measures, commonly referred to as statistical divergence. There are a number of statistical divergences which quantify the discrepancy between the PDFs, such as the Kullback-Leiber divergence, Jensen–Shannon divergence, Hellinger distance (cf. e.g. [250] for a summary). Herein, the Bhattacharyya distance d^B is utilized to formulate the PDF metric as it is commonly used to measure the overlapping degree of PDF [238], and it can be easily related to the formulation in Definition 4.15. Assuming the signals a and b are random variables, the relative exponent of the PDF metric is defined as follows:

$$\mathcal{A}_{\text{pdf}} := d^B(a,b) = -\ln \int_{-\infty}^{\infty} \sqrt{P_{e,a_n}(s) P_{e,b_n}(s)} \mathrm{d}s. \tag{4.21}$$

where P_{e,a_n} and P_{e,b_n} are estimates of the PDFs of the standardized signals (standard score) a_n and b_n, respectively. For $\varepsilon_{\text{PDF}} = 1$, the PDF metric yields

$$\mathcal{M}_{\text{pdf}} = \int_{-\infty}^{\infty} \sqrt{P_{e,a_n}(s) P_{e,b_n}(s)} \mathrm{d}s = BC(a_n, b_n), \tag{4.22}$$

where $BC = BC(a_n, b_n)$ is the Bhattacharyya coefficient which can take values in the range $0 \leq BC \leq 1$, which is in a similar fashion as the constructed comparison metrics. Formulated as such, the PDF metric can be related to Hellinger's distance and Rényi divergence (i.e. relative Rényi entropy) (cf. [238] for details). The integration area in (4.22) for a Gaussian and uniform distribution is schematically depicted in Fig. 4.6.

In (4.21) and (4.22), the standard scores of the signals are used to asses the discrepancies in the third and higher-order standardized moments of the PDF. This is done to avoid redundancy in the metrics to some extent, as the first and second-order moments are included in the RMS metric. The estimated PDFs, P_{e,a_n} and P_{e,b_n}, are obtained by nonparametric kernel density estimation, utilizing the Gaussian kernel and the Improved Sheather-Jones algorithm for bandwidth selection introduced by Botev et al. [34] (including a MATLAB code). Alternatively, the estimated PDFs can be modeled by parametric approaches utilizing for e.g. Hermite polynomials [126].

4.3.6 Wavelet metric

The time-frequency representation can unveil the frequency content at each time-instance of the signal. One of the methods to represent a signal in the time-frequency plane is the continuous wavelet transform. Several studies have utilized the wavelet transform to quantify the discrepancies in the time-frequency plane for the two time-histories (cf. e.g. [152, 180, 322]). Jiang et al. [152] used the wavelet coherence and phase map to discuss the goodness-of-fit between two time-histories, while Teferra et al. [322] constructed a single value metric based on the squared difference of the wavelet coefficients.

The time-frequency plane is of significant importance in bridge aerodynamics and aeroelasticity as it reveals particular features of the aerodynamic forces and response, such as stationary and non-stationary frequency content, aerodynamic coupling, modal contribution, and local "bursts" of signal energy, etc. Hence, the interpretation in the time-frequency plane has been extensively utilized in wind engineering (cf. e.g. [127, 160]).

To obtain the time-frequency representation, the wavelet transform of a signal a is

$$W_a(s_c, t) = \frac{1}{\sqrt{s_c}} \int_{-\infty}^{\infty} a(t_1) \overline{\Psi} \left(\frac{t - t_1}{s_c} \right) \mathrm{d}t_1, \tag{4.23}$$

where $W_a = W_a(s_c, t)$ are the complex wavelet coefficients, s_c is the scale parameter, $\Psi = \Psi(t)$ is the mother wavelet and its conjugate-complex is $\overline{\Psi}$. Herein, the Morlet wavelet, normalized w.r.t. the wavelet energy [150], is utilized and is given as follows:

$$\Psi = \pi^{-1/4} \exp(-i 2\pi f_{ce} t - t^2/2), \tag{4.24}$$

where f_{ce} is the central frequency of the wavelet which is crucial for defining the time and frequency resolution and should be adjusted accordingly [171]. For the Morlet wavelet, the Fourier frequency f is related to the scale parameter as $f = f_{ce}/s_c$. The squared magnitude of the wavelet coefficients (i.e. the scalogram) reveals the frequencies where the energy is concentrated in a time-localized manner. As the interpretation in this work is based on the time-frequency instead of the time-scale representation, the wavelet coefficients are based on the frequency in the following, i.e. $W_a = W_a(f, t)$.

The relative exponent of the wavelet metric is obtained as a normalized RMS deviation of the magnitude of the wavelet coefficients yields

$$\mathcal{A}_w := \frac{\sqrt{\int_0^T \int_0^{\infty} \left[|W_a(f,t)| - |W_b(f,t)| \right]^2 \mathrm{d}f \mathrm{d}t}}{\sqrt{\int_0^T \int_0^{\infty} |W_a(f,t)|^2 \, \mathrm{d}f \mathrm{d}t}}. \tag{4.25}$$

By obtaining the wavelet metric in such a manner, the discrepancies between the two signals in the time-frequency plane are quantified (cf. Fig. 4.7). From a practical aspect, it is important that the properties of the wavelet transform, such as the mother wavelet, central wavelet frequency, and the frequency range, remain the same for both signals. Moreover, for the wavelet-based metrics, the integration of the time-frequency plane should encompass an area which neglects the wavelet end effects [171, 327], commonly referred to as the cone of influence (COI). In case of the Morlet wavelet [327], the COI yields

$$\mathrm{COI} : \left\{ \frac{f_{ce}}{f\sqrt{2}} \leq t \leq T - \frac{f_{ce}}{f\sqrt{2}}. \right. \tag{4.26}$$

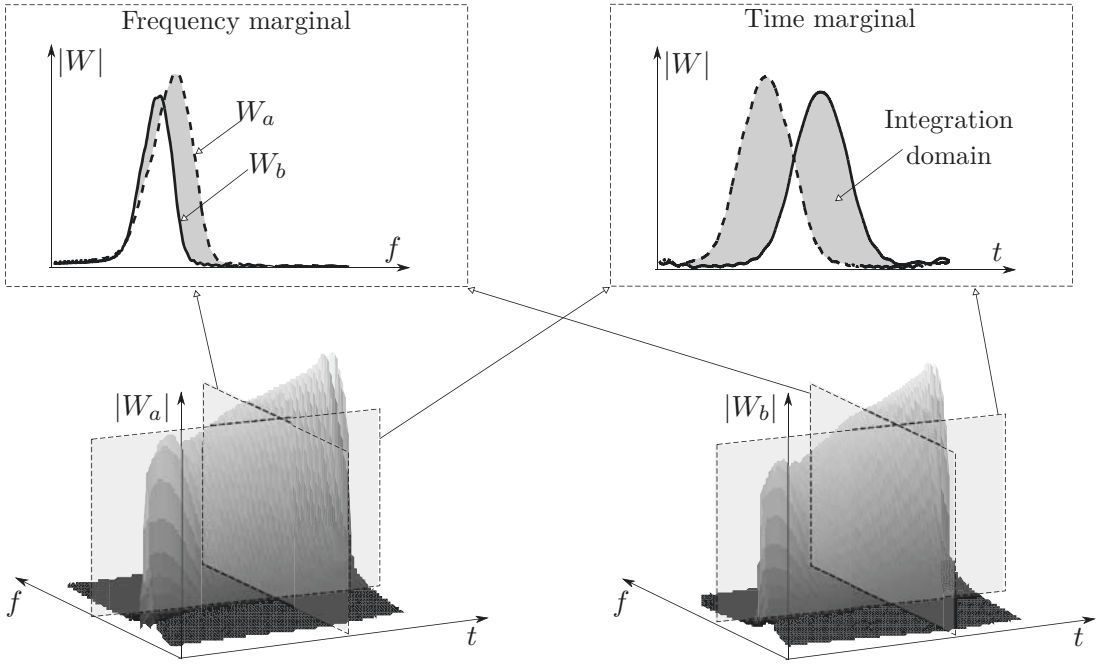

Figure 4.7: Wavelet metric: absolute wavelet coefficient of two signals (bottom) and the corresponding domain of integration shown on the frequency (top-left) and time (top-right) marginals.

4.3.7 Frequency-normalized wavelet metric

The wavelet metric incorporates the total discrepancy in the time-frequency plane. To further study whether this discrepancy is due to the amplitude or frequency difference, the frequency-normalized wavelet metric is introduced by normalizing the instantaneous wavelet amplitude w.r.t. the frequency marginal. The relative exponent for this metric is given as

$$\mathcal{A}_{wf} := \frac{1}{T}\int_0^T \frac{\sqrt{\int_0^\infty \left[\frac{|W_a(f,t)|}{W_{fa}(t)} - \frac{|W_b(f,t)|}{W_{fb}(t)}\right]^2 \mathrm{d}f}}{\sqrt{\int_0^\infty \left[\frac{|W_a(f,t)|}{W_{fa}(t)}\right]^2 \mathrm{d}f}} \mathrm{d}t, \tag{4.27}$$

where the normalization factor, e.g. for signal a, is

$$W_{fa}(t) = \max_f |W_a(t,f)| \,. \tag{4.28}$$

Practically, this metric quantifies the distortion in the shape of the local spectrum, which is of particular interest for aerodynamic models resulting in multiple-frequency output for single-frequency input. A metric normalized w.r.t. the magnitude marginal can be constructed in a similar fashion [180]; however, this metric is not considered herein, since it is deemed to be a redundant addition to the magnitude metric.

4.3.8 Stationarity metric*

To quantify and compare the non-stationary part of the two time-histories is of particular interest for mechanical systems that can exhibit nonlinear or divergent behavior. Despite

having a stationary input, stable nonlinear mechanical models can result in a non-stationary output in terms of amplitude and frequency. Such manifestation in aeroelasticity is related to the amplitude-dependent aerodynamic forces due to strong stationary wind gusts and large oscillations (cf. e.g. [84, 86]). Moreover, the local turbulence effects can lead to a non-stationary hysteresis behavior for a sinusoidal input motion as noted by Zhang et al. [375] in a numerical study (cf. Fig. 4.1). Non-stationary amplitude modulations in the response and forces are also present during flutter or even in terms of frequency modulation during post-flutter limit cycle oscillations, as seen later in the chapter involving applications from bridge aerodynamics.

Herein, to evaluate the discrepancies in non-stationary parts of the time-histories, a stationarity metric is introduced that yields the following relative exponent:

$$\mathcal{A}_s : \begin{cases} \to \infty & \text{if} \quad \Upsilon_s(a) \neq \Upsilon_s(b) \\ = 0 & \text{if} \quad \Upsilon_s(a) = \Upsilon_s(b) = 0, \\ = \dfrac{\sqrt{\int_0^T \int_0^\infty \left[\left| W_a^F(f,t) \right| - \left| W_b^F(f,t) \right| \right]^2 \mathrm{d}f\mathrm{d}t}}{\sqrt{\int_0^T \int_0^\infty \left| W_a^F(f,t) \right|^2 \mathrm{d}f\mathrm{d}t}} & \text{if} \quad \Upsilon_s(a) = \Upsilon_s(b) = 1. \end{cases} \tag{4.29}$$

where Υ_s is a binary indicator of signal non-stationarity, while $W^F = W^F(f,t)$ represents the filtered non-stationary part of the wavelet coefficients. To determine whether the signal is non-stationary and if so, to filter the non-stationary part of the wavelet coefficients, a local and a global method based on surrogates and hypothesis testing are utilized (cf. [32, 221]). In the following, these methods are briefly revisited and combined in a two-step process.

A surrogate of a signal is obtained by manipulating the original time-histories to satisfy the null hypothesis while retaining most of the properties such as the power spectrum or PDF. There are various ways of obtaining suitable surrogates based on the null hypothesis, which were summarized recently by Lanchester et al. [185]. Since the null hypothesis, in this case, is that the signal is stationary, the Fourier-based surrogates have shown to be adequate (cf. [221, 264]). A Fourier-based surrogate of a signal $a = a(t)$ is obtained by randomizing the phase of its Fourier transform $\hat{a} = \hat{a}(f)$ while retaining the modulus at each frequency and then applying the inverse Fourier transform. With this, the surrogate signal $a_{\mathrm{sur}} = a_{\mathrm{sur}}(t)$ is obtained as

$$a_{\mathrm{sur}}(t) = \int_{-\infty}^{\infty} \exp(i2\pi f t) \left| \hat{a}(f) \right| \exp[i\varphi^R(f)] \mathrm{d}f, \tag{4.30}$$

where $\varphi^R = \varphi^R(f)$ is a uniformly distributed random phase as

$$\varphi^R \sim \mathcal{U}[-\pi, \pi). \tag{4.31}$$

It is clear that (4.30) is similar as (3.34) that was utilized for generation of a univariate stationary Gaussian process.

When performing hypothesis testing, a N_{sur} number of surrogates is required yielding the ensemble

$$\left\{ a_{\mathrm{sur},1}(t), a_{\mathrm{sur},2}(t), \ldots, a_{\mathrm{sur},N_{\mathrm{sur}}}(t) \right\}. \tag{4.32}$$

The first step is to determine whether the signal is stationary by comparing it to surrogate data utilizing discriminating statistics, based on the statistical distance between the local and global spectrum. If the discriminating statistic of the original signal $\sigma_{d_a}^2$ falls out of the one-sided

confidence interval of the probability density of the discriminating statistic of the surrogates $\sigma^2_{d_{\text{sur}}}$, the null hypothesis is rejected for the original signal. This is formulated as

$$\Upsilon_s(a) = \begin{cases} 0 & \text{if} \quad \Pr(\sigma^2_{d_{\text{sur}}} \leq \sigma^2_{d_a}) \leq \text{CL}; \ \text{"stationary"}, \\ 1 & \text{if} \quad \Pr(\sigma^2_{d_{\text{sur}}} \leq \sigma^2_{d_a}) > \text{CL}; \ \text{"non-stationary"}, \end{cases} \tag{4.33}$$

where CL corresponds to the confidence level. The discriminatory statistic $\sigma_{d_{\text{sur}}}$ is, in fact, a random variable for which an estimated parametric PDF is obtained, such as the Gaussian or Gamma density, for an ensemble of surrogates in (4.32). For a single time-history, the discriminatory statistic is obtained based on the divergence $d = d(t)$ between the local and global wavelet-based spectrum as follows:

$$\sigma^2_d = \text{Var}\left[d(t)\right]. \tag{4.34}$$

A combination of the Kullback-Leiber divergence and log-spectral deviation is utilized herein for the distance since it has shown to be adequate for both cases of amplitude and frequency modulation (cf. [32] for discussion). For the signal a, this distance is

$$d_a^{\text{LSD+KL}}(t) = \left\{ \int_0^\infty \left[W^2_{a,n}(f,t) - S^W_{a,n}(f) \right] \log \frac{W^2_{a,n}(f,t)}{S^W_{a,n}(f)} \mathrm{d}f \right\} \left\{ 1 + \int_0^\infty \left| \log \frac{W^2_a(f,t)}{S^W_a(f)} \right| \mathrm{d}f \right\}, \tag{4.35}$$

where the $W^2_a = W^2_a(f,t)$ and $S^W_a = S^W_a(f)$ are the scalogram (i.e. local spectrum) and wavelet-based spectrum (i.e. global spectrum), respectively, while $W^2_{a,n} = W^2_{a,n}(f,t)$ and $S^W_{a,n} = S^W_{a,n}(f)$ are their normalized versions, respectively. The wavelet-based spectrum is obtained as

$$S^W_a(f) = \frac{1}{T} \int_0^T W^2_a(f,t) \mathrm{d}t, \tag{4.36}$$

In the second step, if a signal is determined to be non-stationary (cf. (4.33)), the non-stationary part of the wavelet coefficients $W^F_a = W^F_a(f,t)$ is filtered using a threshold scalogram based on stationary surrogates (cf. [221]). This yields the following:

$$W^F_a(f,t) = \begin{cases} 0 & \text{if} \quad W^2_a(f,t) \leq \max\limits_t W^2_{\text{a,tr}}(f,t), \\ W_a(f,t) & \text{if} \quad W^2_a(f,t) > \max\limits_t W^2_{\text{a,tr}}(f,t), \end{cases} \tag{4.37}$$

where $W^2_{a,tr} = W^2_{a,tr}(f,t)$ is a threshold scalogram. Herein, the maximum of the threshold scalogram is considered w.r.t. the time marginal instead of a localized value as by McCullough and Kareem [221]. The reason for this is that the threshold peak can occur at any time, under the stationarity assumption. Assuming normality of the scalogram, the threshold is obtained based on the surrogate scalograms as

$$W^2_{\text{a,tr}} = \left\langle W^2_{\text{sur}} \right\rangle + g^*_s \sqrt{\frac{\sum\limits_{j=1}^{N_{\text{sur}}} \left(W^2_{\text{sur},j} - \left\langle W^2_{sur} \right\rangle \right)^2}{N_{\text{sur}} - 1}} \tag{4.38}$$

where g^*_s is a factor depending on the probability of exceeding the threshold and W^2_{sur} is the scalogram of the surrogates, which represents an ensemble for (4.32).

It should be noted that it can be determined whether the signal is stationary only with the local method in (4.37); hence, the global method in the first step (cf. (4.33)) can be considered

redundant. However, the computation of the standard deviation of the surrogate scalograms in (4.38) requires either retaining all surrogate scalograms in computer memory or their re-computation once $\langle W_{sur}^2 \rangle$ is determined. Hence, utilizing the two-step process can help to reduce computational memory when obtaining $\mathcal{M}_s$ for stationary signals. Moreover, to filter the complete stationary part of the signal for finely discretized time marginal, a large number of surrogates is required. Otherwise, local spurious peaks may be still present in the filtered scalogram, which would result in a sensitive stationarity metric. As shown in the fundamental application, detecting stationarity with a global binary test followed by a local quantification of the non-stationary parts alleviates this problem for a reasonable number of surrogates.

4.3.9 Bispectrum metric*

The higher-order spectrum has been proven to be a useful tool to detect nonlinearities in mechanical systems [103, 150], plasma physics [174], neuronal networks [202], and intermittent effects of turbulence [333]. From a bridge aerodynamics perspective, a single harmonic motion with large amplitudes can result in a force with multiple harmonics as a result of a nonlinear relationship between input-output [86, 139, 204]. To detect and quantify the nonlinearities up to the second-order in the aerodynamic forces, Wu and Kareem [358] utilized the Fourier-based bispectrum. Herein, the wavelet-based bispectrum is used to formulate the bispectrum metric and quantify the discrepancies in the second-order nonlinearities between the two time-histories. The main advantage of utilizing the wavelet-based instead of the Fourier-based bispectrum is that it can detect intermittent nonlinearities and the statistical error is reduced, as discussed by Jamsek et al. [150].

Analogous to the Fourier bispectrum, van Milligen et al. [333] introduced the wavelet bispectrum. For a signal a, the wavelet bispectrum $B_{Wa} = B_{Wa}(f_1, f_2)$ is obtained from the wavelet coefficients (cf. (4.23)) as

$$B_{Wa}(f_1, f_2) = \int_{T_B} W_a(f_1, t) W_a(f_2, t) \overline{W_a}(f_3, t) \mathrm{d}t, \tag{4.39}$$

where $f_3 = f_1 + f_2$ and T_B is the integration time interval of interest. Since the wavelet bispectrum is a complex quantity, it can be expressed in terms of amplitude $G_B = G_B(f_1, f_2)$ and biphase $\varphi_B = \varphi_B(f_1, f_2)$, yielding

$$B_{Wa} = G_{Ba} \exp(i\varphi_{Ba}). \tag{4.40}$$

The instantaneous biphase can be obtained from (4.39) and (4.40) as

$$\varphi_{Ba}(f_1, f_2, t) = \varphi_{Wa}(f_1, t) + \varphi_{Wa}(f_2, t) - \varphi_{Wa}(f_3, t), \tag{4.41}$$

where $\varphi_W = \varphi_W(f, t)$ is the phase for the wavelet coefficients in (4.23).

The bispectrum in (4.39) can indicate whether there is nonlinear interactions (i.e. quadratic phase coupling) between the f_1 and f_2 harmonics, yielding non-trivial values of the bispectrum magnitude at the $f_2 - f_1$ and $f_2 + f_1$ frequency couples. In addition to non-trivial magnitude, the condition $\varphi_{Ba} = 0$ for the biphase in (4.41) is necessary to be satisfied at these frequency pairs for quadratic phase coupling to occur [102]. lf this condition is not satisfied, the normalized bispectrum, i.e. bicoherence (Fourier- or wavelet-based), can yield in non-trivial value despite the absence of nonlinearities in the signal. This is particularly true for synthetically generated signals with a constant phase, such as broadband forces/response, for which the bispectrum

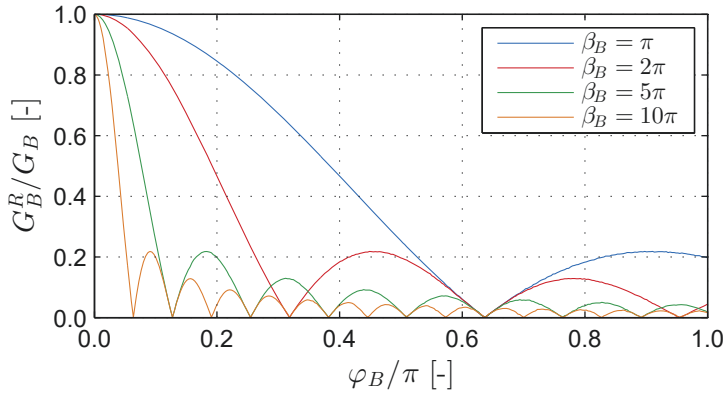

Figure 4.8: Wavelet-based bispectrum phase randomization: effect of the randomization factor β_B on the bispectrum amplitude for false the detection of quadratic-phase coupling ($\varphi_B \neq 0$) .

can have multiple peaks corresponding to the discrete frequencies or natural signal frequencies. Therefore, further adjustment of the bispectrum is required to detect the quadratic nonlinearity.

Herein, a slightly modified quadratic-phase coupling detector is utilized, based on the phase-randomized bispectrum introduced by Kim and Powers [173] for the Fourier-based and by Li et al. [202] and Scully et al. [292] for the wavelet-based bispectrum. The phase-randomized bispectrum $B_{Wa}^R = B_{Wa}^R(f_1, f_2)$ is obtained as follows

$$B_{Wa}^R(f_1, f_2) = \int_{T_B} G_{Ba}(f_1, f_2, t) \exp\left[i\varphi_B^R(f_1, f_2, t)\varphi_{Ba}(f_1, f_2, t)\right] \mathrm{d}t, \tag{4.42}$$

where

$$\varphi_B^R = \varphi_B^R(f_1, f_2, t) \sim \mathcal{U}[-\beta_B, \beta_B) \tag{4.43}$$

is the uniform random biphase for β_B being the randomization factor. From (4.42), it can be deduced that if $\varphi_B = 0$, the exponential term amounts to 1, while, if $\varphi_B \neq 0$, the random value φ_B^R can considerably reduce the bispectrum. This reduction depends on the randomization factor β_B. In previous studies (cf. e.g. [292]) this factor is taken as $\beta_B = \pi$; however, this does not offer insight into how the phase-randomized bispectrum behaves. Considering a bispectrum amplitude G_B and biphase φ_B that are constant in time, and are not necessarily zero, the influence of the β_B factor on the resultant phase-randomized bispectrum amplitude G_B^R is shown in Fig. 4.8. It can be seen that the larger β_B factor is, the faster G_B^R attenuates towards zero for biphase angles deviating from zero. Moreover, there is a "ripple" effect after G_B^R reaches zero. Theoretically, there should be no deviation of the biphase φ_B from zero in case of quadratic phase coupling; however, noise can affect the bispectrum [99] and thus, the angle φ_B can take small values. Although it would be the most appropriate to select the β_B factor based on the level of noise, in this study this factor is selected as $\beta_B = 10\pi$. This corresponds to an angle of $\varphi_B = 2\pi/\beta_B = 0.2$ rad, for which it is assumed that quadratic phase coupling is present, i.e. when G_B^R first intercepts the x axis (cf. Fig. 4.8).

The phase-randomized bispectrum is still affected by noise and, additionally, due to the ripple effect of the biphase randomization. In addition a zero biphase, i.e. $\varphi_B = 0$, the amplitude of G_B^R should be also significant to indicate that the quadratic phase coupling between two harmonics is not due to noise [102]. In order to obtain a statistically significant estimation of the B_w^R, a surrogate method can be employed. The generation of surrogates can be conducted in a similar fashion as for the stationarity metric, by manipulating the original signal properties. For the wavelet bispectrum, Fourier-based surrogates cannot be utilized as stationarity is

not assumed; thus, more advanced surrogates should be utilized such as the wavelet iterative amplitude adjusted Fourier transform surrogates (cf. e.g. [185]). However, these surrogates are computationally very demanding; therefore, the surrogate bispectrum map is obtained simply by destroying the biphase information in the original bispectrum directly [292]. This can be done by simply including a surrogate random biphase in (4.42) as

$$B^R_{W\mathrm{sur}}(f_1,f_2)=\int_{T_B} G_{Ba}(f_1,f_2,\tau)\exp\left[i\varphi^R_B(f_1,f_2,t)\varphi^R_{B,\mathrm{sur}}(f_1,f_2)\right]\mathrm{d}t, \tag{4.44}$$

where

$$\varphi^R_{B,\mathrm{sur}}=\varphi^R_{B,\mathrm{sur}}(f_1,f_2)\sim\mathcal{U}[-\pi:-\beta_{\mathrm{sur}},\beta_{\mathrm{sur}}:\pi) \tag{4.45}$$

is the random surrogate biphase for $0<\beta_{\mathrm{sur}}<\pi$. Again, a N_{sur} number of surrogates is required to test a null hypothesis, yielding the ensemble

$$\left\{B^R_{W\mathrm{sur},1},B^R_{W\mathrm{sur},2},\ldots,B^R_{W\mathrm{sur},N_{\mathrm{sur}}}\right\}. \tag{4.46}$$

The null hypothesis for the surrogate bispectrum amplitude map is that the signal does not exhibit quadratic phase coupling. Hence, the biphase $\varphi^R_{B,\mathrm{sur}}$ should not amount to zero. This is controlled by the random factor β_{sur}. Li et al. [202] obtain the surrogate random biphase $\varphi^R_{B,\mathrm{sur}}$ by adding to the initial biphase φ_{Ba} a time-varying random phase within the $[\pi,\pi)$ interval. In this study, $\varphi^R_{B,\mathrm{sur}}$ is taken to be constant as it is a more critical case for which the bispectrum can result in false detection of nonlinearities. This creates a bispectrum surrogate map which is based on the original phase-randomized bispectrum B^R_W and additionally ensuring that the biphase φ_{Ba} does not amount to zero by the factor β_{sur}. Since the factor β_B assures quadratic phase coupling, the factor β_{sur} should complement in a way; hence, it is obtained as $\beta_{\mathrm{sur}}=2\pi/\beta_B$. In this manner, the wavelet bispectrum is filtered for non-zero biphase and insignificant amplitude, corresponding to the ripples (cf. Fig. 4.8).

Similarly as for the stationarity metric and again assuming normality, the threshold bispectrum amplitude map $G^R_{Ba,\mathrm{tr}}=G^R_{Ba,\mathrm{tr}}(f_1,f_2)$ yields

$$G^R_{Ba,\mathrm{tr}}=\left\langle G^R_{B\mathrm{sur}}\right\rangle+g^*_b\sqrt{\frac{\sum_{j=1}^{N_{\mathrm{sur}}}\left(G^R_{B\mathrm{sur},j}-\left\langle G^R_{B\mathrm{sur}}\right\rangle\right)^2}{N_{\mathrm{sur}}-1}}, \tag{4.47}$$

where g^*_b is a factor depending on the probability of exceeding the threshold.

The filtered phase-randomized bispectrum amplitude $G^F_{Wa}=G^F_{Wa}(f_1,f_2)$ can be obtained from the phase-randomized bispectrum amplitude as

$$G^F_{Ba}(f_1,f_2)=\begin{cases}0 & \text{if}\quad G^R_{Ba}(f_1,f_2)\le\max G^R_{Ba,\mathrm{tr}}(f_1,f_2),\\ G^R_{Ba}(f_1,f_2) & \text{if}\quad G^R_{Ba}(f_1,f_2)>\max G^R_{Ba,\mathrm{tr}}(f_1,f_2).\end{cases} \tag{4.48}$$

Although the noise level is frequency-dependent [333], the maximum value of $G^R_{Ba,\mathrm{tr}}$ is taken for filtering as a threshold, since spurious peaks could remain for finely discretized frequencies. This would result in a very sensitive bispectrum metric. Moreover, the bispectrum for signals without quadratic phase coupling should be zero anyway. Alternatively, the values at each individual frequency pair can be taken; however, this requires a larger number of surrogates,

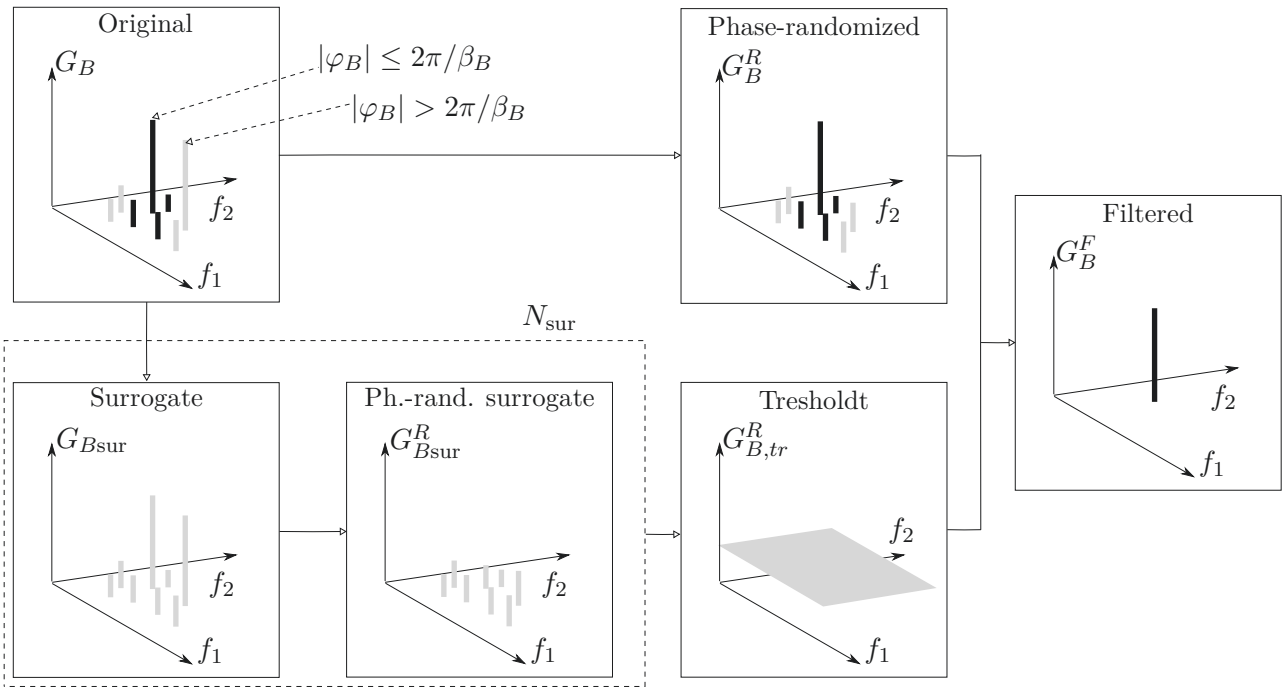

Figure 4.9: Detection of quadratic-phase coupling in signals using phase randomization and surrogates: from original bispectrum amplitude G_B, containing false and true frequency couples, to filtered G_B^F, containing only true frequency couples.

which is of high computational cost. The explained process for detection of quadratic-phase coupling is illustrated in Fig. 4.9.

Finally, the relative exponent for the wavelet-based bispectrum metric is defined as

$$\mathcal{A}_b : \begin{cases} \to \infty & \text{if} \quad \Upsilon_b(a) \neq \Upsilon_b(b), \\ = 0 & \text{if} \quad \Upsilon_b(a) = \Upsilon_b(b) = 0, \\ = \dfrac{\sqrt{\int_0^\infty \int_0^\infty \left[G_{Ba}^F(f_1,f_2) - G_{Bb}^F(f_1,f_2)\right]^2 \mathrm{d}f_1 \mathrm{d}f_2}}{\sqrt{\int_0^\infty \int_0^\infty \left[G_{Ba}^F(f_1,f_2)\right]^2 \mathrm{d}f_1 \mathrm{d}f_2}} & \text{if} \quad \Upsilon_b(a) = \Upsilon_b(b) = 1, \end{cases} \tag{4.49}$$

where Υ_b is binary and it indicates whether there is a quadratic phase coupling in a signal as

$$\Upsilon_b(a) = \begin{cases} 0 & \text{if} \quad \max G_{Ba}^F(f_1,f_2) = 0; \ \text{"linear"}, \\ 1 & \text{if} \quad \max G_{Ba}^F(f_1,f_2) > 0; \ \text{"nonlinear"}. \end{cases} \tag{4.50}$$

From (4.49), it can be gathered that the bispectrum metric quantifies the discrepancies in the nonlinear portion of the two time-histories, should both contain quadratic phase coupling. In practice, the integration in (4.49) is only about the part of the bispectrum that is encompassed by the inner triangle (IT), to avoid the redundant part of the bispectrum. Depending on the sampling frequency f_s, the region of the IT [103] is defined as follows:

$$\text{IT} : \begin{cases} f_2 \leq f_1 & \text{for} \quad 0 \leq f_1 \leq \dfrac{f_s}{2}, \\ f_2 \leq \dfrac{f_s}{2} - f_1 & \text{for} \quad \dfrac{f_s}{4} \leq f_1 \leq \dfrac{f_s}{2}. \end{cases} \tag{4.51}$$

4.4 Summary

In summary, a methodology for comparison of aerodynamic models was introduced in this chapter. The methodology is constituted of two parts. The first part entails a categorical modeling approach to evaluate the complexity of the models based on their aerodynamic assumptions in a qualitative manner. The second part includes comparison metrics for time-histories that can quantify the effect of aerodynamic model assumptions on a SRQ for complexity-related aerodynamic models in the time domain for identical input wind time-histories.

Initially, the categorical modeling approach was briefly revisited and extended in terms of defining comparison metrics, model comparability and completeness. Utilizing the advantages offered by this approach, complexity relations for the aerodynamic models presented in the previous chapter were formalized. The outcome is a clear and organized diagram which distinguishes which model is more complex, and hence, better, based on its mathematical construction. This diagram represents a fundamental basis of the presented methodology for model comparison and quantification of the effect of model assumptions on a selected SQR. Moreover, model completeness of the aerodynamic models w.r.t. the classical flutter phenomenon has been defined, resulting in a subcategory of models. Such a clear structure narrowed a set of aerodynamic models from a category which accounts for multiple aerodynamic phenomena.

As a subsequent step, a set of comparison metrics for time-histories was presented to quantify the discrepancies of particular signal features. All of the metrics were constructed in a unified manner, tailored for comparative studies of time-domain aerodynamic models. Nine metrics were considered, including seven adapted from previous studies based on the phase, peak, RMS, magnitude, PDF, wavelet, frequency-normalized wavelet; and two newly introduced, based on the stationarity and bispectrum. With this set of metrics, the difference in a time-dependent SRQ for two complexity-related aerodynamic models can be quantified in a judicious manner.

In the next two chapters, the methodology for comparison of aerodynamic models is applied in a quantitative manner, first to fundamental applications and then to real-world problems from bridge aerodynamics. Since the diagram of mathematical models already provides a qualitative sense of model quality for the aerodynamic models, it will be mostly used to identify the aerodynamic assumptions and provide information on model comparability, i.e. whether two models can be compared or not. Thus, the practical application of the methodology is more related to the comparison metrics as they supply a result of a quantitative character.

Chapter 5

Fundamental Applications

5.1 Introduction

Before using the introduced framework for practical applications from the field of bridge aerodynamics, individual parts of the framework are applied to fundamental problems in this chapter. The motivation is to verify and study their behavior for problems with simple or analytical solutions. Initially, the performance of the comparison metrics for time-histories is studied for generic signals in Sec. 5.2. By modifying particular signal property, the sensitivity of the comparison metrics is observed to develop a general conception of their response.

Section 5.3 presents a verification of the free-stream turbulence for both deterministic and random gusts. In the case of random free-stream, specific SRQs such as the velocity field, turbulence intensity, length scales, spectra, and PDFs are compared against their prescribed values. Moreover, it is ensured that span-wise coherence and correlation are maintained for the presented turbulent Pseudo-3D VPM. This is of major importance for the Pseudo-3D buffeting analysis conducted in the next chapter for a long-span bridge. In the case of the deterministic free-stream, the gust quality is assessed including the predictive capabilities of the derived closed-form solution that relates the target gust amplitudes and inflow circulation. Parametric studies are performed for both deterministic and random free-stream turbulence to provide guidelines for the choice of numerical and physical parameters.

Finally, a complete analysis of a flat plate is conducted in Sec. 5.4, which includes verification of the aerodynamic coefficients and aeroelastic response against their analytical counterpart. The aerodynamic coefficients that are of interest are the static wind coefficients, flutter derivatives and aerodynamic admittance for both random and deterministic free-stream. For the latter case of the aerodynamic admittance, the complete complex form is obtained, which was not previously possible for the random free-stream. The aeroelastic response from buffeting and flutter analyses is compared to the response for the analytical flat plate model in both frequency and time domain. Constructed as such, this study represents the first complete verification of the VPM for buffeting analyses.

To ensure reproducibility of the results, the choice of the numerical parameters is as explicit as possible, although, in some instances, tedious.

5.2 Comparison metrics: Generic signals

As a part of the first fundamental application, the comparison metrics for time-histories presented in Sec. 4.3 are applied to for four generic signals, $a_j = a_j(t)$ for $j \in \{1, \ldots, 4\}$. The goal is to study their behavior w.r.t. a reference signal $a_r = a_r(t)$ by modification of certain signal features.

The reference signal is given as follows

$$a_r = A_1 \cos(\omega_1 t) + A_2 \cos\left(\omega_2 t + \frac{\pi}{3}\right) + \varrho_r. \tag{5.1}$$

The generic signals are labeled corresponding to the particular signal feature that is being modified, yielding the following four signals:

- Signal 1 - Phase shift

$$a_1 = A_1 \cos(\omega_1 t + \varphi_1) + A_2 \cos\left(\omega_2 t + \frac{\pi}{3} + \varphi_2\right) + \varrho_1; \tag{5.2}$$

- Signal 2 - Amplitude scaling

$$a_2 = 2A_1 \cos(\omega_1 t) + 2A_2 \cos\left(\omega_2 t + \frac{\pi}{3}\right) + \varrho_2; \tag{5.3}$$

- Signal 3 - Frequency modulation

$$a_3 = A_1 \cos(\omega_1 t) + A_2 \cos\left(\omega_2 t + A_3 t^2 + \frac{\pi}{3}\right) \exp(-\xi_1 t) + \varrho_3; \tag{5.4}$$

- Signal 4 - Nonlinearity

$$a_4 = A_1 \cos(\omega_1 t) + A_2 \cos\left(\omega_2 t + \frac{\pi}{3}\right) + \frac{A_1 + A_2}{2} \cos(\omega_1 t) \cos(\omega_2 t + \varphi_3) \exp(-\xi_2 t) + \varrho_4. \tag{5.5}$$

Initially, the following parameters are considered: $A_1 = 1$, $A_2 = 1.3$, $\omega_1 = 2 \times 2\pi$, $\omega_1 = 2.8 \times 2\pi$, $\varphi_1 = \pi$, $\varphi_2 = \pi/6$, $A_3 = (\omega_3 - \omega_2)/T$, $\omega_3 = 3.6 \times 2\pi$, $\varphi_3 = \pi/3$, $\xi_1 = \xi_2 = 0$, $T = 100$ s is the signal length with a sampling frequency f_s=100 Hz, and $\varrho = \varrho(t)$ is a white noise with a zero mean and signal-to-noise ratio amounting to 10.

The parameters for computation of the comparison metrics are given in Tab. 5.1. For the local stationarity analysis, selecting two hundred surrogates has shown to be sufficient (cf. [32]). A

Metric parameter		Value
Normalization time:	T_c	$2\pi/\omega_2$
Central wavelet frequency:	f_{ce}	$3\omega_1/(2\pi)$
Confidence level:	CL	95 %
Surrogates - Stationarity:	N_{sur}	200
Exceedance - Stationarity:	g_s^*	2
Surrogates - Nonlinearity:	N_{sur}	100
Exceedance - Nonlinearity:	g_b^*	2

Table 5.1: Comparison metrics for generic signals: metric parameters.

hundred surrogates is commonly appropriate for the threshold bispectrum map (cf. [292]). The normalization T_c time is case-dependent and should be related to the main harmonics of the signal. For the chosen generic signals, it is prescribed to correspond to the second harmonic. The resulting comparison metrics are given in Fig. 5.1, while in Fig. 5.2, the normalized wavelet coefficients are depicted for all the signals except for the phase shift signal a_1, since they are similar as for the reference one a_r. The following discussion for each signal is based on these two figures.

Signal 1 - Phase shift

The first signal is constructed to study the effect of phase shift since a time lag is a common manifestation of the fluid memory in the unsteady aerodynamic models. As expected, the phase metric $\mathcal{M}_{\varphi}^{a_r,a_1}$ results in a low (cf. Fig. 5.1, top-left). Moreover, the magnitude metric obtained using the warped signals results in a value of $\mathcal{M}_{m}^{a_r,a_1} = 0.88$. For comparison, this metric amounts to a value of 0.27 for unwarped signals, which is unrealistic as the signals are only phase-shifted (the original and warped signals for this particular case are also shown in Fig. 4.4 from Sec. 4.3.4). Due to the added noise, the wavelet metrics amount to $\mathcal{M}_{w}^{a_r,a_1} = \mathcal{M}_{wf}^{a_r,a_1} = 0.96$, which is slightly less than 1. The reference a_r and the phase shift signal a_1 are similar considering the features accounted in the remaining comparison metrics.

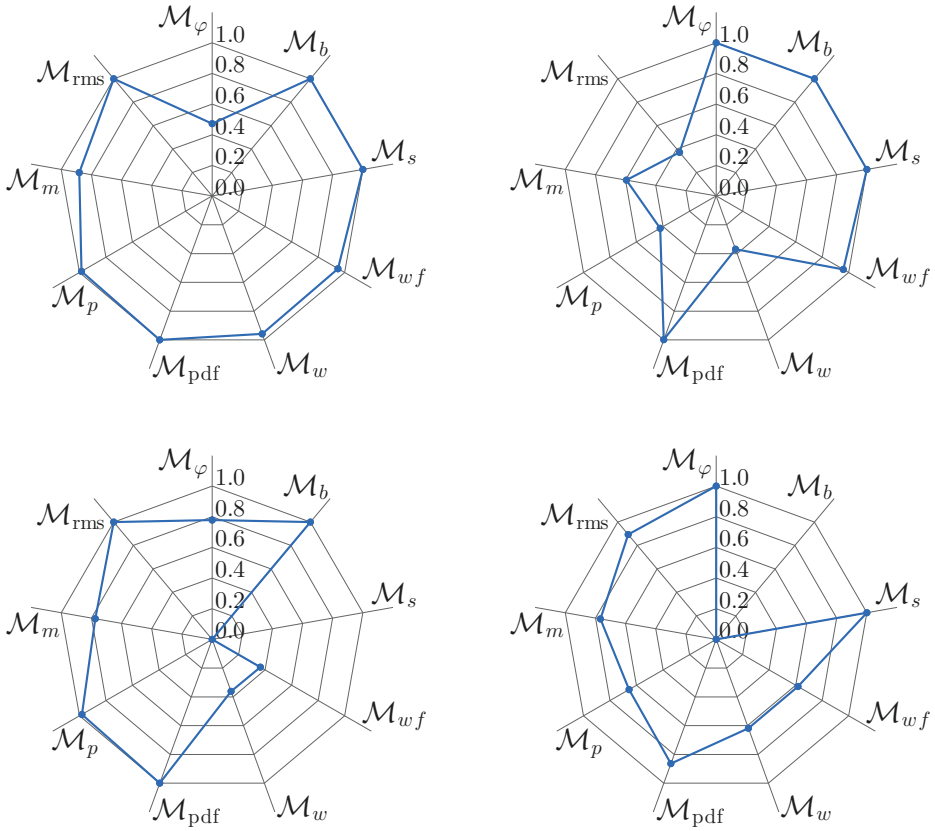

Figure 5.1: Comparison metrics for generic signals w.r.t. a reference signal: phase shift $\mathcal{M}^{a_r,a_1}$ (top-left); amplitude scaling $\mathcal{M}^{a_r,a_2}$ (top-right); frequency modulation $\mathcal{M}^{a_r,a_3}$ (bottom-left); and non-linearity $\mathcal{M}^{a_r,a_4}$ (bottom-right).

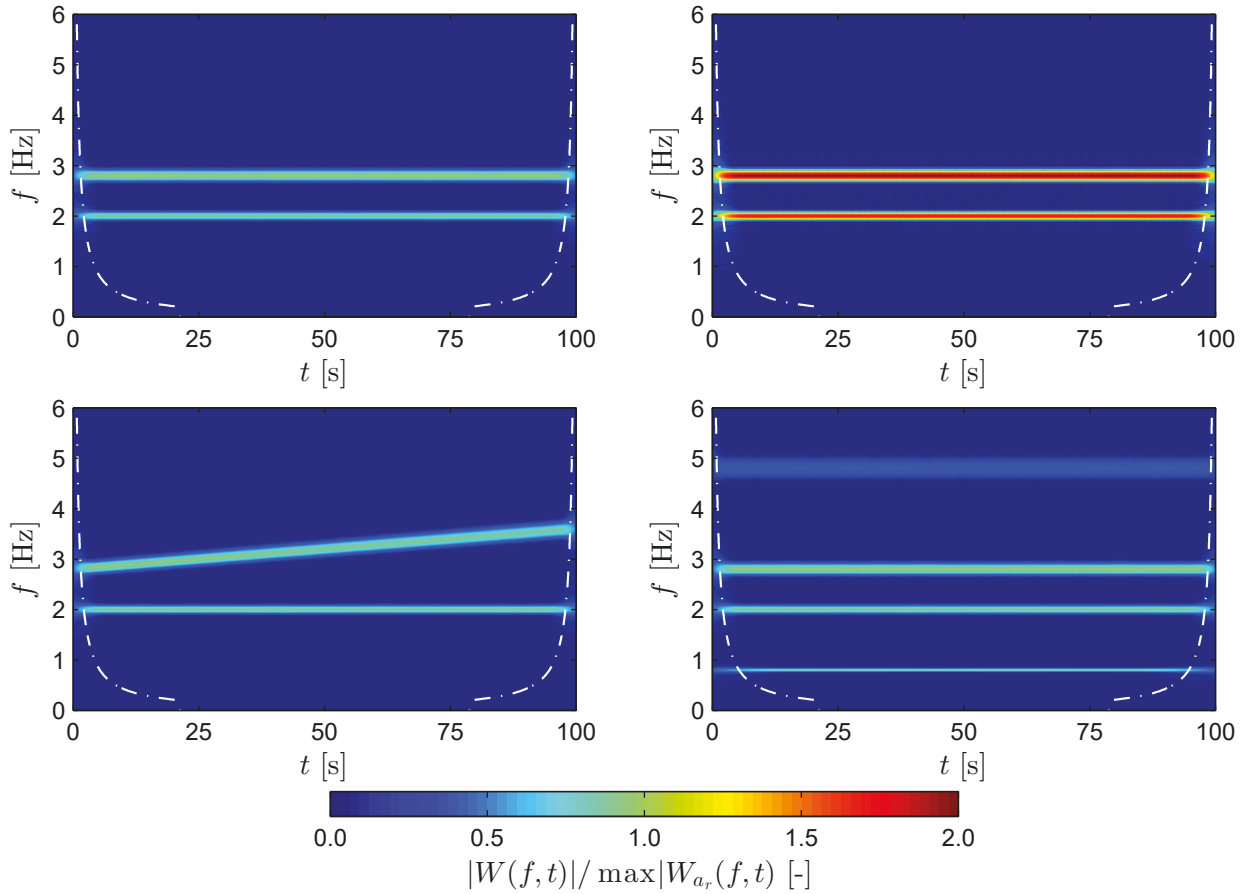

Figure 5.2: Comparison metrics for generic signals: normalized wavelet amplitude $|W(f,t)|$ for the reference W_{a_r} (top-left); amplitude scaling W_{a_2} (top-right); frequency modulation W_{a_3} (bottom-left); nonlinearity W_{a_4} (bottom-right). The dashed-dot line indicates the cone of influence COI.

Signal 2 - Amplitude scaling

Comparing the second signal to the reference, the behavior of the comparison metrics due to amplitude discrepancy is analyzed. The signal amplitude of a_2 is two times larger than the amplitude for a_r. Increasing the amplitude in such way, affects the RMS $\mathcal{M}_{\text{rms}}^{a_r,a_2}$, magnitude $\mathcal{M}_m^{a_r,a_2}$, peak $\mathcal{M}_p^{a_r,a_2}$, and wavelet metric $\mathcal{M}_{\text{w}}$ (cf. Fig. 5.1, top-right). With exception of the magnitude metric, the rest of the metrics amount to $\mathcal{M}_{\text{rms}}^{a_r,a_2} \cong \mathcal{M}_{\text{p}}^{a_r,a_2} \cong \mathcal{M}_{\text{w}}^{a_r,a_2} \cong 0.4$, which is logical as a discrepancy of 100 % yields $\exp(-1) \cong 0.37$. The magnitude metric resulted in a higher value due to the warping of the signal using the dynamic time warping algorithm. Another particularity is that the value of the frequency normalized wavelet metric is $\mathcal{M}_{wf}^{a_r,a_2} \cong 1$. This is due to the fact that both signals have the same relative frequency content, as it can be seen from the absolute value of the wavelet coefficients in Fig. 5.2. As anticipated, no discrepancies are detected by the phase, PDF, stationarity and bispectrum metrics, i.e. $\mathcal{M}_{\varphi}^{a_r,a_2} = \mathcal{M}_{\text{pdf}}^{a_r,a_2} = \mathcal{M}_s^{a_r,a_2} = \mathcal{M}_b^{a_r,a_2} = 1$.

Signal 3 - Frequency modulation

The third signal is devised to investigate the effect of frequency modulation. Practically, the signal x_3 contains a linear chirp, which can also be observed in the wavelet coefficients (cf. Fig. 5.2). Since the stationarity null hypothesis (cf. (4.33)) is accepted for a_r and rejected for a_3, the stationarity metric amounts to $\mathcal{M}_s^{x_r,x_3} = 0$. The magnitude $\mathcal{M}_m^{a_r,a_3}$ and wavelet-based

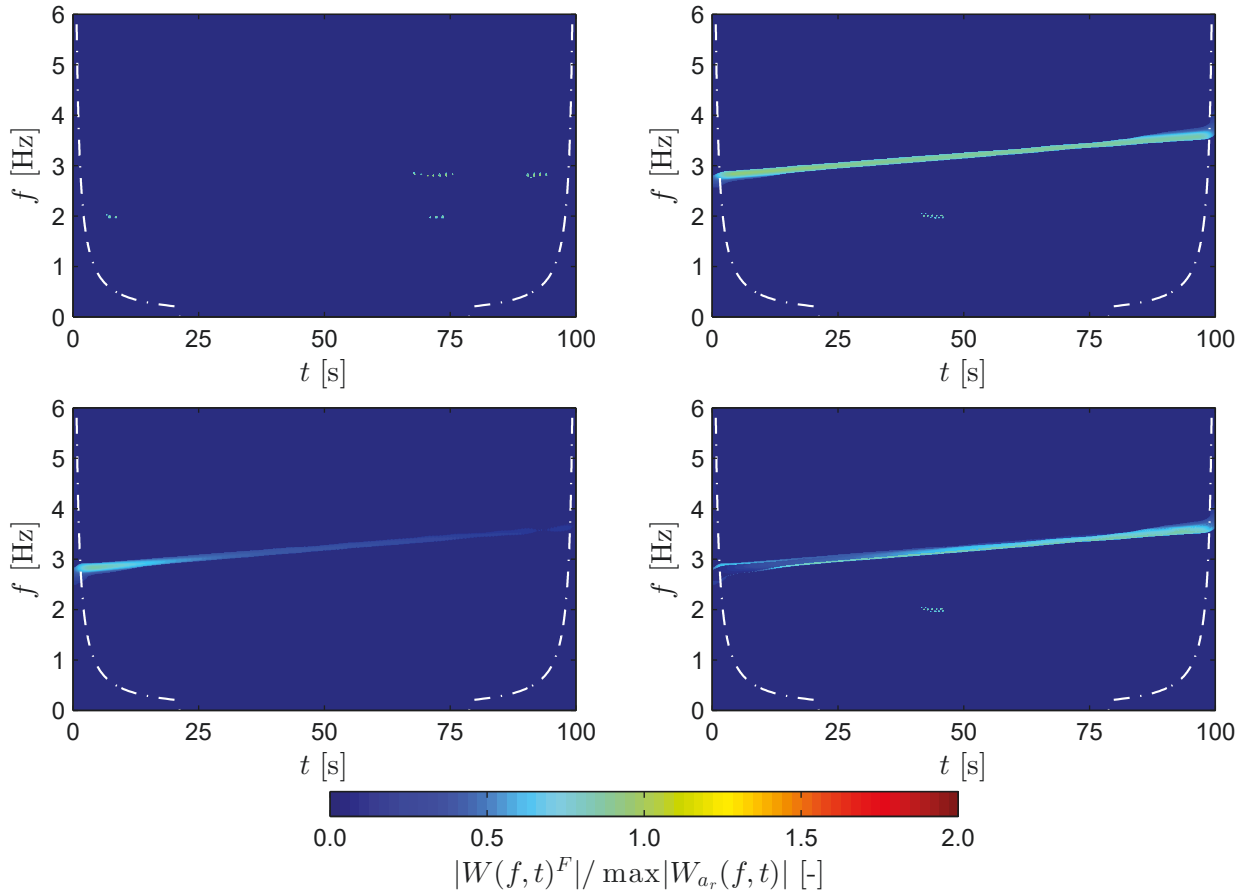

Figure 5.3: Comparison metrics for generic signals: filtered non-stationary wavelet amplitude $|W^F(f,t)|$ for the reference $|W^F_{x_r}|$ (top-left); frequency modulation $|W^F_{x_2}|$ (top-right); damped frequency modulation $|W^F_{x^*_3}|$ (bottom-left); difference $||W^F_{x_3}| - |W^F_{x^*_3}||$ (bottom-right). The dashed-dot line indicates the cone of influence COI.

metrics, $\mathcal{M}_w^{a_r,a_3}$ and $\mathcal{M}_{wf}^{a_r,a_3}$, result in substantially lower values than 1, while the peak and RMS metrics are $\mathcal{M}_p^{a_r,a_3} = \mathcal{M}_{\text{rms}}^{a_r,a_3} \cong 1$. This further reinforces the claim why multi-criteria assessment is required beyond discussions based on averaged or global features of the signals. Unlike the previous example, the wavelet metric $\mathcal{M}_{wf}^{a_r,a_3}$ has similar value as its frequency-normalized version $\mathcal{M}_w^{a_r,a_3}$, which brings the conclusion that the discrepancies in $\mathcal{M}_{wf}^{a_r,a_3}$ are due to relative frequency modulation, rather than amplitude modulation. Although the mean phase metric amounts to $\mathcal{M}_\varphi^{a_r,a_3} < 1$, quantifying the mean phase between a stationary and frequency modulated non-stationary signal is obsolete, as noted in the preceding section. The frequency modulation did not result in appreciable deviation of the PDF; hence, $\mathcal{M}_{\text{pdf}} \cong 1$.

To further investigate the stationarity metric for two non-stationary signals, the frequency-modulated harmonic in (5.4) is additionally damped by a factor $\xi_1 = 0.025$ and the resulting signal is denoted as x_3^*. Figure 5.3 depicts the filtered non-stationary part of the normalized absolute wavelet coefficients $|W^F|$ of the signals a_r (top-left), a_3 (top-right), a_3^* (bottom-left), and the difference $||W^F_{a_3}| - |W^F_{a_3^*}||$ (bottom-right). It can be observed that there are some spurious peaks for the reference signal, despite the fact that the univariate test correctly accepted the null hypothesis (cf. (4.33)). This is the reason why the two-level process is employed for the stationarity metric. For the frequency-modulated signal a_3 and additionally damped signal a_3^*, the stationarity null hypothesis was rejected and the effect of the linear and damped linear chirp can be seen in the filtered wavelet coefficients. The discrepancy in the non-stationary

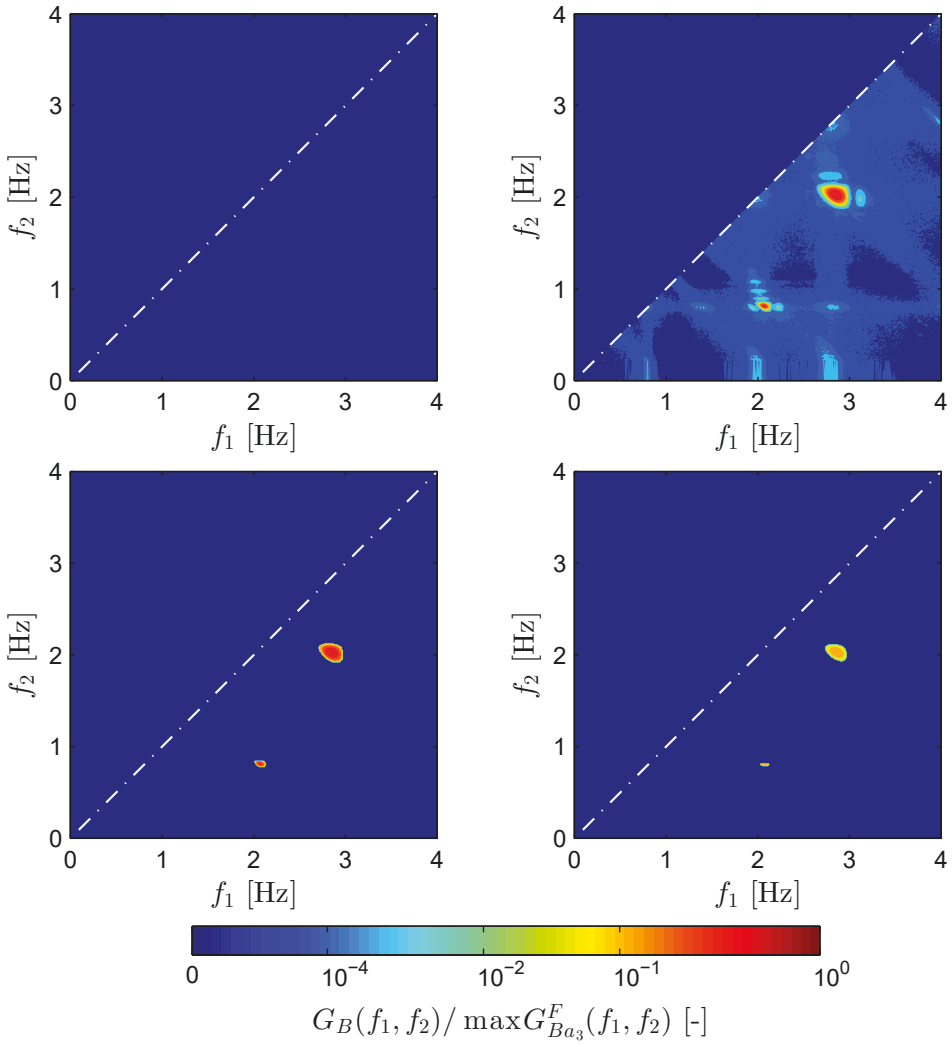

Figure 5.4: Comparison metrics for generic signals: phase-randomized bispectrum amplitude $G^R_B(f_1, f_2)$ and filtered phase-randomized bispectrum amplitude $G^F_B(f_1, f_2)$ for the reference $G^F_{Ba_1}$ (top-left), nonlinearity $G^R_{Ba_4}$ (top-right), nonlinearity $G^F_{Ba_4}$ (bottom-left); damped nonlinearity $G^F_{Ba^*_4}$ (bottom-right). The dashed-dot line indicates the inner triangle IT.

part for a_3 and a^*_3 is quantified based on (4.49). Hence, the stationarity metric amounts to $\mathcal{M}_s^{a_3,a^*_3} = 0.48$ for these two signals.

Signal 4 - Nonlinearity

In the last case, the difference of the nonlinearity in terms of quadratic phase coupling is explored between the reference a_r and nonlinear signal a_4. The wavelet bispectrum metric amounts to $\mathcal{M}_b^{a_r,a_4} = 0$ (cf. Fig. 5.1, bottom-right) as the reference signal is linear and a_4 is nonlinear due to multiplication of the harmonics at ω_1 and ω_2. The filtered wavelet bispectrum of the reference signal is trivial (cf. Fig. 5.4, top-left), while the filtered bispectrum is not (cf. Fig. 5.4, center-right). Hence, it is clear that the corresponding frequency couples at $(f_1, f_2) = (2, 2.8 - 2)$ and $(f_1, f_2) = (2.8, 2)$ are due to nonlinear interaction of ω_1 and ω_2 for the signal a_4. Moreover, the magnitude of the wavelet coefficients indicates two additional frequencies at 0.8 Hz and 4.8 Hz (cf. Fig. 5.2, bottom-right). Thus, most of the metrics which involve signal amplitude indicated discrepancies.

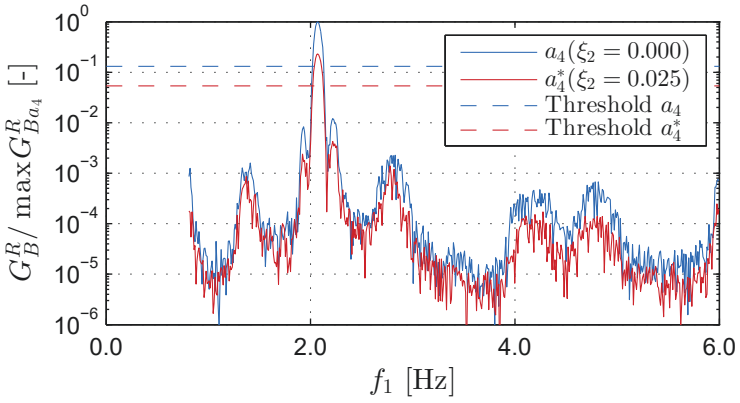

Figure 5.5: Comparison metrics for generic signals: phase-randomized bispectrum amplitude for nonlinearity $G^R_{Ba_4}(f_1, 0.8)$ and damped nonlinearity $G^R_{Ba_4^*}(f_1, 0.8)$ signals, including the filtering threshold.

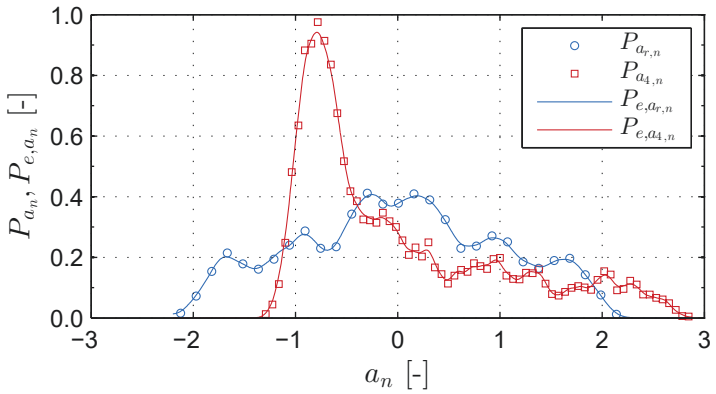

Figure 5.6: Comparison metrics for generic signals: histogram estimate PDFs P_{a_n} and kernel estimate PDFs P_{e,a_n} of the normalized (standard score) reference $a_{r,n}$ and nonlinearity $a_{4,n}$ signals.

The filtering of the nonlinear part of the signal is demonstrated in Fig. 5.4, where the unfiltered (cf. Fig. 5.4, top-right) and filtered (cf. Fig. 5.4, bottom-left) wavelet bispectrum are depicted. It is clear that the additional noise of the bispectrum is removed by utilizing the presented surrogate method (cf. (4.48)). To quantify a discrepancy in the nonlinear portions of two signals, a signal a_4^* is constructed based on (5.5) by introducing a damping coefficient of $\xi_2 = 0.025$. The wavelet bispectrum amplitude of a_4^* is shown in Fig. 5.4 (bottom-right), and additionally, a plane of the wavelet bispectrum amplitude at $f_2 = 0.8$ Hz is given in Fig. 5.5. Both of these figures indicate a difference in the wavelet bispectrum magnitude. Using (4.39) for the partial area of the IT (separated by the white dashed-dot line in Fig.5.4), the wavelet bispectrum metric amounts to $\mathcal{M}_b^{a_4,a_4^*} = 0.46$. The filtering threshold can be also observed in Fig. 5.5. Further, by modifying a_4 in (5.5) for $\varphi_3 = 0$, the filtered bispectrum amplitude resulted in zero values as the condition of $\varphi_B = 0$ is not satisfied. Hence, no quadratic phase coupling is detected. In this case, the filtered wavelet bispectrum is not shown as it is similar to a_r.

Further, the PDF metric amounts to $\mathcal{M}_{\text{pdf}}^{a_r,a_4} = 0.86$, indicating a discrepancy in the PDFs. Figure 5.6 depicts the histogram and the corresponding estimated PDFs using kernels of the normalized versions of the signals a_r and a_4. It is apparent that the PDF of the signal $a_{4,n}$ is asymmetric, which is due to the quadratic part of (5.5). It can be argued that for such a discrepancy, the PDF metric should be more sensitive. This can accounted for by adjusting the sensitivity parameter $\varepsilon_{\text{pdf}} > 1$ (cf. Definition 4.15). For e.g., $\mathcal{M}_{\text{pdf}}^{a_r,a_4} = 0.74$ for $\varepsilon_{\text{pdf}} = 2$.

5.3 Free-stream turbulence

Here, the flow fields of the CFD model for random and deterministic free-stream turbulence are verified. The verification is conducted for a CFD domain that does not contain an immersed body. In particular, the objectives of this section are to:

i) verify the flow field and conduct parametric studies for the 2D random free-stream turbulence for von Kármán spectra (cf. Sec. 3.6.2),

ii) study the span-wise correlation for the novel Pseudo-3D VPM presented in Sec. 3.6.4,

iii) study the flow field for the deterministic free-stream turbulence presented in Sec. 3.7.4, in terms of predicted amplitude and frequency content,

iv) verify the derived closed-form analytical solution for prediction of deterministic gust amplitudes (cf. 3.224) with its discrete inverse counterpart (cf. (3.227)).

5.3.1 Random gusts

Thorough investigation and parametric studies on the free-stream turbulence statistics for anisotropic turbulence based on the ESDU spectra have been performed by Prendergast [257] and the research group at the Technical University of Denmark [134, 261]. Herein, the turbulent statistical properties for the isotropic and anisotropic von Kárman spectra are investigated in 2D first, to understand the behavior of the flow field. Parametric studies are then performed to identify the sensitivity of relevant numerical parameters. Based on these findings, the discussion is continued for the Pseudo-3D case.

Two cases of free-stream turbulence are considered with isotropic and anisotropic properties. For these cases, the prescribed statistical (physical) properties of the free-stream turbulence and numerical parameters are given in Tab. 5.2. Additionally, the numerical discretization parameters are given in Tab. 5.3. How some of these parameters are selected will be discussed in the following. A reference dimension of $B = 31$ m is selected that corresponds to a body chord as the final goal of using the free-stream turbulence is to study its effect on an immersed body. For easier discussion, the turbulent properties are distinguished as:

- Target - prescribed statistics, denoted by the subscript t,
- Generated - properties that are sampled on the ladder (cf. Fig. 3.10 from Ch. 3), prior to conversion into particles (cf. (3.181) and (3.182)),
- Simulated - properties that are tracked down within the CFD domain.

Flow field: 2D

Preliminary, a trial run is performed for the isotropic case with a wide trial domain ($l_d/B \times l_h/B = 90 \times 90$) in order to investigate the spatial behavior of the turbulence energy along the centerline of the domain $\boldsymbol{x} = (x, 0, 0)$. Figure 5.7 presents an instantaneous particle map and the turbulence intensity along the centerline. Three different regions of the flow are distinguished, namely: (i) convergent region - where the kinetic energy converges; (ii) convection region - in which the particles are convected without major interaction and (iii) mixing free-flow region - where there is a mixing of rotational and free flow. It is observed that the longitudinal turbulence energy peaks at $x/B \approx 1$ and then a constant decay is noted. The vertical turbulence intensity peaks further downstream at $x/B \approx 20$ and it remains relatively constant up to

Turbulent case	Physical parameter		Value
Isotropic	Wind speed:	U	30 m/s
	Longitudinal intensity:	TI_{ut}	6 %
	Vertical intensity:	TI_{wt}	6 %
	Longitudinal length scale:	L_{ut}/B	1.75
	Vertical length scale:	L_{wt}/B	0.87
	Reynolds number:	Re	1.03×10^5
	Turbulent Reynolds number:	Re_{L_u}	1.79×10^5
	Coherence coefficient:	$\boldsymbol{c}_x = (C_x, C_y, C_z)$	$(3, 5, 10)$
Anisotropic	Wind speed:	U	30 m/s
	Longitudinal intensity:	TI_{ut}	11 %
	Vertical intensity:	TI_{wt}	6 %
	Longitudinal length scale:	L_{ut}/B	3.48
	Vertical length scale:	L_{wt}/B	0.48
	Reynolds number:	Re	1.03×10^5
	Turbulent Reynolds number:	Re_{L_u}	3.59×10^5
	Coherence coefficient:	$\boldsymbol{c}_x = (C_x, C_y, C_z)$	$(3, 5, 10)$

Table 5.2: Random free-stream turbulence: prescribed physical parameters for the two turbulent cases for reference dimension $B = 31$ m.

Numerical parameter		Value
Domain length:	l_d/B	21
Domain height:	l_h/B	21
Reduced time-step	$\Delta\tau = \Delta t U/B$	1.65×10^{-2}
Total time:	$\tau = tU/B$	677
Core radius:	ϵ/B	9.7×10^{-3}
Poisson grid:	$N_x \times N_z$	511×511
$\mathrm{P^3M}$ neighboring cells:	N_r	3
Particle release factor:	$\Delta p = \Delta t_{in}/\Delta t$	4
Particle band height:	l_G/B	18
Span-wise increment:	$\Delta y/B$	0.16
Number of strips:	N_{str}	6
Correction factor:	β_{in}	0.7 (0.65)

Table 5.3: Random free-stream turbulence: numerical parameters for reference dimension $B = 31$ m. The value of the correction factor β_{in} is given for the isotropic case, while the value in brackets is for the anisotropic case.

$x/B \approx 60$, after which it starts to reduce slowly due to the free-space boundary condition. Similar observations are noted by Rasmussen et al. [261], who reported that the reduction of vertical turbulent energy starts to decay at approximately $x = 3.5l_G$. To accommodate a uniform turbulence field and sufficiently developed wake, a domain with $10B$ upstream distance from the leading edge and $10B$ behind the trailing edge is considered appropriate. Thus, the selected domain ($l_d/B \times l_h/B = 21 \times 21$) is marked by the red box on the particle map in Fig. 5.7. All further analyses are conducted for the selected domain.

Figure 5.8 depicts a sample of the time-histories from the generated velocity components at the ladder $\boldsymbol{x}_g = (0.5B, 0, 0)$ and simulated velocities at the center of the domain $\boldsymbol{x}_c = (10.5B, 0, 0)$,

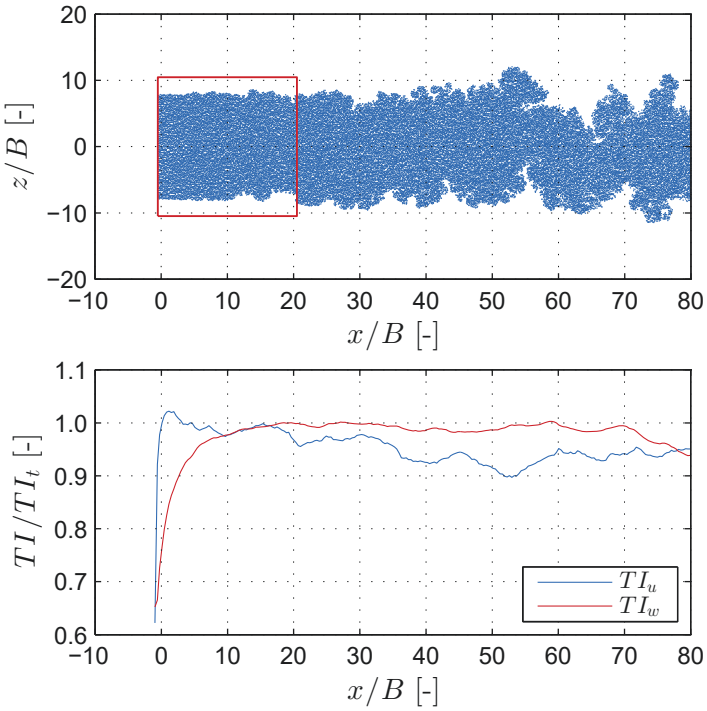

Figure 5.7: Random free-stream turbulence, 2D: sample particle map (top); normalized turbulence intensity TI/TI_t along the centerline $z/B = 0$ (bottom) for the isotropic case. The test domain size is $l_d/B \times l_h/B = 90 \times 90$, while the red box on the particle map indicates the selected domain.

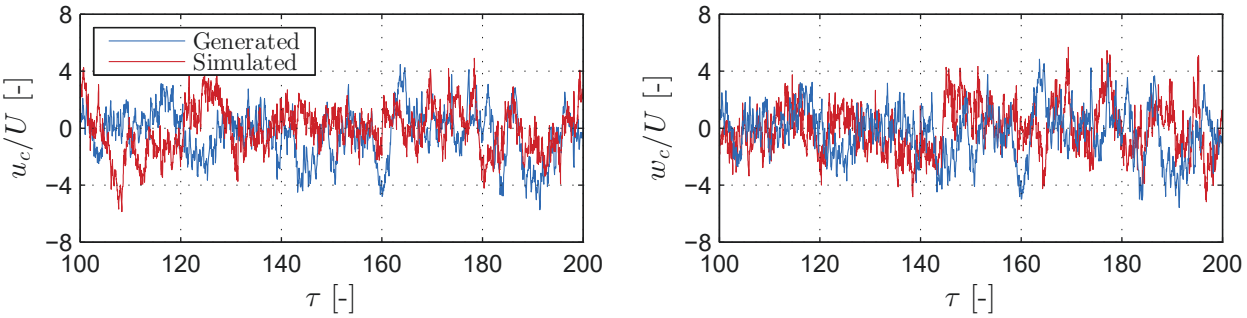

Figure 5.8: Random free-stream turbulence, 2D: sample generated (at $\boldsymbol{x}_g = (0.5B, 0, 0)$) and simulated (at $\boldsymbol{x}_c = (10.5B, 0, 0)$) time-histories of the longitudinal u (left) and vertical w (right) fluctuations for the isotropic case.

while Fig. 5.9 depicts instantaneous magnitude of the fluctuating velocity for the selected domain. From the latter figure, it appears that the fluctuating velocity is simply convected by the mean wind speed, i.e. Taylor's hypothesis holds. Due to this hypothesis, the time-histories should appear relatively similar with a phase-shift corresponding to the distance between the particle band and $\boldsymbol{x}_c$. This is not the case herein as the generated velocity is not divergence-free; however, similar amplitude and frequency content may be observed and the following discussion shows that the turbulence statistics are mostly retained.

The target, generated (at $\boldsymbol{x}_g$) and simulated (at $\boldsymbol{x}_c$) turbulence intensities are given in Tab. 5.4. Good correspondence can be observed for the isotropic case, while a reduction in longitudinal turbulence energy is noted for the anisotropic case. By converting the ladder velocities into circulation by (3.182), the divergent-free condition is imposed, which results in loss of turbulent kinetic energy. This is also noted for ESDU spectra with anisotropic turbulence [135, 257, 261].

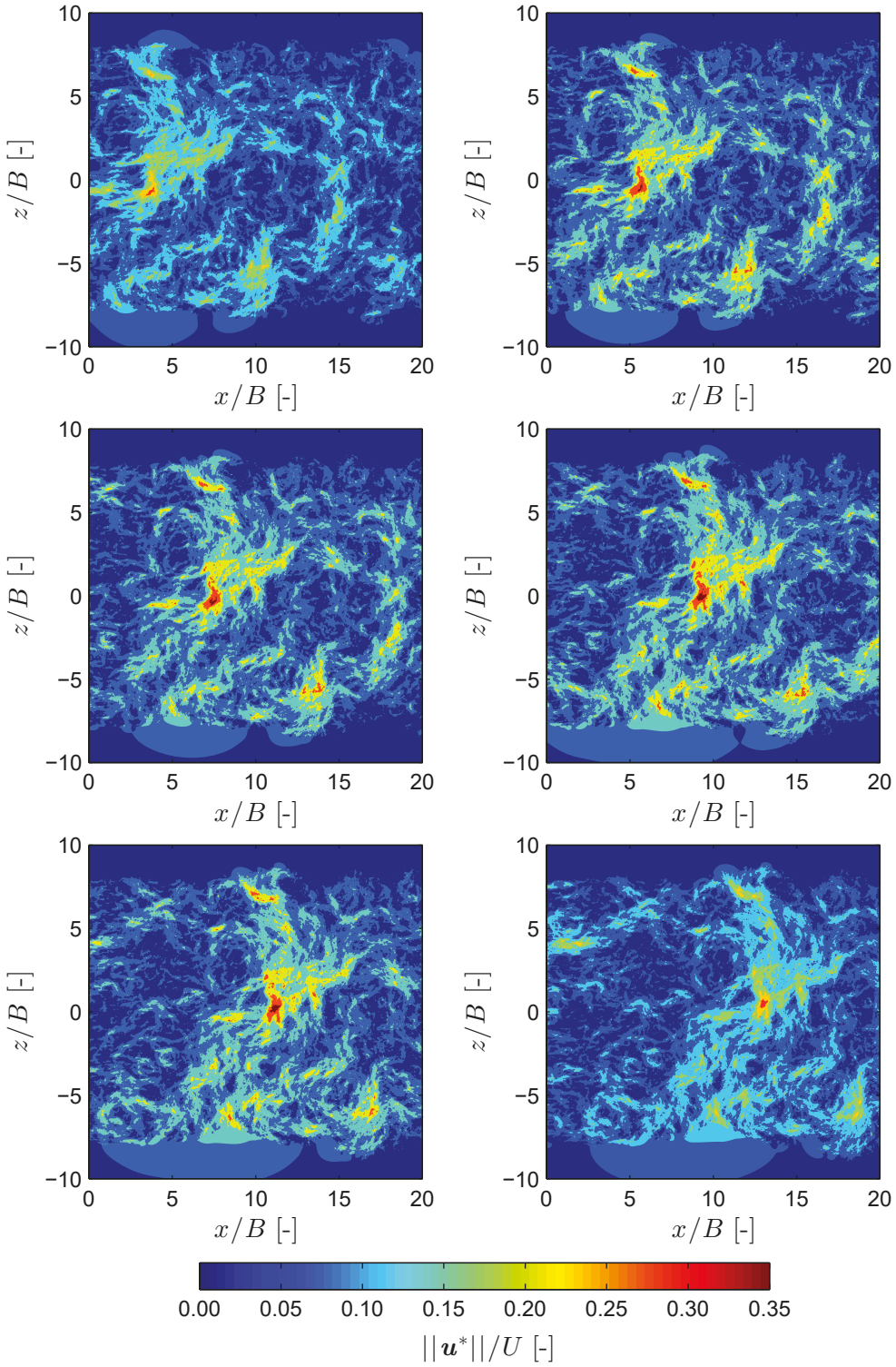

Figure 5.9: Random free-stream turbulence, 2D: sample fields of fluctuating velocity magnitude $\|\boldsymbol{u}^*\|$ for the isotropic case at $\tau = 88.0, 89.9, 91.7, 93.6, 95.4, 97.3$ (from left to right, top to bottom), i.e. the time shift between consecutive snapshots corresponds to a convection distance of approximately one length scale $L_u/B \approx 1.75$ due to mean wind speed.

The results obtained herein for the isotropic case suggest that the loss of turbulent kinetic energy is minor. Further, mostly uniform turbulence intensity is noted across the selected domain, particularly in the area of expected motion and wake of a body (cf. Fig. 5.10).

Case	Parameter	TI_u [%]	TI_w [%]	$L_{u\tau}/B$ [-]	L_{ux}/B [-]	$L_{w\tau}/B$ [-]	L_{wx}/B [-]
Isotropic	Target	6.0	6.0	1.74	1.74	0.87	0.87
	Generated	6.0	6.1	1.70	/	0.99	/
	Simulated	5.9	5.8	1.70	1.69	1.09	1.10
Anisotropic	Target	11.0	6.0	3.48	3.48	0.48	0.48
	Generated	11.0	5.89	2.79	/	0.61	/
	Simulated	7.65	6.45	2.06	2.12	0.98	1.01

Table 5.4: Random free-stream turbulence, 2D: turbulent intensities and length scales for the generated (at $\boldsymbol{x}_g = (0.5B, 0, 0)$) and simulated (at $\boldsymbol{x}_c = (10.5B, 0, 0)$) velocities compared w.r.t prescribed quantities. The temporal length scales L_τ are obtained from the fluctuating time-histories at $\boldsymbol{x}_g$ or $\boldsymbol{x}_c$, while the spatial length scale for the simulated velocity L_x is obtained from signals at points along the centerline $z/B = 0$.

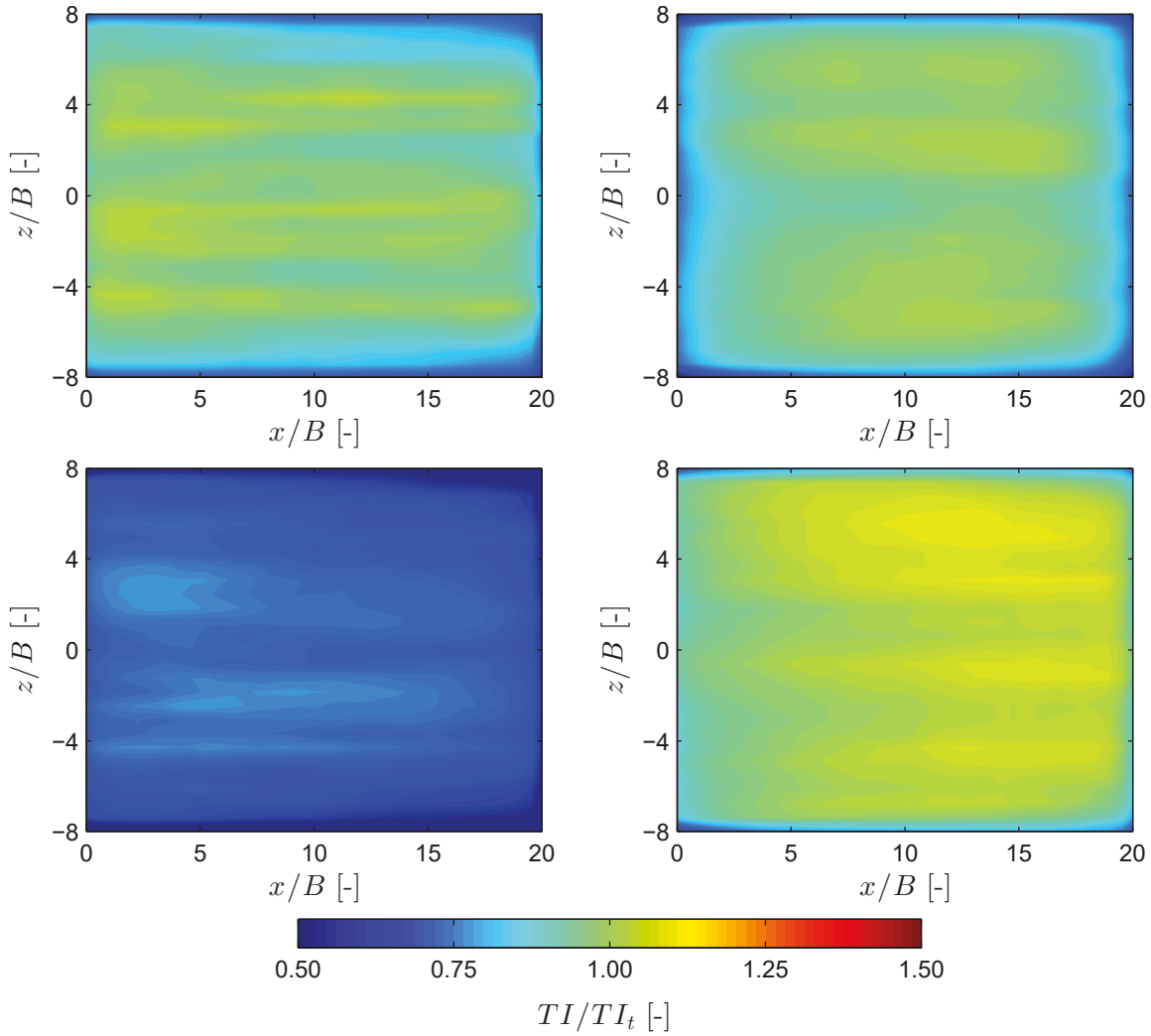

Figure 5.10: Random free-stream turbulence, 2D: spatial distribution of normalized turbulence intensity for the horizontal TI_u/TI_{ut} (left) and vertical TI_w/TI_{wt} (right) fluctuations for the isotropic (top) and anisotropic (bottom) cases.

The normalized PSDs of the generated and simulated wind velocities are compared to the von Kármán PSDs in Fig. 5.11 for both isotropic and anisotropic cases. All PSDs are normalized w.r.t. target length scales and target variances of the corresponding fluctuating components.

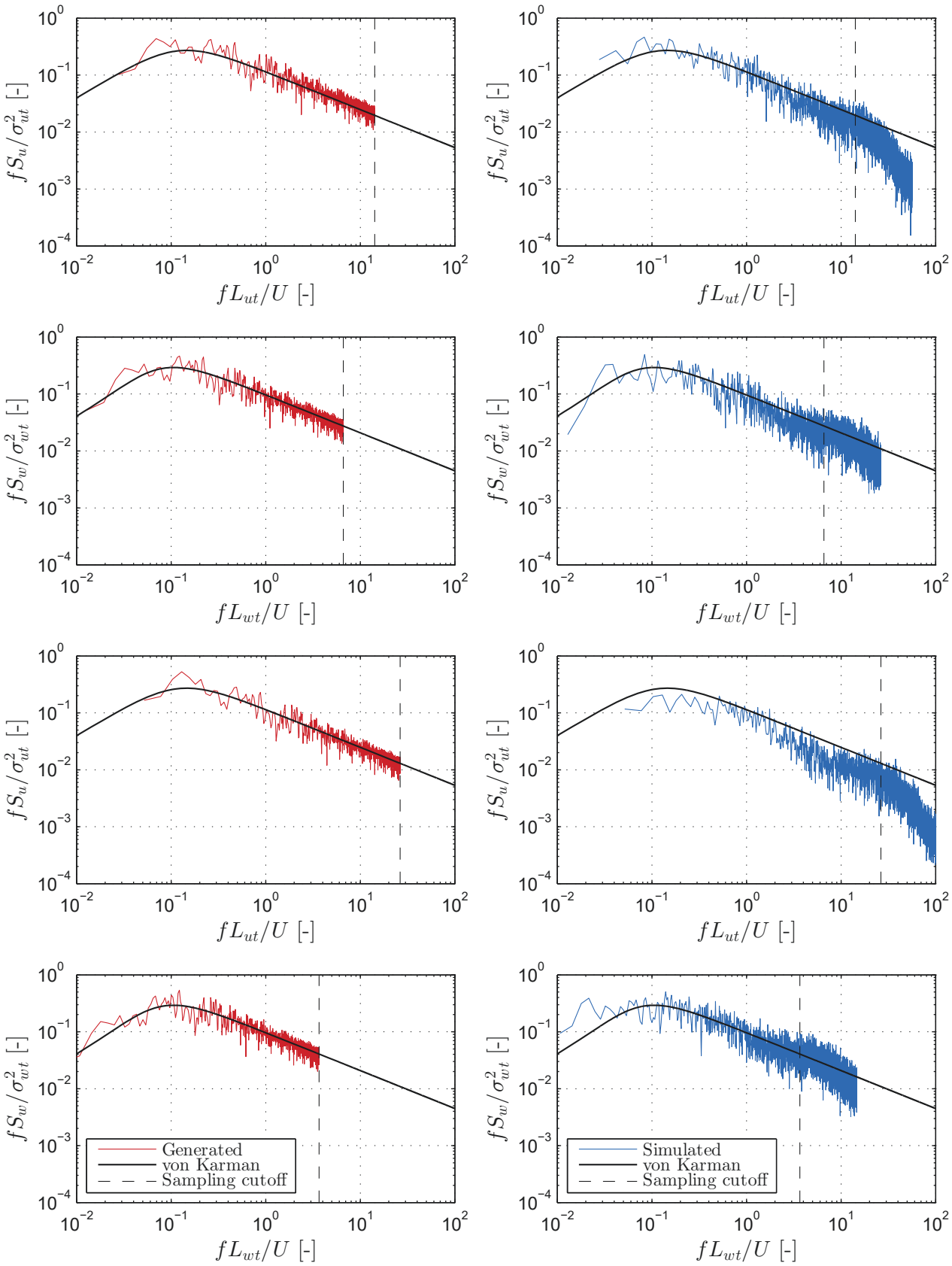

Figure 5.11: Random free-stream turbulence, 2D: PSDs of the generated at $\boldsymbol{x}_g$ (left) and simulated at $\boldsymbol{x}_c$ (right) velocities for the isotropic longitudinal (top), isotropic vertical (center-top), anisotropic longitudinal (center-bottom) and anisotropic vertical (bottom) fluctuations. These are further compared to the prescribed von Kármán spectra, while the sampling cutoff represents a Nyquist frequency f_{sg} for particle release factor $\Delta p = 4$, i.e. the Nyquist frequency of the generated velocity.

Normalizing the PSDs in such a way, vertical shifts in the spectra correspond to a discrepancy in the turbulent energy (i.e. intensity), lateral shifts to a discrepancy in the length scales, while any other distortion means discrepancy of the relative frequency content w.r.t. the target quantities. As expected, the generated PSDs matches the target spectra. The sampling cutoff frequency corresponds to the Nyquist frequency of the generated velocity. Below the sampling frequency, the PSDs of the simulated wind velocities for the isotropic case correspond well with the target ones for both velocity components with a minor relative discrepancy in the lowest frequencies for the vertical component. In the anisotropic case, the spectral distribution is retained for the PSD of the longitudinal velocity component; however, a vertical shift is noted. This means that imposing the divergence-free condition, the velocities are simply averaged without disturbing the relative frequency content. Better correspondence is noted for the PSD of the vertical component than the longitudinal, with deviation from the target spectrum in the low-frequency range.

Further, the turbulent length scales of the generated (at $\boldsymbol{x}_g$) and simulated (at $\boldsymbol{x}_c$) are given in Tab. 5.4. The simulated length scales are computed as a function of time L_τ (cf. (2.9)) and as a function of the spatial coordinate L_x (cf. (2.6)). In the isotropic case, the generated and simulated longitudinal length scales correspond good to the target one, while minor overestimation is noted for the vertical ones. In the anisotropic case, the length scale for the longitudinal component is somewhat underestimated for both the generated and simulated case, while the lateral is overestimated. Overestimation of such magnitude for the generated length scales has been previously reported (cf. Rossi et al. [267]), and is generally connected to the computation of the length scale in terms of the noise threshold of the autocorrelation. For the simulated length scales, there is an additional "averaging" due to the conversion of ladder velocities into particle. In fact, this averaging can be seen for both turbulence intensities and length scales. Since the discrepancy in the length scales is not up to an order of magnitude, it is not visible in the PSDs. For both cases, Taylor's hypothesis is generally valid as there is a good correspondence for the spatial and temporal length scales ($L_t \approx L_x$). The validity of this hypothesis can also be quantitatively evaluated from Fig. 5.12, where the coefficient of correlation R^* (or normalized cross-correlation R) is depicted w.r.t. the reduced dimensional time τ and normalized spatial dimension x/B. As established in Sec. 3.6.4, Taylor's hypothesis is the basis for the span-wise correlation in the Pseudo-3D method with free-stream turbulence.

The histogram estimate PDFs of the wind fluctuations are important for the buffeting forces as

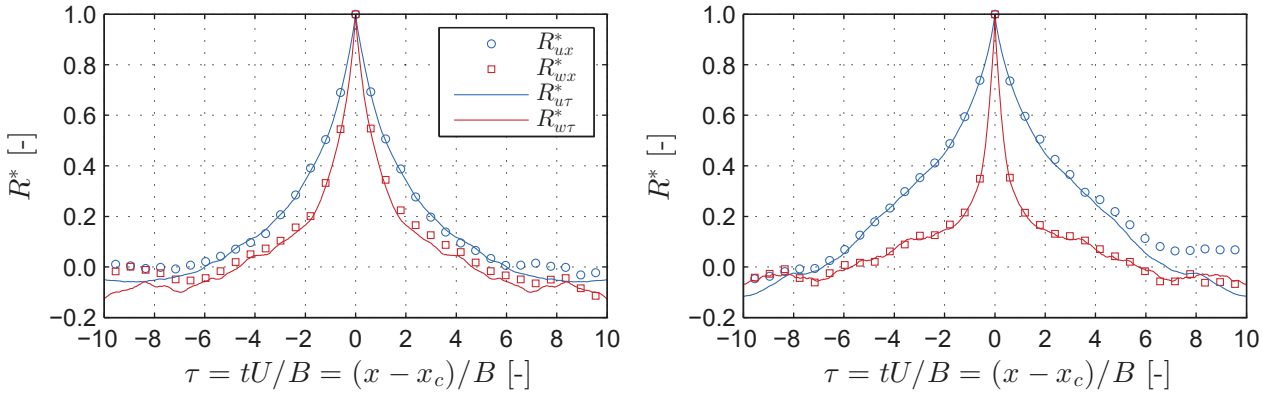

Figure 5.12: Random free-stream turbulence, 2D: spatial correlation R^*_x and autocorrelation R^*_τ coefficients of the simulated velocity fluctuations at $\boldsymbol{x}_c$ for the isotropic (left) and anisotropic (right) cases.

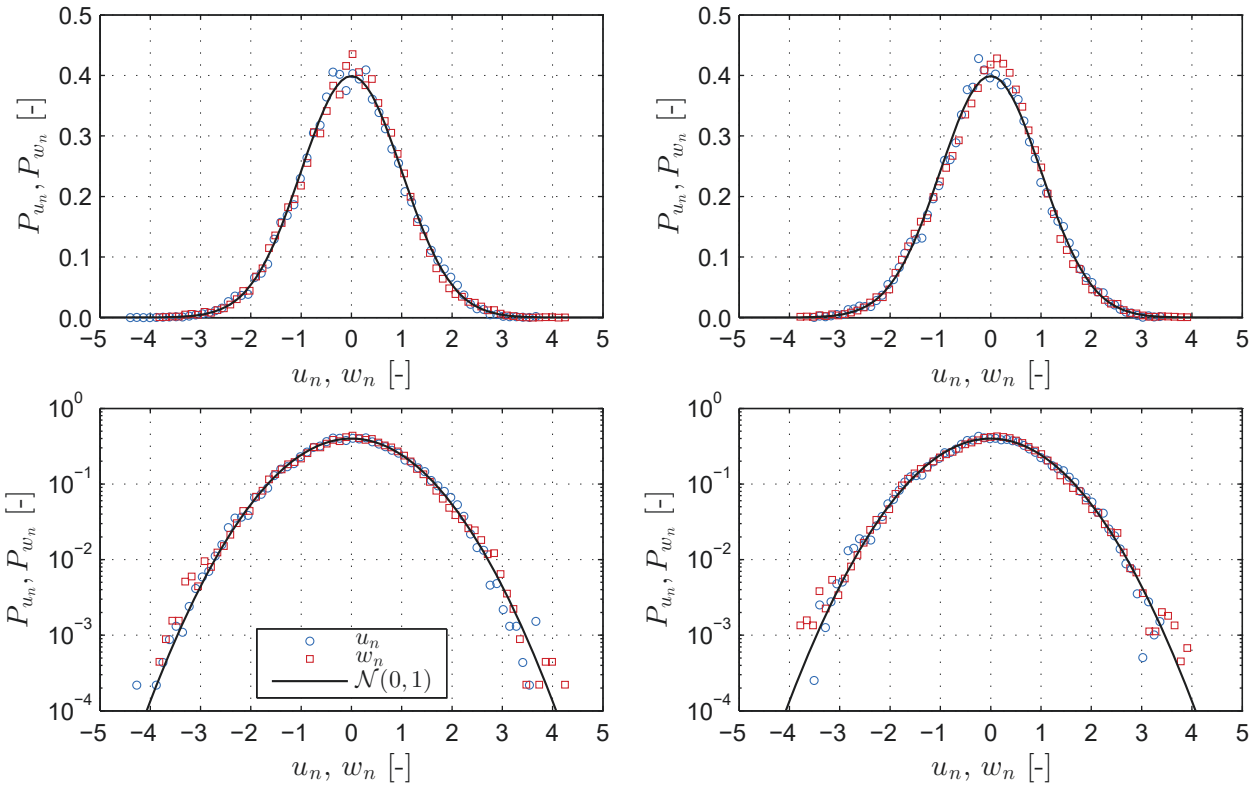

Figure 5.13: Random free-stream turbulence, 2D: histogram estimate PDFs of normalized (standard score) simulated velocity fluctuations P_{u_n} and P_{w_n} for the isotropic (left) and anisotropic (right) cases, compared a standard normal distribution $\mathcal{N}(0,1)$. The bottom figures provide better representation of the tail of the PDF as logarithmic scale is used for the ordinate.

Gaussian input would result in Gaussian output only for linear aerodynamic models. Figure 5.13 depicts the PDFs of the standard score wind fluctuations for both cases. It is observed that both fluctuating components for both cases generally follow the normal probability distribution $\mathcal{N}(0,1)$, even in the tail of the distribution which is visible in the logarithmic representation (cf. Figure 5.13, bottom). However, the Kolmogorov-Smirnov test for normality rejected the null hypothesis at 5 % significance level, which may be attributed to three factors, namely: (i) the conversion from ladder velocities to circulation, (ii) artificial energy above the cutoff frequencies and (iii) due to the non-Gaussianity of 2D turbulence (cf. Boffeta and Ecke [30] for discussion). Further investigations are required to support the latter statement as the current numerical resolution does not resolve all turbulent scales and no closure model is implemented. The generated velocity is determined to be Gaussian (not shown).

Parametric studies

Next, parametric studies are conducted w.r.t. four numerical parameters: circulation correction factor β_{in}, particle release factor Δp, core radius ϵ, and particle band height l_G. Additionally, the effect of Reyolds number as a physical parameter is studied. The discussion is mainly based on the PSDs of the velocities for the isotropic case. Before continuing with the parametric studies, a remark is made regarding the computation of a PSD, its smoothing, and representation.

The "full" PSD of a signal, i.e. without any smoothing, can contain significant noise, which makes it difficult to interpret the results. To be able to make a meaningful interpretation, the PSDs need to be smoothened. Typically, Welch's method is used for 8 averaging segments with

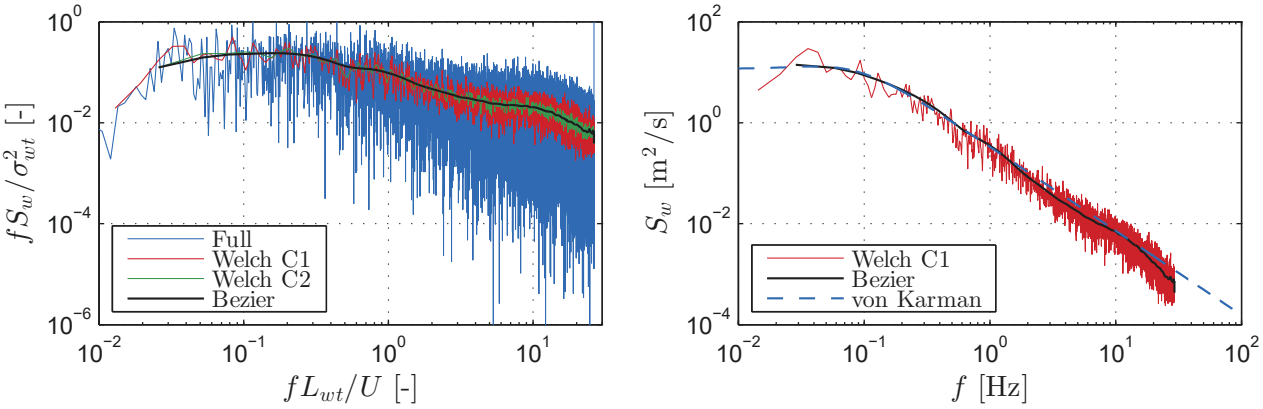

Figure 5.14: Random free-stream turbulence, 2D: effects of smoothing (left) and normalization (right) on the representation of the PSD of the simulated vertical fluctuations for the isotropic case. The "Full" PSD is obtained without any smoothing; the Welch spectrum corresponds to a smoothened spectrum with 8 averaging segments and 50 % overlap (C1) and 20 averaging segments and 50 % overlap (C2); Berzier curves are fitted to the Welch C2 spectrum. The unnormalized spectrum (right) is corresponding to the normalized spectrum in Fig. 5.11 (right, center-top).

a 50 % overlap (as shown previously in Fig. 5.11). While this is sufficient for representation of a single PSD for comparison with an analytical curve, further smoothing is required for comparison of several PSDs. Rasmussen et al. [261] suggested to sub-sample the full spectrum and subsequently use Bezier curves. The sub-sampling is required as the Bezier curves require the computation of factorial; thus, a large number of points results in numerical instability. Herein, the Bezier curves are fit to a smoothened Welch spectrum using 20 averaging segments with a 50 % overlap, which is the minimum number of segments that resulted in a Bezier curve without numerical instability. The smoothing process is depicted in Fig. 5.14 (left), where the Welch C1 corresponds to 8 averaging segments, while Welch C2 to 20 averaging segments with 50 % overlap. Moreover, by normalizing the PSD with the frequency, the discrepancy in the whole frequency range is illuminated. For e.g., the unnormalized PSD of the vertical component for the Welch C1 in Fig. 5.14 (right), appears to be in better correspondence with von Kármán spectra than normalized PSD shown in Fig. 5.11 (top-right).

First, the effect of the circulation correction factor β_{in} is considered. Generally, β_{in} can take values from 0.6 up to 1, depending on the target spectra and the hight of the particle ladder [257]. Figure 5.15 depicts the PSDs for varying this factor for the isotropic case. Modifying this factor proportionally scales the global turbulent energy in a uniform manner for the whole frequency content for both fluctuating components. Thus, this factor is directly connected to the turbulence intensity. Figure 5.16 depicts the turbulence intensity along the centerline $\boldsymbol{x} = (x, 0, 0)$, for both isotropic (left) and anisotropic (right) cases. In the isotropic case, the turbulence intensity for both components converges for values of β_{in} approximately amounting to $\beta_{in} = 0.7$. The reason for the factor β_{in} not having a value of one is due to the "smudging" effect of the vortices when they are generated from a velocity ladder, as the circulation Γ_p only for a single cell tends to the approximated one Γ_a. This was shown by Prendergast [257], who used the corner point velocities of a square grid instead of a ladder to replicate a circular vortex and concluded that in case the grid is larger than 3×3 cells, the factor $\beta_{in}\pi/2 \to 1$. Furthermore, Chawdhury and Morgenthal [51] used the method for conversion of ladder velocities into particles to reproduce a wake behind a bluff body where the velocities sampled on the ladder are obtained from the solution of the Navier-Stokes equation. The factor β_{in} is reported to

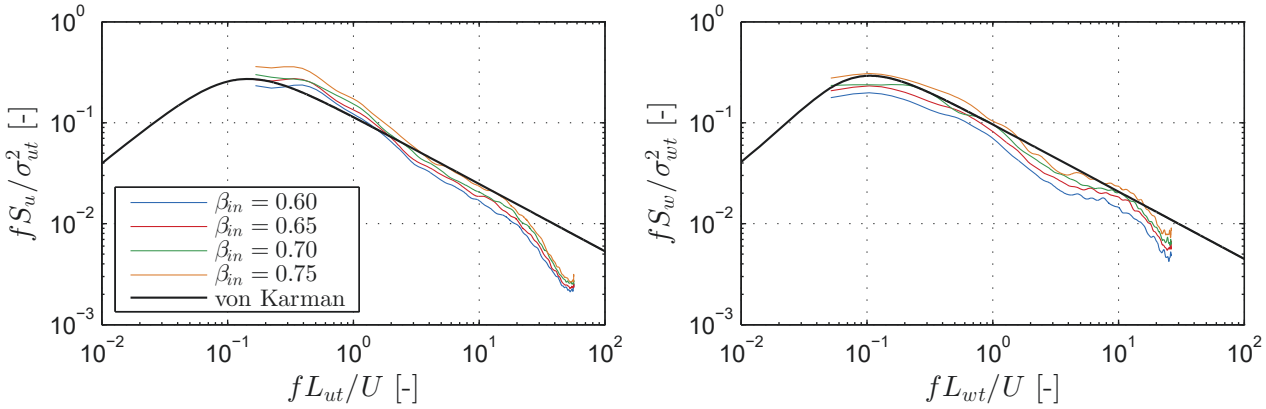

Figure 5.15: Random free-stream turbulence, parametric studies: effect of circulation correction factor β_{in} on the PSDs of longitudinal S_u (left) and vertical S_w (right) simulated velocities for the isotropic case.

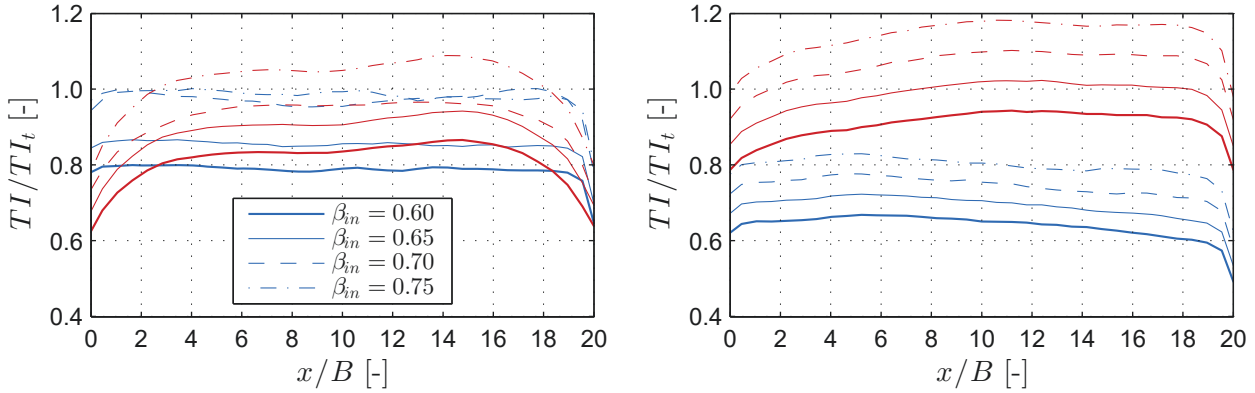

Figure 5.16: Random free-stream turbulence, parametric studies: effect of circulation correction factor β_{in} on the turbulence intensity of longitudinal TI_u (blue) and vertical TI_w (red) simulated velocities for the isotropic (left) and anisotropic (right) cases along the centerline $z/B = 0$.

be around 0.6 to match the reproduced flow turbulence properties. In the anisotropic case, it can be seen that for β_{in}=0.65 (i.e. $\beta_{in}\pi/2 \rightarrow 1$) the vertical turbulence intensity converges to the prescribed value, while for the lateral component the turbulence intensity is found to be reduced to 70 %, as noted in Tab. 5.4.

Second, the effect of particle release factor Δp is studied. From the PSDs shown in Fig. 5.17, it can be gathered that there is an artificial rise of energy at a particular frequency that corresponds to the Nyquist frequency of the generated velocity, f_{sg}. Based on the particle release factor, this frequency is

$$f_{sg} = \frac{1}{2\Delta p \Delta t}. \tag{5.6}$$

Of course, setting $\Delta p = 1$ would result in no artificial rise of energy. However, this means higher computational demand as a larger number of time-steps are needed for the generation of the time-histories, i.e. $\lfloor N_s/\Delta p \rfloor$ (cf. Sec. 3.6.2). Moreover, the number of inflow particles N_{ip} increases as they are injected at a higher rate and with a larger number of particles per seeding step due to the smaller cell size, i.e. $\Delta c = U\Delta p \Delta t$. For e.g., 240 particles are injected every 4-th simulation step for $\Delta p = 4$, while 480 particles are injected every 2-nd simulation step for $\Delta p = 2$. Selecting $\Delta p = 4$ is considered to balance the accuracy and numerical efficiency for the particular turbulent properties.

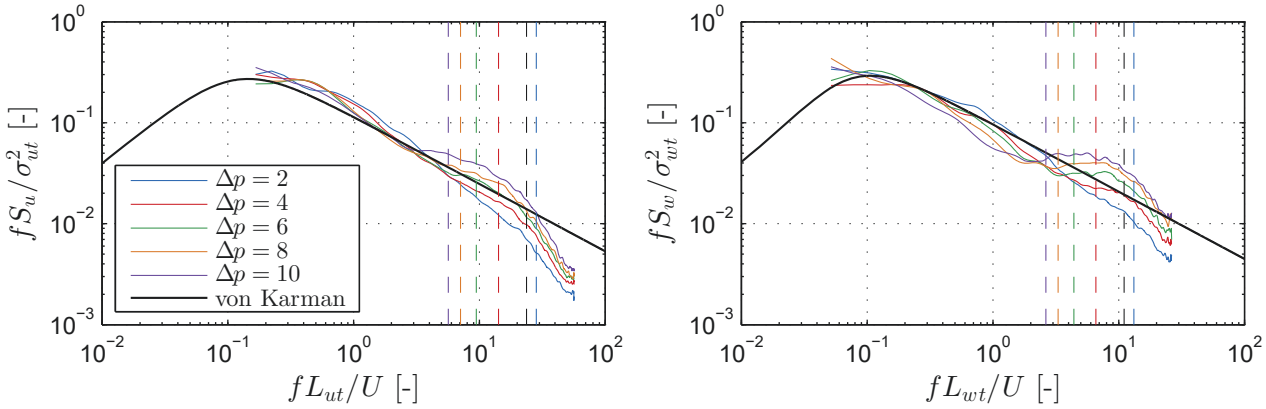

Figure 5.17: Random free-stream turbulence, parametric studies: effect of particle release factor factor Δp on the PSDs of longitudinal S_u (left) and vertical S_w (right) simulated velocities for the isotropic case. The dashed lines in corresponding colors depict to the Nyquist frequency f_{sg} obtained as in (5.6). The black dashed line correspond to the core cutoff frequency $f_{s\epsilon}$ (cf. (5.9)) for the baseline $\Delta c/\epsilon = 6.6$.

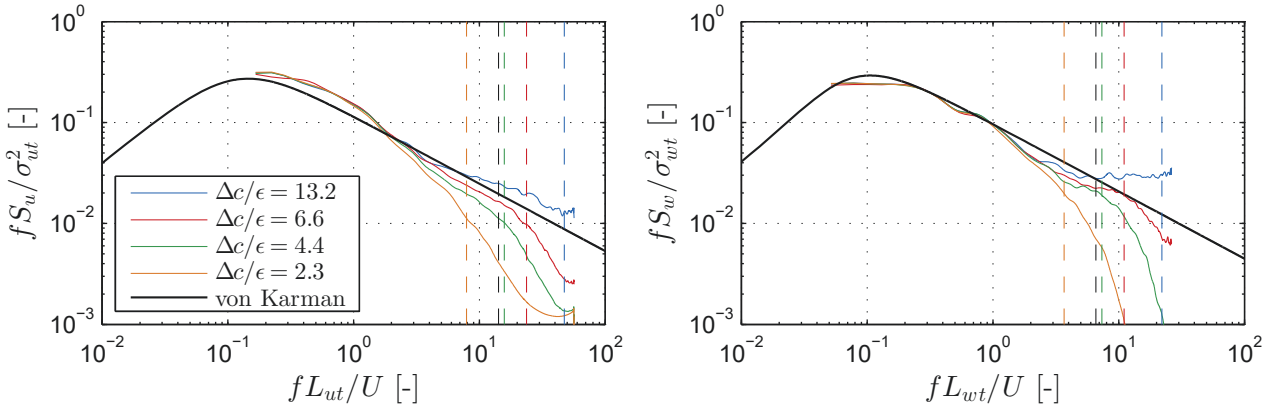

Figure 5.18: Random free-stream turbulence, parametric studies: effect of the ratio between the cell size and core radius $\Delta c/\epsilon$ on the PSDs of longitudinal S_u (left) and vertical S_w (right) simulated velocities for the isotropic case. The dashed lines in corresponding colors depict the core cutoff frequency $f_{s\epsilon}$ obtained as in (5.9). The black dashed line correspond to the core cutoff f_{sg} frequency (cf. (5.6)) for $\Delta p = 4$.

Third, the influence of the core radius examined. As the core radius ϵ is used to resolve the numerical instabilities by mollifying the particles' velocity (cf. (3.173)), it is logical to relate it to the particle spacing and the average distance between a vortex and velocity sampling point of interest. Under Taylor's hypothesis, the inflow particles are assumed to be advected only by the mean flow; thus, the average particle spacing is equal to the cell size Δc. The results of a parametric study for different $\Delta c/\epsilon$ is depicted in Fig. 5.18. It can be observed that reducing this ratio, a loss of turbulent kinetic energy starts to be significant at lower frequencies. The relationship between the core radius and a particular cutoff frequency $f_{s\epsilon}$, for which the smoothing is considered to be significant, depends on the type of mollified kernel used. For the Gaussian core, a distance of 2ϵ between a velocity sampling point and a vortex particle would result in a reduction of $\approx$2 % of velocity (similarly as the 98 % interval for Gaussian distribution). Taking that for a vortex at the center of the quadratic cell (cf. Fig. 3.10 from Ch. 3), the induced velocity at a sample point positioned on the inner circle of the cell should

not be reduced less than 98 %, the ratio

$$\frac{\Delta c/2}{\epsilon} = 2 \tag{5.7}$$

can be obtained. This ratio is more conservative than the ratio proposed by Prendergast [257], which corresponds to a distance equivalent to the radius of the outer circle of the quadratic cell. Hence, significant smoothing can be expected for wavelengths smaller than the distance $\Delta c/2$ (i.e. the inner radius of the cell). The Nyquist frequency for this wavelength yields

$$f_{s\epsilon} = \frac{\Delta c/2}{2U}. \tag{5.8}$$

Plugging this into (5.7) yields the relation between core cutoff frequency and core radius

$$f_{s\epsilon} = \frac{U}{8\epsilon}. \tag{5.9}$$

The core radius cutoff frequencies are represented by the dashed lines in Fig. 5.18. Above these frequencies, it can be seen that there is a significant smoothing. It is also interesting to note that for $\Delta c/\epsilon = 13.2$, there is an artificial increment. This is a consequence of the particle release factor corresponding to f_{sg} (cf. (5.6)), which is represented by the black dashed line in Fig. 5.18. Similarly, for all Δp cases in Fig. 5.17, the smoothing below $f_{s\epsilon}$ (black dashed line) is a consequence of the selected core radius. Generally, both $f_{s\epsilon}$ and f_{sg} should correspond to frequencies that are not of interest for the analysis. In this case, $f_{s\epsilon}$ is set corresponding to $\Delta c/\epsilon = 6.6$ and is generally governed by the panel length of the immersed body.

Forth, the consequence of varying the particle band height l_G is investigated. Naturally, the domain size is also changed to accommodate higher particle bands. For the ratios $l_G/B = 8$, $l_G/B = 12$ and $l_G/B = 20$, the dimension of the quadratic domain corresponds to $l_d/B = 11$, $l_d/B = 17$ and $l_d/B = 28$, respectively. The simulated velocity is tracked at position $x = 0.625 l_G$ downstream from the particle band height to assure similar convergence of the turbulent energy as in Fig. 5.7. Figure 5.19 depicts the PSDs for varying l_G/B ratio. Only minor increments in the low frequencies of the longitudinal fluctuations can be observed. Similar findings were reported by Rassmusenn et al. [261] for the ESDU spectra.

Finally, the effect of the Reynolds number is considered by varying the kinematic viscosity ν. The PSDs of the velocity fluctuations for three Reynolds numbers are depicted in Figure 5.20.

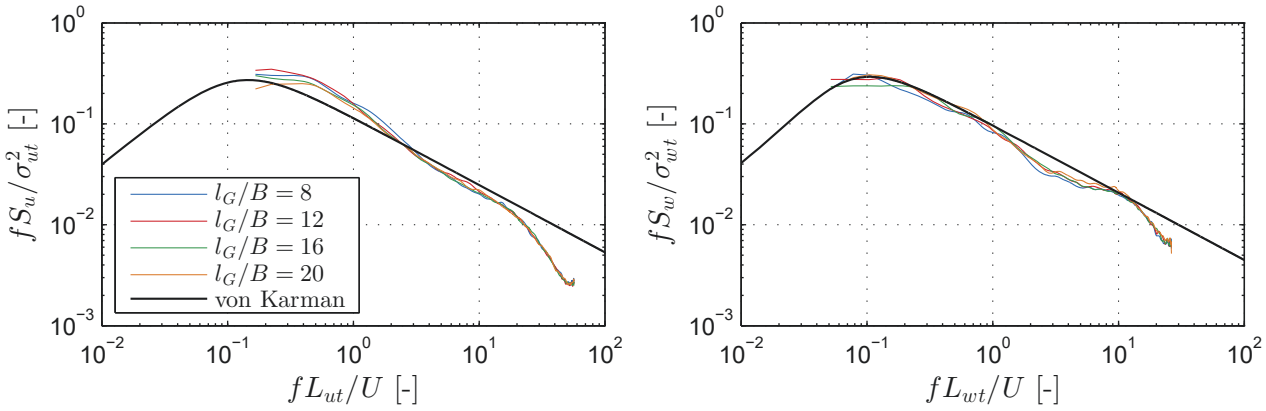

Figure 5.19: Random free-stream turbulence, parametric studies: effect of particle band height l_G/B on the PSDs of longitudinal S_u (left) and vertical S_w (right) simulated velocities for the isotropic case.

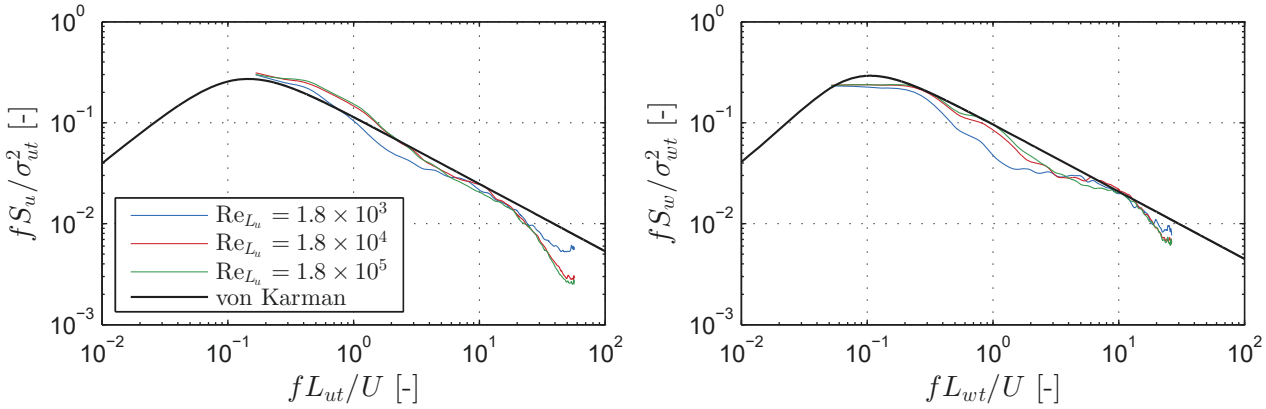

Figure 5.20: Random free-stream turbulence, parametric studies: effect of turbulent Reynolds number Re_{L_u} on the PSDs of longitudinal S_w (left) and vertical S_w (right) simulated velocities for the isotropic case.

It can be observed that for $\mathrm{Re}_{L_u} = 1.8 \times 10^3$ (i.e. $\mathrm{Re} = 1.03 \times 10^3$) there is additional loss of turbulent energy, compared to the cases with higher Reynolds numbers. It is reasonable to state that this is a consequence of the increased role of turbulent viscosity. No significant difference in the PSDs of the velocities is noted for Reynolds number with orders of magnitude 10^4 and 10^5.

Flow field: Pseudo-3D

The correlation of wind fluctuations between strips in the turbulent Pseudo-3D VPM represents an essential part. Thus, the span-wise correlation and coherence are studied between six strips for the isotropic and anisotropic cases with the numerical parameters noted previously in Tab. 5.2. Two coherence models are used as a target for generation of the ladder velocities, and are denoted as:

- VC - Vickery coherence model (cf. (3.25)),
- MC - Modified coherence model (cf. (3.198)).

These two types of coherence models along with the two cases of turbulence make a total of four cases which will be the topic of discussion of this section. The span-wise correlation and coherence are studied for points that lie on a horizontal line, i.e. there is no vertical separation $z = 0$. Thus, the target coherence is similar for both input coherence models.

Figure 5.21 depicts the span-wise correlation coefficient $R_y^* = R^*(y)$ for of the first strip w.r.t. the rest of the strips for the simulated velocity at the center of the fluid domain, $\boldsymbol{x}_c = (0, y, 0)$ (cf. Fig. 3.12 from Ch. 3 for graphical representation of two slices). The span-wise correlation coefficient of the simulated velocities is further compared to the one from the generated fluctuations at the ladder. Since there is no vertical separation, the generated span-wise correlation coefficient is identical for the VC and MC models. At a point close to the particle band ($y/B = 2.5$), R_y^* of the simulated velocities for the MC model yields good results for both vertical and longitudinal fluctuations. Utilizing the VC model, there is a reduction in R_y^* for both fluctuating components. In the anisotropic case, excellent agreement of R_y^* is noted the vertical velocity for both VC and MC, while there is a partial loss for the longitudinal one. For points further downstream, a loss of correlation is observed only in the longitudinal fluctuating components for both VC and MC models in both isotropic and anisotropic cases. Nevertheless,

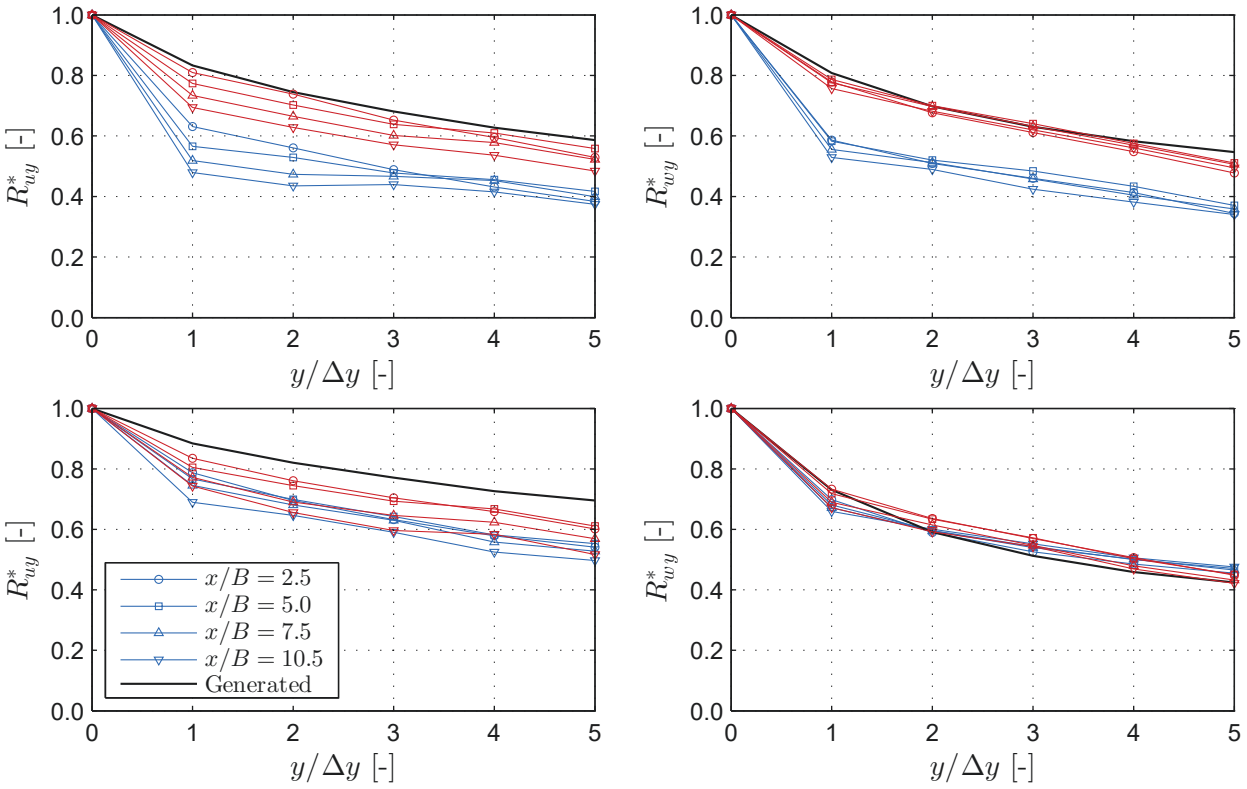

Figure 5.21: Random free-stream turbulence, Pseudo-3D: span-wise correlation coefficient of the generated velocity at the grid and simulated velocity along the centerline $z/B = 0$ for the longitudinal R^*_{uy} (left) and vertical R^*_{wy} (right) components in the isotropic (top) and anisotropic (bottom) cases. Blue color corresponds to VC target coherence model, while red color corresponds to the MC target coherence model for the generated velocity.

this loss is not substantial. This and the fact that the correlation of the vertical fluctuations is constant downstream is a consequence of Taylor's hypothesis. It is important to note that, the simulated correlation coefficients for all cases maintain the exponential shape of decay.

As noise may affect the correlation coefficient, coherence is a more reliable measure to study how the strips are correlated with each other. In particular, the magnitude-squared coherence (from here on referred to as coherence) is used as a basis of discussion as it is straightforward to be obtained from Welch PSD for random signals. In a similar manner as in the previous section, Berzier curves are used to smoothen the magnitude-squared coherence for easier comparison. Initially, the coherence of the generated velocity at the ladder is verified for points with only lateral separation $\boldsymbol{x}_g = (-10.5B, y, 0)$. Figure 5.22 depicts the generated coherence of all slices for VC and MC models in the case of isotropic turbulence. Good correspondence is observed for all strips, without any particular difference between them due to the principle of geometric similarity (cf. Sec. 3.3.1). Further, there is no difference in which target coherence model (VC or MC) is used for the generated velocity. Since the wind generation is a standard method, similar results were obtained for the anisotropic case (not shown).

Figure 5.23 depicts the span-wise coherence of the simulated velocities at the center of the strip $\boldsymbol{x}_c = (0, y, 0)$ for both isotropic (top) and anisotropic (bottom) cases. In both turbulent cases, the simulated coherence for the vertical fluctuation component (cf. Fig. 5.23, right) yielded better results than for the longitudinal one (cf. Fig. 5.23, left). Two reasons seem plausible for this. First, the vertical velocity governs the circulation spectrum, and thus, the circulation

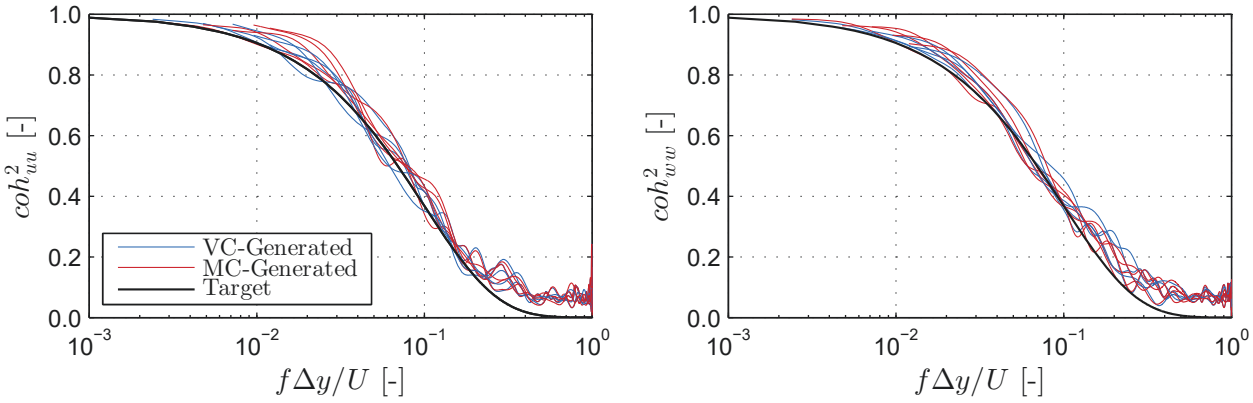

Figure 5.22: Random free-stream turbulence, Pseudo-3D: span-wise coherence of the generated velocity at the grid for the longitudinal coh_{uu} (left) and vertical coh_{ww} (right) components in the isotropic case, obtained using Berzier curves and Welch PSD. Each line corresponds to the coherence of the first strip w.r.t. rest of the strips.

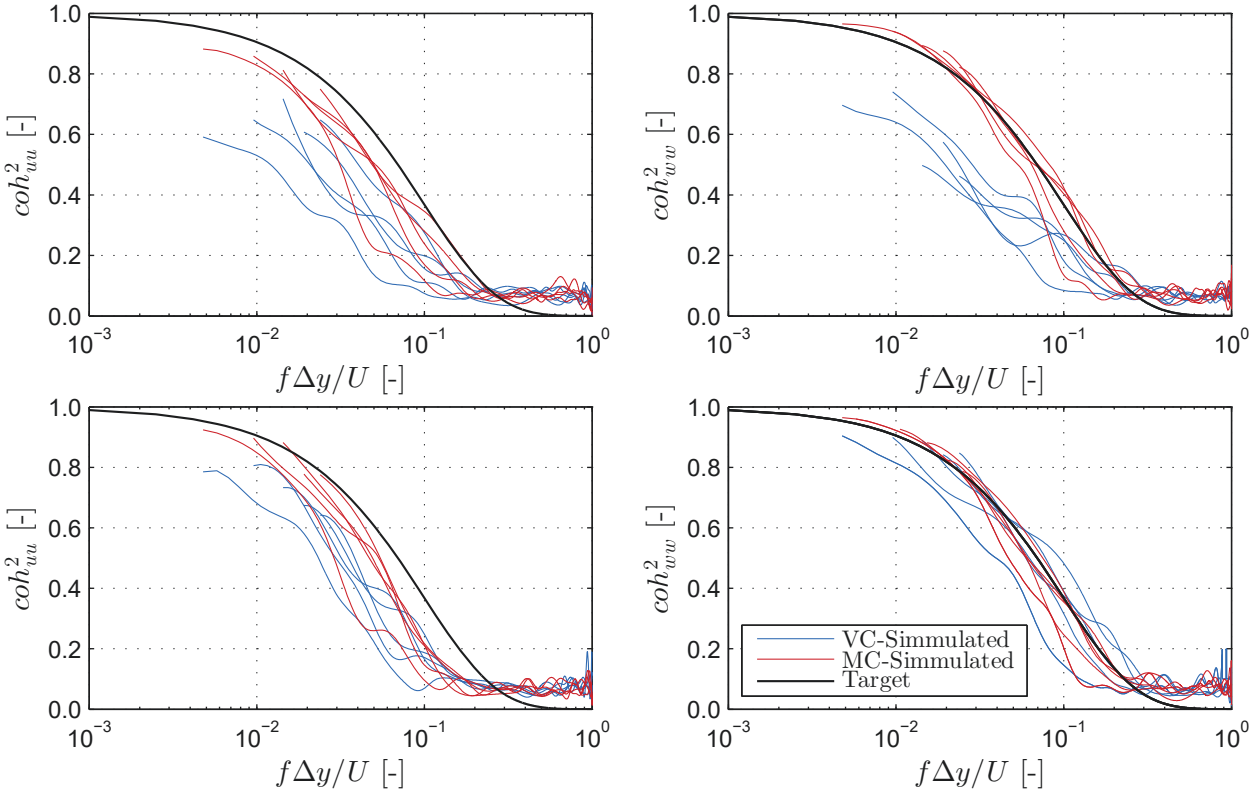

Figure 5.23: Random free-stream turbulence, Pseudo-3D: span-wise coherence of the simulated velocity in the CFD domain at $\boldsymbol{x}_c = (10.5B, y, 0)$ for the longitudinal coh_{uu} (left) and vertical coh_{ww} (right) components in the isotropic (top) and anisotropic (bottom) cases. The coherence is obtained using Berzier curves and Welch PSD. Each line correspond to the coherence of the first strip w.r.t. rest of the strips.

cross-spectrum, which could be seen from the limiting version of the point spectrum S_Γ^{lim} derived in Sec. 3.6.4 (cf. (3.195)). Second, there is a stronger decay of R^* (cf. Fig. 5.21) for the lateral component and thus, simulated coherence is reduced for the point $\boldsymbol{x}_c$. This will be discussed later. Similarly, as for the correlation coefficient, the simulated coherence yields better results if the ladder velocities are generated using the MC model. This is particularly true for the

isotropic case (cf. Fig. 5.23, top), while the difference in the simulated coherence is minor for both VC and MC models in the anisotropic case (cf. Fig. 5.23, bottom). Moreover, the discrepancies in the simulated coherence are similar for both turbulent cases for the MC model. This is not the situation for the VC model since the anisotropic case yield better results than the isotropic. Nevertheless, it is important to note that the shape of the simulated coherence is maintained for all cases w.r.t. the target.

Figure 5.24 depicts the coherence of the simulated velocities between the first and third slice for three points along the centerline $\boldsymbol{x}_g = (0, y, 0)$ in the isotropic case. A decay can be observed in the simulated coherence of the longitudinal velocity for the MC. This explains the discrepancy for the coherence of the simulated longitudinal velocity for the MC model in Fig. 5.23 (left). No such consistent trend can be observed for the VC model and thus, the coherence loss is suspected to be due to numerical uncertainty. In case of the vertical velocity, no decay is noted for both VC and MC models, which is in line with the observation from the correlation coefficient in Fig. 5.21.

To further illuminate the reason why the MC yields better results than the VC for the simulated velocities, the coherence of the circulation at $\boldsymbol{x}_g = (0, y, 0)$ is depicted in Fig. 5.25 for the isotropic case. This circulation coherence is obtained after converting the grid velocities into particles and prior to their release into the CFD domain. In the case of the MC model (cf. Fig. 5.25, left), it can be seen that the target coherence of the circulation is similar as for the velocities i.e. the principle of geometric similarity applies. On the other hand, the target coherence of the circulation is different for each slice for the VC model, i.e. the principle of geometric similarity does not apply. This was noted previously in Sec. 3.6.4. Larger relative discrepancies can be observed for the VC (cf. Fig. 5.25, right) than for the MC model (cf. Fig. 5.25, left). The suspected reason is the numerical noise that is introduced during the conversion from grid velocities into particles (i.e. enforcing divergence-free condition) is relatively high for low absolute values of the target circulation coherence. The values of the target coherence (up to 0.15) are relatively low in the case of the VC model compared to the MC model.

Finally, a parametric study is conducted for different Reynolds numbers for the isotropic case

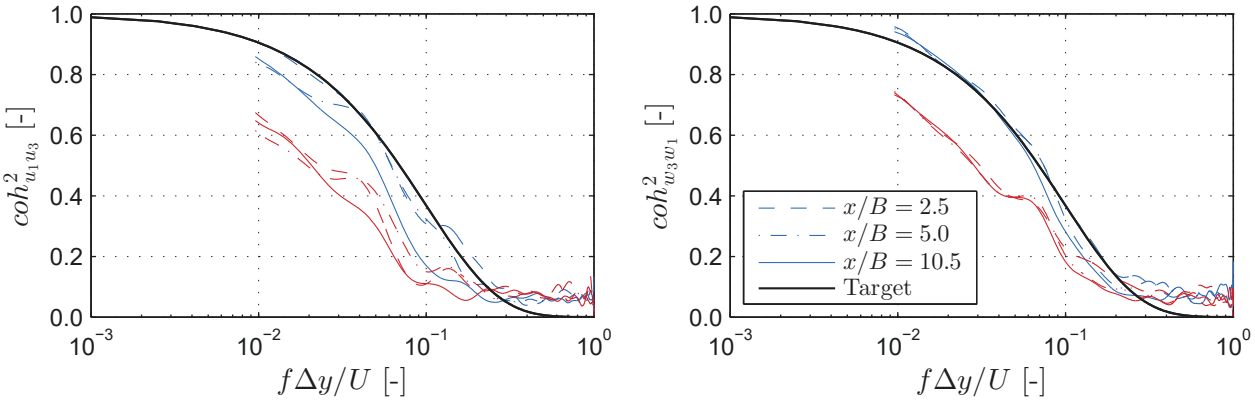

Figure 5.24: Random free-stream turbulence, Pseudo-3D: span-wise coherence of the simulated velocity in the CFD domain at the first $\boldsymbol{x}_{c1} = (x, 0, 0)$ and third strip at $\boldsymbol{x}_{c3} = (x, 2\Delta y, 0)$. The velocities are sampled at three downstream locations of the particle release band in the CFD domain for the longitudinal (left) and vertical (right) components in the isotropic case. Blue color corresponds to the VC target coherence model, while the red color corresponds to the MC target coherence model for the generated velocity.

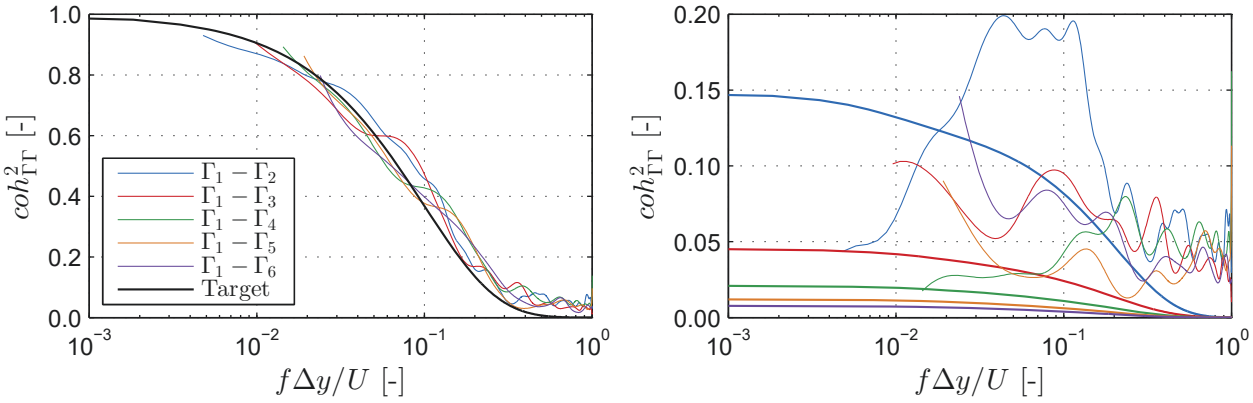

Figure 5.25: Random free-stream turbulence, Pseudo-3D: generated span-wise coherence of the inflow circulation $coh_{\Gamma\Gamma}$ for the MC (left) and VC (right) target coherence model of the ladder velocity. The thick lines represent the target circulation coherence, which in the case of the MC model is a single (black) line due to the principle of geometric similarity. In the case of the VC model, the target circulation coherence of the first strip w.r.t. the rest is different for each strip and is denoted by a thick line in the corresponding color.

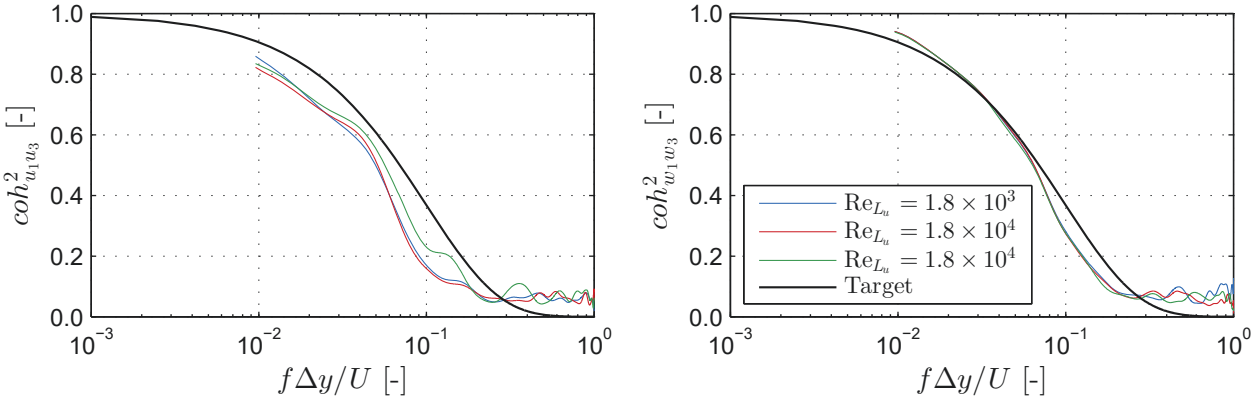

Figure 5.26: Random free-stream turbulence, Pseudo-3D: influence of Reynolds number on the simulated span-wise coherence of the simulated velocity in the CFD domain at the first $\boldsymbol{x}_{c1} = (10.5B, 0, 0)$ and third strip at $\boldsymbol{x}_{c3} = (10.5B, 2\Delta y, 0)$ for the longitudinal (left) and vertical (right) fluctuations for the isotropic case and MC model.

for the MC model. Figure 5.26 depicts the results for the coherence of the simulated velocities between the first and third slice at points $\boldsymbol{x}_{c1} = (0, 0, 0)$ and $\boldsymbol{x}_{c3} = (0, 2\Delta y, 0)$, respectively. Minor loss of coherence for the longitudinal velocity can be seen for lower Reynolds numbers, while the coherence of the vertical velocity appears to be insensitive.

In summary, with the presented turbulent Pseudo-3D VPM method, a significant part of the correlation between strips is retained for both MC and VC models. The MC model yields better results than the VC model for the simulated velocity, particularly for the isotropic case. The discrepancy is not as significant for the anisotropic case. It is important to note that this is a purely numerical consequence for the CFD velocities and it has nothing to do with the underlying physics, i.e. which target coherence model better describes the natural turbulence. Thus, there is no difference in the generated coherence. Further, it is noteworthy to mention that the coherence within the CFD domain is not reported in the studies dealing with bridge vibration due to turbulent wind (cf. e.g. [172, 326]).

5.3.2 Deterministic gusts

In this section, the flow field including a sinusoidal gust with prescribed amplitude and frequency is verified for the introduced numerical active turbulence generator, without a body in the CFD domain. Later this method is used to determine the aerodynamic admittance of bridge decks under sinusoidal gusts. First, the derived analytical closed-form solution (cf. (3.224)) for circulation amplitude prediction is verified with the discrete inverse solution (3.227). With this, the circulation amplitude of the inflow particles can be prescribed for a selected sinusoidal gust amplitude. Next, the flow field across the CFD domain is investigated to study and ensure that the simulated velocity behaves as prescribed along the centerline, i.e. to test the planar wake and non-interference of the wakes assumptions (cf. assumptions i) and ii) from Sec. 3.7.4). Finally, parametric studies are performed for numerical and physical parameters.

The general configuration of the numerical active turbulence generator was presented previously in Fig. 3.14 (cf. Sec. 3.7.4 from Ch. 3). Two cases are studied, in which the fictitious airfoils are assumed to be oscillating out-of- and in-phase, generating longitudinal and vertical sinusoidal gusts, respectively. In the following, these two cases are recalled as the "out-of-phase" and the "in-phase" case. For each case, the prescribed (physical) are given in Tab. 5.5. Further, the selected numerical parameters are given in Tab. 5.6. The particle release factor Δp is selected as such to accommodate either 30 particles per gust length or a minimum of N_{ip}=200 particles for the spatial range of summation l_v. With this condition, the particle release factor amounts to $12 \leq \Delta p \leq 21$ for the prescribed reduced velocity range of $2 \leq V_{rt} \leq 50$.

For easier discussion, a prescribed gust property is denoted by the subscript "t", the gust amplitude by the subscript "0", and the velocity along the centerline by the subscript "c".

Circulation amplitude

Initially, the given closed-form solution for the analytical method (cf. (3.224)) for the computation of the circulation of the amplitude of the inflow particles Γ_{F0}^{in} is verified with the inverse one (cf. (3.227)). Figure 5.27 depicts the normalized circulation amplitude for the selected reduced velocity range. The results correspond well between both methods, except at $V_{rt} = 2$, where issues were noted in the pseudo-inverse procedure for the inverse method.

Turbulent case	Physical parameter		Value
Out-of-phase	Wind speed:	U	30 m/s
	Longitudinal amplitude:	u_{ct0}/U	5 %
	Vertical amplitude:	w_{ct0}/U	0 %
	Airfoil distance:	l_R/B	1
	Reduced velocities:	V_r	2-50
	Reynolds number:	Re	1×10^4
In-phase	Wind speed:	U	30 m/s
	Longitudinal amplitude:	u_{ct0}/U	0 %
	Vertical amplitude:	w_{ct0}/U	5 %
	Airfoil distance:	l_R/B	1
	Reduced velocities:	V_r	2-50
	Reynolds number:	Re	1×10^4

Table 5.5: Deterministic free-stream turbulence: prescribed physical parameters for the two turbulent cases for reference dimension $B = 31$ m.

Numerical parameter		Value
Domain length:	l_d/B	21
Domain height:	l_h/B	10.5
Vorticity support:	l_v/B	20.5
Reduced time-step	$\Delta\tau = \Delta t U/B$	$5{\times}10^{-3}$
Total time:	$\tau = tU/B$	$22 - 550$
Core radius:	ϵ/B	$5.5{\times}10^{-3}$
Poisson grid:	$N_x \times N_z$	1023×511
P^{3}M neighboring cells:	N_r	4
Particle release factor:	$\Delta p = \Delta t_{in}/\Delta t$	$12 - 21$

Table 5.6: Deterministic free-stream turbulence: numerical parameters for reference dimension $B =$ 31 m. The value of the particle release factor Δp is based on the reduced velocity V_r.

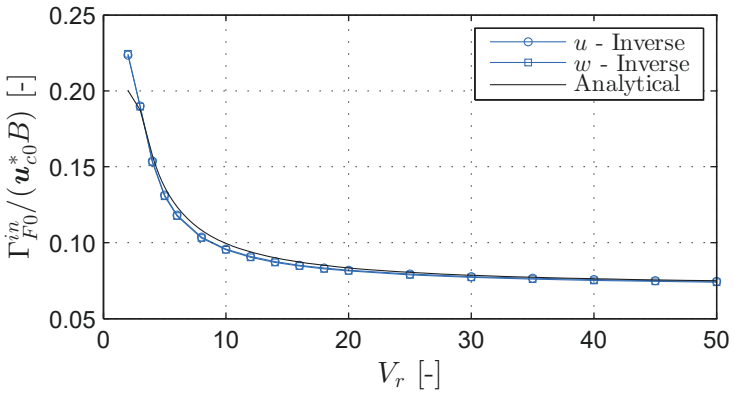

Figure 5.27: Deterministic free-stream turbulence: verification of closed-form analytical solution (cf. (3.224)) with the inverse method (cf. (3.227)) for prediction of the circulation amplitude Γ^{in}_{F0}. The vertical and longitudinal components correspond to the out-of- and in-phase cases, respectfully, which are computed separately.

Flow field

Figure 5.28 depicts time-histories of the velocity fluctuations and their corresponding FFTs at point $\boldsymbol{x}_c = (5B, 0, 0)$ at $V_{rt} = 16$ for both cases. Clear sinusoidal signals can be observed for the longitudinal and vertical velocity fluctuations. In the in-phase case, there is a longitudinal component in addition to the vertical fluctuations. However, the amplitude of this component is an order of magnitude lower than the amplitude of the vertical fluctuations. Theoretically, for an in-phase motion of the airfoils, there should not be a longitudinal component. Moreover, the vertical fluctuation amplitude is slightly underestimated.

To study the origin of these discrepancies, Figs. 5.29 and 5.30 present three instantaneous particle maps and instantaneous magnitude of the fluctuating velocity at $V_{rt} = 16$, for both cases. The snap-shots corresponding to the minimum, zero and maximum velocity at $\boldsymbol{x}_c$, as indicated on the time-histories in Fig. 5.28. It can be observed that the particles are not convected along a horizontal line, particularly for the in-phase case. The planar-wake assumption is more reasonable for the out-of-phase case, as the instability of one wake is counteracted by the other. On the contrary, this instability is enhanced in the in-phase case. Thus, the discrepancies in the gust amplitudes and the secondary fluctuating components are a consequence of violating the planar wake and non-interference assumptions. The sinusoidal variation of

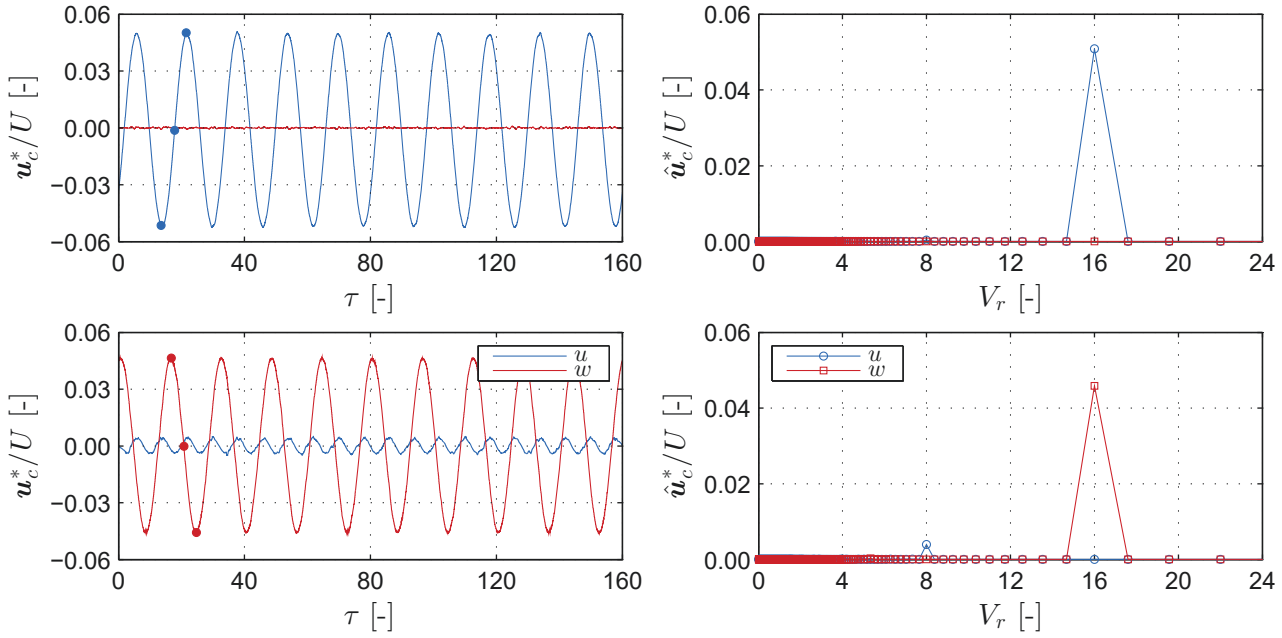

Figure 5.28: Deterministic free-stream turbulence: sample velocity time-histories, u_c and w_c (left), and their corresponding FFTs, $\hat{u}_c$ and $\hat{w}_c$ (right), for the out-of-phase (top) and in-phase (bottom) cases at gust tracking point $\boldsymbol{x}_c = (5B, 0, 0)$. The indicated full circles on the time-histories correspond to the instantaneous snapshots in Figs. 5.29 and 5.30.

the velocity for the out-of-phase case is only between the wakes, while for the in-phase case there is variation outside this region (cf. Fig. 5.29 and 5.30, right). Figure 5.31 depicts the instantaneous particle maps of three reduced velocities. As expected, this discrepancy is more prominent for lower reduced velocities in the neighborhood of the particle release locations due to the variation of the circulation over shorter gust-lengths. Nevertheless, it is important that the body is positioned in the region between the two wakes to avoid particles entering the body.

For the computation of the aerodynamic admittance, it is important that the body is immersed in a uniform sinusoidal gust, while the gust amplitude is of minor significance as the aerodynamic forces are considered to be linear. In order to correctly position a section within the domain, it is of interest to study the gust uniformity and its harmonic component. Thus, a relative quality parameter Q is introduced. This parameter quantifies the energy of a fluctuating velocity at a single prescribed frequency f_t, relative to the total energy of both fluctuating velocities. The gust quality for the out-of-phase and in-phase cases, respectively, is defined based on the PSDs of the longitudinal $S_u = S_u(\boldsymbol{x}; f)$ and vertical $S_w = S_w(\boldsymbol{x}; f)$ velocities as

$$Q_u = \frac{S_u\left(f_t\right)}{\int_0^\infty \left[S_u\left(f\right) + S_w\left(f\right)\right] \mathrm{d}f}, \quad Q_w = \frac{S_w\left(f_t\right)}{\int_0^\infty \left[S_u\left(f\right) + S_w\left(f\right)\right] \mathrm{d}f}. \tag{5.10}$$

Therefore, the gust quality Q and relative gust amplitude ratios, u_0/u_{t0} and w_0/w_{t0}, are the SRQ of interest for the flow field involving deterministic gusts.

Figure 5.32 depicts the influence of the reduced velocity on flow quantities of interest along the centerline $\boldsymbol{x}_c = (x_c, 0, 0)$ for both cases. After the particle release location, there is a certain length, in which the gust amplitudes converge (cf. Fig. 5.32, left). This convergence length is longer for the in-phase case and is also dependent on the reduced velocity. In the out-of-phase case, the gust amplitudes generally agree well with the prescribed ones. In the in-phase case, the situation is slightly different. Beyond the convergence length, the gust amplitudes begin

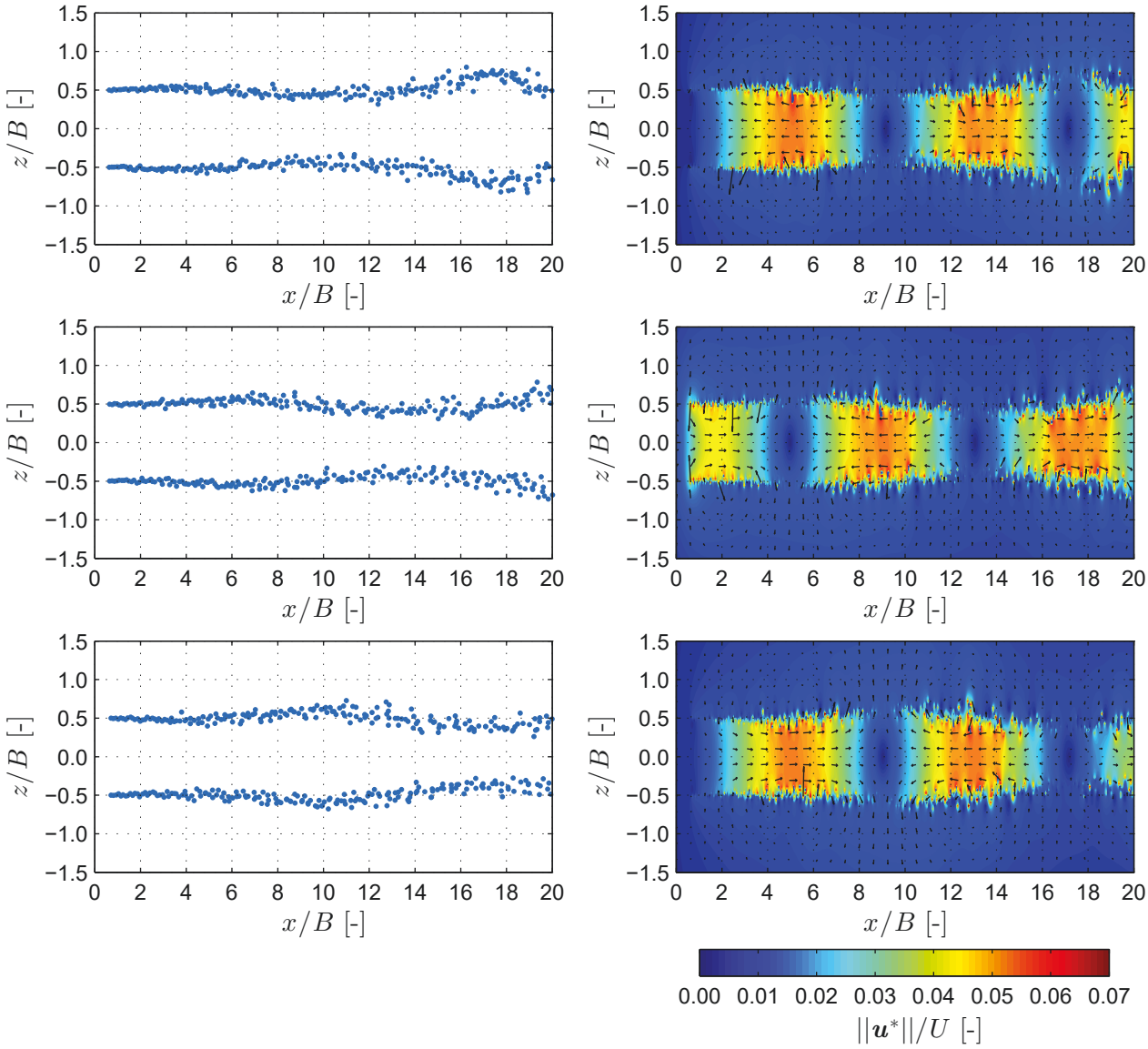

Figure 5.29: Deterministic free-stream turbulence: instantaneous particle maps (left) and fluctuating velocity magnitude fields $\|\boldsymbol{u}^*\|$ (right) for the out-of-phase case at $\tau = 13.5, 17.5, 21.5$ (top to bottom) for $V_{rt} = 16$. The instantaneous snapshots correspond to the indicated full circles in Fig. 5.28 for the out-of-phase case (top).

to "wobble", which is probably due to the distortion of the particle path (cf. Fig. 5.31). For gust lengths which are longer than half of the domain (i.e. $V_{rt} \geq 10$), the convergence length is not reached and this behavior is not observed. The prediction of the magnitude of oscillation is within the ± 20 % range, taking the "wobbling" into account in the region of $2 < x_c/B < 10$. Eighty percent of the prescribed gust amplitude is achieved at $V_{rt} = 45$, i.e. $w_{c0}/w_{ct0} = 0.8$.

The gust quality Q is more important than the prediction of gust amplitude for the aerodynamic admittance. Figure 5.32 depicts the quality parameters for the out-of-phase (top-right) and in-phase (bottom-right) case. It can be observed that the quality decays for points which are further downstream of the particle release locations for the in-phase case, which is due to violation of the planar wake assumption. Nevertheless, for a quality parameter more than 0.9, it can be assumed that the gust is considered as sinusoidal and most of the fluctuating energy is concentrated at a single vertical frequency, which is the situation for the out-of-phase case.

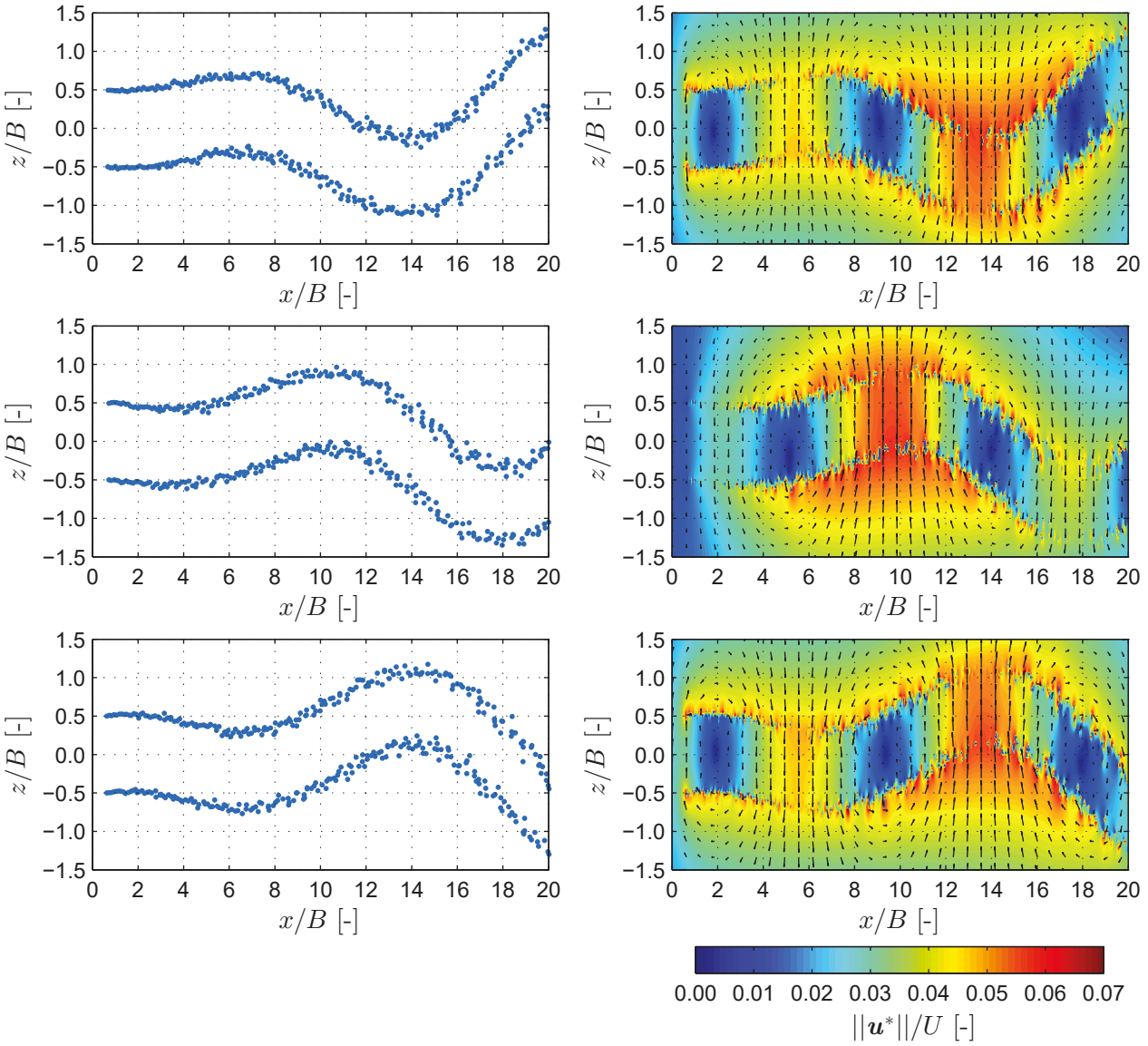

Figure 5.30: Deterministic free-stream turbulence: instantaneous particle maps (left) and fluctuating velocity magnitude fields (right) for the out-of-phase case at $\tau = 13.5, 17.5, 21.5$ (top to bottom) for $V_{rt} = 16$. The instantaneous snapshots correspond to the indicated full circles in Fig. 5.28 for the in-phase case (bottom).

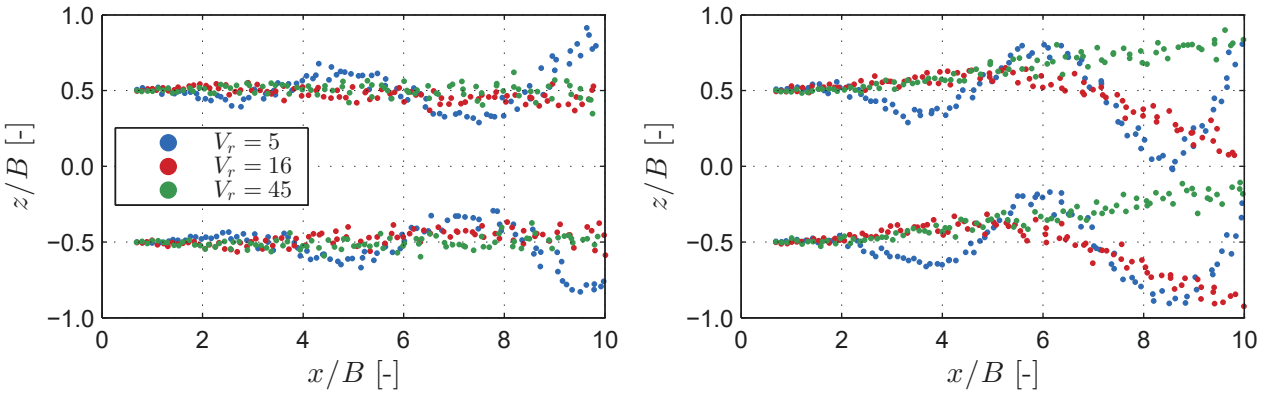

Figure 5.31: Deterministic free-stream turbulence: instantaneous particle maps of various reduced velocities for the out-of-phase (left) and in-phase (right) cases.

Besides sufficient gust quality and amplitude uniformity along the centerline, it should be ensured that these quantities are uniform along the depth of the section. Figure 5.33 depicts the deviation of the gust amplitude along the height w.r.t. the one at the centerline for three vertical profiles. Moreover, the gust quality is included in the figure. The difference in the amplitude is appearing mostly for the out-of-phase case nearby the particle release locations and is more prominent for low reduced velocities. This is in line with the previous observations based on the velocity vector field (cf. Fig. 5.29). For the in-phase case, the deviation of the gust amplitude is even less obvious. Generally, the deviation of the gust amplitude along the height is relatively mild for both cases. The discrepancies of gust quality along the height are somewhat larger than the gust amplitudes. It can be observed that there is a certain band w.r.t. the centerline, for which the quality is relatively constant (cf. Fig. 5.33). This band reduces for vertical profiles, positioned further downstream of the particle release locations. It is important that the section is within the limits of this band for the aerodynamic admittance is computed.

Stapountzis [309] introduces a non-dimensional gust intensity to quantify the relation between the gust amplitude and oscillation amplitude of the airfoils $\boldsymbol{u}^*_{c0}/(U\alpha_F 0)$, valid for both components separately. In the case of the analytical method for the solution of the mathematical model, this relation is in closed-form. For the inverse method, the input variable is the gust intensity, u_{ct0} or w_{ct0}, while α_{F0} is obtained from the circulation (cf. Eqs. (3.227)), as noted by Harding and Bryden [130]. The input variable in the CFD model is the airfoil amplitude α_{F0}, since it is directly related to the circulation amplitude Γ^{in}_{F0}, while the simulated gust intensity u_{c0} or w_{c0} is the output variable. Figure 5.34 depicts the non-dimensional gust intensities for

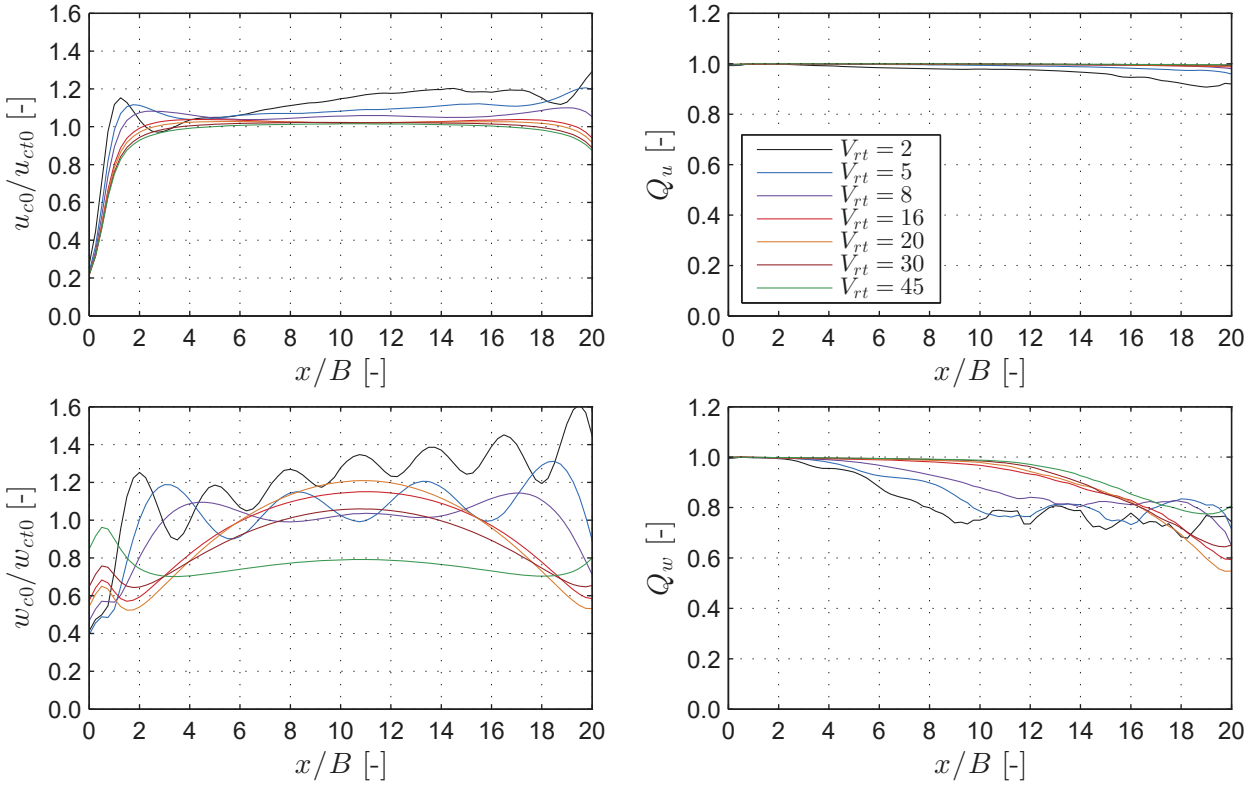

Figure 5.32: Deterministic free-stream turbulence: relative gust amplitude (left) and quality (right) for various reduced velocities for the out-of-phase (top) and in-phase (bottom) cases along the centerline $z/B = 0$.

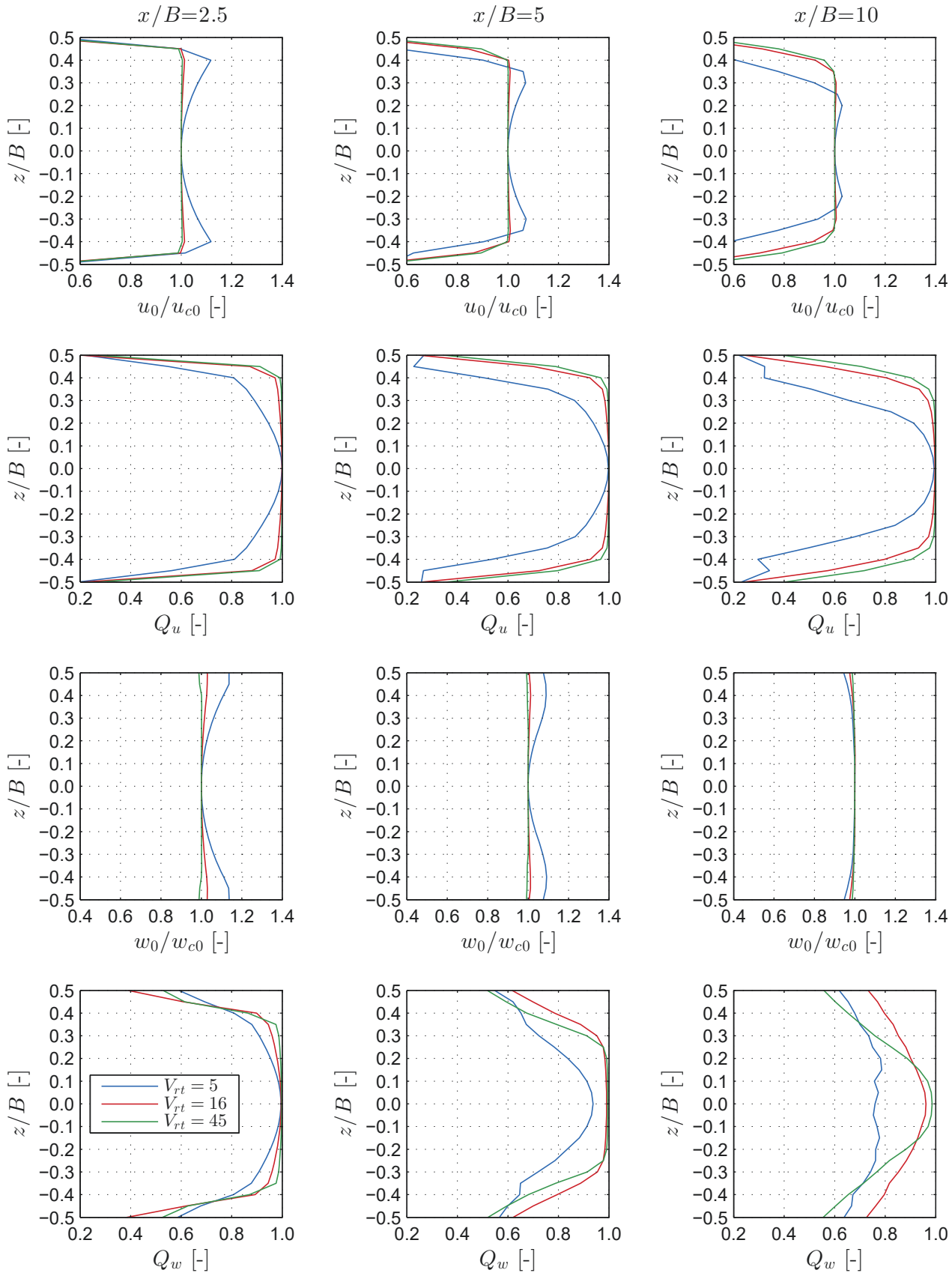

Figure 5.33: Deterministic free-stream turbulence: relative gust amplitude for out-of-phase case $u_0/uc0$ (top); gust quality for out-of-phase case Q_u (center-top); relative gust amplitude for in-phase case $w_0/wc0$ (center-bottom); gust quality for in-phase case Q_w (bottom). The quantities of interest are plotted for various reduced velocities and are sampled at three profiles downstream (see title).

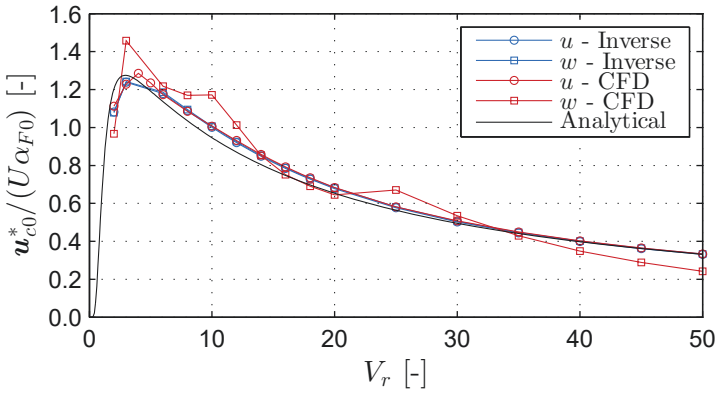

Figure 5.34: Deterministic free-stream turbulence: dimensionless gust intensity $\boldsymbol{u}_{c0}/(U\alpha_{F0})$ for the inverse and analytical solution of the mathematical model and the CFD model. The vertical and longitudinal components correspond to the out-of- and in-phase cases, respectfully, which are computed separately.

the CFD and mathematical model, the latter solved using the inverse and analytical methods. For the CFD model, the point for the gust amplitude is selected such to ensure a gust quality above $Q \geq$0.9 and the inflow particles are not crossing the centerline. Thus, the tracking point for the simulated velocity is selected as x_c/B=2 for $V_{rt} \leq$4; x_c/B=5.5 for $4 < V_{rt} \leq 16$; and x_c/B=10 for $V_{rt} <$16. Generally, good correspondence is obtained for the models, with small discrepancies for very low reduced velocities and for gust lengths which are significantly longer than the domain length for the in-phase case.

Parametric studies

Parametric studies are conducted for one numerical and three physical parameters. The numerical parameter considered is the domain length l_d, while the physical parameters considered are the gust amplitudes u_{ct0} and w_{ct0}, and airfoil distance l_R and Reynolds number Re.

First, the influence of the domain length is depicted in Fig. 5.35. It can be observed that only the vertical gust amplitudes for high reduced velocities are in better correspondence with the prescribed values for increasing l_d/B ratio. This is expected as there is sufficient vorticity support to describe the whole gust length. The rest of the numerical parameters (e.g. particle release factor or core radius) are expected to influence the gust quality and amplitude in a similar fashion as discussed in the previous section for random free-stream (cf. Sec. 5.3.1). Thus, the lowest reduced frequency should be larger than the one corresponding to the Nyquist frequency for the generated velocity f_{sg} or core cutoff frequency $f_{s\epsilon}$ (cf. (5.6) and (5.9)).

Second, the influence of gust amplitude is shown in Fig. 5.36. The quality of the vertical gusts decays more rapidly for higher gust amplitudes. It is also expected that for high gust amplitudes, the wake is significantly distorted.

Third, from Fig. 5.37 it can be gathered that increasing the l_R/B ratio increases the vertical gust quality for high reduced velocities. However, for very large l_R/B ratios, the quality of the gust is expected to be reduced due to the high circulation amplitudes required for a specific gust amplitude. This would effectively contribute to the violation of the planar wake assumption.

Finally, Fig. 5.36 depicts the influence of Reynolds number. No particular influence of the viscosity is observed on the gust amplitude nor quality for selected gust lengths.

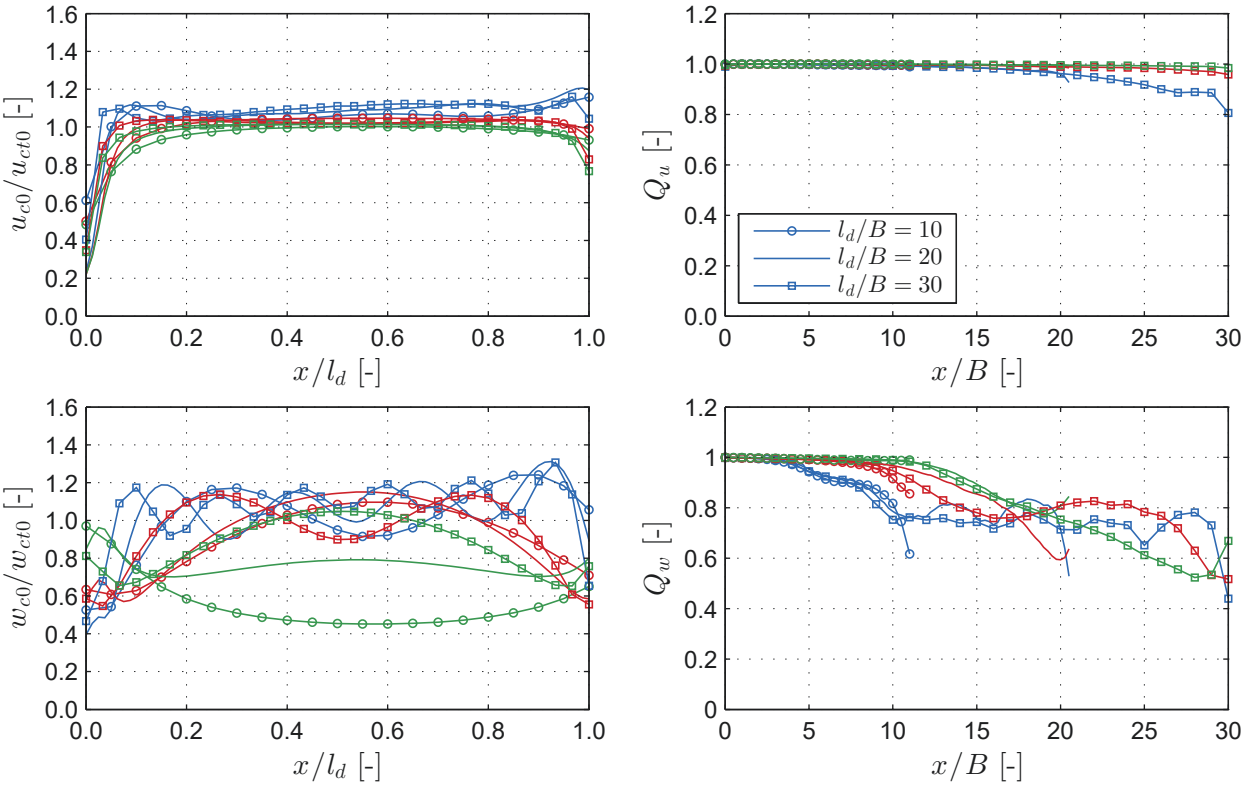

Figure 5.35: Deterministic free-stream turbulence, parametric studies: effect of domain length on the relative gust amplitude (left) and quality (right) for the out-of-phase (top) and in-phase (bottom) cases along the centerline $y/B = 0$. Reduced velocities considered: $V_{rt} = 5$ (blue), $V_{rt} = 16$ (red), $V_{rt} = 45$ (green).

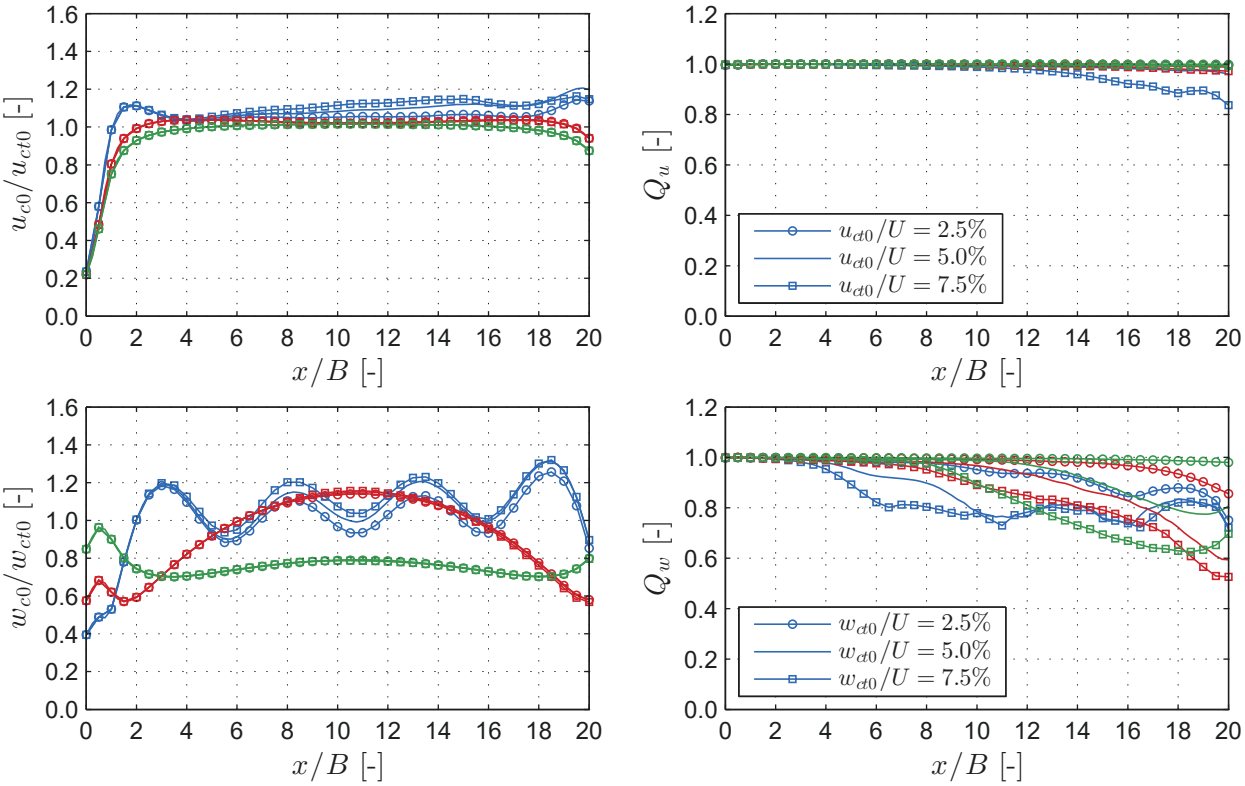

Figure 5.36: Deterministic free-stream turbulence, parametric studies: effect of gust amplitude on the relative gust amplitude (left) and quality (right) for the out-of-phase (top) and in-phase (bottom) cases along the centerline $y/B = 0$. Reduced velocities considered: $V_{rt} = 5$ (blue), $V_{rt} = 16$ (red), $V_{rt} = 45$ (green).

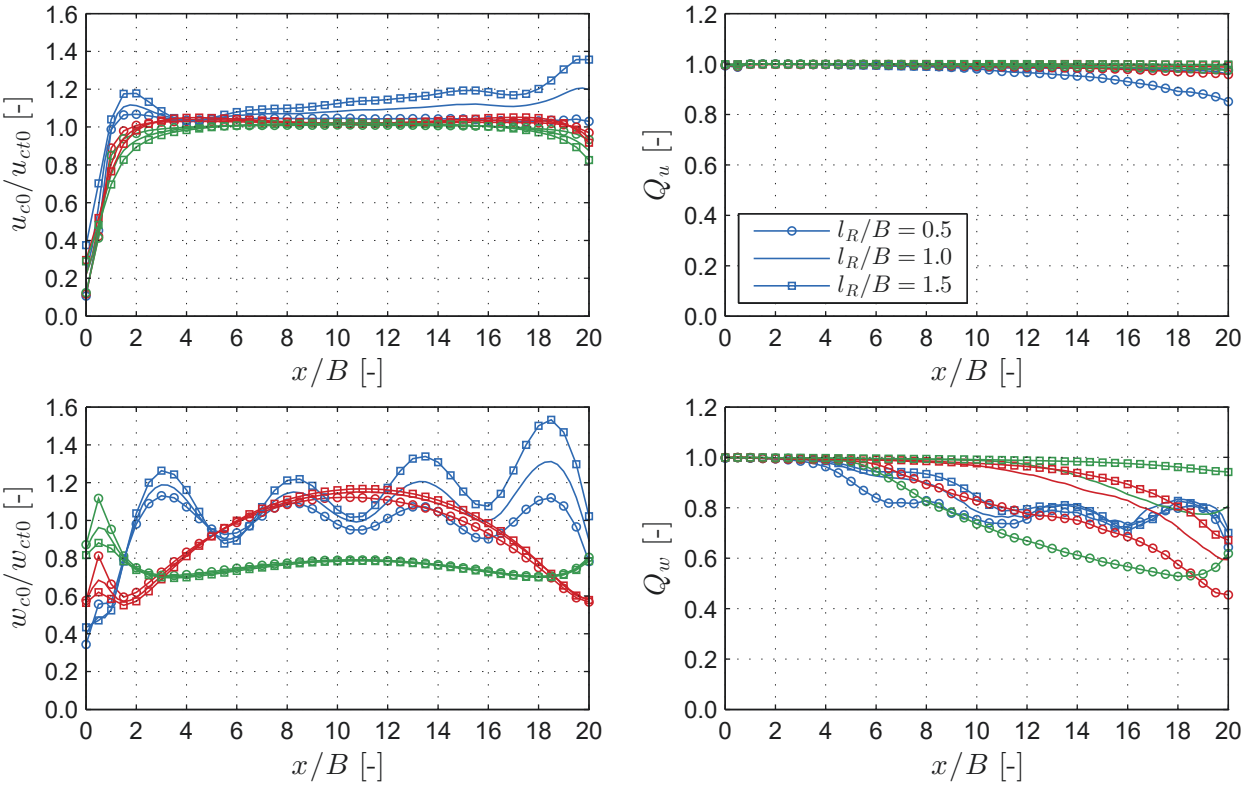

Figure 5.37: Deterministic free-stream turbulence, parametric studies: effect of airfoil distance on the relative gust amplitude (left) and quality (right) for the out-of-phase (top) and in-phase (bottom) cases along the centerline $y/B = 0$. Reduced velocities considered: $V_{rt} = 5$ (blue), $V_{rt} = 16$ (red), $V_{rt} = 45$ (green).

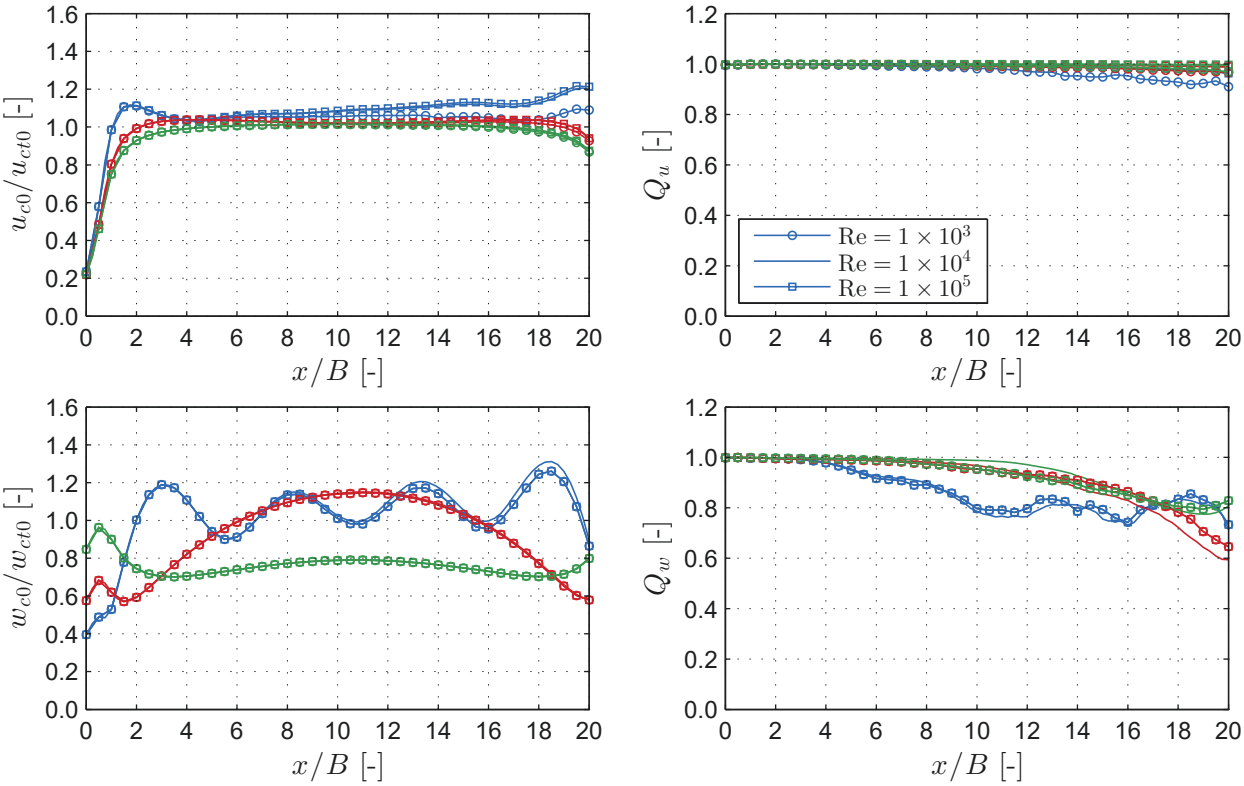

Figure 5.38: Deterministic free-stream turbulence, parametric studies: effect of Reynolds number on the relative gust amplitude (left) and quality (right) for the out-of-phase (top) and in-phase (bottom) cases along the centerline $y/B = 0$. Reduced velocities considered: $V_{rt} = 5$ (blue), $V_{rt} = 16$ (red), $V_{rt} = 45$ (green).

5.4 Flat Plate

The aerodynamics of an infinitely thin flat plate represents a simple, yet a benchmark study for verification of the aerodynamic forces and response in the linear range. The potential flow solution for the linear aerodynamic forces presented in Sec. 3.4 can be used for verification of the CFD model for an appropriate Reynolds number.

The main goal of this section is to verify the CFD model (cf. (3.184)) in a synergistic manner for both laminar and turbulent free-stream. Having verified the turbulent free-stream, the aerodynamic coefficients and results from aeroelastic analyses are compared against their analytical counterparts. Particular aspects that relate to the novel contribution of this work are:

i) verification of the complex aerodynamic admittance for deterministic free-stream turbulence (cf. Sec. 3.6.2),

ii) verification and comparison of the aerodynamic admittance for random free-stream based on von Kármán spectra (cf. Sec. 3.7.3),

iii) verification of the presented FFT method for computation of the unsteady buffeting forces (cf. Sec. 3.5.7)

iv) verification of the CFD buffeting response with time- and frequency-domain analytical flat plate model (one-to-one and statistical comparisons),

v) application the comparison metrics to the buffeting response (cf. Sec. 4.3).

In addition to these aspects, a verification is performed for the laminar boundary layer, static wind coefficients, rational approximation, and critical flutter velocity. The aerodynamic forces are of main interest for the present work; thus, quantities from fluid dynamics such as the boundary layer are only briefly discussed.

The simulations performed are for a laminar and turbulent free-stream with a static or dynamic section depending on the quantity of interest. Thus, the structural and flow physical parameters are given in Tab. 5.7, while the numerical parameters are given in 5.7. The center of the plate is positioned at $\boldsymbol{x}_s = (x_s, 0, 0) = (10.5B, 0, 0)$. These parameters represent the baseline and are used for the analyses unless noted otherwise. As the plate is very thin, it is expected that the particles cross the plate due to motion, free-stream turbulence or due to the random walk in the viscous step. These crossing particles are deleted in a simple manner as adopted by Morgenthal [226].

5.4.1 Boundary layer

The surface boundary layer of a viscous fluid for an infinitely long flat plate was first analytically derived by Blasius in his Ph.D. thesis [24, 25] in 1907, who even solved it numerically by hand for four discrete values. Although the fluid behavior, and thus boundary layer, is not of primary importance for this study, it can give an overall idea of how well the simulation can replicate flow around immersed boundaries and what are the Reynolds number effects. With this, an appropriate Reynolds number can be selected for the aeroelastic analyses that assures potential flow to some extent and the flat plate analytical model can be used for verification. Thus, the Reynolds number should be high enough, so that the viscous effects are minimized, and low enough, so that the aftermath of laminar to turbulent transition is reduced.

Property type	Physical parameter		Value
Structural	Plate width:	B	31 m
	Plate depth:	H_D/B	1/200
	Mass:	m_h	22.74 t/m
	Inertial mass:	m_α	2.47×10^3 tm^2/m
	Vertical frequency:	f_h	0.1 Hz
	Torsional frequency:	f_α	0.278 Hz
	Damping ratio:	ξ	0.5 %
	Forced oscillation:	V_r	$2-50$
	Forced oscillation amplitude:	$\alpha_0 = \dot{h}_0/U$	3 deg
Laminar free-stream	Wind speed:	U	20 m/s
	Reynolds number:	Re	1×10^4
Random free-stream	Longitudinal intensity:	TI_u	5 %
	Vertical intensity:	TI_w	5 %
	Longitudinal length scale:	L_u/B	4
	Vertical length scale:	L_w/B	2
	Turbulent Reynolds number:	Re_{L_u}	4×10^4
	Coherence coefficient:	$\boldsymbol{c}_x = (C_x, C_z)$	(3, 10)
Deterministic free-stream	Longitudinal amplitude:	u_{c0}/U	0
	Vertical amplitude:	w_{c0}/U	5 %
	Airfoil distance:	l_R/B	1
	Reduced velocities:	V_r	$2-50$

Table 5.7: Flat plate: prescribed physical parameters for all analyses. These parameters represent the baseline and are used unless noted otherwise.

Numerical parameter		Value
Domain length:	l_d/B	21
Domain height:	l_h/B	21
Number of panels:	N_{pan}	402
Panel length:	$\Delta l_{pan}/B$	5×10^{-3}
Reduced time-step:	$\Delta\tau = \Delta t U/B$	5×10^{-3}
Core radius:	ϵ/B	5.5×10^{-3}
Poisson grid:	$N_x \times N_z$	1023×1023
P^{3}M neighboring cells:	N_r	4
Vorticity support:	l_v/B	20.5
Particle release factor (deterministic):	$\Delta p = \Delta t_{in}/\Delta t$	12-21
Particle release factor (random):	$\Delta p = \Delta t_{in}/\Delta t$	4
Particle band height:	l_G/B	18
Correction factor:	β_{in}	0.7

Table 5.8: Flat plate: prescribed numerical parameters for all analyses. These parameters represent the baseline and are used unless noted otherwise.

The boundary layer profile can be obtained from a third-order differential equation as

$$gg'' + 2g''' = 0, \tag{5.11}$$

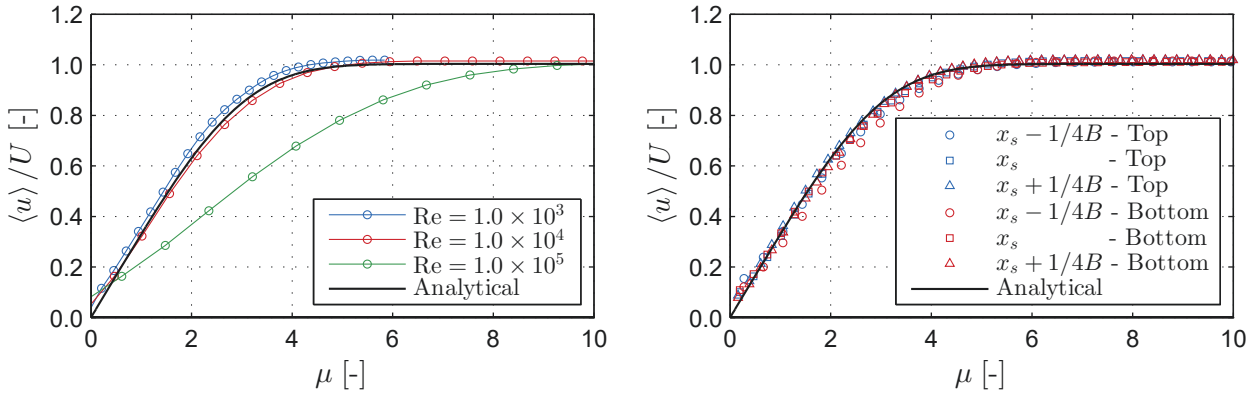

Figure 5.39: Flat plate: boundary layer at center of the plate $\boldsymbol{x}_s = (x_s, 0, 0)$ for various Reynolds numbers (left); boundary layer at top and bottom surface at three locations for Reynolds number $\mathrm{Re} = 1 \times 10^4$ (right). The analytical result is according to the Blasius solution.

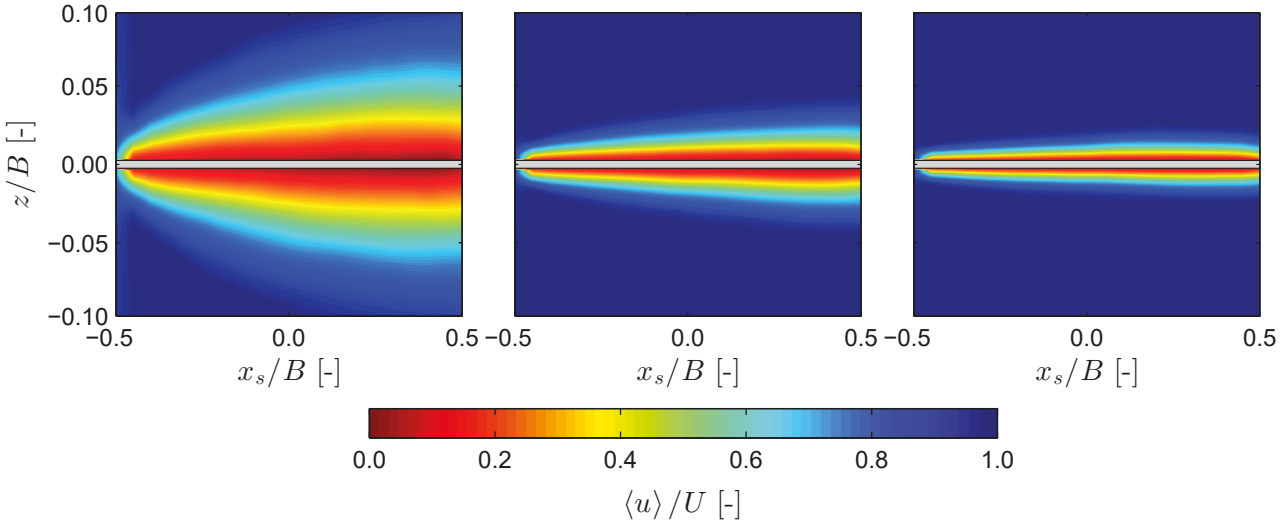

Figure 5.40: Flat plate: averaged longitudinal velocity field $\langle u \rangle$ for laminar free-stream at Reynolds number $\mathrm{Re} = 1 \times 10^3$ (left); $\mathrm{Re} = 1 \times 10^4$ (center); $\mathrm{Re} = 1 \times 10^5$ (right).

where $g = g(\mu) = u(\mu)/U$, the similarity parameter μ is

$$\mu = z\sqrt{\frac{U}{\nu x_s}}, \tag{5.12}$$

and the prime denotes differentiation w.r.t. μ.

The boundary layer is computed at three Reynolds numbers $\mathrm{Re} \in \{1 \times 10^3, 1 \times 10^4, 1 \times 10^5\}$. To reduce the statistical error due to the viscous step, the results are averaged for a reduced time equivalent to one chord i.e. $\tau = 1$. Figure 5.39 (left) depicts the results at the center of the plate for all Reynolds numbers. Good correspondence can be observed for $\mathrm{Re} = 1 \times 10^4$, while small overshooting is present for $\mathrm{Re} = 1 \times 10^3$. As expected, the boundary layer is unstable for $\mathrm{Re} = 1 \times 10^5$ and completely deviated from the Blasius profile due to laminar to turbulence transition. Figure 5.39 (left) depicts the results for the top and bottom surface at the center, front and back quarter points of the plate for $\mathrm{Re} = 1 \times 10^4$. Based on this and the velocity field depicted in Fig. 5.40, it can be concluded that the symmetry of the flow is mostly preserved. Figure 5.41 shows instantaneous particle maps of all Reynolds numbers. Unlike for the lower

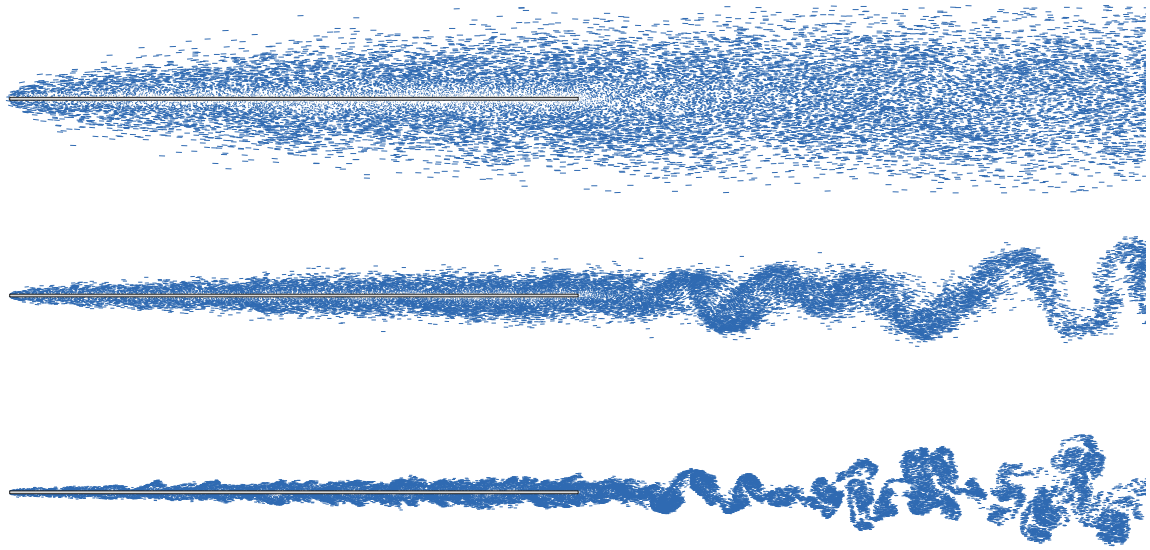

Figure 5.41: Flat plate: instantaneous particle maps of horizontal plate ($\alpha_s = 0$) at Reynolds number $\mathrm{Re} = 1 \times 10^3$ (top); $\mathrm{Re} = 1 \times 10^4$ (center); $\mathrm{Re} = 1 \times 10^5$ (bottom).

Reynolds numbers, coherent structures formed by vortex blobs transmit along the plate for $\mathrm{Re} = 1 \times 10^5$ indicating breaking of the boundary layers. Similar results have been obtained using the Vortex methods first by Chorin [64] nearly 40 years ago, and then by Walther [342] and Morgenthal [226].

Based on the previous discussion and results, the Reynolds number of $\mathrm{Re} = 1 \times 10^4$ is selected as a baseline for the aeroelastic analyses and verification. The aerodynamic coefficients are determined for all three Reynolds numbers.

5.4.2 Static wind coefficients

The initial step to verification of the aerodynamics is the static wind coefficients for varying angle of attack. The linear hypothesis for a thin flat plate, used to obtain the analytical slopes of the lift and moment coefficients (cf. Sec. 3.4 and (3.49)), is valid for small angles of attack. For large angles of attack, the flow completely separates from the top surface leading to "dead air" in the wake [9]. This results in a peak of the lift coefficient, i.e. stall (cf. Fig. 3.6 from Sec. 3.5), in which region the lift coefficient is nonlinear. As the purpose of the present analysis is verification, in which the analytical flat plate model is valid, only the linear range is of interest. Early experiments conducted by Zahm et al [372] indicate that this range is 6 deg$< \alpha_s <$ 6 deg for a flat plate with $H_D/B \approx 50$ at $\mathrm{Re} \approx 1.5 \times 10^5$ (calculated by the author).

Figure 5.42 depicts the lift and moment coefficients for varying static angle of attack at the selected Reynolds numbers for averaging time $\tau = 75$. Generally, a linear trend and good correspondence can be observed with the theoretical lift and moment slopes of 2π and 0.5π, particularly for the at Reynolds numbers of 1×10^4 and 1×10^5. The lift slope is determined as $C'_L \in \{2.34\pi, 1.94\pi, 2.00\pi\}$, while the moment slope is $C'_M \in \{0.50\pi, 0.46\pi, 0.48\pi\}$ corresponding to the Reynolds number $\mathrm{Re} \in \{1 \times 10^3, 1 \times 10^4, 1 \times 10^5\}$, respectively. The highest discrepancy is found in the increase of the lift slope at 1×10^3. This is not in line with some numerical (cf. Wang et al. [343] for $\mathrm{Re} = 3 \times 10^2$) and experimental (cf. Suanda et al. [314] for $\mathrm{Re} = 4 \times 10^3$) studies for insect and birds flights for very low Reynolds number that show

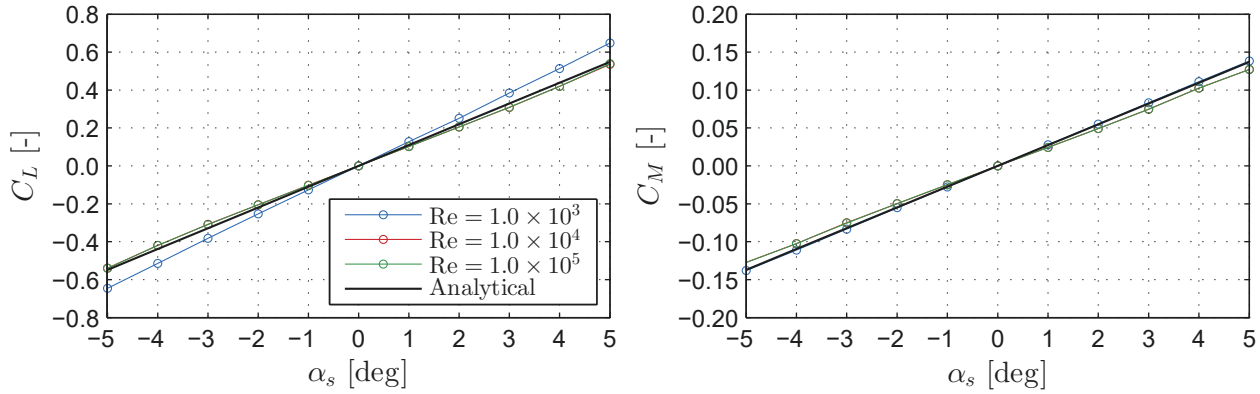

Figure 5.42: Flat plate: lift C_L (left) and moment C_M (right) static wind coefficients.

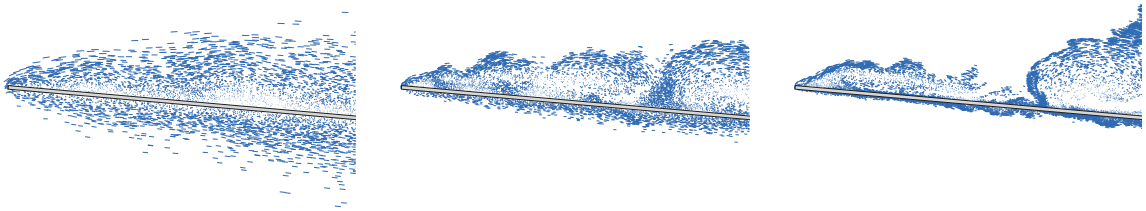

Figure 5.43: Flat plate: instantaneous particle maps of inclined plate ($\alpha_s = 4$ deg, only quarter plate is shown) at Reynolds number $\mathrm{Re} = 1 \times 10^3$ (left); $\mathrm{Re} = 1 \times 10^4$ (center); $\mathrm{Re} = 1 \times 10^5$ (right).

reduction of the thin-airfoil theory slope. The loss of lift is typically a consequence of separation at the top surface [9]. For very low Reynolds numbers, the viscous forces delay or even permit reattachment of the laminar separated bubble, as discussed comprehensively by Shyy et al. [300]. Figure 5.43 depicts instantaneous particle maps at $\alpha_s = 5$ deg for the three Reynolds numbers. One can observe that there are reattaching vorticial structures for the Reynolds numbers of order 10^4 and 10^5, while that is not obvious for 10^3. Although the observation from the particle maps is reasonable and consistent to some extent with previous studies, the inconsistencies in the lift are believed to be due to the deleting the vortex particles that cross the plate for $\mathrm{Re} = 1 \times 10^3$. At this Reynolds number, the viscous forces are the strongest, thus, the particle displacement is the highest in the random walk. In fact, the plate thickness was constrained by Walther [342] depending on the Reynolds number to reduce the probability of particles crossing the plate due to the random walk. However, further analyses are required on this account. In the case of thin airfoils for $\mathrm{Re} > 3 \times 10^4$, most of the experimental studies show that the stall is delayed with insignificant changes in the lift slope (cf. e.g. [149]). Hence, the baseline for $\mathrm{Re} = 1 \times 10^4$ is verified with excellent correspondence.

5.4.3 Flutter derivatives

To verify the self-excited forces, the flutter derivatives are compared with Theodorsen's solution for a flat plate performing sinusoidal oscillations. The flutter derivatives are determined by the forced vibration method (cf. Sec. 3.7.2), for the forcing properties given in Tab. 5.7 at three Reynold numbers $\mathrm{Re} \in \{1 \times 10^3, 1 \times 10^4, 1 \times 10^5\}$. At each reduced velocity, the simulation time corresponds to 10 periods, yielding averaging time from $\tau = 20$ up to $\tau = 500$. The formulation of the analytical flutter derivatives given in (3.126) is used for the analytical flutter derivatives as the apparent mass effect cannot be separated in the forces obtained from the CFD analyses (cf. Sec. 3.5.5).

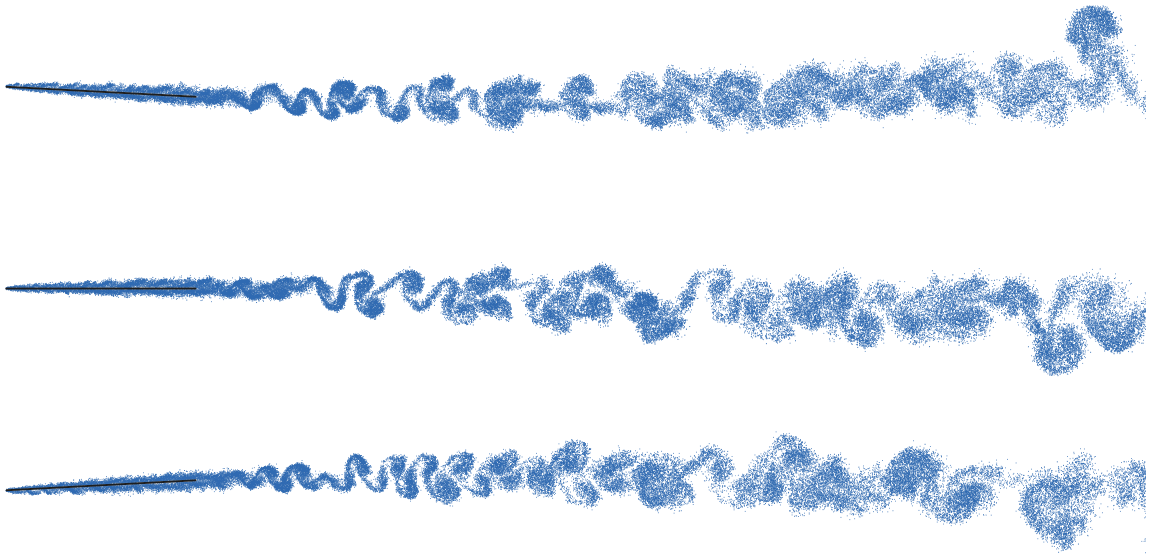

Figure 5.44: Flat plate: instantaneous particle maps of a rotating plate at maximum (top), zero (center), and minimum (bottom) amplitude for a reduced velocity of $V_r = 16$. The Reynolds number is $\mathrm{Re} = 1 \times 10^4$.

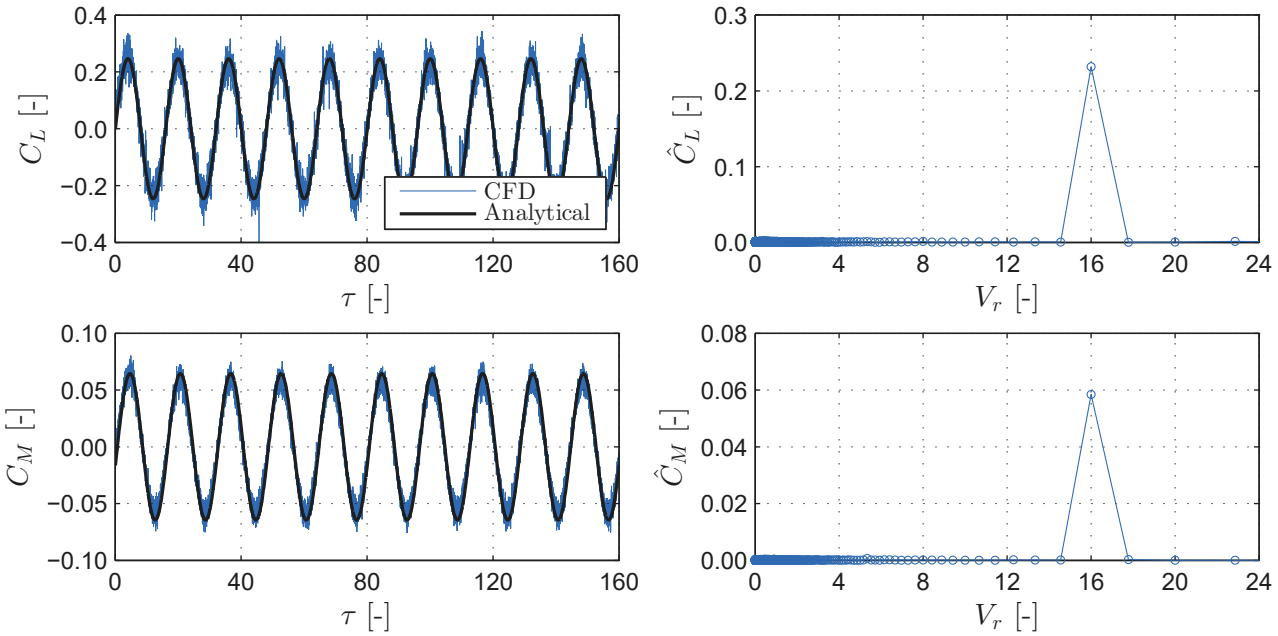

Figure 5.45: Flat plate: sample lift C_L (top-left) and moment C_M (bottom-left) time-histories, and their corresponding FFTs, $\hat{C}_L$ (top-right) and $\hat{C}_M$ (bottom-right), for a rotating plate at reduced velocity of $V_r = 16$. The analytical solution is obtained based on Theodorsen function including apparent mass terms, while the Reynolds number is $\mathrm{Re} = 1 \times 10^4$.

Figure 5.44 depicts three particle maps for the from maximum to minimum rotation angle at $V_r = 16$ for $\mathrm{Re} = 1 \times 10^4$. No leading-edge separation vortex is observed, which would violate the Kutta condition. The leading edge separation is a typical indicator of nonlinearity at high angles of attack and stall flutter (cf. e.g. Walker [340], McCrosky and coworkers [219, 220] for comprehensive discussions, or more recently Ramesh et al. [260] who also included CFD results based on the vortex methods). For these reduced velocities, the lift and moment time-histories

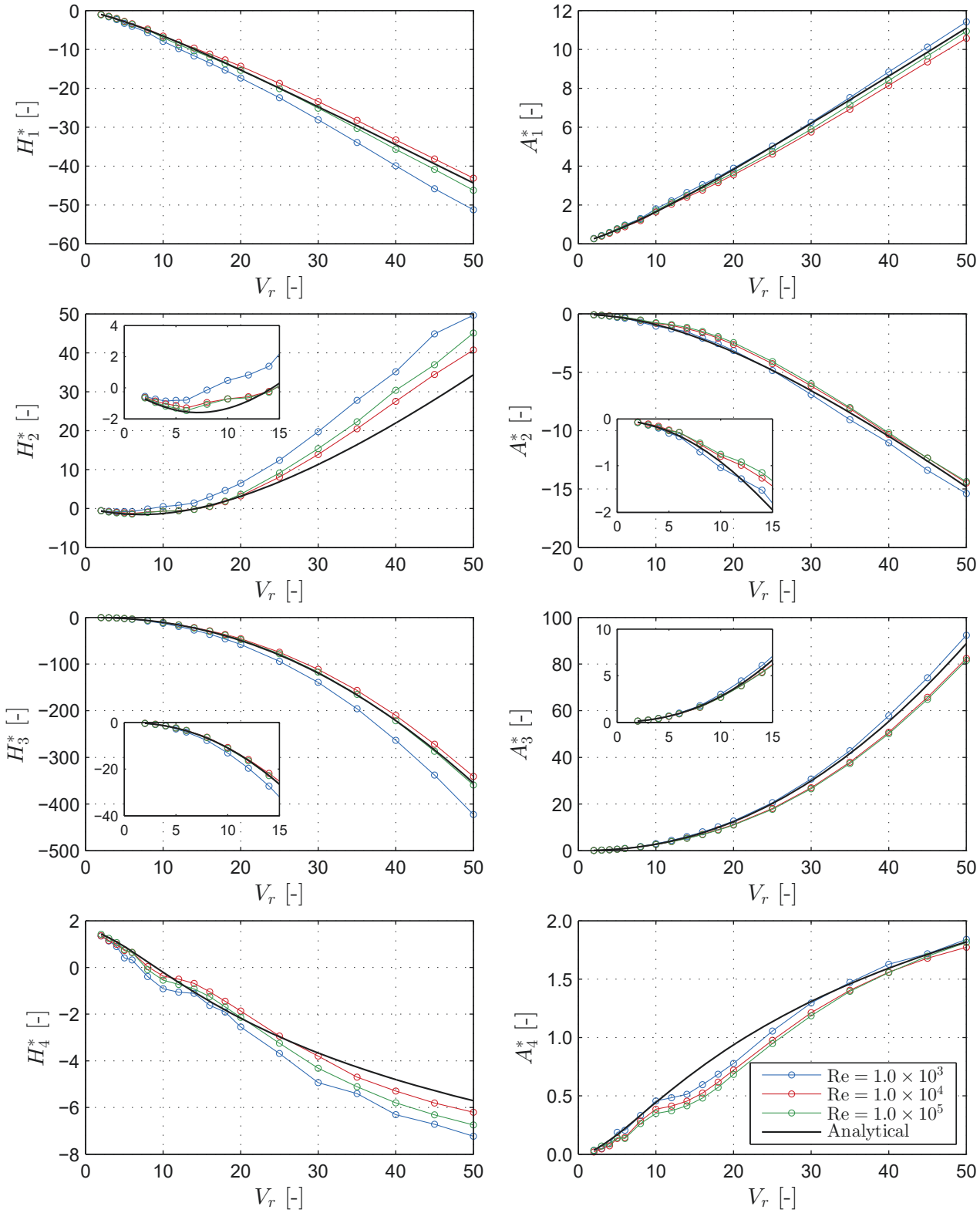

Figure 5.46: Flat plate: flutter derivatives for various Reynolds numbers. The analytical solution is obtained based on Theodorsen function including the apparent mass terms (cf. (3.126)).

and the corresponding analytical solution based on potential flow (cf. (3.57)) are depicted in Fig. 5.45 (left). Further, the corresponding FFTs are shown in Fig. 5.45 (right). A clear sinusoidal force can be observed which agrees well with the analytical forces in both phase and

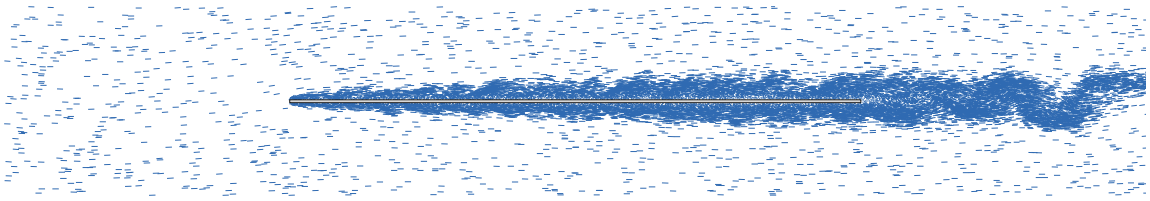

Figure 5.47: Flat plate: instantaneous particle map of a horizontal plate under random free-stream turbulence at Reynolds number $\mathrm{Re} = 1 \times 10^4$.

magnitude. No sub- or super-harmonics; thus, the forces are mostly linear.

The flutter derivatives at the prescribed Reynolds numbers are given in Fig. 5.46 along with the analytical solution. Generally, good results are obtained that verify the CFD model. To a certain extent, the correspondence is better for higher Reynolds numbers, although no uniform pattern is observed between $\mathrm{Re} = 1 \times 10^4$ and $\mathrm{Re} = 1 \times 10^5$. Roughly speaking, monotonic behavior corresponding to the Reynolds number change is observed for A_2^*, A_3^* and A_4^*. Instead of A_3^*, Bruno and Fransos [36] reported the monotonic behavior for H_1^* and H_3^* based on the FVM without sub-grid turbulence modeling for a flat plate with $B/H_D = 400$. However, these two derivatives seem to be in very good agreement for $\mathrm{Re} = 1 \times 10^4$ and $\mathrm{Re} = 1 \times 10^5$; thus, any discrepancies might be a numerical artifact. Further, the lack of turbulence modeling generally affects the grid-based methods more than the VPM. As expected, the poorest performance is observed for H_2^*, H_4^* and A_4^*. The latter two are prone to high uncertainty and are not of significant importance for the flutter analysis (cf. e.g. [217, 287]). Although not compared in-detail, the deviations are in line with the experimental results for a flat plate by Matsumoto et al. [217] for $B/H_D = 20$, Starossek [311] for $B/H_D = 25$ by Gu et al. [124] for $B/H_D = 22.5$ with a wind nose. Moreover, the present results are consistent, and in some instances with better correspondence, compared other CFD studies of flat plates and airfoils, based on both the VPM (cf. e.g. [2, 226, 341]) and the grid-based methods (cf. e.g. [15, 36, 77]).

5.4.4 Aerodynamic admittance

Having verified the free-stream turbulence in Sec. 5.3, the aerodynamic admittance from CFD analyses is compared against Sears function (cf. (3.56)) to assure the reliability of the buffeting forces. Both cases of random and deterministic free-stream turbulence are used to compute the admittance including a comparison.

Random free-stream turbulence

The static flat plate is subjected to free-stream turbulence with turbulent characteristics and numerical parameters given previously in Tabs. 5.7 and 5.8, respectively. Figure 5.47 depicts an instantaneous particle map of the flat plate subjected to turbulence for Reynolds number $\mathrm{Re} = 1 \times 10^4$. Turbulent coherent structures appear to propagate along the plate, which were not observed for laminar free-stream (cf. Fig. 5.41 (center)) at $\mathrm{Re} = 1 \times 10^4$. However, conclusive statements of the effect of 2D free-stream turbulence on the boundary layer cannot be made on this account and further investigations are required. Given that the scale of turbulence and eddies of interest that carrying most of the turbulent energy are relatively large compared to the boundary layer thickness, the effect of local turbulence is assumed to be insignificant for the aerodynamic admittance and buffeting response (cf. Hunt [141] for discussion).

The aerodynamic admittance is computed for Reynolds number $\mathrm{Re} \in \{1 \times 10^3, 1 \times 10^4, 1 \times 10^5\}$

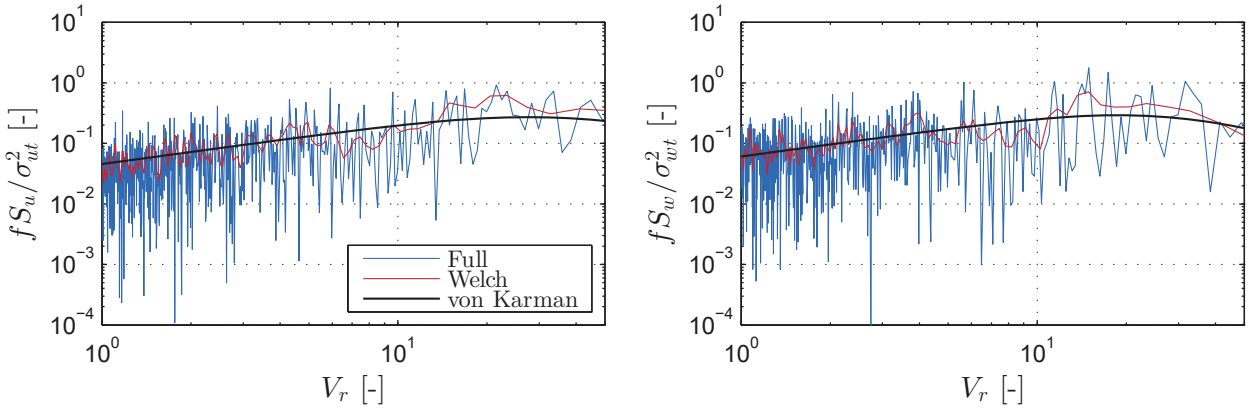

Figure 5.48: Flat plate: PSDs of simulated random free-stream turbulence at $\boldsymbol{x}_c$ of the lateral (left) and longitudinal (right) fluctuations at Reynolds number $\mathrm{Re} = 1 \times 10^4$.

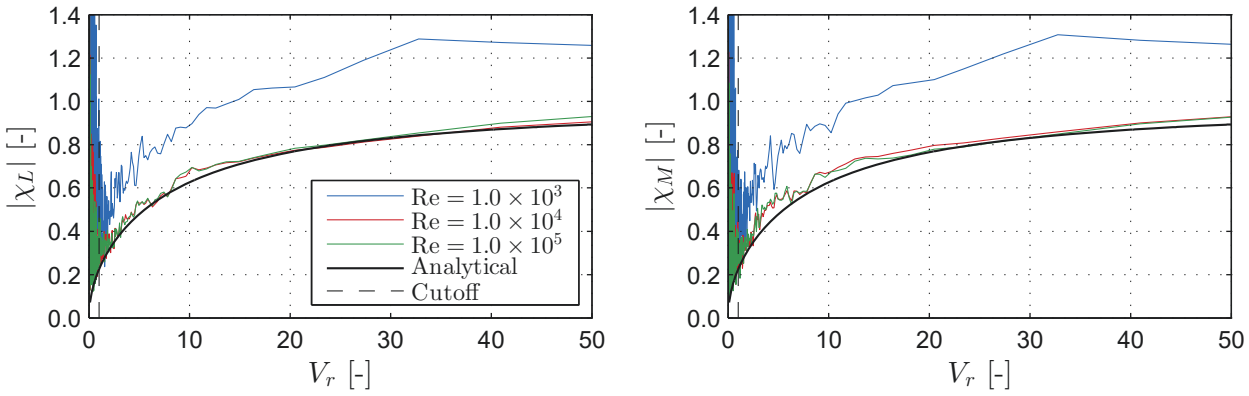

Figure 5.49: Flat plate: absolute value of the lift $|\chi_L|$ (left) and moment $|\chi_M|$ (right) aerodynamic admittances for random free-stream turbulence at various Reynolds numbers. Sears function is taken as analytical solution. The cutoff reduced velocity is $V_r = 1$, below which there is significant noise.

by a simple division of the PSDs of the buffeting forces and the velocity fluctuations (cf. (3.207)), as described in Sec. 3.7.3. The velocity fluctuations are obtained at the gust tracking point $\boldsymbol{x}_c$ from a simulation without a section in the CFD domain. The gust tracking point is selected to be at the stiffness center, i.e. $\boldsymbol{x}_s \equiv \boldsymbol{x}_c$. Figure 5.48 depicts the PSDs of the velocity based on the Welch method and without any filtering (Full) at $\mathrm{Re} = 1 \times 10^4$. The reduced time for computation of the aerodynamic admittance amounts to $\tau = 500$, which corresponds to approximately 10 cycles for the lowest frequency of interest (i.e. reduced velocity $V_r = 50$). Good correspondence can be seen with the target von Kármán spectra.

Figure 5.49 shows the absolute value of the aerodynamic admittances $|\chi_L|$ and $|\chi_M|$ for the three cases of Reynolds number, computed using the Welch PSD in (3.207), and the theoretical Sears admittance (cf. 3.56). Good correspondence can be observed for the high Reynolds numbers $\mathrm{Re} \in \{1 \times 10^4, 1 \times 10^5\}$ for the range of reduced velocity above the cutoff $V_r = 1$, with a deviation of approximately 10 % that is mainly due to noise. Although the results at $\mathrm{Re} = 1 \times 10^4$ are in slightly better correspondence with the analytical results for $|\chi_L|$, no conclusive statements can be made. Rassmussen et al. [261] used the vortex methods to obtain the admittance for random free-stream turbulence based on the VTG and ESDU spectra. They reported a deviation of up to 75 %. The results obtained herein provide better correspondence with the analytical Sears function. High noise is noted below the cutoff $V_r = 1$. The results in this range are generally

unreliable as they are a result of gust lengths shorter than the chord. For these gust lengths, the local 3D effects are dominant, which cannot be replicated well by the vortex method. However, for the typical turbulence length scales, the strength of the gusts with such short lengths are with several orders of magnitude lower (cf. Fig. 5.48) as well as the admittance amplitudes. Thus, the buffeting forces for these reduced velocities are negligible anyway for applications in bridge aerodynamics. The low Reynolds number $\mathrm{Re} = 1 \times 10^3$ resulted in scaled for a factor, which is probably due to the overestimation of the slopes of the static wind coefficients C'_L and C'_M, which was discussed previously.

Deterministic free-stream turbulence

Next, the aerodynamic admittance is computed for a flat plate subjected to vertical sinusoidal gusts, as introduced in Sec. 3.7.4. The gust and numerical parameters are given in Tabs. 5.7 and 5.8, respectively. Following the flow field verification in Sec. 5.3.2, the stiffness center $\boldsymbol{x}_s = (x_s, 0, 0)$ of the flat plate is positioned at x_s/B=2 for $V_{rt} \leq$4; x_s/B=5.5 for $4 < V_{rt} < 16$; and x_s/B=10 for $V_{rt} \geq$16. With this, a gust quality above $Q \geq$0.9 is ensured the section region and the inflow particles are not crossing the body. Figure 5.50 depicts a sequence of particle

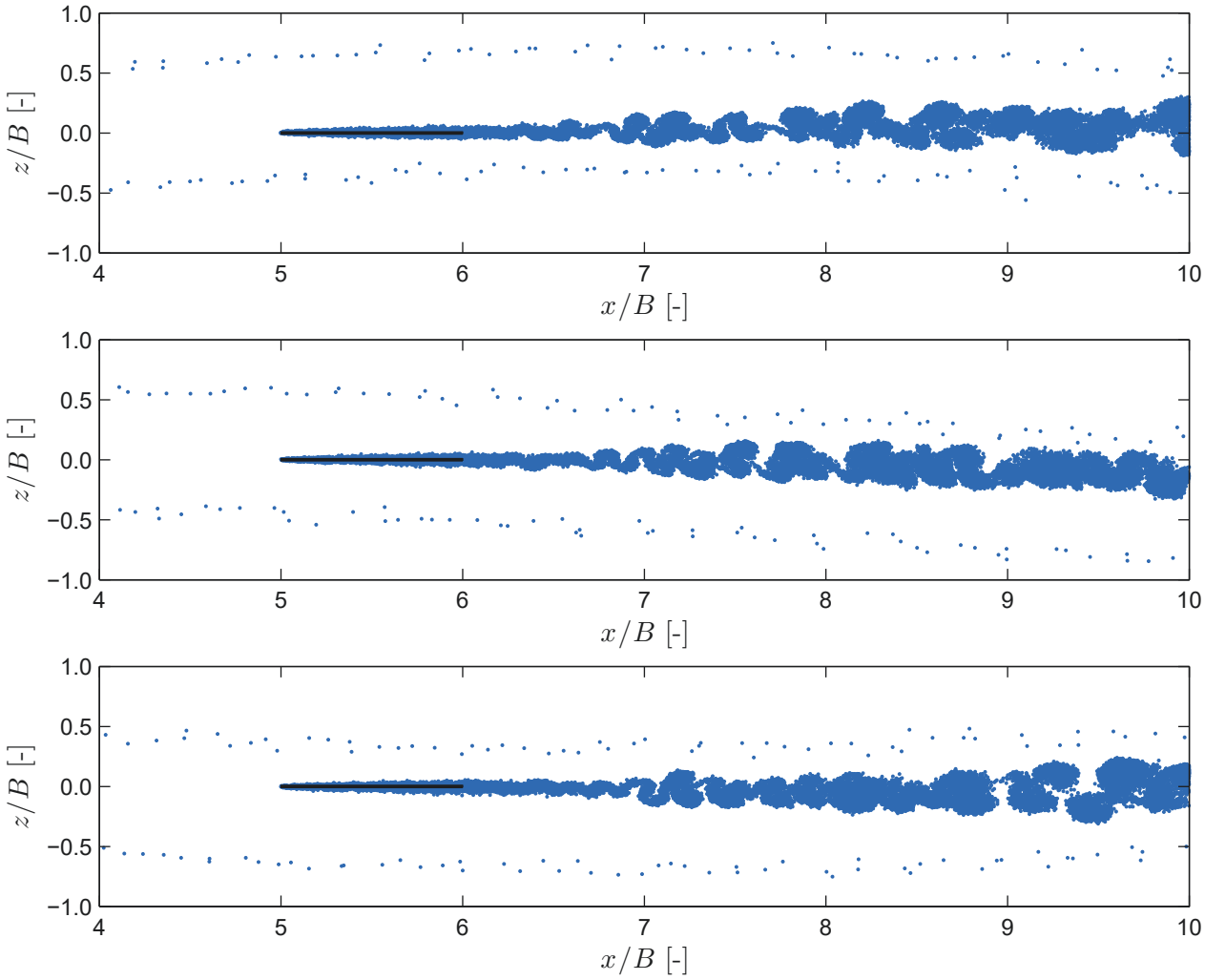

Figure 5.50: Flat plate: instantaneous particle maps of a horizontal plate under deterministic (sinusoidal) free-stream gust at maximum (top), zero (center), and minimum (bottom) amplitude for a gust reduced velocity of $V_r = 16$. The Reynolds number is $\mathrm{Re} = 1 \times 10^4$.

maps from a cycle of sinusoidal gust past a flat plate at a prescribed reduced velocity of V_r=16 for Re $= 1 \times 10^4$. It can be seen that even at the peak velocities (τ=17.5 and τ=25.5), the inflow particles do cross the body. To obtain the aerodynamic admittance, the actual sinusoidal gust needs to be tracked down at a specific location $\boldsymbol{x}_c$ within the CFD domain. For this case, the gust is tracked at the stiffness center, i.e. $\boldsymbol{x}_c \equiv \boldsymbol{x}_s$, as described in the optional step c) from Sec. 3.7.4. Hence, the influence of the body on the upstream velocity is not taken into account. Nevertheless, the analytical flat plate model is based on a potential flow; thus, it does not account for this effect anyway. Moreover, the tracking location can be positioned arbitrarily far upstream of the leading edge. This leads to inconsistent results as the influence of the section depends on the distance between the tracking location and the leading edge. Tracking the gust at the stiffness center $\boldsymbol{x}_s$ is only applicable for CFD analyses, as the simulations with and without section are reproducible. In experiments, the gust needs to be tracked down at a point upstream of the leading edge.

A time-histories of the lift and moment fluctuating coefficients at V_r=16 normalized w.r.t. the gust angle are depicted Fig. 5.51 (left), for Re $= 1 \times 10^4$. These are further compared to their analytical counterparts for the Sears function. From the figure, it can be observed that the forces sinusoidal. The additional high-frequency fluctuations for the CFD model are caused by the viscous random walk and vortex-shedding. It could be observed that the analytical time-histories are sort of a least-square fit to the results from the CFD analyses. The FFTs of the normalized coefficients (cf. Fig. 5.51, right) also depicts a clear harmonic in the forces.

Figure 5.52 (left) depicts the real $\Re(\chi)$ and imaginary $\Im(\chi)$ parts of the complex aerodynamic admittance obtained from the CFD simulations and the Sears function at Re $= 1 \times 10^4$. The aerodynamic admittance is computed based on 10 cycles of sinusoidal gust for each reduced velocity, yielding simulation time up to $\tau = 500$. Very good agreement can be observed for

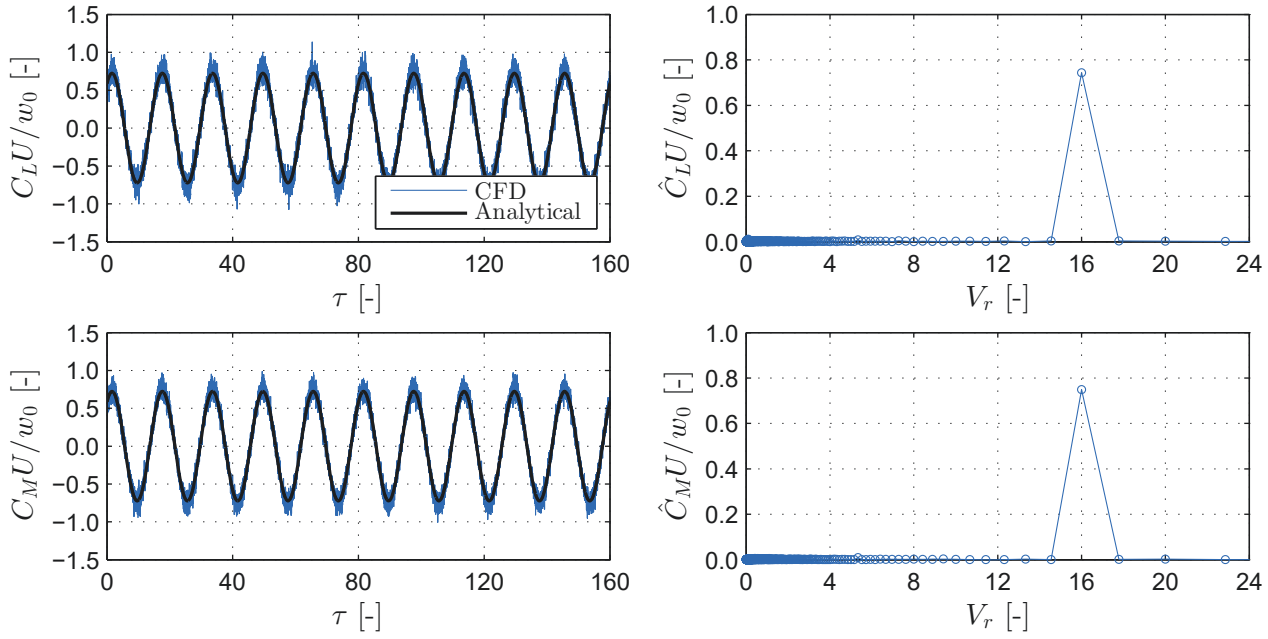

Figure 5.51: Flat plate: sample lift C_L (top-left) and moment C_M (bottom-left) time-histories, and their corresponding FFTs, $\hat{C}_L$ (top-right) and $\hat{C}_M$ (bottom-right), for a horizontal plate under deterministic (sinusoidal) free-stream gust with a reduced velocity of $V_r = 16$. The analytical solution is obtained based on the Sears function, while the Reynolds number is Re $= 1 \times 10^4$.

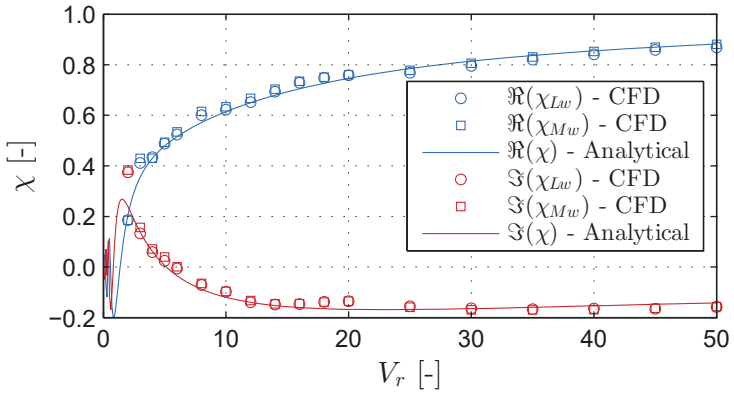

Figure 5.52: Flat plate: real and imaginary parts of the aerodynamic admittances for deterministic free-stream gusts. The Sears function is taken as an analytical solution.

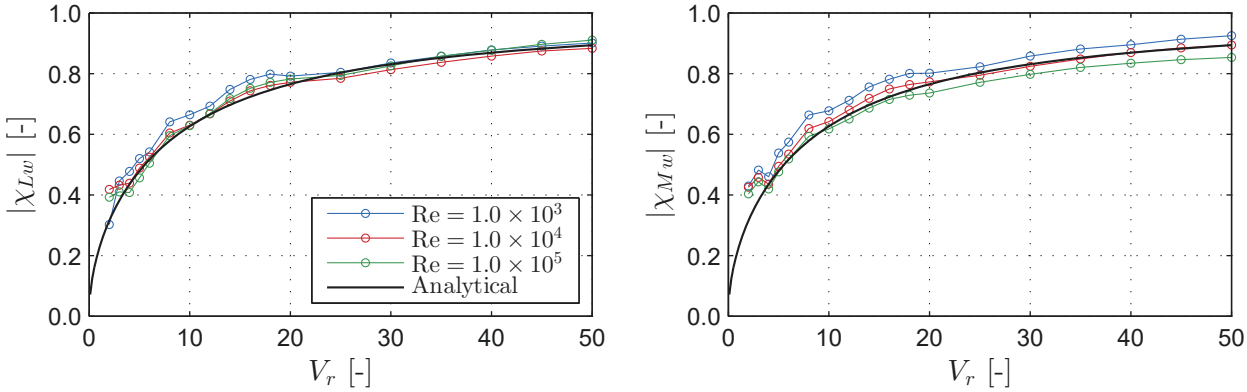

Figure 5.53: Flat plate: absolute value of the lift $|\chi_{Lw}|$ (left) and moment $|\chi_{Mw}|$ (right) aerodynamic admittances for deterministic free-stream gusts at various Reynolds numbers. The Sears function is taken as an analytical solution.

both real and imaginary parts. As it can be observed from the figure, the gust lags behind the aerodynamic forces for reduced velocities up to V_r=8. Another important particularity is that the aerodynamic admittance of the moment and lift force coincide, which effectively means that the lift force is acting on the front quarter-chord point. A maximum deviation of 10 % for the absolute value of the admittance is obtained for a prescribed reduced velocity of V_r=2, while the discrepancies are in the range of ±2 % for higher reduced velocities V_r >3. As noted previously, the range for $V_r < 2$ is of minor interest in bridge aerodynamics. The absolute values of the aerodynamic admittances $|\chi_{Lw}|$ and $|\chi_{Mw}|$ are given in Fig. 5.53 for three Reynolds numbers $\mathrm{Re} \in \{1 \times 10^3, 1 \times 10^4, 1 \times 10^5\}$. Generally, good correspondence is obtained for all cases, with the best results for $\mathrm{Re} = 1 \times 10^4$. For increasing Reynolds number, a constant reduction is observed for the moment aerodynamic admittance. No such monotonic trend for the lift. Surprisingly, no constant overestimation of the aerodynamic admittances is observed for $\mathrm{Re} = 1 \times 10^3$ as in the case for random free-stream turbulence, despite the high lift slope. One explanation could be that the inflow particles for the random free-stream mix with the particles close to the boundary layer causing local effects, while this is not the case for the deterministic free-stream. However, no conclusive statements can be made on this account without further investigation.

Comparison

In what follows, the results obtained in the previous sections are compared. Figure 5.54 depicts the absolute value of the aerodynamic admittance for a flat plate obtained using the deterministic and random free-stream at $\mathrm{Re} = 1 \times 10^4$. The admittances from both deterministic and random free-stream (using Welch PSDs) correspond well with Sears admittance, with a slightly better agreement for the moment admittance from deterministic free-stream turbulence. Significant numerical noise is noted for the aerodynamic admittance if the full PSDs are used for the random free-stream, without any smoothing. Utilizing deterministic as opposed to random free-stream turbulence offers several advantages including: (i) the admittance is obtained in its complex form rather than only the absolute value, (ii) all six components of the aerodynamic admittance can be obtained separately (cf. (3.208) and (3.209)) instead of only three (cf. (3.207)) and, (iii) the numerical uncertainty arising from the smoothing in the PSD is avoided. As a consequence of the latter point, it is difficult to separate the contribution of the incident part from the shear layer and wake fluctuations of the admittance for the random free-stream. A drawback of obtaining the admittance using deterministic gusts is the computational inefficiency since a separate CFD simulation is required at each reduced velocity.

It is important to note that the analogy between deterministic and random free-stream turbulence for the 2D CFD analyses is not the same as the analogy in experiments between gusts obtained using an active turbulence generator and grid turbulence. Using an active turbulence generator represents the strip assumption accurately to some extent. Thus, experimental studies of the aerodynamic admittance of an airfoil or a flat plate corresponded well with the Sears admittance (cf. Jancauskas and Melbourne [151]), while the asymptote $|\chi| \to 1$ at $V_r \to \infty$ is preserved for bridge decks (cf. e.g. [81, 85, 129]). This is in line with the CFD results obtained from this work for both deterministic and random free-stream. In the case of experimental aerodynamic admittance determined for grid free-stream turbulence, the 3D effects can be dominant. This results in significantly reduced amplitude of the aerodynamic admittance even at $V_r \to \infty$, as the effects are averaged over the experimental strip of finite length [101, 186]. The 3D effect for random free-strip generally depends on the length in the span-wise direction and for very long width-to-span ratios, such as long-span bridges, can be insignificant as discussed by Massaro and Graham [215]. This is discussed later in the conclusion as a part of the critical remarks. The random free-stream turbulence in the VPM is 2D; hence, the absolute values of the CFD aerodynamic admittance for both methods are comparable.

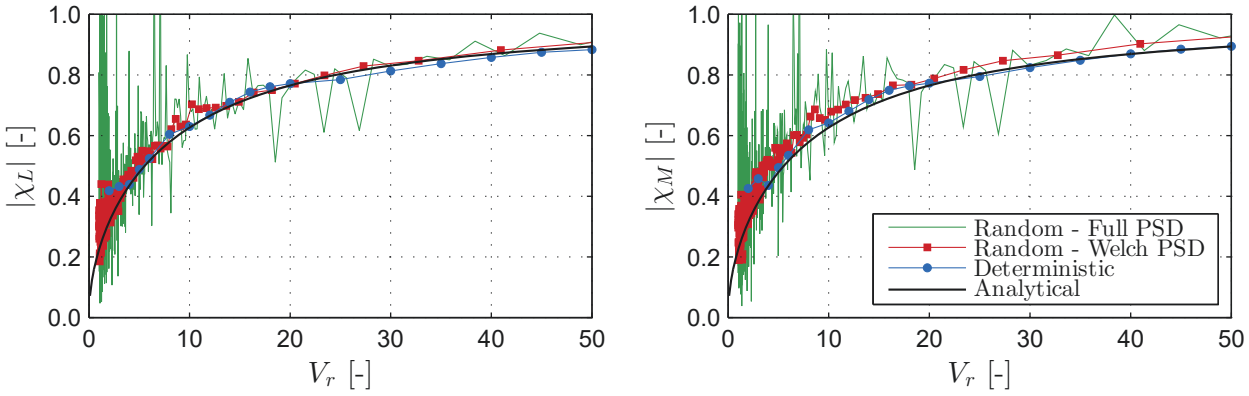

Figure 5.54: Flat plate: comparison of the absolute lift χ_L (left) and moment χ_M (right) aerodynamic admittances for deterministic and random free-stream turbulence. The Sears function is taken as an analytical solution.

5.4.5 Rational approximation

Before advancing to the CFD buffeting and flutter analyses, two parts of the analytical flat plate model (i.e. semi-analytical LU model for bridge decks) are verified, namely: the rational approximation (cf. Sec. 3.5.5) and the FFT-based method for computation of the buffeting forces (cf. Sec. 3.5.7).

The unsteady effects for a flat plate, modeled by Theodorsen and Sears frequency-dependent functions, are mapped into the time domain using rational approximation (cf. (3.106), (3.116)). This can be accomplished either by elementary indicial or impulse functions, as discussed in Sec. 3.5.5. In the case of indicial functions, the time-domain approximation should correspond to Wagner and Küssner functions (cf. (3.59)), i.e. to their approximations (cf. (3.62)), for the self-excited and buffeting forces, respectively.

Figure 5.55 depicts the rational approximation of Theodorsen (left) and Sears (right) functions. In case of Theodorsen function, good correspondence can be observed for both indicial and impulse approximation. For both cases, four extra unsteady states are used ($N_{st} = 4$ in (3.100) and (3.112)). The obtained indicial function is further compared to the Jones' approximate form (cf. (3.62)) of Wagner function (cf. Fig. 5.56, left), given previously in (3.62) for Φ_{se}. Although Jones' approximation utilizes only two unsteady terms, the difference is insignificant. As discussed by Dowell [90], four terms provide better approximation to Theodorsen function.

Difficulties arise when approximating directly Sears function (cf. (3.56)) due to its circulatory behaviour for low reduced velocities ($V_r \leq 5$), which is manifested by "spirals" in both imaginary and real parts (cf. Fig. 5.55, right). These spirals appear since Sears [293] selected the origin of the coordinate system (i.e. point at which the gust is acting) to be the middle of the plate, as noted by Giesing et al. [118]. Therefore, when approximating Sears function directly, values for $V_r \geq 5$ are selected, yielding good approximation for unsteady states $N_{st} = 5$ and $N_{st} = 4$ for the indicial and impulse functions, respectively. The corresponding indicial function is given in Fig. 5.56 (right) and is denoted as "Indicial Approx. Sears". It can be seen that there is a variation w.r.t. the approximate form of Küssner function (cf. (3.62)) with an unstable origin, due to the spirals discussed previously.

Alternatively to the analytical Sears function for the gust problem, the rational approximation

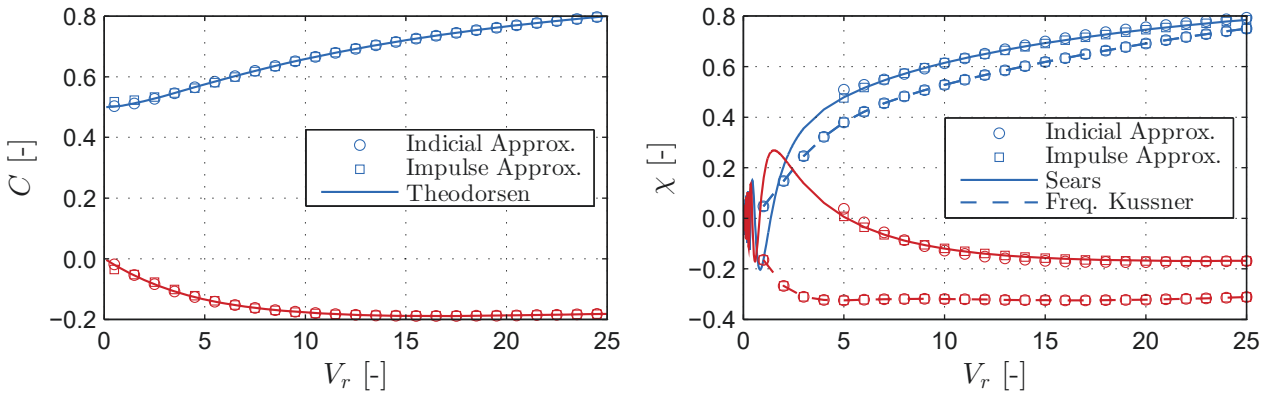

Figure 5.55: Flat plate: rational approximation of Theodorsen (3.52) (left) and Sears (3.56) (right) functions using indicial and impulse function approximation. Blue color denotes the real, while red color the imaginary part of the functions. Additionally, the frequency-domain counterpart of the approximate form of Küssner function ("Freq. Kussner", (5.13)) is rationally approximated.

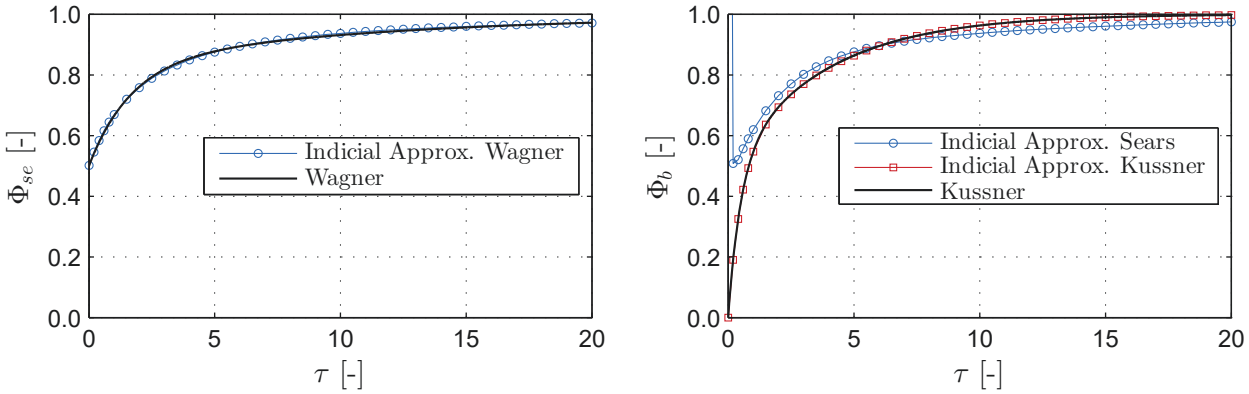

Figure 5.56: Flat plate: self-excited (left) and buffeting (right) indicial functions obtained from the rational approximation of the Theodorsen and Sears functions, respectively, (cf. Fig. 5.55). The approximate form of Wagner and Küssner functions (3.62) is given as a reference. Additionally, the buffeting indicial function, obtained from the rational approximation frequency-domain counterpart of the approximate form of Küssner function ("Freq. Kussner" in Fig. 5.55, left), is given and is denoted as "Indicial Approx. Kussner".

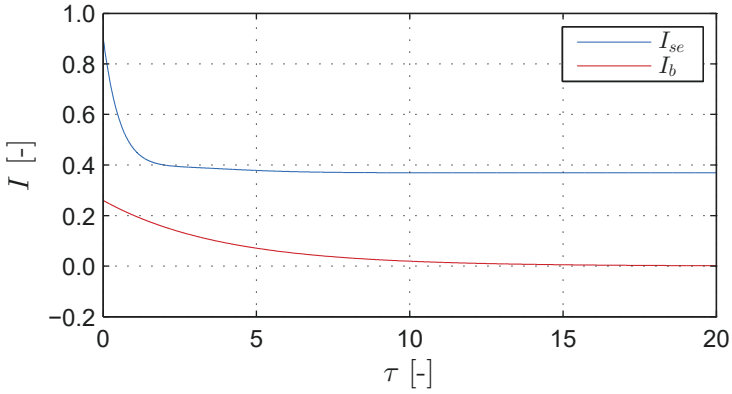

Figure 5.57: Flat plate: self-excited and buffeting impulse functions obtained from the rational approximation of the Theodorsen and Sears functions (cf. Fig. 5.55), respectively.

can be performed for the frequency-domain counterpart of the approximate form of Küssner function (3.62), given as follows [118]:

$$\chi = 1 - \frac{0.5}{K^* - 0.13i} - \frac{0.5}{K^* - i}, \tag{5.13}$$

for K^* being the reduced frequency w.r.t half chord. The frequency-domain counterpart is denoted as "Freq. Kussner" in Fig. 5.55 (right). Giesing et al. [118] noted that Küssner chose the leading edge of the airfoil as a reference point, which is why the spirals do not appear. Performing rational approximation on this function resulted in excellent results for both impulse and indicial functions for $N_{st} = 2$. As expected, the obtained indicial function ("Indicial Approx. Kussner") matches exactly the approximate form Küssner function. The impulse functions in Fig. 5.57 depict the averaged linear fluid memory, and cannot be directly compared to the indicial functions using (3.87), as discussed by Wu and Kareem [361].

Next, the simple method for computation of the unsteady buffeting forces based on FFT is verified (cf. Sec. 3.5.7 and Fig. 3.8). The fluctuating lift coefficient for the vertical wind fluctuations used in the previous section is obtained for three cases: (i) without admittance,

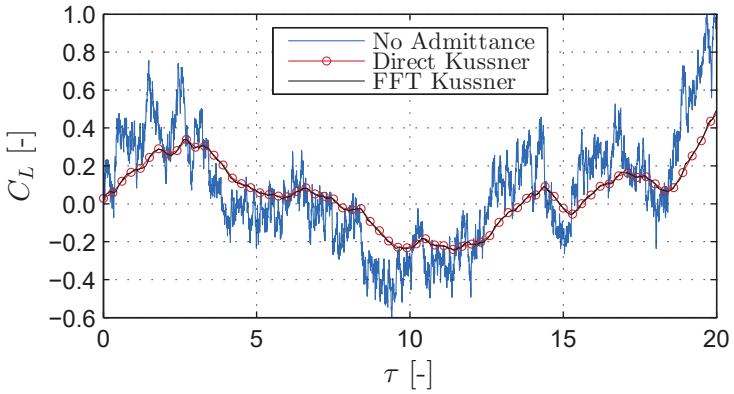

Figure 5.58: Flat plate: verification of the method for computation unsteady buffeting forces using FFT (cf. Sec. 3.5.7 and Fig. 3.8). The lift coefficient C_L obtained using this method is denoted as "FFT Kussner". The "Direct Kussner" denotes the lift coefficient C_L obtained full convolution of the Küssner function and vertical wind velocity.

(ii) with admittance using "direct" convolution (cf. (3.59)) of the approximate form of Küssner function (cf. (3.62)), and (iii) with admittance using FFT (cf. (3.141)) for the frequency-domain counterpart of the approximate form of Küssner function (cf. (5.13)). The result for the three cases is depicted in Fig. 5.58. It can be seen that the presented method using FFT ("FFT Kussner") is almost identical to performing direct convolution using direct convolution ("Direct Kussner"). The relative RMS error for the time-history of $\tau = 500$ is less than 1 %.

5.4.6 Buffeting analysis

Having all aerodynamic coefficients verified, the CFD buffeting response of the flat plate can be studied and compared against its analytical counterpart. The dynamic properties of the flat plate and characteristics of the random free-stream turbulence are given in Tab. 5.7. A wind speed of $U = 20$ m/s is selected to be low enough, to accommodate the linearity assumption, and high enough, for the influence of local effects to be insignificant. The verification is performed in two manners:

- One-to-one comparison - same input wind time-history for both the analytical flat plate and the CFD model;
- Statistical comparison - input of twenty random wind records for both the analytical flat plate and the CFD model.

The results from the flat plate model are denoted as "Analytical". Each analysis is conducted for a run-time amounting to $\tau = 450$, of which the last $\tau = 387$ chords are used for the comparison and statistical analyses. The effective time-window for comparison corresponds to dimensional $t = 600$ s, which is the standard 10-minute wind specified by codes as a reference (cf. e.g. ESDU [100]). The SRQ are the vertical displacements and rotation.

It is noted that the numerical code used for the analytical flat plate model is verified with the results produced from the Task Group 3.1: "Super Long Span Bridge Aerodynamics" from the International Association of Bridge and Structural Engineering (IABSE), of which the author is a contributing member. Buffeting and flutter analyses are used as a basis for verification in both time and frequency domain for a similar example with slightly different aerodynamic coefficients. A fraction of the results is given in the Appendix A.

One-to-one comparison

Within the one-to-one comparison, the buffeting response from the CFD model is compared with the time-domain response from the analytical flat plate model for the same input. The input wind fluctuations are tracked down at the stiffness center $\boldsymbol{x}_s$ from a simulation without a section in the CFD domain. A time-shift for $\tau = 0.5$ is applied as the approximation of the Küssner function in (3.62) is for gusts acting at the leading edge. Although the gust tracking point could have been selected at the leading edge, this was not done to maintain consistency of the verified Sears admittance in the previous section. Also, the shift is justified based on Taylor's hypothesis, which was shown to be valid during the turbulent free-stream verification.

Figure 5.59 depicts a representative sample of 100 chords of the response. The amplitudes of the vertical displacements and rotations are generally small. The maximum effective angle of attack due to rotation and vertical displacements is approximately 4 deg; thus, ensuring a linear range of the self-excited forces. Excellent correspondence can be observed for the vertical displacement, while there is a slight discrepancy for the rotation. The instantaneous velocity field in Fig. 5.60 shows that there is no major separation that can lead to aerodynamic nonlinearity, although the gusts can increase the velocity at the leading edge in some instances.

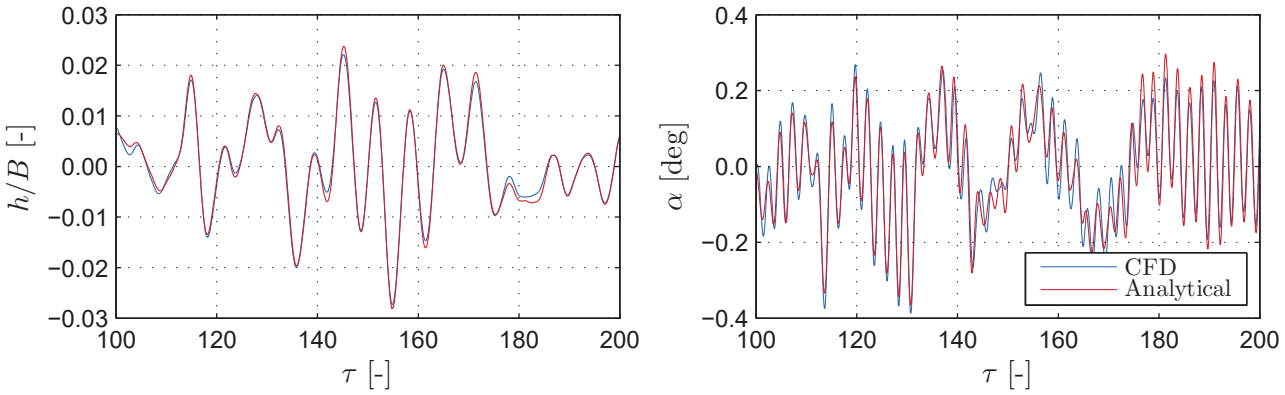

Figure 5.59: Flat plate: sample time-histories of the vertical displacements (left) and rotation (right) from the one-to-one comparison.

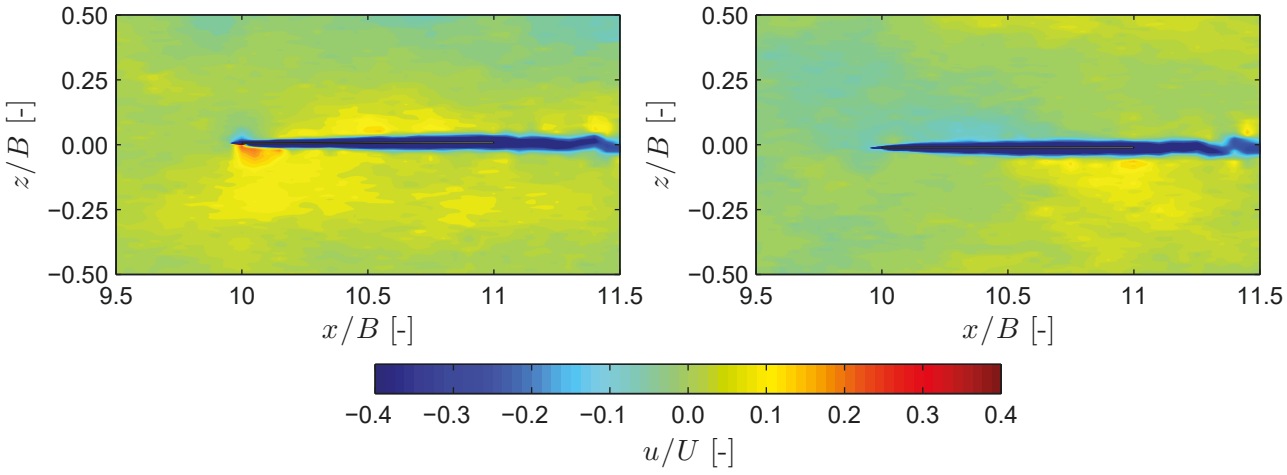

Figure 5.60: Flat plate: instantaneous longitudinal velocity fields from buffeting analysis. The two snapshots are approximately $\tau = 2$ apart and they correspond to the peak of the vertical displacements at $\tau \approx 158$ from Fig. 5.59.

To verify further all aspects of the verification in terms of model assumptions and signal features, the comparative methodology presented from Ch. 4 is applied in a similar manner as for the aerodynamic models for bridges. The flat plate (FP) model (cf. (3.59)) is linear and based on potential flow, while the CFD model (cf. (3.184)) is not. Thus, $\mathbf{Set}_{\mathrm{FP}}$ represents a superset of $\mathbf{Set}_{\mathrm{CFD}}$ as

$$\mathbf{Set}_{\mathrm{FP}} := \mathbf{Set}_{\mathrm{CFD}} \cup \{\boldsymbol{f}_v = 0; \boldsymbol{f}_{noi} = 0; \boldsymbol{f}(t) = \boldsymbol{f}(\boldsymbol{a}(t)); \boldsymbol{f} = \boldsymbol{f}|_{\alpha_s}\}\,, \tag{5.14}$$

since the LU model disregards the vortex shedding $\boldsymbol{f}_v$ and interior noise $\boldsymbol{f}_{noi}$ forces, is time-invariant for input $\boldsymbol{a}(t)$, and is linear. Therefore, the FP model is less complex than the CFD model:

$$\mathbf{FP} \longrightarrow \mathbf{CFD}.$$

Figure 5.61 depicts the comparison metrics $\overline{\mathcal{M}^{\mathrm{FP,CFD}}}$ for the vertical displacement (left) and rotation (right), computed for the metric parameters given in Tab. 5.9. Since the purpose of this example is to verify the CFD model, the FP model is taken as a reference model for the comparison; thus, the comparison is backward according to Definition 4.13. Except for $\overline{\mathcal{M}_w^{\alpha^{\mathrm{FP}},\alpha^{\mathrm{CFD}}}} = \overline{\mathcal{M}_{wf}^{\alpha^{\mathrm{FP}},\alpha^{\mathrm{CFD}}}} \approx 0.87$, all metrics resulted in values higher than 0.95. No indications of non-stationarity or nonlinearity are noted. The sources of the minor discrepancies differences are due to numerical uncertainty in the CFD model and/or the assumptions within the FP model (cf. (5.14)). Particularly, it is plausible to argue that the minor discrepancy in the wavelet metrics for the rotation is due to the local effects. Nevertheless, the effect of these sources cannot be separated. A qualitative criterion for the comparison metrics is not strictly defined yet; however, values larger than 0.9 generally mean very good correspondence.

Metric parameter		Value
Normalization time:	T_c	$(1/f_h{+}1/f_\alpha)/4$
Central wavelet frequency:	f_{ce}	$10.5 f_\alpha$
Confidence level:	CL	95 %
Surrogates - Stationarity:	N_{sur}	200
Exceedance - Stationarity:	g_s^*	2
Surrogates - Nonlinearity:	N_{sur}	100
Exceedance - Nonlinearity:	g_b^*	2

Table 5.9: Flat plate: Comparison metric parameters for one-to-one comparison of buffeting response.

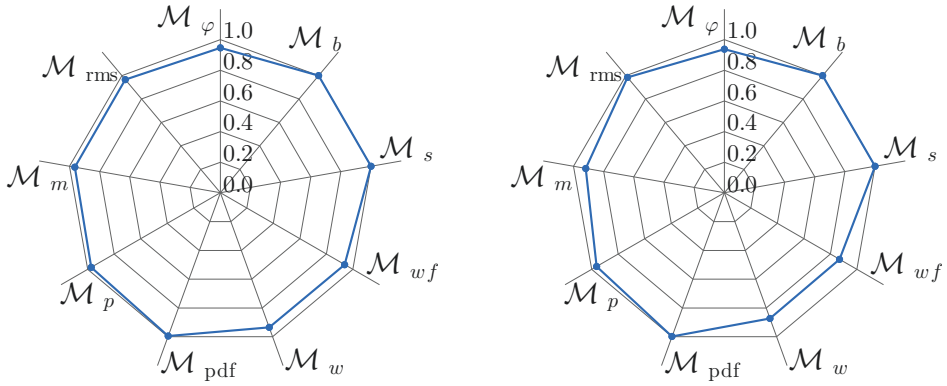

Figure 5.61: Flat plate: comparison metrics of the vertical displacements $\overline{\mathcal{M}^{h^{\mathrm{FP}},h^{\mathrm{CFD}}}}$ (left) and rotation $\overline{\mathcal{M}^{\alpha^{\mathrm{FP}},\alpha^{\mathrm{CFD}}}}$ (right) from the one-to-one comparison between the CFD and analytical model, where the analytical is taken as reference.

The normalized wavelet amplitude is shown in Fig. 5.62 for the CFD (left) and FP (right) models for both components of the response, vertical displacements (top) and rotation (bottom). The vertical natural frequency corresponds to a reduced frequency of approximately $K \approx 1$, while the torsional to $K \approx 2.7$. It can be seen from the figure that the flat plate oscillates mainly

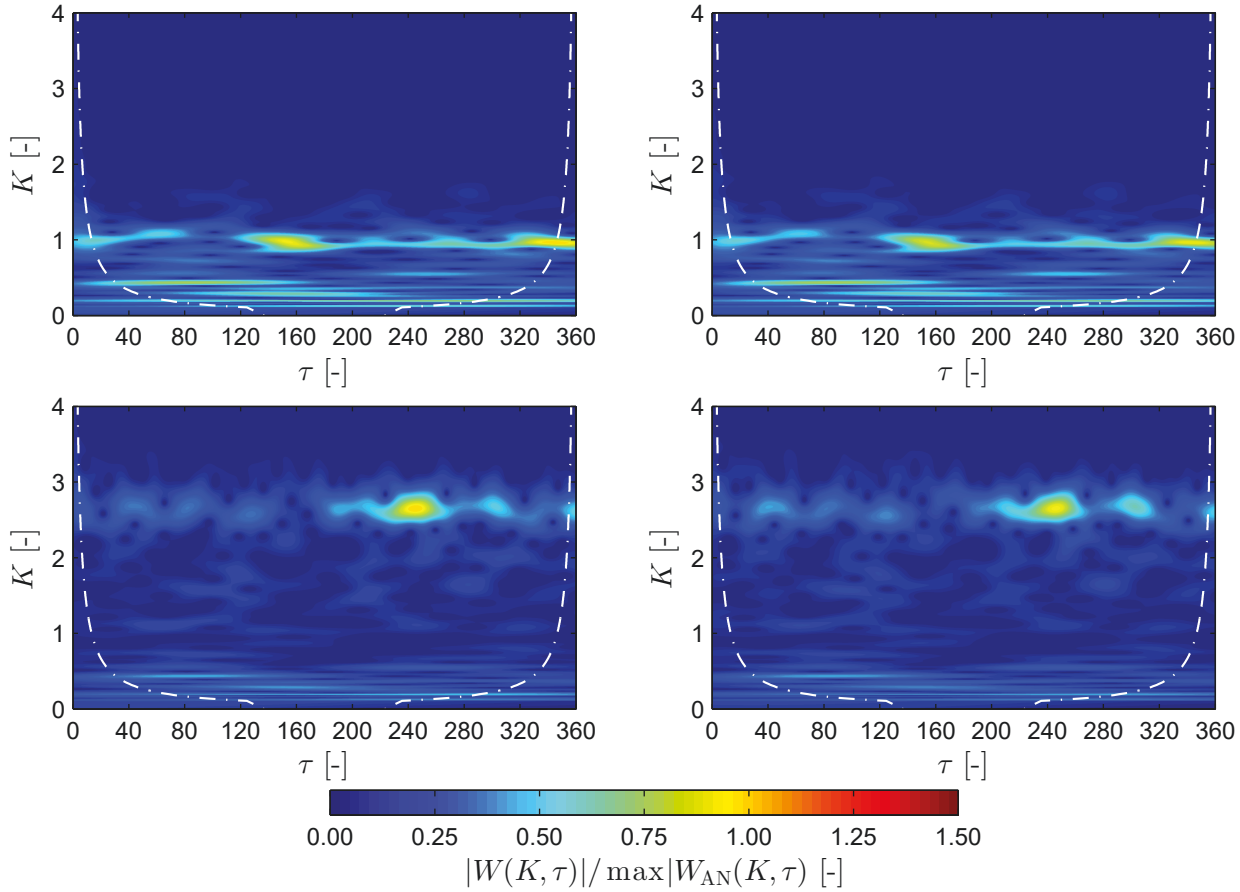

Figure 5.62: Flat plate: normalized absolute wavelet coefficients of the vertical displacements (top) and rotation (bottom) for the CFD (left) and analytical model (right) from the one-to-one comparison. The normalization is performed w.r.t. the corresponding wavelet coefficients (vertical or rotational displacements) of the analytical model. The dashed-dot line indicates the cone of influence COI.

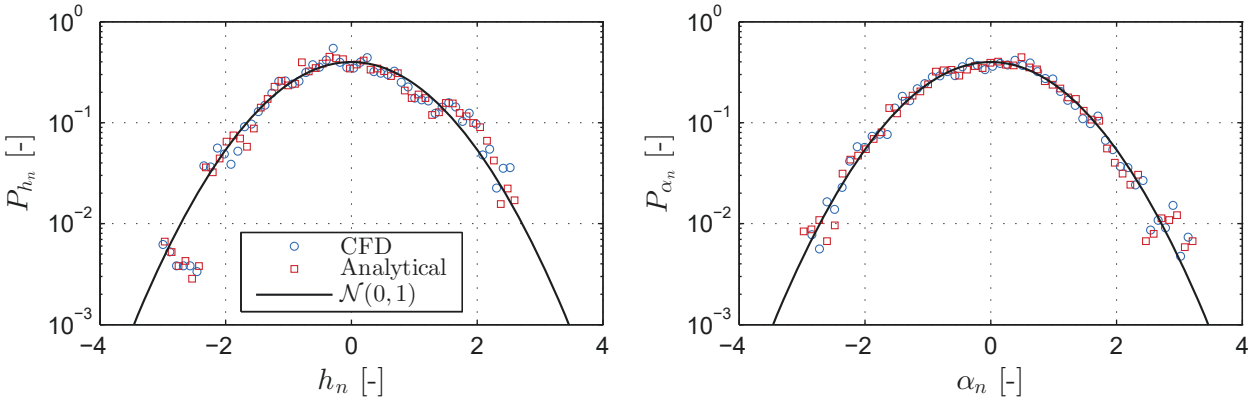

Figure 5.63: Flat plate: histogram estimate PDFs of the normalized (standard score) vertical displacements (left) and rotation (right) from the one-to-one comparison. These are additionally compared to a standard normal distribution $\mathcal{N}(0,1)$.

at the natural frequencies, although the effect of the background turbulence on the very low frequencies for the vertical displacements is also prominent. Both instantaneous magnitude and frequency match which further proves that the CFD and FP models correspond very well.

Further, the histogram estimate PDFs of the displacements are given in Fig. 5.63. Generally, the displacements follow the Gaussian PDF; however, the Kolomorgov-Smirnov test rejected the null hypothesis at 5 % significance. Since the FP is a linear model, the reason is probably due to the non-Gaussianity of the free-stream turbulence discussed previously in this chapter.

Statistical comparison

The comparison performed in the previous section is not completely based on an independent analytical solution as the input wind time-histories are obtained from CFD analysis. To further verify the CFD model to a purely analytical solution, a statistical comparison is performed. Twenty separate CFD analyses are conducted, each with randomly generated free-stream turbulence with the same turbulent statistics. These are then compared to the analytical FP model in both the time and frequency domain. The solution for the analytical FP model in the frequency domain is obtained by reformulating (3.57), in a similar fashion as for the LU model in Sec. 3.5.5. Twenty separate random records of the wind fluctuations are considered for the FP model in the time domain as well.

The results of the RMS displacements are given in Fig. 5.64. The analytical response for the FP model in the frequency domain is denoted as AN-FD, while in the time domain as AN-TD. Further, the 99 % confidence interval is given for the FP model in the time domain and the CFD model. It can be seen that the mean value of the CFD response yields very good results compared to both AN-TD and AN-FD responses. A discrepancy of 4 % and 6 % is noted for the vertical displacement and rotation, respectively. The analytical response is clearly within the 99 % confidence interval of the CFD model. It can be seen that the confidence interval of the FP model in the time domain (AN-TD) is very narrow. This is a consequence of the generation process of the time-history for a single point. In this case, the random wind fluctuations have the exactly prescribed spectrum since the generation process is simply inverse FFT with random phase (cf. (3.35)), i.e. without random amplitudes of the spectrum.

Figure 5.65 depicts the PSD of the vertical displacements (left) and rotation (right). The PSD of the response for the CFD and analytical FP model in the time domain is averaged from the twenty analyses. For the CFD model, the PSD is computed using Welch's method, i.e. it is smoothened. In the case of the FP model in the time domain, no smoothing is necessary as the

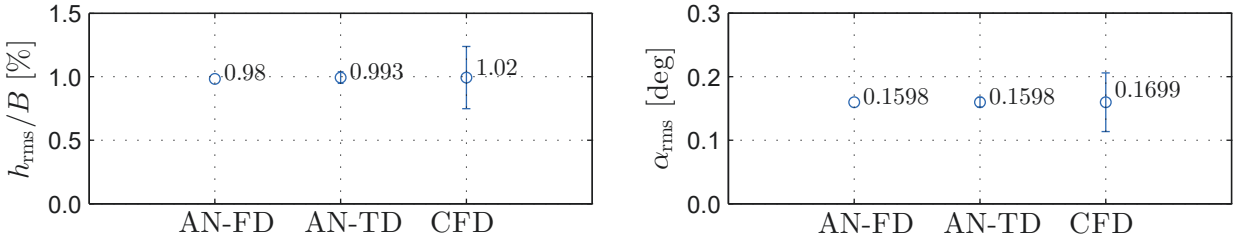

Figure 5.64: Flat plate: RMS of the vertical displacements (left) and rotation (right) from the statistical comparison. The response for the analytical model is obtained in the frequency (AN-FD) and time domain (AN-TD), while the CFD response is only in the time domain. The error bars indicate the 99 % confidence interval for the time-domain models (AN-TD and CFD), while the marker is the mean of 20 response time-histories.

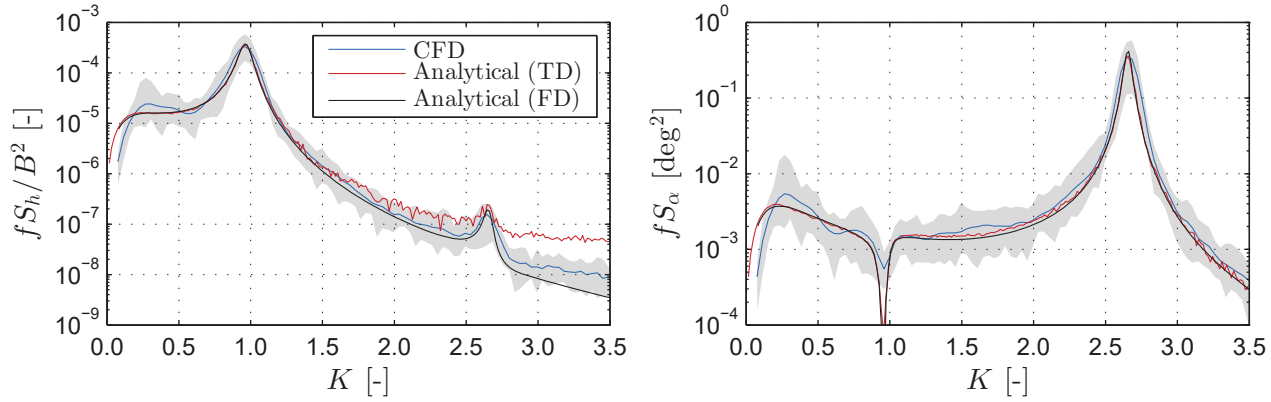

Figure 5.65: Flat plate: PSDs of the vertical displacements (left) and rotation (right) from the statistical comparison. The response for the analytical model is obtained in the frequency (FD) and time domain (TD), while the CFD response is only in the time domain. The shaded area defines the envelope at each frequency for the CFD model, while lines indicate the mean for the time domain models from 20 response time-histories.

random wind fluctuations have the exactly prescribed spectrum. Further, the shaded gray area represents the envelope from all twenty PSDs for the CFD model. As can be observed from the figure, excellent correspondence is obtained across the frequency content, even for a secondary peak of S_h that represents the aerodynamic coupling. The slight deviation in the PSD of the rotation at the reduced frequency corresponding to the first natural mode, i.e. $K \approx 1$, is due to the smoothing as S_α is significantly low for this frequency.

5.4.7 Flutter analysis

Flutter analyses are performed for both models as a final step of the flat plate study. The critical flutter velocity U_{cr} is the SRQ of interest and is determined for the FP model in both the time and frequency domain and the CFD model for laminar free-stream. In the frequency domain, the critical flutter velocity is determined for the forces defined in (3.57) by complex eigenvalue analysis in the state-space, in a similar fashion as in Sec. 3.5.7. The system is simply let to perform free-vibration to obtain the critical flutter limit in the time domain for both FP and CFD models. Figure 5.66 (left) depicts the critical flutter limit, normalized with the central frequency $f_{h\alpha} = (f_\alpha + f_h)/2$. A difference of less than 1 % is noted between the CFD model and the FP model for both the frequency (AN-FD) and time domain (AN-TD). Further, in the same figure (right), the critical flutter frequency f_{cr} is compared. In the time domain, f_{cr} is obtained as the argument corresponding to the peak in the FFT of the response time-histories

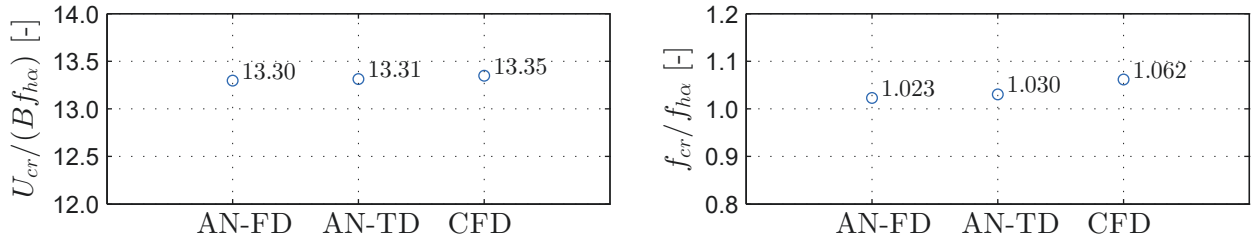

Figure 5.66: Flat plate: critical flutter velocities U_{cr} (left) and critical frequencies f_{cr} (right) for the analytical model in both the frequency (AN-FD) and time domain (AN-TD), and the CFD model.

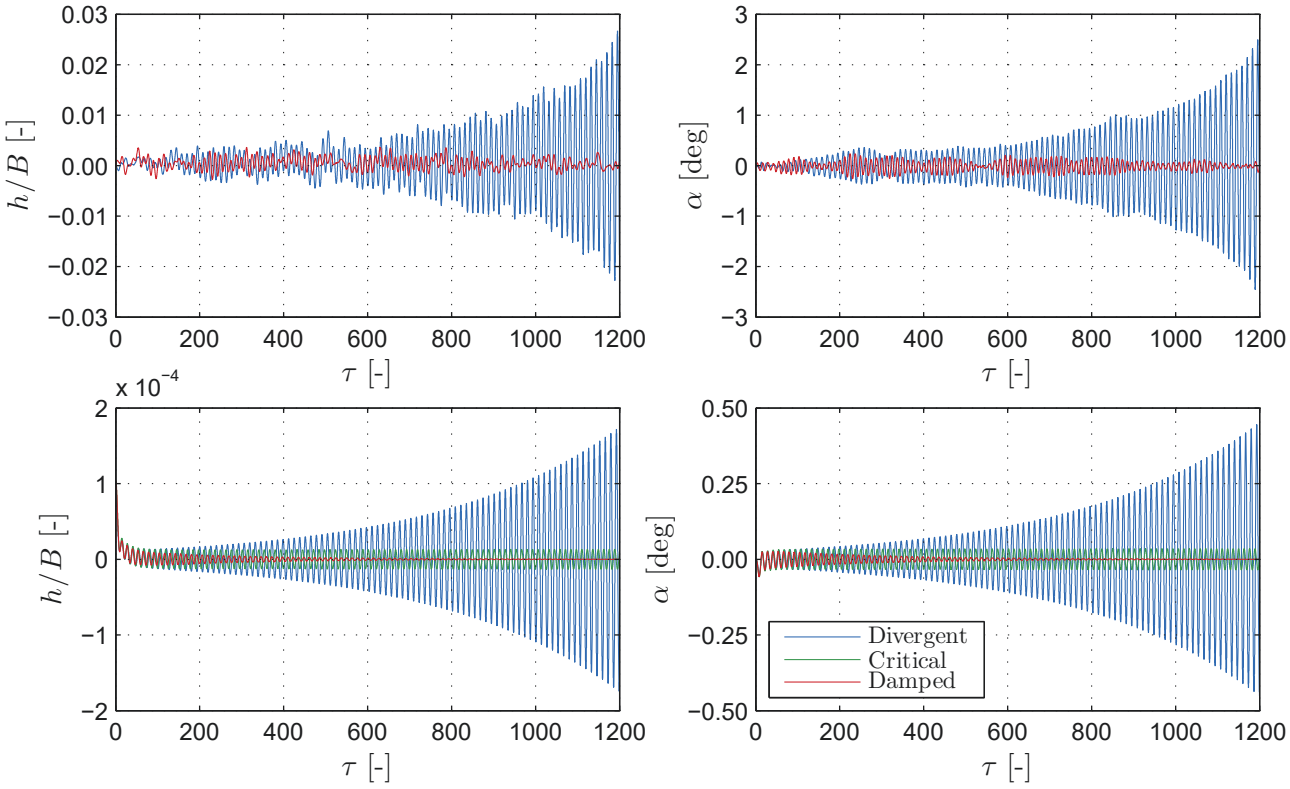

Figure 5.67: Flat plate: time-histories of the vertical displacements (left) and rotation (right) for the CFD (top) and analytical model in the time domain (bottom) near the critical flutter velocity. The following oscillation cases are depicted: CFD damped ($U/(Bf_{h\alpha}) = 13.31$), CFD divergent ($U/(Bf_{h\alpha}) = 13.35$), Analytical damped ($U/(Bf_{h\alpha}) = 13.29$), Analytical critical ($U/(Bf_{h\alpha}) = 13.31$) Analytical divergent ($U/(Bf_{h\alpha}) = 13.40$)

in the flutter region, which is equal for both degrees of freedom. In the frequency domain, f_{cr} corresponds to the governing flutter mode, i.e. the one with negative damping. Again, the discrepancy for the CFD model w.r.t. its analytical counterpart is approximately 3 %, yielding excellent correspondence between the CFD and analytical results.

Figure 5.67 depicts the time-histories of the decaying, critical and post-critical (divergent) regime for the CFD and FP models in the time domain. Below U_{cr}, a decaying response is observed for the CFD model, while there is a divergent trend of the displacements and rotation at U_{cr}. It is difficult to obtain exact U_{cr} in case of CFD free-vibration analysis at which the response would result in critical oscillations, i.e. for which the damping is exactly zero. On the other hand, it is possible to obtain the critical oscillation case for the LU model that maintains a constant amplitude of oscillation at U_{cr}. In the post flutter region, divergent oscillations can be observed for the LU model in the time domain as well.

Instantaneous particle maps and velocity fields are depicted in Fig. 5.68 that correspond to a minimum, zero and maximum rotation for the CFD model at $\tau \approx 1000$. The rotation amplitude is ≈ 1 deg in this region. No clear separation is yet observed that would lead to high aerodynamic nonlinearity, yielding the conclusion that the flutter is still coupled [91, 219, 220].

Figure 5.69 depicts the frequency (left) and damping (right) for each mode from the frequency-domain flutter analysis for the FP model. It is clear that the unstable mode is the torsional mode, exhibiting the critical zero-damping condition $\xi_\alpha = 0$ at U_{cr}.

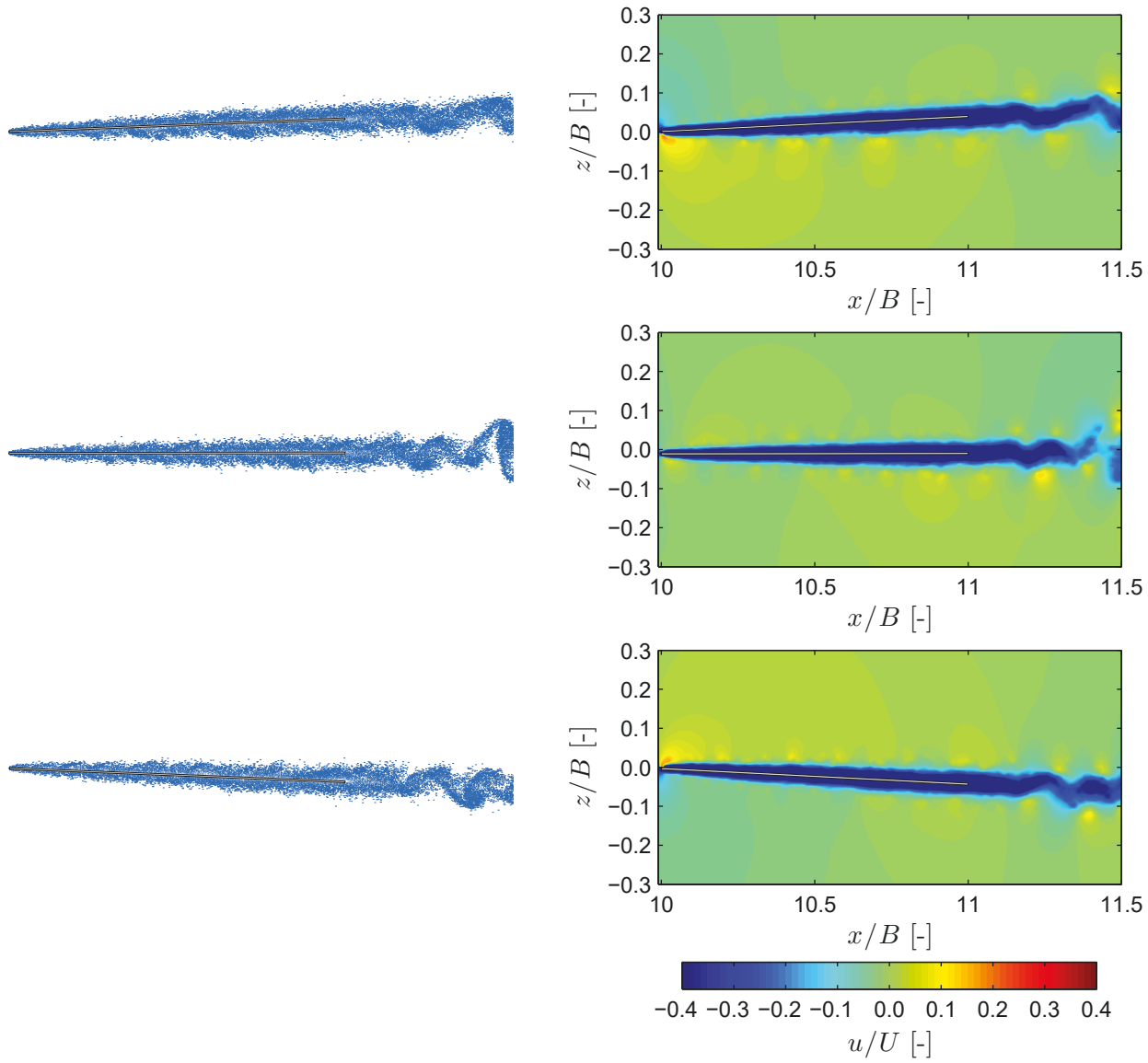

Figure 5.68: Flat plate: instantaneous particle maps and longitudinal velocity fields of a fluttering plate at a consecutive local maximum (top), zero (center) and local minimum (bottom). The cycle is occurring at $\tau \approx 1000$ (cf. Fig. 5.67).

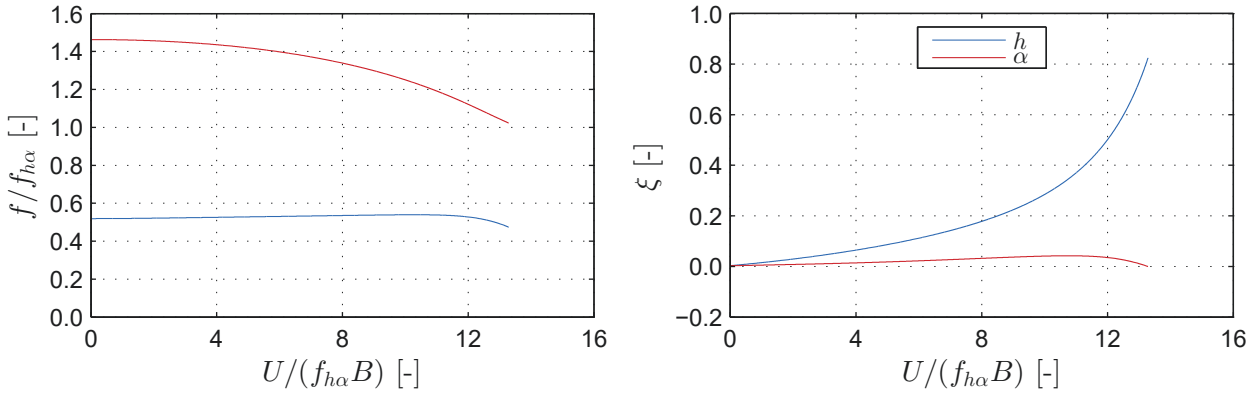

Figure 5.69: Flat plate: frequency (left) and damping ratio (right) from the frequency-domain flutter analysis for the analytical model. The critical flutter velocity is $U_{cr}/(Bf_{h\alpha}) = 13.30$ that corresponds to zero-damping condition $\xi_\alpha = 0$.

5.5 Summary

This chapter presented fundamental applications to study and verify particular aspects of the novel methods and the main framework for aerodynamic analyses and model comparison. Initially, the performance of the comparison metrics presented in Sec. 4.3 was examined on generic signals. By modifying elementary features of the signal, the behavior of the comparison metrics was studied. This demonstrated how and why various global and local signal features should be considered when comparing two time-histories.

Next, the random free-stream turbulence was verified for the CFD model. The turbulent statistics in 2D were examined for the von Kármán spectra, including parametric studies. Generally, good correspondence with the target quantities was observed for the isotropic case, while a reduction in the turbulent energy in the longitudinal fluctuations was reported for the anisotropic case. It was concluded that this discrepancy is a consequence of the grid generated velocities being not divergence-free. Then, the velocity span-wise correlation and coherence between the fluid strips were examined for the novel velocity-based Pseudo-3D VPM, presented in Sec. 3.6.4. The simulated velocity coherence between strips based on the proposed modified coherence model resulted in better correspondence with the target coherence than Vickery's model, particularly for isotropic turbulence. Both coherence models yielded minor underestimation of the coherence for the simulated longitudinal velocity for the isotropic case, which was mainly attributed to the viscous forces. This particular verification provides a basis for an application of the turbulent Pseudo-3D VPM for multimode buffeting analysis of bridges.

Further, the flow field for deterministic gusts was studied. It was shown that sinusoidal gusts can be obtained with sufficient quality and their amplitude can be predicted to some extent using the closed-form solution derived in Sec. 3.7.4. By performing parametric studies, guidelines were given for a selection of numerical and physical parameters for practical applications. Thus, a basis for determination of the complex aerodynamic admittance under deterministic gusts was established.

Finally, a complete aerodynamic analysis of a flat plate was conducted. The results from the aerodynamic coefficients and aeroelastic response were verified with their analytical counterparts. Good agreement was obtained for the boundary layer, static wind coefficients, flutter derivatives and aerodynamic admittance at the baseline Reynolds number. As a particular facet, the novel method for computation of the complex aerodynamic admittance under deterministic gusts was verified w.r.t. the analytical Sears function, yielding excellent results for both real and imaginary parts. Having the aerodynamic coefficients verified, a comparison of the buffeting response for the analytical and CFD models was performed in two manners: one-to-one and statistical comparison. The comparison metrics which ensued from the one-to-one comparison resulted in high values, delivering the conclusion of an excellent correspondence. The outcome of the statistical comparison further supported the overall verification of the buffeting response as the CFD model was completely independent of the analytical one. This represents the first CFD study using the VPM that verifies the buffeting response with an analytical solution. Moreover, the critical flutter velocity for the CFD model was found to be corresponding with the one from analytical frequency- and time-domain flutter analysis with less than 1 % discrepancy.

This chapter was intended to provide clear and convincing results for elementary examples that have either simple or analytical solutions. The utility of the presented methods and framework for applications in bridge aerodynamics is presented in the coming chapter.

Chapter 6

Applications to Bridge Aerodynamics

6.1 Introduction

This chapter shows the applicability of the presented individual methods and synergistic framework to bridge aerodynamics and aeroelasticity. First, the Mersey Gateway Bridge is used as an example to illustrate how the categorical modeling approach can be of practical use. The Great Belt Bridge is used as a second reference object for the application of the complete synergistic framework. Finally, the Third Bosporus Bridge is used as a validation example for the CFD method for the determination of the complex aerodynamic admittance.

6.2 Mersey Gateway Bridge

The Mersey Gateway Bridge spans over the River Mersey and it connects Runcorn and Widnes in Cheshire, UK. A long-held aspiration of the local authorities, the bridge commenced fully operational mode in October 2017. Knight Architects and COWI were commissioned to carry out the design and engineering. Now, the bridge stands as a landmark structure with the main crossing of 988 m, supported by three towers and stay cables.

From a structural aspect, the Mersey Gateway Bridge is a multi-span and cable-stayed, featuring a concrete box deck with varying width in the range approximately between 33 and 34 m. As such, the deck caters to six traffic lanes. The south tower rises 127 m in height, while the north tower 112 m. Both outer towers are considerably higher than the central one, which is 82 m high. The balanced cantilever method was used for the construction, in which first the towers are erected and then the deck is built onwards by casting in-situ segments progressively. For bridges build using this method, the erection stage at maximum cantilever is of special interest in the design check for wind action due to the high bending moments. A particular attribute of the structural system of this bridge is that the deck rests simply supported at the north and south towers, requiring special treatment in the erection stage.

As a part of this case-study, aeroelastic analyses are performed for the south tower at the erection stage, with modified system properties. The goal is to illustrate the practical applicability of the categorical approach to aerodynamic modeling, which was presented in Sec. 4.2. Considering only semi-analytical aerodynamic models, the effect of specific model assumptions on the deck response is studied in a structured manner. Specifically, nine models are considered including the LST, ST, LQS, MQS, CQS, MBM, CMBM, LU, and HNL model. Moreover, the

reference object is chosen to be rather stiff with a bluff cross-section compared to other studies dealing with an assessment of aerodynamic models (cf. e.g. [194, 255, 273, 359]). The results in this section are part of a study by the author (cf. Kavrakov and Morgenthal [167]). Therein, the models are defined slightly different compared to this work and the categorical aspect is not included in the discussion; however, the conclusions stay essentially the same.

This section starts with briefly explaining the structural system, including the modifications made for this particular case. Next, the aerodynamic coefficients, based on CFD analyses, are determined, followed by a buffeting analysis for a range of wind speeds. Finally, a flutter analysis is conducted including a short parametric study of specific aspects of the aforementioned models.

Figure 6.1: Mersey Gateway Bridge: a panoramic impression (picture courtesy Halton Borough Council, from www.merseygateway.co.uk).

Figure 6.2: Mersey Gateway Bridge: south tower in the erection stage, including the temporary pier that was not considered in this study (picture courtesy Halton Borough Council, from www.merseygateway.co.uk).

6.2.1 Modified structural model

In the original design and construction of the Mersey Gateway Bridge, simply supported connection is established between the deck and both south and north pylons. Further, to ensure sufficient stability during the balanced cantilevering stage, a temporary pier was build in addition to the temporary fixing of the deck (cf. Fig. 6.2). Here, the temporary pier is not considered; instead, the deck is rigidly fixed with the tower and additionally stiffened, resulting in relatively higher natural frequencies than the original design.

Figure 6.3 (bottom) depicts the bridge with the considered south tower. Each of the two cantilevers in the maximum cantilever stage is $l_{span} = 205$ m long. At this stage, 57 stay cables are connected to the deck with 8 m distance between the concrete segments. The vertical distance between the tip of the tower and the deck surface amounts to 96 m. With this, the smallest angle between the deck and the cables results in 25.4 deg, while the largest angle results to 68 deg. The cross-section is a concrete box girder with a width of $B = 33.15$ m (cf. Fig. 6.3, top). Inherently, such type of girders poses a high sectional modulus that results in rather high structural stiffness compared to light streamlined sections. Taking this into account, higher natural frequencies are expected compared to flexible suspension bridges.

Based on the basic physical parameters listed in Table 6.1, a Finite Element model was built. The achieved first modes in the lateral, vertical and torsional direction are depicted in Fig. 6.4. Without loss of generality, the wind is applied only to the deck within the aeroelastic analyses. For further information, all considered natural frequencies are included in Tab. B.1 in Appendix B.

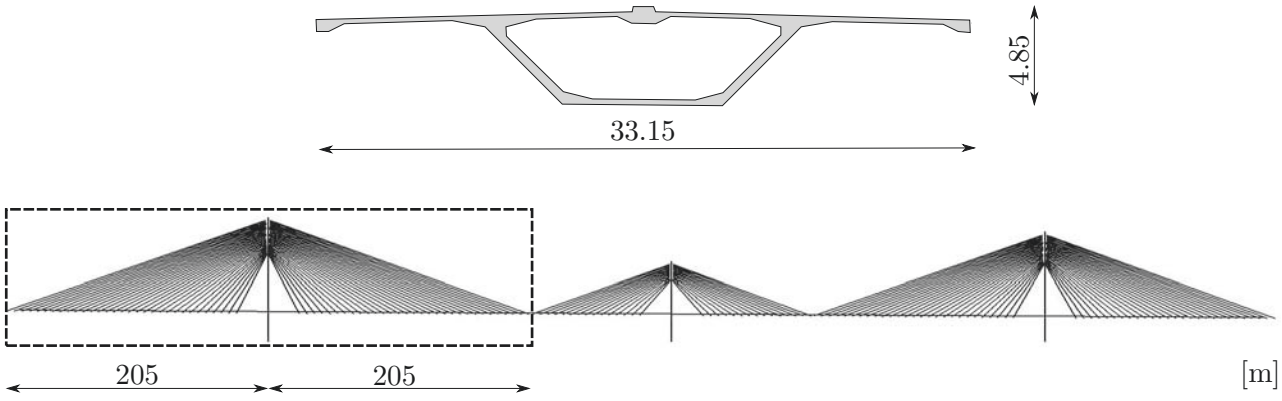

Figure 6.3: Mersey Gateway Bridge: deck cross-section (top) and structural system (bottom), including the considered south tower in the erection stage.

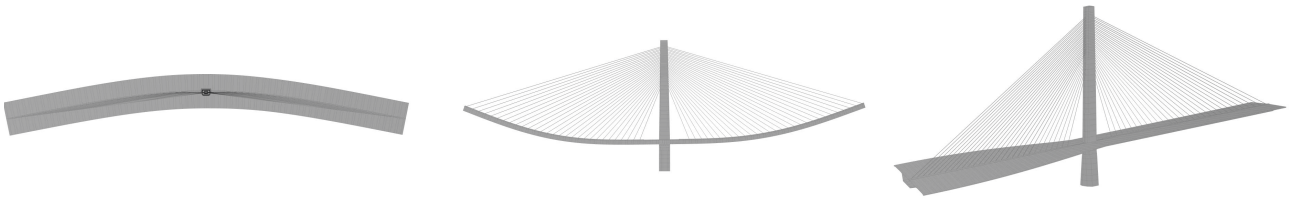

Figure 6.4: Mersey Gateway Bridge: shapes of the first lateral (left, $f_p = 0.401$ Hz), vertical (center, $f_h = 0.444$ Hz) and torsional (right, $f_\alpha = 0.913$ Hz) modes of the south tower in erection stage.

Property type	Physical parameter		Value
Structural	Total span:	l_{span}	2694 m
	Deck width:	B	33.15 m
	Deck depth:	H_D	4.85 m
	Mass:	m_h	28.71 t/m
	Inertial mass:	m_α	2.99×10^3 tm^2/m
	Number of modes:	N_m	15
	First lateral frequency:	f_p	0.401 Hz
	First vertical frequency:	f_h	0.444 Hz
	First torsional frequency:	f_α	0.913 Hz
	Damping ratio:	ξ	1 %
Turbulent	Wind speed:	U	25-75 m/s
	Longitudinal intensity (Low/High):	TI_u	12/24 %
	Vertical intensity (Low/High):	TI_w	6/12 %
	Longitudinal length scale:	L_u	140 m
	Vertical length scale:	L_w	56 m
	Coherence coefficient:	$\boldsymbol{c}_x = (C_x, C_y, C_z)$	(3,8,10)

Table 6.1: Mersey Gateway Bridge: physical parameters.

6.2.2 Aerodynamic coefficients

Static wind coefficients and flutter derivatives are obtained using CFD analyses, for which the section is discretized on $N_{pan} = 280$ panels with a CFD domain spanning approximately $6B$ beyond the trailing edge. As the purpose of this application involves only semi-analytical models that can be based on any set of aerodynamic coefficients, standard numerical parameters described in Sec. 3.6 are used and are not discussed in detail.

Bluff box girders are usually prone to torsional flutter. Their flutter derivatives are rather irregular and sensitive to the angle of incidence, while the moment static wind coefficient may experience negative slope, i.e. stall. Looking at the static wind coefficients in Fig. 6.5, nearly a zero slope is obtained for a static angle of attack amounting to $\alpha_s \approx 6$ deg, which is the first indication for a torsional flutter.

Further, the flutter derivatives for various angles of incidence are depicted in Fig. 6.6 including their rational approximation for the models involving unsteady forces. Impulse functions are

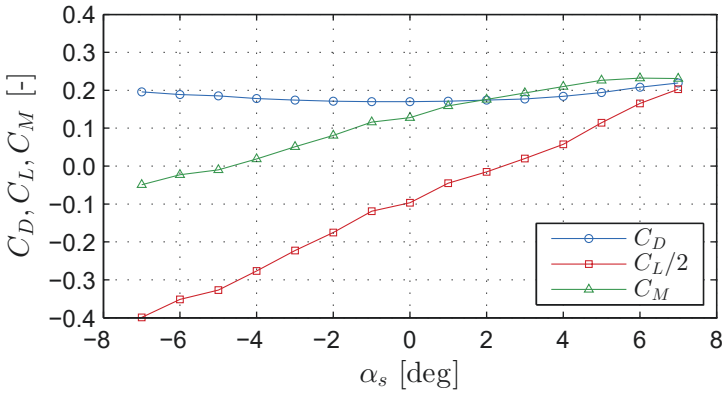

Figure 6.5: Mersey Gateway Bridge: static wind coefficients from CFD analysis.

used for the rational approximation with aerodynamic states ranging in the $N_{st} = 3-5$ interval. A particular point of interest is the derivative A_2^*, which is related to the torsional and which changes sign between the angles $\alpha_s = 3$ deg and $\alpha_s = 6$ deg, indicating torsional flutter. Based on fundamental studies of rectangular cylinders, Matsumoto et al. [216] conclude that as the width-to-depth increases, the flutter mechanism changes from coupled to torsional flutter. Rotating the section about the stiffness center increases the width-to-depth ratio and thus this section is prone to torsional flutter at high angles of attack. For the buffeting analysis,

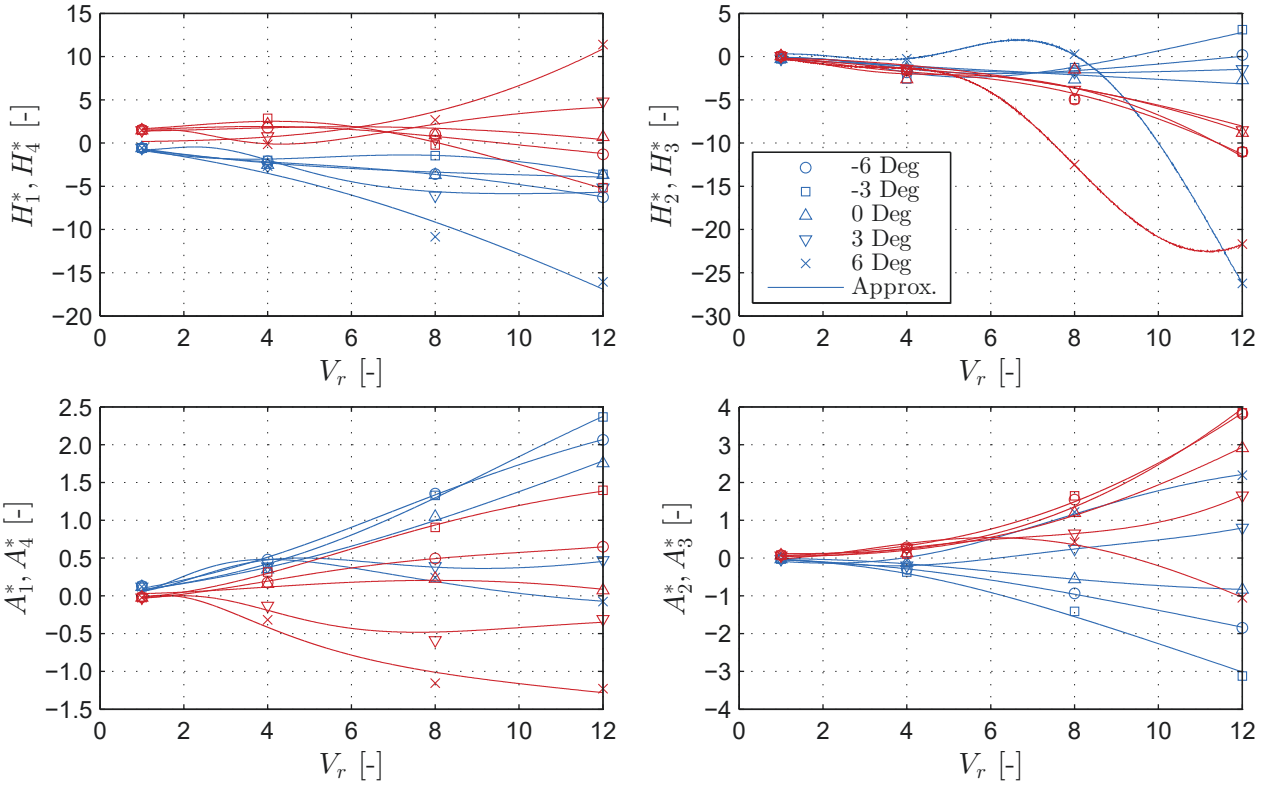

Figure 6.6: Mersey Gateway Bridge: flutter derivatives for various angles of attack from CFD analysis and their rational approximation (Approx.). The derivatives related to the velocity (H_1^*, H_2^*, A_1^*, A_2^*) are given in blue, while the derivatives related to the vertical displacement (H_3^*, H_4^*, A_3^*, A_4^*) are given in red.

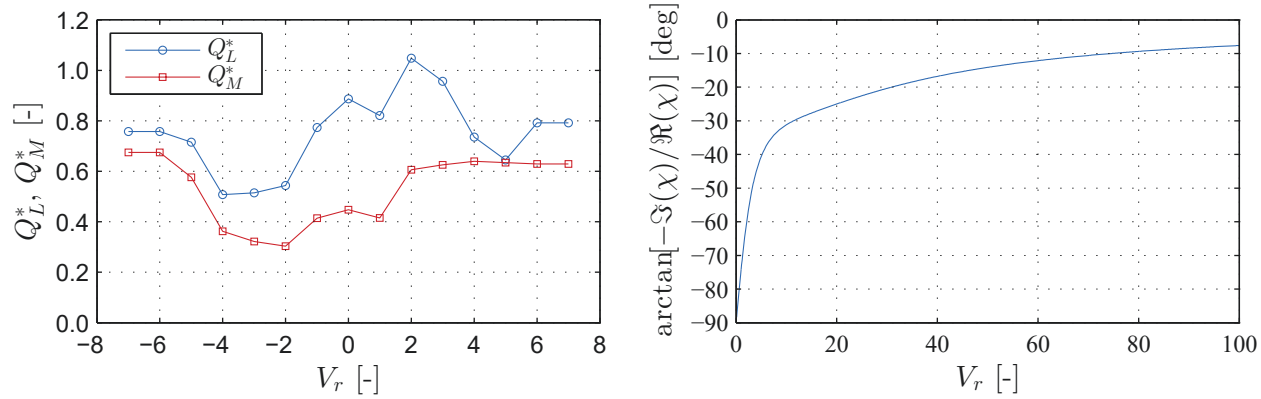

Figure 6.7: Mersey Gateway Bridge: dynamic derivatives at $V_r = 4$ for the CQS model (left) and phase angle between wind fluctuations and buffeting force for Sears aerodynamic admittance (right).

the flutter derivatives P_j^* for $j \in \{1,\dots,6\}$, A_j^* and H_j^* for $j \in \{5,6\}$ are considered to be corresponding to their quasi-steady values (cf. (3.123) from Sec. 3.5.5).

At the time when this particular application was considered, the CFD methods for estimating the aerodynamic admittance were not implemented/developed. Hence, Sears function is used for the aerodynamic admittance to account for the unsteady effects in the buffeting forces. For bluff decks such as the present, the absolute value of the aerodynamic admittance is typically higher than the one for Sears (cf. e.g. [287]). Thus, the unsteady contribution may be overestimated, resulting in lower buffeting forces. The experimental data on the aerodynamic admittance is scarce, which is the reason why many studies also use Sears admittance (cf. e.g. [61, 359]). As the purpose of the present application is mostly a conceptual comparison of assumptions, Sears function is considered to be sufficient and is used for the MBM, CMBM, LU and HNL models.

Apart from the common aerodynamic coefficients, the dynamic derivatives Q^* for the CQS model (cf. (3.145) and (3.146)) are given in Fig. 6.7 (left) for V_r=4. This coefficient accounts for the average fluid memory at a particular reduced velocity. Based on the present results in the figure, the averaged fluid memory is more prominent for the moment than the lift and generally reduces the response. For a larger angle of incidence than zero, the effect seems to be noisier than for the negative angles. In addition, Fig. 6.7 (right) gives the phase angle between the gust and forces for Sears admittance. It can be observed that for $V_r \lessapprox 10$, there is a significant change, while for $V_r \gtrapprox 10$ the phase slowly attenuates. This is important for the lag coefficients n_L and n_M in the HNL model (cf. (3.148) from Sec. 3.5.10) and in order to determine above which V_r quasi-steady assumption becomes valid. Although it is difficult to say when the phase becomes negligible, herein n is obtained based on the interpolation of the admittance at V_r=15. In the case of experimental complex admittance functions, the phase usually converges faster.

6.2.3 Buffeting analysis

Buffeting analysis is performed for the selected models for wind speeds ranging from $U = 25-75$ m/s. A total of seven different wind speeds are selected, each with a duration of 10 minutes (i.e. $t = 600$ s) and time-step amounting to Δt=0.1 s. The spectral properties of the fluctuations are based on the von Kárman spectra and Vickery coherence as in (3.26), with turbulent parameters given in Tab. 6.1 for two turbulent cases: low and high turbulence. At every wind speed in both turbulent cases, the same time-history is used for all of the models, i.e. the input wind fluctuations are identical. The RMS is selected as a SRQ for the following discussion.

Figure 6.8 depicts the RMS across the span of the response for a wind speed of $U = 75$ m/s and the high turbulence case. Three main branches could be distinguished w.r.t. the magnitude of the response. The first branch is the one with the highest amplitudes including the models that neglect the self-excited forces, i.e. the ST and LST models. The second branch involves the QS, LQS, and MQS models, which either neglect the complete fluid memory or the fluid memory of the buffeting forces. In the last branch, consisted of CQS, MBM, CMBM, LU, and HNL models, the fluid memory is included in both self-excited and buffeting forces up to a certain extent. All branches tend to diverge with the rise of the turbulence intensity.

Similar behavior of the models can be observed from the cantilever tip-response for increasing wind speed (cf. Fig. 6.9). The three branches can be also delineated, somewhat more prominent for the vertical displacement than for the rotation. Comparing the two levels of turbulence

intensity, the relative difference between the branches is intensified for the case with high turbulence.

Next, model comparison is conducted based on the diagrammatic ordering of models which was formulated as a part of the categorical approach to aerodynamic modeling in Sec. 4.2.4. The effect of including/excluding a particular aerodynamic assumption is studied for complexity-related models, i.e. only for models that are directly comparable according to Definition 4.12. For the present application, the comparison is based only on the RMS comparison metric $\mathcal{M}_{\text{rms}}$ for the tip-response.

The influence of six assumptions is studied, although many more can be examined based on the current results. Addressing the assumption of interest, based on the model with higher complexity (cf. Sec. 4.2.4), the focus is on the effect of:

- Aerodynamic nonlinearity, based on $\mathbf{Set}_{\text{ST}}$ and metric $\mathcal{M}_{\text{rms}}^{\text{ST,LST}}$, since from (4.14) follows

$$\mathbf{Set}_{\text{ST}}/\mathbf{Set}_{\text{LST}} = \{\boldsymbol{f} = \boldsymbol{f}|_{\alpha_s}\}\,;$$

- Aerodynamic nonlinearity, based on $\mathbf{Set}_{\text{QS}}$ and metric $\mathcal{M}_{\text{rms}}^{\text{QS,LQS}}$, since from (4.12) follows

$$\mathbf{Set}_{\text{QS}}/\mathbf{Set}_{\text{LQS}} = \{\boldsymbol{f} = \boldsymbol{f}|_{\alpha_s}\}\,;$$

- Aerodynamic damping/stiffness, based on $\mathbf{Set}_{\text{LQS}}$ and metric $\mathcal{M}_{\text{rms}}^{\text{LQS,LST}}$, since from (4.13) follows

$$\mathbf{Set}_{\text{LQS}}/\mathbf{Set}_{\text{LST}} = \{\boldsymbol{f}_{se} = 0\}\,;$$

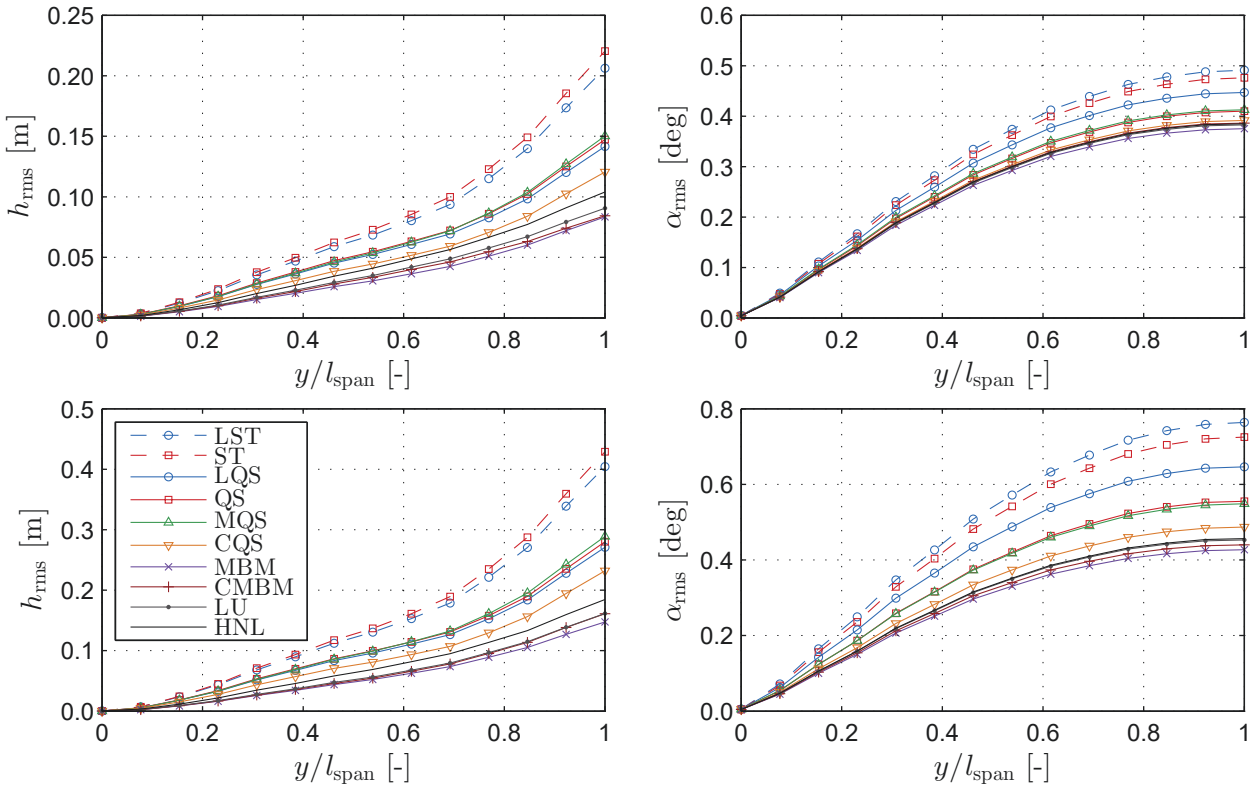

Figure 6.8: Mersey Gateway Bridge: RMS of deck-wise vertical displacement (left) and rotation (right) at $U = 75$ m/s, for the low ($TI_u = 12$ %, TI_w=6 %, top) and high ($TI_u = 24$ %, TI_w=12 %, bottom) turbulent cases.

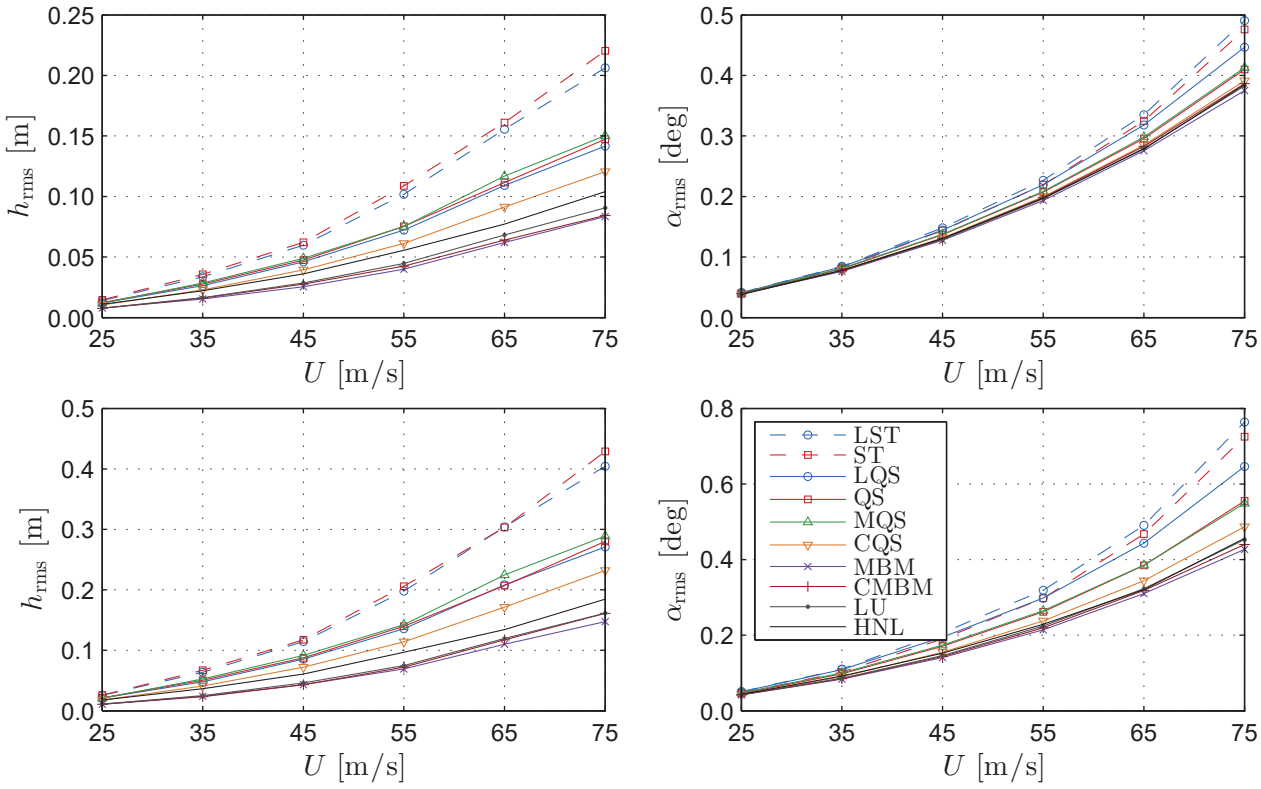

Figure 6.9: Mersey Gateway Bridge: RMS of cantilever tip vertical displacement (left) and rotation (right), for the low ($TI_u = 12$ %, TI_w=6 %, top) and high ($TI_u = 24$ %, TI_w=12 %, bottom) turbulent cases.

- Fluid memory, based on $\mathbf{Set}_{\mathrm{LU}}$ and metric $\mathcal{M}_{\mathrm{rms}}^{\mathrm{LU,LQS}}$, since from (4.12) follows

$$\mathbf{Set}_{\mathrm{LU}}/\mathbf{Set}_{\mathrm{LQS}} = \{V_r \to \infty\}\,;$$

- Aerodynamic coupling, based on $\mathbf{Set}_{\mathrm{LU}}$ and metric $\mathcal{M}_{\mathrm{rms}}^{\mathrm{LU,MBM}}$, since from (4.7) follows

$$\mathbf{Set}_{\mathrm{LU}}/\mathbf{Set}_{\mathrm{MBM}} = \left\{\boldsymbol{f}_{se,\mathrm{coupl}} = 0\right\};$$

- Frequency-dependent fluid memory, based on $\mathbf{Set}_{\mathrm{LU}}$ and metric $\mathcal{M}_{\mathrm{rms}}^{\mathrm{LU,CMBM}}$, since (4.5) follows

$$\mathbf{Set}_{\mathrm{LU}}/\mathbf{Set}_{\mathrm{CMBM}} = \{V_r = V_{rc}\}\,.$$

The term $\boldsymbol{f}_{se,\mathrm{coupl}}$ denotes the coupling terms in the self-excited forces. As the model with higher complexity is taken as a reference for the RMS metric, the comparison is forward according to Definition 4.13.

Figure 6.10 depicts the RMS metric for the above-mentioned comparison couples of aerodynamic models, while Fig. 6.11 depicts a sample of the displacement time-histories. The following discussion is found upon these two figures and the tip-response (cf. Fig. 6.9).

The impact of aerodynamic nonlinearity based on $\mathbf{Set}_{\mathrm{ST}}$ (i.e. steady nonlinearity) is negligent in this case (cf. Fig. 6.10, top-left) as the RMS metric resulted in values of $\mathcal{M}_{\mathrm{rms}}^{\mathrm{ST,LST}} \geq 0.9$ for the response in both turbulent cases. On the other hand, the influence of the aerodynamic nonlinearity based on $\mathbf{Set}_{\mathrm{ST}}$ (i.e. quasi-steady nonlinearity) for the rotation is noteworthy for

the high turbulence case (cf. Fig. 6.10, top-right) and it reduces the response. Thus, including the quasi-steady self-excited forces can affect the influence of aerodynamic nonlinearity.

Neglecting the aerodynamic stiffness and damping, based on $\mathbf{Set}_{\mathrm{ST}}$, significantly increases the vertical response for both turbulence cases. This is a logical observation as the air resistance due to the self-excited forces is in general beneficial for the design before any instability occurs. Thus, the metric $\mathcal{M}_{\mathrm{rms}}^{h^{\mathrm{LQS}},h^{\mathrm{LST}}}$ amounts to a relatively low value of approximately 0.6 for high wind speeds (cf. Fig. 6.10, center-left).

Generally, the largest effect on the response is due to the fluid memory, based on $\mathbf{Set}_{\mathrm{LU}}$

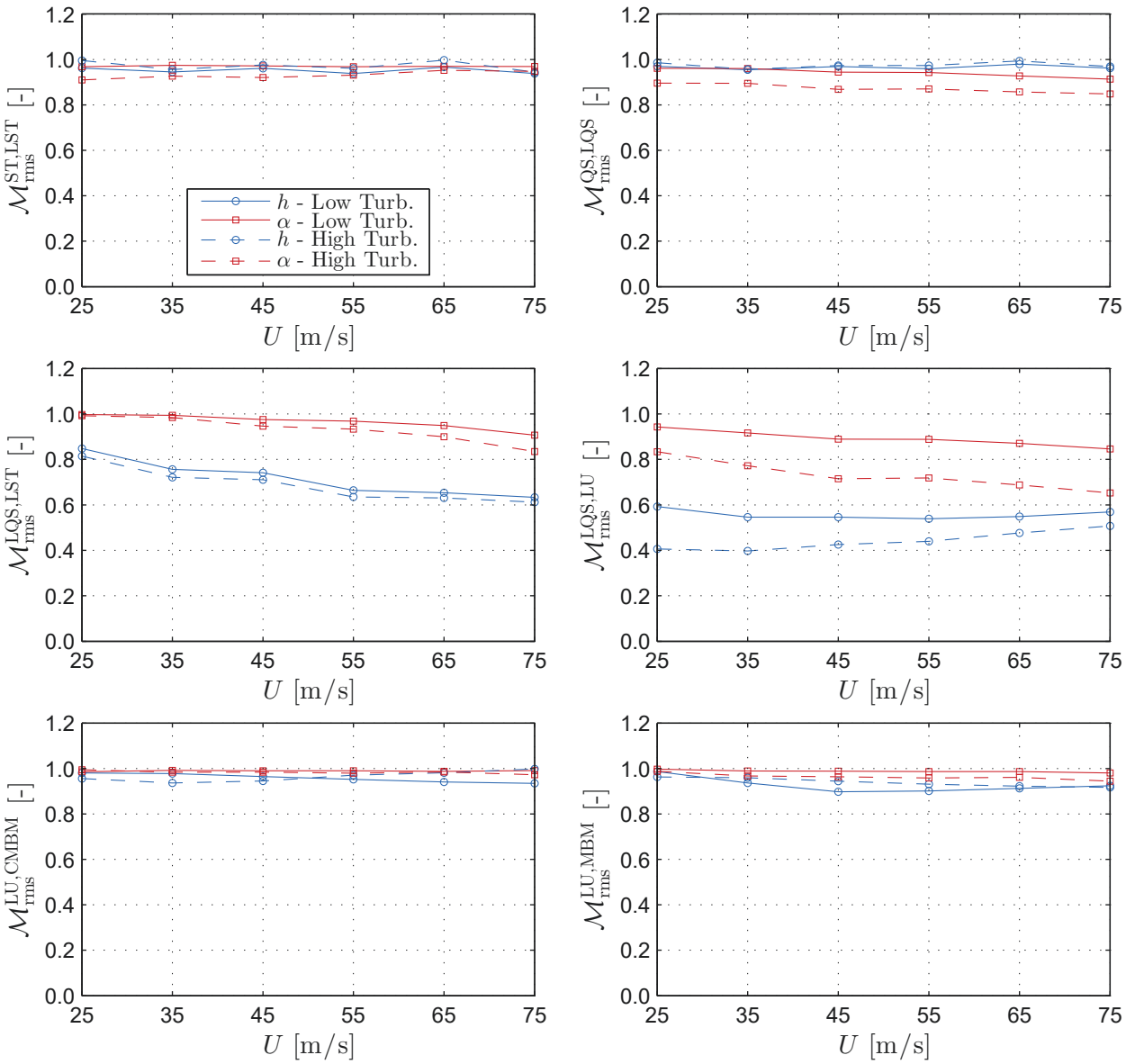

Figure 6.10: Mersey Gateway Bridge: direct and forward comparison of semi-analytical models based on the RMS metric of the response for both turbulent cases to study specific effects of: aerodynamic nonlinearity, based on $\mathbf{Set}_{\mathrm{ST}}$ (top-left); aerodynamic nonlinearity, based on $\mathbf{Set}_{\mathrm{QS}}$ (top-right); aerodynamic damping/stiffness, based on $\mathbf{Set}_{\mathrm{LQS}}$ (center-left); fluid memory, based on $\mathbf{Set}_{\mathrm{LU}}$ (center-right); aerodynamic coupling, based on $\mathbf{Set}_{\mathrm{LU}}$ (bottom-left); frequency-dependent fluid memory, based on $\mathbf{Set}_{\mathrm{LU}}$ (bottom-right).

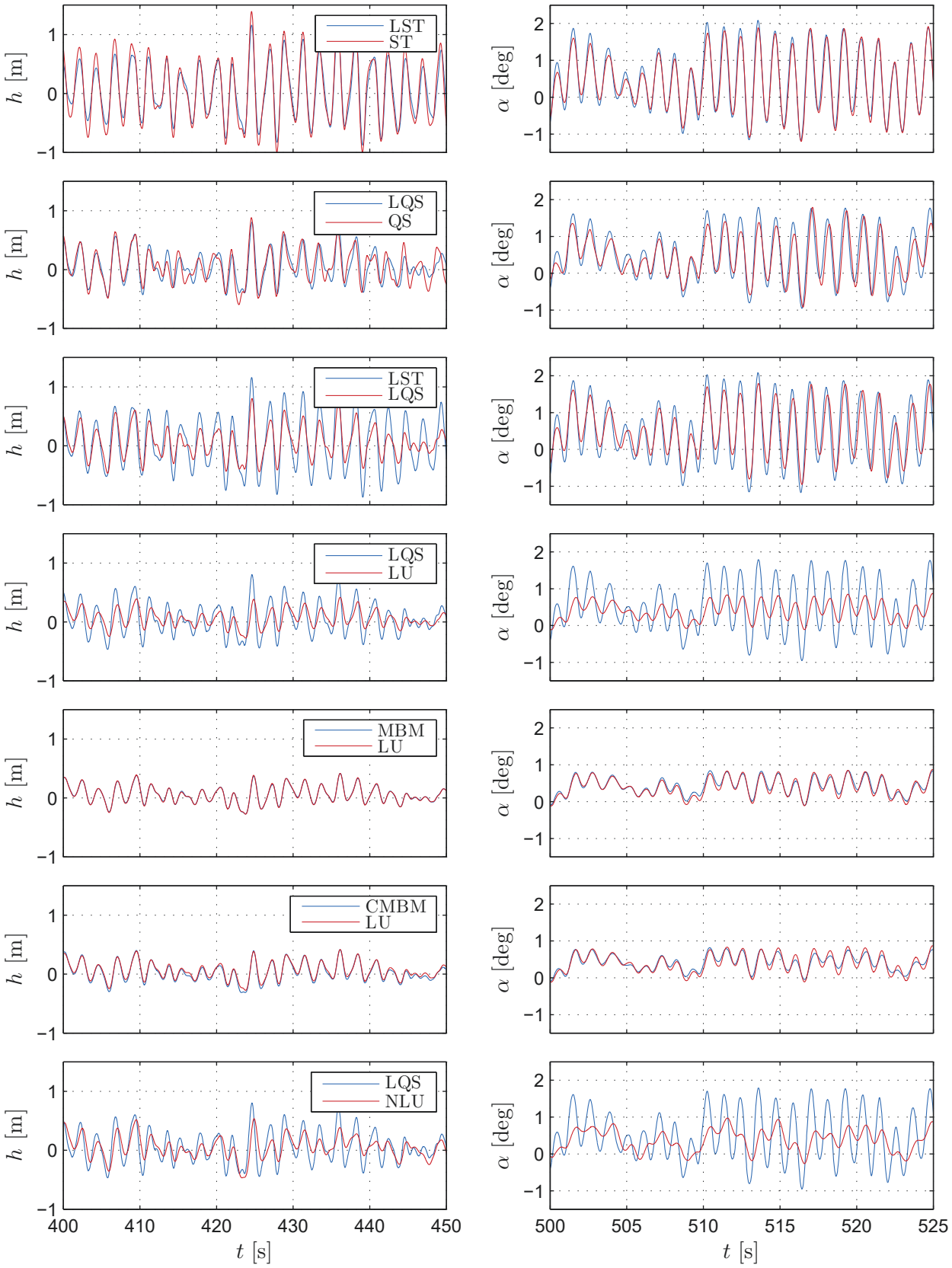

Figure 6.11: Mersey Gateway Bridge: representative sample time-histories of the vertical displacement (left) and rotation (right) for the case of high turbulence ($TI_u = 24$ %, TI_w=12 %) at $U = 75$ m/s. The model couples correspond to the assumptions studied (cf. caption of Fig. 6.10).

(i.e. linear unsteadiness), particularly for the vertical displacement (cf. Fig. 6.10, center-right). Essentially, including the complete linear fluid memory reduces the response and this reduction is more prominent for the high turbulence case. Thus, it is of great importance to consider the unsteady contribution of the aerodynamic forces. This is the main reason why the LU model is, in fact, the baseline model in practice. On the other hand, the influence of the frequency-dependent fluid memory based on $\mathbf{Set}_{\mathrm{LU}}$ is insignificant, which can be observed from the metric $\mathcal{M}_{\mathrm{rms}}^{h^{\mathrm{LU}},h^{\mathrm{CMBM}}}$ (cf. Fig. 6.10, bottom-left). Therefore, assuming averaged fluid memory at the complex-eigenfrequencies is fair.

Interestingly, the effect aerodynamic coupling based on $\mathbf{Set}_{\mathrm{LU}}$ does not have any major impact on the response for the present application (cf. Fig. 6.10, bottom-right). In the typical scenario for streamlined decks, neglecting the aerodynamic coupling can have severe ramifications and result in not detecting the critical flutter limit. This is the case for the next case-study, when the Great Belt Bridge is selected as a reference object.

Finally, the case of comparing models that are not complexity-related is considered, such as the QS, LU and HNL models. To compare these models, first one needs to perform a relative comparison according to Definition 4.12, for which a model of higher or lower complexity than all three models is required. Herein, the LQS model is selected as it is of lower complexity than all other models. According to (4.12), the effect of the aerodynamic nonlinearity for the low-frequency range and fluid memory for the high-frequency range is examined on the metric $\mathcal{M}_{\mathrm{rms}}^{\mathrm{HNL,LQS}}$ since

$$\mathbf{Set}_{\mathrm{HNL}}/\mathbf{Set}_{\mathrm{LQS}} = \left\{ \boldsymbol{f} = \boldsymbol{f}|_{\alpha_s} \text{ for } \alpha_e^l; V_r \to \infty \text{ for } \alpha_e^h \right\}.$$

Figure 6.12 depicts the comparison metrics for the studied models, taking the LQS model as a reference; hence, a backward comparison is in order according to Definition 4.13. Looking at metrics for the vertical displacement, it can be observed that the effect of linear fluid memory has the largest influence, while the effect of quasi-steady nonlinearity is negligible, taking the LQS model as a reference. For the rotation, the impact of the model assumptions on the response is generally lower. However, a conclusion on which of the QS, LQS and HNL models performed better and yielded results of higher quality cannot be drawn. For such comparison, a reference model with higher complexity than all models is necessary.

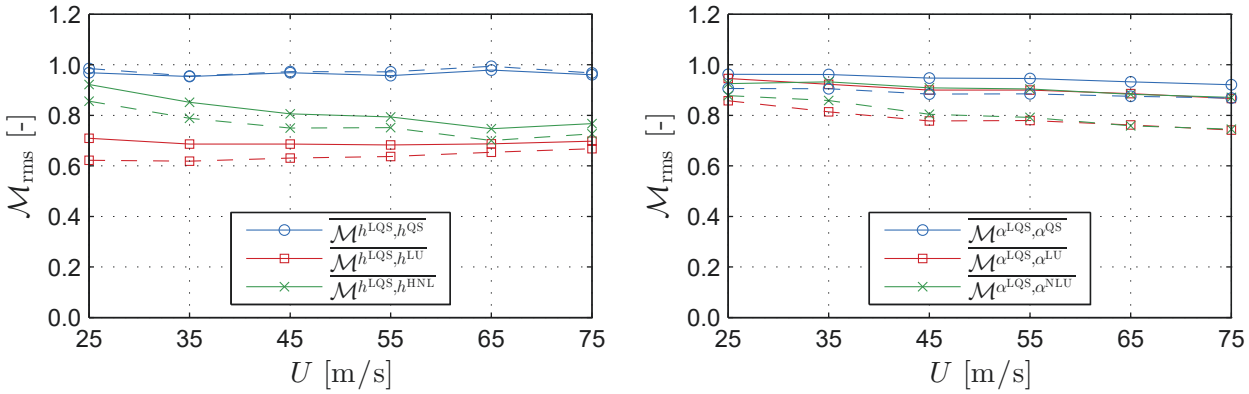

Figure 6.12: Mersey Gateway Bridge: relative and backward comparison of semi-analytical models based on the RMS metric for the vertical displacement (left) and rotation (right) for both low (full line) and high (dashed line) turbulent cases.

6.2.4 Flutter analysis

Stability check during the cantilever erection stage for cable-stayed bridges represents a particular issue as the torsional stiffness of the deck is usually lower than in-service condition. As previously discussed in brief, the structure is prone to torsional flutter for a change of the angle of the incident wind, which can be easily identified by the changing sign of the A_2^* derivative (cf. Fig. 6.13), which is related to the torsional damping of the system. In what follows, flutter analysis is performed for the selected models under uniform free-stream at $\alpha_s = 6$ deg. At a static angle of attack of $\alpha_s = 0$ deg, the structure remained stable for velocities up to $U = 175$ m/s and to consider higher wind speeds would have required extrapolation of the flutter derivatives.

With the exception of the CMBM model, the critical flutter velocity U_{cr} is obtained based on the time-dependent displacements for the rest of the considered models. To illustrate what this means in the time domain, Fig. 6.14 depicts an example of time-history for the LU model below and at the critical wind speed. For wind speeds higher than the critical, the LU model would result in divergent response as the fundamental for the flat plate in the previous chapter. In the post-flutter regime, some of the nonlinear models such as the QS and the CQS models can exhibit limit cycle oscillations. This will be briefly discussed for the next application, while U_{cr} is considered to be the only SRQ addressed herein.

Table 6.2 provides the critical velocity for the selected models. Theoretically, the CMBM and LU models should result in an identical flutter limit as the CMBM has the same complex modal properties as the full frequency-independent system, which was argued by Chen and Kareem [57]. This practically means that the fluid memory is identical for the CMBM and LU models for free-vibration as the structure would oscillate only at the complex eigenfrequencies, where the CMBM model interpolates (i.e. averages) the fluid memory. Nonetheless, the critical flutter velocities are slightly different. In fact, the critical velocity for the LU model using rational approximation is somewhere in between U_{cr} obtained using linear and cubic interpolation for the CMBM model. Thus, this is purely a numerical consequence of the goodness-of-fit of the A_2^* derivative, which could be observed in Fig. 6.13. The assumption of considering the fluid memory the aerodynamic matrices at the complex frequencies ($\mathbf{Set}_{\mathrm{LU}}/\mathbf{Set}_{\mathrm{CMBM}} = \{V_r = V_{rc}\}$, based on $\mathbf{Set}_{\mathrm{LU}}$, from (4.5)) has no influence for the critical flutter velocity. Comparing directly the HNL and LU model is not permitted under the categorical framework, as discussed in the previous section. However, for flutter analysis, the HNL model is governed either by the

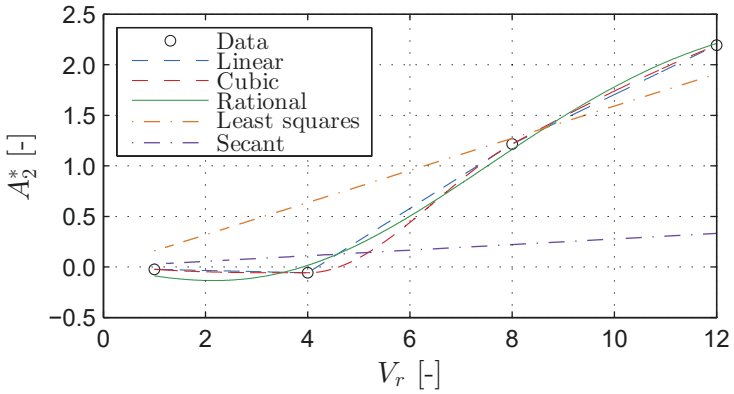

Figure 6.13: Mersey Gateway Bridge: flutter derivative A_2^* with linear and cubic interpolation (CMBM model), rational approximation (MBM, LU, and HNL models), least-squares and secant approximation (MQS model).

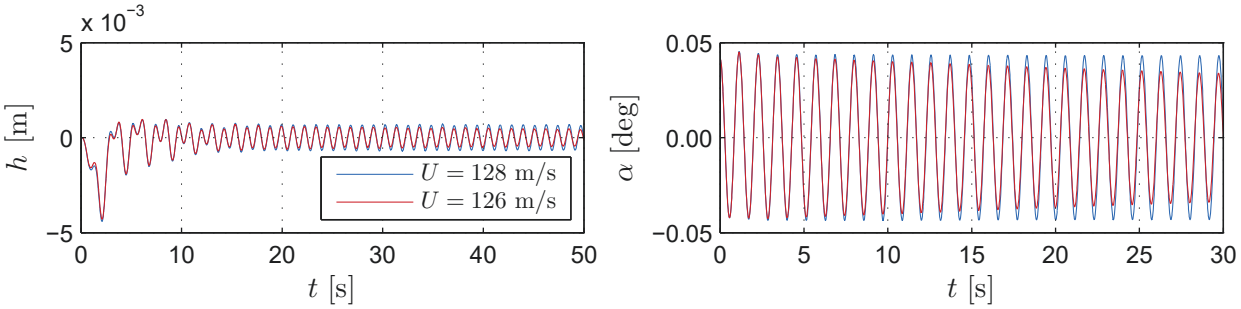

Figure 6.14: Mersey Gateway Bridge: sample time-histories of the vertical displacement (left) and rotation (right) at critical flutter velocity ($U_{cr} = 128$ m/s) and below ($U = 126$ m/s) for the LU model under laminar free-stream at angle of attack of $\alpha_s = 6$ deg.

Model	Note	U_{cr} [m/s]
QS	Aerodyn. center: $m = m(f_{h\alpha})$	106
QS	Aerodyn. center: $m = m(f_{\alpha})$	140
LQS	Aerodyn. center: $m = m(f_{h\alpha})$	99
LQS	Aerodyn. center: $m = m(f_{\alpha})$	131
CQS	Aerodyn. center: $m = m(f_{h\alpha})$	102
CQS	Aerodyn. center: $m = m(f_{\alpha})$	134
MQS	Approx.: Least squares	22
MQS	Approx.: Secant	157
MBM	Approx.: Rational	132
CMBM	Interp.: Linear	125
CMBM	Interp.: Cubic	137
LU	Approx: Rational	128
HNL	Approx: Rational	128

Table 6.2: Mersey Gateway Bridge: critical flutter velocities at $\alpha_s = 6$ deg angle of attack.

quasi-steady or linear unsteady part. Since both models used the flutter derivatives at $\alpha_s = 6$ deg and resulted in identical U_{cr}, the linear unsteady assumption is governing. In general, the results might differ if the response of the HNL model is governed by the quasi-steady part.

When comparing the MQS and CMBM models for free-vibration, the assumption of interest is the complex modes are identical as the natural modes ($\mathbf{Set}_{\text{CMBM}}/\mathbf{Set}_{\text{MQS}} = \left\{\lambda_j = \omega_j; \boldsymbol{\phi}_j = \boldsymbol{\psi}_j\right\}$, based on $\mathbf{Set}_{\text{LU}}$ for $j \in \{1, 2, 3\}$, from (4.6)). Additional uncertainty is included in the approximation of the flutter derivatives for the MQS model, while they are automatically interpolated at the complex eigenfrequencies for the CMBM model. As a result of the nearly quadratic shape of the A_2^* derivative, the U_{cr} obtained using the linear least-squares approximation for the MQS is underestimated significantly. The accuracy of the MQS model is generally good for linear trends for the velocity-related and quadratic trends for the displacement related flutter derivatives. For different trends than this, the secant approximation is used at the reduced velocity of interest, as pointed out in Øiseth et al. [244]. Utilizing the secant approximation for A_2^* w.r.t. the torsional frequency, the analysis with the MQS yielded in overestimation of the flutter limit by 14.6 % w.r.t. the limit for the CMBM with cubic interpolation. Thus, it is difficult to say whether the discrepancy is due to numerical uncertainty or due to the inherent assumption in the mathematical construction of the MQS model.

The effect of aerodynamic coupling is the assumption of interest when comparing the MBM and LU models ($\mathbf{Set}_{\mathrm{LU}}/\mathbf{Set}_{\mathrm{MBM}} = \left\{\boldsymbol{f}_{se,\mathrm{coupl}} = 0\right\}$, based on $\mathbf{Set}_{\mathrm{LU}}$, from (4.7)). For purely torsional flutter, both models should deliver identical results. However, the instability threshold for the MBM was underestimated by 3.1 % due to the effect of the aerodynamic coupling, which is of minor significance. Moreover, the MBM model is able to predict aerodynamic instability as the instability is torsional; i.e. the MBM model is complete w.r.t. torsional flutter. Should the instability has been coupled flutter, this would not have been possible as the MBM model is not a part of the **FlutterModel** category in (4.15).

Before studying the effect of the aerodynamic assumptions for the LQS, CQS and QS models, a brief discussion is given on the influence of the uncertainty in selecting equivalent reduced velocity V_r for the aerodynamic center m_α. Torsional instability for these models occurs if the aerodynamic center is positioned between the trailing edge and the stiffness center, i.e. $m_\alpha > 0$. Flutter can not occur in this case by choosing $V_r \geq 12$ at 6 deg static angle of incidence. Although the value of A_2^* is negative, A_3^* is negative as well (cf. Fig. 6.6), resulting in positive value for the aerodynamic center, based on (3.125). Negative values for A_3^* rarely occur and at high reduce velocities, the quasi-steady values indicate stall, i.e. $C_M^{'} < 0$. However, some studies have reported negative value for the A_3^* such as for the Tacoma Narrows Bridge, reported by Larsen and Walther [193] or the Deer-Isle Sedgewick Bridge, reported by Caracoglia and Jones [45]. Therefore, the assumption of selecting the aerodynamic center at high V_r is challenged for bluff bridge decks which are prone to torsional flutter. Thus, flutter analysis is conducted for two cases w.r.t. the aerodynamic center. In the first case, the aerodynamic center is based on the reduced velocity for the central frequency of oscillation $f_{h\alpha} = (f_h + f_\alpha)/2$, while in the second case, the torsional frequency f_α is used for the determination of the aerodynamic center. For these values, the coefficient H_3^* is still in the positive range; thus, flutter occurs. As an alternative to obtaining the aerodynamic center based on the flutter derivatives (cf. (3.125), this coefficient is set as $m_\alpha = -0.25$ for streamlined bridge decks, which assures no occurrence of torsional flutter.

The flutter limits for the LQS model with $m = m(f_\alpha)$ and the CMBM model are close. This makes sense since the oscillations are driven by the pitching motion and the coupling effects have minor influence. The underestimation of 4.4 % of U_{cr} between this two models is attributed to the linear fluid memory of the self-excited forces contained in the CMBM model, i.e. due to the quasi-steady assumption ($\mathbf{Set}_{\mathrm{CMBM}}/\mathbf{Set}_{\mathrm{LQS}} = \{V_r \to \infty\}$, based on $\mathbf{Set}_{\mathrm{CMBM}}$, from (4.12)). The influence of the quasi-steady aerodynamic nonlinearity contained in the QS model increased the flutter velocity by 6.4 % compared to the LQS model ($\mathbf{Set}_{\mathrm{QS}}/\mathbf{Set}_{\mathrm{LQS}} = \{\boldsymbol{f} = \boldsymbol{f}|_{\alpha_s}\}$, based on $\mathbf{Set}_{\mathrm{QS}}$, from (4.12)). By including the averaged nonlinear fluid memory for the CQS, the flutter limit is reduced for 4.3 % w.r.t. the QS model ($\mathbf{Set}_{\mathrm{CQS}}/\mathbf{Set}_{\mathrm{QS}} = \{V_r \to \infty\}$, based on $\mathbf{Set}_{\mathrm{CQS}}$, from (4.10)). It is worth mentioning that the models, in which the aerodynamic damping is based on the aerodynamic center, may overestimate or underestimate the critical velocity by a relatively large margin; therefore, such models are generally not used for flutter analyses.

6.3 Great Belt Bridge

Little more than two decades have passed since the Great Belt Bridge opened to traffic. The bridge is a part of the Great Belt Link that connects the Danish islands Zealand and Funen. With a main span of 1624 m, it had the second-longest span in the world at the time of the commencement of operation, trailing only Akashi Kaikyō Bridge. Although records of initial plans for linking the two Danish islands can be found dating back to the 1930s, it was not until the late 1980s and early 1990s when the design was finished by COWI, Ramboll and Dissing+Weitling. Today it holds the record of the longest span in Europe and is still undoubtedly considered one of the most remarkable structures (cf. Fig. 6.15).

Structurally, the Great Belt Bridge is a multi-span suspension bridge with a main span of 1624 m and two side-spans of 535 m each, totaling a cable-supported length of $l_{span} = 2694$ m (cf. Fig. 6.16, bottom). Untypical for suspension bridges, the structural system of the Great Belt Bridge is a continuous girder, without joints at the pylons. Such a system benefits the in-service lateral deflections due to both traffic and wind, as noted by Larsen [188]. This made the design possible with only 4.34 m deep steel girder (cf. Fig. 6.16, top). To put things in perspective, the Great Belt Bridge has a 15 % longer span than the Humber Bridge with practically the same depth of the deck [119].

In bridge aerodynamics, the Great Belt Bridge is one of the most studied bridges. It represents sort of a benchmark deck for testing and applying new models and methodologies owning to its streamlined aerodynamic shape and the much-appreciated effort by the Danish government, affiliated consultancies, and design companies to make a large amount of the design data public. Therefore, this bridge is selected as the main application example for all developed methods and methodologies, with the exception of the complex aerodynamic admittance. With this, an attempt is made to show how the individual parts of the synergistic framework fit and contribute together to both the fundamental understanding of the wind-bridge interaction and practical calculation of the response.

Figure 6.15: Great Belt Bridge: a panoramic impression (picture courtesy of Niels Elgaard Larsen (Elgaard), from commons.wikimedia.org).

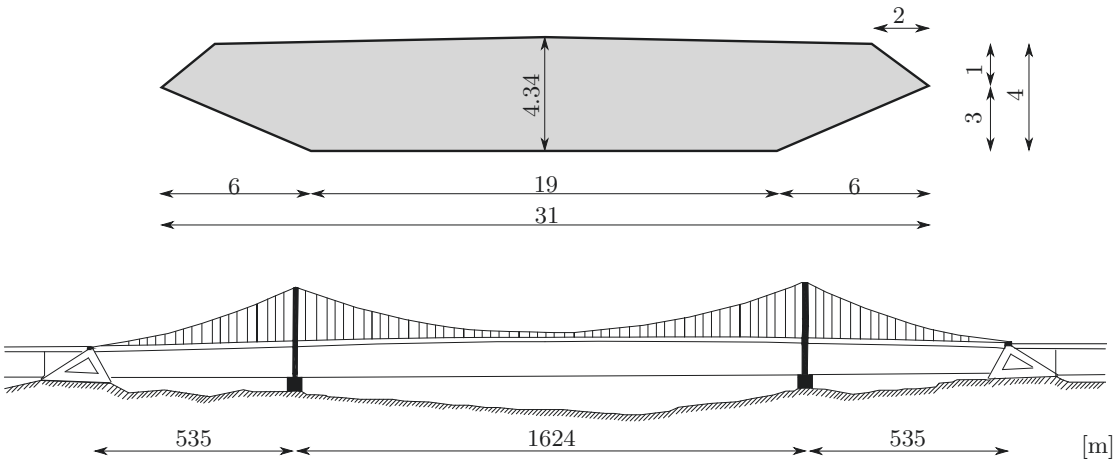

Figure 6.16: Great Belt Bridge: deck cross-section (top) and structural system in elevation (bottom).

The section starts by briefly discussing the structural model. This is followed by describing the numerical and experimental setup for the aerodynamic models and establishing a comparative basis for the CFD and selected semi-analytical models. Next, the aerodynamic coefficients from the CFD analyses are determined and validated with experimental results from this and former studies, where possible. Then both the self-excited and buffeting forces are studied for the CFD model independently and are compared with the selected semi-analytical models to quantify the effect of aerodynamic assumptions. This step is also repeated for the aeroelastic response in a similar fashion for the 2D one-to-one buffeting and flutter analysis. Finally, Pseudo-3D flutter and buffeting CFD analyses are performed and compared with the results for the LU model in a statistical manner.

6.3.1 Structural model

Specific dimensions of the used deck can be found in Fig. 6.16 (top), which is a scaled section of the H9.1 model tested in a wind tunnel by Reinhold et al. [263]. Herein, additional equipment such as barriers and fairings were not considered. The reason for the lack of detailed modeling of additional equipment is to reduce the computational load for the CFD analyses since very fine discretization is required to resolve to small turbulent scales, thin boundary layer and complex flow structures in the region of the deck details.

A Finite Element model of the Great Belt Bridge is constructed to obtain the dynamic properties. The model is based on the information provided by Larsen [188] and Karoumi [162]. Some of the structural parameters are given in Tab. 6.3. Approximately 120 beam elements are used to model the deck, with the appropriately distributed mass and sectional modulus for the steel deck girder. Positioned every 4 m, the hangers are connected to the main cables and to the center of the deck using rigid elements horizontally, suspending the bridge in the vertical direction. The catenary shape was obtained from the 1/9 main span-to-sag ratio, resulting in a total sag of 180 m. The concrete pylons are modeled as beam elements as well, with tapered cross-section. Including the cable saddle, the total height of the pylon reaches 257.6 m. Springs are used to connect the deck to the pylon in the lateral direction.

By varying the prestressing force in the cable and spring stiffness at the support, the modal frequencies are calibrated against the ones given by Larsen [188]. Exact correspondence is obtained w.r.t. the first mode in lateral, vertical, and torsional directions (cf. Tab. 6.3). The

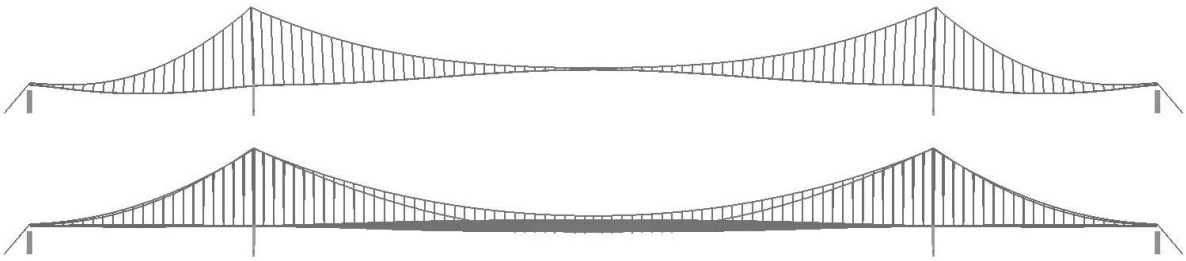

Figure 6.17: Great Belt Bridge: shapes of the first vertical (f_h = 0.100 Hz, top) and torsional (f_α = 0.278 Hz bottom) modes.

first lateral and vertical modes are depicted in Fig. 6.17. Without a loss of generality, the wind is applied only to the deck within the aeroelastic analyses. A total of $N_{str} = 50$ strips are used for the Pseudo-3D analysis for both the CFD and semi-analytical models. The strips are mostly regularly spaced across the deck, with an average length of each strip of approximately 54 m. The modes are then interpolated at the center of the strips. Such span-wise discretization accommodates a total of $N_m = 22$ modes for the Pseudo-3D analysis. It is worth noting that until now, a maximum of 11 strips has been used for Pseudo-3D CFD analysis, yielding the present span-wise discretization as very high resolution. Only two degrees of freedom are used to describe the structural system in 2D. All considered natural frequencies are given in Tab. B.2 in the Appendix B.

6.3.2 Aerodynamic models: Setup and comparative basis

CFD and semi-analytical models

Several types of analyses are performed for this case-study to determine various quantities such as the aerodynamic coefficients, forces, and response. Therefore, the physical and numerical parameters for the CFD and semi-analytical models are generally dependent on the type of analysis and unless noted otherwise, the parameters in Tabs. 6.3 and 6.4 are used. An important remark is that the verification of the 2D and Pseudo-3D free-stream turbulence in Sec. 5.3 is performed using the exact same parameters. Thus, the same inflow particles are directly employed for the CFD buffeting analysis and the determination of aerodynamic admittance for random free-stream turbulence.

Before proceeding with analyses, a comparative basis for the CFD semi-analytical and semi-analytical models is laid out. For all following comparisons, the CFD model is taken as a reference as it is of the highest complexity compared to the rest of the semi-analytical models according to the categorical diagram of model ordering (cf. Sec. 4.2.4).

Property type	Physical parameter		Value
Structural	Total span:	l_{span}	2694 m
	Deck width:	B	31 m
	Deck depth:	H_D	4.4 m
	Mass:	m_h	22.74 t/m
	Inertial mass:	m_α	2.47×10^3 tm^2/m
	Number of modes:	N_m	22
	First lateral frequency:	f_p	0.052 Hz
	First vertical frequency:	f_h	0.100 Hz
	First torsional frequency:	f_α	0.278 Hz
	Damping ratio:	ξ	0.5 %
	Forced oscillation:	V_r	$2-16$
	Forced oscillation amplitude:	$\alpha_0 = \dot{h}_0/U$	1 deg
Laminar	Wind speeds:	U	20-75 m/s
	Reynolds number:	Re	1.03×10^5
2D Random turbulent (isotropic)	Wind speed:	U	20-60 m/s
	Longitudinal intensity (Low/High):	TI_u	6/10 %
	Vertical intensity (Low/High):	TI_w	6/10 %
	Longitudinal length scale:	L_u	54 m
	Vertical length scale:	L_w	27 m
	Turbulent Reynolds number:	Re_{L_u}	1.8×10^5
	Coherence coefficient:	$\boldsymbol{c}_x = (C_x, C_z)$	(3,10)
Pseudo-3D Random turbulent (anisotropic)	Wind speed:	U	30 m/s
	Longitudinal intensity:	TI_u	11 %
	Vertical intensity:	TI_w	6 %
	Longitudinal length scale:	L_u	108 m
	Vertical length scale:	L_w	30 m
	Turbulent Reynolds number:	Re_{L_u}	3.59×10^5
	Coherence function:	coh	Davenport
	Coherence coefficient:	$\boldsymbol{c}_x = (C_x, C_y, C_z)$	(3,5,10)

Table 6.3: Great Belt Bridge: physical parameters for the CFD and semi-analytical models.

Numerical parameter		Value
Domain length:	l_d/B	21
Domain height:	l_h/B	21
Number of panels:	N_{pan}	250
Panel length:	$\Delta l_{pan}/B$	8.08×10^{-3}
Reduced time-step:	$\Delta\tau = \Delta t U/B$	1.65×10^{-2}
Total time:	$\tau = tU/B$	677
Core radius:	ϵ/B	9.77×10^{-3}
Poisson grid:	$N_x \times N_z$	511×511
P^{3}M neighboring cells:	N_r	3
Particle release factor:	$\Delta p = \Delta t_{in}/\Delta t$	4
Particle band height:	l_G/B	18
Number of strips:	N_{str}	50
Correction factor:	β_{in}	0.7 (0.65)

Table 6.4: Great Belt Bridge: numerical parameters.

Six aerodynamic models are studied, including the LQS, QS, CQS, MQS, LU, and HNL models. The assumptions included in these models result in neglecting certain effects that can be captured by the CFD model. Accordingly, none of the semi-analytical models are able to capture the vortex shedding and interior noise forces and they are time-invariant (cf. (4.3)). In addition to these, based on $\mathbf{Set}_{\mathrm{CFD}}$, the following effects are neglected:

- Aerodynamic nonlinearity and fluid memory for the LQS model (cf. (4.12)), as
$$\mathbf{Set}_{\mathrm{CFD}}/\mathbf{Set}_{\mathrm{LQS}} = \{\boldsymbol{f}_v = 0; \boldsymbol{f}_{noi} = 0; \boldsymbol{f}(t) = \boldsymbol{f}(\boldsymbol{a}(t)); \boldsymbol{f} = \boldsymbol{f}|_{\alpha_s}; V_r \to \infty\};$$
- Fluid memory for the QS model cf. (4.10), as
$$\mathbf{Set}_{\mathrm{CFD}}/\mathbf{Set}_{\mathrm{QS}} = \{\boldsymbol{f}_v = 0; \boldsymbol{f}_{noi} = 0; \boldsymbol{f}(t) = \boldsymbol{f}(\boldsymbol{a}(t)); V_r \to \infty\};$$
- Frequency-dependent fluid memory for self-excited forces, fluid memory for buffeting forces and aerodynamic nonlinearity for the MQS model (cf. (4.6)), as
$$\mathbf{Set}_{\mathrm{CFD}}/\mathbf{Set}_{\mathrm{MQS}} = \{\boldsymbol{f}_v = 0; \boldsymbol{f}_{noi} = 0; \boldsymbol{f}(t) = \boldsymbol{f}(\boldsymbol{a}(t)); V_r \to V_{rc}\};$$
- Frequency-dependent fluid memory, conditioned on the origin of the effective angle, for the CQS model (cf. (4.9)), as
$$\mathbf{Set}_{\mathrm{CFD}}/\mathbf{Set}_{\mathrm{CQS}} = \left\{ \boldsymbol{f}_v = 0; \boldsymbol{f}_{noi} = 0; \boldsymbol{f}(t) = \boldsymbol{f}(\boldsymbol{a}(t)); \right.$$
$$\left. \boldsymbol{f}\left(\frac{w}{U+u}\right) = \boldsymbol{f}\left(\frac{\dot{h}}{U-\dot{p}}\right) = \boldsymbol{f}\left(\frac{mB\alpha}{U-\dot{p}}\right); V_r \to V_{rc} \right\};$$
- Aerodynamic nonlinearity for the LU model (cf. (4.4)), as
$$\mathbf{Set}_{\mathrm{CFD}}/\mathbf{Set}_{\mathrm{LU}} = \{\boldsymbol{f}_v = 0; \boldsymbol{f}_{noi} = 0; \boldsymbol{f}(t) = \boldsymbol{f}(\boldsymbol{a}(t)); \boldsymbol{f} = \boldsymbol{f}|_{\alpha_s}\};$$
- Fluid memory for the low-frequency range and aerodynamic nonlinearity for the high frequency range for the HNL model (cf. (4.11)), as
$$\mathbf{Set}_{\mathrm{CFD}}/\mathbf{Set}_{\mathrm{NLU}} = \left\{\boldsymbol{f}_v = 0; \boldsymbol{f}_{noi} = 0; \boldsymbol{f}(t) = \boldsymbol{f}(\boldsymbol{a}(t)); \boldsymbol{f} = \boldsymbol{f}|_{\alpha_s} \text{ for } \alpha_e^l; V_r \to \infty \text{ for } \alpha_e^h\right\}.$$

When performing one-to-one comparisons, all comparison metrics defined in Sec. 4.3 are used to discuss the effect of the aerodynamic assumptions. Unless noted otherwise, the metric parameters given in Tab. 6.5 are used for computing the comparison metrics.

Metric parameter		Value
Normalization time:	T_c	$1/(4f_h{+}4f_\alpha)$
Central wavelet frequency:	f_{ce}	$10.5f_\alpha$
Confidence level:	CL	95 %
Surrogates - Stationarity:	N_{sur}	200
Exceedance - Stationarity:	g_s^*	2
Surrogates - Nonlinearity:	N_{sur}	100
Exceedance - Nonlinearity:	g_b^*	2
Sensitivity - PDF:	$\varepsilon_{\mathrm{PDF}}$	10

Table 6.5: Great Belt Bridge: comparison metric parameters for the one-to-one comparison of buffeting response.

Experimental model

For validation of the static wind coefficients, experiments were conducted at the low-speed wind tunnel at the Bauhaus-Universität Weimar (cf. Fig. 6.18). The tunnel is of the closed return type with a measuring section of size $2.5 \times 1.3 \times 0.8$ m (length×width×height), allowing wind speeds in the range of $U = 1 - 30$ m/s. Such wind tunnels are characterized by superior flow quality in the test section with low turbulence ($TI_u \approx 0.5$ %). However, a high blockage may be an issue for large section ratios. Forces in all six directions were measured using two strain gauge load cells with low cross-talk (cf. Fig. 6.18, e). The signals were then passed through analog amplifies with a sampling frequency of 500 Hz.

Figure 6.18 (a and b) presents the setup for the experiments. A plywood experimental model was constructed by assembling eleven individual cross-sections (cf. Fig. 6.18, c). Using a high precision laser cutting system, superior accuracy was achieved with less than 0.1 mm deviation for the cross-sections. The model was closed using elliptical plates to avoid the end-effects. The geometrical scale of the model w.r.t. the scaled H9.1 section (cf. Fig. 6.16, top) is 1 : 100, yielding a width of $B = 31$ cm and a height of $H_D = 4.4$ cm. Including end-plates, the length of the model that gathers the aerodynamic forces amounts to 1.2 m. Assembled as such, the geometrical properties of the model allow one to perform tests at Reynolds number that is comparable to other experimental studies for a similar section to the selected one (cf. Reinhold et al. [263]), while retaining reasonable blockage ratio.

The measurements for a static section at each angle of attack were performed in a sequence lasting approximately 16 minutes. Figure 6.18 (f) depicts a smoke visualization at $\alpha_s = 0$ at low wind speed. Each measuring sequence consists of four parts, including initial part at $U = 0$ m/s for three minutes, two parts at two separate wind speeds, $U = 5.4$ m/s and $U = 10.8$ m/s, for five minutes each, and final part at $U = 0$ m/s for three minutes. Performing the experiments in such a way permits to set up a baseline for the measurement forces at $U = 0$ m/s. For the static wind coefficients, the measurements at $U = 5.4$ m/s are used, which yields a Reynolds number of $\mathrm{Re} = 1.0 \times 10^5$.

Measuring the static wind coefficients for the H9.1 section is of particular importance, as the experimental results by Reinhold et al. [263] are for the H4.1 section with a ratio of $B/H_D = 6.81$. This section is different from the H9.1 section ($B/H_D = 7.05$), which was used in the experiments by Reinhold et al. [263] for the flutter derivatives. Thus, both static wind coefficients and flutter derivatives from the CFD can be now validated for the H9.1 section. Naturally, it would have been better if the remaining aerodynamic coefficients such as the flutter derivatives and aerodynamic admittances are measured as well using the current experimental setup; however, the present state of wind tunnel equipment still needs further development for such tests.

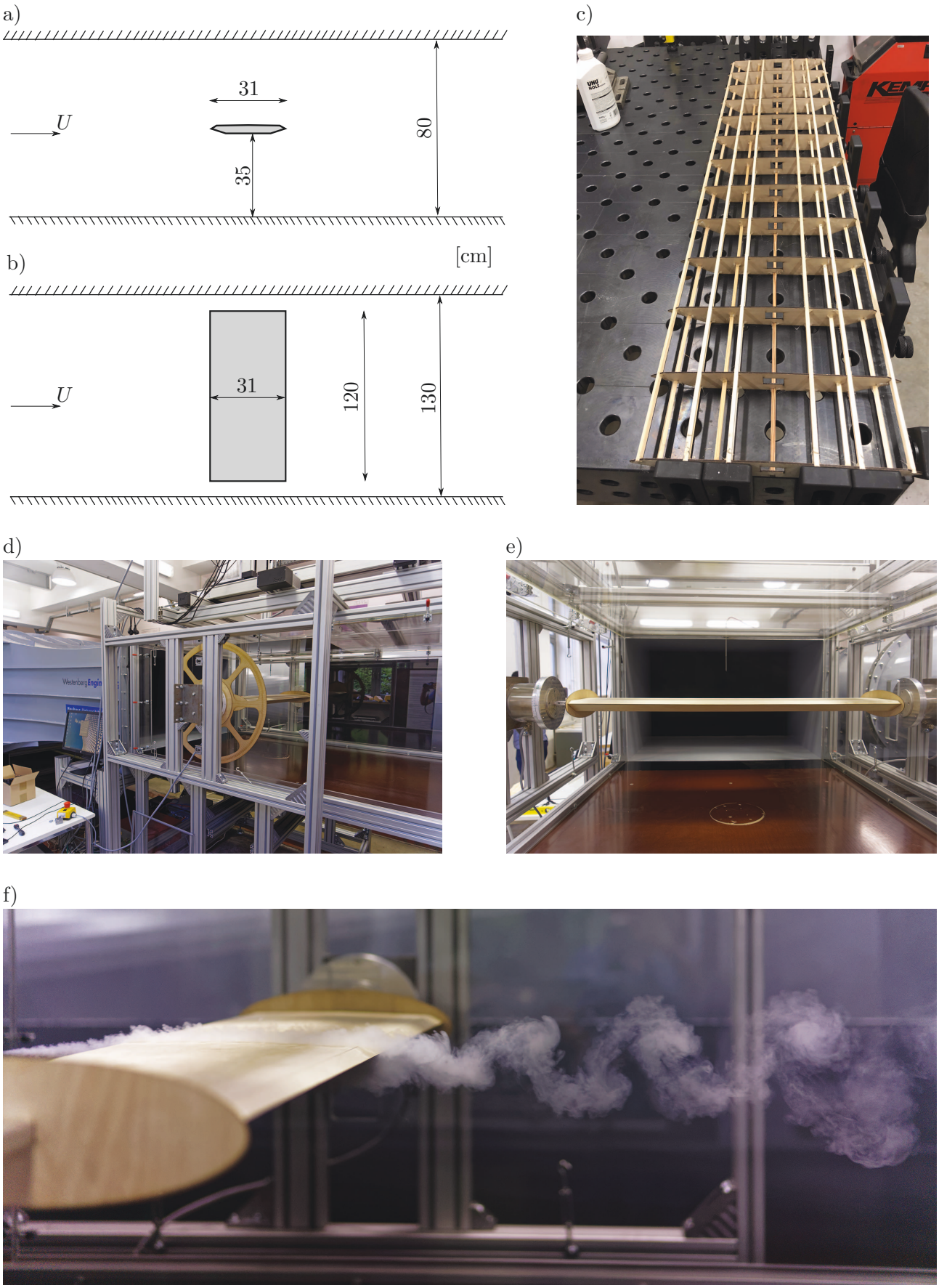

Figure 6.18: Great Belt Bridge: a) experimental setup in elevation, b) experimental setup in plan, c) skeleton of experimental plywood model, d) setup in wind tunnel including a wheel for angle adjustment, e) back view of the model mounted on sensors, f) static tests at $\alpha_s = 0$ deg.

6.3.3 Aerodynamic coefficients

This section is devoted to the aerodynamic coefficients from the CFD analyses. Where possible, a part of the aerodynamic coefficients is validated with experimental results from this study and Reinhold et al. [263]. A further comparison is made with former numerical studies to acquire a sense of validity and comparability of the numerical simulations. Moreover, by studying the distinctive features of the aerodynamic coefficients, the nonlinear effects and fluid memory are preliminarily identified to a certain extent.

Static wind coefficients

The static wind coefficients are determined for a smooth free-stream. Each CFD simulation is performed for a time amounting to τ =450 chords, of which 400 chords are used for the averaging. In the case of the experiments, similar averaging time was used as well. Table 6.6 summarizes the mean values of the static wind coefficients and Strouhal number St= $f_{\text{shed}}H_D/U$ at α_s =0 deg, where f_{shed} is the vortex shedding frequency. Since there is not a clear peak in the spectral amplitude of the lift coefficient, the Strouhal number is computed as a range rather than a value for the CFD analysis. A similar observation is noted by Kuroda [183] for shallow box sections, while Farsani et al. [106] noted broadband frequency spectrum of the lift for the Great Belt Bridge section. Unfortunately, oscillations of the static rig with a frequency of oscillation close to the natural one were noted in the experiments; hence, it was unreliable to select the shedding frequency properly as it may have been influenced by the synchronizing oscillation, i.e. vortex-induced vibration.

Figure 6.19 depicts the static wind coefficients w.r.t. the angle of attack. Looking at the figure, the validation of the present CFD results with experiments is considered fair, compared to other CFD studies. It is evident that the value of the drag coefficient is different compared to the experimental results, and a change of slope is indicated in the moment coefficient at $\alpha_s \approx \pm 5$ deg. As can be seen from the figure, some of these features appear in other numerical studies as well.

Before performing the experiments, it was argued by the author [169] that the width-to-depth ratio of the H4.1 model, higher level of detailing (fences and barriers) and free-stream turbulence ($TI_u = 7.5$ %) in the experiments by Reinhold et al. [263] could partially explain the scattering in the static wind coefficients for the numerical studies. The present experiments indicate that

	Re	C_D	C_L	St
Present (VPM)	1.0×10^5	0.060	0.065	0.106 - 0.173
Present (EXP)	1.0×10^5	0.072	0.00	/
Farsani et al. [106] (VPM)	1.0×10^5	0.071	0.053	0.084
Hejlesen et al. [135] (VPM)	1.0×10^4	0.06	0.07	0.20
Larsen and Walther [192] (VPM)	1.0×10^5	0.061	0.000	0.100 - 0.168
Bruno and Khris [37] (FVM)	1.0×10^5	0.071	-0.195	0.124 - 0.164
Lee et al. [196] (FVM)	1.0×10^5	0.05	0.03	0.160
Fradsen [108] (FEM)	6.2×10^6	0.072	-0.08	0.26
Reinhold et al. [263] (EXP)	1.0×10^5	0.080	0.010	0.109 - 0.158

Table 6.6: Great Belt Bridge: comparison of the static wind coefficients and Strouhal number St at α_s =0 deg with present experimental (EXP) results and results from former studies based on the VPM, Finite Volume Method (FVM) and Finite Element Method (FEM).

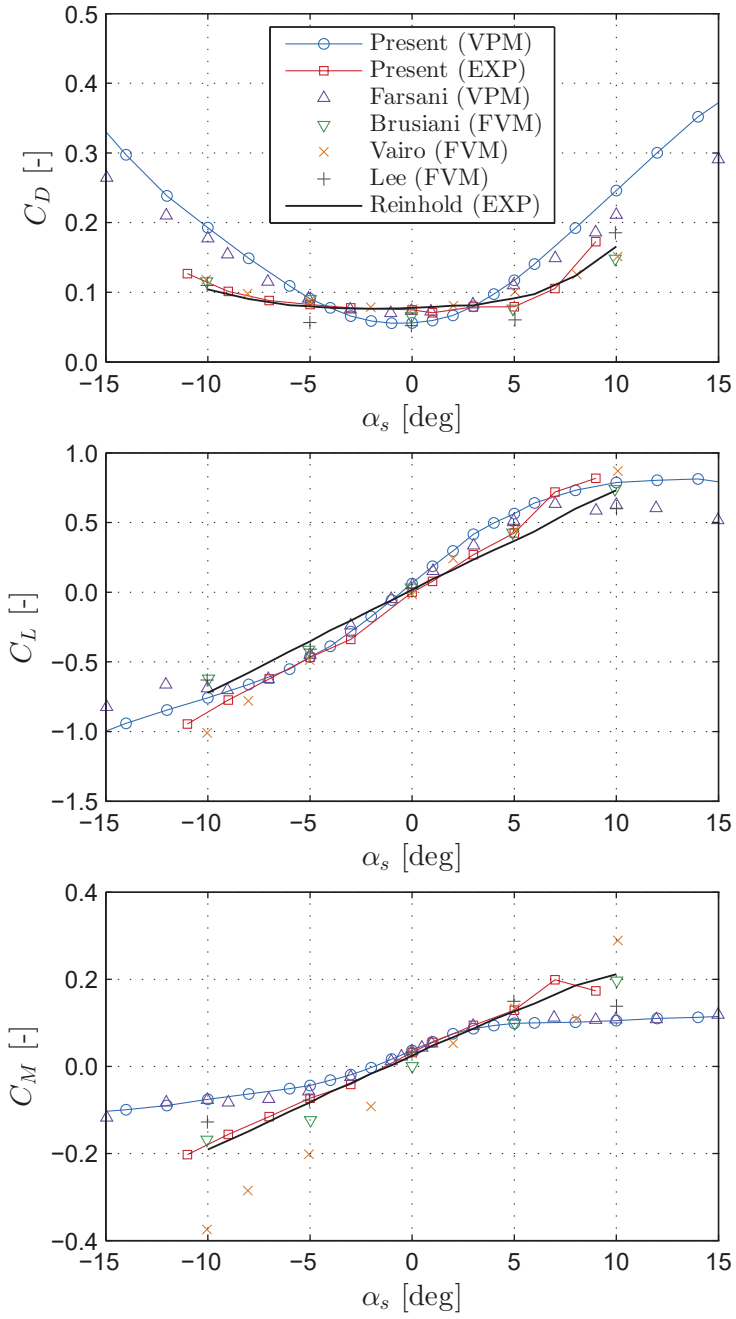

Figure 6.19: Great Belt Bridge: drag C_D (top), lift C_L (center) and moment C_M (bottom) static wind coefficients for the CFD and present experimental (EXP) results and results from former studies (Farsani et al. [106], Brusiani et al. [40], Vairo [332], Lee et al. [196], Reinhold et al. [263]), based on the VPM, EXP, Finite Volume Method (FVM) and Finite Element Method (FEM).

this may be the case for the lift coefficient, as a higher slope is also obtained for the present setup compared to the experiments by Reinhold et al. [263]. Bruno and Khris [37] note that the side barriers influence the reattachment point and prevent the formation of a larger bubble on the upper side, while the blockage effect of the railings contributes to higher suction on the lower surface. Both of these effects influence the lift coefficient compared to a bare section.

Further, the increased surface due to the auxiliary equipment gathers additional drag force and thus a larger mean drag coefficient in Reinhold et al. [263] experimental values at $\alpha_s = 0$,

which is also noted by Larsen and Walther [192]. Considering the present experimental results it can be argued that the effect of the auxiliary equipment does not contribute to such a large discrepancy. Issues in the prediction of the drag coefficient have been noted in several VPM studies (cf. e.g. [193, 229]). Although preliminary indications of a stall are notable in the moment coefficient in the present experimental results at high positive angles, the change of slope is mostly a feature for the present and former CFD models. Moreover, from the trend of the lift and moment coefficients, it can be observed that linearity is valid in $\approx \pm 5$ deg interval for the static wind coefficients.

Flutter derivatives

The flutter derivatives are determined for smooth free-stream and angle of attack ranging from -4 to 4 deg with an increment of 2 deg. Utilizing the forced oscillation method, a minimum time corresponding to 10 cycles is set to obtain the flutter derivatives at each reduced velocity.

At α_s =0 deg, good correspondence is observed between the obtained CFD flutter derivatives and experimental results by Reinhold et al. [263] (cf. Fig. 6.20). It is noted, that determining the flutter derivatives under smooth free-stream for aeroelastic analyses with turbulent free-stream does not account for the effect of the free-stream turbulence on the self-excited forces. Haan and Kareem [128] showed that both turbulence intensity and length scales impact the flutter derivatives. However, a standard procedure for separation of the buffeting from self-

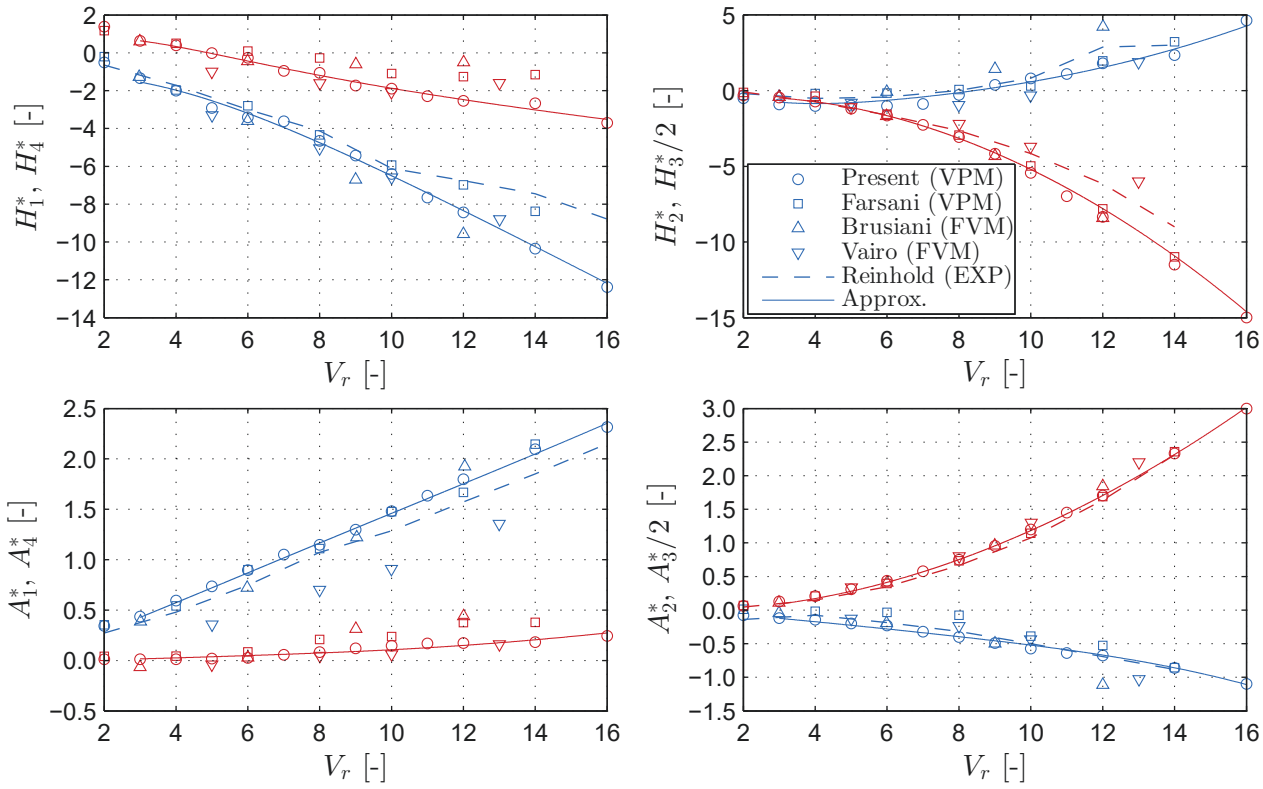

Figure 6.20: Great Belt Bridge: flutter derivatives from CFD analysis and their rational approximation (Approx.). The derivatives related to the velocity (H_1^*, H_2^* A_1^* A_2^*) are given in blue, while the derivatives related to the displacement (H_3^*, H_4^* A_3^* A_4^*) are given in red. These are further compared with from former studies (Farsani et al. [106], Brusiani et al. [40], Vairo [332], Reinhold et al. [263]), based on the VPM, experiments (EXP) and Finite Volume Method (FVM).

excited forces is not well-established. This warrants further investigation including experimental validation.

Figure 6.21 depicts the flutter derivatives for varying angles of attack. A higher sensitivity of the flutter derivatives is observed for the positive angles than for negative angles. For α_s =4 deg, the sign of A_2^* changes to positive for reduced velocities above V_r =6, which indicates torsional flutter. Since the aerodynamic nonlinearity outside the range of $\alpha_s = \pm 4$ deg is evident in the static wind coefficients (cf. Fig. 6.19), a linearization of the self-excited forces in this region might result in erroneous high amplitudes in the displacements for the HNL model. Therefore, the flutter derivatives in the $\alpha_s = \pm 4$ deg range are used.

Furthermore, the indicial functions for the self-excited forces are given in Fig. 6.22. These are obtained by rational approximation of the flutter derivatives. At low angles of attack ($2 \leq \alpha_s \leq 2$), the indicial functions are generally smooth with relatively short rise-time, as expected for a streamlined bridge deck. The abrupt change in the first few steps is due to the temporal singularity at $V_r \to 0$. Significantly longer rise-time and higher overshooting amplitudes are noted for the indicial functions at $\alpha_s = \pm 4$ deg.

The aerodynamic center is an important parameter in the quasi-steady based models. Figure 6.23 (left) depicts the aerodynamic center and the correction coefficients for the selected case, based on the flutter derivatives (cf. (3.125)). It can be observed from the figure that the moment aerodynamic center m_M is in the range between -0.2 and -0.45 with a convergent trend beyond -0.4. The lift aerodynamic center m_L changes from positive to negative due to the changing value of the H_2^* derivative (cf. Fig. 6.20). Commonly for bridge decks, reduced

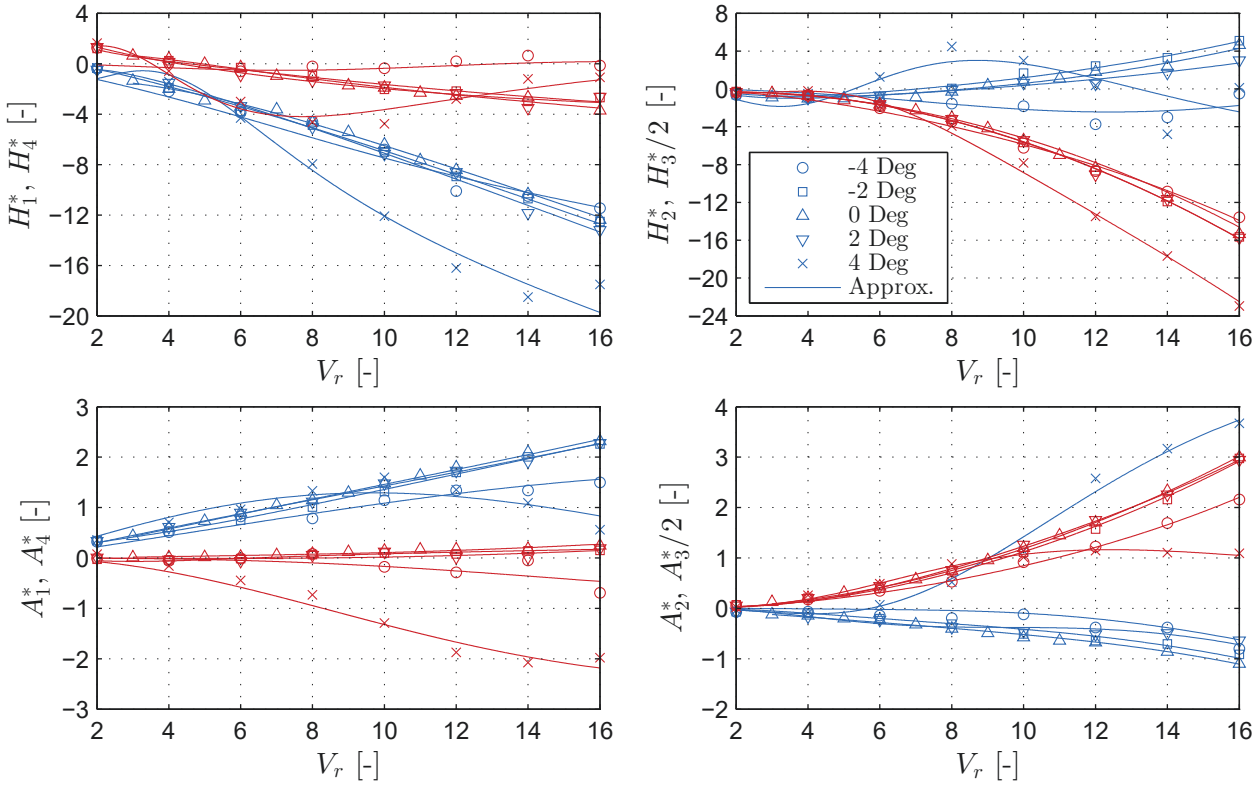

Figure 6.21: Great Belt Bridge: flutter derivatives for various angles of attack and their rational approximation (Approx.). The derivatives related to the velocity (H_1^*, H_2^*, A_1^*, A_2^*) are given in blue, while the derivatives related to the displacement (H_3^*, H_4^*, A_3^*, A_4^*) are given in red.

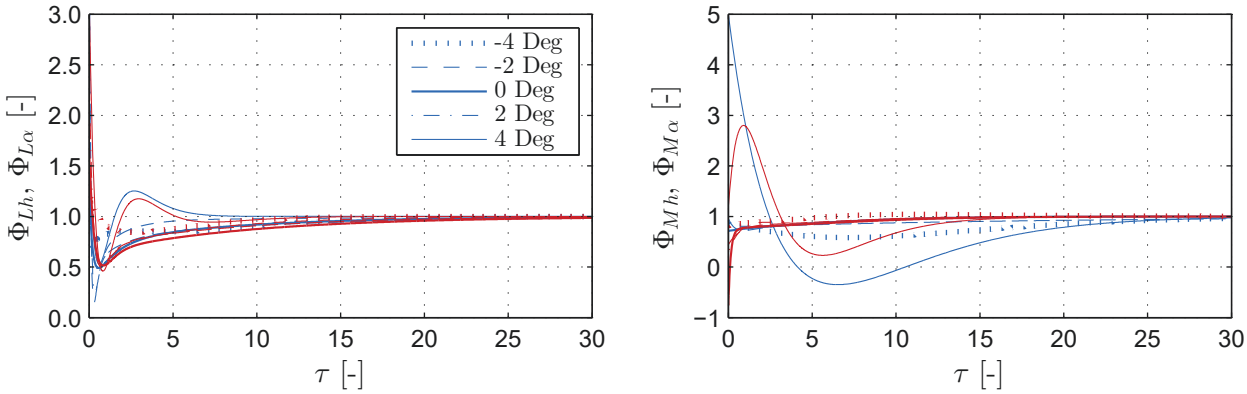

Figure 6.22: Great Belt Bridge: lift (left) and moment (right) self-excited indicial functions for various angles of attack, related to the vertical displacement Φ_h (red) and rotation Φ_α (blue).

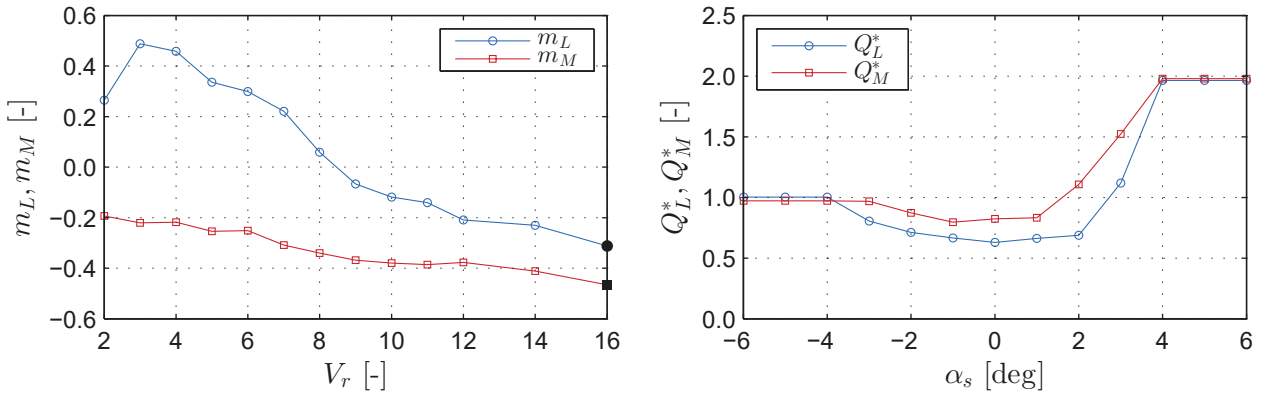

Figure 6.23: Great Belt Bridge: aerodynamic center (left) and dynamic derivatives at $V_r = 12$ (right). The black filled markers indicate the values of the aerodynamic center used in the analyses.

velocities beyond $V_r \geq 15$ are considered to represent an equivalent quasi-steady state; hence, the aerodynamic center is selected in this reduced velocity range [85]. In this case, the values for the aerodynamic center in the subsequent analyses are selected for V_r=16 and they fall in the reasonable range between -0.5 and 0.5, given by Wu and Kareem [359]. The selected values for the aerodynamic center can strongly influence the results in the aeroelastic analysis, by increasing or decreasing the contribution of aerodynamic damping due to rotation. Choosing a large positive value for the moment aerodynamic center may lead to premature torsional flutter for streamlined bridge decks [359]. As seen in the previous case-study, obtaining the aerodynamic center at very high reduced velocities may lead to failure of capturing a torsional flutter for bluff bridge decks prone to torsional flutter. Although obtaining the aerodynamic center from the flutter derivatives may not be accurate for a nonlinear model [364], presently the author is not aware of other standard procedures for its determination. Herein, parametric studies on the influence of the aerodynamic center on the response are beyond the scope of the study (cf. e.g. [85, 359, 364] for discussions). The frequency-dependent correction coefficients Q_L^* and Q_M^* in the CQS model (cf. Fig. 6.23, right) can reduce or increase the slope of the static wind coefficients, based on the aerodynamic characteristics described by the flutter derivatives. In this case, these coefficients attain high value for positive angles of attack due to the prominent nonlinearity, as noted previously. Beyond the range of ± 4 deg, these coefficients are maintained as constant.

Aerodynamic admittance

Next, the aerodynamic admittance is determined for random free-stream turbulence (cf. Sec. 3.7.3). At the time of performing the analyses for this case-study, the novel method for determining the aerodynamic admittance under deterministic gusts was not yet developed.

Figure 6.24 depicts the obtained aerodynamic admittance functions are shown for $\alpha_s \in \{-2, 0, 2\}$ deg, along with the approximate Sears function (cf. (5.13) of Sec. 5.4.5). Approximately $\tau = 400$ chords of wind fluctuations and forces are used to compute the aerodynamic admittance, both recored at the stiffness center $\boldsymbol{x}_s$ (cf. Sec. 3.7.3). As a separation between the influence of the longitudinal and vertical fluctuations in the buffeting forces is not feasible for the admittance under random free-stream, it is assumed that $\chi_L = \chi_{Lu} = \chi_{Lw}$ and $\chi_M = \chi_{Mu} = \chi_{Mw}$.

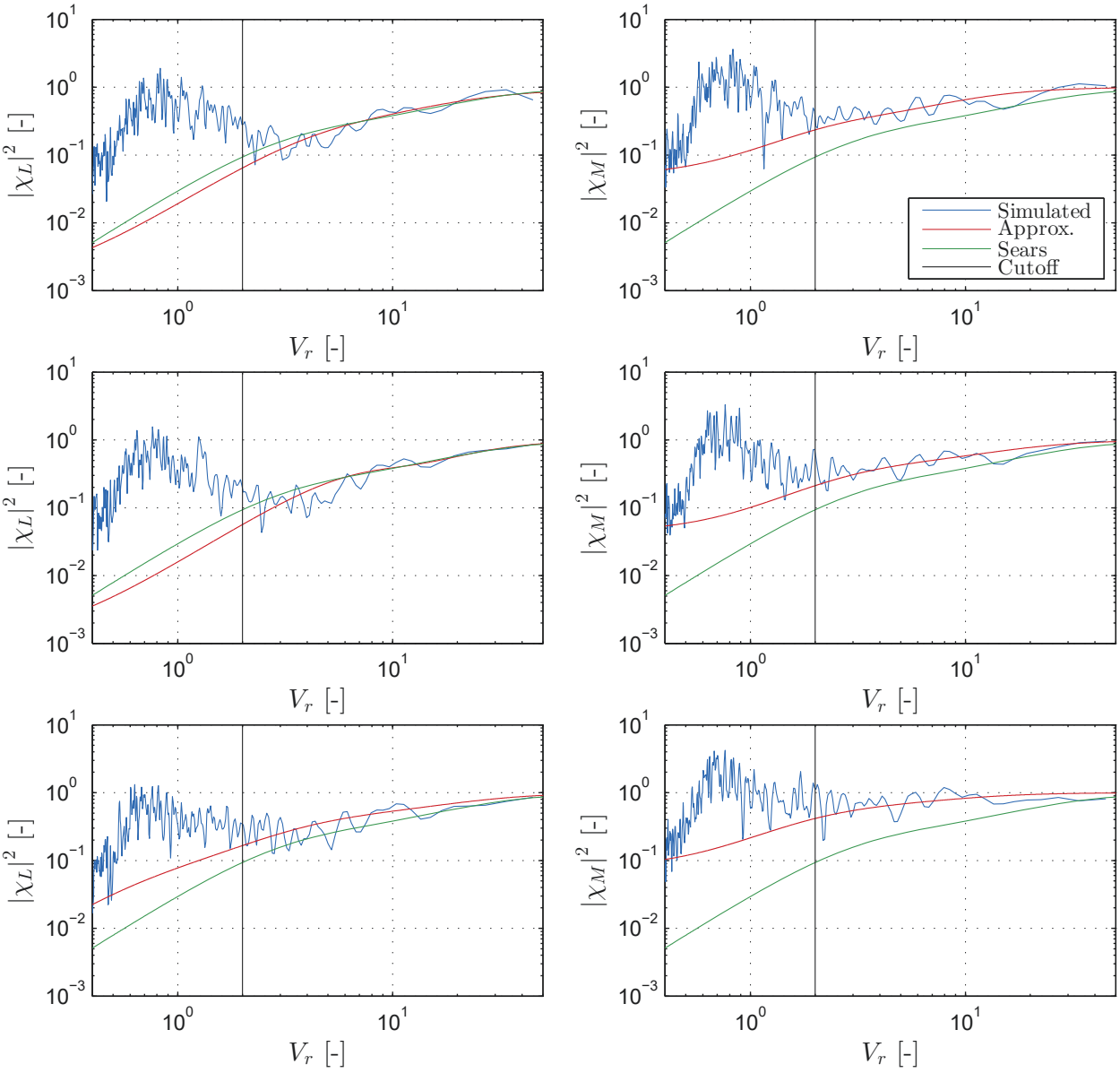

Figure 6.24: Great Belt Bridge: lift (left) and moment (right) aerodynamic admittance for angle of attack of $\alpha_s = -2$ deg (top), $\alpha_s = 0$ deg (center) and $\alpha_s = -2$ deg (bottom) including its rational approximation (Approx.). The cutoff frequency describes the lower limit for the approximation to eliminate vortex shedding effects.

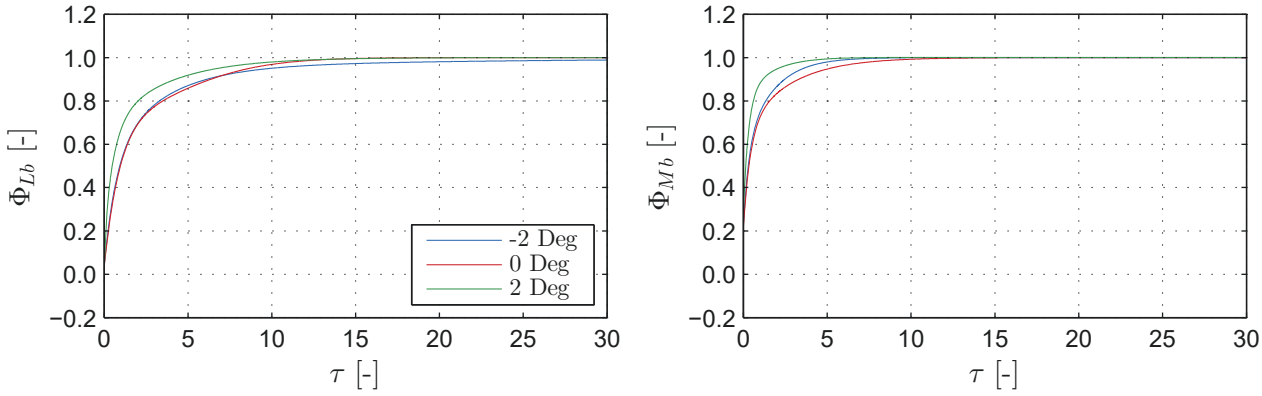

Figure 6.25: Great Belt Bridge: lift (left) and moment (right) buffeting indicial functions for various angles of attack.

Two regions are distinguished in the aerodynamic admittance w.r.t. the reduced velocity: below and above the cutoff reduced velocity (cf. Fig. 6.24). Above the cutoff reduced velocity, the admittance is governed by the incident wind fluctuations, while the wake fluctuations govern the admittance below the cutoff reduced velocity. The latter observation can be linked to the Strouhal number as well, as the vortex shedding frequency corresponds to the peak of the admittance below the cutoff reduced velocity. There are various interpretations of the aerodynamic admittance for a bridge deck. Kareem and Wu [161] separate three distinctive regions of the admittance, characterized by the incident, shear layer or near wake and the wake fluctuations. The LU and HNL models, which model for the fluid memory in the buffeting forces, account only for the region of the aerodynamic admittance governed by the incident fluctuations. Therefore, only the part of the aerodynamic admittance above the cutoff reduced velocity is used for the rational approximation. There is no clear indication for the selection of the cutoff reduced velocity; rather a heuristic distinction between the three regions. In this case, the cutoff limit is chosen at V_r =2, with the same reasoning as for a flat plate (cf. 5.4.4), that gust lengths shorter than the width are dominated by local effects. It should be noted that the incident fluctuations also have a contribution to the admittance below the cutoff reduced velocity. However, this contribution is small compared to the one from the wake fluctuations.

Since with this method the phase and magnitude component of the aerodynamic admittance cannot be obtained separately, it is assumed that the imaginary part from the complex form of the admittance is the same as the one in the complex Sears approximation (5.13). The buffeting indicial functions are relatively smooth with short rise-time and are depicted in Fig. 6.25. The shear layer and wake fluctuations significantly influenced the aerodynamic admittance for angles higher than 2 deg and lower than -2 deg; therefore, the region of the admittance governed by incident fluctuations could not be clearly distinguished for angles outside this range.

6.3.4 Buffeting forces

In this section, the buffeting fluctuating lift and moment coefficients are studied for a static section under turbulent free-stream, in order to single out the discrepancies between the CFD and the semi-analytical models in case of the buffeting forces. As the Reynolds number is kept constant, both cases of low ($TI = 6$ %) and high ($TI = 10$ %) turbulence intensity are studied only for one constant mean wind speed of $U = 30$ m/s. The input free-stream turbulence for the semi-analytical models is the tracked wind fluctuations in the CFD domain at $\boldsymbol{x}_s = (0, 0, 0)$,

from analysis without a section. Additionally, they are shifted for $\tau = -1/2$ as the imaginary part of the approximation of the Sears admittance (cf. (5.13)) corresponds to the Küssner function that is for gusts acting at the leading edge (cf. Sec. 5.4.6 for discussion).

In Fig. 6.26, a representative part of the time-histories of the fluctuating wind coefficients is presented for the CFD and semi-analytical models. It is observed that the high-frequency component of the fluctuating wind coefficients is overestimated by the LQS model, as the peaks in the time-histories are significantly higher than the ones for the reference model. Nonetheless, the low-frequency content of the fluctuating wind coefficients for the LQS model follows the same trend as the CFD model. The peaks in the fluctuating wind coefficients for the QS model have lower amplitudes compared to the LQS model, which effectively shows the influence of the quasi-steady aerodynamic nonlinearity on the buffeting forces for large effective angles of attack. Nevertheless, the effect of nonlinearity on the buffeting forces is overestimated by the QS model, which is observed when the time-histories for this model are further compared to the ones for the CFD model (see e.g. C_{Mb} for $t = 170 - 180$ s). Although the additional high-frequency content in the fluctuating wind coefficients is still overestimated for the CQS model, a better correspondence is achieved between this and the reference model compared to the QS and LQS models. The averaged fluid memory considered in the CQS model is dependent on the correction coefficient Q^* (cf. (3.146)), which is based on the flutter derivatives. When there is no motion, the fluid memory of the buffeting forces is described by the aerodynamic admittance; therefore, the correction coefficient should be based on the admittance. However, the buffeting and self-excited part of the effective angle of attack are inseparable in a nonlinear formulation and thus, the correction coefficient Q^* is computed from the flutter derivatives. This corresponds to the assumption that the fluid memory is independent of the origin of the effective angle. Mainly, the LU and HNL models are in the best agreement with the CFD model for the fluctuating wind coefficients. The effect of fluid memory is manifested as a filter for the fluctuating wind coefficients, resulting in their amplitude and phase alteration. Looking at the time-histories for these models, it is evident that an additional high-frequency component is present in the fluctuating wind coefficients for the CFD model, which is revisited later in this section.

Generally, the observations made from the qualitative assessment of the time-histories correspond to the quantitative assessment based on the RMS of the fluctuating wind coefficients for both turbulent cases (cf. Fig. 6.27). The RMS of the fluctuating wind coefficients for the LU and HNL model corresponds well with the RMS for the CFD model. By including the quasi-steady nonlinearity of the low-frequency wind fluctuations in the HNL model, the RMS of the lift coefficient is slightly increased, while a decrease is noted in the RMS of the moment coefficient. Comparing the results for the LQS and LU model, it can be seen that fluid memory plays a major role in the buffeting forces, particularly in the high turbulence case. The impact of the quasi-steady nonlinearity is prominent for the moment coefficient, which is observed from the results of the QS model in contrast to the LQS model. As discussed previously, the effect of the nonlinearity may be overestimated if the fluid memory is not taken into account concurrently for the buffeting forces.

In order to further examine the discrepancies between the fluctuating wind coefficients for the LU and CFD model, a sequence of snapshots of an instantaneous particle map and corresponding pressure coefficient C_p is depicted in Fig. 6.28. The sequence of snapshots corresponds to the peak moment coefficient for $t = 164 - 165$ s (cf. Fig. 6.26). An incoming vertical gust (given by the resultant velocity vector U_r) initiates a flow separation on the top surface (cf. Fig. 6.28, a), which grows in size as a vortex is entrained. The gust velocity reaches a peak

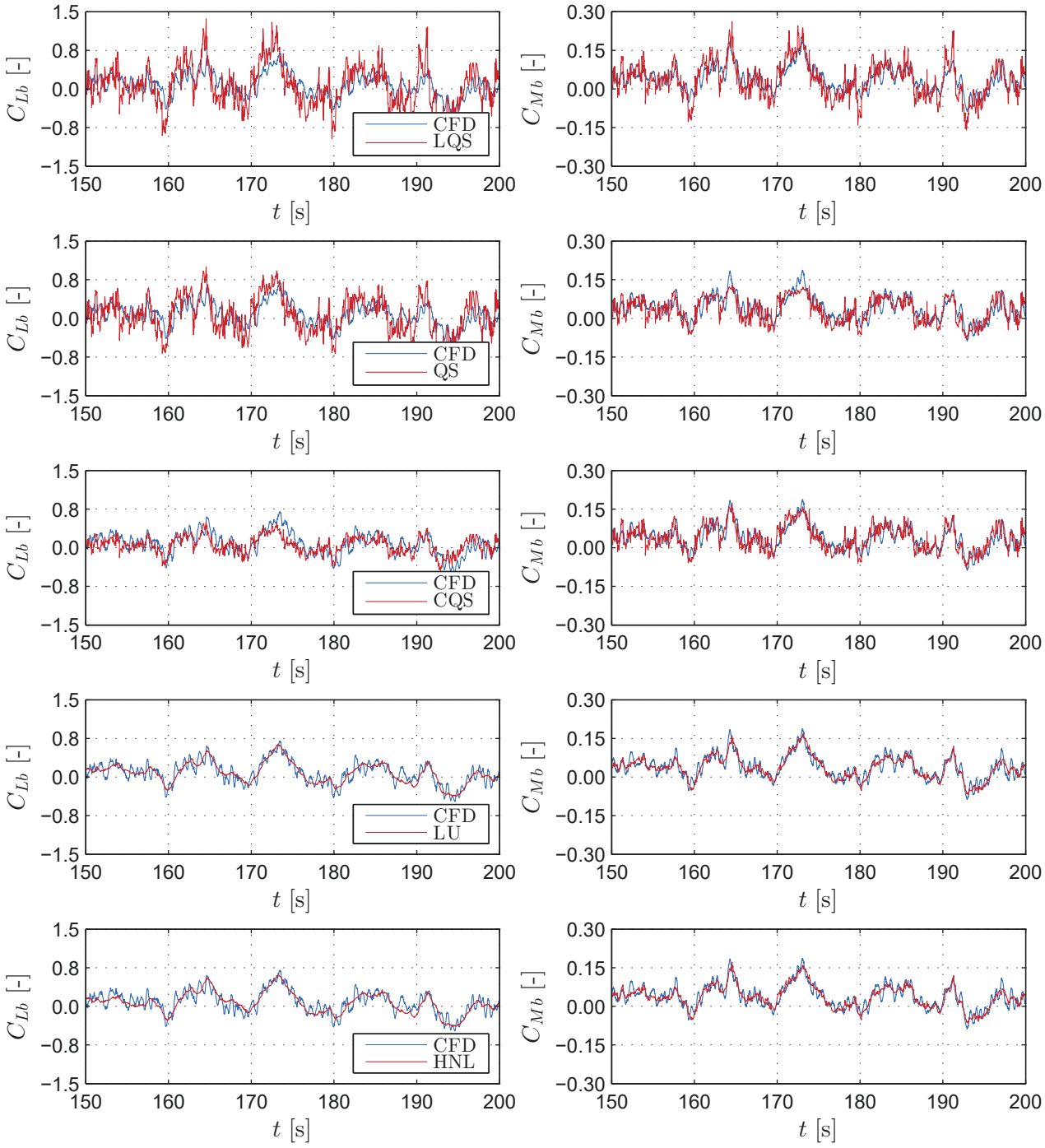

Figure 6.26: Great Belt Bridge: sample time-history of the lift (left) and moment (right) fluctuating buffeting coefficients for the CFD and semi-analytical models and a static deck at $U = 30$ m/s and $TI = 6$ %.

almost simultaneously with the suction pressure at the top surface near the leading edge (cf. Fig. 6.28, b). The vortex is then convected downstream and a secondary vortex is formed, resulting in an additional suction pressure (cf. Fig. 6.28, c). Both of the vortices are then convected downstream (cf. Fig. 6.28, d). Since all of the semi-analytical models resulted in a peak in the fluctuating moment coefficient (cf. Fig. 6.26), the main influence in the moment force is due to the incident fluctuations. Nevertheless, the peak of C_{Mb} for the LU model is slightly reduced compared to the one for the CFD model, which may originate from some local

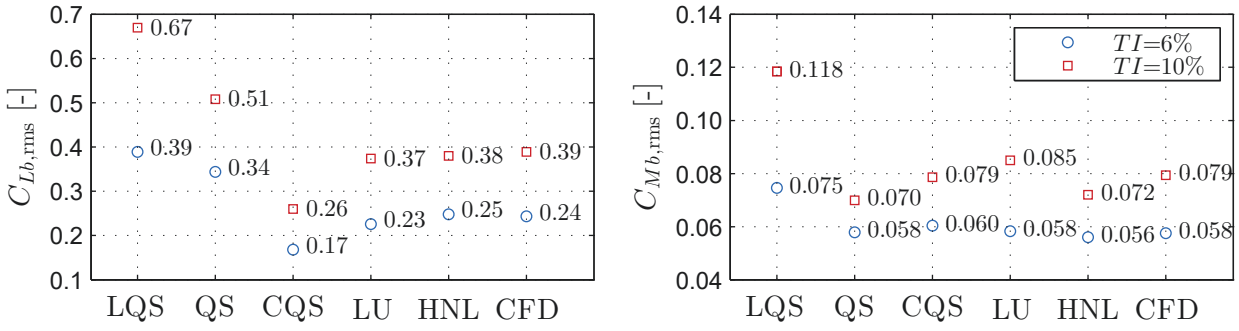

Figure 6.27: Great Belt Bridge: RMS of the lift (left) and moment (right) fluctuating buffeting coefficients for the CFD and semi-analytical models and a static deck at $U = 30$ m/s.

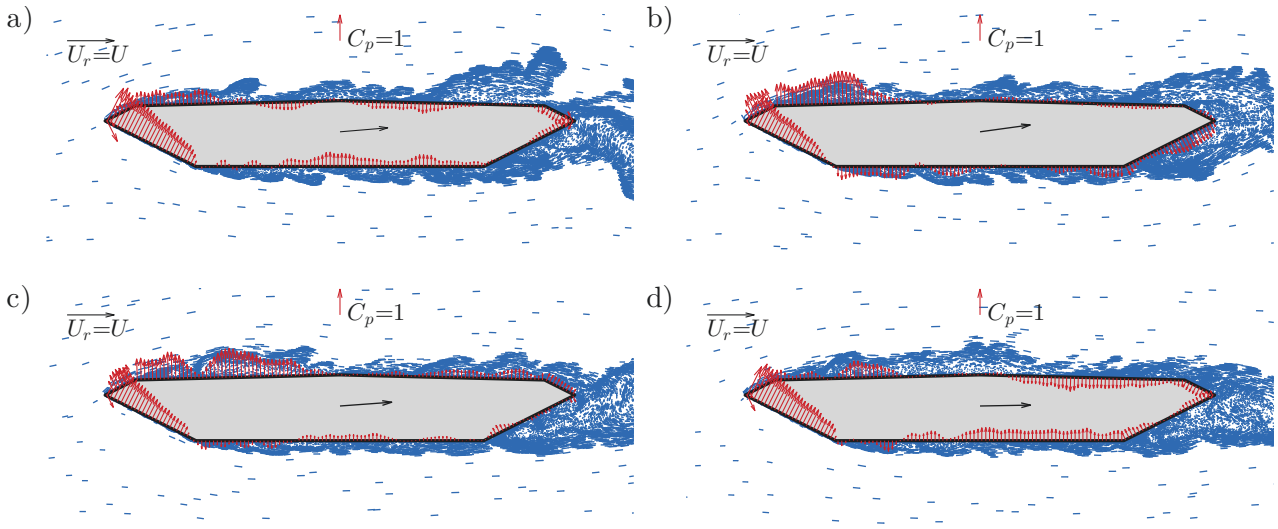

Figure 6.28: Great Belt Bridge: instantaneous particle maps and pressure distribution for a static deck at $U = 30$ m/s and $TI = 6$ %. The snapshots correspond to: a) $t = 159.40$ s; b) $t = 164.04$ s; c) $t = 164.31$ s and d) $t = 165.06$ s from Fig. 6.26. The black arrow corresponds to both direction and magnitude of the instantaneous resultant wind velocity U_r.

effects. Fundamental studies on long rectangular cylinders note that the unsteady behavior of the separation bubble results in quasi-periodic fluctuating pressures as the vortex is convected downstream (cf. Cheri et al. [63]). For a turbulent free-stream, the magnitude of these fluctuating pressures increases significantly and the length of the separation bubble reduces (cf. Saathof and Melbourne [272] and Hiller and Cherry [136] for a detailed discussion on these effects). The local effects are highly influenced by the three-dimensionality of the flow, and therefore they are not well captured by the current CFD model. Presently, it is not well understood how the local 2D effects influence the local pressure. Furthermore, these local effects are length scale-dependent. The experimental studies are conducted for moderate Reynolds number with a significantly lower length scale to depth ratio $L_u/H_D \approx 2.1$ compared to this study $L_u/H_D \approx 25$. Therefore, strong conclusions on the local effects cannot be drawn without further fundamental investigations.

It is noted that the combined effects due to the nonlinearity and non-stationarity are intractable by the selected semi-analytical models. Although the underlying mechanisms of bluff-body aerodynamics are still not fully established, three effects could be mentioned, which are the probable cause for the low-frequency content in the fluctuating wind coefficients for the CFD

model, namely: (i) unsteady aerodynamic nonlinearity, (ii) local effects due quasi-periodic fluctuations and (iii) vortex shedding. As the shape of the fluctuating wind coefficients for the LU and HNL model is similar and the high-frequency fluctuations of the CFD model are mostly quasi-periodic, the claim that these fluctuations are due to the vortex shedding and local turbulence effects seems plausible. Nevertheless, it is difficult to single out these effects. The influence of the vortex shedding can be also seen in the aerodynamic admittance (cf. Fig. 6.24).

To further study the effect of aerodynamic nonlinearity, the PDFs of the fluctuating wind coefficients are shown in Fig. 6.29. For wind fluctuations that follow the Gaussian PDF (cf. Fig. 5.13 from Sec. 5.3.1), a linear force model would also result in a similar PDF of the fluctuating wind coefficients, which is the case for the LU model. The PDFs of the fluctuating wind coefficients for the CFD model generally follow the trend of the Gaussian PDF for the low turbulence case, except for the positive values of the lift coefficient at the tail of the distribution. While the values at the tail for the CFD model can be due to the vortex shedding and/or aerodynamic nonlinearity, it can be seen that the PDF of the lift and especially the moment coefficient for the QS and CQS models significantly depart from the Gaussian trend. This departure fortifies the claim that the effect of nonlinearity on the buffeting forces is overestimated for the QS and CQS model as the fluid memory is not accounted for accordingly.

Besides the difference in the amplitude of the buffeting forces, the consideration of the fluid memory also affects the phase between the buffeting forces and wind fluctuations. Figure 6.30 depicts the envelope of the fluctuating wind coefficients w.r.t. the instantaneous angle of attack for the low turbulence case, filtered using a moving average filter with 30 samples. It is evident that the hysteretic behavior of the fluctuating wind coefficients, appearing for the CFD model, can be only captured by the LU and HNL models. The good correspondence of these models indicates that using the imaginary part for the aerodynamic admittance from the approximation of the Sears function is justified. However, this assumption is case-dependent. The consideration of the phase in the complex form of the aerodynamic admittance can significantly influence the response in aeroelastic analyses at high reduced velocities when the intermodal coupling is meaningful, as noted by Chen [53].

Most of the above observations can be realized by studying the comparison metrics in Fig. 6.31 for the fluctuating wind coefficient, taking the CFD as a reference for the metric parameters in Tab. 6.5. As expected, the LQS model has the poorest performance overall, since it is the most simple model from the selected models. An important remark can be made on the metrics for the QS model for the lift coefficient: while a high value the peak metric $\mathcal{M}_p^{C_{Lb}^{\mathrm{CFD}},C_{Lb}^{\mathrm{QS}}}$ can be observed, this is not consistent with the rest of the metrics, which resulted in poor behavior. When high-frequency vortex shedding is present, the corresponding peaks for the two models, CFD and QS, could be accidental and not occur at the same time. This proves the need for a multicriterial assessment of aerodynamic models. Similarly, despite having good correspondence for the RMS in the moment coefficient for the QS model, the PDF metric $\mathcal{M}_{\mathrm{pdf}}^{C_M^{\mathrm{CFD}},C_{Mb}^{\mathrm{QS}}}$ also resulted in poor value, which supports the statements made above that the aerodynamic nonlinearity is overestimated when the fluid memory is not considered within the model. The CQS model showed some success for the moment coefficient. However, this is not consistent in the case of the lift coefficient. Although not as drastic for the QS model, the PDF metric $\mathcal{M}_{\mathrm{pdf}}^{C_{Mb}^{\mathrm{CFD}},C_{Mb}^{\mathrm{CQS}}}$ also resulted in low values due to the tail of the distribution (cf. Fig. 6.29). Overall, the most consistently high metrics are obtained for the LU and NLU models, which further proves the point that consideration of fluid memory is paramount. For these two models, the magnitude $\mathcal{M}_{\mathrm{m}}$ and both wavelet-based metrics, $\mathcal{M}_{\mathrm{w}}$ and $\mathcal{M}_{\mathrm{wf}}$, are similar, which yields

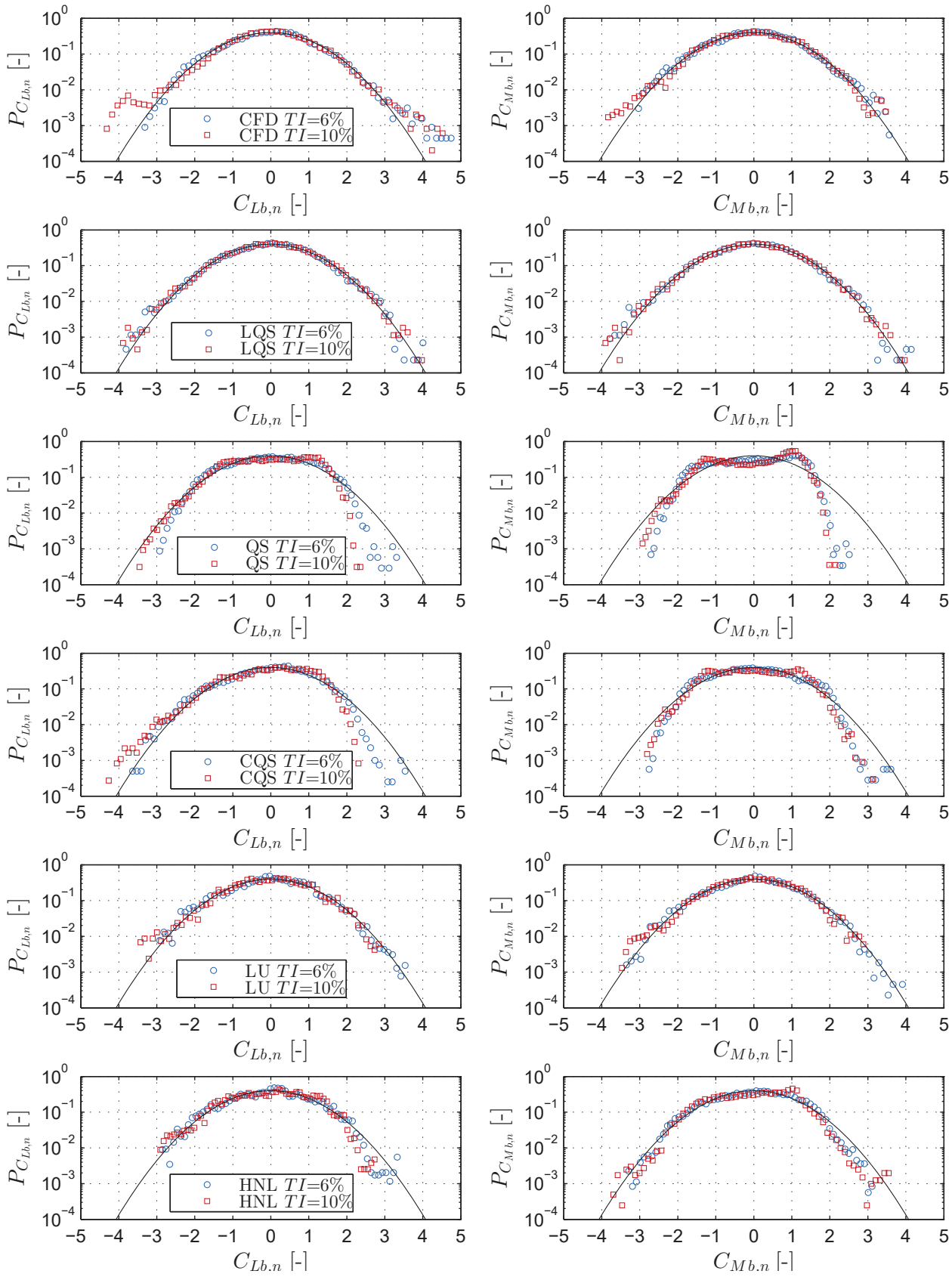

Figure 6.29: Great Belt Bridge: histogram estimate PDF of the normalized (standard score) lift (left) and moment (right) fluctuating buffeting coefficients for a static deck at $U = 30$ m/s and $TI = 6$ %. The black line indicates a standard normal distribution $\mathcal{N}(0, 1)$.

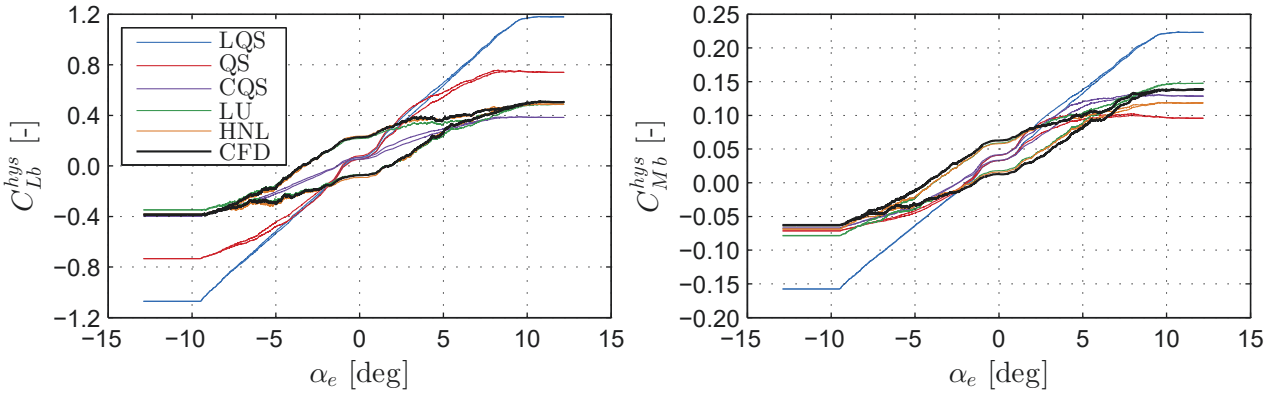

Figure 6.30: Great Belt Bridge: filtered envelope of the aerodynamic hysteresis of the lift C_{Lb}^{hys} (left) and moment C_{Mb}^{hys} (right) buffeting coefficients for a static deck at $U = 30$ m/s and $TI = 6$ %.

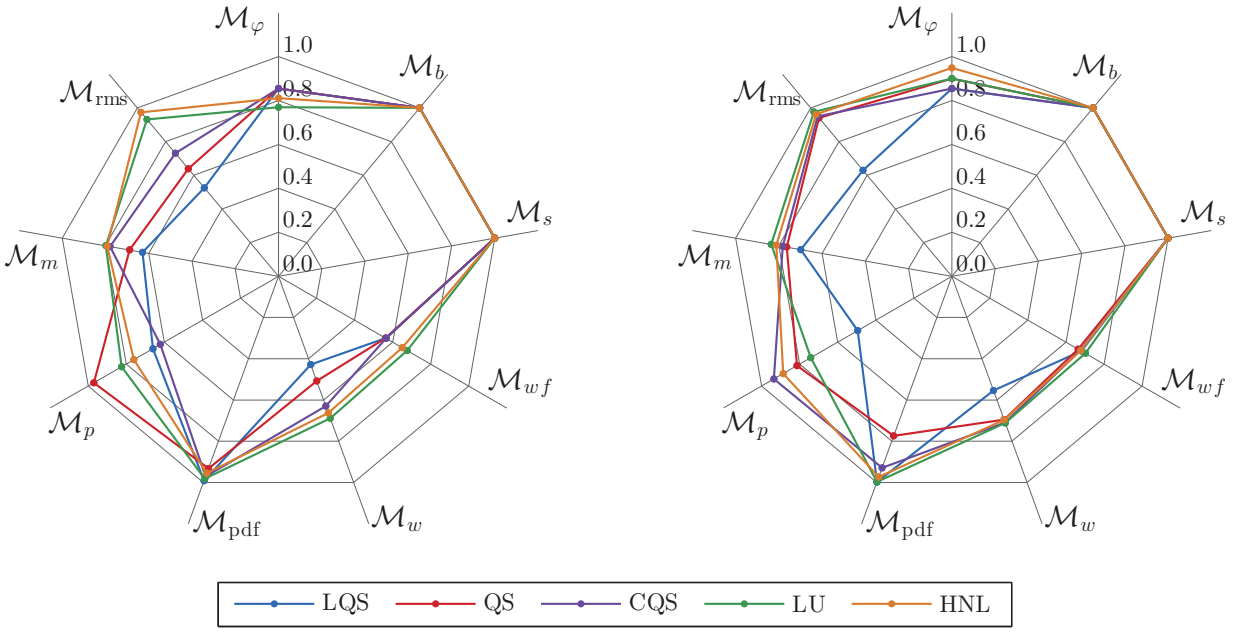

Figure 6.31: Great Belt Bridge: comparison metrics for the lift $\mathcal{M}^{C_{Lb}^{\text{CFD}},C_{Lb}^{j}}$ (left) and moment $\mathcal{M}^{C_{Mb}^{\text{CFD}},C_{Mb}^{j}}$ (right) buffeting coefficients for a static deck at $U = 30$ m/s and $TI = 6$ %, where $j \in \{\text{LQS}, \text{QS}, \text{CQS}, \text{LU}, \text{HNL}\}$. The CFD model is selected as a reference.

the conclusion again that the vortex shedding effects are the reason for the discrepancies. No quadratic phase coupling or non-stationarity is detected, which could be seen from $\mathcal{M}_{\text{b}}$ and $\mathcal{M}_{\text{s}}$ metrics, respectively. It is also important to note that the phase metric might be obsolete in this case, as the buffeting forces are broadband. Thus, the mean phase is distorted by the high-frequency vortex shedding forces for the CFD model. For such cases, the effect of phase-shift is better observed from the hysteresis (cf. Fig. 6.30).

6.3.5 Self-excited forces

The effect of aerodynamic nonlinearity can be prominent in the self-excited forces at large angles of attack. This was also initially indicated based on the flutter derivatives at various angles of attack in the previous section. In the following, the self-excited moment coefficient $C_{M\alpha}$ due to a sinusoidal forced rotation are compared for the LQS, QS, CQS and LU models w.r.t. the

reference CFD model. The MQS and NLU models are not considered, as theoretically both would equal the LU model for a single-frequency sinusoidal excitation, taking into account the flutter derivatives at the oscillation frequency.

Figure 6.32 depicts a portion of the time-history of $C_{M\alpha}$, due to rotation about a static angle of attack amounting to $\alpha_s = 0$ deg (left) and $\alpha_s = 4$ deg (right) for the considered models. The deck is forced to rotate in a sinusoidal manner with an amplitude of $\alpha_0 = 3$ deg at a reduced velocity amounting to $V_r = 16$ for a reduced time of $\tau = 1600$, i.e. 100 cycles. Despite the additional component due to the vortex shedding forces for the CFD model, a single-frequency fit describes the forces sufficiently well for oscillations at $\alpha_s = 0$ deg. However, this is not the case for rotation about $\alpha_s = 4$ deg. Complex behavior is exhibited for the CFD model at this static angle of attack that results in large negative peaks of the moment coefficient.

Before comparing the models, an attempt is made to study the origin of these particular peaks. Figure 6.33 depicts instantaneous particle maps for rotation about $\alpha_s = 0$ deg (left) and $\alpha_s = 4$ deg, at $\tau/V_r \approx 56.4$ that corresponds to one of the negative peaks (cf. Fig. 6.32). A large separating vortex is noted for the $\alpha_s = 4$ deg case, resulting in high negative pressure at the trailing part of the deck. This vortex is a consequence of large separation at the leading edge, i.e. this is a leading-edge vortex. Such vortices are known to be a source nonlinearity in the aerodynamic forces for airfoils (cf. e.g. [139, 219, 220, 260, 340]) and bridge decks (cf. e.g. [376]), resulting in amplitude dependence of the self-excited forces and thus, complex hysteretic behavior.

To quantify the discrepancies between the time-histories, the comparison metrics for the semi-

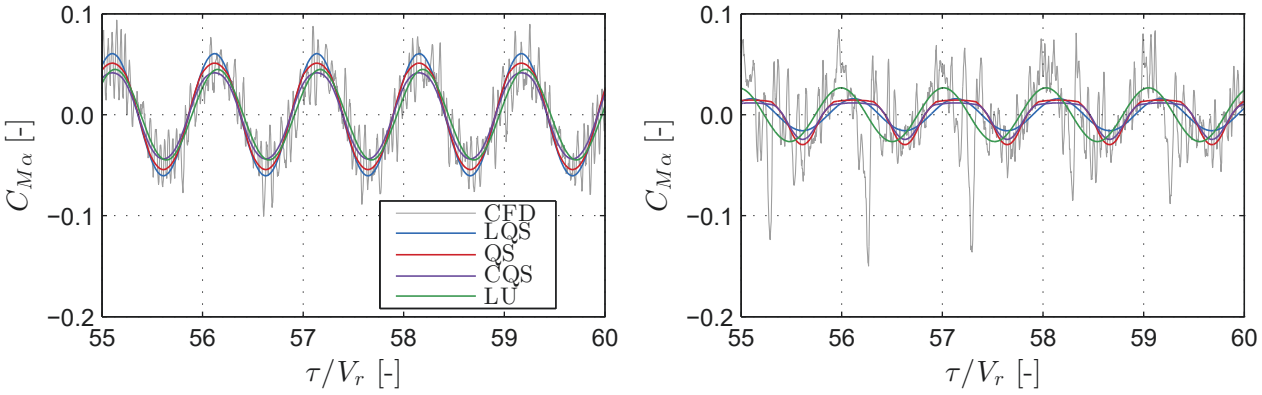

Figure 6.32: Great Belt Bridge: fluctuating moment self-excited coefficient for sinusoidally rotating deck about static angle $\alpha_s = 0$ deg (left) and $\alpha_s = 4$ deg (right) at $V_r = 16$.

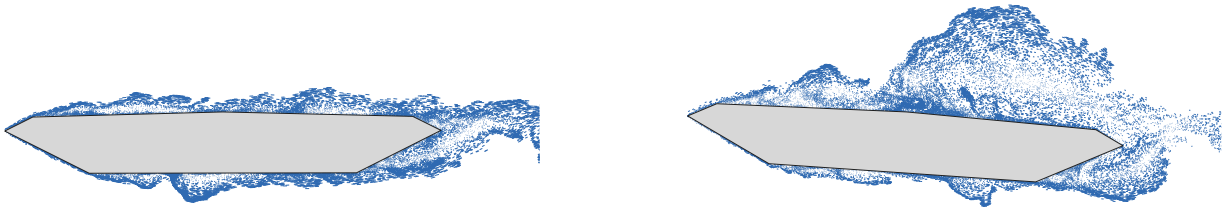

Figure 6.33: Great Belt Bridge: instantaneous particle maps for sinusoidally rotating deck about static angle $\alpha_s = 0$ deg (left) and $\alpha_s = 4$ deg (right) at $V_r = 16$. The snapshots correspond to the negative peak occurring in the moment coefficient for $\alpha_s = 4$ deg at $\tau/V_r \approx 56.3$ (cf. Fig. 6.32, right).

analytical models are given in Fig. 6.34, taking the CFD as a reference. Modified parameters w.r.t. the metric parameters in 6.5 are the central wavelet frequency, taken as $f_0 = 2$ Hz, and the normalization time amounting to $T_c = V_r B/(2U)$ for the phase metric. Significant difference can be noted in the metrics between the case of rotation about $\alpha_s = 0$ deg (cf. Fig. 6.34, left) and the case of rotation about $\alpha_s = 4$ deg (cf. Fig. 6.34, right). Neglecting the fluid memory, completely or partially, results in a lower phase metric for the LQS, QS and CQS models. This is particularly true for the rotation about the static angle of $\alpha_s = 4$ deg. Unlike these models, the LU model resulted in good correspondence for $\mathcal{M}_\varphi$ as it is a linear fit at the main harmonic.

The LQS and QS models showed good correspondence for the RMS $\mathcal{M}_{\text{rms}}$, magnitude $\mathcal{M}_m$ and peak $\mathcal{M}_p$ metrics for the $\alpha_s = 0$ deg case. Although the quasi-steady assumption is close to being valid for such a high reduced velocity of $V_r = 16$, these metrics for the case of sinusoidal forced vibrations may not fully represent the realistic effect of quasi-steady related assumptions. The additional vortex-shedding forces easily affect these metrics for this type of vibration. These forces are not captured by any of the quasi-steady based models.

For the case of self-excited forces with single-frequency input motion, the wavelet metrics $\mathcal{M}_w$ and $\mathcal{M}_{wf}$ are the most important since the major part of the wavelet energy of the forces should be concentrated at few frequencies. Both of these metrics yield the best results for the LU model for the $\alpha_s = 0$ deg case, which is logical as this model directly replicates the amplitude and phase for the main harmonic. However, the results of the quasi-steady based models resulted in similar values, providing that the quasi-steady assumption may be valid at this high reduced velocities. On the other hand, the wavelet metrics resulted in significantly lower values for the case of $\alpha_s = 4$ deg for all models. Both the wavelet and normalized-wavelet metrics resulted in a similar value of $\mathcal{M}_w \approx M_{wf}$, meaning that there is a significant discrepancy in the time-frequency plane mainly due to frequency modulations. Another interesting point, in this case, is that the QS and CQS model yielded better results than the LU model for the wavelet-based metrics.

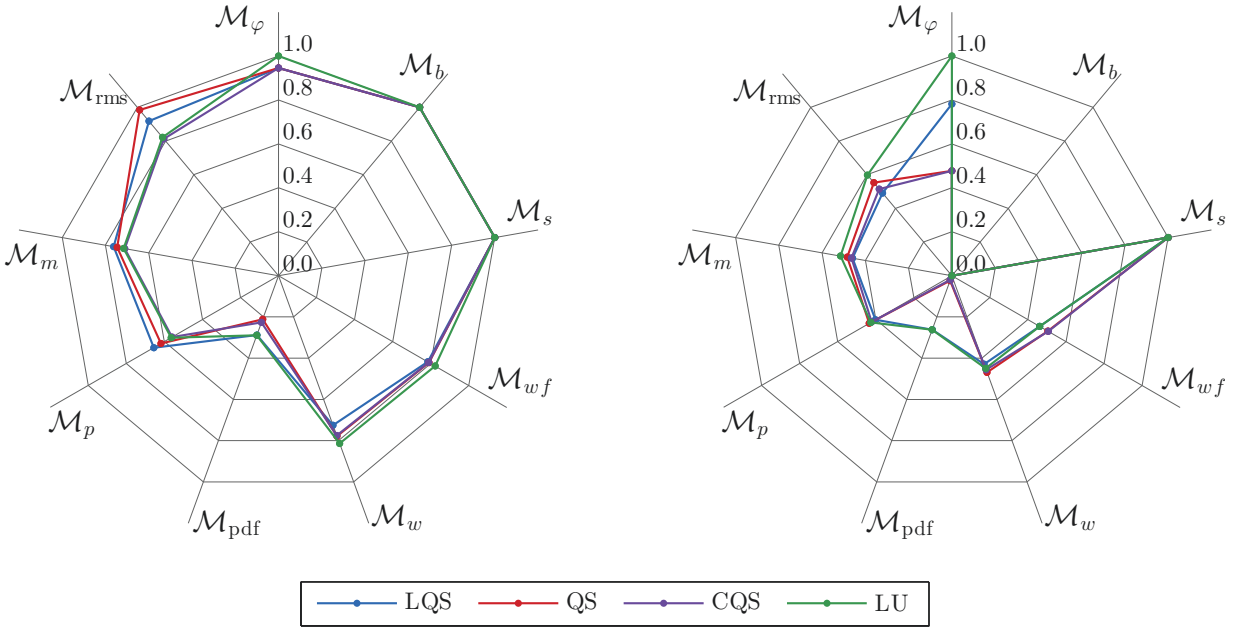

Figure 6.34: Great Belt Bridge: comparison metrics for the moment self-excited coefficient $\mathcal{M}^{C^{\text{CFD}}_{M\alpha}, C^{j}_{M\alpha}}$ for sinusoidally rotating deck about static angle $\alpha_s = 0$ deg (left) and $\alpha_s = 4$ deg (right) at $V_r = 16$, where $j \in \{\text{LQS}, \text{QS}, \text{CQS}, \text{LU}\}$. The CFD model is selected as a reference.

To study the behaviour of the wavelet-based metrics, Fig. 6.35 depicts the magnitude of the wavelet coefficients $|W_{C_{M\alpha}}|$ for the CFD, LU and QS models for rotation about $\alpha_s = 0$ deg (left) and $\alpha_s = 4$ deg (right). Apart from from the main harmonic at $V_r = 16$ (i.e. $K \approx 0.4$), an additional superharmonic contribution is noted for the CFD and QS models at $K = 0.8$ (cf. Fig. 6.35, top-right and bottom-right, respectively). Since the LU model is linear, it models only a single harmonic component; hence, it does not account for the frequency content other than the forcing frequency. On the contrary, the QS model is able to capture this behavior as it

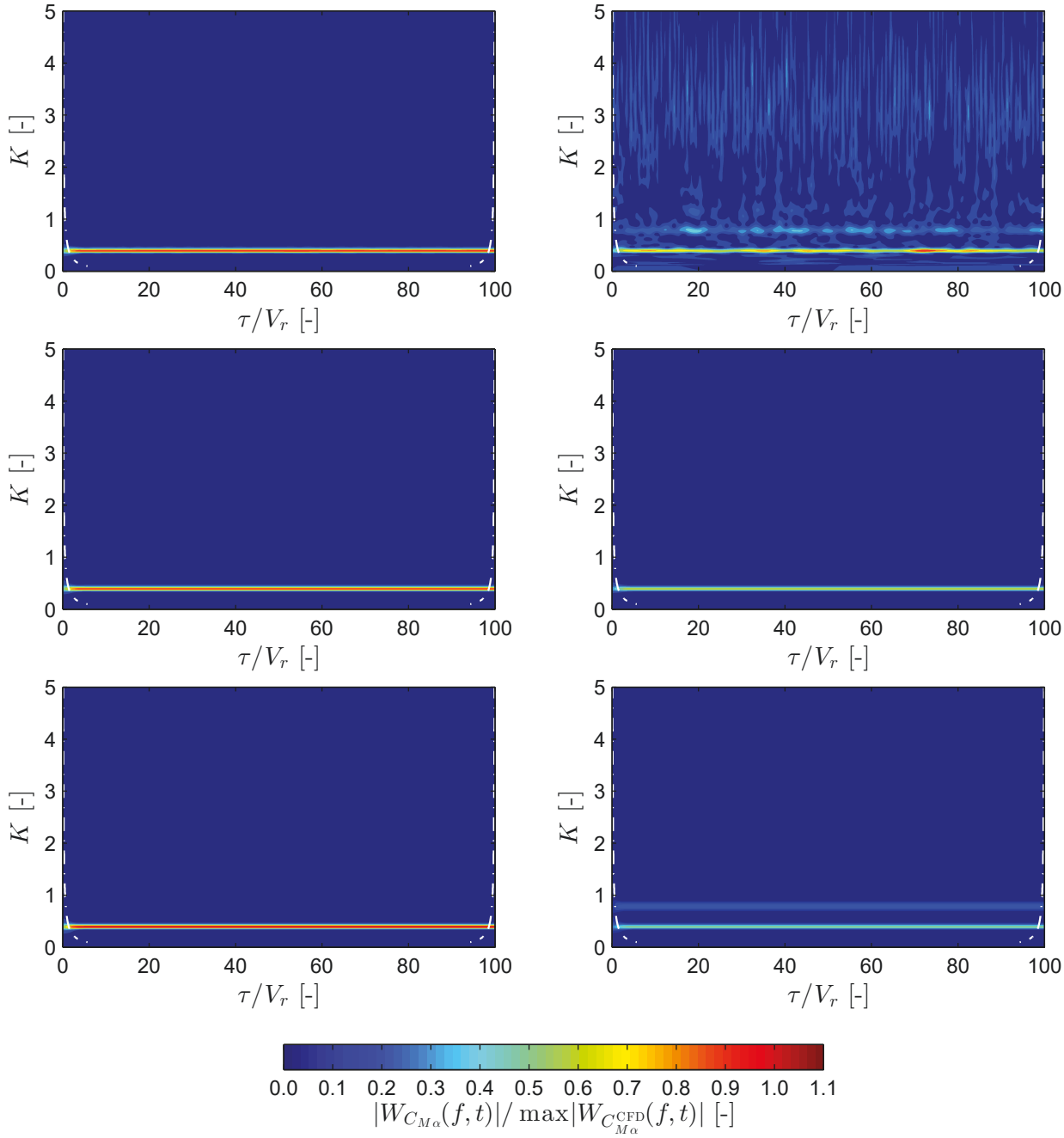

Figure 6.35: Great Belt Bridge: normalized absolute wavelet coefficients of the fluctuating self-excited moment coefficient for a sinusoidally rotating deck about static angle $\alpha_s = 0$ deg (left) and $\alpha_s = 4$ deg (right) at $V_r = 16$. From top to bottom: CFD, LU and QS models. The dashed-dot line indicates the cone of influence COI.

is nonlinear. Moreover, there is a widespread frequency content in the range from $K = 2-4$ for $\alpha_s = 4$ deg for the CFD model, which corresponds to the frequency range of vortex-shedding. At $\alpha_s = 0$ deg, the relative effect of the vortex shedding on the wavelet coefficients is significantly lower (an order of magnitude) than at α_s=4 deg, and it occurs at higher frequencies (i.e. lower Strouhal number); thus, it is not visible in the figure. Both the nonlinearity and vortex shedding are the reason for high discrepancies in the wavelet metrics of the forces for rotation about $\alpha_s = 4$ deg. The LQS and CQS models resulted in similar time-frequency planes as the LU and QS models, respectively; thus, they are not shown in the figure.

Detecting superharmonics is the first indicator of nonlinearity, as observed numerous studies in bluff-body aerodynamics (cf. e.g. [86, 207, 367]). Quadratic phase coupling is the nonlinearity that is related to the superharmonic at twice the frequency of oscillation (i.e. second-order nonlinearity), as observed previously in the wavelet coefficient, and can be revealed by the bispectrum. Figure 6.36 depicts the unfiltered $G_B^R(K_1, K_2)$ (top) and surrogate-filtered $G_B^F(K_1, K_2)$ (bottom) phase-randomized bispectrum magnitude for the CFD (left) and QS models (right) for forced vibration at $\alpha_s = 4$ deg. For both of these models, there is a peak at the frequency

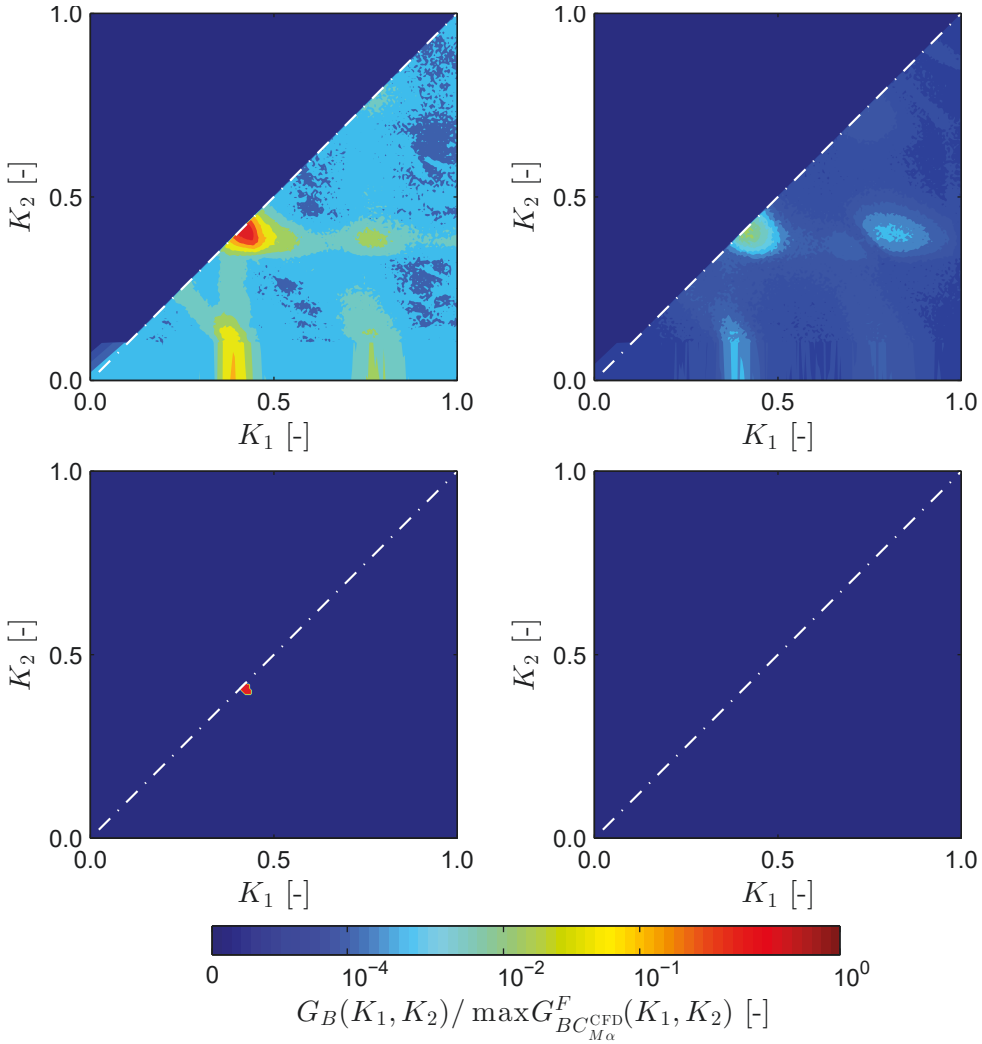

Figure 6.36: Great Belt Bridge: phase-randomized bispectrum amplitude $G^R_{BC_{M\alpha}}$ (top) and filtered phase-randomized bispectrum amplitude $G^F_{BC_{M\alpha}}$ (bottom) of the fluctuating self-excited moment coefficient for the CFD (left) and QS (right) models. The deck is performing sinusoidal rotations about a static angle of $\alpha_s = 4$ deg at $V_r = 16$. The dashed-dot line indicates the inner triangle IT.

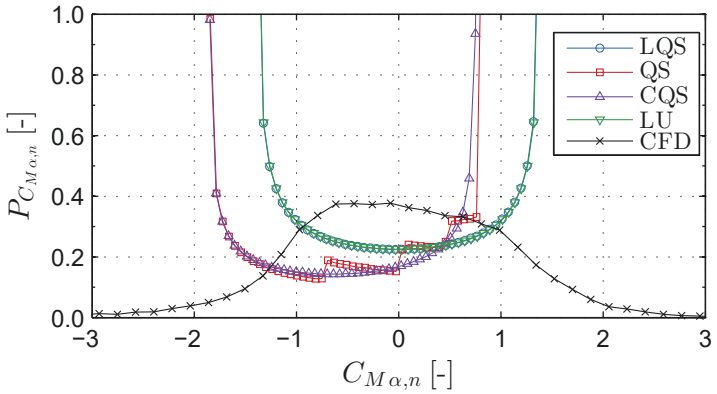

Figure 6.37: Great Belt Bridge: histogram estimate PDF of the normalized (standard score) fluctuating self-excited moment coefficient for a sinusoidally rotating deck about a static angle of $\alpha_s = 4$ deg at $V_r = 16$.

couple of $(K_1, K_2) = (0.4, 0.4)$ for the unfiltered bispectrum magnitude G_B^R, indicating potential quadratic phase coupling (i.e. nonlinearity). However, in case of the QS model (cf. Fig. 6.36, top-right), the peak at $(K_1, K_2) = (0.4, 0.4)$ is significantly lower than for the CFD model (two orders of magnitude). This indicates that the aerodynamic nonlinearity is significantly underestimated for the QS model. Similar observations for a pitching airfoil were realized by McCroskey and his coworkers [219, 220], who observed that the dynamic hysteresis of the self-excited aerodynamic forces attains significantly higher values compared to the static counterparts at a similar angle of attack. Based on the surrogate testing, such small amplitudes of the bispectrum as the ones for the QS model, are detected as noise. Thus, the filtered bispectrum magnitude of the QS model resulted in trivial values (cf. Fig. 6.36, bottom-right). Contrary, the peak for the CFD model is clearly indicated in the filtered bispectrum magnitude (cf. Fig. 6.36, bottom-left), suggesting aerodynamic nonlinearity. As none of the models captured this phenomenon for the present case, the bispectrum metric resulted in $\mathcal{M}_b = 0$.

Significantly small values are noted for the PDF metric $\mathcal{M}_{\text{pdf}}$ for all models. Figure 6.37 depicts the histogram estimate PDFs of the $C_{M\alpha}$ due to rotation at $\alpha_s = 4$ deg. The PDFs of the CFD model are somewhat Gaussian and asymmetric due to the vortex shedding, interior noise, and nonlinearity, despite single-frequency input. A similar observation is noted by Lin et al. [207] for the case of bluff rectangular cylinders. Since all semi-analytical models yield close to sinusoidal forces, the PDF attains vertical asymptotic behavior. In the case of the QS and CQS models, the asymmetry is due to the nonlinear behavior that is different for positive and negative angles of attack. It should be noted that, selecting a sensitivity factor of $\varepsilon_{\text{PDF}} = 10$ (cf. Tab. 6.5) also contributes to the high value of the PDF metric.

6.3.6 Aerostatic analysis: 2D

The aerostatic response is computed for a smooth free-stream at the selected wind speeds using CFD, semi-analytical linear and nonlinear aerostatic analyses. The latter analysis is performed by iterative updating of the static wind coefficients w.r.t. the position of the section until an aerostatic equilibrium is achieved. For the CFD analysis, the section is subjected to a smooth free-stream and undergoes free oscillations with a duration of τ =160. The response is then averaged for τ =110-160, for which the initial impulse is sufficiently damped out. Figure 6.38 shows the vertical h_s and torsional α_s displacements due to laminar free-stream. The figure suggests that nonlinear aerostatic analysis is required for high wind speeds. Similar observa-

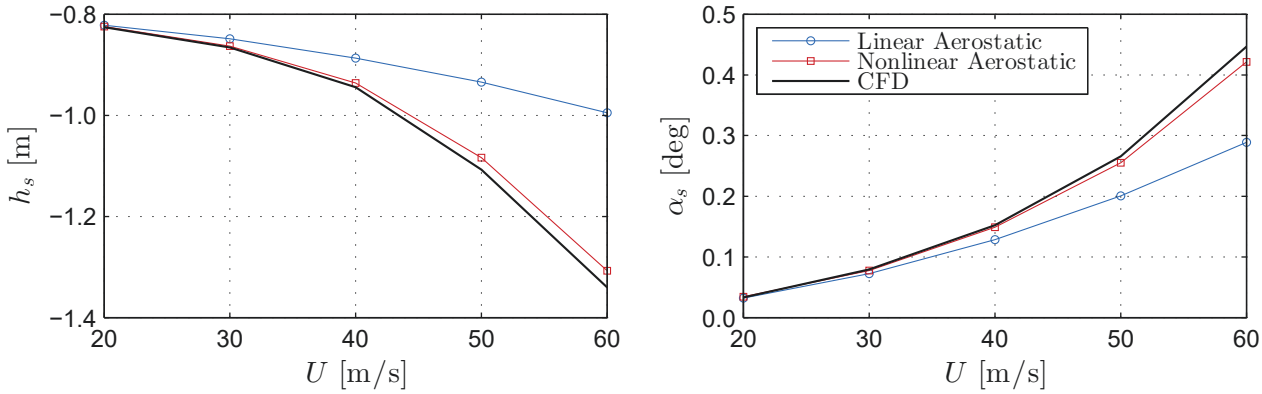

Figure 6.38: Great Belt Bridge: 2D aerostatic vertical displacement h_s (left) and rotation α_s (right) for smooth free-stream.

tions are noted by Zhang et al. [374], where the influence of the geometric and aerodynamic nonlinearities on the flutter velocity are studied. It is noted that for the linear models, the linearization of the static wind coefficients is performed at the angle of nonlinear static equilibrium.

6.3.7 Buffeting analysis: 2D

Aeroelastic analyses under free-stream turbulence are performed for velocities ranging from 20 up to 60 m/s for both turbulent cases. Since the turbulent Reynolds number is constant, the influences of the reduced velocity, turbulence intensity and motion amplitudes on the dynamic response are studied. Figure 6.39 depicts snapshots of the velocity field during bridge oscillation for CFD buffeting analysis, in which upstream fluctuation velocity can be observed due to the free-stream turbulence.

Two types of comparisons are performed: one-to-one comparison, for the same input wind time-history for all models; and statistical comparison, for twenty random wind time-histories for the LU model.

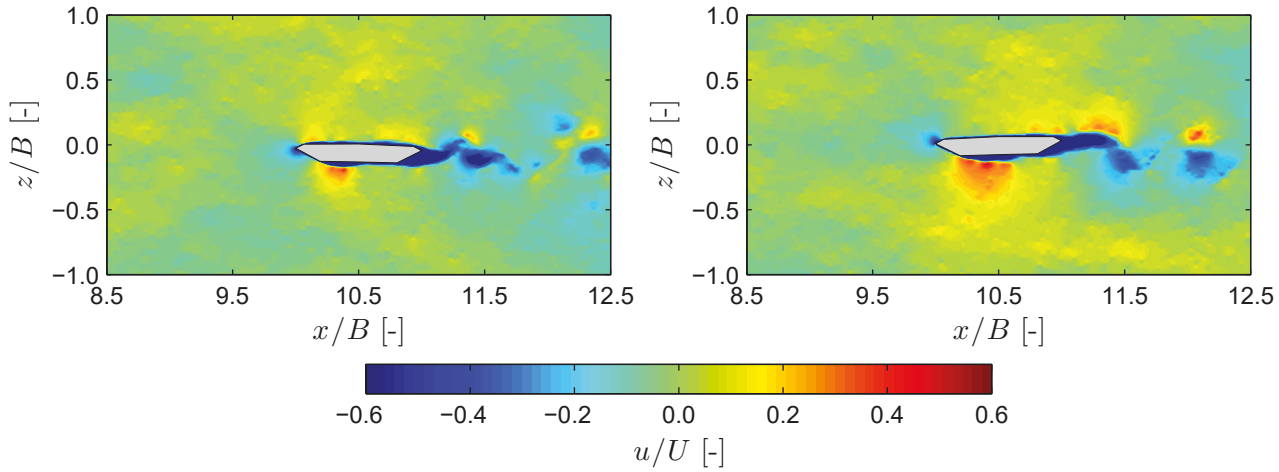

Figure 6.39: Great Belt Bridge: instantaneous longitudinal velocity fields of 2D buffeting analysis at $U = 30$ m/s and $TI = 6$ %.

One-to-one comparison

Input wind fluctuations for the semi-analytical models are tracked down in the section-less CFD domain at $\boldsymbol{x}_s$ within the one-to-one comparison. In what follows, the time-histories are compared based on local and global quantities, as well as the comparison metrics.

Figure 6.40 depicts the RMS values of the vertical and torsional response for the selected wind speed range for both turbulent cases. Specific values of the response are listed in Fig. 6.41 for two representative velocities: high ($U = 30$ m/s) and low ($U = 60$ m/s) w.r.t. the flutter limit $U_{cr} \approx 70$ m/s. Based on the figures containing the RMS of the response, it is observed that the aeroelastic response for the LQS model is overestimated compared to the one for the CFD model for all of the cases. If the response for the LQS model is further compared to the results of the LU and QS models, it is evident that the effects of linear fluid memory and quasi-steady nonlinearity decrease the amplitude of the response, particularly for the case with high turbulence intensity.

The discrepancy between the vertical responses for the QS and CFD models is decreasing for higher wind velocities. Although the good correspondence between these two models can be attributed to the fact that the effect of fluid memory becomes negligible at high reduced velocity, this might not be the case herein. As discussed previously, the effect of the quasi-steady nonlinearity in the buffeting on the aeroelastic response is likely overestimated, while the nonlinearity in the self-excited forces underestimated. Another indication for the incapability of the QS model to represent the nonlinear aeroelastic behavior is the significant difference in the rotation w.r.t. the CFD model for high wind speeds, particularly for the high turbulence.

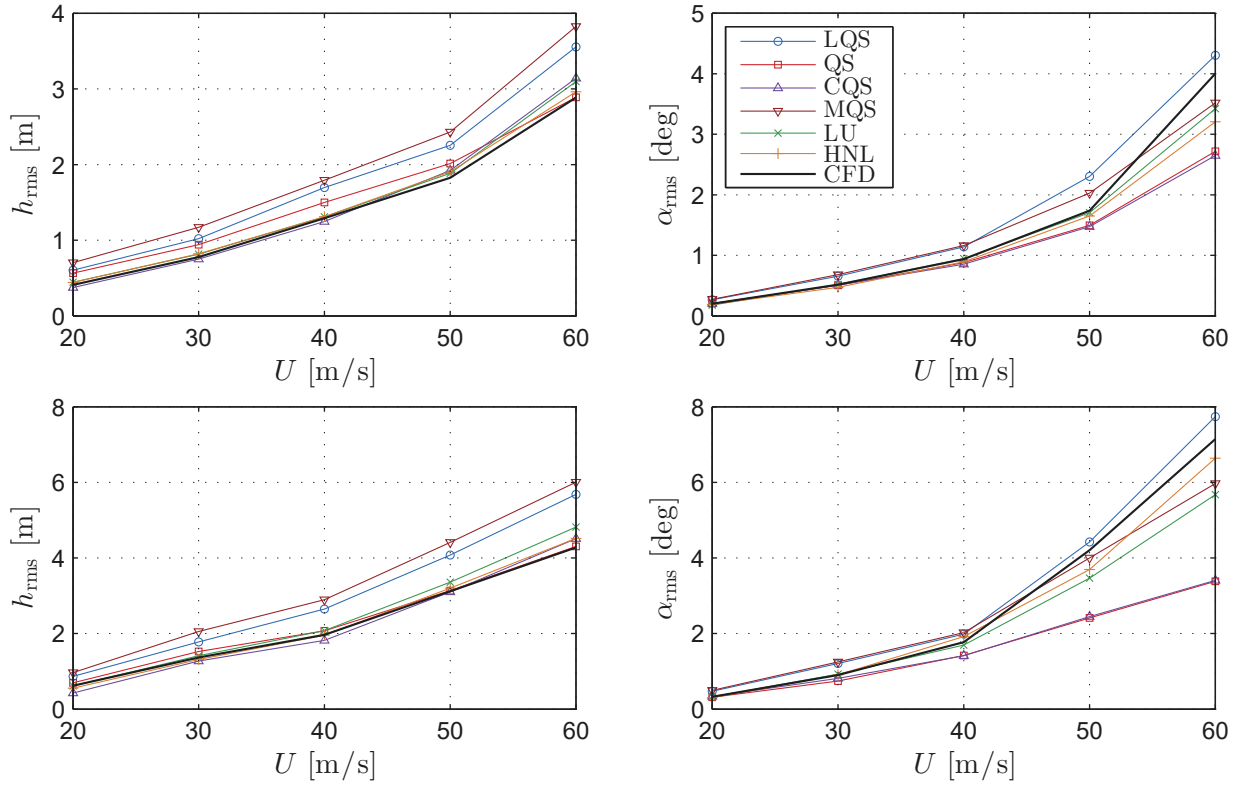

Figure 6.40: Great Belt Bridge: RMS of the vertical displacement (left) and rotation (right) for the CFD and semi-analytical models from 2D buffeting analysis for the selected mean wind speed range at $TI = 6$ % (top) and $TI = 10$ % (bottom).

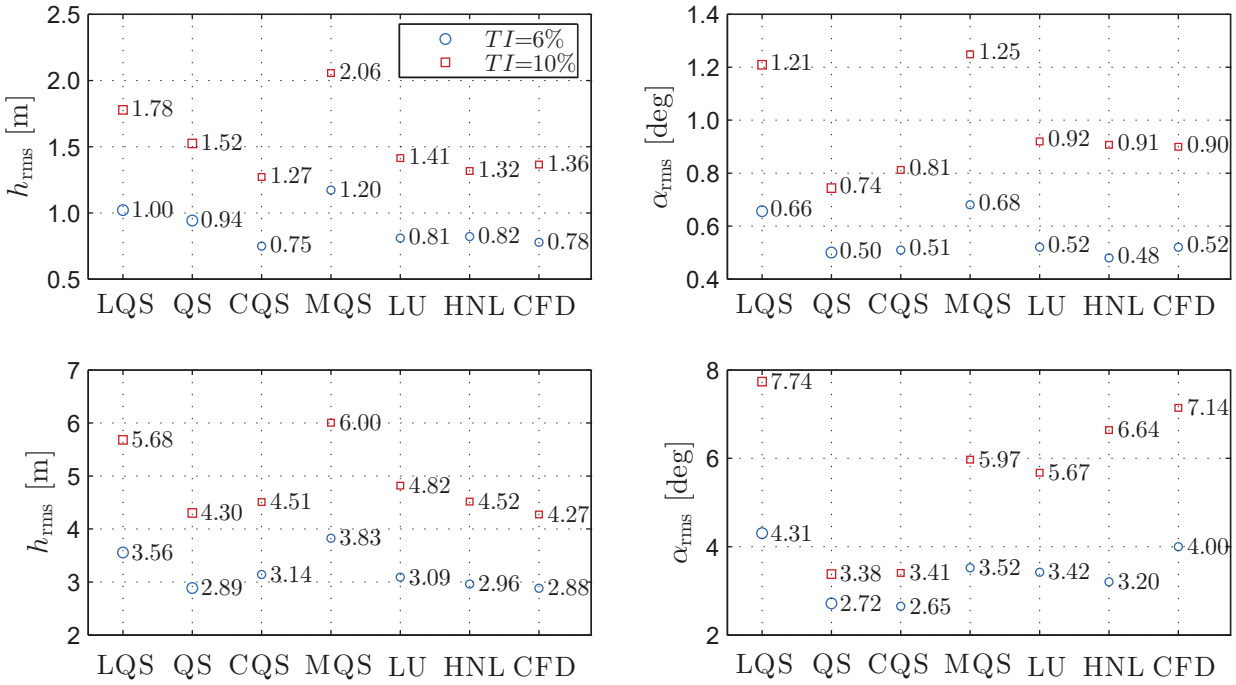

Figure 6.41: Great Belt Bridge: RMS of the vertical displacement (left) and rotation (right) for the CFD and semi-analytical models from 2D buffeting analysis at $U = 30$ (top) m/s and $U = 60$ m/s (bottom).

The trend of the response for the CQS model is essentially the same as the one for the QS model compared to the CFD model. For the case with low turbulence intensity, the vertical displacement for the CQS model is in better agreement with the response for the CFD model than the QS model. Other than this case, there is no clear indication of how the averaged fluid memory affects the aeroelastic response. Although no conclusive statements can be made on this account, the abrupt changes in the correction coefficient in the CQS model might result in irregularity in the trend of the displacements, as noted by Wu and Kareem [359]. The same observations regarding the effect of quasi-steady nonlinearity hold for the CQS model as well. Even though the aim of the MQS model is to better describe the aerodynamic damping than the LQS model, an increased discrepancy for the vertical displacement is noted for the MQS model compared to the LQS model. This is a result of the quadratic trend of H_2^*, in contrast to the linear trend assumed in the MQS model [244]. The slope of the RMS of the torsional response w.r.t. the mean wind speed for the MQS model is lower than the one for the CFD model, which indicates an insufficient quality of approximation for the torsional damping. This can be also observed in Fig. 6.41 as the rotational displacement for the MQS model is overestimated at U =30 m/s and underestimated at $U = 60$ m/s w.r.t. the CFD model. Øiseth et al. [244] used the secant approximation of the torsional flutter derivatives to address this issue; however, this is not considered in this study.

Generally, the smallest discrepancies in the response are obtained for the LU and HNL models w.r.t. the CFD model, taking into account all considered cases and both degrees of freedom. Representative time-histories of the aeroelastic response for the semi-analytical models are compared with the response for the CFD model in Fig. 6.42, for the case with low turbulence and $U = 30$ m/s. The figure suggests that the response for the CFD model lags behind all models based on the quasi-steady assumption. This indicates the phase effect of the fluid memory in the aerodynamic forces. Based on a qualitative assessment, the response time-

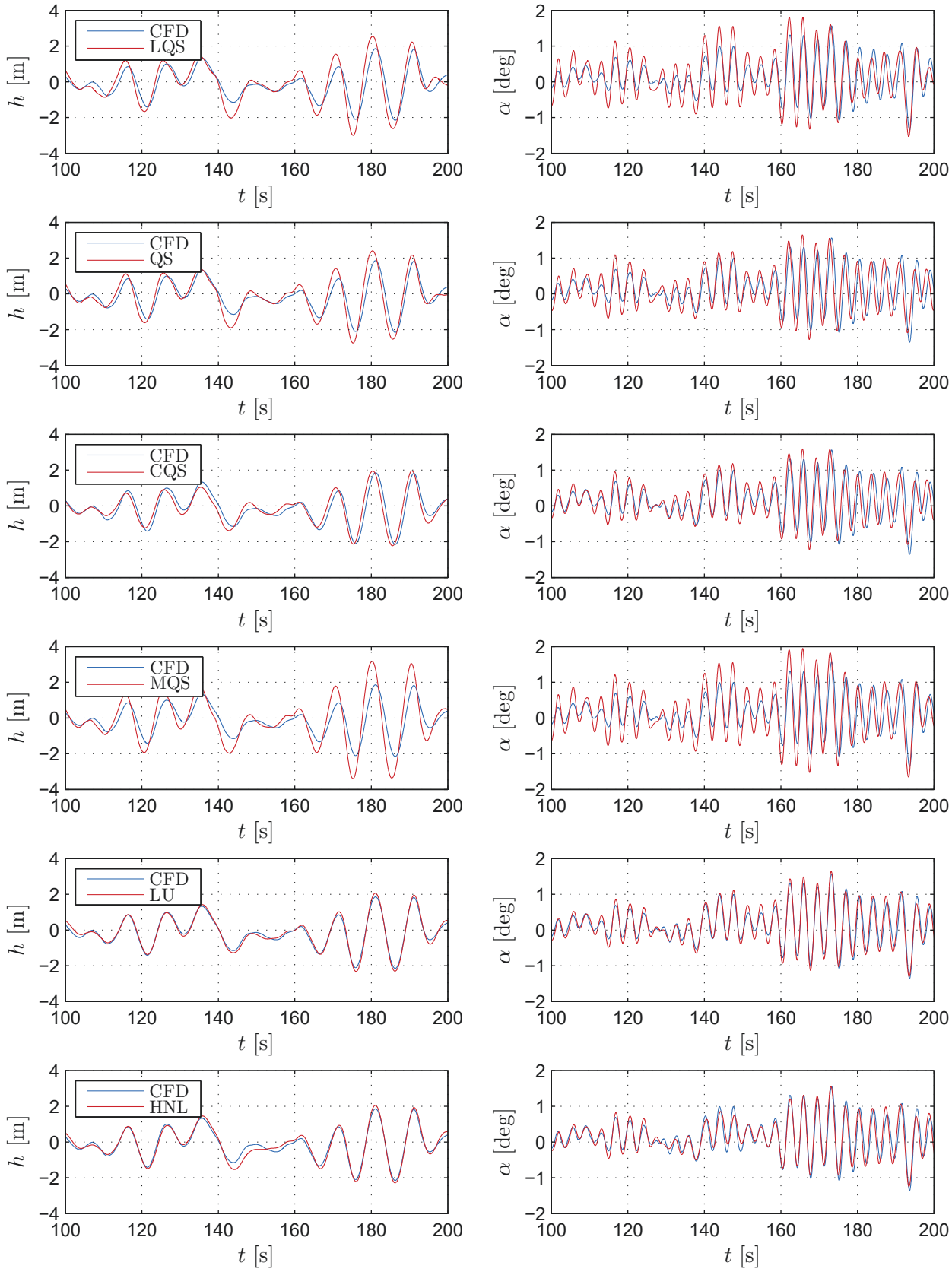

Figure 6.42: Great Belt Bridge: representative sample time-histories of the vertical displacement (left) and rotation (right) for the CFD and semi-analytical models from 2D buffeting analysis at $U = 30$ m/s and $TI = 6$ %.

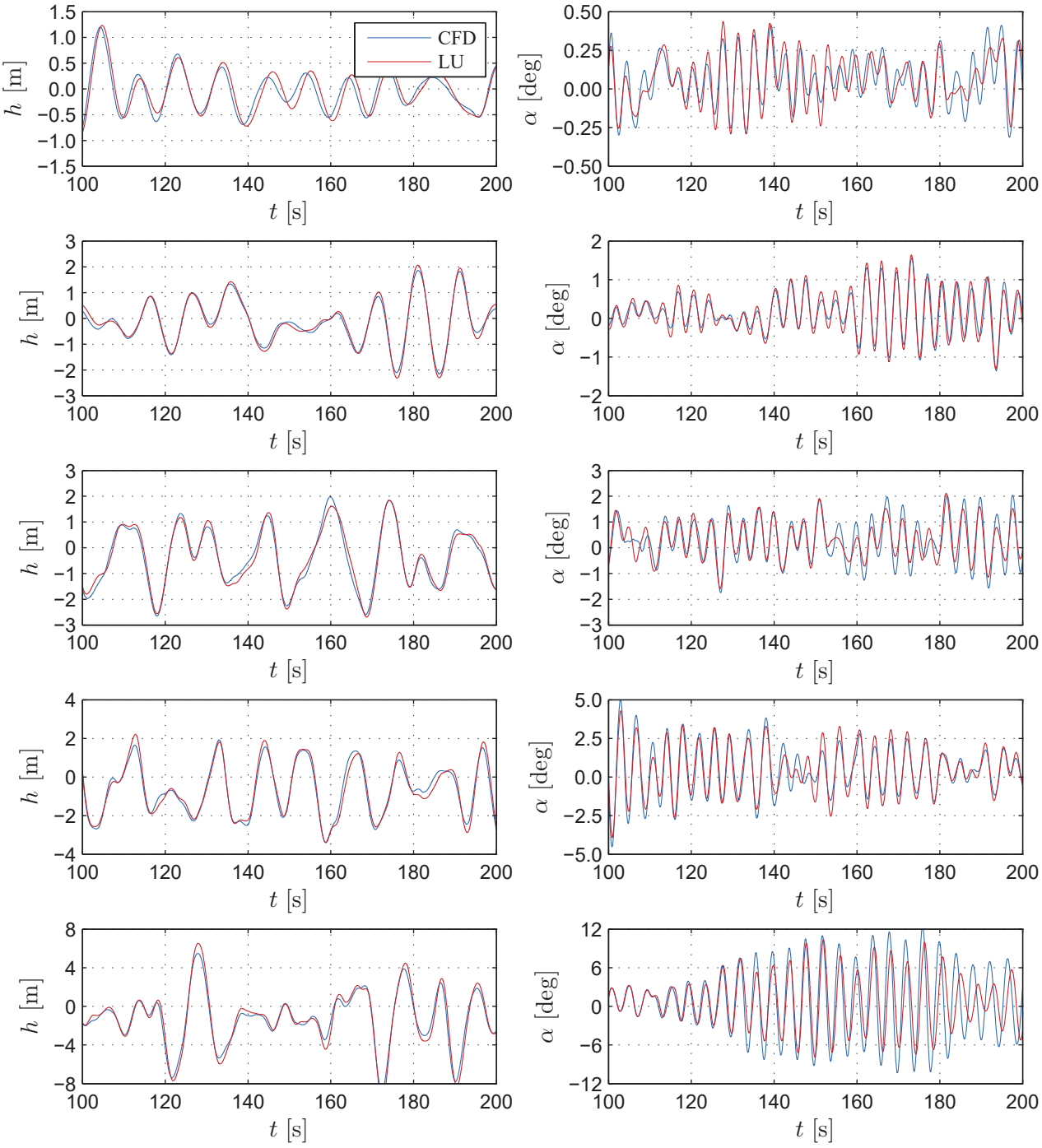

Figure 6.43: Great Belt Bridge: representative sample time-histories of the vertical displacement (left) and rotation (right) for the CFD and LU models from 2D buffeting analysis at $U = 20, 30, 40, 50, 60$ m/s (top to bottom) and $TI = 6$ %.

histories for the LU and HNL models appear to be in the best agreement with the response time-histories for the CFD model.

A particular feature is observed in the torsional response for the CFD model: above a certain velocity ($U = 50$ m/s and $U = 40$ m/s for the low and high turbulence case, respectively), a distinctive change of the slope of RMS of the response is noted (cf Fig. 6.40). For both levels of turbulence, a notable similarity in the torsional responses is the amplitude at which this change of slope occurs ($\alpha_{\text{rms}} \gtrapprox 3$ deg). When a motion is introduced to an aeroelastic

system in addition to the free-stream turbulence, it is even more challenging to describe the origin of discrepancies in the aerodynamic forces for the models. In a dynamic system, the nonlinearity of the self-excited forces is included through their nonlinear amplitude dependence on the motion [117] and multiple output frequencies, excited by a single harmonic input motion [84, 86].

Figure 6.43 shows a comparison of the response time-histories for the LU and CFD models for the studied wind speed range and the case with low turbulence. The torsional responses for the LU and CFD models exhibit an increasing phase-shift and amplitude difference at U =60 m/s. In the time interval between $t = 140 - 180$ s, the amplitudes for the CFD model exceed $\alpha \geq 6$ deg. When studying the self-excited forces in the previous section, it was seen that at such high angles of attack, quadratic phase coupling may occur (i.e. nonlinearity is present). This high peak in the rotation can be also observed from the wavelet coefficients at $U = 60$ m/s for the low turbulence case, depicted in Fig. 6.44 for all models. None of the models is actually capable to capture this high rotation amplitudes at this particular time. Further, this makes the case that although the RMS of the torsional response for the LQS model corresponds well with the response for the CFD model at $U = 60$ m/s (cf. Fig. 6.40, top-right), a conclusion that the LQS model describes well the aerodynamic forces is likely to be inaccurate. To prove this point, it can be observed that the peak of the torsional response for the LQS model does not occur at the same time instance as for the CFD model (cf. Fig. 6.44). Thus, general conclusions should not be made solely on the RMS of the response. Another interesting effect that can be observed from the wavelet magnitude of the vertical displacement (cf. Fig. 6.44, left) is a spectral contribution appears at a frequency corresponding to the torsional frequency $f_\alpha = 0.287$ Hz. This indicates the effect of aerodynamic coupling, which is prominent for all models, except for the MQS model.

All previous observations can be further supported by the comparison metrics depicted in Fig. 6.45 for two wind speeds, $U = 30$ m/s (top) and $U = 60$ m/s (bottom). Again, the CFD model is taken as a reference when comparing the semi-analytical models. Generally, the nonlinear quasi-steady based models, CQS and QS, are in better agreement for the vertical rotation at the higher wind speed, which indicates the validity of the quasi-steady assumption at high wind speeds. Neglecting both nonlinearity and fluid memory yields the highest discrepancy for the LQS model. The effect of fluid memory is clearly the most influential as the LU and HNL models yielded the best overall behavior, local and global. Moreover, by studying the comparison metrics for the vertical displacement h at $U = 60$ m/s, it can be realized why considering the RMS as an only basis for comparison is insufficient. Particularly, the QS model performs slightly better for the RMS metric $\mathcal{M}_{\mathrm{rms}}^{h^{\mathrm{CFD}},h^{\mathrm{LU}}} < \mathcal{M}_{\mathrm{rms}}^{h^{\mathrm{CFD}},h^{\mathrm{QS}}}$, while the situation is reversed for the magnitude metric, i.e. $\mathcal{M}_{\mathrm{m}}^{h^{\mathrm{CFD}},h^{\mathrm{LU}}} > \mathcal{M}_{\mathrm{m}}^{h^{\mathrm{CFD}},h^{\mathrm{QS}}}$. This indicates that only the global quantities of the CFD model are in better correspondence with the QS model and not the local ones. Since the input may be considered as identical, to draw a general conclusion that the quasi-steady nonlinearity is more critical than the linear fluid memory at high wind speeds, all metrics should support such a statement. In this case, it may only be indicated that the influence of the nonlinearity becomes apparent in the RMS at high wind speeds.

A particular point of interest is the stationarity metric $\mathcal{M}_s$ for the rotation at $U = 60$ m/s (cf. Fig. 6.45, bottom-right). Namely, this metric yields a value of zero for all models, which means that a part of the CFD torsional response is actually non-stationary. Figure 6.46 depicts the non-stationary portion of the rotation for the CFD model. It can be observed that this particular time interval is the same as the one discussed previously, where nonlinearities were indicated and the incapability of the semi-analytical models to capture this effect

(cf. Fig. 6.43, bottom-right). For stationary input, which is the case for the wind fluctuations in this study, only a nonlinear model may result in a non-stationary output in the stable range

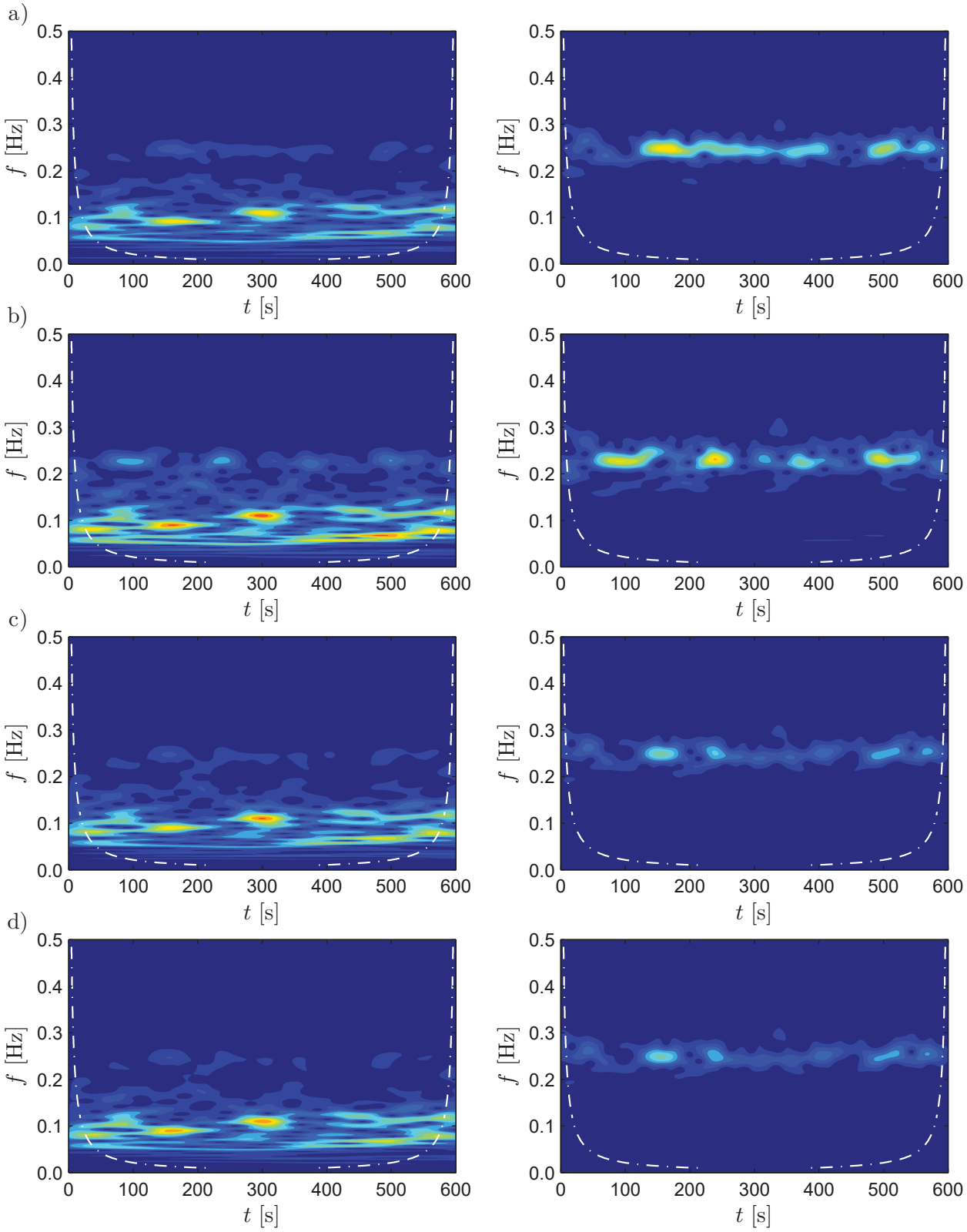

Figure 6.44: Great Belt Bridge: normalized absolute wavelet coefficients of the vertical displacement (left) and rotation (right) for the a) CFD, b) LQS, c) QS, d) CQS, e) MQS , f) LU and g) HNL models from 2D buffeting analysis at $U = 60$ m/s and $TI = 6$ % (continued figure).

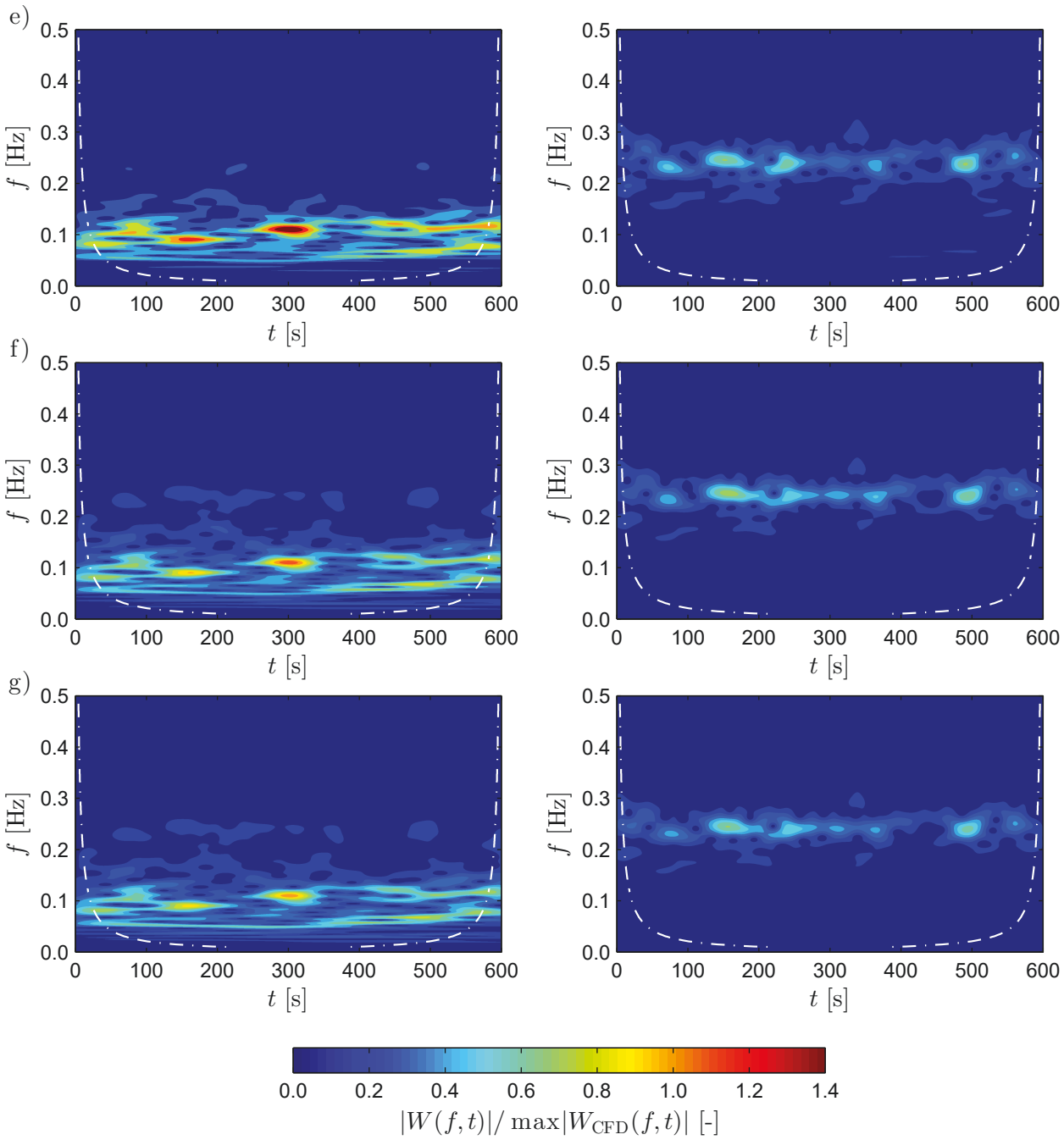

Figure 6.44 (continued)

(i.e. not in the flutter region). Hence, the unsteady nonlinearity in the self-excited forces seems like a plausible reason for the amplitude modulations in this time interval.

The bispectrum showed no appreciable peaks for all models; thus, the bispectrum metric amounts to $\mathcal{M}_b = 1$. Although quadratic phase coupling may be occurring, this effect can be further reduced by the mechanical admittance when looking at the dynamic response. Hence, it is easier to be captured for the self-excited aerodynamic forces due to sinusoidal forced excitation, as shown in the previous section. It should be noted that quadratic phase coupling is just one particular type of nonlinearity. Other types of nonlinearities such as cubic phase coupling cannot be identified by the bispectrum.

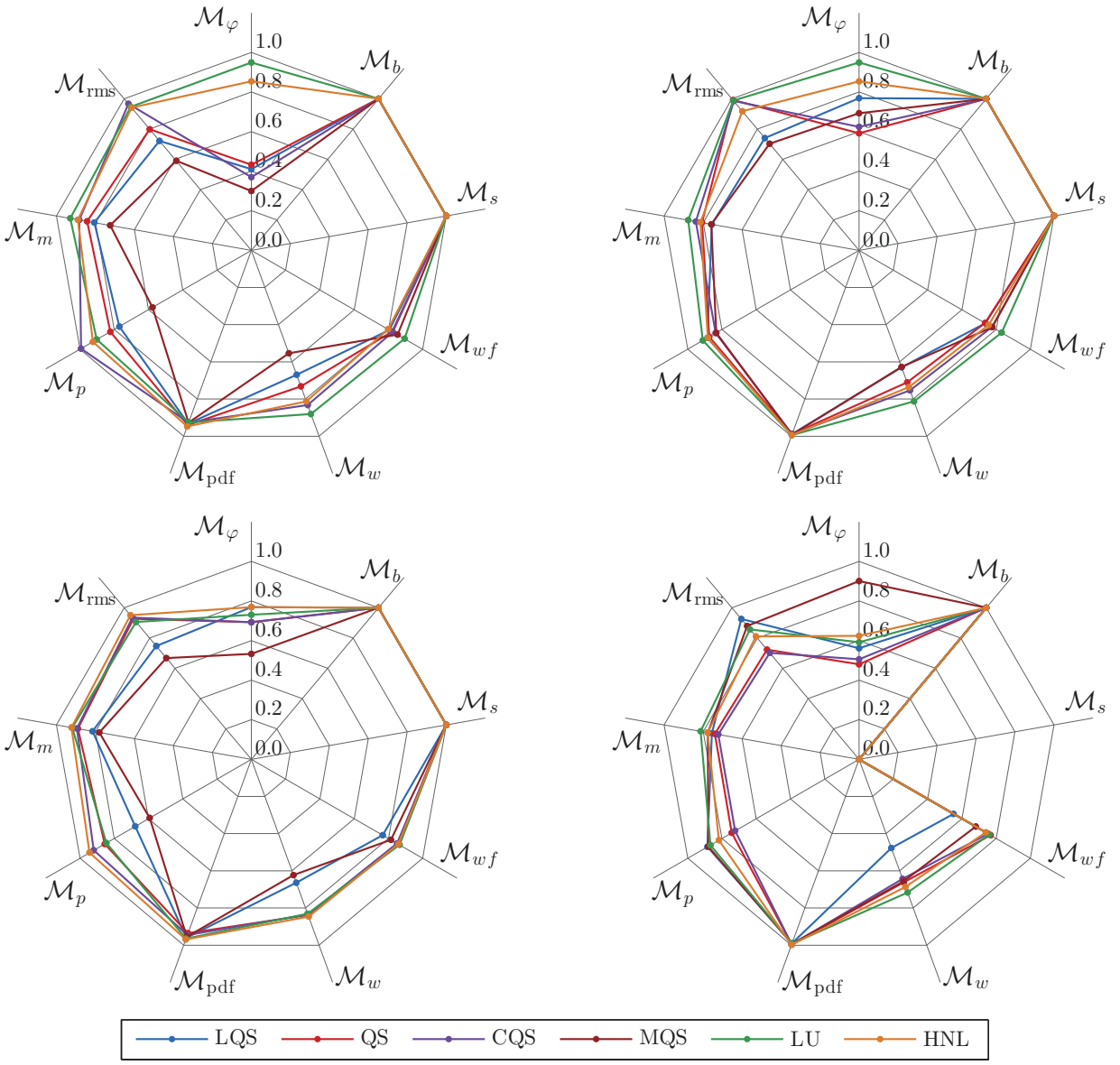

Figure 6.45: Great Belt Bridge: comparison metrics of the vertical displacement $\mathcal{M}^{h^{\text{CFD}},h^j}$ (left) and rotation $\mathcal{M}^{\alpha^{\text{CFD}},\alpha^j}$ (right) from 2D buffeting analysis at $U = 30$ m/s (top) and $U = 60$ m/s (bottom) and TI=6 %, where $j \in \{\text{LQS}, \text{QS}, \text{CQS}, \text{MQS}, \text{LU}, \text{HNL}\}$. The CFD model is selected as a reference.

Statistical comparison

The statistical comparison is performed using twenty time-history records for the input wind fluctuations only of the LU model. In contrast to the flat plate study (cf. Sec 5.4), where the time-histories were generated simply by phase randomization of the wind spectrum, here the wind fluctuations are the ones generated at the particle ladder for the CFD model. In this way, it is avoided that the spectrum of the wind fluctuations is matched exactly due to the imposed correlation between ladder cells. Hence, a more appropriate statistical significance can be obtained for the LU model.

Figure 6.47 depicts the response for the CFD, for a single time-history, and for the LU model, for twenty records. The shaded area represents the 99 % confidence interval for the LU model. Generally, the CFD response for the vertical displacement falls into the confidence interval.

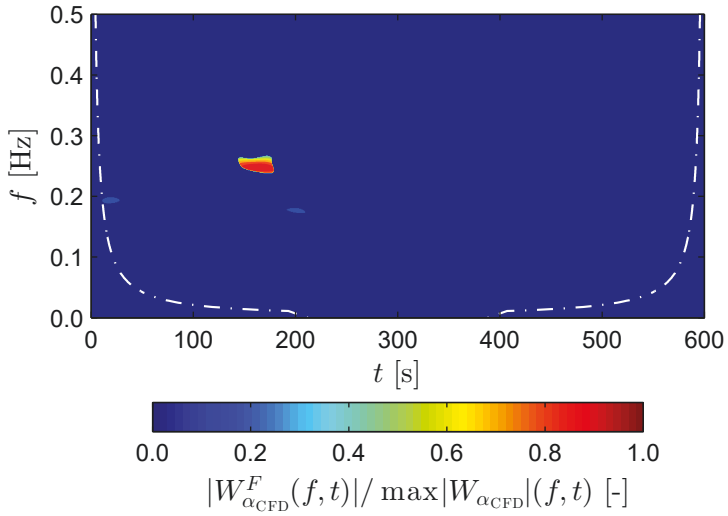

Figure 6.46: Great Belt Bridge: filtered non-stationary part of the absolute wavelet coefficients of the rotation for the CFD model from 2D buffeting analysis at $U = 60$ m/s and $TI = 6$ %.

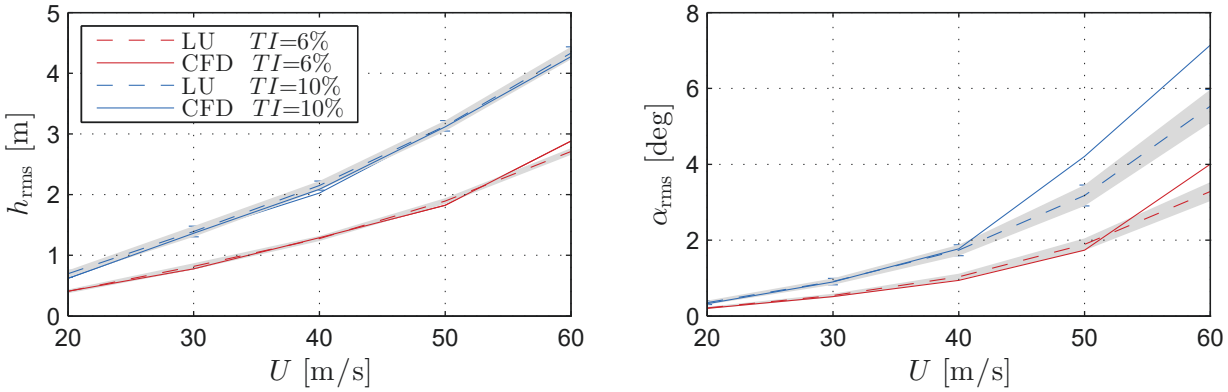

Figure 6.47: Great Belt Bridge: RMS of the vertical displacement (left) and rotation (right) from the statistical comparison for 2D buffeting analysis for the CFD and LU models. The response for the LU model is obtained based on the mean of 20 independent response time-histories. The shaded area represents the 99 % confidence interval for the LU model.

This indicates that regardless of how the wind fluctuations are obtained (from CFD or directly generated), similar conclusions can be made on the assumptions and validity of the CFD model. Again, the LU model underestimates the torsional response for amplitudes $\alpha_{\mathrm{rms}} \gtrapprox 3$ deg for the CFD model. Similarly as for the one-to-one comparison, it can be argued that this is a consequence of the aerodynamic nonlinearity in the self-excited forces.

6.3.8 Flutter analysis: 2D

The critical flutter velocity U_{cr} is computed in the time domain using the semi-analytical and CFD models for smooth free-stream and the results are given in Fig. 6.48 (left). Additionally, the critical flutter range obtained from Larsen's [189] direct section model tests is given by the gray area in the same figure. To obtain the critical frequency f_{cr}, FFT is performed on the motion time-histories at flutter (cf. Fig. 6.48, right). The good correspondence of the results for the HNL and CFD models suggests that good approximation of the flutter velocity can be obtained by a linear dynamic perturbation analysis about the nonlinear static equilibrium. In

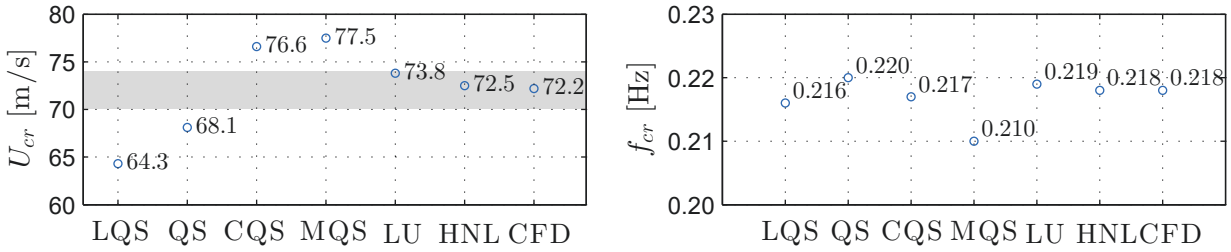

Figure 6.48: Great Belt Bridge: critical flutter velocity U_{cr} (left) and frequency f_{cr} (right) for the CFD and semi-analytical models from 2D flutter analysis. The shaded area represents the range for critical flutter velocity obtained from experimental section model testing by Larsen [188].

the case of the HNL model, the flutter derivatives were linearized at the static angle $\alpha_s = 1.5$ deg for the flutter analysis. However, the effect of the aerostatic nonlinearity is not very significant in this case, since the critical velocity for the LU model is slightly overestimated (≈ 1.5 %) w.r.t. the one for the HNL model. The QS and LQS models underestimate the critical velocity compared to the LU and CFD models, which indicates that the effect of linear fluid memory increases the flutter velocity. This observation is in line with the previous case-study of the Mersey Gateway bridge; however, it is in contradiction to the results presented by Wu and Kareem [359]. A general conclusion cannot be made since the flutter derivatives and the aerodynamic center are case-dependent. Furthermore, from the results for the QS and CQS models, it can be observed that including the averaged fluid memory increases the flutter velocity when the quasi-steady nonlinearity is considered. Nevertheless, considering the fluid memory in an averaged manner overestimates the effect of the fluid memory on the instability limit, as the critical velocity for the CQS model is overestimated compared to the one for the LU, HNL and CFD models. A higher flutter velocity is obtained for the MQS model compared to the CFD model, which is a result of the quadratic trend of the velocity flutter derivatives.

Figure 6.49 depicts the time-histories of the decaying, critical and post-critical response for the CFD, HNL and QS models. The response of the CFD model below U_{cr} has a decaying trend, while limit cycle oscillations can be observed at U_{cr}. In the case of the CFD free vibration analysis, it is difficult to obtain the exact critical velocity, although U_{cr} is computed with an increment of 0.2 m/s. The response for the HNL and QS models maintain a constant amplitude at the critical flutter speed. For a velocity higher than U_{cr}, the response for the HNL model adopts divergent behavior with unlimited amplitudes. Although the post-flutter behavior results in limit cycle oscillations for the QS model, the amplitudes during limit cycle oscillations are not corresponding with the CFD model. The reason for this is that the dynamic wind coefficients considerably exceed their static values, which is also noted by McCroskey [219]. The aerodynamic response from the flutter analysis for the rest of the semi-analytical models is omitted herein since it has a similar trend as the LU and QS models (linear or nonlinear) [359].

An absolute value of the wavelet coefficients of the vertical and torsional response for the CFD model, normalized w.r.t. the frequency marginal, is depicted in Fig. 6.50). The wavelet analysis is performed for a central frequency of $f_0 = 0.5$ Hz. For these wavelet coefficients of the response, the instantaneous frequency is computed by the identification of the local maxima of the ridge (cf. Fig. 6.51, where the wavelet energy is concentrated (cf. Kijewski and Kareem [171]). The results suggest that the initial frequency of oscillation for the CFD model corresponds well with the one obtained for the HNL model. As the divergent behavior progresses to stable limit cycle oscillations, the coupled instantaneous frequency tends to the torsional natural frequency, indicating torsionally driven oscillations in this range.

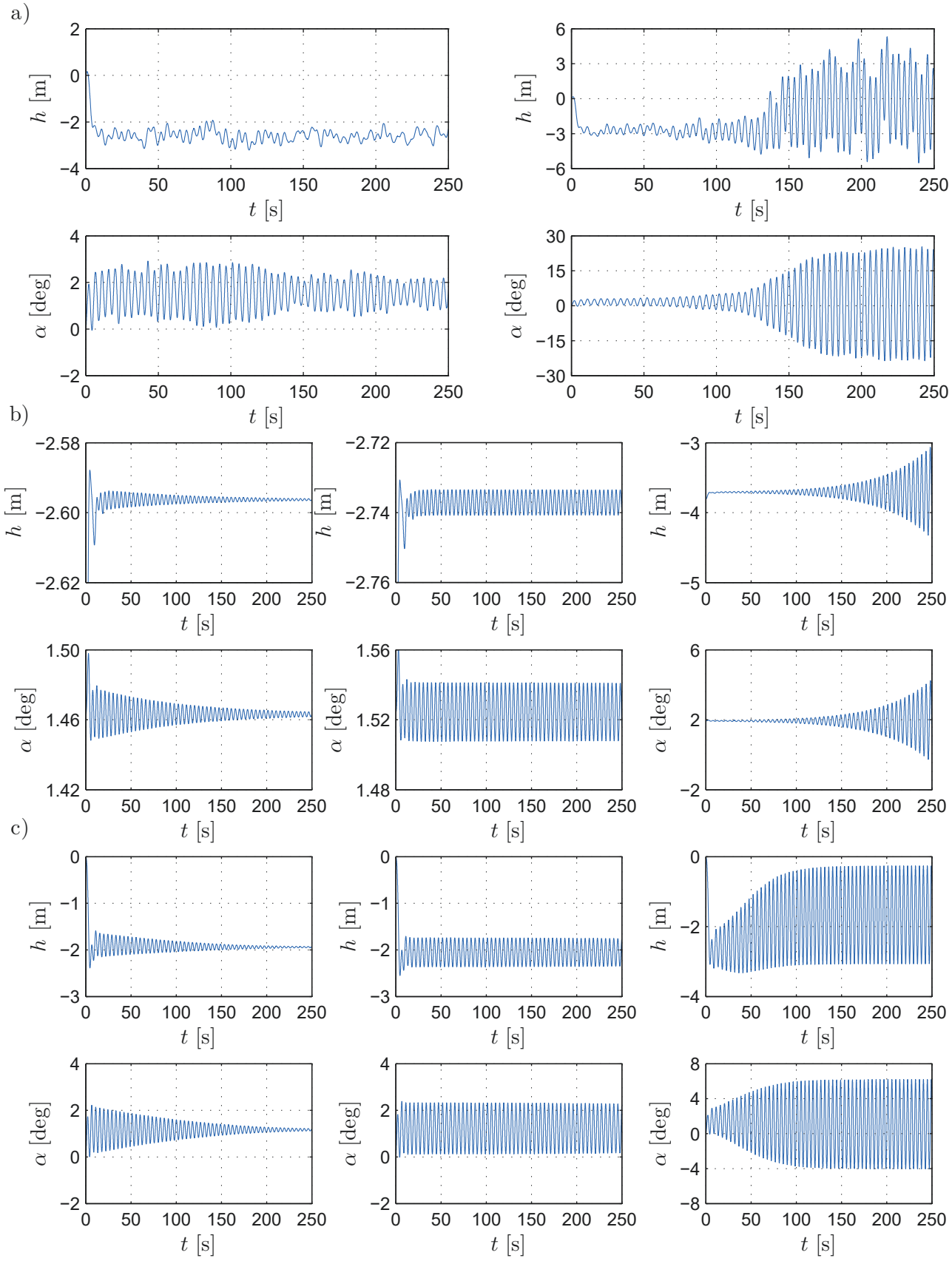

Figure 6.49: Great Belt Bridge: time-histories of the responses near the critical velocity from 2D flutter analysis. The following cases of response are depicted: a) CFD model - damped ($U = 71.0$ m/s, left), limit cycle oscillation ($U_{cr} = 72.2$ m/s, right); b) HNL model - damped ($U = 71.5$ m/s, left), critical ($U_{cr} = 72.5$ m/s, center), divergent ($U = 78.0$ m/s, right); c) QS model - damped ($U = 67.0$ m/s, left), critical ($U = 68.1$ m/s, center), limit cycle oscillation ($U = 72.0$ m/s, right).

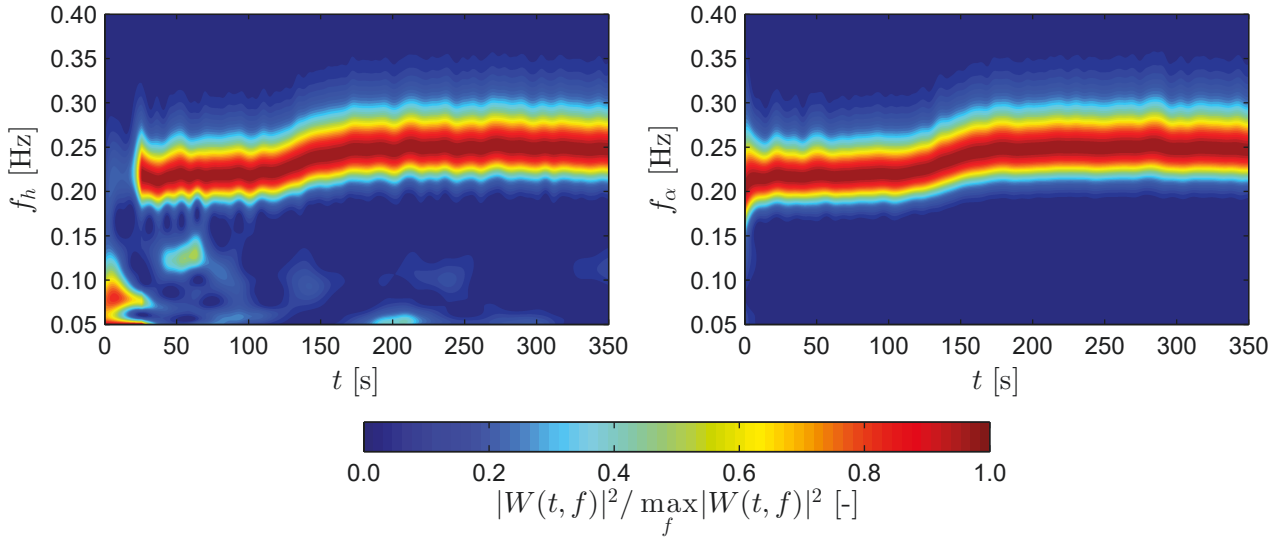

Figure 6.50: Great Belt Bridge: frequency-normalized wavelet magnitude of the vertical displacement $|W_h|$ (left) and rotation $|W_\alpha|$ (right) during limit cycle oscillation (at $U_{cr} = 72.2$ m/s) for the CFD model from 2D flutter analysis.

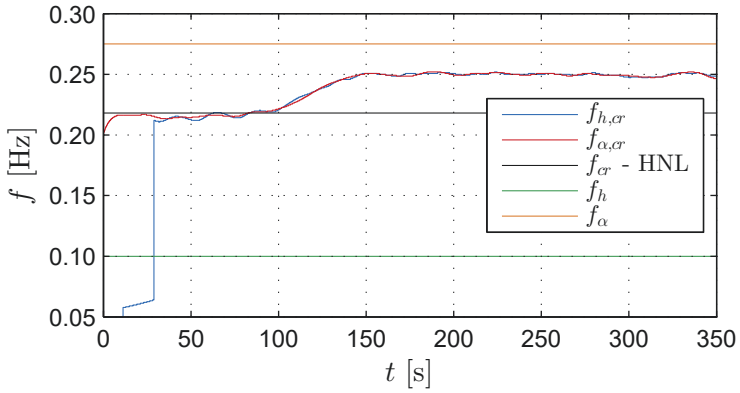

Figure 6.51: Great Belt Bridge: instantaneous frequency of the response during limit cycle oscillation (at $U_{cr} = 72.2$ m/s) for the CFD model from 2D flutter analysis.

Amandolese et al. [7] performed an experimental study on limit cycle oscillation of a flat plate due to aerodynamic nonlinearities and noted that beyond the critical velocity, the coupled frequencies tend towards the rotational branch, which is in line with the observations of this study. The authors also noted that with increasing amplitudes, there might be a change in the driving mechanism of the aeroelastic response from coupled to stall flutter. Unlike coupled flutter, stall flutter for airfoils is characterized by limited amplitudes and by partial or complete separation of the flow at the leading edge [91, 219], leading to high nonlinearity in the aerodynamic forces.

Figure 6.52 depicts instantaneous particle maps and velocity contours during half a period in the limit cycle oscillation range. As seen in the figure, a separation bubble is forming at the leading edge, which is characteristic of a dynamic stall. The transition from coupled to torsional flutter can be also identified from the A_2^* derivative at $\alpha_s = 4$ deg (cf. Fig. 6.21). Generally, the vortex methods are capable of accurately modeling the post-flutter behavior and matching the limit cycle oscillation amplitudes. This was recently validated by Chawdwhury and Morgenthal [52] with experimental results and for energy harvesters, while Akbari and Price [6] showed that the aerodynamic hysteresis can be accurately represented during dynamic stall of airfoils. However,

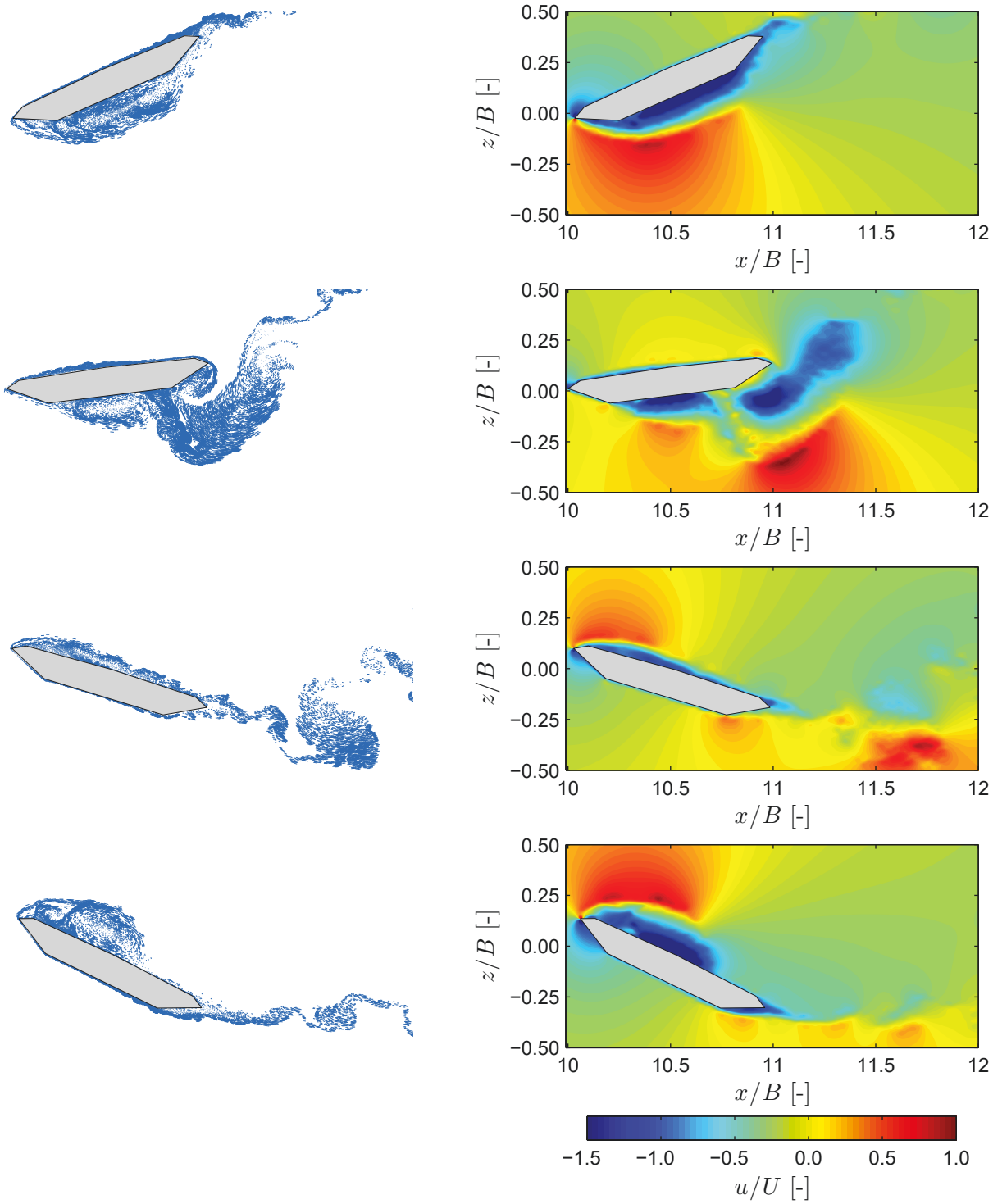

Figure 6.52: Great Belt Bridge: instantaneous particle maps (left) and longitudinal velocity fields (right) during limit cycle oscillation for the CFD model from 2D flutter analysis. The sequence represents half cycle from minimum (nose-down, top) to maximum (nose-up, bottom) rotation.

it is noted that amplitudes in the limit cycle oscillation range might lack numerical accuracy, as issues were noted in the vortex release algorithm for large rotations in the present work. This is attributed to the relatively coarse time-step. Nevertheless, the critical flutter limit for the CFD model corresponds well with the wind tunnel experiments and the LU and HNL models, which is of main interest in bridge aerodynamics.

6.3.9 Buffeting analysis: Pseudo-3D

The fundamental study of a flat plate and extensive analyses in the previous section prove the reliability of using the vortex method for 2D aeroelastic analyses. In what follows, a Pseudo-3D buffeting analysis is performed using the new turbulent Psuedo-3D method, presented in Sec. 3.6.4, and further verification is conducted with the LU model in a statistical manner. As noted in Tabs. 6.3 and 6.4, anisotropic free-stream turbulence ($TI_u = 11$ %; $TI_w = 6$ %) is used for the Pseudo-3D buffeting analysis for a bridge discretized on $N_{str} = 50$ strips. The properties of the free-stream turbulence in terms of achieved coherence and turbulence statistics are identical as in Sec. 5.3.1 since the numerical parameters are similar. Thus, very good correspondence was noted for the vertical turbulence intensity ($TI_w = 6$ %), while the longitudinal was underestimated resulting in $TI_u = 8$ %. It is noted that although isotropic turbulence could have been easily selected, the idea is to show that for conventional streamlined bridge decks, the underestimation of the longitudinal turbulence intensity does not play a significant role.

Before performing the aeroelastic analysis, the span-wise correlation of the buffeting forces is further verified for the Davenport coherence. Considering 5 static strips of the Great Belt section at a distance $\Delta y = 5$ m, the Welch magnitude-squared coherence of the lift and moment force of the first and third strip are given in Fig. 6.53. In the same figure, the magnitude squared-coherence is given for the wind fluctuations, previously obtained in Sec. 5.3.1 (cf. Fig. 5.23). Very good agreement can be observed for the buffeting forces w.r.t. the target Davenport coherence. Moreover, it can be seen that the vertical fluctuations govern the span-wise correlation, which makes the Davenport coherence function sufficient for this case-study. Generally, the modified coherence should be used (cf. Sec. 5.3.1), which was realized at a later point in this work.

Next, buffeting analysis is performed for both CFD and LU models. Selecting the mean wind speed at $U = 30$ m/s ensures that vortex shedding effects do not influence the response significantly while minimizing the potential nonlinear effects. As discussed, both of these phenomena are not captured by the LU model. The analyses are performed for time amounting to $t = 700$ s with approximately 41 thousand time-steps. The fluid domain for each strip is discretized by

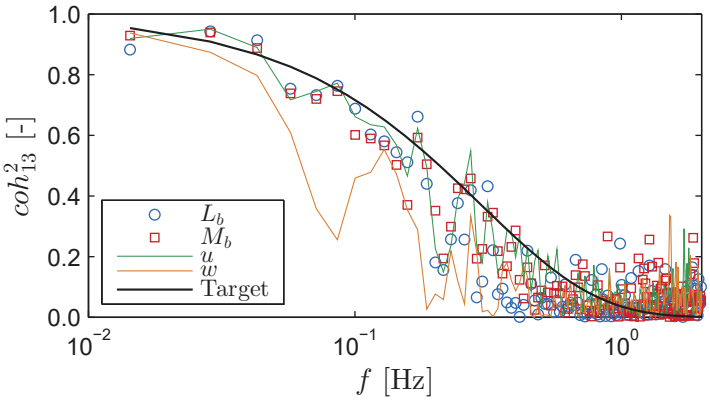

Figure 6.53: Great Belt Bridge: span-wise coherence of the forces and wind fluctuations between the first and the third strip for a static deck and $N_{str} = 5$ number of strips with and distance of $\Delta y = 5$ from a CFD Pseudo-3D buffeting analysis. The results for the wind fluctuations are taken from Sec. 5.3.1 (cf. Fig. 5.23) for a simulation without a body in the CFD domain, as the numerical parameters are identical.

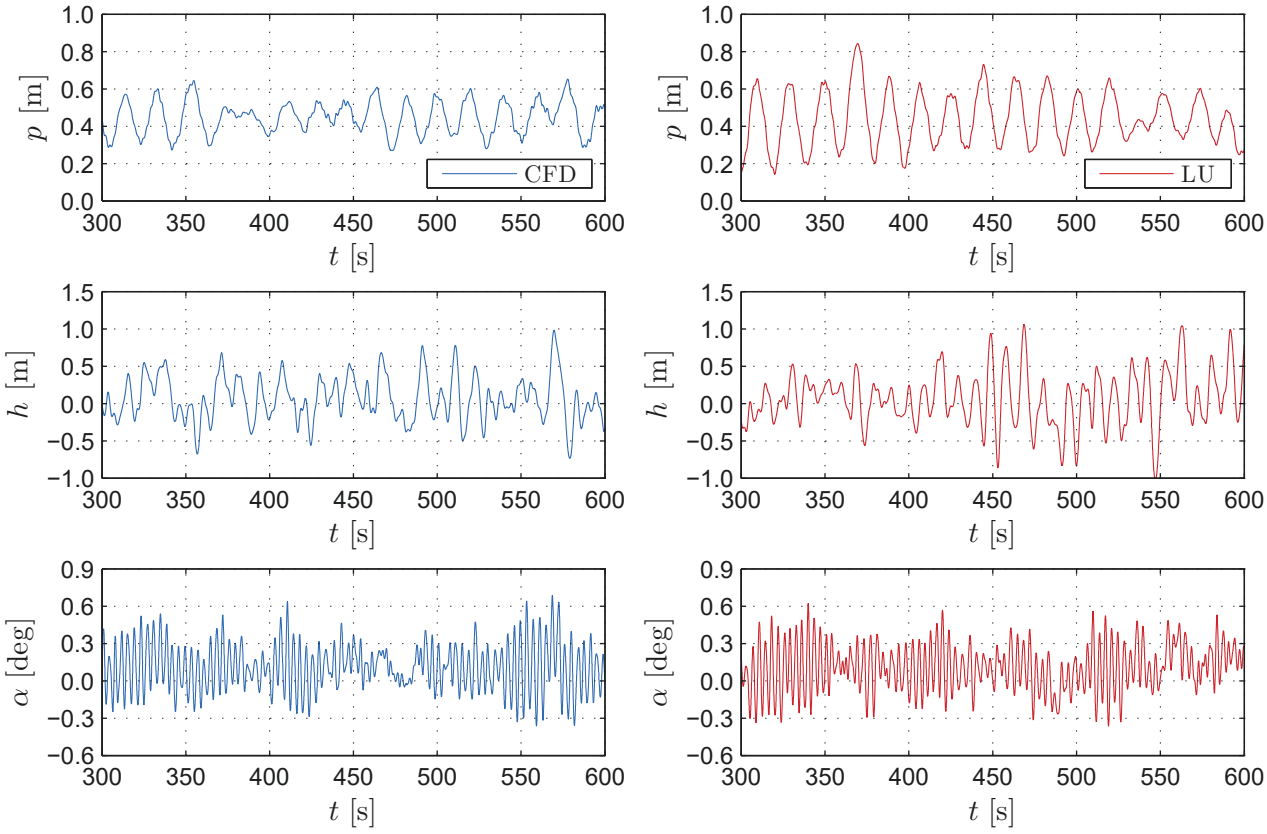

Figure 6.54: Great Belt Bridge: representative sample time-histories of the lateral (top), vertical (center) and rotation (bottom) displacements at midspan ($y/l_{span} = 0.5$) for the CFD (left) and LU (right) model from Pseudo-3D buffeting analysis.

approximately N_p= 175 thousand particles, resulting in a total of N_p=8.75 million particles for all strips. A parallel multi-core CPU architecture is utilized and each strip is run on a single core. The runtime was approximately 100 h, excluding the time required for the generation of inflow particles. A representative sample of the response time-histories for the CFD and LU model are shown in Fig. 6.54. Figure 6.55 depicts instantaneous particle maps for all 50 strips in the initial steps of the analysis, i.e. before the particles reach the section, to achieve sufficient visibility.

Two cases are considered for the free-stream turbulence in the LU model: case one (C1), considering the loss of turbulent energy of the longitudinal fluctuations of the CFD model, i.e. TI_u=8 % and TI_w=6 %, and case two (C2), where the turbulence intensity is taken as the prescribed quantities, i.e. TI_u=11 % and TI_w=6 %. With this, a comparable basis is maintained between the CFD and LU model for C1, whereas the influence of the loss of lateral turbulent energy on the response can be evaluated by studying C1 and C2 for the LU model. For each of the two cases for the LU model, 20 analyses are conducted with randomly generated wind fluctuations in order to facilitate a statistical significance of the results. As per common practice for time-domain buffeting analysis with randomly generated wind fluctuations, the 99 % confidence interval of the results is considered for the comparison [61].

Figure 6.56 depicts the RMS of the response, where the curve for the LU model in both cases is an average from the 20 analyses, while the shaded area corresponds to the 99 % confidence interval of the response for the LU model for C1. The lateral displacement is overestimated from the CFD analysis by 4.4 % compared to the mean value of the response for the LU model

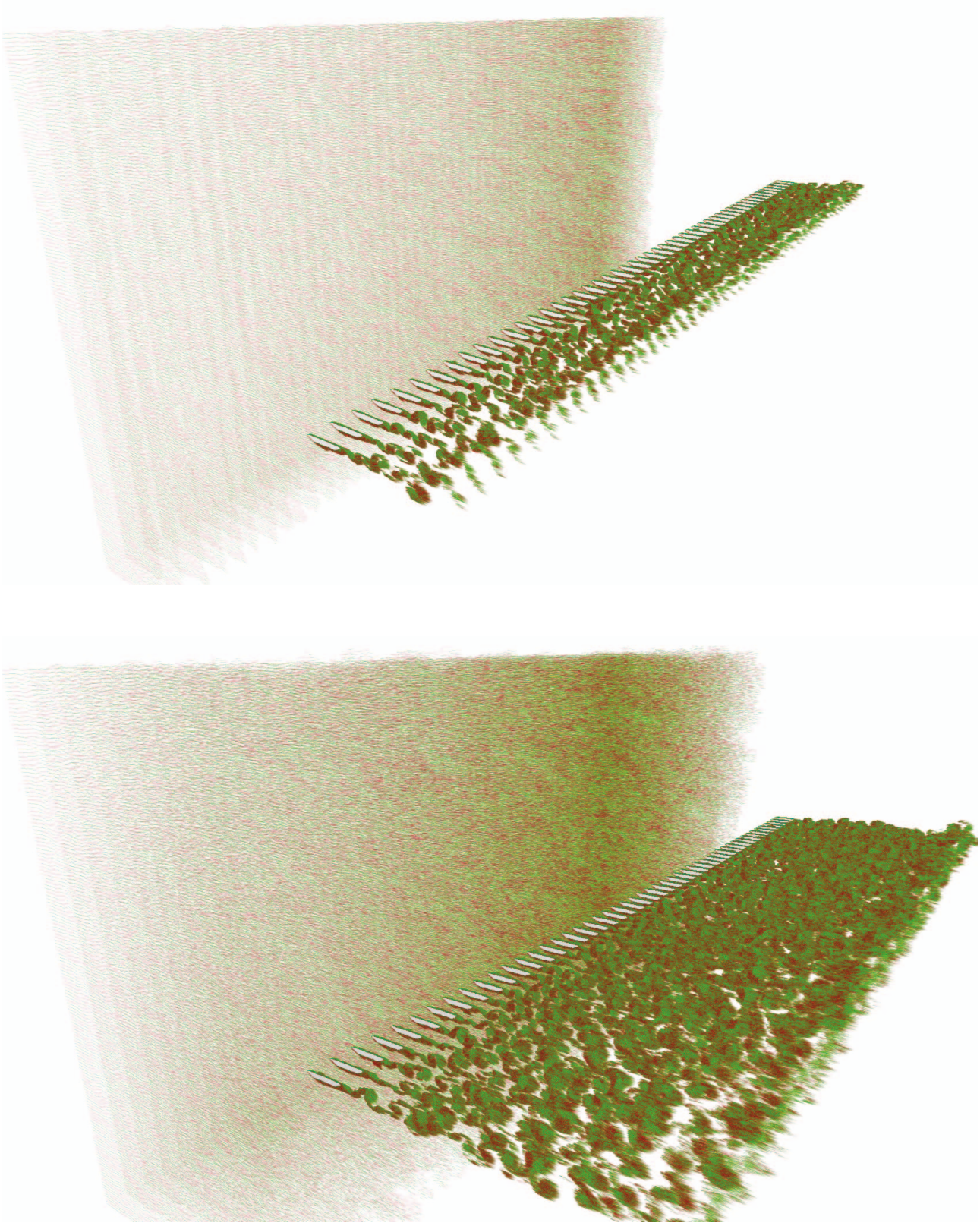

Figure 6.55: Great Belt Bridge: instantaneous particle maps at the initial steps from Pseudo-3D buffeting analysis. The particle maps are shown before the bridge is immersed into the inflow particles for visibility.

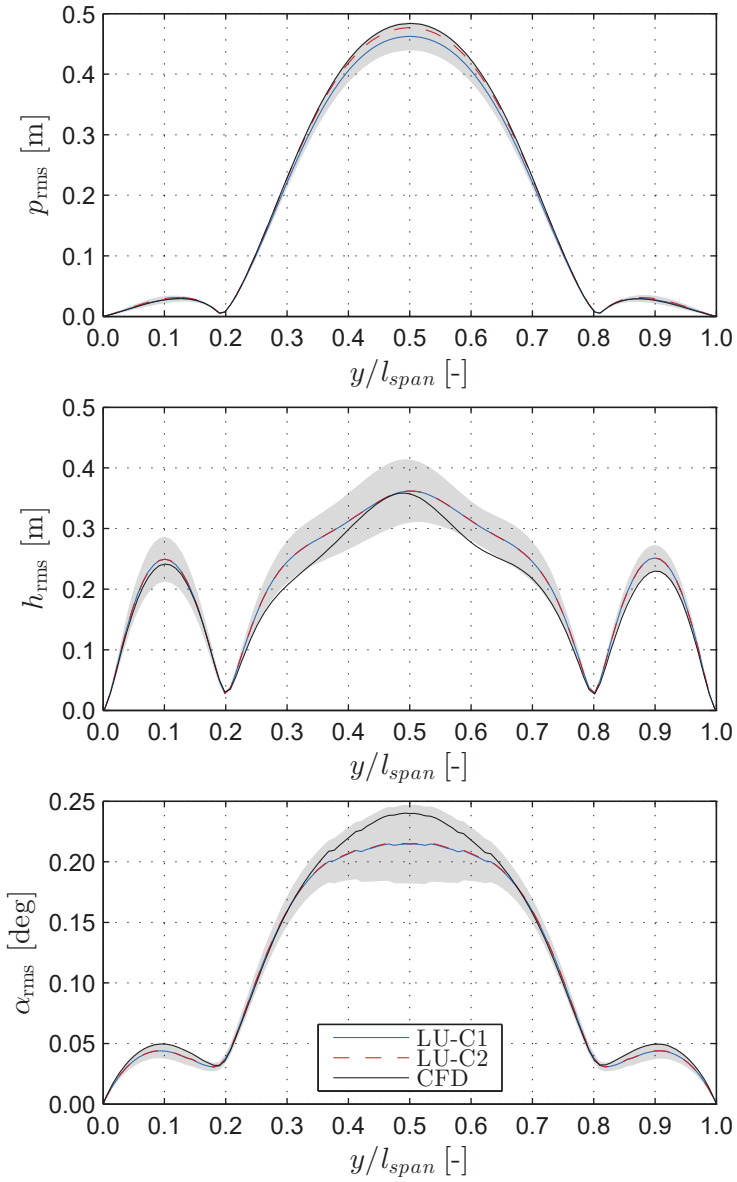

Figure 6.56: Great Belt Bridge: RMS of the span-wise lateral (top), vertical (center) and rotational (bottom) displacements for the LU and CFD models from Pseudo-3D buffeting analysis. The lines representing the response for the LU model in case C1 (TI = 8 %, TI = 6 %) and C2 (TI = 11 %, TI = 6 %) are obtained as an average from 20 generated random wind time-histories with U = 30 m/s. The shaded area defines the 99 % confidence interval of the displacements for the LU model for C1.

for C1, which can be attributed to the quasi-steady values used for the lateral aerodynamic damping and the slower decay from the initial impulse in the CFD model. The RMS of the vertical displacement at the span of the CFD model is in good agreement with the mean value of the LU for C1 with a discrepancy of 2 %. The difference in the mean value of the RMS of the torsion for the LU model for C1 is 10 % w.r.t. the CFD model.

Figure 6.57 (left) depicts the PSDs of the response at mid-span (y/l_{span}=0.5), where the gray shaded area corresponds to the envelope for the LU model for C1. Additionally, the same figure (cf. Fig. 6.57, right) depicts the modal contributions of the first three modes for each component of the response. Judging from the relative modal contribution, there is a good

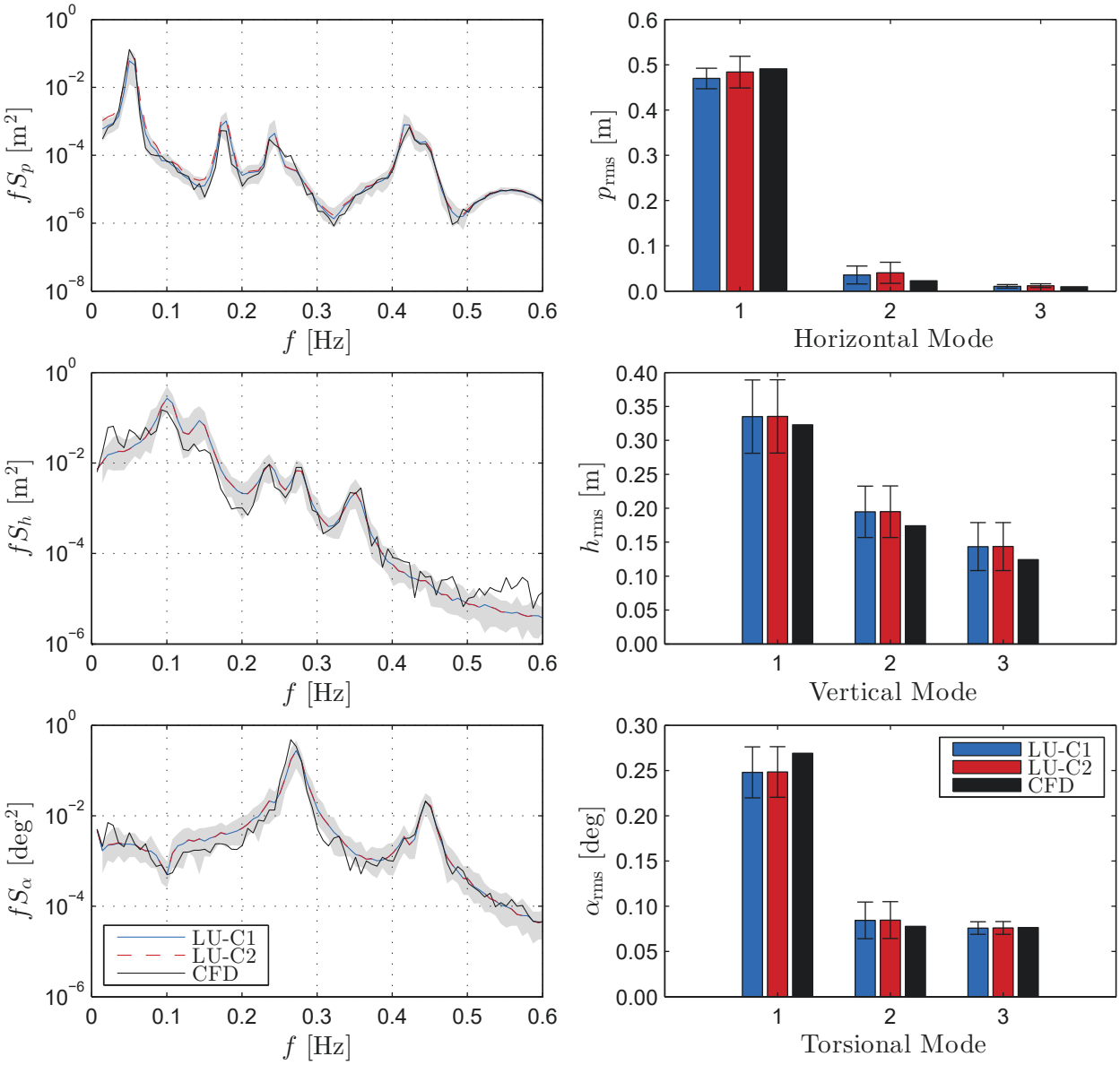

Figure 6.57: Great Belt Bridge: PSD (left) of the response at midspan ($y/l_{span} = 0.5$) and modal contribution (right) the first 3 modes in horizontal (top), vertical (center) and torsional (bottom) directions for the LU and CFD models from Pseudo-3D buffeting analysis. The lines and bars represent the response for the LU model in case C1 ($TI = 8$ %, $TI = 6$ %) and C2 ($TI = 11$ %, $TI = 6$ %), are obtained as an average from 20 generated random wind time-histories with $U = 30$ m/s. The shaded area (left) defines the envelope, while the error bars (right) the 99 % confidence interval for the displacements of LU model for C1.

correspondence between the CFD and LU model for C1. The frequency content of the vertical and rotational displacements shows that the CFD model results in a slightly increased value in the part of the response due to background turbulence. This is the probable reason why the shape of the RMS vertical response of the CFD model is slightly distorted and unsymmetrical compared to the LU model (cf. Fig. 6.56). Nevertheless, it is noted that the response for the CFD model is within the confidence interval of the RMS and envelope of the PSD of the response for the LU model, from which it can be concluded that a good agreement is obtained for the vertical and rotational displacements. The loss of lateral turbulent energy affected only

the lateral displacement, where C1 underestimated the response compared to the C2 by 3.1 %. Therefore, for bridge decks with low drag coefficient at the angle of static equilibrium compared to the lift slope, which is commonly the case for most of the streamlined sections, the loss of lateral turbulent energy can be negligible for the vertical and torsional displacements.

6.3.10 Flutter analysis: Pseudo-3D

A multimode flutter analysis is conducted as a final step of the aeroelastic analyses for the Great Belt Bridge. The critical flutter velocity U_{cr} is determined using the laminar Pseudo-3D VPM and the LU model in the time domain. Figure 6.58 depicts the time-histories of the vertical and torsional displacements for the LU and the CFD model, for velocities below and at critical flutter velocity. Furthermore, the displacements for a divergent velocity for the LU model are given. The static displacements due to the mean wind velocity for the LU model are omitted in the time-histories in order to distinctively show the difference between the damped, critical and divergent oscillations. Limit cycle oscillations are evident in the post-flutter range (approx. $t > 300$ s) for the CFD model, in a similar fashion as for the 2D analysis with slightly lower amplitudes.

Figure 6.59 shows the instantaneous particle maps of the bridge deck during limit cycle oscillation from peak negative (nose-down) to peak of the positive rotation (nose-up). The con-

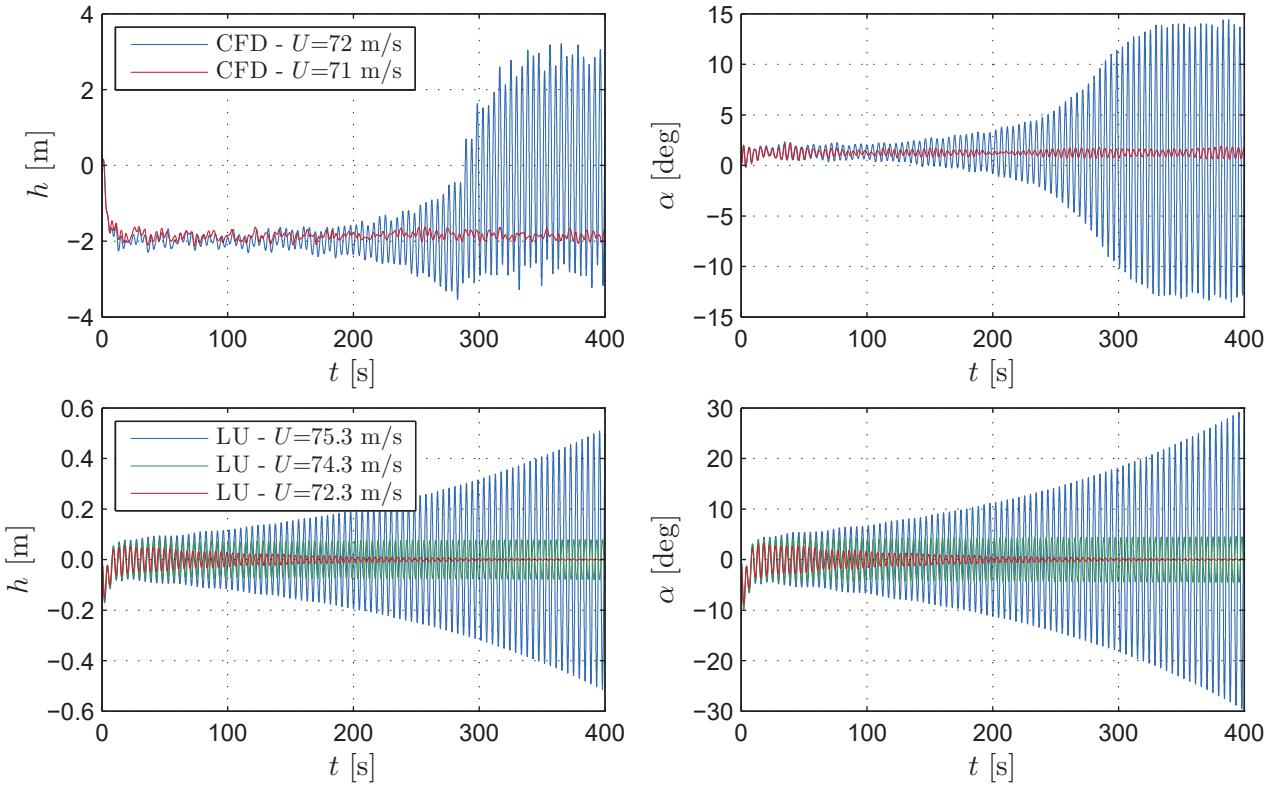

Figure 6.58: Great Belt Bridge: time-histories of the vertical displacement (left) and rotation (right) near the critical velocity for the CFD (top) and LU (bottom) models from Pseudo-3D flutter analysis. The following cases of response are depicted: CFD model - damped ($U = 71.0$ m/s), limit cycle oscillation ($U_{cr} = 72$ m/s); LU model - damped ($U = 72.3$ m/s), critical ($U_{cr} = 74.3$ m/s), divergent ($U = 75.3$ m/s). In case of the LU model, the mean is subtracted from the response and aerodynamics (indicial functions and flutter derivatives) are used for static angle of attack of $\alpha_s = 2$ deg.

tribution of the first vertical and torsional modes is clear during the limit cycle oscillations; however, vibrations of higher modes can be seen as well. Since the self-excited forces are usually considered as fully correlated in the span-wise direction, the utility of the Pseudo-3D VPM for the determination of the instability threshold in multimode flutter analysis is prominent.

Similarly, as for the 2D analysis, the critical flutter velocity U_{cr} appeared to be sensitive to the positive angles of incidence. In 2D, this was manifested by comparing the LU and HNL models. Therein for the HNL model, the instability threshold was determined directly from the flutter analysis using interpolated rational coefficients for the indical functions at the angle of static equilibrium. Herein, the critical flutter limit at the angle of static equilibrium for the LU model (U_{cr}-LU for $\alpha = \alpha_s$) is computed by linearly interpolating of the critical velocity, obtained for flutter derivatives at various angles of attack. As the flutter derivatives were additionally obtained determined an increment of 1 degree (not shown), the deviations are expected to be small for the simple approach of interpolation of U_{cr} using the LU model herein.

Figure 6.60 shows the critical flutter velocity for the CFD and LU models. The CFD model resulted in lower instability limit w.r.t. the LU model at the angle of static equilibrium α_s, with a difference of 5.5 %. The angle at static equilibrium for the CFD model is obtained by averaging the rotations at a velocity that is 1 m/s less than the critical one. Since critical flutter velocity for the CFD model lies on the α_s-LU curve, it can be further concluded that the nonlinear aerostatic analysis of the LU model yielded good correspondence with the CFD model.

Compared to the 2D case, performing a multimode flutter analysis resulted in higher flutter velocity for the LU model. This means that there is a contribution of the higher modes, yielding higher instability threshold ($U_{cr} = 73.8$ m/s in 2D at $\alpha = \alpha_s$ for HNL model, that is equivalent to LU for this case with $U_{cr} = 76.2$ m/s for Pseudo-3D at $\alpha = \alpha_s$). Interestingly, this is not the case for the CFD model as the critical velocity in 2D is identical as in Pseudo-3D. Due to the unsymmetrical shape of the deck, the Great Belt experiences a relatively large static angle of attack compared to other symmetrical streamlined sections. This, and the fact that the flutter regime changes to stall flutter at high angles of attack are the plausible reasons why there is no increment of the flutter velocity for the 3D case. Such observation means that the unsteady aerodynamic nonlinearity can govern the flutter velocity and suppress the contribution of the higher modes. In the case of the symmetrical deck of the Little Belt Bridge, Abbas [2] found that the critical flutter limit is increased by performing a multimode CFD Pseudo-3D analysis.

Larsen [188] reported an instability threshold amounting to $U_{cr} \approx 72$ m/s from free-vibration experimental tests for a taut strip model, which is similar to the results from the Pseudo-3D analysis. For free-vibration tests, the angle of attack is automatically corresponding to the angle of static equilibrium. Hence, the good overall correspondence between the CFD and experimental results further proves the reliability of the laminar Pseudo-3D VPM. Even in experiments, the critical velocity taut-strip model (3D) is in the critical range ($U_{cr} = 70 - 74$ m/s) for the sectional model (2D). This further confirms the findings of this study for the Pseudo-3D VPM.

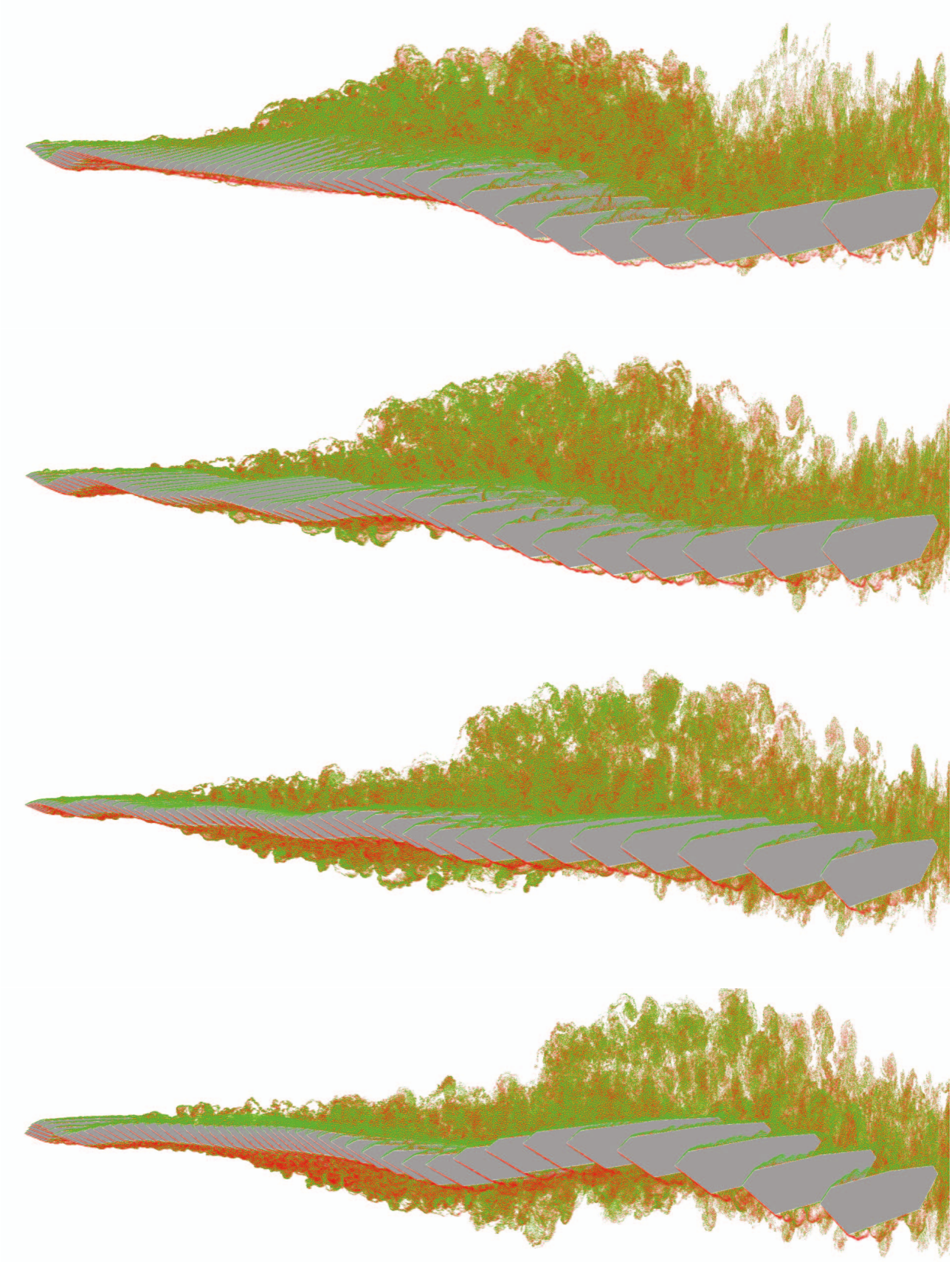

Figure 6.59: Great Belt Bridge: instantaneous particle maps during limit cycle oscillation for the CFD model from Pseudo-3D flutter analysis. The sequence represents half cycle from minimum (nose-down, top) to maximum (nose-up, bottom) rotation.

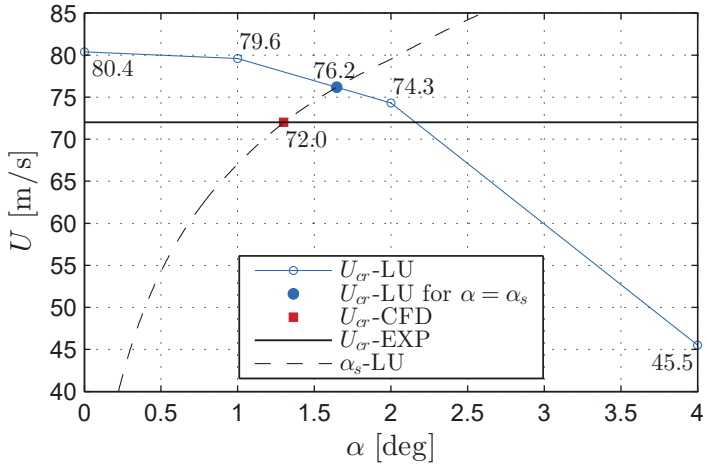

Figure 6.60: Great Belt Bridge: critical flutter velocity U_{cr} for the LU and CFD models from Pseudo-3D flutter analysis. The experimental results (EXP) are for the taut strip model reported by Larsen [188]. In the case of the LU model, U_{cr} is determined for a positive angle of incidence and the corresponding value is computed using linear interpolation at the intersection with the angle at static equilibrium α_s (U_{cr}-LU for $\alpha = \alpha_s$).

6.4 Third Bosphorus Bridge

The new Third Bosphorus Bridge, officially named Yavuz Sultan Selim Bridge, stands as a link between Europe and Asia (cf. Fig. 6.61). With a main span of 1408 m and a total length of 2164 m, it connects the two villages of Garipçe, on the European side, and Poyrazköy, on the Asian side, both located near Istanbul, Turkey. An unconventional hybrid between a cable-stayed and suspension bridge was selected for the structural system by the Swiss engineer Jean-François Klein and the French engineer Michel Virlogeux, to assure the required high rigidity for the in-service condition [335]. Standing as such, the Third Bosphorous Bridge is certainly one of the most innovative civil structures of the decade.

From a wind engineering aspect, the deck is aerodynamically shaped with a high width-to-depth aspect ratio. With a width of 58.4 m, the deck accommodates four road, two railway and two pedestrian lanes (cf. Fig. 6.62, (c) for a schematic illustration of the shape). The high aspect ratio and cutting-edge aerodynamic shape were the two of several reasons why this deck was selected to be the experimental benchmark for code verification as a part of the IABSE Task Group 3.1, "Super Long Span Bridge Aerodynamics". Thus, extensive experimental tests were conducted at the boundary layer wind tunnel at Politecnico di Milano by the wind engineering group. These tests included determination of static wind coefficients, flutter derivatives, aerodynamic admittance and buffeting response under deterministic gusts.

This section presents a validation of the novel method for the determination of complex aerodynamic admittance, presented in Sec. 3.7.4. The experimental results are taken from the tests conducted as a part of the aforementioned IABSE task group. During his research stay at Politecnico di Milano, the author was present for the model building and instrumentation had extensive discussions with the wind engineering group. The data from the tests and post-processing codes were supplied by the Politecnico di Milano wind engineering group [12], and were further advanced and elaborated by the author.

The section starts with a description of the experimental setup, followed by validation of the static wind coefficients and aerodynamic admittance for vertical sinusoidal gusts. Moreover, the aerodynamic admittance for longitudinal gusts is obtained from CFD simulations.

Figure 6.61: Third Bosphorous Bridge: a panoramic impression (picture courtesy of Rolf Cosar (Rolfcosar), from commons.wikimedia.org).

6.4.1 Experimental setup

As a part of the experimental tests, aerodynamic forces were measured for laminar free-stream and deterministic gusts using an active turbulence generator, for the experimental setup depicted in Fig. 6.62. The sectional model was made of carbon fiber with a geometrical scale of 1:50 and is equipped with four rings of pressure taps connected to high-frequency pressure scanner (cf. Fig. 6.63, a and d). Each ring consists of 62 pressure taps and is positioned at different locations along the length of the model, denoted as $R1 - R4$ in Fig. 6.62 (b). Having such a configuration enables one to measure the pressure correlation in the lateral direction. Compared to the real deck on-site, the experimental model does not include windshields; nevertheless, fences were considered (cf. Fig. 6.63, d). Due to high porosity, the aerodynamic forces are obtained by integration of the pressure taps positioned on the deck only, i.e. the effect of the fences is assumed to be negligible; however, they might influence the local aerodynamics.

An active turbulence generator consisting of ten NACA 0012 airfoils with a chord of 20 cm was utilized to generate vertical sinusoidal gusts (cf. Fig. 6.62, b). All airfoils are mechanically linked and forced to perform sinusoidal pitching motion by two brushless motors with user-defined frequency and amplitude. The active turbulence generator is 4 m long, i.e. 40 cm longer than the model, and it was positioned at a distance of $6B$ upstream of the section.

Four four-holes cobra probes were installed at distance B upstream of the leading edge for each pressure ring (cf. Fig. 6.62, c). With this, the instantaneous wind fluctuations were measured in both horizontal and vertical directions, which is required for the computation of the aerodynamic admittance.

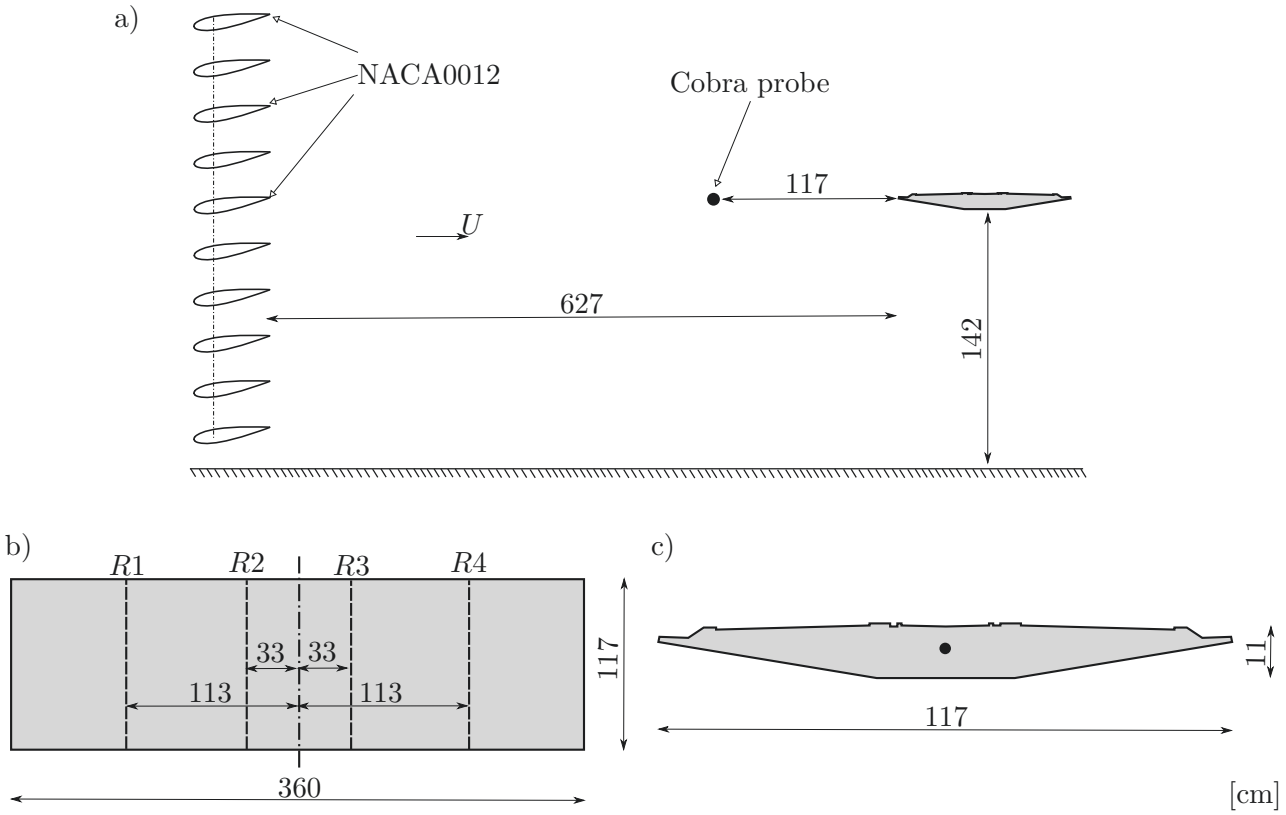

Figure 6.62: Third Bosphorous Bridge: experimental setup in a) elevation, b) plan including four pressure rings denoted as $R1 - R4$, and c) cross-section.

a)

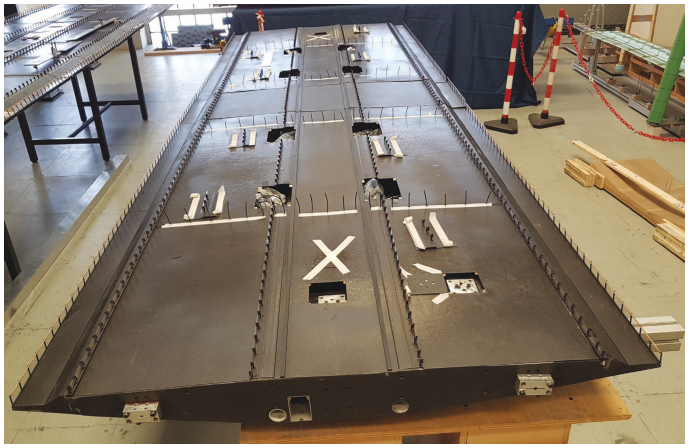

b)

c)

d)

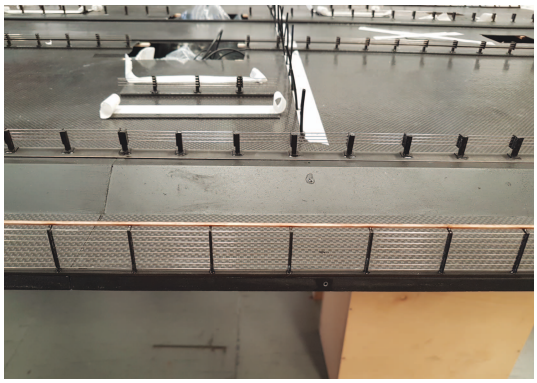

e)

Figure 6.63: Third Bosphorous Bridge: a) experimental model, b) active turbulence generator, c) experimental model with cobra probes, d) fences and pressure taps, e) aerodynamic admittance tests (pictures b), c) and e) are courtesy of T. Argentini, S. Omarini, and D. Rocchi.)

Low residual turbulence intensity was noted during the admittance tests with an intensity of TI_u=1.6 % in the horizontal and TI_w= 1.1 % in the vertical direction and corresponding length scales of L_u=0.124 m and L_w=0.025 m, respectively. These values are negligible w.r.t. the actively generated turbulent component. Thus, the experimental setup ensured, up to a certain degree, that the deck aerodynamics is two-dimensional for both laminar and deterministic turbulent free-stream, i.e. the strip assumption is valid.

6.4.2 Static wind coefficients

Before validating the aerodynamic admittance, the static wind coefficients obtained using CFD simulations are compared to the experimental results. The common physical parameters for the CFD simulations and experiments are given in Tab. 6.7. In the case of the CFD model, the numerical parameters are given in Tab. 6.8. The lift and moment coefficients are averaged for a minimum period amounting to τ=50 at each angular increment, for a deck positioned at $\boldsymbol{x_s}$=(6.5B, 0) in the CFD domain. An instantaneous velocity field and particle map of the section under laminar free-stream is depicted in Fig. 6.64.

Figure 6.65 depicts the static wind coefficients, obtained from the CFD simulations and experimental tests. As noted previously for the experimental tests, the static wind coefficients are obtained from the pressure taps positioned on the deck only, neglecting the fences and auxiliary equipment. The Reynolds number in the experimental tests amounts to Re=7.70×10^5. A slight overestimation is noted in the lift coefficient for positive angles; while there is an offset in the moment coefficient. The drag coefficient can be underestimated by the VPM, which has been also observed in other studies (cf. e.g. Larsen and Walther [193]). Although the aerodynamic forces from the experimental tests are obtained using the pressure taps only, the separation and reattachment point is still influenced by the auxiliary equipment. Taking this into account, the correspondence is considered to be fair.

Property type	Physical parameter		Value
Shape	Deck width:	B	1.17 m
	Deck depth:	H_D	0.11 m
Experimental	Wind speed:	U	6.5-11 m/s
	Reynolds number:	Re	4.9×10^5-1.16×10^6
	Vertical amplitude:	w_{c0}/U	1.1-7.4 %
	Longitudinal amplitude:	u_{c0}/U	/
	Airfoil distance:	l_R/B	1.5
	Reduced velocities:	V_r	$2-54$
CFD	Wind speed:	U	10 m/s
	Reynolds number:	Re	7.78×10^5
	Vertical amplitude:	w_{c0}/U	3.5 %
	Longitudinal amplitude:	u_{c0}/U	3.5 %
	Airfoil distance:	l_R/B	1.5
	Reduced velocities:	V_r	$2-54$

Table 6.7: Third Bosphorous Bridge: prescribed physical parameters for the experimental and CFD models under laminar and turbulent free-stream.

Numerical parameter		Value
Domain length:	l_d/B	17
Domain height:	l_h/B	8.5
Number of panels:	N_{pan}	750
Panel length:	$\Delta l_{pan}/B$	2.75×10^{-3}
Reduced time-step:	$\Delta\tau = \Delta t U/B$	2.75×10^{-3}
Core radius:	ϵ/B	3.3×10^{-3}
Poisson grid:	$N_x \times N_z$	1023×511
P^{3}M neighboring cells:	N_r	3
Vorticity support:	l_v/B	16.5
Particle release factor:	$\Delta p = \Delta t_{in}/\Delta t$	12-21

Table 6.8: Third Bosphorous Bridge: prescribed numerical parameters the CFD model.

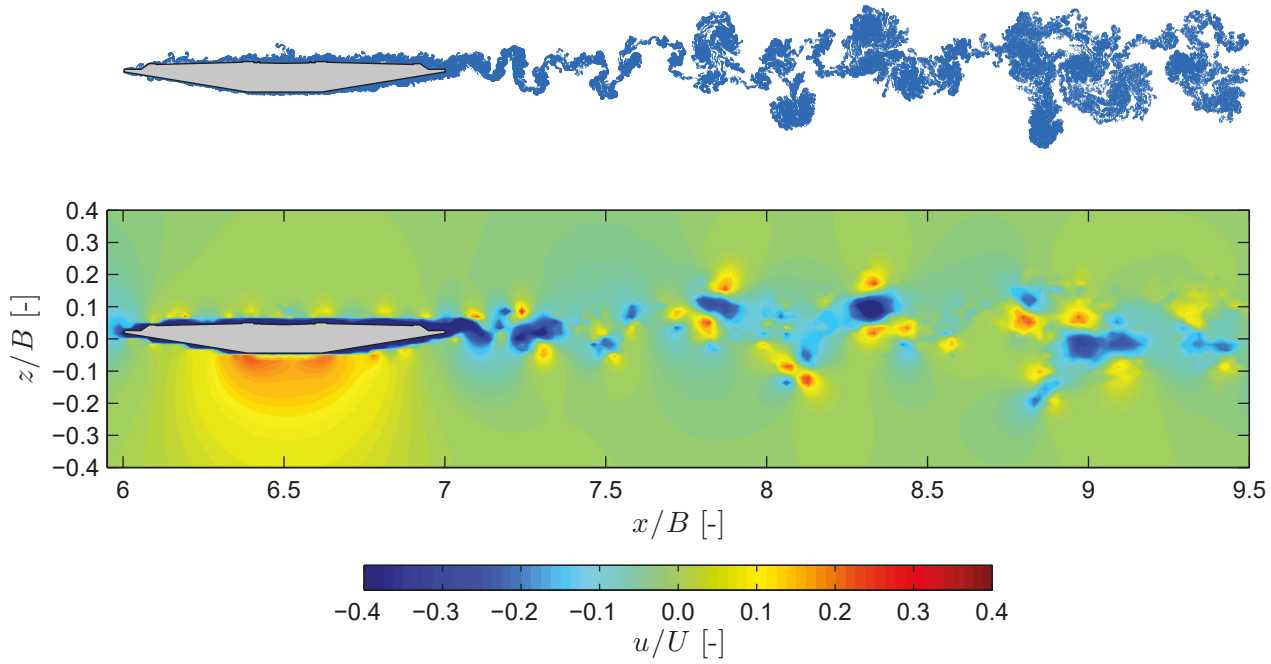

Figure 6.64: Third Bosphorous Bridge: instantaneous particle map (top) and velocity field (bottom) under laminar free-stream.

6.4.3 Aerodynamic admittance

Having validated the static wind coefficients, the aerodynamic admittance for vertical gusts is determined herein for both experimental and CFD models. The section is subjected to vertical sinusoidal gusts with prescribed amplitude (cf. Tab. 6.7). For experiments, it is difficult to obtain exactly the prescribed reduced velocities and gust amplitude. Hence, the Reynolds number and the gust amplitudes are given in a range. As an example, Fig. 6.66 depicts the time-histories and their corresponding FFTs of the longitudinal and vertical velocity components. Despite the high frequency and additional longitudinal components, a clear sinusoidal harmonic is observed at $V_{rt} = 9.52$. The gust quality (cf. (5.10)) for this particular experimental time-history amounts to $Q_w \approx 0.7$.

Figure 6.67 depicts instantaneous snapshots of particle maps from minimum to maximum peak

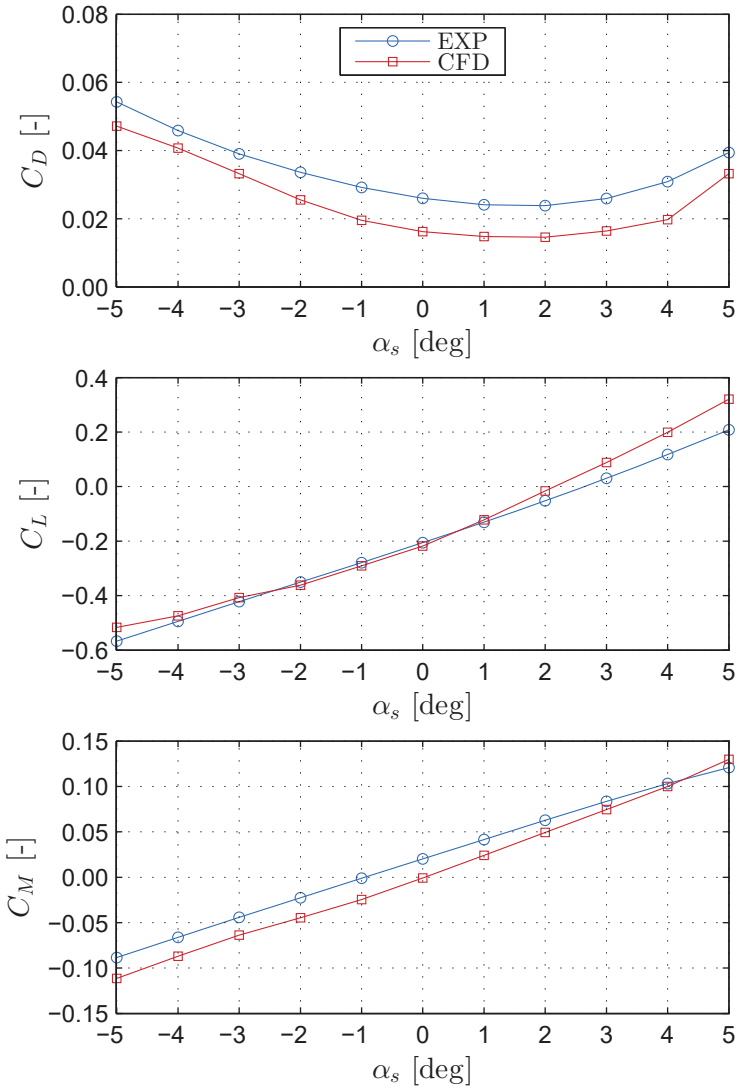

Figure 6.65: Third Bosphorous Bridge: drag C_D (top), lift C_L (center) and moment C_M (bottom) static wind coefficients for the CFD and experimental (EXP) model.

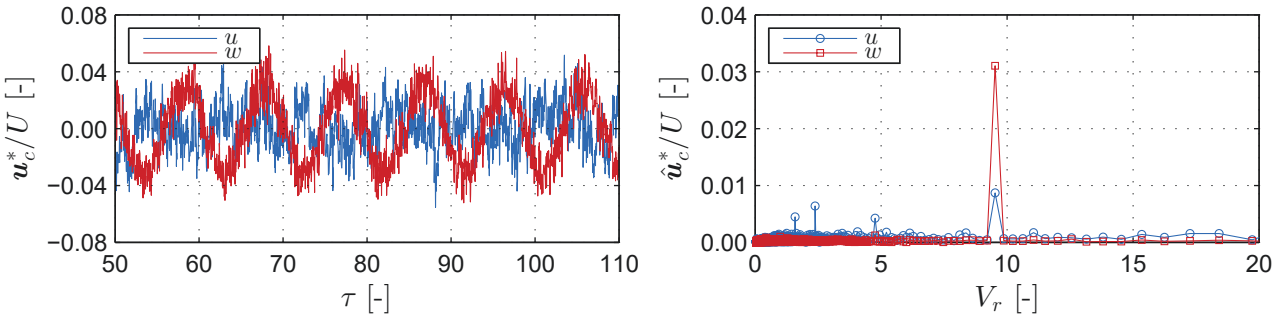

Figure 6.66: Third Bosphorous Bridge: sample wind velocity time-histories, u and w (left), and corresponding FFTs, $\hat{u}$ and $\hat{w}$ (right), recorded from the cobra probe corresponding to the pressure ring $R3$ at gust with reduced velocity $V_{rt} = 9.52$.

of a sinusoidal gust past the bridge deck at a reduced velocity of V_{rt}=10. It is evident that the particles do not cross the section. Figure 6.68 depicts the fluctuating wind coefficients due to buffeting forces, C_{Db}, C_{Lb} and C_{Mb} (i.e. the mean is subtracted), which are normalized

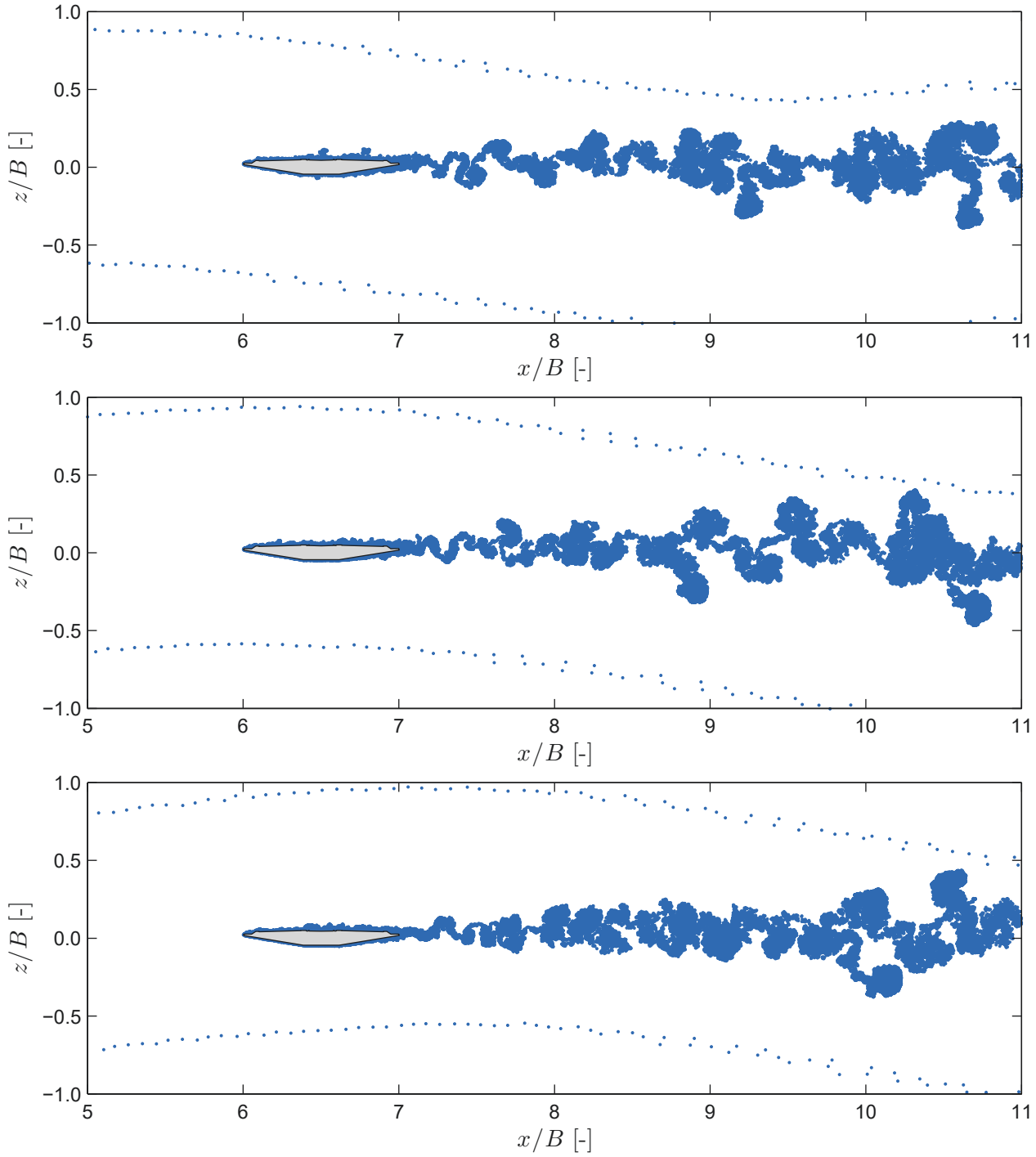

Figure 6.67: Third Bosphorous Bridge: instantaneous particle maps of the section under vertical sinusoidal gust with reduced velocity $V_{rt} = 10$.

w.r.t. the gust amplitude w_0/U. The reduced velocity, Reynolds number and gust amplitudes are approximately similar for this case for the CFD analyses and experiments. To obtain comparable results, the abscissa is normalized w.r.t. the gust reduced velocity for each model ($V_{rt} = 10$ for the CFD and $V_{rt} = 9.52$ for the experimental results). Very good correspondence can be observed, with a slight overestimation by the CFD model for the lift and moment. In the case of the drag, the amplitudes at the prescribed reduced velocities correspond well, while an additional low reduced velocity component can be observed from the experimental results. The

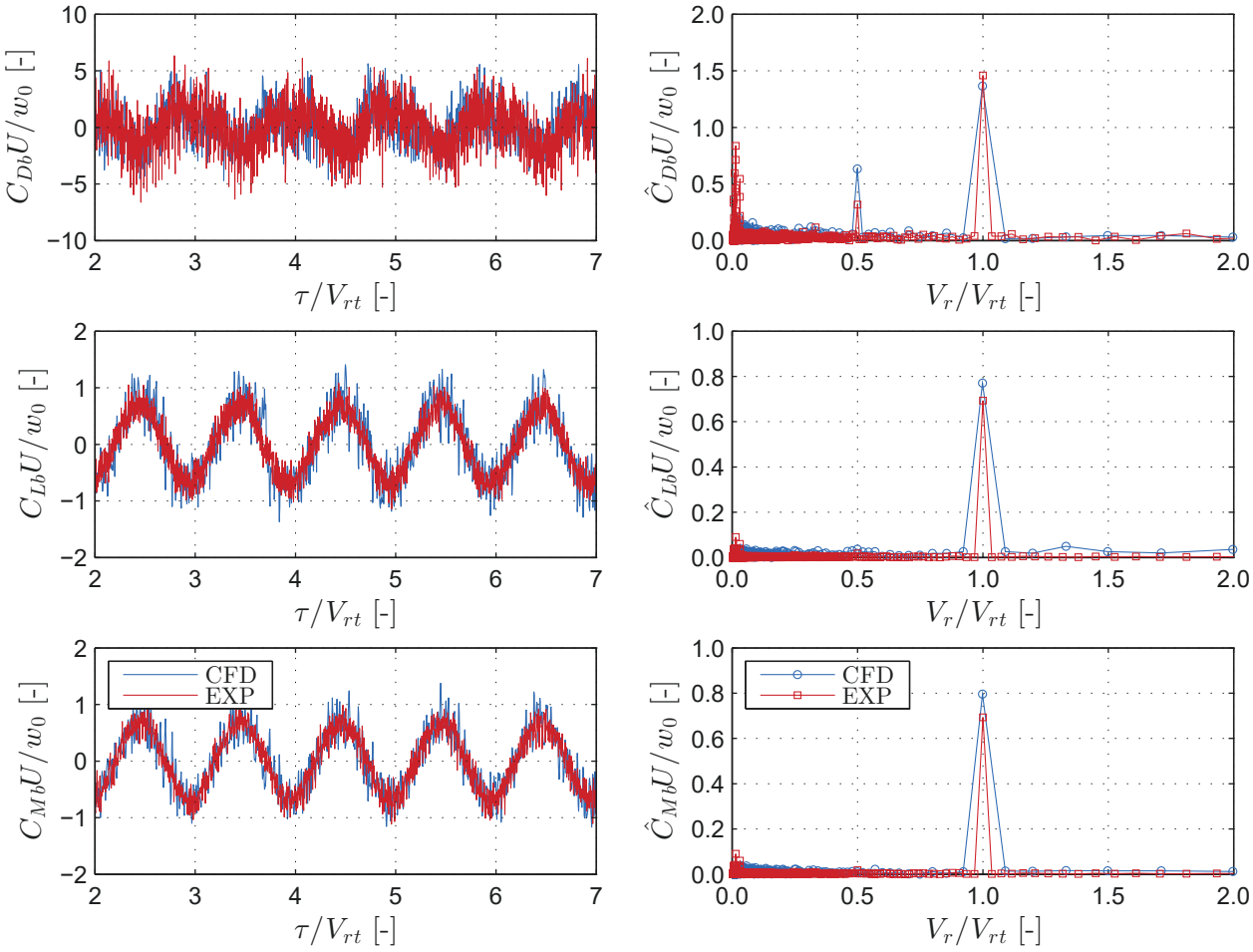

Figure 6.68: Third Bosphorous Bridge: sample normalized drag C_{Db} (top-left), lift C_{Lb} and moment C_{Mb} time-histories of the buffeting forces (no mean), and their corresponding FFTs (right), for a section under vertical sinusoidal gust for the CFD ($V_{rt} = 10$, Re $= 7.78 \times 10^5$, $w_{c0}/U = 3.5$ %) and experimental (EXP) model ($V_{rt} = 9.52$, Re $= 7.78 \times 10^5$, $w_{c0}/U = 3.1$ %). The abscissa is normalized w.r.t. the corresponding gust reduced velocity.

drag force at $V_r = 0.5V_{rt}$ is higher for the experimental results due to the higher contribution of the additional longitudinal velocity component.

In Fig. 6.69, the aerodynamic admittance for vertical gusts for the CFD and experimental models is depicted. The experimental results are for the inner pressure rings, R2 and R3 (cf. Fig. 6.62). These two rings are selected in order to alleviate the end effects of the flow on the model. The aerodynamic admittance for the CFD model is computed for two setups. In the first setup (S1), the sinusoidal gust is tracked down at B upwind of the leading edge (i.e. $\boldsymbol{x}_c = (5B, 0)$), in a similar fashion as for the experimental results. The aerodynamic admittance for the second setup (S2) is computed with a sinusoidal gust tracked at the position of the stiffness center (i.e. $\boldsymbol{x}_c \equiv \boldsymbol{x}_s = (6.5B, 0)$), from a simulation without a section in the CFD domain as previously discussed in Sec. 3.7.4 from Ch. 3. In order to obtain comparable results with the experiments for the imaginary value of the aerodynamic admittance, the sinusoidal gust is shifted for $\tau_{\text{shift}} = 1.5$ for S2. It is noted that this does not influence the absolute value of the aerodynamic admittance. As it can be observed from the figure, the CFD results for the lift and moment correspond well with the experimental results for both real and imaginary components. In the case of the drag aerodynamic admittance, the correspondence of the CFD

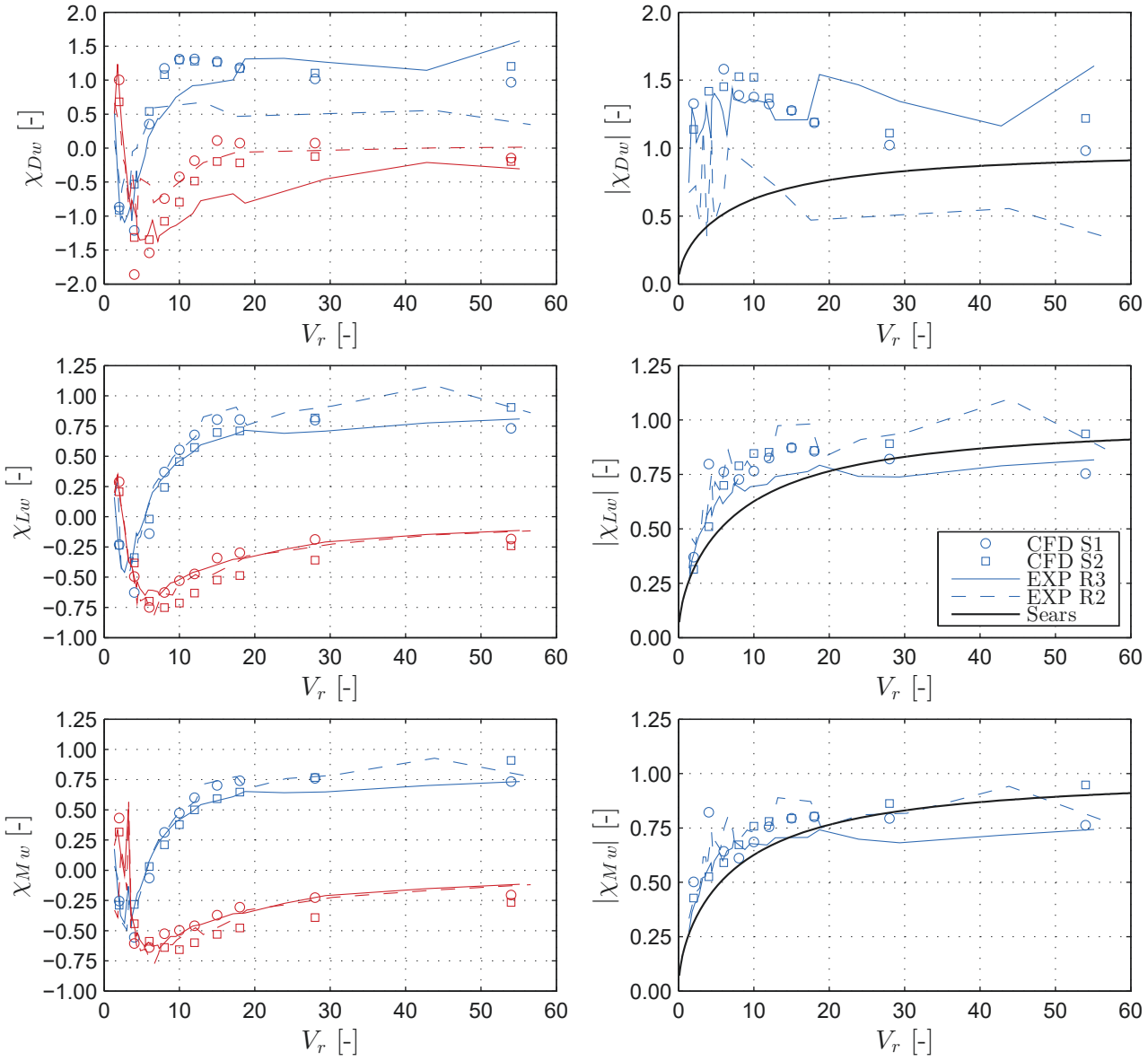

Figure 6.69: Third Bosphorous Bridge: aerodynamic admittance of the drag χ_{Dw} (top), lift χ_{Lw} (center), and moment χ_{Mw} (bottom) forces for a section under vertical sinusoidal gusts for the CFD and experimental (EXP) model. The complex description (left) is given for the real (blue) and imaginary (red) values, while the absolute admittance (right) is further compared to Sears function.

results is better for R3, while some discrepancies are observed for R2. Obtaining the drag admittance implies division of the drag force with the difference $C_D' - C_L$ (cf. (3.209)), which value is very low. As seen from the static wind coefficients (cf. Fig. 6.65), the drag is highly nonlinear in the region of $\alpha_s \approx 0$ and the value of drag derivative C_D' is very small. The low-frequency components in the experimental results govern the drag force at particular reduced velocities as well, which means that the sensitivity of the drag due to vertical gusts is indeed very low. This explains partially the discrepancies for the drag admittance component. It is worthy to notice that, the drag aerodynamic admittance exceeds unity in both models.

Two reasons seem plausible for the difference between S1 and S2 for the CFD model. First, the distortion of the incoming gust due to the influence of the section, and second, the variation of the gust amplitude in the along-wind direction. As discussed previously, the linear unsteady

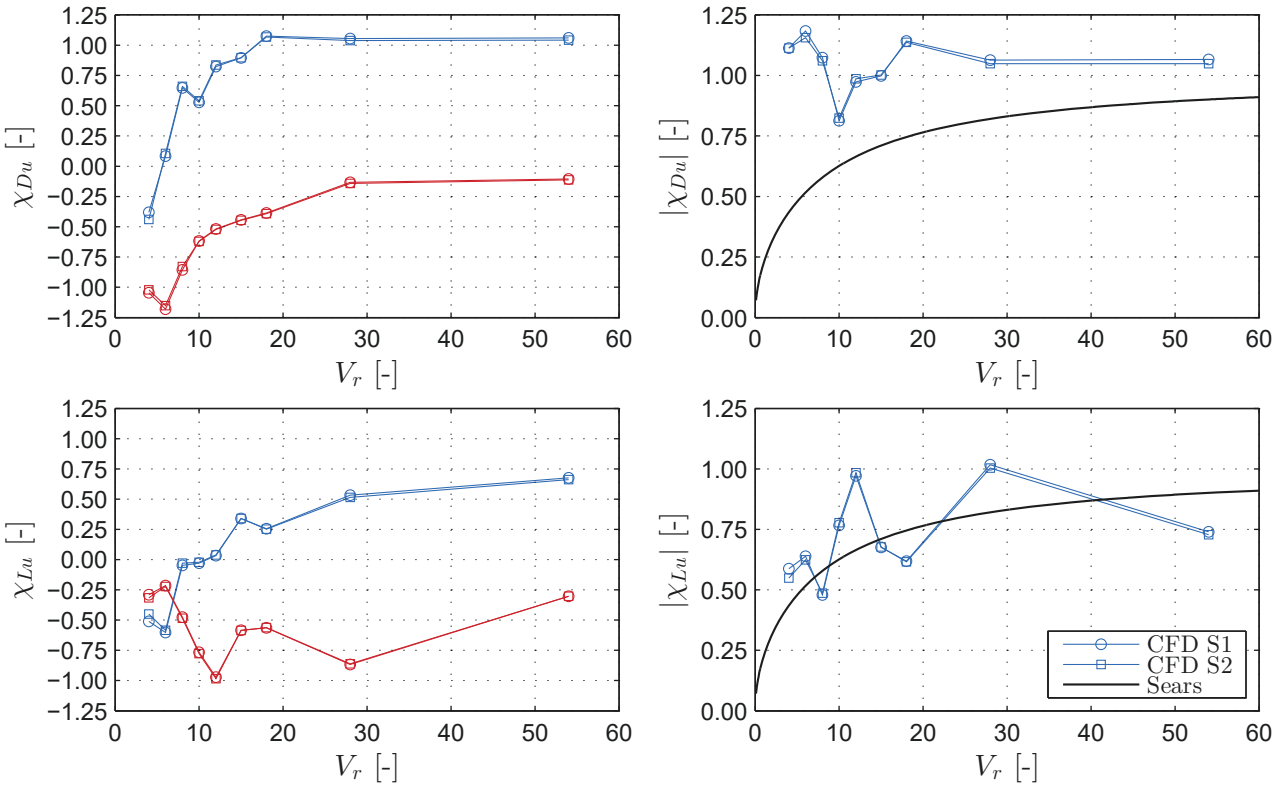

Figure 6.70: Third Bosphorous Bridge: aerodynamic admittance of the drag χ_{Du} (top) and lift χ_{Lu} (bottom) forces for a section under longitudinal sinusoidal gusts for the CFD model. The complex description (left) is given for the real (blue) and imaginary (red) values, while the absolute admittance (right) is further compared to Sears function.

aerodynamic model does not take the effect of the section on the gust amplitudes into account. It is noteworthy to mention that for S1, the absolute value of the aerodynamic admittance tends faster towards unity than in the S2 case.

Furthermore, the aerodynamic admittance due to longitudinal gusts is determined only for the CFD model. All of the airfoils used in the experimental tests are mechanically connected and oscillate in-phase. Hence, a pure longitudinal gust cannot be generated. Figure 6.71 depicts the aerodynamic admittance for the drag and moment forces. Although some alteration can be observed, the absolute value of the drag admittance is mostly unitary. The lift admittance is somewhat irregular w.r.t. Sears function. The imaginary values for the drag and lift admittances are always negative, meaning that the forces lag behind the longitudinal gust for this particular point of tracking of the wind. This was not the case for the vertical gusts (cf. Fig. 6.69). No significant difference between the two setups, S1 and S2, is observed.

The moment admittance due to longitudinal gusts is not obtained for this particular case. The reason for this is that the moment forces resulted in rather low values, which for most of the reduced velocity range are even lower than the vortex-shedding forces. This can be observed in the FFTs of the fluctuating coefficients in Fig. 6.71. Furthermore, the value of the moment coefficient C_M at $\alpha_s = 0$ is very close to zero (cf. Fig. 6.65); hence, the results are prone to high numerical uncertainties in the averaging procedure for the static wind coefficients. Therefore, the moment admittance resulted in very high values due to the small values in the denominator in (3.208) for moment aerodynamic admittance due to longitudinal gusts χ_{Mu}. In a general case for a deck with $C_M \not\approx 0$, obtaining χ_{Mu} is straightforward using the presented method.

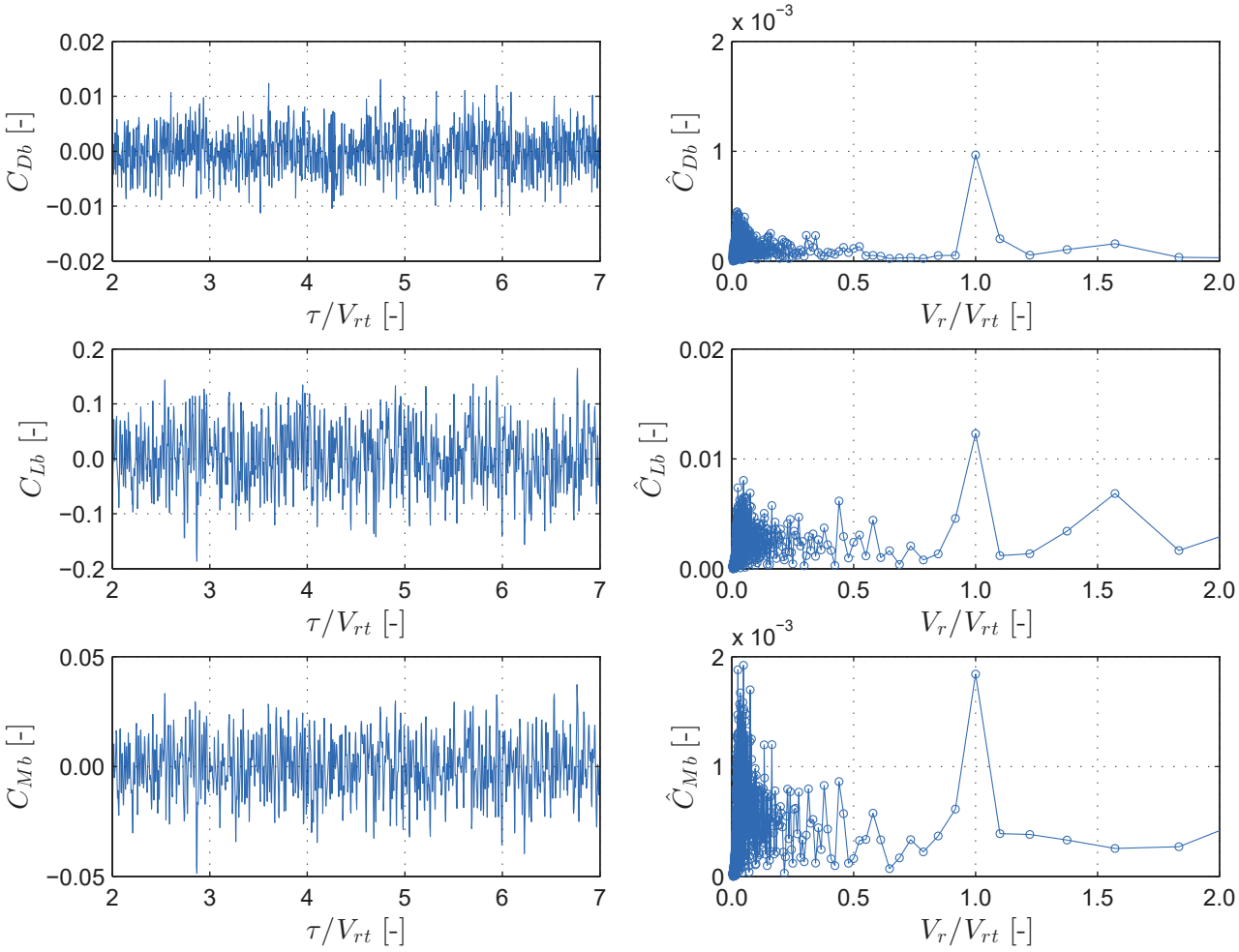

Figure 6.71: Third Bosphorous Bridge: sample normalized drag C_{Db} (top-left), lift C_{Lb} and moment C_{Mb} time-histories of the buffeting forces (no mean), and their corresponding FFTs (right), for a section under vertical sinusoidal gust for the CFD model ($V_{rt} = 10$, Re $= 7.78 \times 10^5$, $u_{c0}/U = 3.5$ %). The abscissa is normalized w.r.t. the corresponding gust reduced velocity.

6.5 Summary

Applications of the whole or parts of the presented synergistic framework were made in this chapter to practical problems from bridge aerodynamics and aeroelasticity. Three bridges were considered as reference objects, including the Mersey Gateway Bridge, Great Belt Bridge, and Third Bosporus Bridge.

The Mersey Gateway Bridge was used as an illustrative example to show how the categorical modeling approach can help to study the influence of specific assumptions on the response. This particular reference object was selected as not many studies focused on evaluating aerodynamic models for a cable-stayed bridge with a bluff cross-section in the erection stage. Aeroelastic analyses were performed for nine semi-analytical models and the effects of six assumptions were studied based on the RMS metric for complexity-related models using direct comparison. Based on the results from buffeting analysis, it was argued that considering the self-excited forces and fluid memory has the largest influence on such type of structures. On the other hand, the nonlinearity, steady or quasi-steady, did not have a significant contribution. Similar findings on the effects of the aerodynamic model assumptions were noted from the flutter analysis. In contrast to streamlined decks, it was found out that the effect of aerodynamic coupling on the critical velocity does not play a major role for bluff girders as the flutter is mostly torsional.

The Great Belt Bridge was selected as an application example to show how most of the presented methods fit together and how they can aid the aerodynamic and aeroelastic analyses. With exception of the CFD method for determination of the complex aerodynamic admittance, all presented methods were used in a synergistic manner to study the influence of the aerodynamic assumptions, perform and verify the results of 2D and Pseudo-3D aeroelastic analysis. Where possible, the aerodynamic coefficients were first validated with present and past experimental results. This was followed by 2D analyses using a CFD and six semi-analytical models. Applying the presented comparative methodology, the effects of aerodynamic assumptions on the self-excited forces, buffeting forces, aeroelastic response from one-to-one comparison and critical flutter limit were highlighted. This effectively showed which aerodynamic phenomena can or cannot be captured by the semi-analytical models compared to the CFD model. As the LU and HNL model yielded the best overall correspondence, the fluid memory was determined to be the most influential effect within the fluid-structure interaction. However, the discrepancies between these models increased for the rotation at high amplitudes, which was attributed to the nonlinearity of the self-excited forces. The nonlinearity was not appropriately considered by the nonlinear quasi-steady models. None of the semi-analytical models was able to replicate the effect of vortex shedding and local non-stationary effects included in the CFD model. Buffeting and flutter analyses were conducted using the Pseudo-3D VPM. The results corresponded well with the results for the LU model. As linear behavior is expected for the prescribed wind, it could be concluded that this method is readily available for practical applications.

Finally, the Third Bosphorous Bridge was utilized as a validation example for the presented CFD method for the determination of the complex aerodynamic admittance. Results from experiments, conducted in the boundary layer wind tunnel at Politecnico di Milano, were used as a basis for validation. Initially, the static wind coefficients were compared, followed by validation of the aerodynamic admittance due to vertical gusts for all aerodynamic forces, including drag lift and moment. Both real and imaginary parts of the CFD complex aerodynamic admittance corresponded well with their experimental counterparts. In addition, the aerodynamic admittance due to longitudinal gusts was determined, showing the versatility of the method to determine six complex aerodynamic admittances.

Chapter 7

Summary and Conclusions

7.1 Summary

The main aim of this work was to develop a comparative methodology for aerodynamic models. Three additional, by no means less important, methods were developed including a turbulent Pseudo-3D VPM for buffeting analysis, a CFD method for determination of the complex aerodynamic admittance and a simple FFT-based method for computation of the unsteady buffeting forces. Ultimately, all of the developed methodologies were presented as a synergistic framework with the notion to perform both model assessment and analyses in bridge aerodynamics and aeroelasticity.

To address the issue of model assessment in both qualitative and quantitative manner, a comparative methodology was established in two steps. In the first step, the complexity of a CFD and twelve semi-analytical models was evaluated on an abstract level based on their mathematical constructions using a categorical modeling approach. The result is a diagrammatic ordering of models which clearly shows which model is more complex, and thus, better. Further, the categorical modeling approach was extended in terms of model comparability and completeness to clearly delineate which models can be compared and which not.

In the second step of the comparative methodology, nine comparison metrics for time-histories were constructed on a uniform basis. Two of these metrics were introduced as new, which could evaluate the discrepancy in the non-stationary and nonlinear parts of the signal. Considering that the aerodynamic forces and response are time-histories for analyses in the time domain, the effect of the aerodynamic assumptions was studied using these metrics. The need for metrics that quantify a SRQ beyond the RMS, as per standard practice in bridge aerodynamics, was demonstrated on generic signals in Chapter 5.

The turbulent Pseudo-3D VPM was composed using two previously developed methods, namely, the laminar Pseudo-3D VPM and the velocity-based random free-stream turbulence generation. It was shown in analytical manner that the span-wise correlation of the velocity within the CFD domain remains correlated between strips. Based on the verification of the velocity field within the fundamental applications, it was confirmed in a numerical manner that the velocity span-wise correlation between strips is maintained within the CFD domain up to a certain extent. The minor loss of span-wise correlation was attributed to the application of kinematic constrains on a non-divergence-free velocity field.

To determine the complex aerodynamic admittance, deterministic free-stream turbulence was simulated by modeling the wakes of two fictitious pitching airfoils with inflow vortex particles. Positioning a section downstream of the particle release locations yielded sinusoidal buffeting forces. The complex aerodynamic admittance was then determined as a transfer function between the buffeting forces and the deterministic free-stream gusts. Moreover, a closed-form relation, based on an existing mathematical model, was deduced to relate the gust amplitudes and vortex particles' circulation. This closed-form relation and the quality of the deterministic gusts were verified based on simulation without a body in the domain.

The complete verification of the CFD aerodynamic and aeroelastic analyses of flat plate w.r.t. their analytical counterpart served several purposes for the novel aspects of this work. Initially, the complex aerodynamic admittance was verified against the Sears analytical function. Then, it was shown that there is virtually no difference when a simple FFT-based method for computation of the unsteady buffeting forces is used compared to the standard approach based on the convolution of indicial functions. As a final step of the flat plate analysis, the results of the buffeting and flutter response were compared w.r.t. an analytical solution, rendering very good results. The comparison metrics from one-to-one verification of the buffeting response resulted in high values as well, indicating excellent correspondence.

Chapter 6 was devoted to applications of the presented methods and synergistic framework in bridge aerodynamics and aeroelasticity. The Mersey Gateway Bridge was used as an example to demonstrate how the categorical modeling approach can be used to study the effect of aerodynamic model assumptions in the case of semi-analytical aerodynamic models. The most complete application of the synergistic framework was for the Great Belt Bridge. Aerodynamic coefficients were compared with wind tunnel results where possible, and then the 2D buffeting and flutter responses were studied for six semi-analytical and a CFD model. Employing the comparison metrics for time-histories, it was shown that in the case of both, the Great Belt Bridge and Mersey Gateway Bridge, the most influential assumption is the fluid memory. Moreover, the analysis revealed that although nonlinearities may be present in the CFD response, these cannot be appropriately captured by the quasi-steady based models. The results from the Pseudo-3D flutter and buffeting analyses corresponded well with the semi-analytical models. Finally, a study was undertaken to validate the CFD complex aerodynamic admittance with experimental results for the deck of the Third Bosporus Bridge.

7.2 Critical remarks

Before proceeding with the conclusions, three remarks on the modeling in this work are made on the strip assumption, sub-grid turbulence modeling and the validity of results.

Strip assumption

The present investigation is based on the 2D strip assumption, which inevitably influences the fluid-structure interaction and turbulent energy transfer compared to a 3D case. From a perspective of aerodynamic forces, the linear motion-induced forces have been commonly assumed as fully correlated (cf. e.g Scanlan [285]), indicating that the 2D effects are predominant for these forces. Thus, the flutter derivatives from 2D CFD simulations are in good correspondence with experimental results, as it was the case herein for the Great Belt Bridge. Similar observations were reported by Bai et al. [15] for the flutter derivatives obtained using 2D and 3D numerical simulations.

The 3D effect in the incident part of the buffeting forces is, however, not negligible and it is dependent on the free-stream turbulence characteristics such as the turbulent length scale and span-wise coherence [187]. Herein, all employed 2D aerodynamic models, CFD or semi-analytical, depend only on the chord-wise wavenumber. This situation closely resembles experimental tests involving an active turbulence generator (cf. e.g. [81, 86]), as the forces are assumed to be fully correlated over the strip. It is well-established that the aerodynamic forces dependent on both span- and chord-wise wavenumbers. Experimental studies such as the ones by Larose [187] and Etkin [101] have shown that the buffeting forces per unit span are reduced and their and span-wise correlation is increased in the 3D case.

Analytical models for thin airfoils including both wavenumbers have been long developed, such as the one by Graham [121]. Utilizing the general two-wavenumber analytical model of the aerodynamic forces, Massaro and Graham [215] showed why there is an increase in the span-wise correlation of the buffeting forces for random free-stream. The most recent semi-analytical model in bridge aerodynamics involves both, span-wise and chord-wise, wavenumbers (cf. e.g. [200, 201]). Presently. This model is linear and only applicable in the frequency domain.

An important finding in the analytical study by Massaro and Graham [215] was that for bridges with a large span-to-width ratio, such as the Great Belt Bridge, the strip assumption may be used with sufficient accuracy as the reduction of the lift in the 3D admittance is balanced by its increased span-wise correlation. Probably, the largest influence of the three-dimensionality is in the local effects in the aerodynamic forces due to the small turbulent scales and vortex shedding, which also has been observed in some experimental studies (cf. e.g. [136, 199]).

Looking at the strip assumptions from a fluid dynamics point of view, it is also well established that the 2D flow characteristics lack physical merit. The mechanism of energy transfer between scales for 2D turbulence is different from the mechanism for the 3D case [30]. Moreover, the phenomena due to fluid-structure interaction such as vortex shedding are three-dimensional. However, the large number of validation studies shows that the VPM can reasonably well approximate the aerodynamic forces, which is of main interest for this work.

Sub-grid turbulence

Another factor that influences the aerodynamic forces is the sub-grid turbulence. In this work, a sub-grid turbulent model has not been included and the resolved scales are significantly larger than the Kolmogorov length scale, hence the name CFD "model". However, it is noted that the unresolved scales do not significantly affect the resolution of the resolved scales in the VPM [71] and the angular impulse and energy are mostly conserved. Although a partial turbulence modeling is implied in the mollification process, this is not a controlled procedure [70].

Nevertheless, the influence of sub-grid turbulence, 2D or 3D, on the aerodynamic forces is not well understood and warrants further investigations, as discussed by Wu and Kareem [362]. In case the aerodynamic coefficients are validated to a certain extent with experimental and numerical results from former studies, it is reasonable to assume that the computational model describes the fluid-structure interaction adequately.

Validity of numerical results

Where possible, a wind tunnel validation was performed in this work with good to fair correspondence. In particular, most of the aerodynamic coefficients for the Great Belt Bridge and the aerodynamic admittance in the case of the Third Bosporus bridge were validated. Further, the critical flutter velocity for the Great Belt Bridge was also validated with the experimental results from past studies for both 2D and Pseudo-3D.

The 2D or Pseudo-3D aeroelastic response due to random free-stream turbulence was not validated with experimental results. This would require further experimental tests performed on a taut-strip model with very large length scale-to-deck width ratio in order to alleviate the 3D effects.

However, as the aerodynamic coefficients are validated to a certain extent with experimental and numerical results from former studies, it is reasonable to assume that the CFD model describes the fluid-structure interaction adequately, at least in the linear range. On the other hand, a point can be made that even though experiments represent the reality, the influence of measuring uncertainty and non-corresponding scaling of both structure and fluid may not completely resemble the situation on-site.

7.3 Conclusions

As a part of the proposed synergistic framework, the comparative methodology offers a straightforward way to determine the assumption responsible for the discrepancies in a particular metric of a SRQ by using the diagrammatic ordering of models. A newly developed model can be easily integrated into the diagram, and the advantages and limitations of its mathematical constructions can be observed immediately. In case the SRQ is a signal, the comparison metrics for time-histories allow one to quantify discrepancies in particular signal features for two models individually. In other words, one can obtain a deeper insight into the effect of the aerodynamic assumptions by looking at individual comparison metrics. Based on this, a judgment can be made which phenomena can or cannot be captured by this model and how does this reflect on particular signal features. The present methodology can be easily extended to any other engineering field. Thus, it shows the potential to be used in model assessment studies beyond the field of bridge aerodynamics.

Both the laminar and novel turbulent Pseudo-3D VPM provide a new instrument to unveil some of the nonlinear and local non-stationary effects for wind-bridge interaction. Utilizing the Pseudo-3D VPM, the vortex shedding, local turbulence effects, and aerodynamic nonlinearities are inherent in a 2D manner. These effects may be of major significance for high amplitudes of oscillation in severe wind conditions. Thus, this provides an advantage of the Pseudo-3D VPM over any semi-analytical model that includes aerodynamic coefficients predicated on 2D CFD studies. Taking into account the critical remarks made previously and obvious limitations of a 2D analysis, the notion was to show that the Pseudo-3D VPM may be readily applicable for aeroelastic analyses of bridges. It is indeed indented that this method is considered from a modeling aspect, rather than as a simulation, serving as a compromise between the limitations of the semi-analytical models and high computational demand of the 3D CFD simulations.

Having verified and validated, the CFD method for obtaining the six-component complex aerodynamic admittance under deterministic gusts is promising. Both real and imaginary parts can be obtained separately at a clearly delineated frequency. A complex transfer function in

the time domain is necessary for the buffeting forces to be real signals. In contrast, only the absolute value of the aerodynamic admittance can be obtained for random free-stream gusts. Moreover, there is no presently available two-wavenumber semi-analytical model in the time domain. Thus, assuming fully correlated gusts (i.e. two-dimensionality) seems appropriate. These arguments, and the fact that remarkably few studies exist that compute the aerodynamic admittance using grid-based CFD methods, makes the case for using the VPM for practical design applications.

It is envisioned that the presented synergistic framework is applied in bridge aerodynamics in part or as a whole. Studying the effects of the assumptions in a systematic manner can provide the range of applicability for the semi-analytical aerodynamic models from a CFD perspective. Moreover, if one can establish grounds of a reliable CFD model by validating the aerodynamic coefficients, there is a convincing argument that the results of the Pseudo-3D analyses are valid.

In light of the previous statements, it can be concluded the model performance is highly dependent on the case-study and it is in the designers' interest to conduct the analysis with various models to check the range of deviation due to the effect of aerodynamic assumptions. The outcome of this work is indented to shed some light on the complex processes occurring during fluid-structure interaction and to unveil some of the nonlinear and non-stationary aerodynamic effects.

7.4 Outlook

Both the individual presented methods and the proposed synergistic framework leave room for improvement and open new avenues for further study.

A potential advancement of the categorical modeling approach would be to provide a definition of empirical and experimental models. With this, a clear approach using category theory could be defined for different types of models, i.e. experimental w.r.t. mathematical.

Presently, all comparison metrics for time-histories are considered individually as some of them are redundant. Future studies may involve combining these metrics in a unified metric by utilizing weighting factors. These factors, as well as a qualitative interpretation of the comparison metrics, should involve subject matter experts. Moreover, new metrics to quantify discrepancies in higher-order nonlinearities could be developed by employing mathematical tools such as the higher-order spectra.

Extending the comparative methodology in a probabilistic fashion remains a viable outlook as well. Thus, previous approaches used for various verification and validation frameworks based on sensitivity and uncertainty analyses could be incorporated into this methodology.

Several extensions can be made on the account of the CFD model and the Pseudo-3D method in terms of the random free-stream turbulence. Generating a divergence-free random free-stream turbulence will alleviate the loss of kinetic energy and thus, yield better anisotropic properties. Moreover, if the divergence-free velocity fields for multiple strips fields are additionally correlated in the span-wise direction, the loss of correlation for the turbulent Pseudo-3D VPM may be reduced.

To address the limitation of strip assumption, the Pseudo-3D CFD model can be coupled with a semi-analytical model in a hybrid fashion. In this sense, the aerodynamic forces for a single CFD strip could be adjusted to take into account the effects of three-dimensionality such as loss

of span-wise correlation of the buffeting forces. Additionally, simple quasi-steady models can be used to apply the wind on the remaining elements of the bridge such as cables and towers.

Further, applications of the method for simulation of deterministic gusts could entail verification of the superposition principle for the buffeting and self-excited forces within the linear hypothesis and band superposition tests. Moreover, studying the effect of free-stream turbulence, deterministic or random, on the critical flutter limit still remains an open question in the community dealing with bridge aerodynamics and aeroelasticity. Although only 2D, the VPM involving both deterministic and random free-stream turbulence could provide insight into this topic.

Finally, the presented synergistic framework could be validated using an aeroelastic response from wind tunnel experiments for both section and taut-strip experimental models. With this, the effect of the aerodynamic assumptions would be quantified by taking an experimental model as a reference. Moreover, such validation would certainly contribute to the acceptance of the Pseudo-3D vortex methods by the wind engineering community.

Bibliography

[1] Aas-Jakobsen, K. and Strømmen (2001). Time domain buffeting response calculations of slender structures. *J. Wind Eng. Ind. Aerodyn.* 89, 341–364.

[2] Abbas, T. (2016). *Assessment of numerical prediction models for aeroelastic instabilities of bridges*. Ph. D. thesis, Bauhaus-University Weimar.

[3] Abbas, T., Kavrakov, I., and Morgenthal, G. (2017). Methods for flutter stability analysis of long-span bridges: a review. *Proc. Inst. Civ. Eng.-Bridge Eng.* 170 (4), 271–310.

[4] Abbas, T. and Morgenthal, G. (2016). Framework for sensitivity and uncertanty quantification in the flutter assessment of bridges. *Prob. Eng. Mech.* 43, 91–105.

[5] Adowey, S. (2006). *Category theory*. Oxford University Press.

[6] Akbari, M. H. and Price, S. J. (2003). Simulation of dynamic stall for a NACA 0012 airfoil using a vortex method. *J. Fluids Struct.* 17, 855–874.

[7] Amandolese, X., Michelin, S., and Choquel, M. (2013). Low speed flutter and limit cycle oscillations of two-degree-of-freedom flat plate in wind tunnel. *J. Fluids Struct.* 43, 244–255.

[8] Ammann, O., von Kárman, and Woodruff, G. B. (1941). The failure of the Tacoma Narrows Bridge. Technical report, Board of Engineers.

[9] Anderson, F. (2001). *Fundamentals of aerodynamics*, Third ed. McGraw-Hill.

[10] Arena, A., Lacarbonara, W., and Marzocca, P. (2015). Post-critical behaviour of suspension bridges under nonlinear aerodynamic loading. *J. Comput. Nonlin. Dyn.* 11, 011005–011005–11.

[11] Argentini, T., Rocchi, D., Muggiasca, S., and Zasso, A. (2012). Cross-sectional distributions versus integrated coefficients of flutter derivatives and aerodynamic admittances identified with surface pressure measurement. *J. Wind Eng. Ind. Aerodyn.* 104–106, 152–158.

[12] Argentini, T., Rocchi, D., and Omarini, S. (2017). Personal communication.

[13] Babuska, I. and Oden, J. T. (2004). Verification and validation in computational engineering and science: basic concepts. *Comput. Methods Appl. Mech. Engrg.* 193, 4057–4066.

[14] Baele, J. T. and Majda, A. (1985). Higher order accurate vortex methods and explicit velocity kernels. *J. Comput. Phys.* 58, 188–208.

[15] Bai, Y., Sun, D., and Lin, J. (2010). Three dimensional numerical simulations of long-span bridge aerodynamics, using block-iterative coupling and DES. *Comput. Fluids* 39, 1549–1561.

[16] Baker, G. R. (1979). The "Cloud in Cell" technique applied to roll up of vortex sheets. *J. Comput. Phys.* 31, 76–95.

[17] Barnes, J. and Hut, P. (1988). A hierarchical $O(N \log N)$ force-calculation algorithm. *Nature* 9, 669–686.

[18] Bartoli, G. and Righi, M. (2006). Flutter mechanism for rectangular prisms in smooth and turbulent flow. *J. Wind Eng. Ind. Aerodyn.* 94, 275–291.

[19] Batchelor, G. K. (1959). *The theory of homogeneous turbulence*, Third ed. Cambridge University Press.

[20] Bathe, K. (1996). *Finite Element Procedures.* Prentice Hall.

[21] Bienkiwicz, B. (1993). Aerodynamic loading and flow past bluff bodies using discrete vortex method. *J. Wind Eng. Ind. Aerodyn.* 46 & 47, 619–628.

[22] Bienkiwicz, B. and Kutz, R. F. (1990). Applying the discrete vortex method to flow about bluff bodies. *J. Wind Eng. Ind. Aerodyn.* 36, 1011–1020.

[23] Bisplinghoff, R. L., Ashley, H., and Halfman, R. L. (1996). *Aeroelasticity*, Dover ed. Dover Publications.

[24] Blasius, H. (1907). *Grenzschichten in Flüssigkeiten mit kleiner Reibung (in German).* Ph. D. thesis, University of G ottingen.

[25] Blasius, H. (1950). Boundary layers in fluids with little friction. Tech. Memorandum NASA-TM-1256, NASA, Washington, USA.

[26] Bleich, F. (1949). Dynamic instability of truss-stiffened suspension bridges under wind action. *Trans. ASCE* 114, 1117–1222.

[27] Blevins, R. D. (2001). *Flow-induced vibration*, Second ed. Krieger publishing company, Malabar, Florida.

[28] Bliemel, F. (1973). Theil's forecast accuracy coefficient:A clarification. *J. Mark. Res.* 10, 444–446.

[29] Blocken, B. (2014). 50 years of computational wind engineering: Past, present and future. *J. Wind Eng. Ind. Aerodyn.* 129, 69–102.

[30] Boffeta, G. and Ecke, R. E. (2012). Two-dimensional turbulence. *Annu. Rev. Fluid Mech.* 44, 427–451.

[31] Boonyapinyo, V., Miyata, T., and Yamada, H. (1999). Advanced aerodynamic analysis of suspension bridges by state-space approach. *J. Struct. Eng.* 125, 1357–1366.

[32] Borgant, P., Flandrin, P., Hoene, P., Richard, C., and Xiao, J. (2010). Testing stationarity with surrogates:A time-frequency approach. *IEEE Trans. Signal Process.* 58, 3459–3470.

[33] Borri, C. and Costa, C. (2004). Quasi-steady analysis of a two-dimensional bridge deck element. *Comput. Struct.* 82, 993–1006.

[34] Botev, Z., Grotowski, J., and Kroese, D. (2010). Kernel density estimation via diffusion. *Ann. Stat.* 38, 2916–2957.

[35] Brar, P. S., Raul, R. H., and Scanlan, R. H. (1996). Numerical calculation of flutter derivatives via indicial functions. *J. Fluids Struct.* 10, 337–351.

[36] Bruno, L. and Fransos, D. (2008). Evaluation of Reynolds number effects on flutter derivatives of a flat plate by means of a computational approach. *J. Fluids Struct.* 24, 1058–1076.

[37] Bruno, L. and Khris, S. (2003). The validity of 2D numerical simulations of vortical structures around bridge deck. *Math Comput Model* 37, 795–828.

[38] Bruno, L., Khris, S., and Marcillat, J. (2001). Contribution of numerical simulation for evaluation of the effect of section details and partial streamlining on the aerodynamic behaviour of bridge decks. *Wind Struct.* 4, 315–332.

[39] Bruno, L., Tubino, F., and Solari, G. (2005). Aerodynamic admittance functions of bridge deck sections by CWE. In *6th EURODYN*, Rotterdam, Netherlands.

[40] Brusiani, F., de Miranda, S., Patruno, L., Ubertini, F., and Vaona, P. (2013). On the evaluation of bridge deck flutter derivatives using RANS. *J. Wind Eng. Ind. Aerodyn.* 119, 39–47.

[41] Bucher, C. G. and Lin, Y. K. (1988). Stochastic stability of bridges considering coupled modes. *J. Eng. Mech.* 114, 2055–2071.

[42] Bucher, C. G. and Lin, Y. K. (1989). Stochastic stability of bridges considering coupled modes: II. *J. Eng. Mech.* 115 (2), 384–400.

[43] Camara, A., Kavrakov, I., Nguyen, K., and Morgenthal, G. (2019). Complete framework of wind-vehicle-bridge interaction with random road surfaces. *J. Sound Vib.* 458, 197–217.

[44] Cao, S., Tamura, Y., Kikuchi, N., Saito, M., Nakayama, I., and Yutaka, M. (2009). Wind characteristics of a strong typhoon. *J. Wind Eng. Ind. Aerodyn.* 97, 11–21.

[45] Caracoglia, L. and Jones, N. P. (2003). Time domain vs frequency domain characterization of aeroelastic forces for bridge deck sections. *J. Wind Eng. Ind. Aerodyn.* 91, 371–402.

[46] Carasalle, L. and Solari, G. (2006). Monte carlo simulation of wind velocity fields on complex structures. *J. Wind Eng. Ind. Aerodyn.* 94, 323–339.

[47] Carassale, L., Wu, T., and Kareem, A. (2014). Nonlinear aerodynamic and aeroelastic analysis of bridges:Frequency domain approach. *J. Eng. Mech.* 140, 1–14.

[48] Carrier, J., Greengard, L., and Rokhlin, V. (1988). A fast adaptive multipole algorithm for particle simulations. *SIAM J. Sci. Stat. Comput.* 9, 669–686.

[49] Casalotti, A., Arena, A., and Lacarbonara, W. (2014). Mitigation of post-flutter oscillations in suspension bridges by hysteretic tuned mass dampers. *Eng. Struct.* 69, 62–71.

[50] Chawdhury, S., Milani, D., and Morgenthal, G. (2018). Modeling of pulsating incoming flow using vortex particle methods to investigate the performance of flutter-based energy harvesters. *Comp Struct* 209, 130–149.

[51] Chawdhury, S. and Morgenthal, G. (2016). Flow reproduction using vortex particle methods for simulating wake buffeting response of bluff structures. *J. Wind Eng. Ind. Aerodyn.* 151, 122–136.

[52] Chawdhury, S. and Morgenthal, G. (2017). Numerical simulations of aeroelastic instabilities to optimize the performance of flutter-based electromagnetic energy harvesters. *J. Intell. Material Syst.* 29, 479–495.

[53] Chen, X. (2006). Analysis of long span bridge response to winds: building nexus between flutter and buffeting. *J. Struct. Eng.* 132 (12), 2006–2017.

[54] Chen, X. (2013). Typhoon-induced non-stationary buffeting response of long-span bridges in complex terrain. *Eng. Struct.* 57, 406–415.

[55] Chen, X. (2014). Analysis of multimode coupled buffeting response of long-span bridges to nonstationary winds with force parameters from stationary wind. *J. Struct. Eng.* 141, 04014131.

[56] Chen, X. and Kareem, A. (2001). Aeroelastic analysis of bridges under multicorrelated winds: Integrated state-space approach. *J. Eng. Mech.* 127 (11), 1124–1133.

[57] Chen, X. and Kareem, A. (2002). Advanced analysis of coupled buffeting response of bridges: a complex modal decomposition approach. *Prob. Eng. Mech.* 17, 201–213.

[58] Chen, X. and Kareem, A. (2002). Advances in modeling of aerodynamic forces on bridge decks. *J. Eng. Mech.* 128, 1193–1205.

[59] Chen, X. and Kareem, A. (2003). Aeroelastic analysis of bridges: Effects of turbulence and aerodynamic nonlinearities. *J. Eng. Mech.* 129 (8), 885–895.

[60] Chen, X., Matsumoto, M., and Kareem, A. (2000). Aerodynamic coupling effects on flutter and buffeting of bridges. *J. Eng. Mech.* 126 (1), 17–26.

[61] Chen, X., Matsumoto, M., and Kareem, A. (2000). Time domain flutter and buffeting response analysis of bridges. *J. Eng. Mech.* 126, 7–16.

[62] Chen, Z., Han, Y., Hua, X., and Luo, Y. (2009). Investigation on influence factors of buffeting response of bridges and its aeroelastic model verification for Xiaoguan bridge. *Eng. Struct.* 31, 417–431.

[63] Cherry, N. J., Hiller, R., and Latour, M. E. M. P. (1984). Unsteady measurements in a separated and reattaching flow. *J. Fluid Mech.* 144, 13–46.

[64] Chorin, A. (1973). Numerical study of slightly viscous flow. *J. Fluid Mech.* 27, 785–796.

[65] Chorin, A. and Marsden, J. E. (2000). *A mathematical introduction to fluid mechanics*, Third ed. Springer-Verlag.

[66] Christiansen, J. P. (1973). Numerical simulation of hydrodynamics by the method of point vortices. *J. Comput. Phys.* 13, 363–379.

[67] Clough, R. W. and Penzien, J. (1995). *Dynamics of structures*, Third ed. Computers & Structures.

[68] Collar (1978). The first fifty years of aeroelasticity. *Aerospace* 5, 12–20.

[69] Costa, C. and Borri, C. (2006). Application of indicial functions in bridge deck aeroelasticity. *J. Wind Eng. Ind. Aerodyn.* 94, 859–881.

[70] Cottet, G. and Koumoutsakos, P. (2000). *Vortex methods: Theory and Practice*. Cambridge University Press.

[71] Cottet, G. H., Michaux, B., Ossia, S., and VanderLinden, G. (2002). A comparison of spectral and vortex methods in three-dimensional incompressible flows. *J. Compt. Phys.* 175, 1–11.

[72] Davenport, A. G. (1961). The application of statistical concepts to the wind loading of structures. *Proc. Inst. Civ. Eng.* 19, 449–472.

[73] Davenport, A. G. (1962). The response of slender, line-like structures to a gusty wind. *Proc. Inst. Civ. Eng.* 23, 389–408.

[74] Davenport, A. G. (1962). The spectrum of horizontal gustiness near the ground in high winds. *Quart. J. Roy. Meteorol. Soc.* 88, 197–198.

[75] de Maré, M. and Mann, J. (2014). Validation of the Mann spectral tensor for offshore wind conditions at different atmospheric stabilities. *J. Phys.: Conf. Ser.* 524, 012016.

[76] de Miranda, S., Patruno, L., Ubertini, F., and Vairo, G. (2013). Indicial functions and flutter derivatives: A generalized approach to the motion-related wind loads. *J. Fluids Struct.* 42, 466–487.

[77] de Miranda, S., Patruno, L., Ubertini, F., and Vairo, G. (2014). On the identification of flutter derivatives of bridge decks via RANS turbulence models: Benchmarking on rectangular prisms. *Eng. Struct.* 76, 359–370.

[78] Den Hartog, J. P. (1932). Transmission line vibration due to sleet. *Trans. AIEE* 51, 1074–1076.

[79] Deodatis, G. (1996). Simulation of ergodic multivariate stochastic processes. *J. Eng. Mech.* 122, 778–787.

[80] Diana, G., Bruni, S., Cigada, A., and Collina, A. (1993). Turbulence effect on flutter velocity in long span suspended bridges. *J. Wind Eng. Ind. Aerodyn.* 48, 329–342.

[81] Diana, G., Bruni, S., Cigada, A., and Zappa, E. (2002). Complex aerodynamic admittance function role in buffeting response of a bridge deck. *J. Wind Eng. Ind. Aerodyn.* 90, 2057–2072.

[82] Diana, G., Falco, M., Bruni, S., Cigada, A., Larose, G. L., Damsgaard, A., and Collina, A. (1995). Comparisons between wind tunnel tests on fur aeroelastic model for proposed bridge over stretto di messina and numerical results. *J. Wind Eng. Ind. Aerodyn.* 54/55, 101–113.

[83] Diana, G., Resta, F., Belloli, M., and Rocchi, D. (2006). On the vortex shedding forcing on suspension bridge deck. *J. Wind Eng. Ind. Aerodyn.* 94, 341–363.

[84] Diana, G., Resta, F., and Rocchi, D. (2008). A new numerical approach to reproduce bridge aerodynamic non-linearities in the time domain. *J. Wind Eng. Ind. Aerodyn.* 96, 1871–1884.

[85] Diana, G., Rocchi, D., and Argentini, T. (2013). An experimental validation of band superposition model of the aerodynamic forces acting on a multi-box deck sections. *J. Wind Eng. Ind. Aerodyn.* 113, 40–58.

[86] Diana, G., Rocchi, D., Argentini, T., and Muggiasca, S. (2010). Aerodynamic instability of a bridge deck section model: Linear and nonlinear approach to force modeling. *J. Wind Eng. Ind. Aerodyn.* 98, 363–374.

[87] Diana, G., Stoyanoff, S., Aas-Jakobsen, K., Allsop, A., Andersen, M., Argentini, T., Montoya, M. C., , Hernández, S., Juardo, J. A., Katsuchi, H., Kavrakov, I., Kim, H., Larose, G., Larsen, A., Morgenthal, G., Øiseth, O., Omarini, S., Rocchi, D., Svendsen, M., and Wu, T. (2019). IABSE Task Group 3.1 benchmark results. Part 2: Numerical analysis of a 3-degree-of-freedom bridge deck section based on experimental aerodynamics. *Struct. Eng. Int.*. doi:10.1080/10168664.2019.1661331.

[88] Diana, G., Stoyanoff, S., Aas-Jakobsen, K., Allsop, A., Andersen, M., Argentini, T., Montoya, M. C., , Hernández, S., Juardo, J. A., Katsuchi, H., Kavrakov, I., Kim, H., Larose, G., Larsen, A., Morgenthal, G., Øiseth, O., Omarini, S., Rocchi, D., Svendsen, M., and Wu, T. (2019). IABSE Task Group 3.1 benchmark results. Part 1: Numerical analysis of a two-degree-of- freedom bridge deck section based on analytical aerodynamics. *Struct. Eng. Int.*. doi:10.1080/10168664.2019.1639480.

[89] Ding, Q., Zhu, L., and Xiang, H. (2011). An efficient ergodic simulation of multivariate stochastic process with spectral representation. *Prob. Eng. Mech.* 26, 350–356.

[90] Dowell, E. H. (1980). A simple method for converting frequency-domain aerodynamics to the time domain. Tech. Memorandum NASA-81844, NASA, Virginia, USA.

[91] Dowell, E. H. e. a. (2004). *A modern course in aeroelasticity*, Fourth ed. Kluwer Academic Publishers.

[92] Dryden, H. L. (1936). Air flow in the boundary layer near a flat plate. report 562, NACA.

[93] Dutailly, J. C. (2014). Common structures in scientific theories. *HAL ID: hal-01003869*, 34 pp.

[94] Dutailly, J. C. (2014). Hilbert spaces in modelling of systems. *HAL ID: hal-00974251*, 47 pp.

[95] Ebrahimnejad, L., Janoyan, K. D., Valentine, D. T., and Marzocca, P. (2014). Investigation of the aerodynamic analysis of super long-span bridges using ERA-based reduced-order models. *J. Bridge. Eng.* 19, 1–13.

[96] Ehsan, F. and Scanlan, R. H. (1990). Vortex-induced vibrations of flexible bridges. *J. Eng. Mech.* 116, 1392–1411.

[97] El Ossmani, M. and Poncet, P. (2010). Efficiency of multiscale hybrid grid-particle methods. *Multiscale Model Simul.* 8, 1671–1690.

[98] Eldrege, J. D. (2007). Numerical simulation of the fluid dynamics of 2D rigid body motion with the vortex particle method. *J. Comput. Phys.* 221, 626–648.

[99] Elgar, S. and Sebert, G. (1989). Statistics of bicoherence and biphase. *J. Geophys. Res.* 94, 993–998.

[100] ESDU85020 (2001). Characteristics of atmospheric turbulence near the ground. part II: single point data for strong winds (neutral atmosphere). Technical report, Engineering Sciences Data Unit.

[101] Etkin, B. (1981). Turbulent wind and its effect on flight. *J. Aircraft* 18, 327–35.

[102] Fackrell, J. W. A. and McLaughlin, S. (1995). Quadratic phase coupling detection using higher order statistics. In *IEEE Colloq. on Higher Order Statistics in Signal Processing: Are They of Any Use?*, 9/1–9/8.

[103] Fackrell, J. W. A., White, P. R., Hammond, J. K., and Pinnington, R. J. (1995). The interpretation of the bispectra of vibration signals-I. Theory. *Mech. Syst. Signal Process.* 9, 257–266.

[104] Farquharson, F. B. (1940). A dynamic model for the Tacoma-Narrows suspension bridge. Bulletin 1, University of Washington.

[105] Farquharson, F. B. (1940). Part I: Investigations prior to October, 1941. aerodynamic stability of suspension bridges with special reference to the Tacomma Narrows Bridge. Bulletin 116, University of Washington.

[106] Farsani, H. Y., Valentine, D. T., Arena, A., Lacarbonara, W., and Marzocca, P. (2014). Indicial functions in the aeroelasticity of bridge decks. *J. Bridge Eng.* 19, 1–13.

[107] Ferzinger, J. H. and Peric, M. (2002). *Computational methods for fluid dynamics*. Springer.

[108] Frandsen, J. B. (2004). Numerical bridge deck studies using finite elements. Part I: Flutter. *J. Fluids Struct.* 19, 171–191.

[109] Fransos, D. and Bruno, L. (2006). Determination of the aeroelastic transfer functions for streamlined bodies by means of a Navier-Stokes solver. *Math. Comput. Model.* 43, 506–529.

[110] Fujino, Y. and Siringoringo, D. M. (2013). Vibration mechanisms and controls of long-span bridges: A review. *Struct. Eng. Int.* 23, 248–268.

[111] Fujiwara, A., Kataoka, H., and Ito, I. (1993). Numerical simulation of flow field around an oscillating bridge using finite difference method. *J. Wind Eng. Ind. Aerodyn.* 46, 567–575.

[112] Fung, Y. (1993). *An introduction to the theory of aeroelasticity*, Dover ed. New York: Dover Publications.

[113] Garrick, I. E. (1938). On some reciprocal relations in the theory of nonstationary flows. Technical Report NACA-TR-629, NASA.

[114] Ge, Y. and Tanaka, H. (2000). Aerodynamic flutter analysis of cable-supported bridges by multi-mode and full-mode approaches. *J. Wind Eng. Ind. Aerodyn.* 86, 123–153.

[115] Ge, Y. J. and Xiang, H. F. (2008). Computational models and methods for aerodynamic flutter of long-span bridges. *J. Wind Eng. Ind. Aerodyn.* 96, 1912–1924.

[116] Geers, T. (1984). Objective error measure for the comparison of calculated and measured transient response histories. *Shock Vib. Bull.* 54, 99–107.

[117] Giesing, J. P. (1968). Nonlinear two-dimensional unsteady potential flow with lift. *J. Aircr.* 5, 135–143.

[118] Giesing, J. P., Rodden, W. P., and Stahl, B. (1968). Sears function and lifting surface theory for harmonic gust fields. *J. Aircraft* 7, 252–255.

[119] Gimsing, N. J. and Georgakis, C. T. (2012). *CAble supported bridges: Concept and design*, Third ed. John Wiley & Sons.

[120] Goldburg, A., Washburn, W. K., and Florsheim, B. H. (1965). Strouhal numbers for the hypersonic wakes of spheres and cones. *AIAA J.* 7, 1332–1333.

[121] Graham, J. M. R. (1970). Lifting surface theory for the problem of an arbitrarily yawed gust incident of a thin aerofoil in incompressible flow. *Aeronaut. Quart.* 18, 182–198.

[122] Griffin, O. M. and Koopmann, G. H. (1977). The vortex-excited lift and reaction forces on resonantly vibrating cylinders. *J. Sound Vib.* 54, 435–448.

[123] Gu, M. and Qin, X.-R. (2004). Direct identification of flutter derivatives and aerodynamic admittances of bridge decks. *Eng. Struct.* 26, 2161–2172.

[124] Gu, M., Zhang, R., and Xiang, H. (2000). Identification of flutter derivatives of bridge decks. *J. Wind Eng. Ind. Aerodyn.* 84, 151–162.

[125] Gürlebeck, K., Hofmann, D., and Legatiuk, D. (2017). Categorical approach to modelling and to coupling of models. *Math. Meth. Appl. Sci.* 40, 523–534.

[126] Gurley, K. and Kareem, A. (1997). Analysis interpretation modeling and simulation of unsteady wind and pressure data. *J. Wind Eng. Ind. Aerodyn.* 69-71, 657–669.

[127] Gurley, K., Kijewski, T., and Kareem, A. (2003). First- and higher-order correlation detection using wavelet transforms. *J. Eng. Mech.* 129, 188–201.

[128] Haan, F. L. and Kareem, A. (2016). Anatomy of turbulence effect on aerodynamics of an oscillating prism. *J. Eng. Mech.* 135, 987–999.

[129] Han, Y., Chen, Z., and Hua, X. G. (2010). New estimation methodology of six complex aerodynamic admittance functions. *Wind Struct.* 13, 293–307.

[130] Harding, S. and Bryden, I. G. (2012). Generating controllable velocity fluctuations using twin oscillating hydrofoils. *J. Fluid Mech.* 713, 150–158.

[131] Harding, S., Payne, G. S., and Bryden, I. G. (2014). Generating controllable velocity fluctuations using twin oscillating hydrofoils: experimental validation. *J. Fluid Mech.* 713, 113–123.

[132] Harris, R. I. (1971). The nature of wind. In *Proc. of the modern design of wind sensitive structures*, London, UK.

[133] Hatanaka, A. and Tanaka, H. (2002). New estimation method of aerodynamic admittance function. *J. Wind Eng. Ind. Aerodyn.* 90, 2073–2086.

[134] Hejlesen, M. M., Rasmussen, J. T., Larsen, A., and Walther, J. H. (2015). On estimating aerodynamic admittance of bridge section by mesh-free vortex method. *J. Wind Eng. Ind. Aerodyn.* 146, 117–127.

[135] Hejlesen, M. M. and Walther, J. H. (2016). A multiresolution method for solving the poisson equation using high order regularization. *J. Comput. Phys.* 326, 188–196.

[136] Hiller, R. and Cherry, N. J. (1981). The effects of stream turbulence on separation bubbles. *J. Wind Eng. Ind. Aerodyn.* 8, 49–58.

[137] Hockney, R. and Eastwood, J. (1988). *Computer Simulation Using Particles*. Taylor & Francis.

[138] Hora, J. and Campos, P. (2015). A review of performance crietria to validate simulation models. *Expert Syst.* 32, 578–595.

[139] Huang, L., Xu, Y.-L., and Liao, H. (2014). Nonlinear aerodynamic forces on thin flat plate: Numerical study. *J. Fluids. Struct.* 44, 182–194.

[140] Hui, M. C. H., Larsen, A., and Xiang, H. F. (2009). Wind turbulence characteristics study at the Stonecutters bridge site: Part II: Wind power spectra, integral lengthscales and coherences. *J. Wind Eng. Ind. Aerodyn.* 97, 48–59.

[141] Hunt, J. C. R. (1973). A theory of turbulent flow round two-dimensional bluff bodies. *J. Fluid Mech.* 4, 625–706.

[142] IABSE Task Group 3.1: Super-long span bridge aerodynamics (2017). Step 1.1a results. Technical Report IABSE/WG-10-N-004, IABSE.

[143] Irwin, H. P. A. H. (1979). Cross-spectra of turbulence velocities in isotropic turbulence. *Bound.-Layer Meteorol.* 16, 237–243.

[144] Irwin, P. A. (2008). Bluff body aerodynamics in wind engineering. *J. Wind Eng. Ind. Aerodyn.* 96, 701–712.

[145] ISO 4354:2009 (2009). Wind actions on structures. Standard, International Organization for Standardization.

[146] Isyumov, I. (2012). Alan g. davenport's mark on wind engineering. *J. Wind Eng. Ind. Aerodyn.* 102, 12–24.

[147] Jain, A., Jones, N. P., and Scanlan, R. H. (1996). Coupled aeroelastic aerodynamic response analysis of long-span bridges. *J. Wind Eng. Ind. Aerodyn.* 60, 69–80.

[148] Jain, A., Jones, N. P., and Scanlan, R. H. (1996). Coupled flutter and buffeting analysis of long-span bridges. *J. Struct. Eng.* 122 (7), 716–725.

[149] Jakobs, E. N. and Sherman, A. (1939). Airfoil section characteristics as affected by variations of Reynolds number. Technical Report NACA-TR-586, NASA.

[150] Jamšek, J., Stefanovska, A., and McClintock, P. V. E. (2007). Wavelet bispectral analysis for the study of interactions among oscillators whose basic frequencies are significantly time variable. *Phys. Rev. E* 76, 046221–046221–11.

[151] Jancauskas, E. D. and Melbourne, W. H. (1986). The aerodynamic admittance of two-dimensional rectangular section cylinders in smooth flow. *J. Wind Eng. Ind. Aerodyn.* 23, 395–408.

[152] Jiang, X. and Mahadevan, S. (2010). Wavelet spectrum analysis approach to model validation of dynamic systems. *Mech. Syst. Signal Process.* 25, 575–590.

[153] Jones, R. T. (1940). The unsteady lift of a wing of finite aspect ratio. Technical Report NACA-TR-681, NASA.

[154] Jones, R. T. (1979). Classical aerodynamic theory. Technical Report NASA-RP-1050, NASA.

[155] Jung, K., Kim, H.-K., and Lee, H. S. (2012). Evaluation of impulse response functions for convolution integrals of aerodynamic forces by optimization with a penalty function. *J. Eng. Mech.* 138, 519–529.

[156] Jung, K., Kim, H.-K., and Lee, H. S. (2014). New unified approach for aeroelastic analyses using approximate transfer functions of aerodynamic forces. *J. Eng. Mech.* 140, 04013002.

[157] Kaimal, J., Wyngaard, Y. C., Izumi, Y., and Coté, O. R. (1972). Spectral characteristics of surface layer turbulence. *Quart. J. Roy. Meteorol. Soc.* 98, 563–589.

[158] Kaimal, J. C. and Finnigan, J. J. (1994). *Atmospheric Boundary Layer Flows.* Oxford University Press.

[159] Kareem, A. (2008). Numerical simulation of wind effects: A probabilistic perspective. *J. Wind Eng. Ind. Aerodyn.* 96, 1472–1497.

[160] Kareem, A. and Kijewski (2002). Time-frequency analysis of wind effects on structures. *J. Wind Eng. Ind. Aerody.* 90, 1435–1452.

[161] Kareem, A. and Wu, T. (2013). Wind-induced effects on bluff bodies in turbulent flows:Nonstationary, non-Gaussian and nonlienar features. *J. Wind Eng. Ind. Aerody.* 122, 21–37.

[162] Karoumi, R. (1999). Some modeling aspects in the nonlinear finite element analysis of cable supported bridges. *Comput. Struct.* 71, 397–412.

[163] Katsuchi, K., Jones, N. P., Scanlan, R. H., and Akiyama, H. (1998). Multi-mode flutter and buffeting analysis of the Akashi-Kaikyo bridge. *J. Wind Eng. Ind. Aerodyn.* 77&78, 431–441.

[164] Katz, J. and Plotkin, A. (2001). *Low-speed aerodynamics.* Cambridge University Press.

[165] Kavrakov, I., Argentini, T., Omarini, S., Rocchi, D., and Morgenthal, G. (2019). Determination of complex aerodynamic admittance of bridge decks under deterministic gusts using the vortex particle method. *J. Wind Eng. Ind. Aerodyn.* 193, 103971.

[166] Kavrakov, I., Legatiuk, D., Gürlebeck, K., and Morgenthal, G. (2019). A categorical perspective towards aerodynamic models for aeroelastic analyses of bridge decks. *R. Soc. Open Sci.* 6, 181848.

[167] Kavrakov, I. and Morgenthal, G. (2017). A comparative assessment of aerodynamic models for buffeting and flutter of long-span bridges. *Eng.* 3, 823–838.

[168] Kavrakov, I. and Morgenthal, G. (2018). Aeroelastic analyses of bridges using a Pseudo-3D vortex method and velocity-based synthetic turbulence generation. *Eng. Struct.* 176, 825–839.

[169] Kavrakov, I. and Morgenthal, G. (2018). A synergistic study of a CFD and semi-analytical models for aeroelastic analysis of bridges in turbulent wind conditions. *J. Fluids Struct.* 82, 59–85.

[170] Keitel, H., Karaki, G., Lahmer, T., Nikulla, S., and Zabel, V. (2011). Evaluation of coupled partial models in structural engineering using graph theory and sensitivity analysis. *Eng. Struct.* 33, 3726–3736.

[171] Kijewski, T. and Kareem, A. (2003). Wavelet transforms for system identification in civil engineering. *Comput.-Aided Civ. Infrastrcut. Eng.* 18, 339–355.

[172] Kim, C. B. and Yhim, S. S. (2014). Buffeting analysis of cable-stayed bridge using three-dimensional computational fluid dynamics. *J. Bridge Eng.* 19, 319–329.

[173] Kim, T., Powers, E. J., Grady, W. M., and Arapostathis, A. (2007). A novel qpc detector for the health monitoring of rotating machines. In *IEEE Instrumentation Measurement Technology Conference*, 1–6.

[174] Kim, Y. C. and Powers, E. J. (1979). Digital bispectral analysis and its applications to nonlinear wave interactions. *IEEE Trans. Plasma Sci.* 7, 120–131.

[175] Klebanoff, P. (1971). Effect of free stream turbulence on a laminar boundary layer. *Bull. Am. Phys. Soc.* 16, 203–216.

[176] Klöpper, K. (1963). Teilmodellversuche zur beurteilung des aerodynamischen verhaltens von brücken. *Der Stahlbau* 32, 75–79.

[177] Kondo, K., Murakami, S., and Mochida (1997). Generation of velocity fluctuations for inflow boundary conditions of LES. *J. Wind Eng. Ind. Aerodyn.* 67 & 68, 51–64.

[178] Kondo, K., Murakami, S., and Mochida, A. (1997). Generation of velocity fluctuations for inflow boundary condition of LES. *J. Wind Eng. Ind. Aerodyn.* 67&68, 51–64.

[179] Kovacs, I., Svensson, H. S., and Jordet, E. (1992). Analytical aerodynamic investigation of cable-stayed Helgeland bridge. *J. Struct. Eng.* 118, 147–168.

[180] Kristeková, M., Kristek, J., and Moczo, P. (2009). Time-frequency misfit and goodness-of-fit criteria for quantitative comparison of time signals. *Geophys. J. Int.* 178, 813–825.

[181] Kristensen, L. (1979). On longitudinal spectral coherence. *Bound.-Layer Meteorol.* 16, 145–153.

[182] Kristensen, L., Panovsky, H. A., and Smith, S. D. (1981). Lateral coherence of longitudinal wind components in strong winds. *Bound.-Layer Meteorol.* 21, 199–205.

[183] Kuroda, S. (1997). Numerical simulation of flow around a box girder of a long span suspension bridge. *J. Wind Eng. Ind. Aerodyn.* 67 & 68, 239–252.

[184] Küssner, H. (1936). Zusammenfassender bericht über den instationären auftrieb von flügeln. *LuftfahrtForshung* 13, 410–424.

[185] Lancester, G., Iatsenko, D., Pidde, A., Ticcinelli, V., and Stefanovska, A. (2018). Surrogate data for hypothesis testing of physical systems. *Phys. Rep.* 748, 1–60.

[186] Larose, G. L. (1999). Experimental determination of the aerodynamic admittance of a bridge deck segment. *J. Fluids Struct.* 13, 1029–1040.

[187] Larose, L. (2002). The dynamic action of gusty winds on long-span bridges. Technical Report BYG-DTU R-029, Technical University of Denmark.

[188] Larsen, A. (1993). Aerodynamic aspects of the final design of the 1624m suspension bridge across the Great Belt. *J. Wind Eng. Ind. Aerodyn.* 48, 261–285.

[189] Larsen, A. (1997). Prediction of aeroelastic stability of suspension bridges during erection. *J. Wind Eng. Ind. Aerodyn.* 72, 265–274.

[190] Larsen, A. (1998). Advances in aeroelastic analyses of suspension and cable-stayed bridges. *J. Wind Eng. Ind. Aerodyn.* 74&76, 73–90.

[191] Larsen, A. and Larose, G. (2015). Dynamic effects on suspension and cable-stayed bridges. *J. Sound Vib.* 334, 2–28.

[192] Larsen, A. and Walther, J. H. (1997). Aeroelastic analysis of bridge girder sections based on discrete vortex simulations. *J. Wind Eng. Ind. Aerodyn.* 67&68, 253–265.

[193] Larsen, A. and Walther, J. H. (1998). Discrete vortex simulation of flow around five generic bridge deck sections. *J. Wind Eng. Ind. Aerodyn.* 72&78, 591–602.

[194] Lazzari, M. (2005). Time domain modeling of aeroelastic bridge decks: a comparative study and an application. *Int. J. Num. Meth. Eng.* 62, 1064–1104.

[195] Lazzari, M., Vitalini, R. V., and Saetta, A. V. (2004). Aeroelastic forces and dynamic response of long-span bridges. *Int. J. Num. Meth. Eng.* 60, 1011–1048.

[196] Lee, N., Lee, H., Baek, C., and Lee, S. (2016). Aeroelastic of bridge deck flutter with modified implicit coupling method. *J. Wind Eng. Ind. Aerodyn.* 155, 11–22.

[197] Legatiuk, D. and Nilsson, H. (2017). Abstract modelling: towards a typed declarative language for the conceptual modelling phase. In *Proc. 8th International Workshop on Equation-Based Object-Oriented Modeling Languages and Tools*, Munich, Germany.

[198] Leonard, A. (1980). Vortex methods for flow simulation. *J. Compt. Phys.* 37, 2891–355.

[199] Li, M., Li, S., Liao, H., Zeng, J., and Wang, Q. (2016). Spanwise correlation of aerodynamic forces on oscillating rectangular cylinder. *J. Wind Eng. Ind. Aerodyn.* 154, 47–57.

[200] Li, S., Li, M., and Larose, G. L. (2018). Aerodynamic admittance of streamlined bridge decks. *J. Fluid Struct.* 78, 1–23.

[201] Li, S., Li, M., and Liao, H. (2015). The lift on an airfoil in grid-generated turbulence. *J. Fluid Mech.* 771, 16–35.

[202] Li, X., Duan, L., Logan, J. V., and Sleigh, J. W. (2009). The comodulation measure of neuronal oscillations with general harmonic wavelet bicoherence and application to sleep analysis. *NeuroImage* 48, 501–514.

[203] Li, Y. and Kareem, A. (1990). ARMA system in wind engineering. *Prob. Eng. Mech.* 5, 50–59.

[204] Li, Y. and Kareem, A. (1990). Stochastic response of tension leg platforms to wind and wave fields. *J. Wind Eng. Ind. Aerodyn.* 36, 915–926.

[205] Liepmann, H. W. (1952). On the application of statistical concepts to the buffeting problem. *AIAA J.* 19, 793–800.

[206] Lin, R. M. and Ng, T.-Y. (2018). Identification of Volterra kernels for improved predictions of nonlinear aeroelastic vibration responses and flutter. *Eng. Struct.* 171, 15–28.

[207] Lin, S., Wang, Q., Nikitas, N., and Liao, H. (2019). Effects of oscillation amplitude on motion-induced forces for 5:1 rectangular cylinders. *J. Wind Eng. Ind. Aerodyn.* 186, 68–83.

[208] Lin, Y. K. and Yang, J. N. (1983). Multimode bridge response to wind excitations. *J. Eng. Mech.* 109 (2), 586–603.

[209] Lin, Z. and Ge, Y. (2015). Cross-spectral recognition method of bridge deck aerodynamic admittance function. *Earthq. Eng. Eng. Vib* 14, 595–609.

[210] Lindgren, G. (2006). Lectures on stationary stochastic processes.

[211] Lumley, J. L. (1970). *Stochastic tools in turbulence.* Academic Press.

[212] Mann, J. (1994). The spatial structure of neutral atmospheric surface-layer turbulence. *J. Fluid Mech.* 273, 141–168.

[213] Mann, J. (1998). Wind field simulation. *Prob. Eng. Mech.* 13, 269–282.

[214] Mann, J., Kristensen, L., and Jensen, N. O. (1998). Uncertainties of extreme winds, spectra and coherences. In Larsen, A. and Esdahl, S. (Eds.), *Bridge Aerodynamics*, Copenhagen, Denmark, 49–56.

[215] Massaro, M. and Graham, J. (2015). The effect of three-dimensionality on the aerodynamic admittance of thin sections in free stream turbulence. *J. Fluids Struct.* 57, 81–90.

[216] Matsumoto, M., Daito, Y., Yoshizumi, F., Ichikawa, Y., and Yabutani, T. (1997). Torsional flutter of bluff bodies. *J. Wind Eng. Ind. Aerodyn.* 93, 69–71.

[217] Matsumoto, M., Shiraishi, N., Shirato, H., Shigetaka, K., and Niihara, Y. (1993). Aerodynamic derivatives of coupled/hybrid flutter of fundamental structural sections. *J. Wind Eng. Ind. Aerodyn.* 49, 575–584.

[218] Matsumoto, M., Yagi, T., Tamaki, H., and Tsubota, T. (2008). Vortex-induced vibration and its effect on torsional flutter instability in the case of /D=4 rectangular cylinder. *J. Wind Eng. Ind. Aerodyn.* 96, 971–983.

[219] McCroskey, W. J. (1982). Unsteady airfoils. *Ann Rev Fluid Mech* 14, 285–311.

[220] McCroskey, W. J., Carr, L. W., and McAlister, K. W. (1976). Dynamic stall experiments on oscillating airfoils. *AIAA J.* 14, 57–63.

[221] McCullough, M. and Kareem, A. (2013). Testing stationarity with wavelet-based surrogates. *J. Eng. Mech.* 139, 200–209.

[222] McWilliams, J. C. (1984). The emergence of isolated coherent vortices in turbulent flow. *J. Fluid Mech.* 146, 21–43.

[223] McWilliams, J. C. (1990). A demonstration of the suppression of turbulent cascades by coherent vortices in two-dimensional turbulence. *Phys. Fluids A* 2, 547–552.

[224] Mignolet, M. P. and Spanos, P. D. (1992). Simulations of homogenous two dimensional random field. *J. Appl. Mech.* 59, 260–277.

[225] Miyata, T. (2003). Historical view of long-span bridge aerodynamics. *J. Wind Eng. Ind. Aerodyn.* 91, 1393–1410.

[226] Morgenthal, G. (2002). *Aerodynamic analysis of structures using high-resolution vortex particle methods*. Ph. D. thesis, Unversity of Cambridge.

[227] Morgenthal, G. (2005). Advances in numerical bridge aerodynamics and recent applications. *Struct Eng Int* 2, 95–100.

[228] Morgenthal, G., Corriols, A., and Bendig, B. (2014). A GPU-accelerated Pseudo-3D vortex method for aerodynamic analysis. *J. Wind Eng. Ind. Aerodyn.* 125, 69–80.

[229] Morgenthal, G. and McRobie, F. (2002). A comparative study of numerical methods for fluid-structure interaction analysis in long-span bridge design. *Wind Struct.* 5, 101–114.

[230] Morgenthal, G. and Walther, J. (2007). An immersed interface method for the Vortex-In-Cell algorithm. *Comput. Struct.* 85, 712–726.

[231] Mukhopadhyay, V. (1979). The galloping oscillation of a cable of square section suspended in a smooth wind flow. *J. Wind Eng. Ind. Aerodyn.* 5, 35–51.

[232] Müller, M. (2007). *Information retrieval for music and motion*. Springer-Verlag.

[233] Nakamura, Y. (1979). On the aerodynamic mechanism of torsional flutter of bluff structures. *J. Sound Vib.* 67, 163–177.

[234] Nakamura, Y. (1993). Bluff-body aerodynamics and turbulence. *J. Wind Eng. Ind. Aerodyn.* 49, 65–78.

[235] Nakamura, Y. and Mizota, T. (1975). Torsional flutter of rectangular prisms. *J. Eng. Mech.* 101, 125–142.

[236] Náprstek, J., Posíšil, S., and Hračov, S. (2007). Analytical and experimental modelling of non-linear aeroelastic effects on prismatic bodies. *J. Wind Eng. Ind. Aerodyn.* 95, 1315–1328.

[237] Nefzi, B., Schott, R., Song, Y., Staples, G., and Tsiontsiou, E. (2015). An operator calculus approach for multi-constrained routing in wireless sensor networks. In *Proc. 16th ACM International Symposium on Mobile Ad Hoc Networking and Computing*, New York, USA.

[238] Nielsen, F. and Boltz, S. (2011). The Burbea-Rao and Bhattacharyya centroids. *IEEE Trans. Inf. Theory* 57, 5455–5466.

[239] Nieto, F., Owen, J. S., Hargreaves, D., and Hernández, S. (2015). Bridge deck flutter derivatives: Efficient numerical evaluation exploiting their interdependence. *J. Wind Eng. Ind. Aerodyn.* 136, 138–150.

[240] Novak, M. (1972). Galloping oscillations of prismatic structures. *J. Eng. Mech.* 98, 27–46.

[241] Oberkampf, W. L. and Barone, M. F. (2006). Measures of agreement between computation and experiment: validation metrics. *J. Comput. Phys.* 217, 5–36.

[242] Oberkampf, W. L. and Barone, M. F. (2006). Measures of agreement between computation and experiment: validation metrics. *J. Comp. Phys.* 217, 5–36.

[243] Oberkampf, W. L. and Trucano, T. G. (2002). Verification and validation in computational fluid dynamics. *Prog. Aerosp. Sci.* 38, 209–272.

[244] Øiseth, O., Rönnquist, A., and Sigbjörnsson (2010). Simplified prediction of wind-induced response and stability limit of slender long-span suspension bridges, based on quasi-steady theory: A case study. *J. Wind Eng. Ind. Aerodyn.* 98, 730–741.

[245] Øiseth, O., Rönnquist, A., and Sigbjörnsson (2011). Time domain modeling of self-excited aerodynamic forces for cable supported bridges: A comparative study. *Comput. Struct.* 89, 1306–1322.

[246] Øiseth, O., Rönnquist, A., and Sigbjörnsson (2013). Effects of co-spectral densities of atmospheric turbulence on the dynamic response of cable-supported bridges: A case study. *J. Wind Eng. Ind. Aerodyn.* 116, 83–93.

[247] Ostashev, V. E. and Wilson, K. D. (2016). *Acoustics in moving inhomogeneousus media*, Second ed. CRC Press.

[248] Panofsky, H. A. and Dutton, J. (1984). *Atmospheric turbulence.* Wiley-Interscience.

[249] Paola, M. (1998). Digital simulation of wind field velocity. *J. Wind Eng. Ind. Aerodyn.* 74-76, 91–109.

[250] Pardo, L. (2006). *Statistical Inference Based on Divergence Measures.* Chapman & Hall/CRC.

[251] Park, J., Morgenthal, G., Kim, K., Kwon, S.-D., and Law, K. H. (2014). Power evaluation of flutter-based electromagnetic energy harvesters using computational fluid dynamics simulation. *J. Intell. Material Syst.* 25, 1–13.

[252] Parkinson, G. V. and Brooks, N. P. H. (1961). On the aeroelastic instability of bluff cylinders. *J Appl Mech* 61, 252–257.

[253] Paxton, R. (1977). Menai Bridge (1818–1826) and its influence on suspension bridge development. *Trans. Newcomen Soci.* 49 (1), 87–110.

[254] Peng, Y., Wang, S., and Li, J. (2018). Field measurement and investigation of spatial coherence for near-surface strong winds in Southeast China. *J. Wind Eng. Ind. Aerodyn.* 172, 423–440.

[255] Petrini, F., Giuliano, F., and Bontempi, F. (2007). Comparison of time domain techniques for evaluation of the response of the stability in long span suspension bridges. *Comput. Struct.* 85, 1032–1048.

[256] Piccardo, G., Pagnini, L. C., and Tubino, F. (2015). Some research perspectives in galloping phenomena: critical conditions and post-critical behaviour. *Continuum Mech. Thermodyn.* 27, 261–285.

[257] Prendergast, J. (2007). *Simulation of 2D unsteady wind by a vortex method*. Ph. D. thesis, Cambridge University.

[258] Prendergast, J. and McRobie, F. (2006). Simulation of 2D unsteady wind by a vortex method and application to studying bluff body flow. In *7th UK Conf. Wind. Eng.*

[259] Priestly, M. B. (1981). *Spectral analysis and time series*. Academic Press.

[260] Ramesh, K., Gopalarathnam, A., Granlund, K., Ol, M. V., and Edwards, J. R. (2014). Discrete-vortex method with novel shedding criterion for unsteady aerofoil flows with intermittent leading-edge vortex shedding. *J. Fluid Mech.* 751, 500–538.

[261] Rasmussen, J. T., Hejlesen, M. M., Larsen, A., and Walther, J. H. (2010). Discrete vortex method simulations of the aerodynamic admittance in bridge aerodynamics. *J. Wind Eng. Ind. Aerodyn.* 99, 776–785.

[262] Rassmusen, J. T., Cottet, G., and Walther, J. H. (2011). A multiresolution remeshed Vortex-In-Cell algorithm using patches. *J. Comput. Phys.* 230, 6742–6755.

[263] Reinhold, T., Brinch, M., and Damsgaard, A. (1992, February). Wind tunnel tests for the Great Belt Link. In Larsen, A. (Ed.), *Aerodynamics of Large Bridges*, Copenhagen, Denmark, 255–267.

[264] Richard, C., Ferrari, A., Amoud, H., Honeine, P., Flandrin, P., and Borgnat, P. (2010). Statistical hypothesis testing with time-frequency surrogates to check signal stationarity. In *IEEE Inter. Conf. on Acoustics, Speech and Signal Processing*, 3666–3669.

[265] Roger, K. L. (1977). Airplane math modeling methods for active control design. Tech. Report CP–228, AGARD.

[266] Roshko, A. (1955). On the wake and drag of bluff bodies. *J. Aeronaut. Sci.* 22, 124–132.

[267] Rossi, R. and Lazzari, M.and Vitaliani, R. (2004). Wind field simulation for structural engineering purposes. *Int. J. Num. Meth. Eng.* 61, 738–763.

[268] Roy, C. J. and Oberkampf, W. L. (2011). A comprehensive framework for verification, validation, and uncertainty quantification in scientific computing. *Comput. Methods Appl. Mech. Engrg.* 200, 2131–2144.

[269] Ruan, F. and McLaughlin, D. (1998). An efficient multivariate random field generator using the fast Fourier transform. *Adv. Water Resour.* 21, 385–399.

[270] Russel, J. S. (1939). On the vibration of suspension bridges and other structures and the means of preventing injury from this cause. *Edinburgh New Phil. J.* 26, 386–395.

[271] Rutz, F. R. and Rens, K. L. (2007). Wind loads of the 19th century bridges: Design evolution, historic failures and modern preservation. *J. Perform. Constr. Fac.* 21, 157–165.

[272] Saathof, P. J. and Melbourne, W. H. (1997). Effects of free-stream turbulence on surface pressure fluctuations in a separation bubble. *J. Fluid Mech.* 338, 1–24.

[273] Salvatori, L. and Borri, C. (2007). Frequency- and time-domain methods for numerical modeling of full bridge aeroelasticity. *Comput. Struct.* 85, 675–687.

[274] Sankaran, R. and Jancauskas, E. D. (1992). Direct measurment of aerodynamic admittance of two-dimensional rectangular cylinders in smooth and turbulent flows. *J. Wind Eng. Ind. Aerodyn.* 41, 601–611.

[275] Sarin, H., Kokkolaras, M., Hulbert, G., Papalambros, P., Barbat, S., and Yang, R. J. (2010). Comparing time histories for validation of simulation models:Error measures and metrics. *J. Dyn. Syst. Meas. Contr.* 132, 061401–061401–10.

[276] Sarkar, P. P., Caracoglia, L., Haan, F. L. J., Sato, H., and Murakoshi, J. (2009). Numerical simulations and experimental validations of force coefficients and flutter derivatives of a bridge deck. *Eng. Struct.* 31, 158–169.

[277] Šarkić, A., Höffer, R., and Brčić, B. (2015). Numerical simulations and experimental validations of force coefficients and flutter derivatives of a bridge deck. *J. Wind Eng. Ind. Aerodyn.* 144, 172–182.

[278] Sarpkaya, T. (2004). A critical review of the intrinsic nature of vortex-induced vibrations. *J. Fluids Struct.* 19, 389–447.

[279] Sarwar, M. W., Ishihara, T., Shimada, K., Yamakasi, Y., and Ikeda, T. (2008). Prediction of aerodynamic characteristics of a box girder bridge section using LES turbulence model. *J. Wind Eng. Ind. Aerodyn.* 96, 1895–1911.

[280] Scanlan, R. H. (1978). The action of flexible bridges under wind, I: Flutter theory. *J. Sound Vib.* 60, 187–199.

[281] Scanlan, R. H. (1978). The action of flexible bridges under wind, II: Buffeting theory. *J. Sound Vib.* 60 (2), 201–211.

[282] Scanlan, R. H. (1984). Role of indicial functions in buffeting analysis of bridges. *J. Struct. Eng.* 110, 1433–1446.

[283] Scanlan, R. H. (1988). On flutter and buffeting mechanisms in long-span bridges. *Prob. Eng. Mech* 1 (3), 22–27.

[284] Scanlan, R. H. (1993). Problematics in formulation of wind-force models for bridge decks. *J. Eng. Mech.* 119 (7), 1353–1375.

[285] Scanlan, R. H. (1997). Amplitude and turbulence effects on bridge flutter derivatives. *J. Struct. Eng.* 123, 232–236.

[286] Scanlan, R. H. (2000). Motion-related body-force functions in two-dimensional low-speed flow. *J. Fluids Struct.* 14, 49–63.

[287] Scanlan, R. H. (2001). Reexamination of sectional aerodynamic force functions for bridges. *J. Wind Eng. Ind. Aerodyn.* 89, 1257–1266.

[288] Scanlan, R. h., Bélveau, J.-G., and Budlong, K. S. (1974). Indicial aerodynamic functions for bridge decks. *J. Eng. Mech. Div.* 100, 657–672.

[289] Scanlan, R. H. and Jones, N. P. (1990). Aeroelastic analysis of cable-stayed bridges. *J. Struct. Eng.* 116 (2), 279–297.

[290] Scanlan, R. H. and Tomko (1971). Airfoil and bridge deck flutter derivatives. *J. Eng. Mech.* 97 (6), 1717–1737.

[291] Scott, R. (2001). *In the wake of Tacoma*. American Society of Civil Engineers (ASCE.

[292] Scully, C. G., Mitrou, N., Braam, B., Cupples, W. A., and Cho, K. H. (2017). Detecting interactions between renal autoregulation mechanisms in time and space. *IEEE Trans. Biomed. Eng.* 64, 690–698.

[293] Sears, W. R. (1941). Some aspects of non-stationary airfoil theory and its practical application. *AIAA J.* 8, 104–108.

[294] Sears, W. R. and Sparks, B. O. (1941). On the reaction of an elastic wing to vertical gusts. *J. Aeron. Sci.* 9, 64–67.

[295] Selberg, F. (1963). Oscillation and aerodynamic stability of suspension bridges. *Acta Polytechnica Scandinavica* 6, Ci 13.

[296] Selvam, R. P., Tarini, M. J., and Larsen, A. (1998). Computer modeling of flow around bridges using LES and FEM. *J. Wind Eng. Ind. Aerodyn.* 77&78, 643–651.

[297] Sharp, N. S., Neuscamman, S., and Warhaft, Z. (2009). Effects of large-scale free stream turbulence on a turbulent boundary layer. *Phys. Fluids* 26, 095105.

[298] Shinozuka, M. and Deodatis, G. (1996). Simulation of multi-dimensional Gaussian stochastic fields by spectral representation. *Appl. Mech. Rev.* 49, 29–53.

[299] Shinozuka, M. and Jan, C. M. (1972). Digital simulation of random processes and its applications. *J. Sound Vib.* 25, 111–128.

[300] Shy, W., Lian, Y., Tang, J., Vieeru, D., and Liu, H. (2008). *Aerodynamics of low Reynolds number flyers*. Cambridge University Press.

[301] Simiu, E. and Scanlan, R. (1996). *Wind effects on structures*, Third ed. Wiley-Interscience.

[302] Solari, G. (1987). Turbulence modeling for gust loading. *J. Struct. Eng.* 113 (7), 1550–1569.

[303] Solari, G. (2017). Wind loading of structures: framework, phenomena, tools and codification. *Structures* 12, 265–285.

[304] Solari, G. and De Gaetano, P. (2018). Dynamic response of structures to thunderstorm outflows: Response spectrum technique vs time-domain analysis. *Eng. Struct.* 176, 188–207.

[305] Solari, G. and Piccardo, G. (2000). Probabilistic 3-D turbulence modeling for gust buffeting of structures. *Prob. Eng. Mech.* 16, 73–86.

[306] Spivak, D. I. (2014). *Category Theory for the Sciences*. MIT Press.

[307] Sprague, M. A. and Geers, T. (2004). A spectra-element method for modelling cavitation in transient fluid-structure interaction. *Int. J. Numer. Meth. Eng.* 60, 2467–2499.

[308] Stapountzis, H. (1978). *Lift forces on cylindrical bodies in unsteady flow.* Ph. D. thesis, Imperial College London.

[309] Stapountzis, H. (1982). An oscillating rig for the generation of sinusoidal flows. *J. Phys. E. Sci. Instrum.* 15, 1173–1176.

[310] Stapountzis, H. and Graham, J. M. R. (1982). The unsteady lift on bluff cylindrical bodies in unsteady flow. *Aeronaut. Quat.* 3, 219–236.

[311] Starossek, U., Aslan, H., and Theisemann, L. (2009). Experimental and numerical identification of flutter derivatives for nine brdige deck sections. *Wind and Struct.* 12, 519–540.

[312] Stoyanoff, S. (2001). A unified approach for 3d stability and time domain response with application of the quasi-steady theory. *J. Wind Eng. Ind. Aerodyn.* 89, 1591–1606.

[313] Su, C., Fan, X., and He, T. (2007). Wind-induced vibration analysis of cable-stayed bridge during erection by a modified time-domain method. *J. Sound Vib.* 303, 330–342.

[314] Suanda, S., Yasuda, T., Yasuda, K., and Kawachi, K. (2002). Comparison of wing characteristics at an ultralow Reynolds number. *J. Aircraft* 39, 331–338.

[315] Tamura, Y. and Kareem, A. (2013). *Advanced Structural Wind Engineering.* Springer Japan.

[316] Tang, D. and Dowel, E. H. (2002). Limit cycle oscillations of two-dimensional panels in low subsonic flow. *Int. J. Nonlin. Mech.* 37, 1199–1209.

[317] Tao, t., Wang, H., and Wu, T. (2017). Comparative study of the wind characteristics of a strong wind event based on stationary and nonstationary models. *J. Struct. Eng.* 143, 04016230.

[318] Taylor, G. I. (139). Some recent developments in the study of turbulence. In *Proc. 5th int. Congress for Applied Mech.*, Cambridge, USA,.

[319] Taylor, G. I. (1935). Statistical theory of turbulence. *Proc. R. Soc. Lond. A.* 151, 421–444.

[320] Taylor, I. J. and Vezza, M. (1999). Calculation of the flow field around a square section cylinder undergoing forced transverse oscillations using a discrete vortex method. *J. Wind Eng. Ind. Aerodyn.* 82, 271–291.

[321] Taylor, I. J. and Vezza, M. (2009). A numerical investigation into the aerodynamic characteristics and aeroelastic stability of a footbridge. *J. Fluids Struct.* 144, 155–177.

[322] Teferra, K., Schields, M. D., Hapij, A., and Daddazio, R. P. (2014). Mapping model validation metrics to subject matter expert scores for model adequacy assessment. *Reliab. Eng. Syst. Safe.* 132, 9–19.

[323] Theodorsen, T. (1935). General theory of aerodynamic instability and the mechanism of flutter. Technical Report NACA-TR-496, NASA.

[324] Tiffany, S. H. and Adams, W. M. J. (1984). Fitting aerodynamic forces in the laplace domain: an application of nonlinear nongradient technique to multilevel constrained optimization. Tech. Memorandum NASA-TM-86317, NASA, Virginia, USA.

[325] Tiffany, S. H. and Adams, W. M. J. (1988). Nonlinear programming extensions to rational function approximation methods for unsteady aerodynamic forces. Tech. Memorandum NASA-TP-2776, NASA, Virginia, USA.

[326] Tolba, K. I. and Morgenthal, G. (2017). Pseudo three-dimensional simulation of aeroelastic response to turbulent wind using vortex particle methods. *J. Fluids Struct.* 72, 1–24.

[327] Torrence, C. and Compo, G. P. (1998). A practical guide to wavelet analysis. *Bull. Amer. Meteor. Soc.* 79, 61–78.

[328] Tubino, F. (2005). Relationships among aerodynamic admittance functions, flutter derivatives and static coefficients for long-span bridges. *J. Wind Eng. Ind. Aerodyn.* 93, 929–950.

[329] Tubino, F. and Solari, G. (2007). Gust buffeting of long span bridges: Double modal transformation and effective turbulence. *Eng. Struct.* 29, 1698–1707.

[330] Turbelin, G. and Gibert, J. G. (2001). CFD calculations of indicial lift responses for bluff bodies. *Wind and Structures* 4, 245–256.

[331] Uejima, H., Kuroda, S., and Kobayashi, H. (1992, July). Estimation of aerodynamic admittance by numerical computation. In *BBAA VI International Colloquium*, Milan, Italy.

[332] Vairo, G. (2003). A numerical model for wind loads simulation on long-span bridges. *Simul. Model Pract. Theory* 11, 315–351.

[333] van Milligen, B. P., Carreras, B., and Garcia, L. (1995). Wavelet bicoherence: A new turbulence analysis tool. *Phys. Plasmas* 2, 3017–3032.

[334] Vickery, B. J. (1969). On the reliability of gust loading factors. In *Proc. of Tenchincal meeting concerning wind loads on buildings and structures*, Maryland, USA, 93–104.

[335] Virlogeux, M. (2018). Long span bridges. In *Proc. 40th IABSE Symposium*, Nantes, France, K65–K73.

[336] von Kármán, T. (1948). Progress in the statistical theory of turbulence. *Proc. Nat. Acad. Sci.* 34, 530–539.

[337] von Kármán, T. and Biot, M. A. (1940). *Mathematical methods in engineering*, First ed. McGraw-Hill.

[338] von Kármán, T. and Sears, W. R. (1938). Airfoil theory for non-uniform motion. *J. Aeron. Sci.* 5, 379–390.

[339] Wagner, H. (1925). Über die entstehung des dynamischen auftriebes von tragflügeln (in German). *Zeitschrf. Angew. Math. Mech.* 5, 17–35.

[340] Walker, J. M., Helin, H. E., and Strickland, J. H. (1985). An experimental investigation of an airfoil undergoing large amplitude pitching motions. Final Report USAFA-TR-85-2, Air Force Academy Aeronautics Digest, Colorado, USA.

[341] Walther, J. and Larsen, A. (1997). Two dimensional discrete vortex method for application to bluff body aerodynamics. *J. Wind Eng. Ind. Aerodyn.* 67&68, 183–193.

[342] Walther, J. H. (1994). *Discrete vortex method for two-dimensional flow past bodies of arbitrary Shape undergoing prescribed rotary and translational motion.* Ph. D. thesis, Technical University of Denmark.

[343] Wang, S., Zhang, X., He, G., and Liu, T. (2013). A lift formula applied to low-Reynolds-number unsteady flows. *Phys. Fluids* 25, 093605.

[344] Wardlaw, R. L., Tanaka, H., and Utsunomiya, H. (1983). Wind tunnel experiments on the effects of turbulence on aerodynamic behaviour of bridge road decks. *J. Wind Eng. Ind. Aerodyn.* 14, 247–257.

[345] Washizu, K., Ohya, A., Otsuki, Y., and Fujii, K. (1978). Aeroelastic instability of rectangular cylinders in a heaving mode. *J. Sound Vib.* 59, 195–210.

[346] Washizu, K., Ohya, A., Otsuki, Y., and Fujii, K. (1980). Aeroelastic instability of rectangular cylinders in a torsional mode due to a transverse wind. *J. Sound Vib.* 72, 507–521.

[347] Wilde, K., Fujino, Y., and Masukawa, J. (1996). Time domain modeling of bridge deck flutter. *J. Struct. Mech. Earthq. Eng.* 13, 19–29.

[348] Willamson, C. H. K. and Govardhan, R. (2004). Vortex-induced vibrations. *Annu. Rev. Fluid Mech.* 36, 413–455.

[349] Willden, R. and Graham, J. (2001). Numerical prediction of VIV on long flexible circular cylinders. *J. Fluids. Struct.* 15, 659–669.

[350] Willden, R. and Graham, J. (2004). Multi-modal vortex-induced-vibrations of a vertical riser pipe subjected to a uniform current profile. *Euro. J. Mech. B Fluid* 23, 209–218.

[351] Willmott, C. J., Ackleson, S. G., Davis, R. E., Feddema, J. J., Klink, K. M., Legates, D. R., O'Donnel, J., and Rowe, C. (1985). Statistics for the evaluation of comparison of models. *J. Geophys. Res.* 90, 8995–9905.

[352] Wilson, K. D. (1998). Turbulence models and the synthesis of random fields for acoustic wave propagation calculations. Technical Report ARL-TR-1677, Army Research Laboratory.

[353] Wu, B. C. (1976). Numerical boundary conditions for viscous flow problems. *AIAA J.* 14, 1042–1049.

[354] Wu, B. C. and Gulcat, U. (1980). Separate treatment of attached and detached flow regions in general viscous flows. *AIAA J.* 19, 20–27.

[355] Wu, B. C. and Thompson, J. F. (1973). Numerical solutions of time-dependent incompressible Navier-Stokes equation using an integro-differential formulation. *Comput. Fluids* 1, 197–215.

[356] Wu, T. and Kareem, A. (2011). Modeling hysteretic nonlinear behavior of bridge aerodynamics via cellular automata nested neural network. *J. Wind Eng. Ind. Aerodyn.* 99, 378–388.

[357] Wu, T. and Kareem, A. (2012). An overview of vortex-induced vibration (VIV) of bridge decks. *Front. Struct. Civ. Eng.* 6, 335–347.

[358] Wu, T. and Kareem, A. (2013). Aerodynamics and aeroelasticity of cable-supported birdges: Identification of nonlinear features. *J. Eng. Mech.* 139, 1886–1893.

[359] Wu, T. and Kareem, A. (2013). Bridge aerodynamics and aeroelasticity: A comparison of modeling schemes. *J. Fluids Struct.* 43, 347–370.

[360] Wu, T. and Kareem, A. (2014). A nonlinear convolution scheme to simulate bridge aerodynamics. *Comput. Struct.* 128, 259–271.

[361] Wu, T. and Kareem, A. (2014). Revisiting convolution scheme in bridge aerodynamics: Comparison of step and impulse functions. *J. Eng. Mech.* 140 (5), 1–13.

[362] Wu, T. and Kareem, A. (2015). A nonlinear analysis framework for bluff-body aerodynamics: A Volterra representation of the solution of Navier-Stokes equations. *J. Fluids Struct.* 54, 479–502.

[363] Wu, T. and Kareem, A. (2015). Vortex-induced vibration of bridge decks: A Volterra series based model. *J. Eng. Mech.* 139, 1831–1843.

[364] Wu, T., Kareem, A., and Ge, Y. (2013). Linear and nonlinear aeroelastic analysis frameworks for cable-supported bridges. *Nonlin. Dyn.* 74, 487–516.

[365] Wu, X. (2017). Inflow turbulence generation methods. *Annu. Rev. Fluid Mech.* 49, 23–49.

[366] Wu, X., Jacobs, R. G., Hunt, J. C. R., and Durbin, P. A. (1999). Simulation of boundary layer transition induced by periodically passing wakes. *J. Fluid Mech.* 398, 625–706.

[367] Xu, F., Wu, T., Ying, X., and Kareem, A. (2016). Higher-order self-excited drag forces on bridge decks. *J. Eng. Mech.* 132, 06015007.

[368] Xu, K., Zhao, L., and Ge, Y. (2017). Reduced-order modeling and calculation of vortex-induced vibrations for large-span bridges. *J. Wind Eng. Ind. Aerodyn.* 167, 228–241.

[369] Xu, Y.-L. (2013). *Wind Effects on Cable-supported Bridges*. John Wiley & Sons.

[370] Ying, X., Xu, F., Zhang, M., and Zhang, Z. (2017). Numerical explorations of the limit cycle flutter characteristics of a bridge deck. *J. Wind Eng. Ind. Aerodyn.* 169, 30–38.

[371] Yokota, R. and Obi, S. (2011). Vortex methods for simulation of turbulent flows: Review. *J. Fluid Sci. Techn.* 6, 14–29.

[372] Zahm, A. F., Smith, R. H., and Louden, F. A. (1928). Forces on elliptic cylinders in uniform airstream. Technical Report NACA-TR-289, NASA.

[373] Zhang, M., Xu, F., and Ying, X. (2017). Experimental investigations on the nonlinear torsional flutter of a bridge deck. *J. Bridge Eng.* 22, 04017048.

[374] Zhang, X., Xiang, H., and Sun, B. (2002). Nonlinear aerostatic and aerodynamic analysis of long-span suspension bridges considering wind-structure interactions. *J. Wind Eng. Ind. Aerodyn.* 90, 1065–1080.

[375] Zhang, Z., Chen, Z., Cai, Y., and Ge, Y. (2011). Indicial functions for bridge aeroelastic forces and time-domain flutter analysis. *J. Bridge Eng.* 16, 546–557.

[376] Zhang, Z., Zhang, X., Yang, Y., and Ge, Y. (2017). Nonlinear aerodynamic and energy input properties of a twin-box girder deck section. *J. Fluids Struct.* 74, 413–426.

Appendix A: IABSE Benchmark

As a part of the International Association of Structural and Bridge Engineering (IABSE), a Task Group (TG) 3.1: "Super-long span bridge aerodynamics" was formed with the purpose of developing a benchmark for code verification for buffeting and flutter analyses. The TG consists of experienced members including academics, consultants and designers from nine universities and ten companies worldwide. The author is a contributing member as well.

The goal of the TG is to provide reference results for buffeting and flutter analysis for well-defined input. All members of the group contributed with results using their codes and semi-analytical models, for the identical input data. All results are then compared and reference values are provided based on statistical analysis.

The work of the TG was split in three principal steps with sub-steps. The first step is to provide numerical results for a 2D system with two degrees of freedom. Step two is a comparison of numerical results from the members with common wind tunnel experimental results. The third step is planned to be a comparison of numerical results against full scale measurements of a real bridge. So far, the first and part of the second steps are completed.

In this Appendix, the results from the LU model, based on the code used throughout this work, are verified using the reference data provided from Step 1.1a of the IABSE TG3.1 [87, 88]. This step is the simplest case and it involves buffeting and flutter analysis of a flat plate for analytical aerodynamic coefficients. The input parameters resemble the ones used in the flat plate study (cf. Sec. 5.4, Tabs. 5.7 and 5.8), with some differences. The main difference is in the aerodynamic admittance function, for which the TG 3.1 provided the empirical Davenport's admittance instead of the analytical Sears, given as:

$$\chi = \frac{2}{(7/V_r)^2}\left[\frac{7}{V_r} - 1 + \exp\left(-\frac{7}{V_r}\right)\right]. \tag{A.1}$$

Moreover, fluid density of $\rho = 1.22$ is used instead of $\rho = 1.20$, a damping ratio of $\xi = 0.3$ % and the term $\pi/64$ for the A_3^* derivative (cf. (3.126)) is missing for the self-excited forces.

Buffeting analysis was performed in both the time and frequency domain for wind speeds in the range of $U = 15 - 75$ m/s. For the time domain, twenty identical records were provided to all members. The reference results in Fig. A.1 by the mean and standard deviation provided by the TG members [142]. Moreover, the results for both the time and frequency domain are given for the present implementation of the LU model, yielding excellent correspondence. Unfortunately, the results from the TG cannot be directly compared for the CFD model as in Sec. 5.4, since Davenport's admittance was used for the TG benchmark.

Further, the critical flutter velocity was determined to be $U_{cr}/(Bf_{h\alpha}) = 13.22$ for both time and frequency domain for the present code implementation, where $f_{h\alpha}$ is the central frequency. This matches exactly the mean reference value of $U_{cr}/(Bf_{h\alpha}) = 13.22$ provided by the TG.

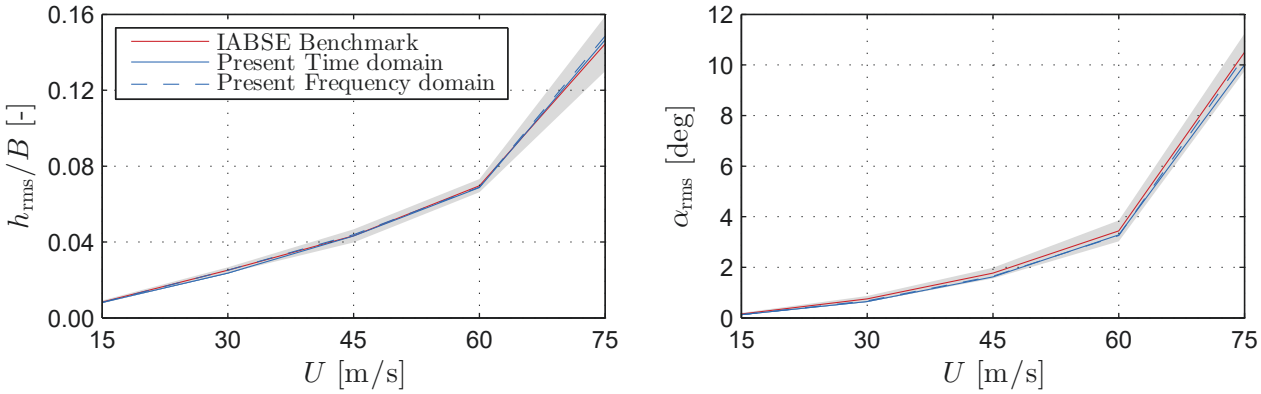

Figure A.1: IABSE Benchmark: RMS of the vertical displacement (left) and rotation (right) from the statistical comparison for 2D buffeting analysis for the present code and results from the IABSE TG3.1. The response for the present time-domain analysis is obtained based on the mean of 20 independent response time-histories. The response for the IABSE benchmark is obtained as a mean of all members of IABSE TG 3.1 from both frequency- and time-domain analyses. The shaded area represents the $\pm\sigma$ interval for the IABSE TG 3.1 Benchmark.

Appendix B: Modal Information

Tables B.1 and B.2 are included in this Appendix.

Mode No.	Mode Type	f [Hz]
1	Tower/Lateral	0.302
2	Lateral	0.401
3	Vertical	0.444
4	Vertical	0.731
5	Vertical	0.810
6	Torsional	0.913
7	Torsional	0.934
8	Vertical	1.505
9	Vertical	1.598
10	Tower/Torsional	1.945
11	Tower/Torsional	2.194
12	Torsional	2.832
13	Lateral	2.833
14	Vertical	2.914
15	Torsional	2.960

Table B.1: Mersey Gateway Bridge: natural frequencies and mode types of the 15 vibration modes included in the analyses.

Mode No.	Mode Type	f [Hz]
1	Lateral	0.053
2	Vertical	0.100
3	Lateral	0.108
4	Vertical	0.118
5	Vertical	0.144
6	Lateral	0.177
7	Vertical	0.193
8	Vertical	0.225
9	Lateral	0.228
10	Vertical	0.238
11	Lateral	0.242
12	Torsional	0.278
13	Vertical	0.279
14	Vertical	0.299
15	Lateral	0.303
16	Vertical	0.321
17	Vertical	0.321
18	Vertical	0.353
19	Torsional	0.377
20	Vertical	0.411
21	Lateral	0.419
22	Torsional	0.449

Table B.2: Great Belt Bridge: natural frequencies and mode types of the 22 vibration modes included in the analyses.